Universidad de Oviedo
Universidá d'Uviéu
University of Oviedo

Department of Electrical, Electronic, Communications, and Systems Engineering

PhD Thesis

PhD Program in Energy and Process Control

Optimization of Torque and Adhesion Control Capabilities for Railway Traction Drives

Author

Ahmed Fathy Youssef Mohamed Abouzeid

MAY 2023

Universidad de Oviedo
Universidá d'Uviéu
University of Oviedo

Departamento de Ingeniería Eléctrica, Electrónica, de
Comunicaciones y de Sistemas

Tesis Doctoral

Programa de Doctorado en Energía y Control de Procesos

Optimización del Control de Par y Adhesión en Sistemas de Tracción Ferroviaria

Autor

Ahmed Fathy Youssef Mohamed Abouzeid

MAYO 2023

Universidad de Oviedo
Universidá d'Uviéu
University of Oviedo

Department of Electrical, Electronic, Communications, and Systems Engineering

PhD Thesis

PhD Program in Energy and Process Control

Optimization of Torque and Adhesion Control Capabilities for Railway Traction Drives

Author

Ahmed Fathy Youssef Mohamed Abouzeid

Dissertation submitted in partial fulfillment of the requirements for the degree of Doctor of Philosophy in Electrical Engineering with International Mention

Advisor: Fernando Briz del Blanco.
Full Professor, Department of Electrical, Electronic, Computer and Systems Engineering, University of Oviedo, Gijón, Spain

Co-advisor: Juan Manuel Guerrero Muñoz.
Full Professor, Department of Electrical, Electronic, Computer and Systems Engineering, University of Oviedo, Gijón, Spain

MAY 2023

Universidad de Oviedo
Universidá d'Uviéu
University of Oviedo

Departamento de Ingeniería Eléctrica, Electrónica, de Comunicaciones y de Sistemas

Tesis Doctoral

Programa de Doctorado en Energía y Control de Procesos

Optimización del Control de Par y Adhesión en Sistemas de Tracción Ferroviaria

Autor

Ahmed Fathy Youssef Mohamed Abouzeid

Tesis presentada en cumplimiento parcial de los requisitos para el grado de Doctor por la Universidad de Oviedo con Mención Internacional

Tutor: Fernando Briz del Blanco
Catedrático, Departamento de Ingeniería Eléctrica, Electrónica, de Computadores y Sistemas, Universidad de Oviedo, Gijón, España
Co-tutor: Juan Manuel Guerrero Muñoz
Catedrático, Departamento de Ingeniería Eléctrica, Electrónica, de Computadores y Sistemas, Universidad de Oviedo, Gijón, España

MAYO 2023

RESUMEN DEL CONTENIDO DE TESIS DOCTORAL

1.- Título de la Tesis	
Español/Otro Idioma: OPTIMIZACIÓN DEL CONTROL DE PAR Y ADHESIÓN EN SISTEMAS DE TRACCIÓN FERROVIARIA	Inglés: OPTIMIZATION OF TORQUE AND ADHESION CONTROL CAPABILITIES FOR RAILWAY TRACTION DRIVES

2.- Autor	
Nombre: AHMED FATHY YOUSSEF MOHAMED ABOUZEID	
Programa de Doctorado: Doctorado en Energía y Control de Procesos	
Órgano responsable: Centro Internacional de Postgrado	

RESUMEN (en español)

La electrificación del transporte se ha impuesto últimamente en el sector del transporte para reducir las emisiones de gases de efecto invernadero y mitigar los efectos del cambio climático en el planeta. Por electrificación del transporte se entiende el proceso de sustitución de vehículos propulsados por combustibles fósiles por otros eléctricos, incluidos vehículos de carretera, todoterreno, ferroviarios, aviones y barcos. Los ferrocarriles eléctricos, entre otros medios de transporte, ofrecen una eficiencia energética sustancialmente mayor, menos emisiones y menores costes de explotación. Además, algunos sistemas de tracción eléctrica ofrecen una función de frenado regenerativo que convierte la energía cinética del tren en energía eléctrica, devolviéndola al sistema de suministro para que la utilicen otros trenes o la red eléctrica. Además, los ferrocarriles eléctricos pueden abastecerse de diversas fuentes, incluidas las energías renovables, en comparación con las locomotoras diésel.

Los trenes eléctricos tienen una relación potencia-peso superior a la de los trenes propulsados por depósitos de combustible a bordo. Esto permite una aceleración más rápida, mayor potencia y límites de velocidad con menor producción de contaminación acústica. Desgraciadamente, el coste de capital de la electrificación ferroviaria es el principal, ya que requiere una nueva infraestructura que incluye estaciones de suministro eléctrico, líneas aéreas, sistemas de señalización y circuitos de protección contra interferencias, etc. Por lo tanto, las soluciones optimizadas para la electrificación ferroviaria deben ser consideradas durante las fases de diseño y operación para lograr los ingresos deseados.

Esta tesis aborda las soluciones optimizadas para los accionamientos de tracción eléctrica en ferrocarriles desde la perspectiva del control. Se presentan en detalle los principales elementos que conforman el control de los accionamientos de tracción eléctrica, incluyendo las técnicas de modulación, el control del par y el control antideslizamiento rueda-carril. A continuación, se presentan varias estrategias propuestas para aprovechar al máximo las capacidades de par y tracción del motor de inducción alimentado por inversor en ferrocarriles. Se han analizado los principios físicos, la implementación y la evaluación del rendimiento de las estrategias propuestas.

Además, se implementa la protección contra la vibración torsional como parte del control de tracción para mejorar la capacidad de tracción. La vibración torsional se ha simulado con éxito de acuerdo con las mediciones en pista. A partir de este logro, el modelo de simulación se aplicará a otros vehículos para validar la predicción de los valores de par dinámico máximo. La capacidad de predecir valores de par dinámico máximo es muy demandada por los fabricantes de vehículos ferroviarios, para permitir un desarrollo más eficiente de nuevos juegos de ruedas. Del mismo modo, estas simulaciones pueden ayudar a los fabricantes a probar la eficacia de sus implementaciones de protección contra las oscilaciones torsionales.

RESUMEN (en Inglés)

Transportation electrification has become more dominant recently in the transport sector for reducing greenhouse gas emissions and mitigating the effects of climate change on the planet. Transportation electrification means the process of replacing fossil fuel-powered vehicles with electric ones including on-road, off-road, rail vehicles, airplanes, and ships. Electric railways, amongst other means of transportation, offer substantially better energy efficiency, lower emissions, and lower operating costs. Besides, some electric traction systems offer regenerative braking feature that turns the train's kinetic energy back into electric form, returning it to the supply system to be used by other trains or the utility grid. Additionally, electric railways can be supplied from diverse sources, including renewable energy compared to diesel locomotives.

Electric trains have a superior power-to-weight ratio compared to trains powered by onboard fuel tanks. This allows faster acceleration, higher power, and speed limits with less noise pollution production. Unfortunately, railway electrification capital cost is the main disadvantage as it requires new infrastructure including power supply stations, overhead lines, signaling systems, interference protection circuits, etc. Therefore, optimized solutions for railway electrification should be considered during the design and operation phases to achieve the desired revenue.

This dissertation addresses the optimized solutions for electric traction drives in railways from the control perspective. The main elements forming the electric traction drive control including modulation techniques, torque control, and wheel-rail anti-slip control are presented in detail. Then, various proposed strategies are introduced to fully utilize the torque and traction capabilities of the inverter-fed induction motor in railways. The proposed strategies' physical principles, implementation, and performance evaluation have been analyzed.

Additionally, torsional vibration protection is implemented as part of the traction control to improve traction capability. Torsional vibration has been successfully simulated in accordance with on-track measurements. Based on this achievement, the simulation model shall be applied to other vehicles in order to validate the prediction of maximum dynamic torque values. The capability of predicting maximum dynamic torque values is highly demanded by railway vehicle manufacturers, to enable more efficient development of new wheelsets. In the same way, such simulations can help manufacturers to prove evidence of the effectiveness of their torsional oscillation protection implementations.

SR. PRESIDENTE DE LA COMISIÓN ACADÉMICA DEL PROGRAMA DE DOCTORADO EN _____

A mi familia y amigos
y en especial, a mis padres

Acknowledgements

Abstract

Transportation electrification has become more dominant recently in the transport sector for reducing greenhouse gas emissions and mitigating the effects of climate change on the planet. Transportation electrification means the process of replacing fossil fuel-powered vehicles with electric ones including on-road, off-road, rail vehicles, airplanes, and ships. Electric railways, amongst other means of transportation, offer substantially better energy efficiency, lower emissions, and lower operating costs. Besides, some electric traction systems offer regenerative braking feature that turns the train's kinetic energy back into electric form, returning it to the supply system to be used by other trains or the utility grid. Additionally, electric railways can be supplied from diverse sources, including renewable energy compared to diesel locomotives.

Electric trains have a superior power-to-weight ratio compared to trains powered by onboard fuel tanks. This allows faster acceleration, higher power, and speed limits with less noise pollution production. Unfortunately, railway electrification capital cost is the main disadvantage as it requires new infrastructure including power supply stations, overhead lines, signaling systems, interference protection circuits, etc. Therefore, optimized solutions for railway electrification should be considered during the design and operation phases to achieve the desired revenue.

This dissertation addresses the optimized solutions for electric traction drives in railways from the control perspective. The main elements forming the electric traction drive control including modulation techniques, torque control, and wheel-rail anti-slip control are presented in detail. Then, various proposed strategies are introduced to fully utilize the torque and traction capabilities of the inverter-fed induction motor in railways. The proposed strategies' physical principles, implementation, and performance evaluation have been analyzed.

Additionally, torsional vibration protection is implemented as part of the traction control to improve traction capability. Torsional vibration has been

successfully simulated in accordance with on-track measurements. Based on this achievement, the simulation model shall be applied to other vehicles in order to validate the prediction of maximum dynamic torque values. The capability of predicting maximum dynamic torque values is highly demanded by railway vehicle manufacturers, to enable more efficient development of new wheelsets. In the same way, such simulations can help manufacturers to prove evidence of the effectiveness of their torsional oscillation protection implementations.

Resumen

La electrificación del transporte se ha impuesto últimamente en el sector del transporte para reducir las emisiones de gases de efecto invernadero y mitigar los efectos del cambio climático en el planeta. Por electrificación del transporte se entiende el proceso de sustitución de vehículos propulsados por combustibles fósiles por otros eléctricos, incluidos vehículos de carretera, todoterreno, ferroviarios, aviones y barcos. Los ferrocarriles eléctricos, entre otros medios de transporte, ofrecen una eficiencia energética sustancialmente mayor, menos emisiones y menores costes de explotación. Además, algunos sistemas de tracción eléctrica ofrecen una función de frenado regenerativo que convierte la energía cinética del tren en energía eléctrica, devolviéndola al sistema de suministro para que la utilicen otros trenes o la red eléctrica. Además, los ferrocarriles eléctricos pueden abastecerse de diversas fuentes, incluidas las energías renovables, en comparación con las locomotoras diésel.

Los trenes eléctricos tienen una relación potencia-peso superior a la de los trenes propulsados por depósitos de combustible a bordo. Esto permite una aceleración más rápida, mayor potencia y límites de velocidad con menor producción de contaminación acústica. Desgraciadamente, el coste de capital de la electrificación ferroviaria es el principal, ya que requiere una nueva infraestructura que incluye estaciones de suministro eléctrico, líneas aéreas, sistemas de señalización y circuitos de protección contra interferencias, etc. Por lo tanto, las soluciones optimizadas para la electrificación ferroviaria deben ser consideradas durante las fases de diseño y operación para lograr los ingresos deseados.

Esta tesis aborda las soluciones optimizadas para los accionamientos de tracción eléctrica en ferrocarriles desde la perspectiva del control. Se presentan en detalle los principales elementos que conforman el control de los accionamientos de tracción eléctrica, incluyendo las técnicas de modulación, el control del par y el control antideslizamiento rueda-carril. A continuación, se presentan varias estrategias propuestas para aprovechar al máximo las ca-

pacidades de par y tracción del motor de inducción alimentado por inversor en ferrocarriles. Se han analizado los principios físicos, la implementación y la evaluación del rendimiento de las estrategias propuestas.

Además, se implementa la protección contra la vibración torsional como parte del control de tracción para mejorar la capacidad de tracción. La vibración torsional se ha simulado con éxito de acuerdo con las mediciones en pista. A partir de este logro, el modelo de simulación se aplicará a otros vehículos para validar la predicción de los valores de par dinámico máximo. La capacidad de predecir valores de par dinámico máximo es muy demandada por los fabricantes de vehículos ferroviarios, para permitir un desarrollo más eficiente de nuevos juegos de ruedas. Del mismo modo, estas simulaciones pueden ayudar a los fabricantes a probar la eficacia de sus implementaciones de protección contra las oscilaciones torsionales.

Contents

List of Figures

List of Tables

Acronyms

AC	Alternating Current
ABS	Anti-lock Braking Systems
CPWM	Continuous Pulse-Width Modulation
CSVPWM	Conventional Space-Vector PWM
CLVFC	Closed loop V/F Control
CLVFC&FF	Closed loop V/F Control with Feedforward Compensation
DC	Direct Current
DPWM	Discontinuous Pulse-Width Modulation
DSP	Digital Signal Processor
DFVC	Direct Flux Vector Control
DTC	Direct Torque Control
DSC	Direct-Self Control
DTC – SVM	Direct Torque Control with Space-Vector Modulation
EV	Electric Vehicle
EMU	Electric Multiple Units
4QC	Four-quadrant Power Converter
FOC	Field-Oriented Control
FLC	Fuzzy Logic Control
FIR	Finite Impulse Response
GHG	Greenhouse Gas
GPWM	Generalized Pulse-Width Modulation
HST	High-Speed Trains
HVAC	Heating, Ventilation, and Air Conditioning
IM	Induction Motor
IIR	Infinite Impulse Response
IGBT	Insulated Gate Bipolar Transistor
LQR	Linear Quadratic Regulator

LQC	Linear Quadratic Gaussian
MPE	Minimum-Phase Error Overmodulation
MME	Minimum-Magnitude Error Overmodulation
MDTC	Modified Direct-Torque Control
MTPA	Maximum Torque Per Ampere
MAT	Maximum Adhesion Tracking
MBS	Multi-body Simulation
OVM	Overmodulation
OFC	Optical Fibber Cable
PMSM	Permanent Magnet Synchronous Machines
PWM	Pulse-Width Modulation
PI	Proportional Integral Controller
PID	Proportional Integral Derivative Controller
PR)	proportional-Resonant Controller
PSO	Particle Swarm Optimization
P&O	Perturb and Observe
RFOC	Rotor Field-Oriented Control
SPWM	Sinusoidal Pulse-Width Modulation
SVPWM	Space-Vector Pulse-Width Modulation
SHE	Selective Harmonic Elimination
ST − DTC	Switching-Table Direct Torque Control
SG	Steepest Gradient Method
3L − NPC	Three-level Neutral-Point-Clamped Inveter
THD	Total Harmonic Distortion
VSI	Voltage-Source Inverter
V/F	Voltage/Frequency (Volt/Hertz)
ZSV	Zero-Sequence Voltage

List of Symbols

V_{ln}^*	Line-neutral voltage command
M_i	Modulation index
θ^*	Stator voltage angle command
V_s^{s*}	Stator voltage vector command in stationary reference frame
$V_{0,1,\cdots 7}$	Stator voltage vectors in stationary reference frame
T_s	Switching period
$T_{0,1,\cdots 7}$	Effective time corresponding to zero and active vectors
K, δ	Adaptation factor and angle for generalized PWM method
F_t^*	Traction force command
T_e^*	Electromagnetic torque command
V_{dc}	DC-link voltage
C_{dc}	DC-link capacitance
$2F$	Second harmonic content of line frequency (AC catenary) filter
ω_m	Measured mechanical speed
ω_r	Rotor angular speed
ω_e	Stator angular speed
ω_{sl}	Slip angular speed
P	Number of pole pairs
p	Derivative operator
v_{abcs}	Three-phase stator voltage components
i_{abcs}	Measured stator currents components
R_s	Stator winding resistance
λ_{abcs}	Stator flux components
L_h	Stator self-inductance
$L_{\sigma s}$	Stator leakage inductance
L_s	Stator winding inductance
L_m	Mutual inductance

v_{abcs}^*	Stator voltages command
R_r	Rotor winding resistance
λ_{abcr}	Rotor flux components
i_{abcr}	Measured rotor currents
v_{abcr}	Three-phase rotor voltage components
L_r	Rotor winding inductance
$L_{\sigma r}$	Rotor leakage inductance
σ	Leakage coefficient
$x_{\alpha\beta}$	Arbitrary complex vector in stationary reference frame
$v_{\alpha\beta s/r}$	Stator/Rotor voltage vector in stationary reference frame
$i_{\alpha\beta s/r}$	Stator/Rotor current vector in stationary reference frame
$\lambda_{\alpha\beta s/r}$	Stator/Rotor flux vector in stationary reference frame
$v_{dqs/r}$	Stator/Rotor voltage vector in dq reference frame
$i_{dqs/r}$	Stator/Rotor current vector in dq reference frame
$\lambda_{dqs/r}$	Stator/Rotor flux vector in dq reference frame
θ_{sf}	Stator flux vector angle
θ_{rf}	Rotor flux vector angle
$\Im$	Imaginary term of complex vector
t	Time
F_N	Normal force
F_t	Traction force
T_m	Motor torque referred to wheelset side
μ	Adhesion coefficient
r_w	Wheel radius
N_m	Number of motors/vehicle
v_t	Train linear velocity
m_t	Train total mass
g	Acceleration of gravity
ω_w	Vehicle wheel angular speed
J	Moment of inertia
B	Viscus friction
R_g	Gear ratio
v_{slip}	Linear slip velocity
a	Acceleration
d	Damping factor
c	Stiffness factor
ϑ	Angular position
G_x	Transfer function

s Laplace complex variable

Superscripts

x^* Commanded value
$\hat{x}$ Estimated value
$\overline{x}$ Conjugate of the complex vector
x^s Vector is rotating with synchronous reference frame
x^{sf} Vector is rotating with stator flux reference frame
x^{rf} Vector is rotating with rotor flux reference frame

Chapter 1

Introduction

1.1 Background

The transport sector is considered one of the most significant contributors to global greenhouse gas (GHG) emissions and climate change, accounting for more than one-third of total energy consumption among European Environment Agency member countries [1]. GHG emissions can be mitigated by involving integrated solutions like replacing fossil fuels with low-carbon sustainable sources (i.e. renewable energy sources) and emerging new technologies such as transportation electrification [2–7]. Powertrain electrification combined with battery energy storage systems provides a promising solution for a fast and efficient mode of transportation with reduced energy consumption [8–10].

Rolling stock is considered to be the most energy-efficient compared to other modes of transportation, such as vehicles and airplanes (see Fig. 1.1). Trains and locomotives can transport large numbers of passengers and goods over long distances with relatively low energy consumption levels [11]. Additionally, rail traction systems are often powered by electricity which facilitates the integration with renewable energy sources and reduces their carbon footprint. In contrast, electric vehicles (EV) minimize GHG associated with personal mobility [12,13]. EVs are becoming more feasible for many consumers with the development of battery technology [14]. However, EVs spreading still face challenges due to range anxiety, charging infrastructure, and overall cost compared to traditional gasoline-powered vehicles [15].
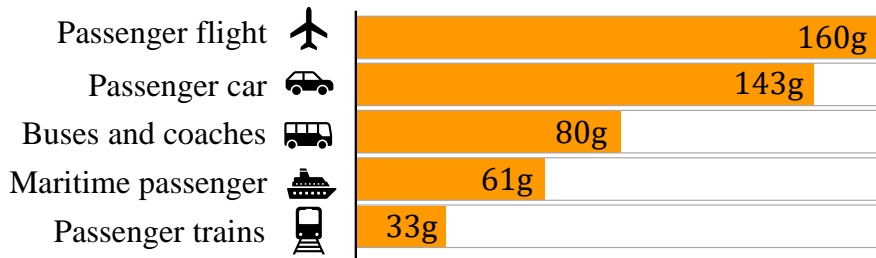
Figure 1.1: Average greenhouse gas GHG emissions (gCO_2e per tonne-km) for freight transport in the European Union (EU-27), 2022 [11].

Rolling stock can be classified according to the power level of the traction system, ranging from several tens of kW for Light Rail systems, to several MW for High-Speed Trains (HST) and Heavy Rail Locomotives [16]. Traction systems can be concentrated or distributed. In concentrated systems, one or more locomotives pull non-motorized coaches. On the contrary, distributed traction systems use Electric Multiple Units (EMU), i.e., self-propelled carriages. Both options have advantages and disadvantages. EMUs can provide superior performance in terms of acceleration and deceleration times, adhesion effort, and transport capacity. However, passenger comfort, maintenance, and pantograph operation can be compromised in this case [17,18]. For the case of HST, European manufacturers have predominantly adopted the concentrated traction option, while the distributed option has been preferred by Japanese manufacturers [19]. Fig. 1.2 shows the main elements of a modern European high-performance locomotive [20].

Despite being one of the most energy-efficient means for mass transportation [21–23], there is pressure to develop a more efficient, reliable, cheap, and compact railway traction system, which should be achieved without compromising customer satisfaction [24–26]. To achieve this, optimized solutions and strategies for traction systems can be improved and developed from both electrical and mechanical perspectives.

From the electrical perspective, the development of a cost-effective traction system for a given application involves a complex, iterative process to decide the number of traction motors, motor size, inverter-rated power, cooling system, etc.
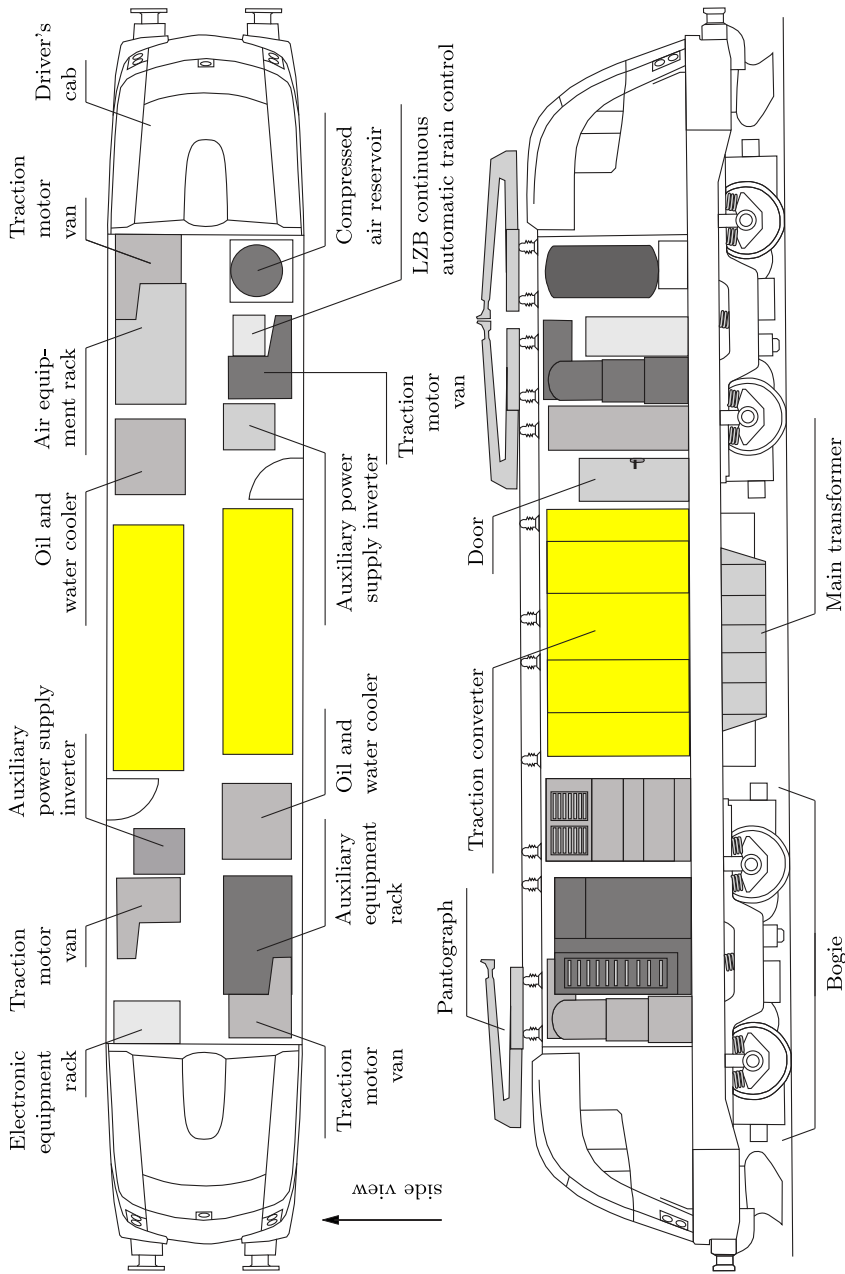
Figure 1.2: Cross section of a European high-performance locomotive (top and side view) [20].

Once the physical elements of the traction system have been decided, the control and modulation strategies need to be defined. Again, in this case, a complex iterative process can be required as the traction system must comply with a number of requirements. These include those imposed by the desired train performance (e.g., torque-speed characteristic, maximum torque and speed, acceleration/deceleration times, etc.), electric drive performance (e.g., machine and inverter efficiency, temperature limits, maximum torque ripple, etc.), existing standards (e.g., electromagnetic interference, acoustic noise, etc.), and so on.

Unfortunately, these targets will often be in conflict. The reduction of inverter losses requires low switching frequencies, which in turn result in higher losses and large torque pulsations in the motor, and can also compromise the dynamic response or even the stability of the drive. Especially challenging is the operation of the traction drive at high speeds. The large back-electromotive force, in this case, forces the inverter to operate in the overmodulation region, including square-wave modes. The control operates in this case with a reduced (or even no) voltage margin and large distortions in the currents, which can further deteriorate the drive performance.

A schematic representation of the main elements involved in the operation of a traction drive is shown in Fig. 1.3. The pantograph transfers the electrical power from the overhead line (AC or DC) to the locomotive. The AC transmission voltage can be 25 kV/50 Hz or 15 kV/16.7 Hz while the DC voltage can be 3 kV or 1.5 kV. For AC catenaries, the main transformer normally consists of a primary high-voltage winding with multiple secondary windings supplying both the traction converters and the auxiliary systems for heating, ventilation, and air conditioning (HVAC), lighting, etc. A four-quadrant power converter (4QC) provides the DC-link voltage feeding the traction inverters, which are responsible for controlling the torque produced by motors according to the locomotive driver commands. Motor torque is transferred to the wheels through the mechanical drivetrain, producing the traction force.

Three-phase induction motors (IMs) were adopted in the 1990s for traction systems in railways replacing DC machines [27] due to their increased robustness and reduced cost and maintenance requirements. In addition, precise control of the IM torque/speed is perfectly possible thanks to the development of new power devices and digital signal processors, combined with the advances in AC-drives control methods. Furthermore, the inherent slip of IM allows multiple motors to be fed from a single inverter, even if they rotate at different
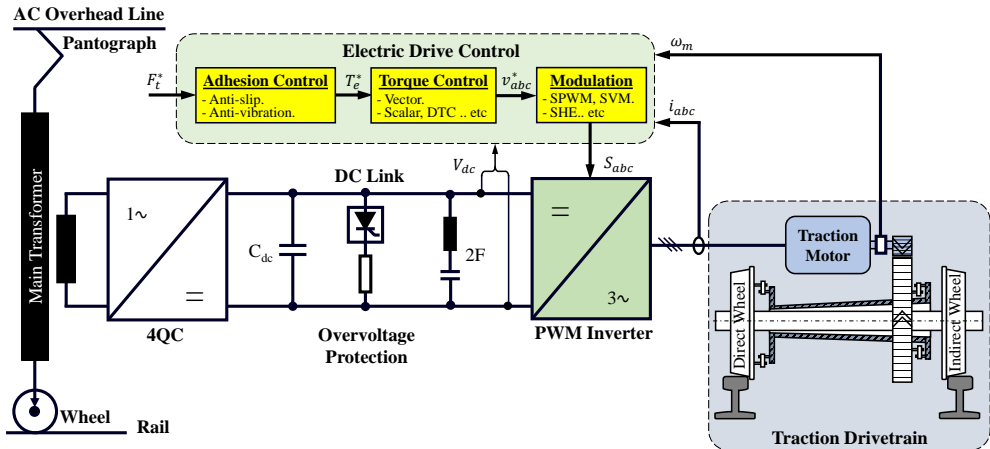
Figure 1.3: Schematic representation of a single-driven axle for a high-performance locomotive.

speeds due to differences in wheel diameters. As a result, the voltage-source inverter-fed IM drive (VSI-IM) is currently the preferred option in traction systems for railways [28]. While Permanent Magnet Synchronous Machines (PMSM) have also been considered and can be found in several traction systems, cost and reliability concern intrinsic to this type of machine, mainly due to magnets, have so far prevented their widespread use [29].

The electric drive control is responsible for achieving the traction force F_t^* commanded by the driver (see Fig. 1.3). The drive will normally receive a torque command coming from outer control loops (e.g., the train driver or speed control loop). From the torque command and the operating condition of the machine, a flux command is derived; different criteria can be followed for this purpose. Torque and flux are controlled by the inner control loops; a number of solutions are available for this purpose. Inner control loops will provide the voltage command to the Voltage Source Inverter (VSI) feeding the machine, with the selection of the modulation method being of the highest importance.

High-power traction drives usually operate with low switching frequencies (< 1 kHz) to reduce switching losses. This results in significant current and consequently torque ripples, which can have implications for mechanical transmission stress, train comfort, standards compliance, etc. Trading-off switching losses and torque pulsations is a challenge for the selection of modulation methods. Furthermore, modulation and control strategies often change with the output frequency. Typically, Asynchronous Pulse-Width Modulation (PWM)
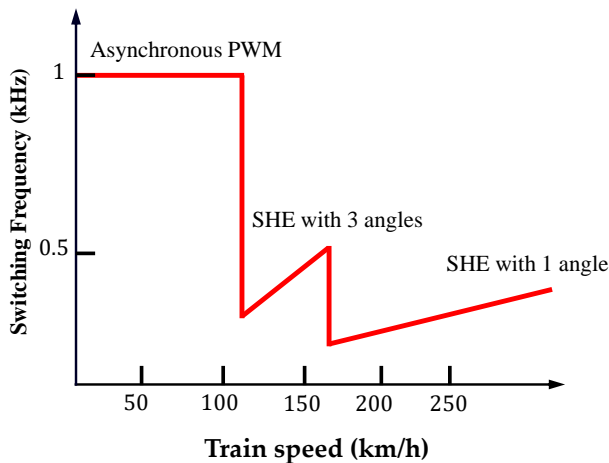
Figure 1.4: Modulation technique vs. train speed for a High-Speed Train (HST).

is used at low speeds, changing to Synchronous Modulation with Selective Harmonic Elimination (SHE) and finally single pulse modes as the speed increases (see Fig. 1.4) [30].

Overmodulation is used in electric drives to maximize the fundamental output voltage of the inverter. This has two beneficial effects: 1) an increase of the fundamental output voltage allows to get more torque at high speed, and consequently more power; 2) the number of commutations, and consequently, the switching losses in the inverter are reduced [31]. Unfortunately, this is at the price of an increase in the distortion of the currents creating torque harmonics with the subsequent effects such as noise, vibration, additional losses in the machine, etc [32]. Many efforts have been devoted to improving drive performance in overmodulation [33–39]. However, the analyses reported in the literature primarily focus on voltage utilization and harmonic content, the effect on switching losses is normally ignored.

On the other hand, optimized solutions for traction systems from the mechanical perspective require advanced techniques capable of detecting and preventing locomotives from the derailment. Derailment is one of the serious problems that should be avoided in railways for ensuring passengers' safety and reducing maintenance costs. Derailment occurs when the train vehicle comes off the track (i.e. the rail) which could lead to major accidents and collisions [40]. Failure in the mechanical components of the vehicle, track geometry defect (due to excessive wear of wheels or rails), and wheel-rail interaction

such as excessive creepage are the most significant reasons for the train vehicle derailment [41, 42]. Therefore, many efforts have been devoted to limiting the creep (i.e. slip) between the wheel and the rail [43–45].

However, a certain amount of slip between the wheel and rail is needed to increase the tractive force generated by the traction motor to the rail. Traditional creep controllers, also known as re-adhesion controllers, avoid slippage (i.e. the condition when the wheel-rail slip velocity dramatically increases) by limiting the slip velocity within a predefined threshold [46, 47]. They can be divided into two types:

1. **Direct methods:** they compare either the wheel circumference slip velocity or the wheel acceleration with a predefined threshold [48–50]. The threshold is chosen based on field tests and trains' driver experience [51, 52]. The main drawback of the direct methods is that the re-adhesion controller cannot optimally utilize the adhesion in different rail surface conditions.

2. **Indirect methods:** they are intended for rolling stocks where multiple motors are fed from the same inverter. It is assumed that the speed of all paralleled motors is not measured [53], some form of sensorless vector control is therefore normally used. Slip is detected in this case from unbalances in the current consumed by the paralleled motors. An obvious limitation of this method is that it can only be used when the traction converter feeds multiple motors.

Finding the optimal slip velocity is a challenging task due to the high unpredictability of adhesion-slip phenomena and the subsequent uncertainty in the estimations. Several approaches have been proposed for this purpose, including: perturb and observe methods (P&O) [54, 55]; recursive least squares searching [56–58]. Model predictive control and particle swarm intelligence methods are also be found in [59, 60]. However, these search algorithms increase the complexity of the control and their implementation in real trains has not been reported in the literature.

While slip controllers enhanced with maximum adhesion tracking increase the utilization of tractive force for high-performance locomotives, they can potentially enter the unstable adhesion region during the searching. As a result, oscillations can arise in the torsional elements of the locomotives power train [61]. These oscillations can also be provoked by the slip-stick phenomenon due to changes in the adhesion condition and track irregularities.

Excitation of torsional resonances by the torque ripple and the interaction between the electric and mechanical elements are the main source of such vibrations [62]. Torsional vibrations in mechanical systems fed from electrical drives can be either passively or actively damped [63]. Passive cancellation can be implemented using Infinite Impulse Response (IIR) notch filters. The filter is designed to remove dangerous oscillations from the torque command [64], avoiding their propagation to the mechanical system. However, notch filters might fail to suppress completely the resonant frequency due to the output delays and the uncertainty in the location of the resonance poles and zeros due to changes in the inertia constant of the mechanical system. A Finite Impulse Response (FIR) notch filter compensator can be used instead [65], taking advantage of FIR systems intrinsic stability and linear phase shift [66,67]. Excitation of resonant modes can be also avoided using an FIR compensator by halving the output of the speed controller and delaying one of the halves by half the resonance period, later adding it to the non-modified half signal, which eventually cancels the oscillation [65]. The limitation of this approach relies on torque control transient response and the noise in the feedback speed sensor.

Active damping of torsional vibration can be achieved by using state feedback compensation where the torque command can be adapted through the feedback signals of the torque control loop, speed control loop, or both [68]. Thus, all system poles can be placed at the desired location by choosing the appropriate feedback gains [69,70]. Usually, these methods require an estimator or observer for non-measurable states [70,71]. Moreover, advanced control techniques using Linear Quadratic Regulator (LQR), Linear Quadratic Gaussian (LQC), and H_∞ have been also proposed in [72–74]. However, these methods are highly sensitive to system parameters, meaning that for successful implementation they might need to be combined with parameter identification methods. Furthermore, the aforementioned torsional vibration mitigation methods use simplified mechanical models, ignoring therefore system dynamics, sensor noise, and other unexpected disturbances, which can be highly relevant in railways due to wheel-rail slippage phenomena.

Analysis and modeling of self-excited torsional vibrations phenomena in railways have been discussed in [75–78]. In [79], an indirect passive anti-vibration control is proposed. Torsional vibrations are extracted from the estimated dynamic of the wheelset axle. If they exceed a predefined limit, the control reduces the torque command. The effectiveness of this method strongly relies on the quick detection of slips. While simple and therefore easy to implement, the main shortcomings of this method are the decrease in traction

capability during the oscillation mitigation process, and the need for additional wheel sensors, which increase the cost and require the reconfiguration of existing locomotives in service. In [80], a state-space active anti-vibration control integrated with a slip re-adhesion control is proposed. This control strategy was capable of damping slip-stick vibrations up to a certain negative gradient of the adhesion force characteristic. The method was further improved by adding a virtual absorber at the indirectly driven wheel to suppress the torsional vibrations [20]. Complete vibration damping at any negative value of adhesion force gradient and without losing the traction capability is feasible with the virtual damper approach. The drawbacks of this method are its complexity and the difficult tuning of the controller and the observer. Furthermore, natural frequency identification is required to adapt the mechanical drive-train parameters to reflect variations due to wear and aging.

1.2 Dissertation Aims and Objectives

Optimized utilization of traction force is a key aspect in modern railway traction systems for multiple reasons as safety, reliability, energy management, and economical concerns. Traction force is defined as the force developed by the traction motor being transferred to the train vehicle's wheel to move the train. Maximizing the traction force leads to efficient and fast acceleration/deceleration rates. This allows for following the planned travel speed-distance profile precisely, avoiding trip delays and reducing energy consumption. Therefore, implementation of control methods able to maximize the traction force becomes crucial to traction systems manufacturers and trains service providers being beneficial from revenue aspect and punctuality as well.

As mentioned in the previous section, the optimization of torque and adhesion control capabilities for railway traction drives requires a complex iterative process not only in the design and selection stage of the traction system elements but also during the operation. Introducing new strategies and improving existing methods in the electric traction drive can lead to higher efficiency compared to the same drive with unchanged elements.

The aim of this dissertation is twofold: first, to investigate and bridge the gap between theory and practice in the field of electric traction drives for railways. This is achieved by addressing recent control advances, and considering both electrical and mechanical challenges. Second, to improve existing methods such as motor torque control and modulation techniques, as well as propose

novel control methods for wheel-rail slip and its impact on the mechanical drivetrain elements, such as torsional vibrations.

1.3 Dissertation Outlines

This thesis is organized into six chapters and two appendices:

- **Chapter 1**: introduces the research line of this dissertation, including an overview of control strategies and recent challenges of traction drives for railways. Moreover, the objectives and outlines of the dissertation are presented.

- **Chapter 2**: describes the modulation techniques used in traction applications, including synchronous and asynchronous pulse-width modulation (PWM) methods. The investigation expands to cover overmodulation strategies existing in the literature and proposes a novel generalized form of space-vector PWM (SVPWM) overmodulation strategy. Additionally, a comparative analysis of overmodulation strategies are performed and validated experimentally.

- **Chapter 3**: gives a brief discussion of induction motor (IM) modeling and design aspects. Additionally, it summarizes IM control strategies for traction applications and proposes a dynamic torque enhancement to the scalar control scheme for high-speed operation. Furthermore, it introduces a remagnetization strategy during reduced flux operation at light loads to improve IM efficiency.

- **Chapter 4**: discusses the wheel-rail slippage phenomenon occurs in railways. Then, summarizes the existing anti-slip control methods in literature and proposes new optimized techniques aim to track maximum adhesion and preventing excessive slippage as well. A scaled roller rig is used for fair comparison of all described methods.

- **Chapter 5**: summarizes the origins and mitigation methods of torsional vibrations in railways. The mathematical and simulation models of mechanical various drivetrains are presented. Moreover, active anti-vibration control based on proportional-resonant (PR) controller is proposed, verified by means of simulation, and compared to real locomotive drivetrain measurements.

- **Chapter 6**: summarizes the main findings obtained throughout this dissertation and future research lines aimed to improve the addressed methods.

- **Appendix A** includes parameters of the electrical and the mechanical elements used in this dissertation as well as controllers gains.

- **Appendix B** includes publications conducted during this dissertation and journal matrices.

Chapter 2

Modulation Techniques in Traction Applications

2.1 Introduction

This chapter presents short notes on asynchronous and synchronous modulation techniques including carrier-based PWM methods, space-vector modulation, and selective harmonic elimination. Linear and overmodulation extending to six-step operation will be discussed in more detail. Finally, a comparative analysis of overmodulation methods for AC electric drives using three criteria: output vs. commanded modulation index (i.e. linearity); harmonic content; and the number of commutations (i.e. switching losses). Thus, the analysis will primarily focus on existing methods reported in the literature, followed by a generalized form for improving some of these methods will be also addressed.

In this chapter the modulation index used is referred to six-step operation, calculated in (2.1), where $V^*_{ln_{(peak)}}$ is the peak line-neutral and V_{dc} is the DC bus voltage.

$$M_i = \frac{V^*_{ln_{(peak)}}}{\frac{2}{\pi}V_{dc}} \tag{2.1}$$

The carrier-based PWM can be classified into Continuous PWM (CPWM) and Discontinuous PWM (DPWM) categories. In the CPWM, all the inverter switches are continuously switching at each switching cycle when the reference magnitude is lower than the peak of the carrier signal (linear region). In

contrast, for DPWM methods there is always one of the three inverter branches clamped to the positive or negative DC bus. The branch being clamped does not switch as there is no intersection between the modulated and carrier signals. In the following sections, some of the CPWM and DPWM methods will be considered [81].

2.2 Continuous PWM (CPWM)

2.2.1 Sinusoidal PWM (SPWM)

In SPWM, the modulating signals at steady-state are sinusoidal waveforms (2.2)-(2.4), which are compared with a high-frequency triangular carrier signal. The intersection between these signals generates the switching signals of the inverter power devices. SPWM offers the simplest implementation method of carrier-based PWM. However, the maximum magnitude of the output voltage $V^*_{ln_{(peak)}}$ for linear operation is limited to $\frac{V_{dc}}{2}$, which corresponds to 78.5% of the six-step voltage, i.e. $M_i = 0.785$. Therefore, the main drawback of this method is the low utilization level of the DC bus voltage.

$$V^*_a = V^*_{ln_{(peak)}} \cos\left(\theta^*\right); \quad \text{where} \quad V^*_{ln_{(peak)}} = \frac{4}{\pi} M^*_i \tag{2.2}$$

$$V^*_b = V^*_{ln_{(peak)}} \cos\left(\theta^* - \frac{2\pi}{3}\right) \tag{2.3}$$

$$V^*_c = V^*_{ln_{(peak)}} \cos\left(\theta^* + \frac{2\pi}{3}\right) \tag{2.4}$$

In order to increase the DC bus voltage utilization, a zero-sequence signal V_0 can be added to the reference signals (2.5)-(2.7) that increases the $V^*_{ln_{(peak)}}$ to $\frac{V_{dc}}{\sqrt{3}}$. The injected zero-sequence signal is commonly referred to as triplen harmonic injection which is calculated by (2.8). Hence, from (2.1) the linear operation is extended to $M_i \cong 0.907$. Since SPWM without triplen harmonics does not fully utilize the DC link voltage, it is disregarded. Hereafter any reference to SPWM assumes triplen harmonic injection. Fig. 2.1 shows a comparison of phase voltages for SPWM with and without triplen harmonic component and its block diagram for three-level inverter.

(a)

(b)

(c)
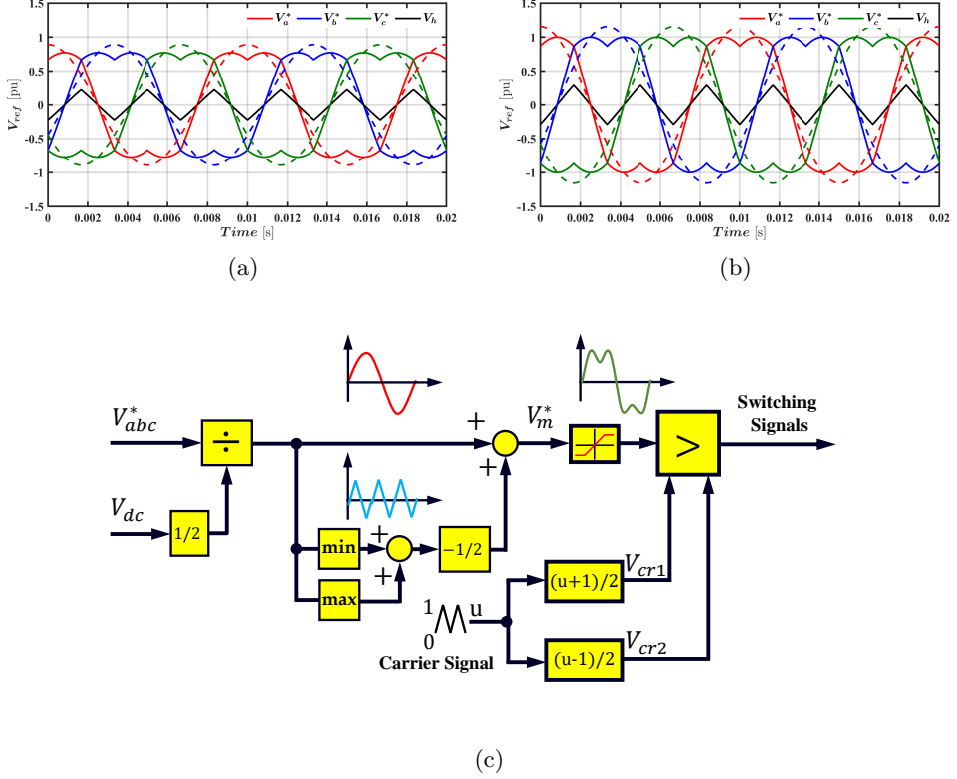
Figure 2.1: Reference voltages of SPWM method: (a) $M_i= 0.7$; (b) $M_i= 0.907$; (c) block diagram. Dashed line (- -) for conventional SPWM; Solid line (-) for SPWM with triplen harmonic injection.

$$V^*_{a(min,max)} = V^*_a + V_0 \tag{2.5}$$

$$V^*_{b(min,max)} = V^*_b + V_0 \tag{2.6}$$

$$V^*_{c(min,max)} = V^*_c + V_0 \tag{2.7}$$

where

$$V_0 = -\frac{(v^*_{max} + v^*_{min})}{2}; \qquad \begin{cases} v^*_{max} &= \max\left(V^*_a, V^*_b, V^*_c\right) \\ v^*_{min} &= \min\left(V^*_a, V^*_b, V^*_c\right) \end{cases} \tag{2.8}$$

2.2.2 Conventional Space-Vector PWM (CSVPWM)

CSVPWM is based on the volt-second balance principle, i.e. the reference voltage vector in sector n can be generated using zero vector (V_0 or V_7) in

15

combination with the two nearest active vectors (V_n, V_{n+1}). Assume that the reference voltage vector be in the first sector as shown in Fig. 2.2, the reference voltage vector can be calculated as in (2.9) where (T_1, T_2) are the applied effective time corresponding to the active vectors, and T_s is the switching period. The effective times can be deduced as in (2.10) where θ^* is the voltage angle between the reference vector and the active vector in the clockwise direction.

$$T_s \cdot V_s^{s*} = T_1 \cdot V_1 + T_2 \cdot V_2 \tag{2.9}$$

$$\begin{cases} T_1 & = \dfrac{|V_s^{s*}| \cdot T_s}{2/3 V_{dc}} \cdot \dfrac{\sin(\pi/3 - \theta^*)}{\sin(\pi/3)} \\ T_2 & = \dfrac{|V_s^{s*}| \cdot T_s}{2/3 V_{dc}} \cdot \dfrac{\sin(\theta^*)}{\sin(\pi/3)} \\ T_Z & = T_s - T_1 - T_2; \qquad T_0 = T_7 = T_Z/2 \end{cases} \tag{2.10}$$
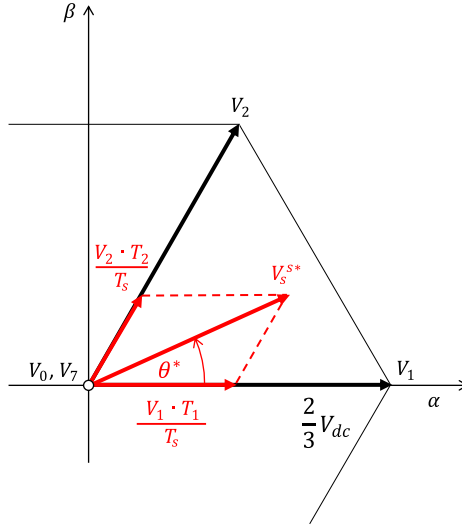
Figure 2.2: Space-vector diagram of the reference voltage vector in the stationary reference frame located in the first sector.

(a) $M_i = 0.7$

(b) $M_i = 0.907$
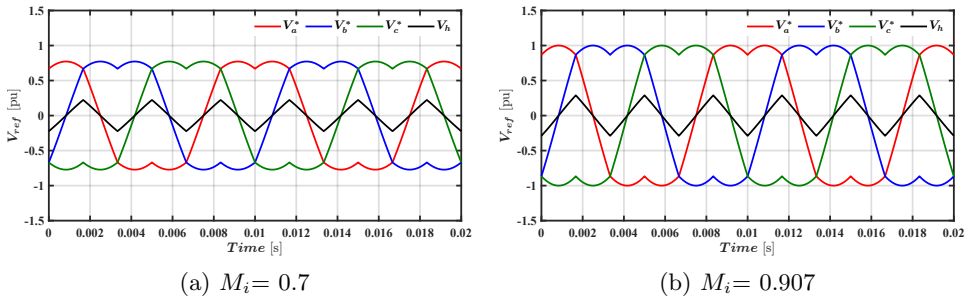
Figure 2.3: Reference voltages of CSVPWM method.

(a)

(b)
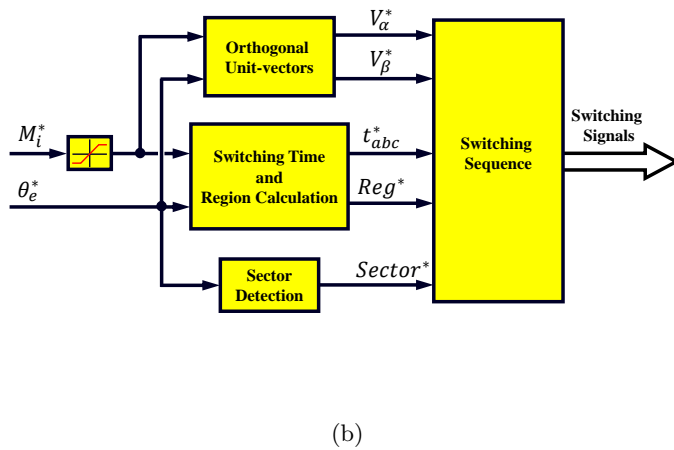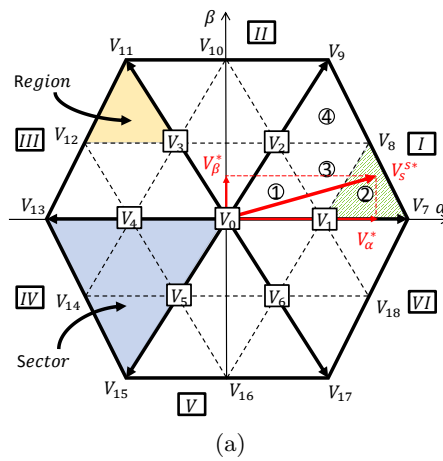
Figure 2.4: Space-Vector Modulation (SVM) of 3L-NPC inverter: (a) Space-vector diagram of reference voltage with all possible switching states; (b) SVM block diagram.

17

CSVPWM provides a maximum modulation index of $M_i \cong 0.907$ in the linear operation, as shown in Fig.2.3. Although CSPVM requires more computational effort and the transformation of complex vectors, the CSVPWM shows low harmonic distortion and more flexibility to use redundant states in multi-level inverters. Space-vector modulation of the three-level Neutral-Point-Clamped (3L-NPC) inverter considered for the following analysis in this chapter is shown in Fig. 2.4 [82–84].

2.3 Discontinuous PWM (DPWM)

The DPWM method aims to reduce the switching losses of the inverter by introducing discontinuous zero-sequence voltage (ZSV). The introduced ZSV modifies the reference sinusoidal voltage to clamp the positive or negative DC bus ($\frac{Vdc}{2}$) for a total duration of 120° electrical degrees at each fundamental cycle. Several DPWM methods have been implemented by using different ZSV, but each DPWM method splits the clamping period into several segments [81]. Generally, DPWM methods utilize the DC bus voltage in the linear modulation range to $M_i \cong 0.907$ with reduced switching losses by 33% compared to the CSVPWM. However, the main drawback of DPWM methods is the high current harmonic distortion and worse waveform quality at low and medium modulation indexes.

2.3.1 120º DPWM

In this method, the modulating signals have only one segment at each fundamental period of a duration of 120° electrical degrees at which they are clamped to the DC bus. It is divided into two subcategories:

- **DPWMMAX**: the modulating signals are clamped to the positive DC bus and the zero-space vector V_0 is removed.

- **DPWMMIN**: the modulating signals are clamped to the negative DC bus and the zero-space vector V_7 is removed.

Fig. 2.5a and 2.5b show the DPWMMAX and DPWMMIN with the injected ZSV respectively. The main disadvantage of these methods is the unequal stress distribution on the inverter switching devices during the clamped period.

2.3.2   60º DPWM

In this method, the total clamping period of 120° is split into two 60° intervals by alternately changing the homopolar voltage V_h between V_0 and V_7 at each fundamental cycle. Based on the placement of the two 60° intervals in the 120° clamping region, different 60° DPWM schemes can be implemented as following (see Fig. 2.5c, 2.5d and 2.5e):

- **DPWM0**: It is generated when the phase difference between the clamped segment and the peak of the reference phase is leading by 30°.

- **DPWM1**: It is generated when the two 60° is placed in the middle of the peak (positive and negative) of the reference phase.

- **DPWM2**: It is generated when the phase difference between the clamped segment and the peak of the reference phase is lagging by 30°.

Among these various DPWM methods, DPWM1 shows minimum switching losses making it the most interesting for AC motors applications [85].

2.3.3   30º DPWM

In this method, the total clamping period per phase of 120° is split into four segments with a 30° electrical degrees interval. DPWM3 is an alternative common name to this method which has low harmonic distortion. The reference modulating signals with the injected ZSV are shown in Fig. 2.5f.
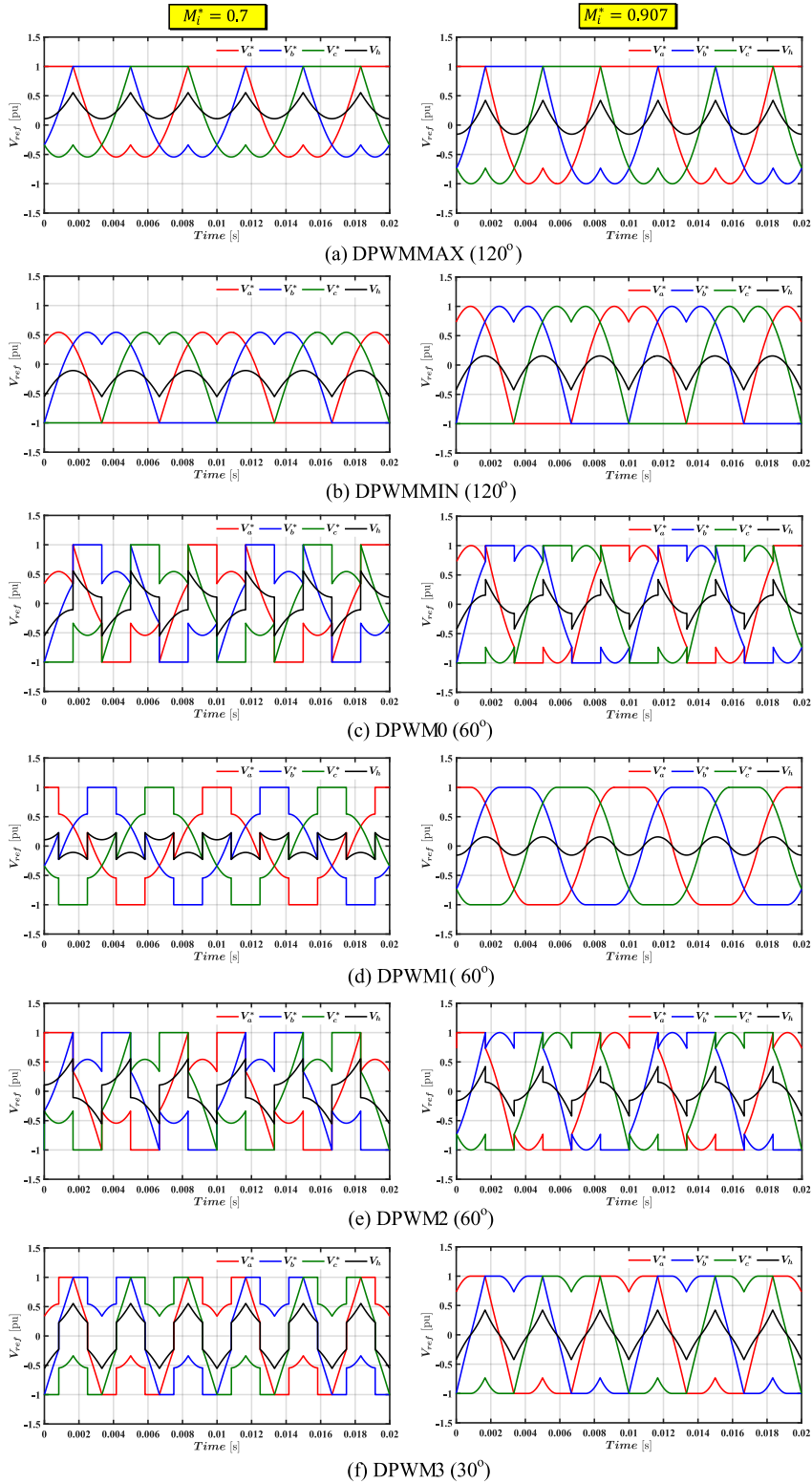
Figure 2.5: Summary of reference voltages of discontinuous PWM (DPWM) methods.

2.4   Generalized PWM Algorithm (GPWM)

In this algorithm, different PWM methods mentioned above can be implemented by changing the zero-sequence signal [85, 86]. It is also called Hybrid PWM as a combination of different modulation methods that can be used based on the voltage magnitude, i.e., using CSVM in the low modulation index then it changes to one of the DPWM methods. Recalling equations (2.5)-(2.7), the zero-vector voltage, calculated in (2.11), is added to the instantaneous reference phase voltages. Where K and δ are variables in table 2.1 that depends on each PWM method and ω is the angular speed of the reference voltage.

$$V_0 = [-K \cdot v_{max}^* + (K - 1) \cdot v_{min}^* + (2K - 1)] \tag{2.11}$$

Table 2.1: K and δ variables for different PWM methods.

Method	K	δ
CSVPWM	0.5	-
DPWMMAX	1	-
DPWMMIN	0	-
DPWM0		$\delta = -\pi/6$
DPWM1	$-\frac{1}{2}\left[1 - sign\left(cos\left(3 \cdot (\omega t + \delta)\right)\right)\right]$	$\delta = -\pi/3$
DPWM2		$\delta = 0$
DPWM3		$\delta = +\pi/6$

2.5   Unified Voltage Modulation Technique of the Space Vector PWM

From the previous GPWM, it can be noted that the unified voltage modulation algorithm deals with the instantaneous three-phase reference voltages and a zero-sequence signal with triplen harmonic of the fundamental. The GPWM is suitable for steady-state operation but during the transients, its performance is not satisfactory. Besides, commonly in high-performance drives like field-oriented schemes, the whole control process is made on the reference space vector (magnitude and angle) combined with CSVPWM method. In [87, 88],

a new unified voltage modulation technique based on the space voltage vector is proposed. This strategy offers simple implementation, less computational effort, and does not involve any look-up tables or logic operation for actual switching time calculations. In addition, all PWM methods (SPWM, CSVPWM, DPWM) can be implemented from the space voltage vector in the stationary frame by only changing one variable (offset time).

Considering the reference voltage vector shown in Fig. 2.2 in the stationary reference frame, the unified PWM strategy procedure is described as follows:

1. The reference phase voltages are obtained from the reference voltage vector in the stationary reference frame.

$$
\begin{bmatrix} V_{as}^* \\ V_{bs}^* \\ V_{cs}^* \end{bmatrix} = \begin{bmatrix} 1 & 0 \\ -1/2 & \sqrt{3}/2 \\ -1/2 & -\sqrt{3}/2 \end{bmatrix} \cdot \begin{bmatrix} V_{\alpha s}^* \\ V_{\beta s}^* \end{bmatrix} \tag{2.12}
$$

2. Calculate a virtual time proportional to each phase voltage:

$$
\begin{cases} T_{as} = \frac{T_s}{V_{dc}} \cdot V_{as}^* \\ T_{bs} = \frac{T_s}{V_{dc}} \cdot V_{bs}^* \\ T_{cs} = \frac{T_s}{V_{dc}} \cdot V_{cs}^* \end{cases} \quad \text{where,} \quad \begin{cases} V_{as}^* + V_{bs}^* + V_{cs}^* = 0 \\ T_{as} + T_{bs} + T_{cs} = 0 \end{cases} \tag{2.13}
$$

3. Calculate the active and zero times. The effective time is the time in which an active voltage is supplied to the load (machine):

$$
T_{eff} = T_{max} - T_{min}; \text{ where } \begin{bmatrix} T_{max} = max(T_{as}, T_{bs}, T_{cs}) \\ T_{min} = min(T_{as}, T_{bs}, T_{cs}) \end{bmatrix} \tag{2.14}
$$

$$
T_z = T_s - T_{eff} \tag{2.15}
$$

4. Calculate the offset time which is required to distribute the zero voltage during one switching period. The offset time is a degree of freedom that can change the modulation method as listed in table 2.2. The DPWM0 and DPWM2 also can be implemented by the same way if needed.

5. Calculate the actual ON gate time signals (switching times) of the top T_{abcT} and bottom T_{abcB} devices for each inverter leg.

$$
\begin{cases} T_{aT} = T_{as} + T_{offset} \; ; \; T_{aB} = T_s - T_{aT} \\ T_{bT} = T_{bs} + T_{offset} \; ; \; T_{bB} = T_s - T_{bT} \\ T_{cT} = T_{cs} + T_{offset} \; ; \; T_{cB} = T_s - T_{cT} \end{cases} \tag{2.16}
$$

Table 2.2: Offset time calculation for unified voltage modulation technique.

PWM Method	Offset time, T_{offset}
SPWM	$T_{offset} = \frac{T_s}{2}$
CSVPWM	$T_{offset} = \frac{T_Z}{2} - T_{min}$
DPWMMAX	$T_{offset} = T_s - T_{max}$
DPWMMIN	$T_{offset} = - T_{min}$
DPWM1	$\text{if}(T_{min} + T_{max}) \geq 0 \quad \text{then } T_{offset} = T_s - T_{max}$ $\text{if}(T_{min} + T_{max}) < 0 \quad \text{then } T_{offset} = -T_{min}$
DPWM3	$\text{if}(T_{min} + T_{max}) \geq 0 \quad \text{then } T_{offset} = -T_{min}$ $\text{if}(T_{min} + T_{max}) < 0 \quad \text{then } T_{offset} = T_s - T_{max}$

2.6   Selective Harmonic Elimination (SHE)

Selective Harmonic Elimination (SHE) is an attractive option for high-power applications providing low switching frequency PWM for reducing the switching losses of the semiconductors. It eliminates the low order-harmonics that would appear in the output voltage hence improving the machine performance. SHE technique uses a number of switching angles per quarter fundamental cycle which are pre-defined via Fourier analysis to ensure the elimination of undesired low-order harmonics [89]. However, the eliminated harmonic energy in the switched waveform is redistributed over the other harmonic components causing an increase in the non-eliminated harmonics. The idea of the SHE method is to make the Fourier coefficients (harmonic components) of the reference switched waveform equal to zero for those undesired harmonics, while the fundamental component is equal to the desired reference amplitude. This can be achieved by solving a set of non-linear equations offline using numerical methods to obtain the desired switching angles [90, 91]. The phase-to-neutral output voltage is given by equation (2.17), while the Fourier coefficients of the predefined waveform with the switching angles as unknown variables are given in (2.18).

$$V_{ln} = \sum_{n=1}^{\infty} \left[\frac{4V_{dc}}{n\pi} \sum_{k=1}^{N} (-1)^{k+1} \cos(n\alpha_k) \right] \cdot \sin(n\omega t) \qquad (2.17)$$

$$h_n = \frac{4}{n\pi} \left[\sum_{k=1}^{N} (-1)^{k+1} \cos(n\alpha_k) \right], \quad \alpha_1 < \alpha_2 < \ldots < \alpha_k < \frac{\pi}{2} \qquad (2.18)$$

where,

h_n	the amplitude of harmonic order n;
α_k	the corresponding switching angle;
N	the number of switching angles required to eliminate $(N-1)$ of harmonic components.

An example of SHE with three switching angles is shown in Fig. 2.6a. With three angles, it is possible to cancel two harmonics of the output voltage (typically the 5th and 7th), in addition to controlling the magnitude of the fundamental voltage as in (2.19) (see Fig. 2.6b). The third harmonic and its multiples are naturally eliminated by the three-phase load connection. The Newton-Raphson iterative method is usually employed to solve such equations to find the appropriate switching angles [92].

$$\frac{4}{\pi} = \cos(\alpha_1) + \cos(\alpha_2) + \cos(\alpha_3),$$
$$0 = \cos(5\alpha_1) + \cos(5\alpha_2) + \cos(5\alpha_3),$$
$$0 = \cos(7\alpha_1) + \cos(7\alpha_2) + \cos(7\alpha_3) \qquad (2.19)$$

As the speed (i.e fundamental frequency) increases, SHE changes to one pulse mode (see Fig. 2.6c & 2.6d) to reduce switching losses. SHE implementation is schematically shown in Fig. 2.6e for a three-level NPC inverter where α_k^* refers to any number of switching angles.

(a)

(b)

(c)

(d)

(e)
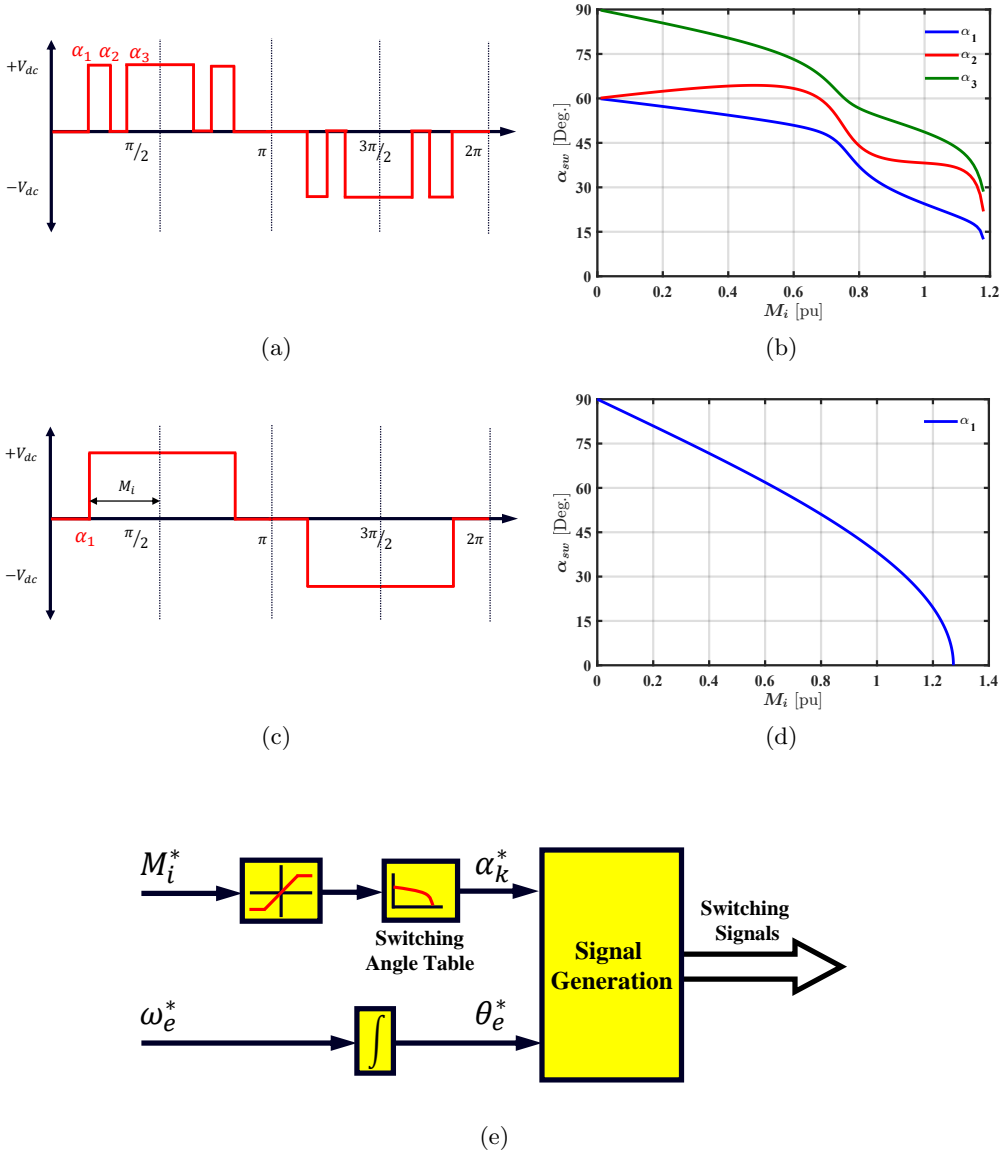
Figure 2.6: Selective Harmonic Elimination (SHE) of 3L-NPC inverter. Phase voltages and switching angles values for the case of: (a) & (b) three switching angles; (b) & (c) one switching angle; (e) SHE block diagram.

2.7 Overmodulation (OVM) Strategies

The actual output-to-reference voltage ratio indicates the linearity of the modulation method used. SPWM in the linear modulation range (output fundamental voltage equal to reference voltage) is $0 \leq M_i \leq \frac{\pi}{4}$, ($0 \leq M_i \leq$

0.7854). Using CSVPM or SPWM with triplen harmonic injection extends the linear region to $0 \leq M_i \leq \frac{\pi}{2\sqrt{3}}$, ($0.7854 \leq M_i \leq 0.907$). In the overmodulation range ($0.907 \leq M_i \leq 1$), the voltage waveform is distorted and results in additional odd harmonics, the fundamental output voltage vs. reference voltage ratio follows a non-linear behavior.

Overmodulation strategies aim to compromise output voltage harmonic distortion, and DC bus utilization when the inverter operates beyond its linear limit. The most widely used OVM methods are (see Fig. 2.7):

- Minimum-phase error (MPE), V_{s1} [86].

- Minimum-distance/magnitude error (MME), V_{s2} [86].

- Switching-state (DPWM1), V_{s3} [86].

- Single-mode (Bolognani), V_{s4} [93].

- Piecewise-fitting dual-mode (Dong-Lee), V_{s5} [94].
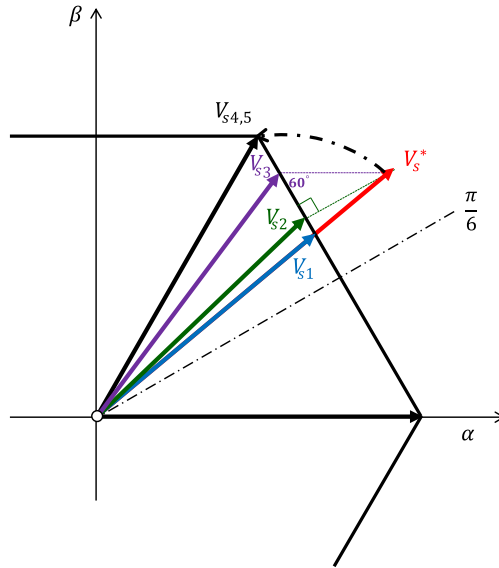
Figure 2.7: Space-vector diagram of the reference voltage vector for different overmodulation strategies.

2.7.1 Minimum-phase Error (MPE), V_{s1}

In this strategy, the reference voltage vector is limited to the hexagon surface in the whole OVM process. Using the unified PWM strategy and recalling equations (2.13)-(2.15), the OVM can be detected when the zero-vector time is negative value [87, 88]. Then the imaginary switching times and the offset time are modified as in (2.16). The output voltage vector is always in phase with its reference vector. The results for this method have been omitted as it requires infinity gain to reach six-step operation.

$$\begin{cases} T_{as}^* = T_{as} \cdot \frac{T_s}{T_{eff}} \\ T_{bs}^* = T_{bs} \cdot \frac{T_s}{T_{eff}} \\ T_{cs}^* = T_{cs} \cdot \frac{T_s}{T_{eff}} \end{cases} \quad \text{where, } T_{offset} = -T_{min} \cdot \frac{T_s}{T_{eff}} \quad (2.20)$$

2.7.2 Minimum-distance/magnitude Error (MDE), V_{s2}

In this strategy, the output voltage vector is modified to a point which is the projection of the reference on the hexagon limit during the OVM process. This strategy is naturally implemented by limiting the three-phase voltage references in the GPWM method. Fig. 2.10a shows the MME method for different modulation indexes at OVM process. Due to the symmetry of the modulation method, the first sector is only presented in Fig. 2.10. It can be noted that the OVM is applied only when the reference voltage vector is outside the hexagon. Therefore, the produced output voltage will be less than its reference value. The modified output voltage lags and leads the reference vector for each half-sector respectively.

2.7.3 Switching-state (DPWM1), V_{s3}

The switching-state or (DPWM1) modulation method belongs to the 60° DPWM category discussed in Section 2.3.2. However, in this strategy, the output voltage vector is modified to a point at which the vector difference between the reference and the output voltage vector makes a 60° with the hexagon surface during the OVM process (see Fig. 2.10b). The modified output voltage lags and leads the reference vector for each half-sector, respectively.
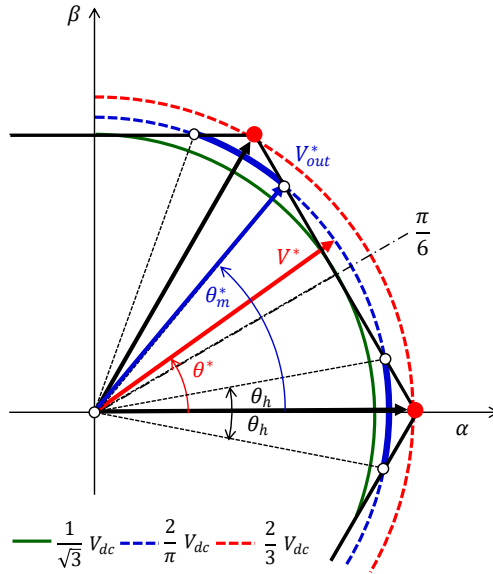
Figure 2.8: Space-vector diagram of the reference voltage vector for for Bolognani overmodulation strategy.

2.7.4 Single-mode (Bolognani), V_{s4}

The operating principle of this strategy is to change the output voltage vector angle while keeping the magnitude as its reference value. The modified output voltage vector angle following the conditions in (2.21), where θ_h is the holding angle [93]. It can be concluded that when the reference vector exceeds the hexagon boundary, the output vector is held at the intersection point until the reference vector enters back inside the hexagon. The intersection point, i.e. the intersection of the reference vector with the hexagon boundary is obtained from the holding angle (2.21). The output voltage vector locations belong to the blue arc shown in Fig. 2.8. As a result, the phase angle of the reference vector shifts to the next or the previous intersection point depending on its location in the sector. Consequently, high harmonic components in the output voltage will be produced. Otherwise, the output voltage vector is equal to the commanded value. The holding angle is inversely proportional to the reference vector where the six-step operation is reached when $V^* = \frac{2}{3}V_{dc}$ (red circles in Fig. 2.8). The modified output voltage lags and leads the reference vector in each half-sector, respectively (see Fig. 2.10c).

$$
\theta_m^* = \begin{cases}
\theta^* & 0 \le \theta^* \le \theta_h \\
\theta_h & \theta_h \le \theta^* \le \frac{\pi}{6} \\
\frac{\pi}{3} - \theta_h & \frac{\pi}{6} \le \theta^* \le \frac{\pi}{3} - \theta_h \\
\theta^* & \frac{\pi}{3} - \theta_h \le \theta^* \le \frac{\pi}{3}
\end{cases}
\; ; \text{where, } \theta_h = \frac{\pi}{6} - cos^{-1}\left(\frac{V_{dc}}{\sqrt{3} \cdot V^*}\right) \quad (2.21)
$$

2.7.5 Piecewise-fitting Dual-mode (Dong-Lee), V_{s5}

To overcome the single-mode disadvantage of having high harmonic components of the output voltage, a dual-mode overmodulation method based on a piecewise-fitting curve is proposed in [94]. In this method the overmodulation region is divided into two regions:

- **OVM region I ($0.9069 < M_i \le 0.9517$):** In this region only the magnitude of the reference vector is changed while the phase angle remains unchanged. The output vector is limited to the hexagon surface if the reference vector is outside the hexagon boundary. When the reference vector is inside the hexagon, the output vector magnitude is increased with an appropriate value to compensate for the difference in the reference vector during the operation outside the hexagon limit as shown in Fig. 2.9a. The modified vector magnitude is a function of the reference angle α_r according to (2.22). The relationship between the α_r and M_i is linearized for the online modulation process in (2.23).

$$
V_{out}^* = \begin{cases}
\dfrac{V_{dc}}{\sqrt{3} \cdot \cos\left(\frac{\pi}{6} - \alpha_r\right)} & 0 \le \theta^* \le \alpha_r \\
\dfrac{V_{dc}}{\sqrt{3} \cdot \cos\left(\frac{\pi}{6} - \theta^*\right)} & \alpha_r < \theta^* \le \frac{\pi}{3} - \alpha_r \\
\dfrac{V_{dc}}{\sqrt{3} \cdot \cos\left(\frac{\pi}{6} - \alpha_r\right)} & \frac{\pi}{3} - \alpha_r < \theta^* \le \frac{\pi}{3}
\end{cases}
\quad (2.22)
$$

$$
\alpha_r = \begin{cases}
\frac{\pi}{6} & (M_i < 0.9069) \\
-30.23 \cdot M_i + 27.94 & (0.9069 \le M_i < 0.9095) \\
-8.58 \cdot M_i + 8.23 & (0.9095 \le M_i < 0.9485) \\
-26.43 \cdot M_i + 25.15 & (0.9485 \le M_i < 0.9517)
\end{cases}
\quad (2.23)
$$

- **OVM region II ($0.9517 < M_i \le 1.0$):** In this region only the magnitude of the reference vector is changed while the phase angle remains
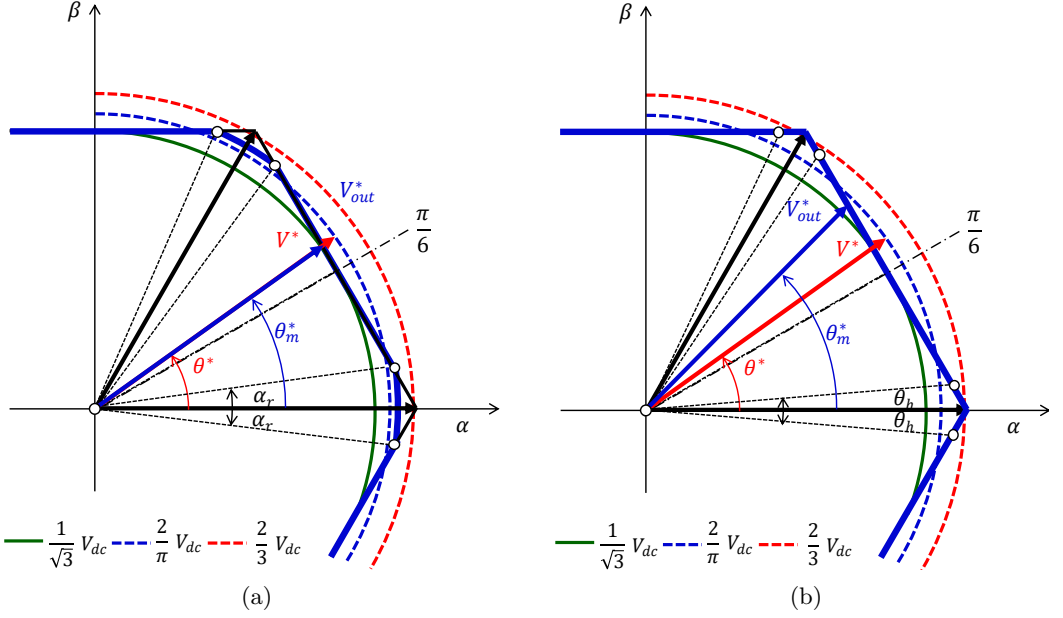
Figure 2.9: Space-vector diagram of the reference voltage vector for Dual-mode over-modulation strategy: (a) OVM region I; (b) OVM region II.

unchanged. The output vector is limited to the hexagon surface if the reference vector is outside the hexagon boundary. When the reference vector is inside the hexagon, the output vector magnitude is increased with an appropriate value to compensate for the difference in the reference vector during the operation outside the hexagon limit as shown in Fig. 2.9b. The modified vector magnitude is a function of the holding angle α_h according to (2.24) and (2.25). The relationship between the α_h and M_i is linearized for the online modulation process in (2.26). The modified output voltage at different modulation indexes can be seen in Fig. 2.10d.

$$V_{out}^* = \frac{V_{dc}}{\sqrt{3} \cdot \cos\left(\frac{\pi}{6} - \theta_m\right)} \tag{2.24}$$

$$\theta_m = \begin{cases} 0 & 0 \leq \theta^* \leq \alpha_h \\ \left(\frac{\pi}{6}\right) \cdot \left(\frac{\theta^* - \alpha_h}{\frac{\pi}{6} - \alpha_h}\right) & \alpha_h < \theta^* \leq \frac{\pi}{3} - \alpha_h \\ \frac{\pi}{3} & \frac{\pi}{3} - \alpha_h < \theta^* \leq \frac{\pi}{3} \end{cases} \tag{2.25}$$

$$
\alpha_h = \begin{cases}
6.40 \cdot M_i - 6.09 & (0.9517 \leq M_i < 0.98) \\
11.75 \cdot M_i - 11.34 & (0.98 \leq M_i < 0.9975) \\
48.96 \cdot M_i - 48.43 & (0.9975 \leq M_i < 1) \\
\frac{\pi}{6} & (1 \leq M_i)
\end{cases} \tag{2.26}
$$

(a) Minimum Distance Error (90°).

(b) Switching State (60°).

(c) Single mode.
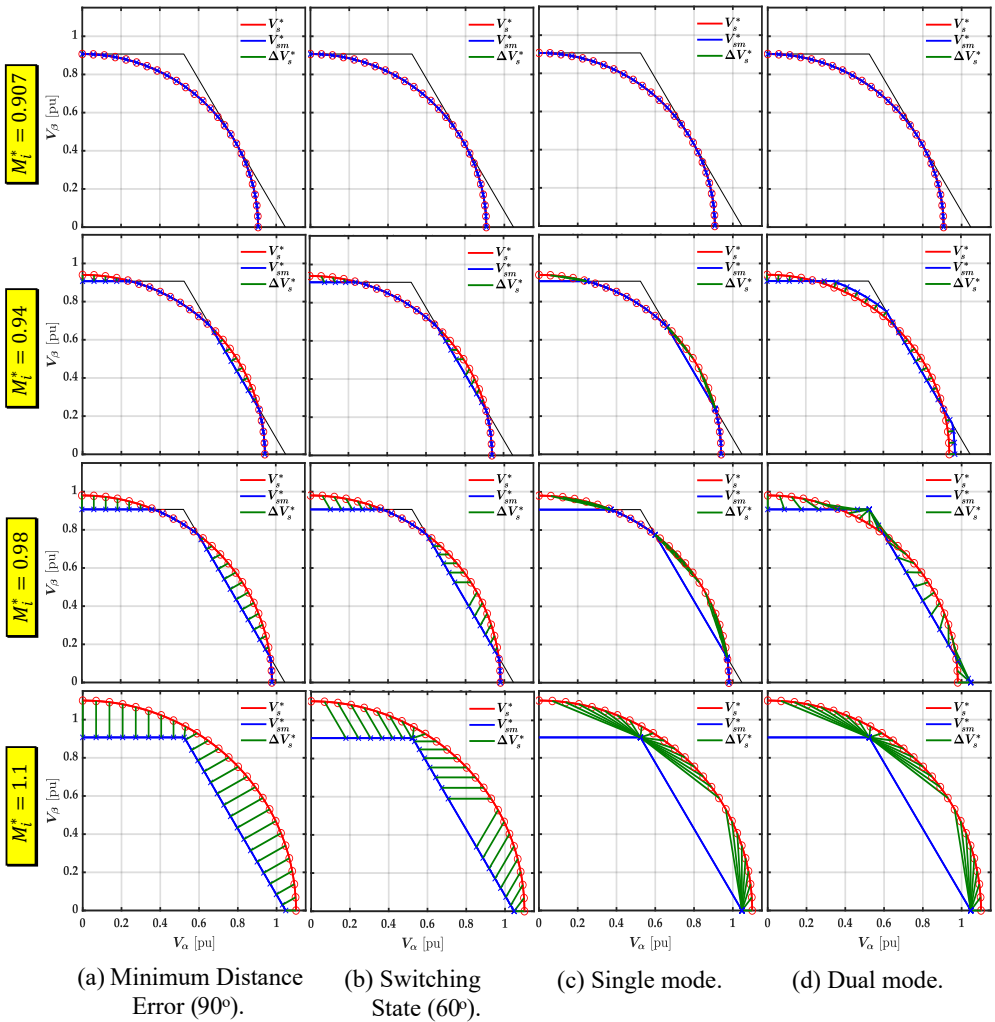
(d) Dual mode.

Figure 2.10: Reference Vs. actual inverter output voltage at different Modulation indexes for conventional overmodulation strategies: (a) Minimum-Distance Error (90°); (b) Switching-State (60°); (c) Single-mode; (d) Dual-mode.

2.8 Proposed Generalized Form of SVPWM in Over-modulation
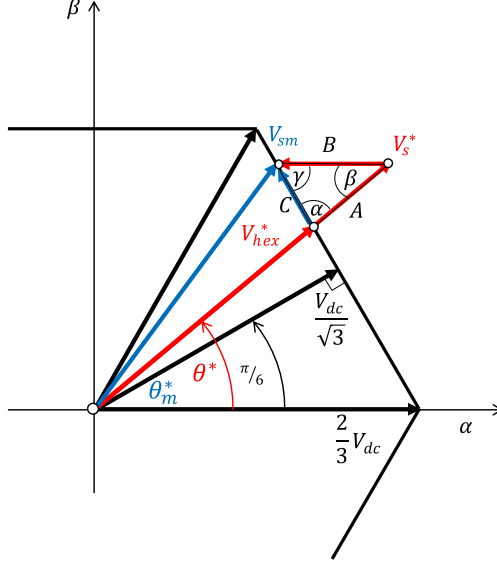
Figure 2.11: Proposed General Form of dynamic OVM with an arbitrary angle γ.

From the previous discussion, it can be noticed that the Minimum-Phase Error, Minimum-Distance Error, and Switching-State methods are based on similar principles, the only difference being the angle between the voltage vector being added to the original voltage command and the hexagon boundary (0°, 90° and 60° respectively), as seen in Fig. 2.7. This type of overmodulation can be generalized to any arbitrary angle γ as described following:

1. Assuming the reference voltage vector is located in the first sector. The reference vector magnitude limited to the hexagon boundary is calculated in (2.27). The new modified reference vector $\vec{V}_{sm}$ (see Fig. 2.11) depends on the angle γ connecting the reference and the modified vector tips with the hexagon border.

$$|V_{hex}^*| = \frac{V_{dc}}{\sqrt{3} \cdot \cos\left(\theta^* - \frac{\pi}{6}\right)} \tag{2.27}$$

2. For a given angle γ the triangle ABC shown in Fig. 2.11 is formed, with the angles α and β being obtained as:

$$\alpha = \begin{cases} \theta^* + \frac{\pi}{3}, & 0 \le \theta^* \le \frac{\pi}{6} \\ \pi - \theta^* - \frac{\pi}{3}, & \frac{\pi}{6} < \theta^* \le \frac{\pi}{3} \end{cases} \tag{2.28}$$

$$\beta = \pi - \alpha - \gamma \tag{2.29}$$

3. The modified output vector can be calculated as follows:

$$|A| = |V_s^*| - |V_{hex}^*| \tag{2.30}$$

$$|C| = |A| \cdot \frac{\sin(\beta)}{\sin(\gamma)} \tag{2.31}$$

$$\vec{V}_{sm} = \begin{cases} \vec{V}_{hex}^* + |C| \cdot e^{-j\pi/3}, & 0 \le \theta^* \le \frac{\pi}{6} \\ \vec{V}_{hex}^* + |C| \cdot e^{j2\pi/3}, & \frac{\pi}{6} < \theta^* \le \frac{\pi}{3} \end{cases} \tag{2.32}$$

2.9 Comparative Analysis of OVM Strategies

This Section compares the performance of the different overmodulation strategies. Three aspects will be considered: a) output to commanded modulation index (linearity); b) harmonic distortion; and c) number of commutations. The analysis will focus on strategies that can reach six-step operation; hence the Minimum-Phase Error (MPE) method is disregarded as it requires an infinite reference modulation index to reach six-step operation.

Fig. 2.12a shows the actual M_i vs. commanded M_i^* modulation index for the overmodulation methods described in section 2.7. It is seen that the Dual-mode strategy provides a nearly linear relationship between the reference and the output voltage while the Minimum-Distance Error (MDE) one shows the worse behavior in this regard. The six-step operation is reached at a very high (in the range of thousands) value of the reference modulation index, therefore the reference modulation index in Fig. 2.12a is only shown up to 2 for clear visualization and comparison with other methods. Switching-State strategy modifies the reference voltage vector to be 60° from the hexagon boundary. Six-step operation is achieved in this case for $M_i^* \cong 1.5$. Holding the reference voltage vector at the hexagon boundary to compensate for the interval being outside the hexagon (i.e. Single-mode) reduces reaching six-step operation to $M_i^* \cong 1.047$ [93].
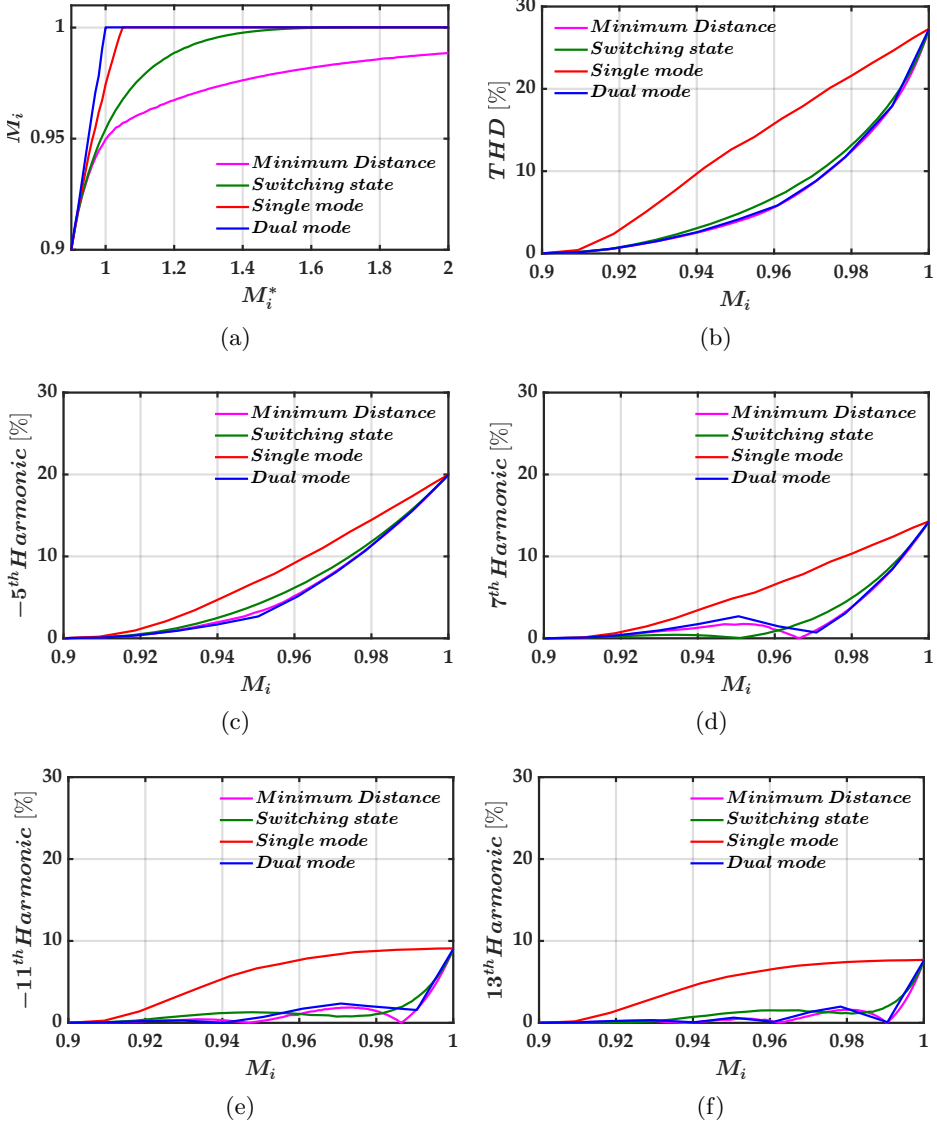
Figure 2.12: Comparative analysis: (a) M_i versus M_i^*; (b) THD, (c) -5th, (d) 7th, (e) -11th and (f) 13th harmonic components vs. M_i respectively.

To conclude this discussion, it is important to note that the non-linear relationship between the commanded and actual modulation index can potentially be compensated by pre-warping the commanded modulation index, either a look-up table or an analytical function can be used for this purpose. The main concern using overmodulation is the low-order harmonics introduced in the output voltage waveform, which will be transferred to the currents and eventually to torque. Fig. 2.12b shows the Total Harmonic Distortion (THD)

considering the -5th, 7th, -11th and 13th harmonic components. It is noted that the Single-mode method shows the worst behavior, while for the other methods only minor differences are observed. The individual harmonic distortion for the -5th, 7th, -11th and 13th components are shown in Fig. 2.12c-f respectively. It is seen that Minimum-Distance Error and Dual-mode have lower harmonic content for most of the overmodulation range. However, the Switching-State method has lower distortion in certain harmonic components for a specific modulation index range. For instance, the 7th from $M_i^* = 0.9$ to $M_i^* = 0.95$ and the -11th from $M_i^* = 0.958$ to $M_i^* = 0.98$, Switching-State method becomes superior for these ranges regarding harmonic content.

Another important aspect that is often neglected in the literature is the switching losses, which are especially relevant for medium-voltage high-power drives. The number of commutations per quarter cycle was obtained by means of simulation. This number is a function of the modulation index and the ratio between switching frequency and fundamental frequency, ($\frac{\omega_{sw}}{\omega_f}$). Fig. 2.13 shows the results for a ratio of 100 and 10 respectively. The Single-mode strategy shows the worst performance, while none of the other methods is superior (i.e., has fewer commutations) for all modulation indexes and switching to fundamental ratios.
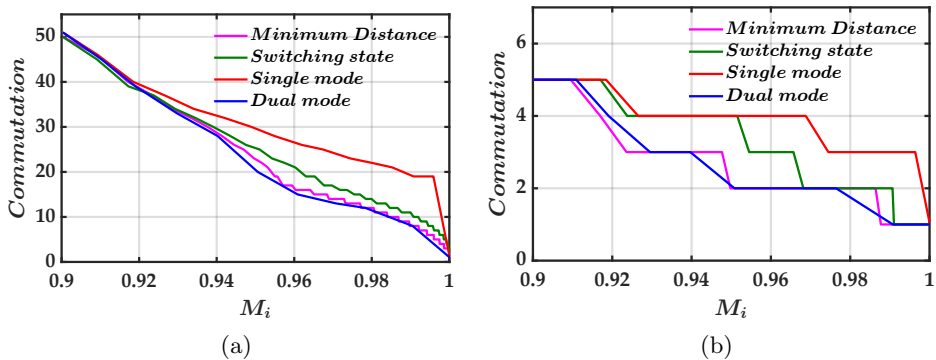
Figure 2.13: Number of commutations per quarter cycle of the fundamental frequency of the different overmodulation methods vs. M_i for a switching to fundamental frequency ratio: (a) $\frac{\omega_{sw}}{\omega_f} = 100$; (b) $\frac{\omega_{sw}}{\omega_f} = 10$.

The same analyses were repeated using the proposed general form discussed in Section 2.8. By comparing the results in Fig. 2.14 and Fig. 2.15, it can be concluded that lower angle, higher linearity, higher THD, and higher number of commutations. The maximum output voltage is found at 1.047 of the commanded modulation indexes, which is similar to the Single-mode method.

Taking into consideration the individual low-order harmonic components, none of the angles provides the best solution over the whole overmodulation range.
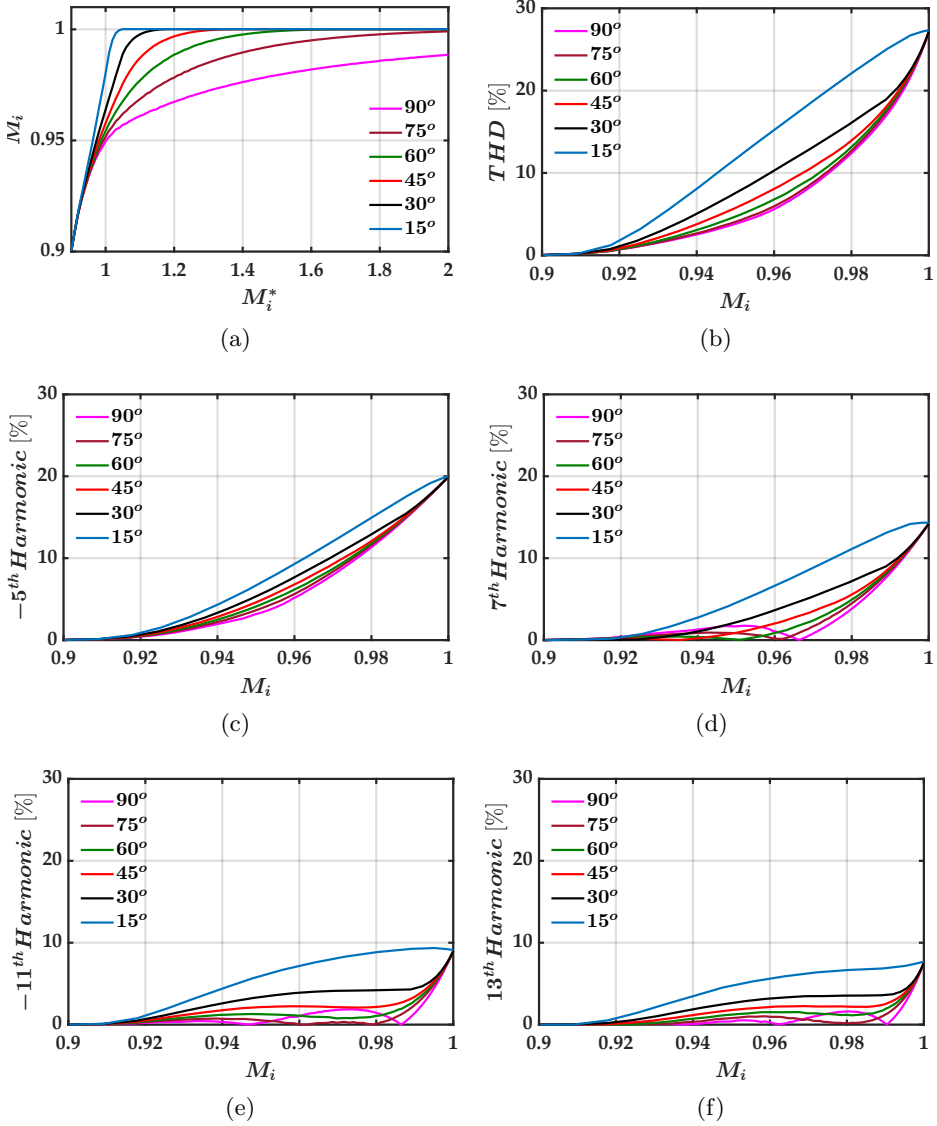
Figure 2.14: Comparative analysis as a function of γ angle: (a) M_i versus M_i^*; (b) THD, (c) -5th, (d) 7th, (e) -11th and (f) 13th harmonic components vs. M_i respectively.

An optimal overmodulation strategy can be achieved by combining at least two overmodulation methods as a function of the modulation index. As the minimum number of commutations and minimum low-order harmonic distor-
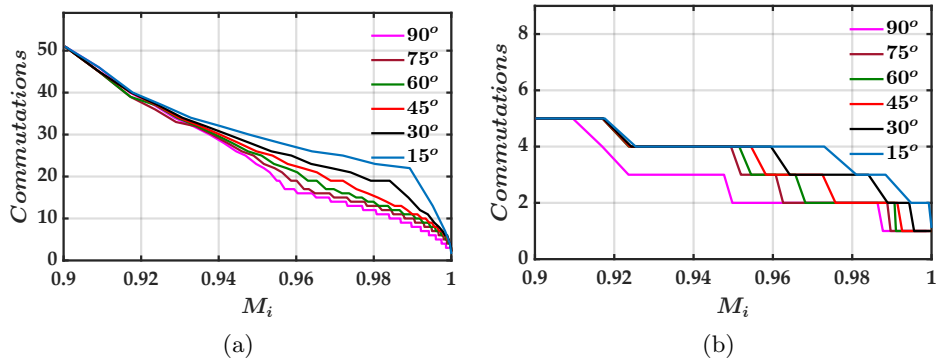
Figure 2.15: Number of commutations per quarter cycle of the fundamental frequency, of the different overmodulation methods as a function of γ angle vs. M_i for a switching to fundamental frequency ratio: (a) $\frac{\omega_{sw}}{\omega_f} = 100$; (b) $\frac{\omega_{sw}}{\omega_f} = 10$.

tion (especially -5th & 7th) are usually the requirements for traction drives, a combination of Switching-State and Dual-mode could provide the best performance over the whole overmodulation range.

2.10 Experimental Validation

A commercial 4 kV three-phase three-level Natural-Point-Clamped (3L-NPC) inverter manufactured by ELINSA company was used for experimental verification of overmodulation strategies discussed in Section 2.7 [95]. The test bench setup is shown in Fig. 2.16a where the NPC inverter is supplied by a MTD4000-36 programmable DC power supply from Magna-Power Electronics [96]. The main circuit elements of the 3L-NPC including the DC charging and protection circuit are shown in Fig. 2.16b. The overmodulation strategies are implemented on a TMS320 F28335 Digital Signal Processor (DSP) combined with input/output interface circuits for current and voltage measurements, and switching signals. All measured data is monitored and stored using a high-precision oscilloscope and then analyzed using MATLAB environment (see Fig. 2.16c).

For the following results, the DC-link was limited to 600V for safety concerns. The switching and sampling frequencies are 1 kHz, and a dead time of 4 µs is used. The measured phase-a to DC mid-point voltages are shown in Fig. 2.17. It can be noticed that the switching pattern of Minimum-Distance Error and Switching-State methods are still far from six-step operation even

(a)

(b)

(c)
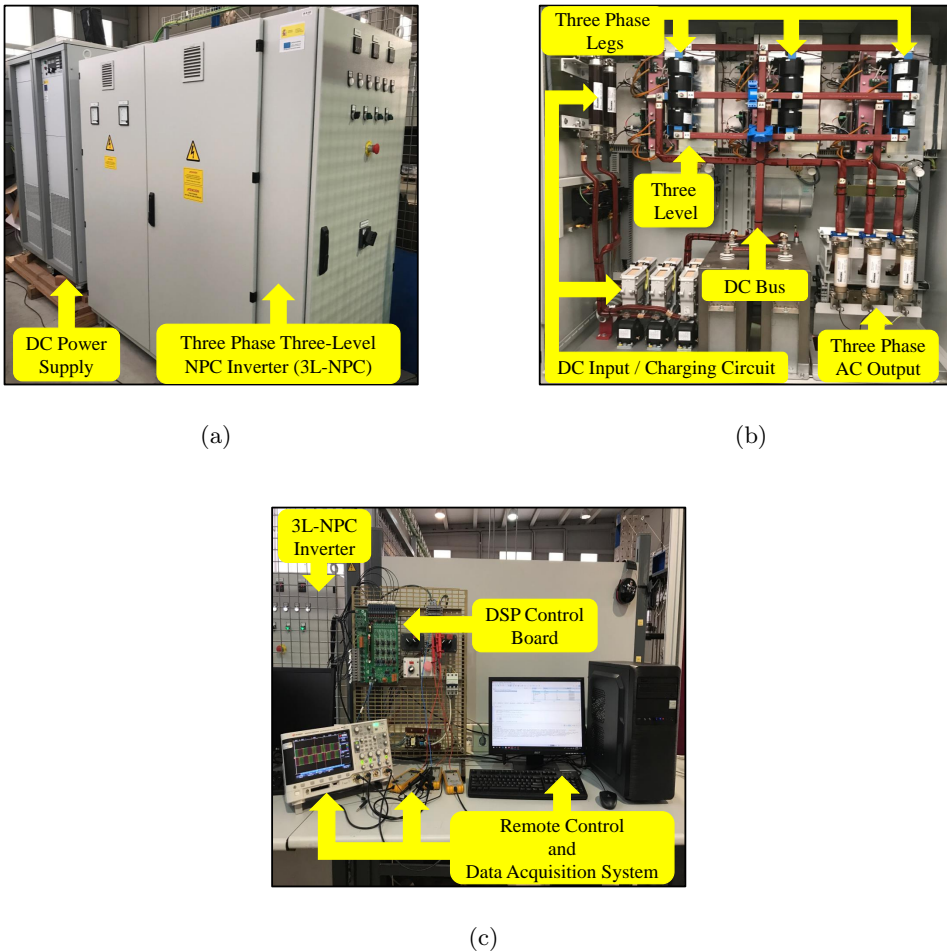
Figure 2.16: Test bench for overmodulation strategies: (a) Schematic representation of the laboratory setup; (b) 4 kV/40A three-level NPC ELINSA inverter.

at ($M_i^* = 1.1$). The transition from linear modulation to six-step is achieved in both Single-mode (see Fig. 2.17c and Dual-mode (see Fig. 2.17d. However, Dual-mode reaches six-step faster with less number of commutations which confirms the simulation results in Section 2.9 (see Fig. 2.17c vs. Fig. 2.17d at $M_i^* = 0.94$ and $M_i^* = 0.98$).

Additionally, Fast Fourier Transform (FFT) has been performed on the output voltage waveform at four different commanded modulation indexes ($M_i^* = 0.94$, 0.98, 1.0, and 1.2) to extract the actual fundamental output voltage. Then, the actual modulation index is calculated and compared with simulation results as seen in Fig. 2.18.
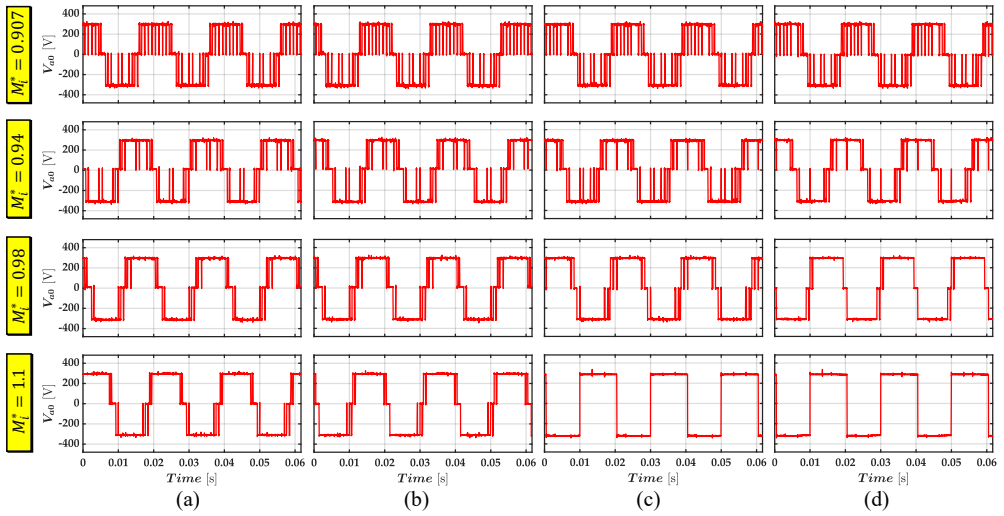
Figure 2.17: Measured voltage of phase A to DC mid-point of three-level NPC (V_{a0}) for different overmodulation methods: (a) Minimum-Distance Error (90°); (b) Switching-State (60°); (c) Single-mode; (d) Dual-mode.
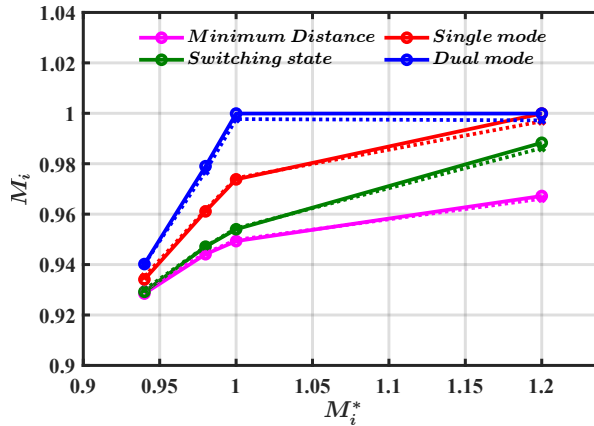
Figure 2.18: Comparison of commanded Vs. output modulation index of three-level NPC for different overmodulation methods: (a) Minimum-Distance Error (90°); (b) Switching-State (60°); (c) Single-mode; (d) Dual-mode. Solid lines with circle marks (-o) for simulation results; Dashed lines with cross marks (- -x) for experimental results.

It is found that both simulation and experimental results are in good agreement. However, the main aspects compared in this Section are done in steady-state, dynamic performance plays an important role in selecting the appropriate overmodulation strategy for electric drives. Usually, overmodulation meth-

ods with larger gains are preferred for such applications which involve current regulators [97, 98]. This might require involving additional compensators or algorithms to improve the dynamic response of the drive control extending the operation into six-step mode [98–103]. Therefore, further investigation is needed for a fair comparison between various overmodulation strategies in closed-loop operation which is kept for future research.

2.11   Conclusions

In this chapter, a comparative analysis of four overmodulation strategies for electric drives reported in the literature is performed: Minimum-Distance Error (90°), Switching-State (60°), Single-mode, and Dual-mode. Furthermore, a generalized overmodulation method with an arbitrary angle γ is presented. Criteria considered for the analysis are: 1) linearity; 2) harmonic distortion, and 3) number of commutations. A finding is that by decreasing the angle between the voltage vector added to the original voltage command and the hexagon boundary, linearity is increased at the price of an increase in the harmonic distortion and number of commutations. It is concluded that none of the analyzed methods achieve the best performance for the whole overmodulation range and switching to fundamental frequency ratio. Optimal performance would be achieved by combining Switching-State and the Dual-mode. Analysis of the dynamic transition between different overmodulation methods, both for open loop operation as well as in current controlled drives is a subject of future research.

Chapter 3

Induction Motor Drives for Traction Applications

3.1 Introduction

This Chapter presents a review of the different aspects involved in the control of IM motor drives for railway applications. Section 3.2 reviews the IM motor model, including a discussion on the machine characteristics. Section 3.3 discusses control strategies, with a special focus on their suitability for use at high speed and low switching frequencies, as this is the most frequent and challenging mode of operation for traction drives. A proposal to enhance torque dynamics of scalar control scheme is presented in Section 3.3.3. Section 3.4 discusses efficient modes of operation and proposed remagnetization strategies in Section 3.4.3. Simulation results will be provided in several Sections, discussion and the experimental validation of the proposed methods will be addressed in Section 3.5. Finally, Section 3.6 addresses the main conclusions.

3.2 Induction Motor (IM) Modeling and Behaviour

IM models as well as a discussion of its behavior are included in this Section, providing the fundamentals for the analysis developed in further Sections.

3.2.1 Dynamic Model Using Complex Vectors

Per-phase equivalent circuits are often used for the analysis of induction machines. Being simple and useful for steady-state operation, per-phase equivalent circuit modeling becomes inadequate for the analysis of machines fed from power converters as the operating point is subject to frequent changes to fulfill the required commands or load variations. Alternatively, complex vector representation is used for dynamic modeling and analysis of three-phase systems in general, as provides a compact, insightful dynamic representation of the physical effects occurring within the machine, i.e., the relationships among electromagnetic variables (voltages, currents, and fluxes) and shaft variables (torque and speed) [104].

Considering a simplified ideal winding model of a three-phase, two-pole induction machine (see Fig. 3.1a) where the stator and rotor phase winding being denoted by $a_s - a_s'$, $b_s - b_s'$, $c_s - c_s'$, and $a_r - a_r'$, $b_r - b_r'$, $c_r - c_r'$ respectively; the displacement between the magneto-motive force (MFF) produced by phase a_s of the stator and the MFF produced by phase a_r of the rotor is denoted as θ_r, ω_r being the angular speed in electrical units in rad/s; P is the number of pole-pairs; ω_m is the mechanical angular speed (rotor shaft speed) in rad/s is given by (3.1).

$$\omega_m = \frac{\omega_r}{P} \tag{3.1}$$

The three-phase stator windings voltage equation v_{abcs} is given by (3.2) in matrix form, where R_s is the stator winding resistance; v_{as}, v_{bs}, v_{cs}, i_{as}, i_{bs}, i_{cs}, and λ_{as}, λ_{bs}, λ_{cs} are the instantaneous stator voltages, currents and fluxes respectively.

$$\begin{bmatrix} v_{as} \\ v_{bs} \\ v_{cs} \end{bmatrix} = R_s \begin{bmatrix} i_{as} \\ i_{bs} \\ i_{cs} \end{bmatrix} + \frac{d}{dt} \begin{bmatrix} \lambda_{as} \\ \lambda_{bs} \\ \lambda_{cs} \end{bmatrix} \tag{3.2}$$

The stator flux component of each phase i.e., λ_{as}, λ_{bs}, λ_{cs} is a function of stator and rotor currents which can be presented in matrix form by (3.3), where L_h represents the stator self-inductance (twice the mutual inductance between stator windings), and $L_{\sigma s}$ is the leakage inductance of the stator windings; $+2\pi/3$ or $-2\pi/3$ being the phase shift between stator/rotor windings.

$$
\begin{bmatrix} \lambda_{as} \\ \lambda_{bs} \\ \lambda_{cs} \end{bmatrix} = \begin{bmatrix} L_{\sigma s} + L_h & -\frac{1}{2}L_h & -\frac{1}{2}L_h \\ -\frac{1}{2}L_h & L_{\sigma s} + L_h & -\frac{1}{2}L_h \\ -\frac{1}{2}L_h & -\frac{1}{2}L_h & L_{\sigma s} + L_h \end{bmatrix} \begin{bmatrix} i_{as} \\ i_{bs} \\ i_{cs} \end{bmatrix}
$$
$$
+ L_h \begin{bmatrix} \cos(\theta_r) & \cos(\theta_r + 2\pi/3) & \cos(\theta_r - 2\pi/3) \\ \cos(\theta_r - 2\pi/3) & \cos(\theta_r) & \cos(\theta_r + 2\pi/3) \\ \cos(\theta_r + 2\pi/3) & \cos(\theta_r - 2\pi/3) & \cos(\theta_r) \end{bmatrix} \begin{bmatrix} i_{ar} \\ i_{br} \\ i_{cr} \end{bmatrix}
$$
$$
(3.3)
$$

The same derivation can be repeated for the rotor circuit to obtain the rotor electromagnetic equations. Hence, the rotor voltage and flux equations in terms of stator and rotor currents are given by (3.4) and (3.5), where R_r is the rotor winding resistance; v_{ar}, v_{br}, v_{cr}, i_{ar}, i_{br}, i_{cr}, and λ_{ar}, λ_{br}, λ_{cr} are the instantaneous rotor voltages, currents and fluxes respectively; $L_{\sigma s}$ being the leakage inductance of the rotor windings

$$
\begin{bmatrix} v_{ar} \\ v_{br} \\ v_{cr} \end{bmatrix} = R_r \begin{bmatrix} i_{ar} \\ i_{br} \\ i_{cr} \end{bmatrix} + \frac{d}{dt} \begin{bmatrix} \lambda_{ar} \\ \lambda_{br} \\ \lambda_{cr} \end{bmatrix} \tag{3.4}
$$

$$
\begin{bmatrix} \lambda_{ar} \\ \lambda_{br} \\ \lambda_{cr} \end{bmatrix} = \begin{bmatrix} L_{\sigma r} + L_h & -\frac{1}{2}L_h & -\frac{1}{2}L_h \\ -\frac{1}{2}L_h & L_{\sigma r} + L_h & -\frac{1}{2}L_h \\ -\frac{1}{2}L_h & -\frac{1}{2}L_h & L_{\sigma r} + L_h \end{bmatrix} \begin{bmatrix} i_{ar} \\ i_{br} \\ i_{cr} \end{bmatrix}
$$
$$
+ L_h \begin{bmatrix} \cos(\theta_r) & \cos(\theta_r - 2\pi/3) & \cos(\theta_r + 2\pi/3) \\ \cos(\theta_r + 2\pi/3) & \cos(\theta_r) & \cos(\theta_r - 2\pi/3) \\ \cos(\theta_r - 2\pi/3) & \cos(\theta_r + 2\pi/3) & \cos(\theta_r) \end{bmatrix} \begin{bmatrix} i_{as} \\ i_{bs} \\ i_{cs} \end{bmatrix}
$$
$$
(3.5)
$$

Considering a generic set of three-phase machine variables, e.g. x_a, x_b and x_c can be represented as a complex vector in space, $x_{\alpha\beta}$ using (3.6), T being Clarke transformation matrix. Gain 2/3 in (3.6) is chosen to maintain the magnitude of x invariant in both domains. The term x_0 is the zero-sequence component which is needed for the matrix T to be invertible. The inverse Clarke transformation is given by (3.7) for returning machine variables into three-phase co-ordinates. The space complex vector $x_{\alpha\beta}$ is referred to a stationary reference frame (see the black arrows in Fig. 3.1b).
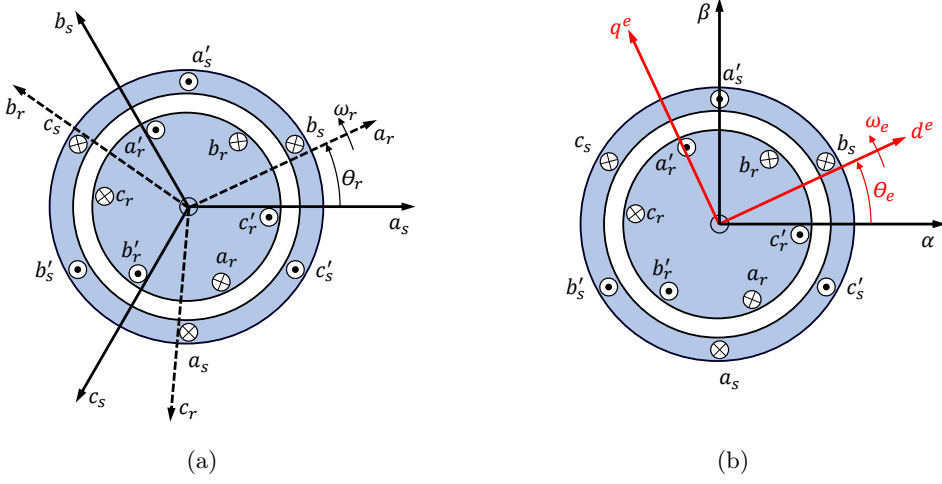
Figure 3.1: Three-phase induction machine model representation using: a) ideal winding; b) complex space vector.

$$
\begin{bmatrix} x_\alpha \\ x_\beta \\ x_0 \end{bmatrix} = T \begin{bmatrix} x_a \\ x_b \\ x_c \end{bmatrix} ; \text{ where } T = \frac{2}{3} \begin{bmatrix} 1 & -\frac{1}{2} & -\frac{1}{2} \\ 0 & \frac{\sqrt{3}}{2} & -\frac{\sqrt{3}}{2} \\ \frac{1}{2} & \frac{1}{2} & \frac{1}{2} \end{bmatrix} \tag{3.6}
$$

$$
\begin{bmatrix} x_a \\ x_b \\ x_c \end{bmatrix} = T^{-1} \begin{bmatrix} x_\alpha \\ x_\beta \\ x_0 \end{bmatrix} ; \text{ where } T^{-1} = \begin{bmatrix} 1 & 0 & 1 \\ -\frac{1}{2} & \frac{\sqrt{3}}{2} & 1 \\ -\frac{1}{2} & -\frac{\sqrt{3}}{2} & 1 \end{bmatrix} \tag{3.7}
$$

Applying Clarke transformation to the voltages, currents and fluxes in induction machines, the stator and rotor voltage equations in stationary reference frame are given by (3.8) and (3.9) respectively. For squirrel cage induction machines $v_{\alpha\beta r} = 0$. The stator and rotor fluxes in terms of stator and rotor currents are given by (3.10) and (3.11) respectively, where $L_m = \frac{3}{2}L_h$ is defined as the mutual inductance; $L_s = L_m + L_{\sigma s}$ and $L_r = L_m + L_{\sigma r}$ are the total stator and rotor inductances respectively. The full derivation of induction machine three-phase variables transformation to stationary frame can be found in [105].

$$v_{\alpha\beta s} = R_s i_{\alpha\beta s} + \frac{d\lambda_{\alpha\beta s}}{dt} \tag{3.8}$$

$$0 = R_r i_{\alpha\beta r} + \frac{d\lambda_{\alpha\beta r}}{dt} - j\omega_r \lambda_{\alpha\beta r} \tag{3.9}$$

$$\lambda_{\alpha\beta s} = L_s i_{\alpha\beta s} + L_m i_{\alpha\beta r} \tag{3.10}$$

$$\lambda_{\alpha\beta r} = L_m i_{\alpha\beta s} + L_r i_{\alpha\beta r} \tag{3.11}$$

Fig. 3.2 shows the electric circuits representation of the above set of equations for the α and β components. It can be noted that the stator and rotor circuits are linked by the magnetizing inductance L_m. Moreover, all machine variables are rotating in steady-state at the fundamental excitation frequency, ω_e.
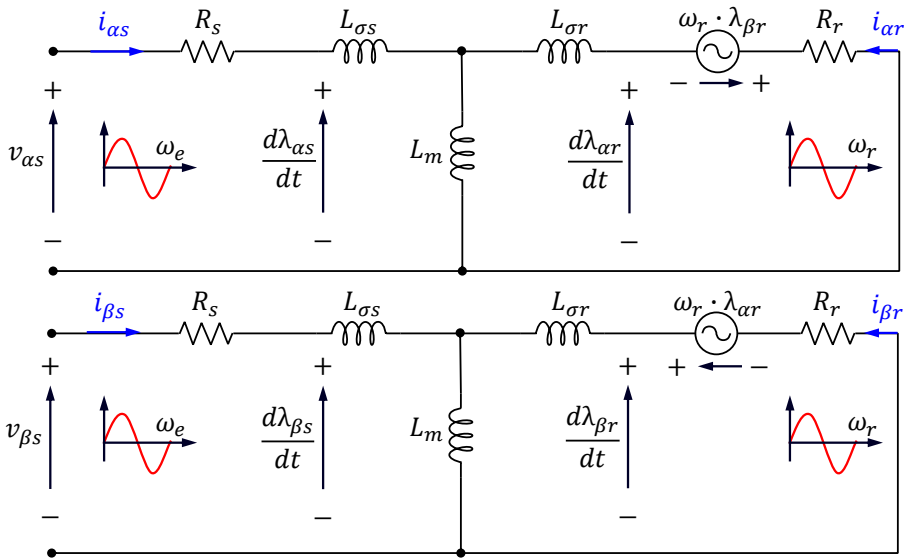
Figure 3.2: IM equivalent circuit in the stationary ($\alpha\beta$) reference frame.

The stator and rotor dynamic equations of the IM in the stationary reference frame (3.8) - (3.11) can be transformed to a reference frame rotating synchronously with the fundamental excitation frequency, ω_e (see red arrows in Fig. 3.1b). The transformation of a generic complex vector quantity between the stationary and the synchronous reference frame, denoted by the superscript " ^{e}" is defined by 3.12 for the case of a single complex vector quantity and 3.13 for its derivative, thus the resulting stator and rotor voltage and fluxes equations are given by (3.14)-(3.17). Note that p is the derivative operator.

45

$$x_{\alpha\beta} = x_{dq}^e e^{j\omega_e t} \tag{3.12}$$

$$px_{\alpha\beta} = (p + j\omega_e)\, x_{dq}^e e^{j\omega_e t} \tag{3.13}$$

$$v_{dqs}^e = R_s i_{dqs}^e + \frac{d\lambda_{dqs}^e}{dt} \tag{3.14}$$

$$0 = R_r i_{dqr}^e + \frac{d\lambda_{dqr}^e}{dt} + j(\omega_e - \omega_r)\lambda_{dqs}^e \tag{3.15}$$

$$\lambda_{dqs}^e = L_s i_{dqs}^e + L_m i_{dqr}^e \tag{3.16}$$

$$\lambda_{dqr}^e = L_m i_{dqs}^e + L_r i_{dqr}^e \tag{3.17}$$
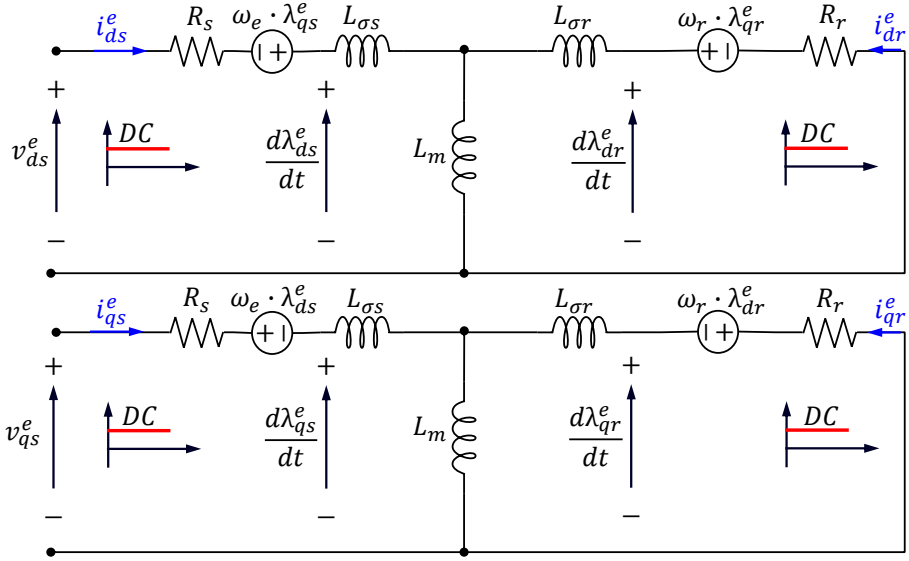
Figure 3.3: IM equivalent circuit in the synchronous (dq) reference frame.

The equivalent circuit of the IM with space vectors referred to the synchronous reference frame is shown in Fig. 3.3. The equivalent circuit is similar to the one in Fig. 3.2, however, the coupling terms between the d and q axis sub-circuits exist in both side, i.e., the stator and the rotor. Also, as all machine variables are rotating in synchronism with the fundamental frequency, they appear as DC signals in steady-state.

3.2.2 Torque Equations

Combining the stator, rotor and flux complex vectors, the electromagnetic torque produced by the IM can be expressed in several forms either in station-

ary reference frame (3.18) or in synchronous reference frame (3.19)-(3.21) [105]; $\overline{x}$ indicates the conjugate of the complex vector; $\sigma = 1 - \frac{L^2}{L_s L_r}$ is the leakage coefficient and $\Im$ is the imaginary term.

$$T_e = \frac{3}{2} \cdot P \cdot \Im\{\lambda_{\alpha\beta s} \cdot \overline{i_{\alpha\beta s}}\} \tag{3.18}$$

$$T_e = \frac{3}{2} \cdot P \cdot \Im\{\overline{\lambda_{dqs}^e} \cdot i_{dqr}^e\} \tag{3.19}$$

$$T_e = \frac{3}{2} \cdot \frac{L_m}{L_r} \cdot P \cdot \Im\{\overline{\lambda_{dqr}^e} \cdot i_{dqs}^e\} \tag{3.20}$$

$$T_e = \frac{3}{2} \cdot \frac{L_m}{\sigma L_r L_s} \cdot P \cdot \Im\{\overline{\lambda_{dqr}^e} \cdot \lambda_{dqs}^e\} \tag{3.21}$$

$$T_e = \frac{3}{2} \cdot P \cdot \frac{|\lambda_r|^2}{R_r} \cdot \omega_{sl} \tag{3.22}$$

3.2.3 Machine Characteristics and Design Aspects

Traction drives commonly receive a torque command from an outer control loop, which is responsible for speed control. The maximum torque that can be produced at a given speed will essentially depend on the current limits of the machine and power converter (due to losses) and on the maximum flux, which is limited by saturation and the available DC link voltage. For most IM designs, the maximum voltage and field weakening occur at the same speed, i.e., field weakening is a direct consequence of reaching the voltage limit. This is shown schematically in Fig. 3.4. For rotor speeds $\omega_r < \omega_{base}$, the machine operates with a rated flux and current, with the voltage increasing proportionally to the rotor speed, mainly due to the back-emf. If $\omega_r > \omega_{base}$, the flux, and consequently torque, must be decreased. The current can still be maintained at its rated value until the machine enters field-weakening region II [106].

IM designs for railway traction are often aimed at reducing the size of the machine, which can be desirable or even imperative due to room constraints. For this purpose, the voltage characteristic of the conventional design in Fig. 3.4 can be modified by rewinding the stator, varying the number of turns, and gauging the wire [106, 107]. If the modification is made such that $N_2 < N_1$, with N_1 and N_2 being the number of turns for the conventional and modified designs, respectively, and the active conductor area in each stator slot remaining unchanged, i.e., $N_1 \cdot S_1 = N_2 \cdot S_2$, and S_1 and S_2 being the area of the conductor for the conventional and modified designs, respectively, both machines should be able to produce the same amount of torque, as the
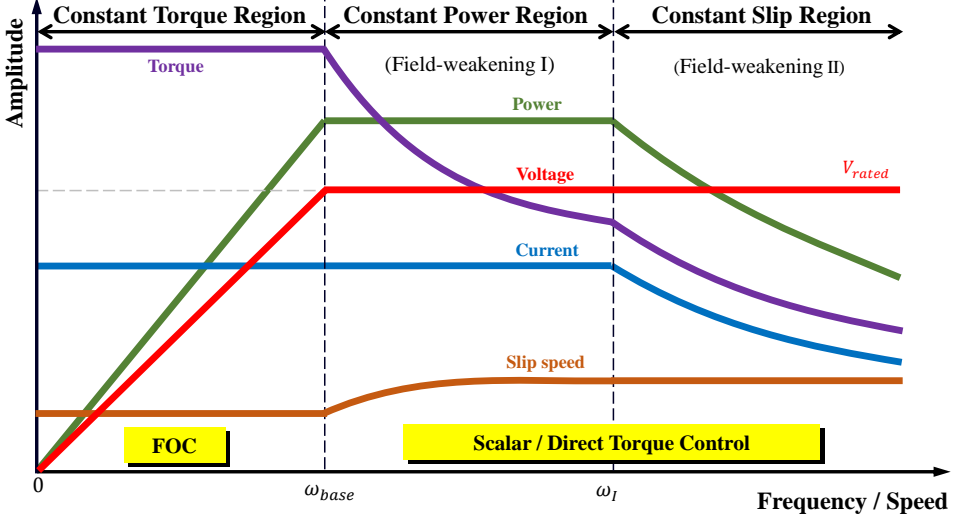
Figure 3.4: IM steady-state regions of operation vs. speed. It is assumed that torque reduction and field weakening occur at the same frequency.

total current circulating within the stator slots and the rest of the machine dimensions are the same in both cases [107]. Since the number of turns have been reduced, the voltage vs. speed characteristic is also modified. As seen in Figure 3.5(a) (dashed line), for $\omega_r = \omega_1$, the machine is far from its voltage limit. It can also be observed that for $\omega_r < \omega_1$, the current of the modified machine design is $\frac{N_1}{N_2}$ larger than for the conventional design. This does not imply an increase of joule losses, as the wire in the modified design is thicker, and the current density is the same in both cases. Since, at $\omega_r = \omega_1$, the modified machine operates well below its voltage limit, there is no need to decrease the flux at this point; instead, the nominal air gap flux density can be maintained until $\omega_r = \omega_2$ (region ② in Fig. 3.5), i.e., the full flux range is extended. The fact that the flux weakening region is reduced while the torque characteristic remains unchanged enables a reduction of the stator current for $\omega_r > \omega_1$. Consequently, assuming that the dimensions of the machine do not change, the extended full flux range design in Fig. 3.5 would allow a significant decrease of the current density in regions ② and ③ (i.e., at high train speeds) and consequently of joule losses, i.e., would be more efficient compared to the conventional design.

However, the design with an extended full flux range offers other possibilities. The torque of an IM can be written as (3.23), where V_{rotor} is the active volume of the rotor, J is the stator surface current density, B is the air gap flux
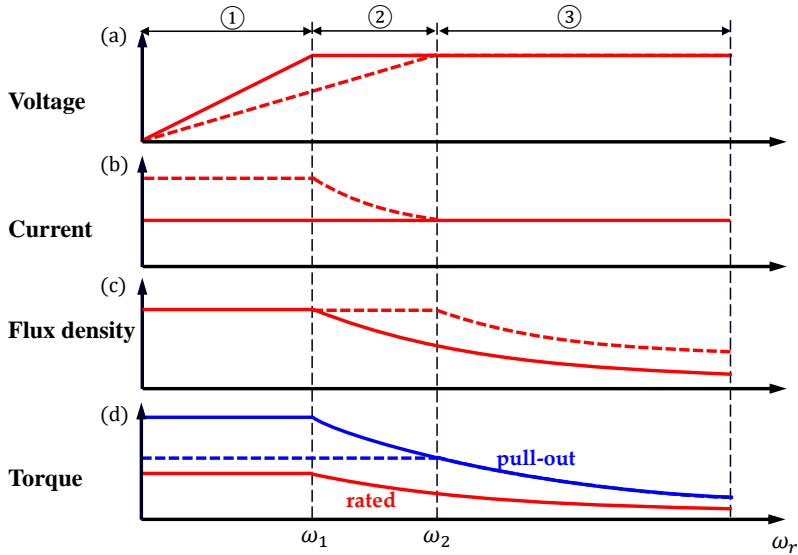
Figure 3.5: Conventional (-) and extended full flux range (- -) IM design behavior: (a) Stator voltage magnitude; (b) Stator current magnitude; (c) Flux density; (d) Electromagnetic torque (rated & pull-out). Both machines are designed to provide the same torque vs. speed characteristic and have the same voltage limit.

density, ϕ is the angle between J and B vectors, and k_1 is a constant which depends on the machine winding design [107].

$$T_e = k_1 \cdot V_{rotor} \cdot J \cdot B \cdot \cos\phi \tag{3.23}$$

As the extended full flux range design provides higher flux densities at high speeds and the current density J remains constant, it is possible to reduce the volume of the rotor, and consequently the size of the machine, without affecting the torque production capability, i.e., the design with extended full flux in Fig. 3.5 will be smaller.

It must be noted, however, that redesigning the machine brings drawbacks that must also be considered. First, the size of the inverter is increased, as the current that the semiconductors must handle is increased by a factor of $\frac{N_1}{N_2}$, while the voltage and power remain unaffected. However, this penalty is often not so relevant nowadays thanks to the latest developments in power devices [106]. Second, the pull-out torque in the low-speed region is significantly decreased, as shown in Fig. 3.5(d), which must be considered to guarantee that the machine meets the application requirements.

3.3 Control Techniques

Control methods for IMs can be classified into scalar and vector types, as shown in Fig. 3.6. The following discussion will primarily focus on the performance at high-speed, as this is normally the most challenging case.
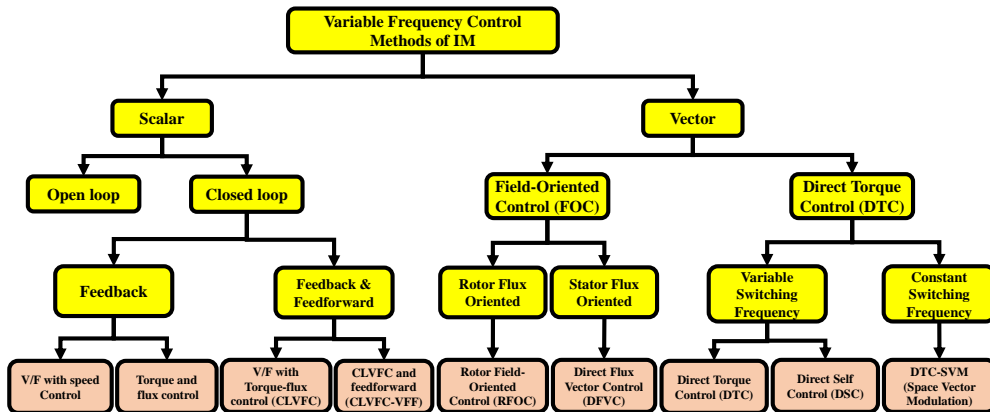
Figure 3.6: Classification of control methods for IMs.

Scalar methods are derived from the machine equivalent circuit in a steady-state. Consequently, they can operate properly in applications in which fast changes in the operating conditions of the machine (torque, speed, flux,...) are not required. On the contrary, vector control methods are based on the dynamic equations of the machine, which, combined with proper control loops, allow the machine's torque capabilities to be fully exploited, without surpassing machine or power converter limits. Both types of methods are briefly discussed in the following. It must be noted, however, that the borderline between scalar- and vector-based methods is sometimes blurred, as there have been several proposals to enhance the dynamic response of scalar methods by adding control loops based on dynamic models.

3.3.1 Scalar Control

3.3.1.1 Open Loop

Open-loop V/F varies the stator voltage magnitude proportional to the frequency. This results in an (almost) constant flux. While simple, V/F control has some relevant limitations. The rotor speed is not precisely controlled due to slip. Additionally, an incorrect voltage to frequency ratio, voltage drop in the

stator resistance, variations of the DC link voltage feeding the inverter, etc., will result in incorrect flux levels, eventually modifying the operating point of the machine from the desired value.

3.3.1.2 Closed Loop

Closed-loop speed control with slip regulation (Fig. 3.7) has been widely used in IM traction drives [108]. Speed error generates the slip command ω_{sl}^* through a Proportional-Integral (PI) controller. Slip is added to the measured speed to produce the angular frequency of the stator voltage ω_e^*.
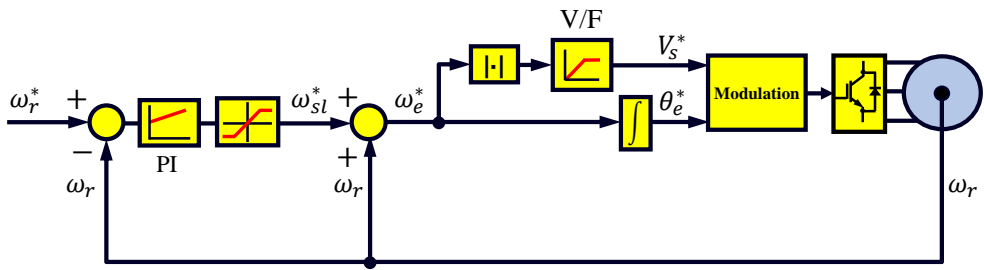
Figure 3.7: Closed loop V/F with speed control scheme.

The method in Fig. 3.7 is relatively simple to implement. However, the fact that coupling between flux and torque is not considered for the control results in very low bandwidths in the control to avoid over currents and torque pulsations. To overcome this problem, decoupling between flux and torque control loops can be used instead of the V/F ratio to obtain the desired stator voltage magnitude and angle (Fig. 3.8). Flux control loop uses the desired V/F characteristic to provide the base value of the stator voltage magnitude, with the rotor flux regulator providing the incremental voltage required to track the desired rotor flux with no error. The second control loop provides the base value for the slip $\hat{\omega}_{sl}$, which is obtained from the desired torque and the estimated rotor flux using (3.22). The torque regulator corrects the slip so that the desired torque is followed with no error.

Torque and flux can be estimated from the (commanded) stator voltages and the (measured) stator currents using the voltage model (3.24) (see Fig. 3.9a); "$\hat{x}$" indicates estimated variables/parameters. From (3.18), the torque is obtained using (3.25).
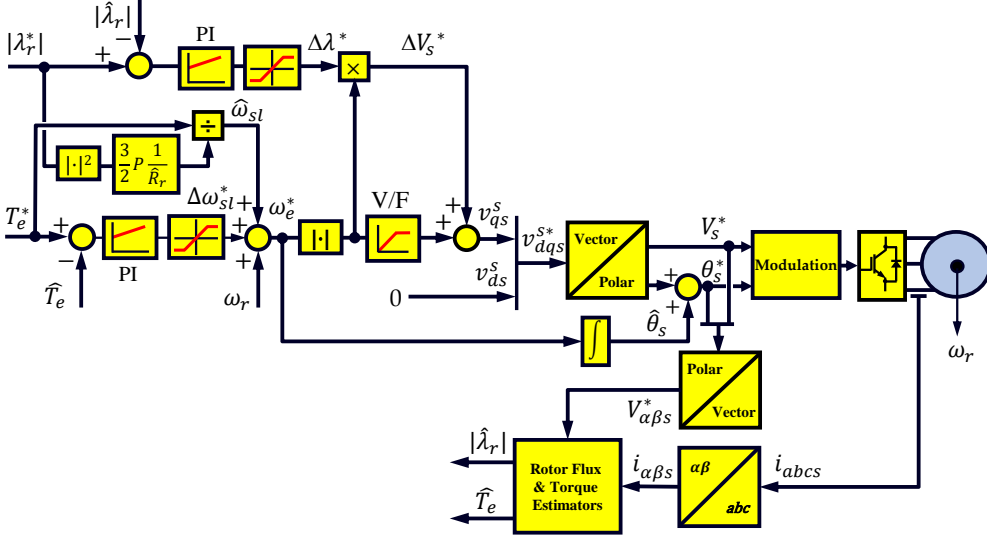
Figure 3.8: Closed loop stator voltage oriented V/F with slip & flux control (CLVF).

$$\hat{\lambda}_{\alpha\beta s} = \int \left(V^*_{\alpha\beta s} - \hat{R}_s i_{\alpha\beta s} \right) \cdot dt \tag{3.24}$$

$$\hat{T}_e = \frac{3}{2} P \left(\hat{\lambda}_{\alpha s} i_{\beta s} - \hat{\lambda}_{\beta s} i_{\alpha s} \right) \tag{3.25}$$

While this approach can provide good results at medium and high speeds, it shows some relevant weaknesses at low and zero speed:

- Drift problems derived from the pure integrator infinite gain at DC value in (3.24). Thus, the pure integrator is replaced in practice by a first-order system to avoid this problem [109].

- The non-ideal behavior of the inverter (dead time, voltage drop in the power switches, etc) will produce a mismatch between the command voltages and the fundamental wave of the actual voltage applied to the machine. This effect becomes significant at low speed, as the stator voltage magnitude varies proportionally to the fundamental frequency.

- Errors in the estimated stator resistance $\hat{R}_s$, which varies with temperature, can be relevant at low speed, as the stator voltage magnitude is small.

Alternatively, stator, rotor fluxes and torque can be estimated using current model shown in Fig. 3.9b at low speeds. However, it has some drawbacks

as parameter sensitivity dependence such as rotor time constant (especially related to rotor resistance $\hat{R}_r$) and magnetizing inductance. Moreover, the knowledge of rotor position is mandatory which requires an additional position sensor.
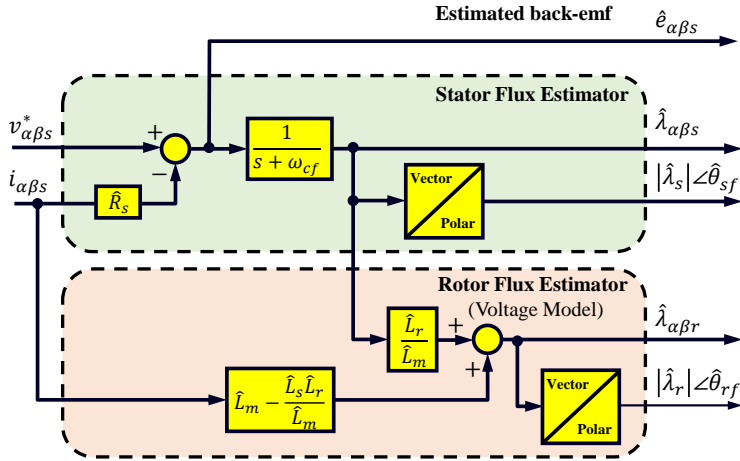
(a)
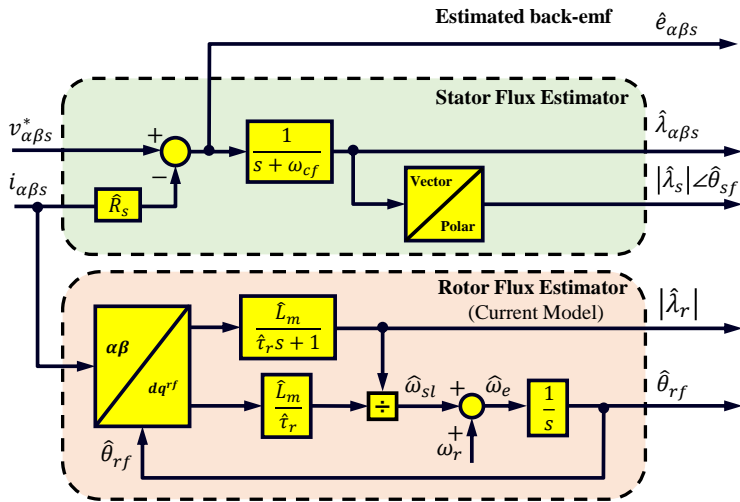
(b)

Figure 3.9: Stator and rotor flux estimation: (a) using voltage model; (b) using current model.

3.3.2 Vector Control

Vector control methods are aimed at directly manipulating the IM fields and torque. These methods are based on the well-known dq-models discussed in subsection 3.2.1.

3.3.2.1 Field-Oriented Control

Field-Oriented Control (FOC) represents flux and torque as a function of stator currents in a synchronous reference frame, with high-bandwidth current regulators being used to provide the voltage command to the inverter. For analysis and control purposes, alignment of the synchronous reference frame into one of the machine fluxes (rotor, stator, or airgap) is advantageous [110]. Common methods can be summarized as follows:

a) **Rotor Flux Orientation**, Substituting (3.16) and (3.17) into (3.14) and (3.15), and aligning the synchronous reference frame with rotor flux (i.e., $\lambda_r^{rf} = \lambda_{dr}^{rf}$), the stator voltage equation is expressed as (3.26)-(3.27) where $\hat{R}_s' = \hat{R}_s + \hat{R}_r \left(\frac{\hat{L}_m}{\hat{L}_r} \right)^2$. The rotor flux and torque equations are given by (3.28) and (3.29) respectively. Thus all variables are referred to a reference frame aligned with the rotor flux which permits independent control of machines' rotor flux and torque through the d and q axis components of the stator current respectively (see Fig. 3.10).

$$v_{ds}^{rf} = \hat{R}_s' i_{ds}^{rf} + \hat{L}_{\sigma s} \frac{di_{ds}^{rf}}{dt} - \hat{\omega}_e \hat{L}_{\sigma s} i_{qs}^{rf} - \hat{R}_r \frac{\hat{L}_m}{\hat{L}_r^2} \hat{\lambda}_{dr}^{rf} \tag{3.26}$$

$$v_{qs}^{rf} = \hat{R}_s' i_{qs}^{rf} + \hat{L}_{\sigma s} \frac{di_{qs}^{rf}}{dt} + \hat{\omega}_e \hat{L}_{\sigma s} i_{ds}^{rf} + \hat{\omega}_r \frac{\hat{L}_m}{\hat{L}_r} \hat{\lambda}_{dr}^{rf} \tag{3.27}$$

$$L_m i_{ds}^{rf} = \tau_r \frac{d\lambda_r^{rf}}{dt} + \lambda_r^{rf} \tag{3.28}$$

$$T_e = \frac{3}{2} P \frac{L_m}{L_r} \lambda_r^{rf} i_{qs}^{rf} \tag{3.29}$$

RFOC is one of the most popular options for the high-performance control of IM drives [111], although RFOC is often used in high-speed trains at relatively low speeds, the inverter operates in the linear region and with an adequate switching to fundamental frequency ratio. However, its use at high speeds presents multiple problems, including the lack of a voltage margin
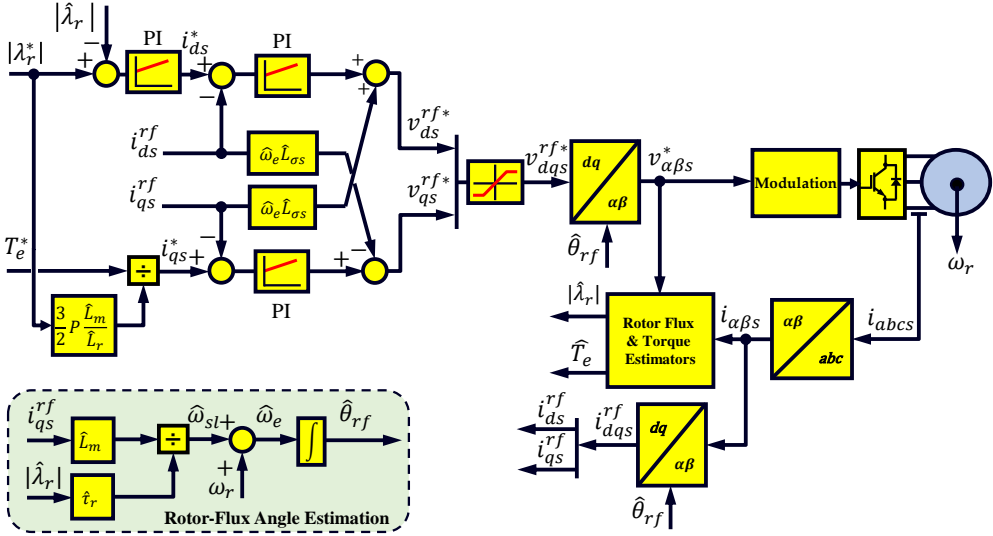
Figure 3.10: Block diagram of rotor flux field-oriented control (RFOC).

in the inverter for proper operation of the current regulator, distortions in the currents due to overmodulation, and delays intrinsic to the reduced switching frequency.

b) **Stator Flux Orientation**, in this case, all variables are referred to a reference frame aligned with the stator flux. Stator voltage equation can be expressed as (3.30) and (3.31). It can be observed that the stator flux variation can be regulated through the d-axis voltage, and the torque is then controlled through the q-axis current (3.32), with a current regulator being used for this purpose.

$$v_{ds}^{sf} = \hat{R}_s i_{ds}^{sf} + \frac{d\hat{\lambda}_{ds}^{sf}}{dt} \tag{3.30}$$

$$v_{qs}^{sf} = \hat{R}_s i_{qs}^{sf} + \hat{\omega}_{sf}\hat{\lambda}_{ds}^{sf} \tag{3.31}$$

$$T_e = \frac{3}{2}P\hat{\lambda}_{ds}^{sf} i_{qs}^{sf} \tag{3.32}$$

Direct Flux Vector Control (DFVC) is one of the methods using stator flux-oriented control (see Fig. 3.11) [112]. Stator flux $\alpha\beta$-components are estimated from the voltage-model-based flux estimator (Fig. 3.9a). The synchronous frequency can be obtained from the estimated stator flux and back-emf (3.33) [113], avoiding the use of stator flux angle derivative and time-consuming trigonometric functions.

$$\hat{\omega}_{sf} = \frac{\hat{\theta}_{sf}}{dt} = \frac{d}{dt}\left[tan^{-1}\left(\frac{\hat{\lambda}_{\beta s}}{\hat{\lambda}_{\alpha s}}\right)\right] = \frac{\hat{\lambda}_{\alpha s} \cdot \hat{e}_{\beta s} - \hat{\lambda}_{\beta s} \cdot \hat{e}_{\alpha s}}{\left|\hat{\lambda}_s\right|^2} \qquad (3.33)$$

At low speeds, DFVC can operate either with rated stator flux or a maximum torque per ampere (MTPA) strategy, same as RFOC, to improve the efficiency (will be discussed in the subsection 3.4.2). Above the base speed, flux is reduced according to $|\lambda_s^*| \leq \frac{V_{max} - \hat{R}_s i_{qs}^{sf}}{|\hat{\omega}_{sf}|}$, where V_{max} is the maximum output voltage of the inverter, which depends on the available DC-link voltage and the modulation method. Operation in overmodulation is feasible, but a voltage margin must be preserved for proper operation of the q-axis current regulator, meaning that operation with a maximum output voltage (i.e., six-step) is not possible. Furthermore, operation in overmodulation forces a reduction of the current regulator bandwidth to mitigate the effects of the resulting current harmonics in this case. Therefore, current regulator gains may need to be adapted to machine speed.

It is finally noted that Fig. 3.11 includes a mechanism to limit the torque angle δ between the stator and rotor fluxes so that it is smaller than the pull-out torque angle of $\delta = 45$ electrical degrees [112].
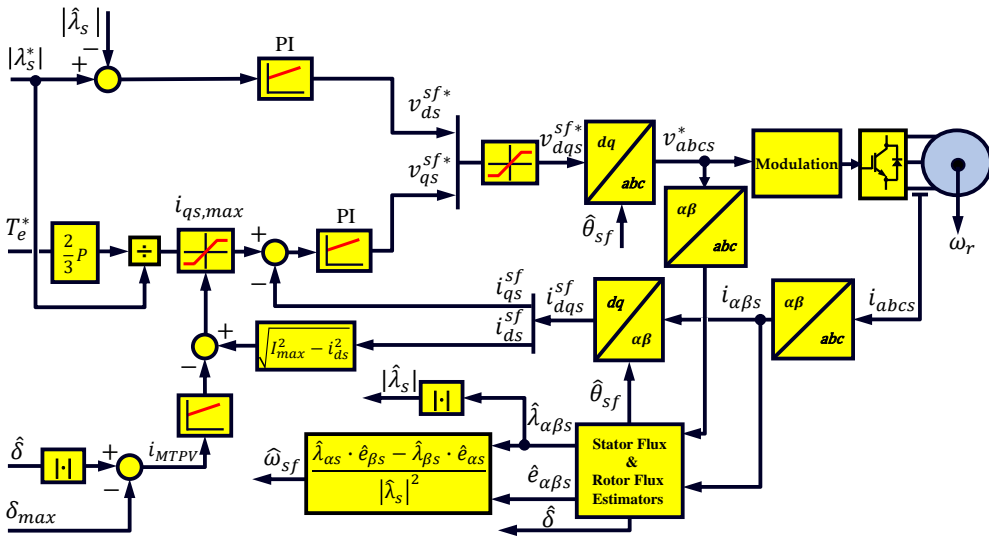
Figure 3.11: Block diagram of Direct Flux Vector Control (DFVC).

3.3.2.2 Direct Torque Control

Direct Torque Control (DTC) methods control torque by controlling the stator flux magnitude and the angle with respect to the rotor flux. Recalling equation (3.21), torque can be expressed as (3.34), with δ being the torque angle. The stator flux is controlled through stator voltage where V_s the inverter output voltage vector. Note that the voltage drop in the stator resistance is neglected.

$$T_e = \frac{L_m}{\sigma L_s L_r} \left| \hat{\lambda}_{\beta s} \right| \left| \hat{\lambda}_{\beta r} \right| \sin(\delta) \tag{3.34}$$

Considering two-level Voltage Source Inverter (VSI) used which can produce six active vectors ($V_1 \rightarrow V_6$) and two zero vectors (V_0,V_7) (see Fig. 3.12(a)). Fig. 3.12(b) shows the effect of every active voltage vector on the torque and stator flux.
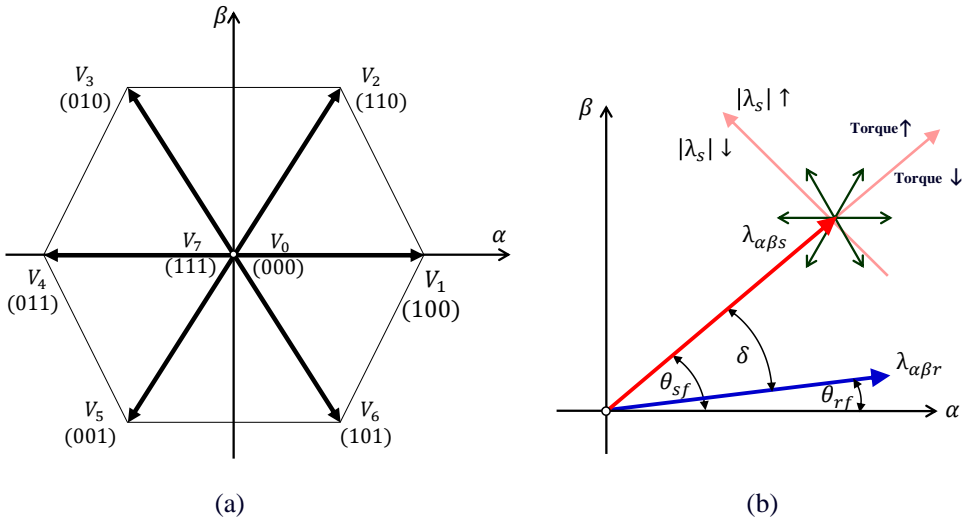
Figure 3.12: Voltage vectors and flux trajectories for Direct Torque Control (DTC) schemes: (a) two-level inverter states, (b) variation of stator flux and torque depending on the voltage vector being applied.

Assuming that the rotor flux is rotating in the anti-clockwise direction, voltage vectors located ahead of the stator will make the stator flux to move forward, increasing the power angle and consequently the torque. On the contrary, voltage vectors located behind the stator flux will force the flux to

move backwards, producing a fast reduction of the power angle and, therefore, of torque. Zero voltage vectors will stop the rotation of stator flux; since the rotor flux is still rotating, torque angle and consequently torque will decrease.

DTC can be divided into two main groups based on the resulting switching frequency as follows:

Variable Switching Frequency. Switching-Table-Based (ST-DTC) was introduced by Takahashi and Noguchi [114] in the mid-1980s. Two hysteresis controllers are used to control the stator flux and torque directly. The hysteresis control signals are sent to a look-up table to select the voltage vectors required to achieve high dynamics (see Fig. 3.14a). The fact that the switching frequency is not defined and operation in overmodulation and six-step is not straightforward, makes this method inadequate for high-power railway drives [115].
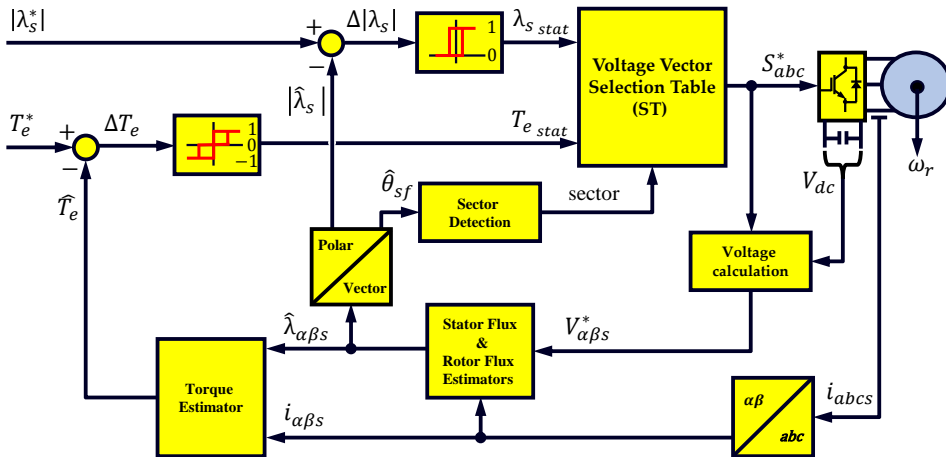
Figure 3.13: Block diagram of Switching-Table-Based Direct Torque Control (ST-DTC).

Direct-Self Control (DSC) was proposed by Depenbrock [116] for high-power drives, its block diagram is shown in Fig. 3.14. Three hysteresis controllers determine the voltage applied to the machine by comparing the command flux magnitude and the estimated for each phase. A two-level hysteresis torque controller determines the amount of zero voltage vector to be used. DSC produces a hexagonal stator flux trajectory as seen in Fig. 3.14b.

From $\approx 30\%$ to $\approx 85\%$ of base speed, DSC offers a high dynamic response

and reduced switching losses, but at the price of a high current ripple. At high speeds ($>\approx 85\%$ of base speed), zero voltage vectors are not selected anymore, DSC providing, therefore, a natural transition into overmodulation and eventually into six-step. A PI controller driven by the torque error can be used to reduce stator flux command once the control enters overmodulation (dashed red box in Fig. 3.14); more elaborated options can be also implemented [117]. Below $\approx 30\%$ of the base speed, there is a degradation of the control performance, a detailed description can be found in [118, 119].

(a)

(b)
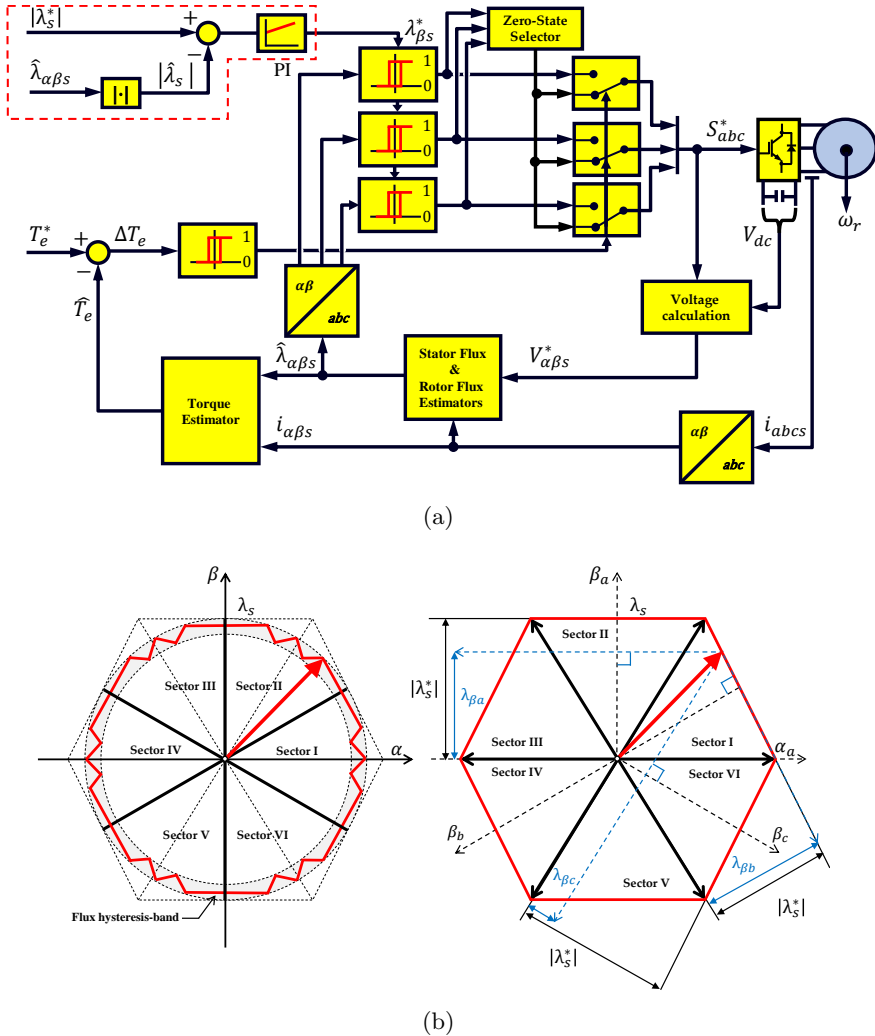
Figure 3.14: Direct-Self Control (DSC) scheme: (a) block diagram; (b) flux trajectory.

Constant Switching Frequency. DTC with constant switching frequency calculates the required stator voltage vector averaged over a sampling period

to achieve the desired torque and stator flux. The voltage vector is synthesized using space vector modulation (SVM), so these methods are often termed as DTC-SVM. DTC-SVM proposed in [120] uses two PI regulators to control stator flux and torque providing respectively the d- and q- reference stator voltage components to the modulator (SVM). However, this scheme suffers from the same limitation of ST-DTC to operate in the overmodulation region and six-step.
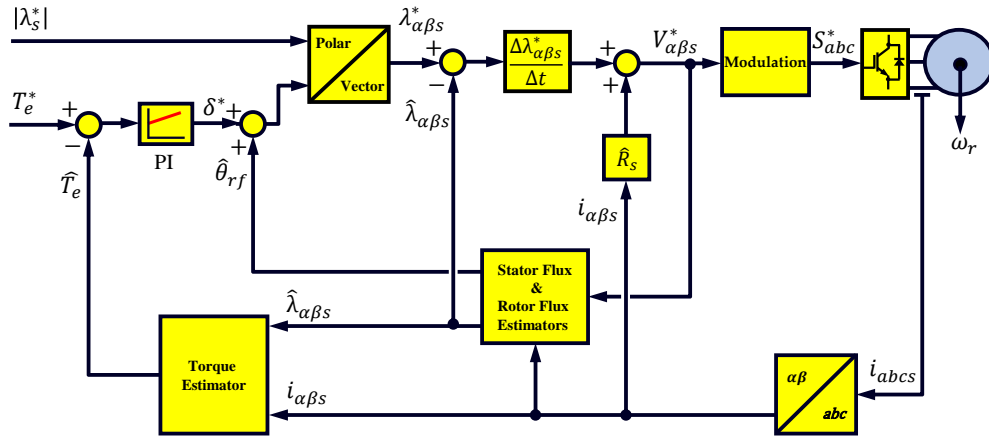
(a)
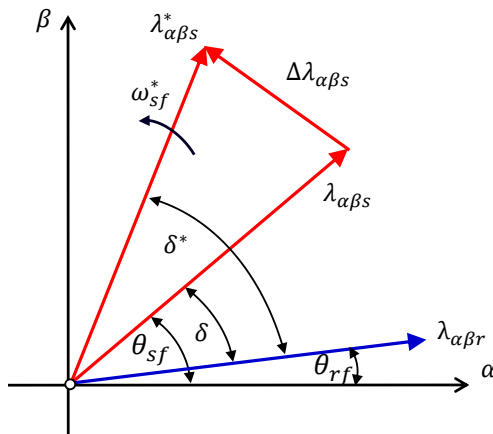
(b)

Figure 3.15: Modified Direct-Torque Control (MDTC) scheme: (a) block diagram; (b) flux trajectory.

The DTC-SVM scheme shown in Fig. 3.15a controls the torque through the torque angle (3.34) [121, 122]. The stator flux angle is obtained from the

estimated rotor flux angle and the reference torque angle provided by a PI controller, Fig. 3.15b. The required stator voltage vector $V^*_{\alpha\beta s}$ to cancel the stator flux error vector $\hat{\lambda}^*_{\alpha\beta s}$ at the end of the next sampling period, Δt, can be obtained as (3.35). This equation considers the voltage drop in the stator resistance.

$$V^*_{\alpha\beta s} = \frac{\Delta\hat{\lambda}^*_{\alpha\beta s}}{\Delta t} + \hat{R}_s i_{\alpha\beta s} \qquad (3.35)$$

The scheme in Fig. 3.15a works properly for relatively small sampling periods (Δt), its implementation being simple and retaining the fast dynamics of DTC in this case. Unfortunately, it is not suitable in the overmodulation region, where voltage constraints eventually result in magnitude and phase errors in the actual stator flux vector, leading into instability problems. DTC-SVM scheme was improved in [123] by including a predictive term to mitigate the stator flux delay and extend the operation to six-step. However, this was at the price of a significant complexity increase compared to the original DTC proposal in [114]. Furthermore, (3.35) applies for relatively small values of the control period, Δt, but can result in meaningful steady-state errors in case of low switching frequencies. Those limitations make the use DTC-SVM for railway traction applications arguable.

Several methods aimed to improve the dynamic response of scalar control have been reported in the literature [124–129]. In [124], a feedforward term is added to the voltage magnitude command to compensate for the voltage variation caused by torque changes, which is claimed to decouple torque and flux and improve both the dynamic and steady-state response of the V/F control. As the parameters required by the decoupling block will change with the operating conditions, the use of look-up tables or adaptation mechanisms might be required. This will increase the complexity of the control. In [127, 128], a transient voltage vector is estimated and added to the voltage vector command improving the transient response of the scalar V/F method. However, the estimated transient vector is obtained from d-q current regulators operating in parallel of the main V/F controllers which could be problematic when the machine enters the overmodulation region and the voltage margin required for the normal operation of the current controller is lost. Methods reported in [125, 126, 129] are targeted to overcome the limitations of scalar control at low fundamental frequencies only, being therefore disregarded.

3.3.3 Proposed Torque Dynamics Enhancement for Scalar Control

In railway traction applications, RFOC is typically used at low speeds, and scalar control is widely used when the drive operates close or at the voltage limit to overcome the deterioration of the current regulator performance in the overmodulation region [130]. However, scalar control methods show slow torque dynamics due to the coupling between torque and flux and the need to prevent overcurrents. This is not a concern for normal operation of traction drives. However, modern trains may require fast torque dynamics for advanced modes of operation, such as adhesion control, torsional torque vibration mitigation, and cancellation of torque ripple in traction drives fed from AC catenaries without an intermediate 2F filter (this topic will be discussed in details later in Chapter 5) [80, 131].

Considering that the induction machine in Fig. 3.10 is operating at a relatively high speed. The q-axis of the synchronous reference is defined to be aligned with the stator voltage vector as in (3.36) and (3.37). If a sudden change in the torque command is applied, the slip angular speed $\hat{\omega}_{sl}$ will increase proportionally (see Fig. 3.8), increasing therefore the angular speed of the stator voltage vector. The magnitude of the stator voltage v_{qs}^s will also increase according to the predefined V/Hz ratio to keep the flux constant. Such sudden changes of the stator voltage angle and magnitude can result in large transient currents. Due to this, the rate of variation of the torque command, i.e. the dynamic response of the scalar control, must be limited.

$$v_{ds}^s = 0 \tag{3.36}$$

$$v_{qs}^s = V_s^* = |\hat{R}_s I_s + j\hat{\omega}_e \hat{\lambda}_s| \cong |\hat{\omega}_e \hat{\lambda}_s| \tag{3.37}$$

To understand how the dynamic response of the scalar control can be enhanced, it is useful to analyze the behavior of the stator voltage from a rotor flux-oriented control perspective. Equations (3.26) and (3.27) can be used to define the feedforward terms aimed to improve the dynamic response of the scalar control in Fig. 3.7. Despite of its apparent complexity, and the associated parameter sensitivity, a number of simplifications are feasible:

1) The resistive voltage drops $\hat{R}_s' i_{ds}^{rf}$ and $\hat{R}_s' i_{qs}^{rf}$ can be neglected in high speed operation;

2) $\hat{L}_{\sigma s} \frac{di_{ds}^{rf}}{dt}$ equals zero assuming that the flux is kept constant;

3) $\hat{R}_r \frac{\hat{L}_m}{\hat{L}_r^2} \hat{\lambda}_{dr}^{rf}$ can be shown to be negligible for high power machines due to the relatively small value of the rotor flux and rotor resistance.

The relationship between the stator voltage, q-axis current and flux can be then simplified as:

$$v_{ds}^{rf} \cong -\hat{\omega}_e \hat{L}_{\sigma s} i_{qs}^{rf} \tag{3.38}$$

$$v_{qs}^{rf} \cong \hat{L}_{\sigma s} \frac{di_{qs}^{rf}}{dt} + \hat{\omega}_e \hat{L}_{\sigma s} i_{ds}^{rf} + \hat{\omega}_r \frac{\hat{L}_m}{\hat{L}_r} \hat{\lambda}_{dr}^{rf} \tag{3.39}$$

Equation (3.38) shows the feedforward term to be added to the d-axis voltage component v_{ds}^{rf} to take into account changes in the torque (i.e. q-axis current). The transient response improvement is achieved by the $\hat{L}_{\sigma s} i_{qs}^{rf}$ term of the stator voltage q-axis component in (3.39). This term is a function of the q-axis current derivative and enhances therefore torque dynamic behavior. Since this action must be applied to the scalar control, the q-axis current is transformed into the slip angular speed using (3.40).

$$\hat{\omega}_{sl} = \frac{\hat{L}_m}{\hat{\tau}_r |\lambda_r^*|} i_{qs}^{rf} \tag{3.40}$$

Finally, the feedforward terms aimed to improve the dynamic response are given in (3.41) & (3.42) by substituting (3.40) in (3.38) & (3.39), where the steady-state value is nearly achieved from the V/F relation, i.e. $|\hat{\omega}_e \hat{\lambda}_s| \cong \hat{\omega}_e \hat{L}_{\sigma s} i_{ds}^{rf} + \hat{\omega}_r \frac{\hat{L}_m}{\hat{L}_r} \hat{\lambda}_{dr}^{rf}$ in (3.37). Fig. 3.16 shows the block diagram of the proposed method.

$$v_{ds_{FF}}^s \cong -\hat{\omega}_e \hat{L}_{\sigma s} \frac{\hat{\tau}_r |\lambda_r^*|}{\hat{L}_m} \hat{\omega}_{sl} \tag{3.41}$$

$$v_{qs_{FF}}^s \cong \hat{L}_{\sigma s} \frac{\hat{\tau}_r |\lambda_r^*|}{\hat{L}_m} \frac{d\hat{\omega}_{sl}}{dt} \tag{3.42}$$

The performance of the proposed method has been validated by simulation using MATLAB/Simulink. Fig. 3.17 shows the response to a torque step from 2 kNm to 3 kNm of RFOC (Fig. 3.10), scalar control (Fig. 3.8), and scalar
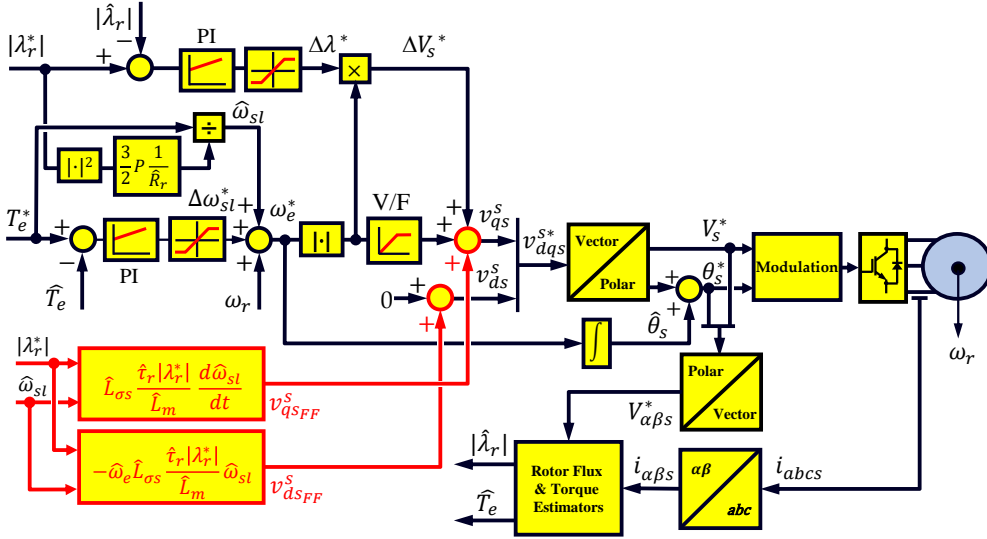
Figure 3.16: Proposed feedforward compensation for stator voltage oriented scalar V/F control (CLVF&FF).

control with both dq-axis feedforward terms (Fig. 3.16). Top subfigures show the torque, stator voltage and current vectors response in the time domain while bottom subfigures show the vector diagrams. For the sake of comparison, all vector diagrams are shown in the rotor-flux reference frame.

The superior dynamic performance of RFOC over scalar control is readily observed from Fig. 3.17a and Fig. 3.17b. The differences in the trajectories followed by the voltage in Fig. 3.17d and Fig. 3.17e explain this behavior. For the RFOC case, current controllers force the current to move along the q-axis, while for the scalar control case, a deviation from the desired trajectory is observed. Adding the d-axis feedforward term is seen to improve the dynamic response providing the correct position of the stator voltage vector, but this results in unwanted torque and current oscillations. The dynamic response with only d-axis feedforward has been omitted as it provides an unsatisfactory response. Full feedforward (Fig. 3.17c and Fig. 3.17f) are seen to provide a dynamic response comparable to that of field-oriented control. However, it is seen the stator voltage vector reaches large values during the transient, which is undesired. This behavior can be avoided by limiting the maximum slope of the torque command, which is a common practice in traction drives.

While the fast changes in the torque command shown in Fig. 3.17 are not normally needed, there is a number of operating conditions in which they might be required. This would include implementing anti-slip control and active
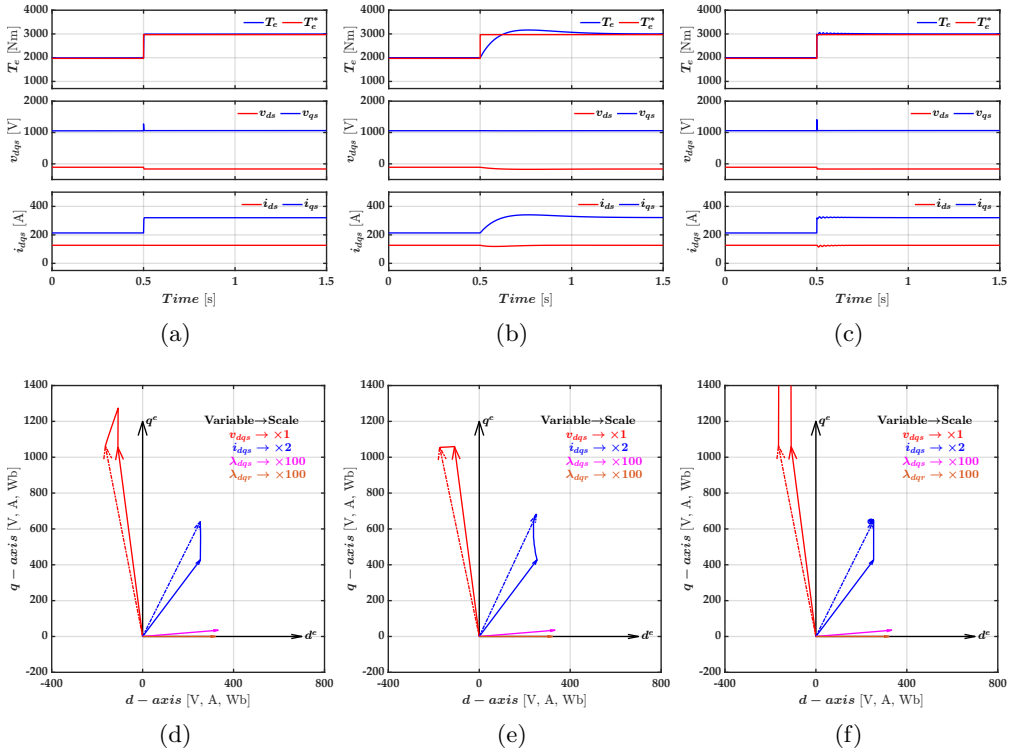
Figure 3.17: Response to a torque command step change: (a), (d) RFOC; (b), (e) CLVF; (c), (f) CLVF&FF. Top: time response. Bottom: vector trajectories. Solid vector: starting position. Dashed vector: steady-state position.

cancellation of torsional torque vibrations. As a common example, mitigating torque ripples produced by the 2F oscillation of the DC-link voltage in AC catenaries when a 2F filter is not used, the control should be able to produce torque oscillations at frequencies around twice the catenary frequency [132]. Fig. 3.18 shows the dynamic response of the control schemes under discussion subjected to a torque command oscillating at 100 Hz (which corresponds to 2F for 50 Hz catenaries). While RFOC (see Fig. 3.18a & 3.18d) precisely follows the torque command, closed loop scalar V/F is unable to track such fast torque variations (see Fig. 3.18b & 3.18e). Use of full feedforward 3.18c & 3.18f) is able to precisely produce the demanded oscillations in torque signal.

All the simulation results have shown so far used a linear voltage source. While this is useful for validation of the concepts, the use of the linear voltage source hides effects that can play a relevant role in the real system, as the current harmonics due to commutation and the delays intrinsic to PWM. The proposed method has also been validated when feeding the IM from a three-

level Neutral-Point Clamped inverter (3LNPC), as shown in Fig. 3.19. A step of 2 kNm is applied at $t = 0.5$s then a ramp of 1 kNm is applied at $t = 1.5$s (see Fig. the left column of Fig. 3.19).

It is observed from Fig. 3.19 that for the case of using a switching converter and the intrinsic delays due to modulation, the proposed method still shows excellent command tracking capabilities.
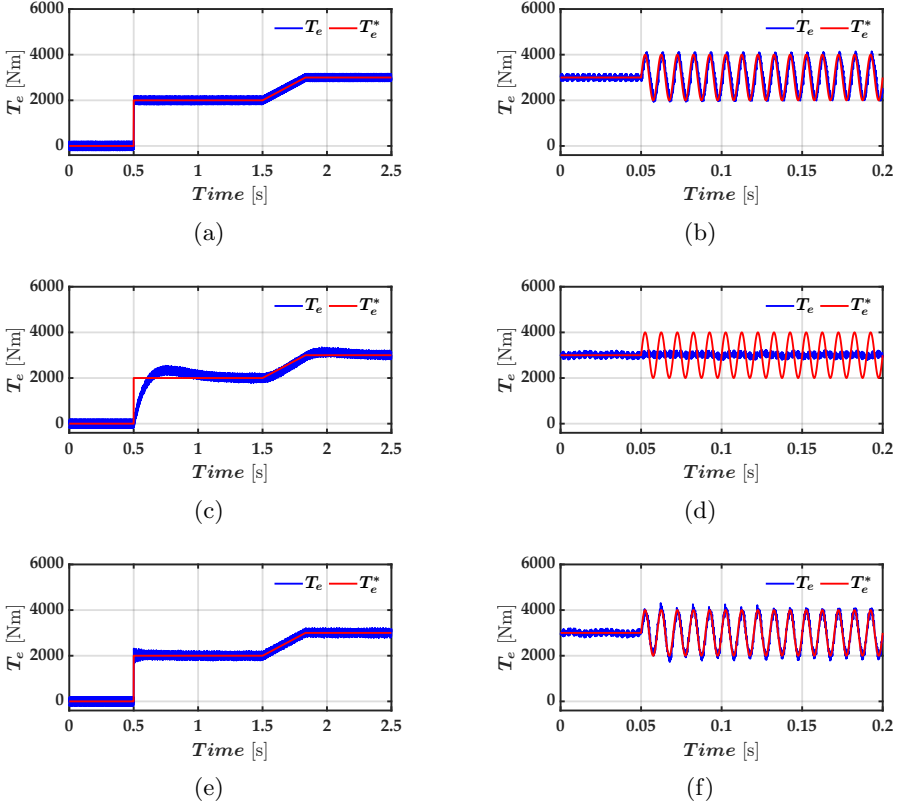
Figure 3.19: Response of IM connected to 3L-NPC: (a), (b) RFOC; (c), (d) CLVF; (e), (f) CLVF&FF. Left: with step/ramp torque command. Right: with 100 Hz injected oscillation torque command.

3.3.4 Comparative Analysis

Table 3.1 summarizes the main features and conclusions for the control methods discussed in subsections 3.3.1 and 3.3.2, including controlled variables and the easiness of operation at low speeds, overmodulation (high speed), and the transition to six-step. Regarding the dynamic response, it is important

to note that the torque ramp is normally limited in railway traction. Consequently, the response time to a step-like torque command might not be the most relevant metric for its evaluation; instead, the drive capability to follow the maximum torque ramp requested by the application might be more relevant, especially when the machine operates at a high speed in the field-weakening region. Closed loop V/F control (CLVFC), proposed Closed loop V/F control with feedforward compensation (CLVFVC&FF), Direct Flux Vector control (DFVC), and Direct Torque Control with space vector modulation (DTC-SVM) have been selected as a representative subset of the methods in Table 3.1, their behavior will be analyzed and compared by means of simulation in this Section.

Table 3.1: Summary of the presented control schemes for traction applications.

Properties / Performance	V/F with Feedback			FOC		DTC		
	V/F	CLVF	CLVF&FF	RFOC	DFVC	ST	DSC	DTC-SVM
Reference frame	λ_r	λ_r	λ_r	λ_r	λ_s	SRF.	SRF.	λ_r
Controlled variables	ω_r [1] λ_r; T_e	λ_r; T_e	λ_r; T_e	$\lambda_r \& i_{ds}$; i_{qs}	λ_s; i_{qs}	λ_s; T_e	λ_s; T_e	λ_s; T_e
Defined switching frequency	✔	✔	✔	✔	✔	✗	✗	✔
Low speed (linear modulation)	✔	✔	✔	✔	✔	✗	✗	✔
High speed (overmodulation)	✔	✔	✔	—	—	✗	✔	✗
Six-step operation	✔	✔	✔	✗	✗	✗	✔	✗
Dynamic response [2]	✗/✗	✗/—	—/✔	✔/—	✔/—	✔/✗	✔/✔	✔/✗

✔: favorable; —: neutral; ✗: unfavorable; "SRF." stands for stationary reference frame.

[1]: Implementation of an outer speed control loop for the rest of the methods is straightforward.

[2]: maximum torque dynamic response/capability to provide 3 kNm/s in overmodulation.

MATLAB/Simulink will be used for simulation. IM parameters for the base speed are given in appendix A.1. The simulation model implements asynchronous SVM with a switching frequency of 1 kHz at low speeds and Selective Harmonic Elimination (SHE) at high speeds. Infinite inertia is assumed. Consequently, the rotor speed remains constant throughout the simulation. This assumption is realistic considering the train mass. However, it is noted that it is not valid if wheel-rail slip occurs, this will be discussed in Chapter 4. The maximum torque ramp was limited to 3 kNm/s, which was imposed by the application. Simulation results are shown in Fig. 3.20.
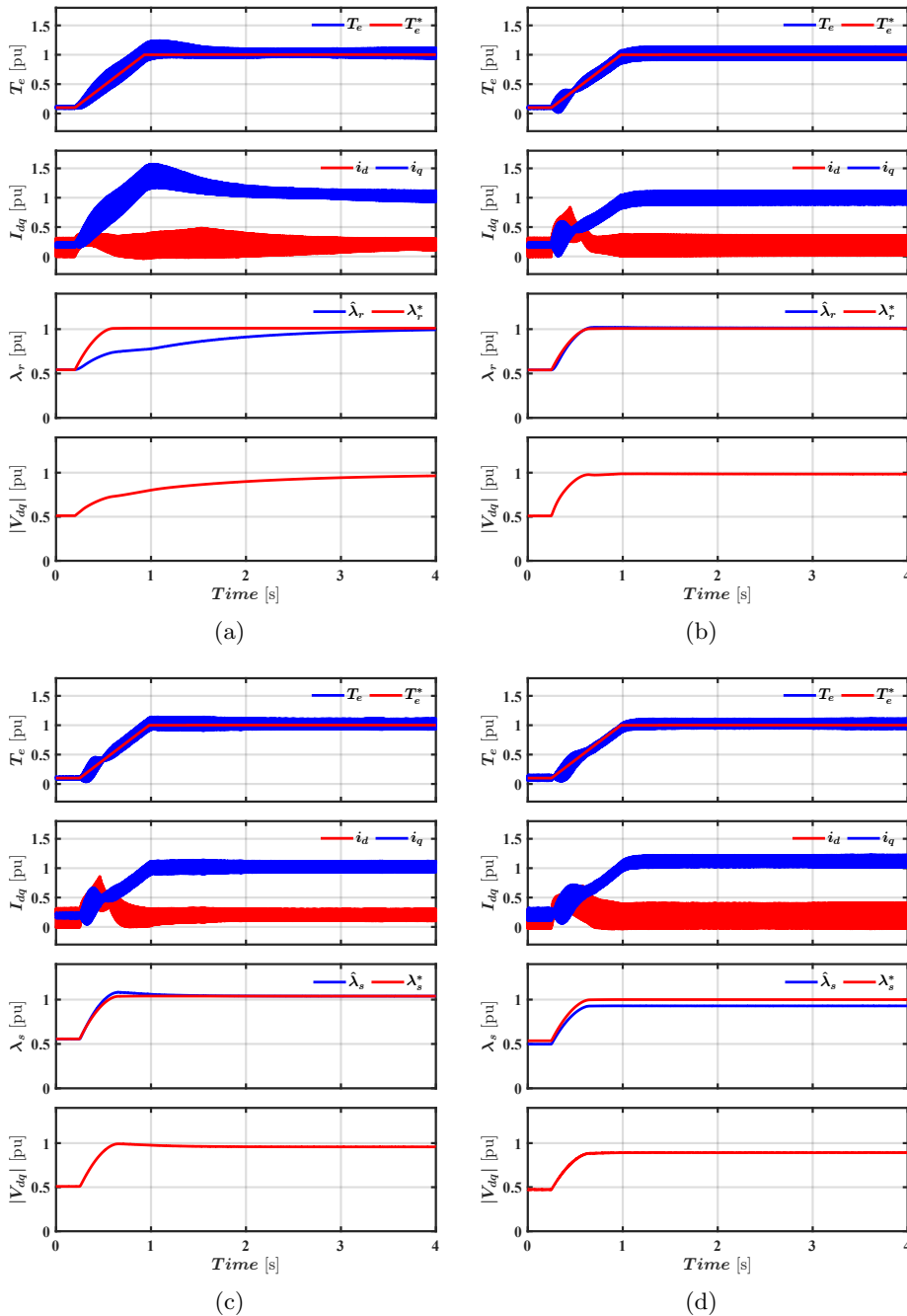
Figure 3.20: Simulation results of using (**a**) CLVFC, (**b**) CLVFC&FF, (**c**) DFVC, and (**d**) DTC-SVM control methods with SHE. Rotor speed $\omega_r = 1.328\,\omega_{base}$; torque was increased from 10% (i.e., with the machine operating with reduced flux in MTPA) to 100%. From top to bottom: commanded and actual torque; d- and q-axis currents; commanded and estimated flux (can be stator or rotor flux, depending on the method); and output voltage magnitude. All the variables are shown in p.u.

The most remarkable difference is the slowest transient response of CLVFC (in Fig. 3.20a) due to dynamic limitations intrinsic to scalar control. The dynamic response is seen to improve and be comparable to the other methods when the feedforward defined by (3.41) & (3.42) are used (CLVFC&FF in Fig. 3.20b). DFVC (in Fig. 3.20c) and DTC-SVM (in Fig. 3.20d) are seen to provide similar dynamic responses to CLVFC&FF.

Regarding DFVC, it must be noted that to achieve proper operation in the overmodulation region, the q-axis current regulator bandwidth should be reduced compared to linear region to avoid the current regulator reaction to low-order current harmonics due to the large harmonic content of inverter voltage. The need to dynamically adapt the gains of the current regulator in the high-speed region is an obvious concern.

It can be observed that DTC-SVM suffers from a steady-state error in the controlled flux due to the intrinsic behavior of hysteresis controllers and the low sampling time (Δt) when SHE is used in the inverter. This results in an increase in the load angle. This could lead to overcurrents or even instability issues if the load angle is not monitored.

Fig. 3.21 summarizes the performance in steady-state, i.e., once the machine is providing its maximum torque, for the four control methods. Error in the flux for DTC-SVM is seen to affect the modulation index and slip. This will eventually affect the machine loses distribution, which is a concern as traction motors can be required to operate close to their thermal limit. CLVFC and CLVFC&FF are seen to have a higher torque error compared to DFVC, but with little impact on the modulation index and slip. It is noted that a torque error in the range of 1% is perfectly assumable.

It can be concluded that the proposed CLVFC&FF performs better compared to the other considered schemes at high speeds due to its high dynamics; also the controllers are not affected by low-order harmonics resulting from a square-wave operation and is simple to implement.
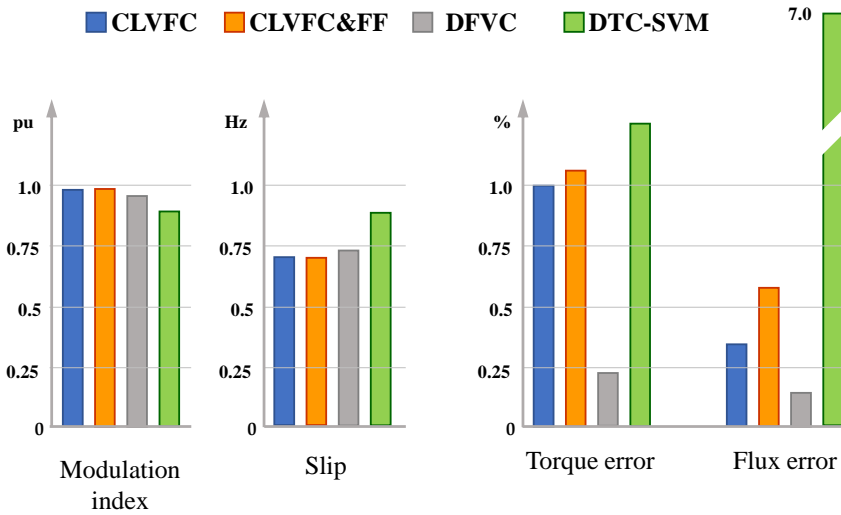
Figure 3.21: From left to right: modulation index, slip, torque error, and error in the flux being controlled for the four control methods being considered, once the machine has reached a steady state, i.e., is its maximum torque. Torque and slip have been low-pass filtered to eliminate the harmonic content produced by modulation.

3.4   Reduced Flux Operation

In high-speed traction applications, the electric drive can work for certain periods of time with light loads. It is possible in this case to decrease the flux level to reduce the stator current and consequently joule and iron losses. A drawback of this approach is that if a torque increase is demanded, the machine must be remagnetized first to achieve the required flux level [133], this is discussed in subsection 3.4.3. Mainly two approaches are involved for optimum selection of the flux level as following:

3.4.1   Loss Minimization Method (Maximum Efficiency)

In this method, optimization of motor's efficiency is achieved by adapting flux level using a model-based approach, which applies analytical equations [134]; online adaptation, which measures the input power and uses adaptive flux controller [135]; and hybrid methods, which combine both solutions to provide the optimal flux level with minimum motor losses [136]. There are two main drawbacks of these methods: 1) the approximation used in the model analysis neglects the leakage inductance of stator and rotor, which causes inaccuracy

in voltage equations, especially in high-speed regions; 2) these minimization techniques are intended for steady-state operation, transient operation is not considered.

3.4.2 Maximum Torque Per Ampere (MTPA)

MTPA strategy is one of the most efficient strategies in motor drives due to its simplicity [137]. MTPA seeks to produce the required torque of the machine with minimum current consumption. Thus, the overall efficiency of the IM is improved by minimizing the joule losses. However, maximizing the efficiency of the machine meanwhile operating at high speeds can't be guaranteed anymore as iron losses become dominant which are normally ignored in MTPA analysis [138]. Some improvements have been introduced into MTPA methods to obtain the optimal flux level considering iron losses but at the cost of complexity increase and increased parameters dependency as well [139, 140].

Another aspect that has to be taken into consideration for MTPA operation of IM is the machine size. For low-power machines, the ratio between the flux-producing current component (i_{ds}) to the torque-producing current component (i_{qs}) is higher compared to big machines with high power levels (as the case of traction motors). Consequently, the reduction of joule losses thanks to MTPA will be less significant in high-power machines compared to low-power machines (see Fig. 3.22).
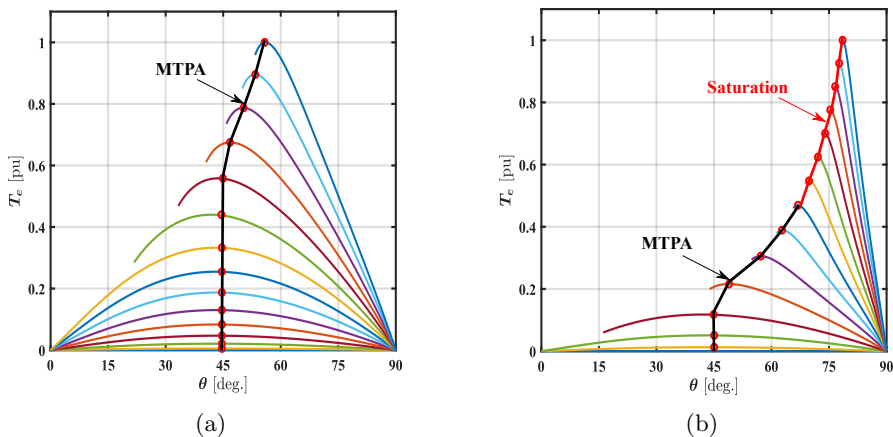
Figure 3.22: MTPA comparison based on machine size: (a) small machine; (b) big machine.

However, the main limitation of the aforementioned methods is that it

controls only the steady-state behavior of the stator current dq-axis trajectories regardless of the dynamic behavior during torque variations. Therefore, an additional strategy should be integrated with the control system to control the machines' dynamics during the transition between low-to-high torque levels (and vice-versa) operating with reduced flux levels. There are few attempts to improve the motor's efficiency during transients [141–143]. An extension of this work will be discussed in detail in the following Section.

3.4.3 Analysis of Remagnetization Strategies

Operating with reduced flux levels might deteriorate the dynamic response of the electric drive whenever a torque increase is demanded. The time required to build the rotor flux will depend on the rotor time constant and the magnetizing current that can be applied. The goal of the remagnetization process would be to determine the most suitable trajectories to move from the initial torque and flux levels $(T_{e_{ini}}, \lambda_{r_{ini}})$ to their final values. In the discussion following it will be assumed that for the final value maximum torque $T_{e_{max}}$ is targeted, the required rotor flux for that case being $\lambda_{r_{max}}$. $T_{e_{max}}$ and $\lambda_{r_{max}}$ will depend on rotor speed and the available voltage (see Fig. 3.23).
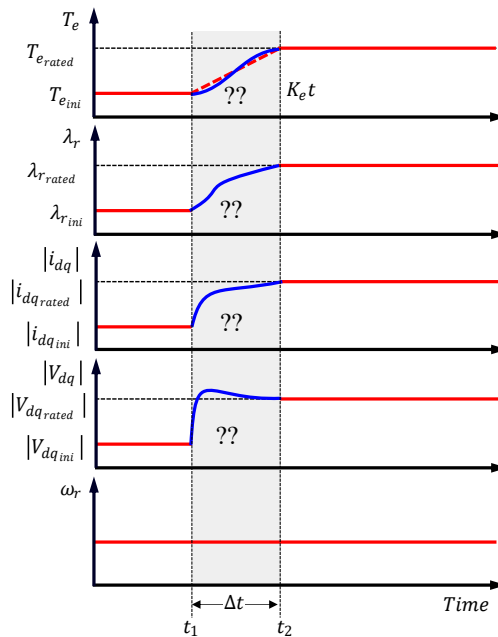
Figure 3.23: Problem statement. From top to bottom, torque, rotor flux, current magnitude, voltage magnitude, and rotor speed during the remagnetization process. Rotor speed is assumed to remain constant during the process.

Some aspects must be considered for remagnetization. In general, sudden changes of torque (jerk) should be avoided in traction systems as they might stress the mechanical transmission, produce wheel slip, and also raise comfort concerns. For this reason, the maximum allowed torque gradient will normally have relatively low values. However, there are exceptions in which faster torque variations might be required. An example would be active cancellation of torsional vibrations [20]. In the discussion following it will be assumed that the load has very large mechanical inertia (train mass), consequently, rotor speed will remain constant during remagnetization. Various possible strategies combining remagnetization and torque increase are discussed following.

- **Remagnetization with step-like rated d-axis change and ramp-like q-axis current change (profile 1)**: If FOC is being used, perhaps the most straightforward implementation for the remagnetization of the machine to achieve rated rotor flux and torque (for the actual operating speed) is to apply the rated d- axis, while q-axis current is commanded to follow a predefined ramp to avoid jerk phenomena, as shown in Fig. 3.24a. The drawback of this solution is the large settling time for remagnetization, in the range of three rotor time constants, and consequently, the reduced dynamic response of torque.

- **Remagnetization with maximum d-axis current (profile 2)**: This strategy prioritizes remagnetization over torque production. As shown in Fig. 3.24b, following an increased torque command, all the available current is used in the d-axis for this purpose (segment 1-2 in Fig. 3.24b). Once the rotor flux is fully established, d-axis current is reduced to the level required to maintain the rotor flux at its target level, the remaining available current being transferred to the q-axis to produce the maximum torque (segment 2-3 in Fig. 3.24b). This strategy reduces the time required to produce the desired final torque (i.e. settling time) and provides the fastest torque production. However, in traction applications, fast torque variation is not allowed as mentioned above.

- **Remagnetization with maximum d-axis current and constant Nm/s (profile 3)**: The main idea behind this strategy is to control the torque to follow a ramp (3.43) (see Fig. 3.24c), where K_{T_e} is the slope in Nm/s.

$$T_e^* = T_{e_{ini}} + K_{T_e}t \ \text{ for } \ t_1 < t < t_2 \tag{3.43}$$

To minimize the settling time, K_{T_e} must be selected such that maximum current is used during the whole transient (3.44).

$$\sqrt{i_{ds}^{*}{}^2 + i_{qs}^{*}{}^2} = I_{s_{max}} \tag{3.44}$$

The desired torque and flux trajectories can be obtained by solving (3.28), (3.29) and (3.44). Finding an analytical solution for this system is not feasible, numerical methods can be used instead. It is seen in Fig. 3.24c that, at the beginning of the transient, all the available current is transferred to the d-axis current to fully establish the rotor flux. Then, the d-axis current is reduced to its rated value while increasing the q-axis current smoothly taking into consideration that fast changes in q-axis current are avoided as they would produce torque impacts.

- **Remagnetization with reduced d-axis current and constant Nm/s (profile 4)**: The strategy in Fig. 3.24d provides the same torque ramp as in Fig. 3.24c but using the smallest possible current during segment 2. This reduces the stress in the power devices, as well as the risk of surpassing the maximum current in case of overshoots. Thus, segment 3 in Fig. 3.24c is omitted to have a continuous trajectory of d-q axis currents. However, this strategy is not straightforward, and the minimum current value is changing with the initial torque value. Therefore, profile 3 strategy can be used with lower current magnitude providing the simplest solution at cost of longer magnetization time.
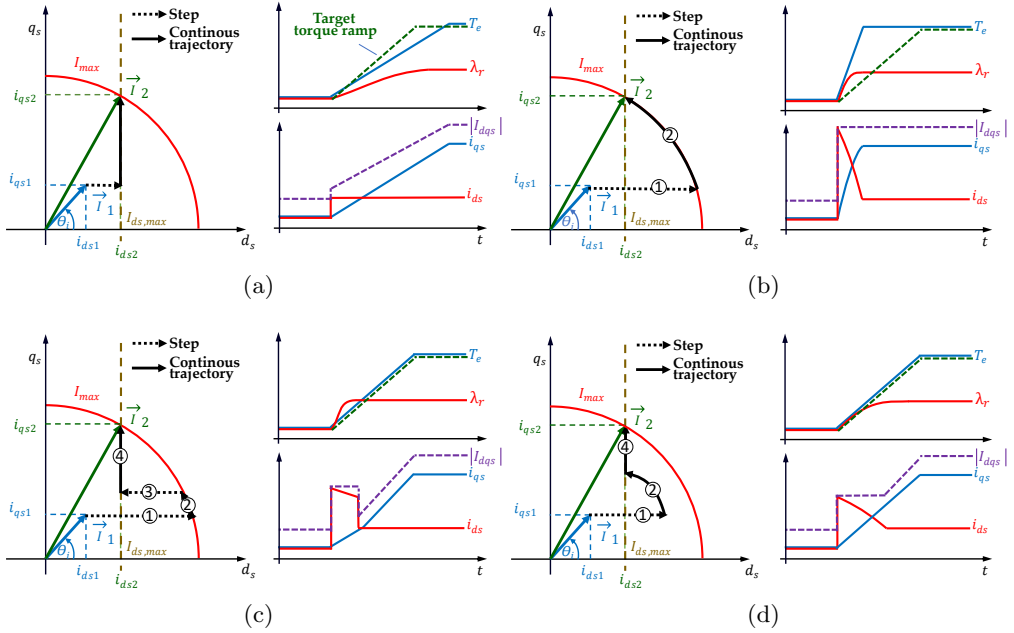
Figure 3.24: Wave shapes for the case of remagnetization using: (a) rated d-axis current; (b) maximum d-axis current; (c) maximum d-axis current and constant Nm/s; (d) reduced d-axis current and constant Nm/s.

The proposed remagnetization strategy (see Fig. 3.25) includes the following process:

1. At light load, the initial rotor flux reference value is obtained from Maximum-Torque per Ampere (MTPA) using a look-up table or polynomial function approximation according to the operating speed.

2. Once an increase/decrease is commanded to the reference torque, the torque and rotor flux references will follow one of the predefined trajectories with rates limited to the application until reach to the new target values.

3. The rotor flux reference is limited in the field-weakening region according to operating speed.

4. The rotor flux trajectory can be a ramp, exponential convergence or other profiles obtained from optimization methods (profiles 1-to-4) that meet the application constraints.

(a)

(b)
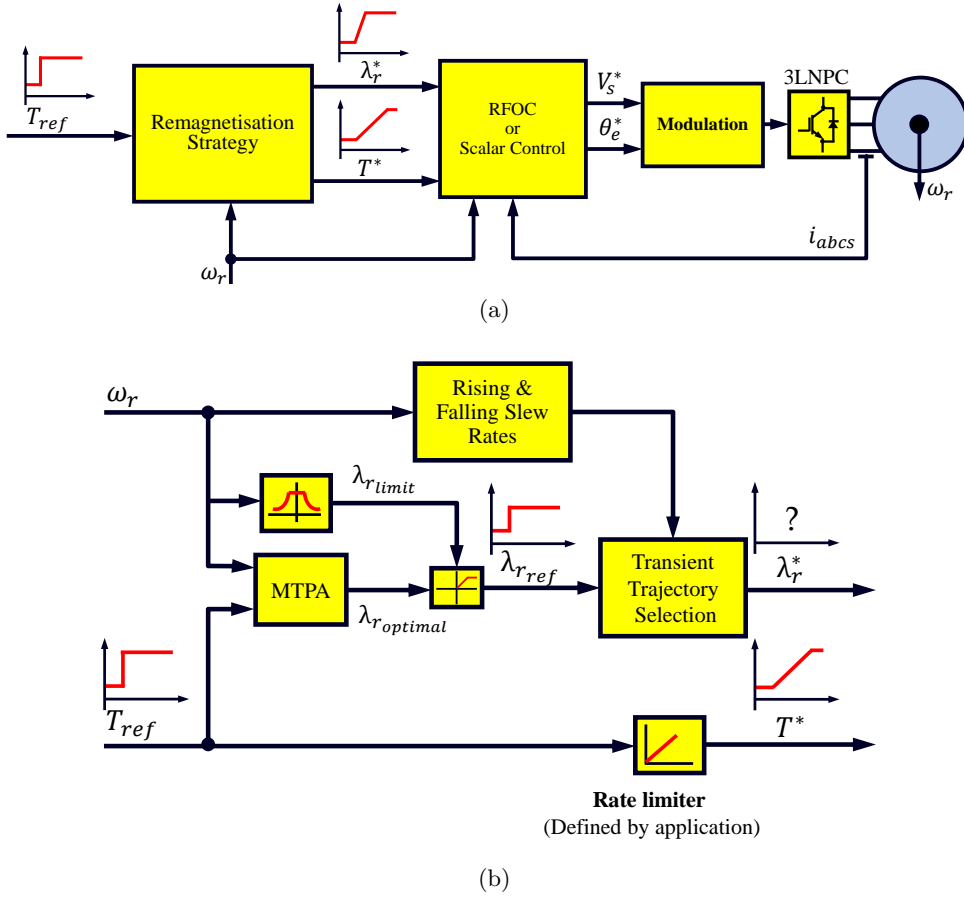
Figure 3.25: Proposed remagnetization strategy: (a) overall control scheme; (b) detailed block diagram of the proposed remagnetization method.

The proposed remagnetization strategies have been simulated using MAT-LAB environment with a sample time of 200 μs. The dynamic d-q model in rotor flux reference frame is used for modeling the induction machine. IM parameters for the base speed are given in table A.1 in the Appendix.

RFOC (Fig. 3.10) is used to evaluate the proposed strategies. Pole-zero cancellation method is used to tune the current regulators to achieve a bandwidth of 200 Hz.

Fig. 3.26 shows a summary of the simulation results for the machine operating at base speed, assuming that the IM is fed from an inverter with ideal power switches. The IM torque is increased from 10% to 100% of the rated torque at t=0.25 s (see Fig. 3.26) following the four remagnetization profiles proposed in this subsection. It is noted that the slowest torque production

is obtained by magnetizing the machine with profile 1, i.e. d-axis current is increased to its rated value then the q-axis current is increased gradually Fig. 3.27. The final torque will be achieved when the machine flux is fully established which could take some time ($\approx$ 3 to 4 times the rotor time constant see Fig. 3.26).
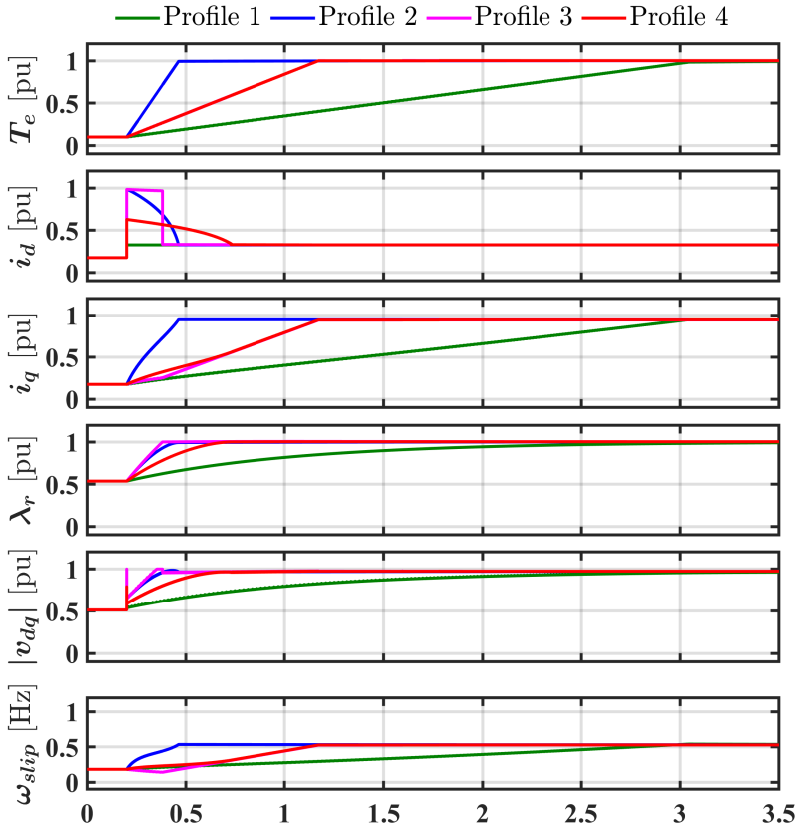
Figure 3.26: Simulation results of different proposed remagnetization strategies.

On the other side, fastest torque production is reached following profile 2 (see the blue color in Fig. 3.26) where all the stator current is used to magnetize the machine. Afterward, the stator current vector follows the current limit trajectory sharing the remaining current into the q-axis component assuring that the total current is not surpassed (see Fig. 3.27).

Profiles 3 and 4 show similar torque rise behavior (magenta vs. red color in Fig. 3.26) as these strategies are designed to follow a predefined kNm/s rate (in this application 3 kNm/s is used). However, the dynamics are different. Profile 3 prioritizes the use of stator current vector on the d-axis component in order to

expedite flux establishment then the priority moves to the q-axis component for torque production (see Fig. 3.27). A reduced remaganetization can be used for profile 4 (see Fig. 3.27) which will penalize the dynamic response of the rotor flux (see Fig. 3.26), which in general is not a concern in traction applications, as the fast torque increase is not needed. The main advantage of this strategy is it compromises the dynamic response of the electric drive and the stresses on the inverter switches during the remagnetization process.

In the previous discussion, remagnetization process has been analyzed based on d- and q-axis currents behavior. This analysis can be therefore easily applied if RFOC is being used. However, other torque control schemes do not rely in d- and q-axis currents. An alternative approach for the remagentization strategy, intended for control schemes without current regulators, is to control the flux trajectory assuming that the torque trajectory is a ramp whose gradient is limited by the application. The simplest flux trajectory is to follow a ramp where the ramp rising/falling rate will be selected according to two criteria: 1) the torque change rate; 2) the magnitude of stator current components. Three different rotor flux change rates 5, 2, and 1 wb/s respectively are evaluated (see Fig. 3.28a and 3.28b). It is noted that the higher the rotor flux rate change, the faster flux establishment, and the higher the d-axis stator current component. It is also observed that the dynamic response of the fastest flux rate change, (i.e. 5 wb/s) is similar to profile 3 in Fig. 3.26. The limitations of this flux rate change are the high current value which increases the stresses on the inverter switches and the risk of demagnetizing the machine during the torque reduction process (see green profile in Fig. 3.28b). A compromising solution could be achieved by relaxing the rotor flux (see blue and magenta profiles in Fig. 3.28a and 3.28b). Further improvement on the dynamic behavior can be achieved using an exponential flux rate change (first-order like behavior) as seen in Fig. 3.28c and 3.28d. As the control scheme does not include current regulators, the d-axis current can surpass the maximum stator current limit.
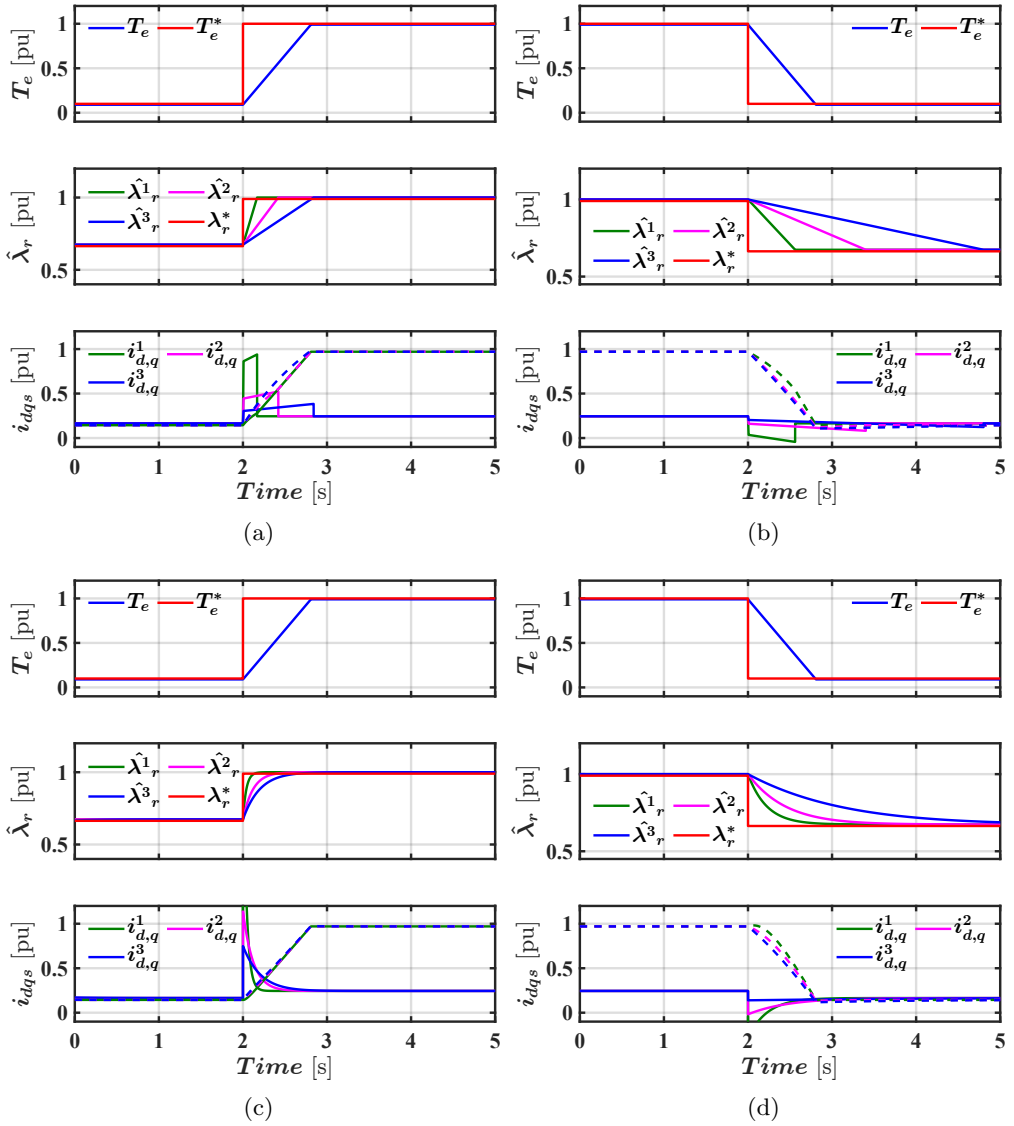
Figure 3.28: Simulation results of IM torque change from 10% to 100% of rated torque: (a) ramp increase; (b) exponential increase; (c) ramp decrease; (d) exponential decrease. Solid line (-) represents the d-axis while dashed line (- -) represetns the q-axis of stator current.

3.5   Experimental Validation

In this Section, IM control techniques and proposed remagnetization strategies discussed in sections 3.3 and 3.4.3 respectively will be tested and evaluated via a full-scale high-speed traction drive used in real trains [144]. A schematic diagram of the high-power traction system test bench is shown in 3.29a. It consists of two identical IMs and converters connected back-to-back, which are supplied from a High-Voltage (HV) power supply with a specially designed traction transformer which is used to filter off catenary harmonics and allow the interconnection of the different converters. A 100 Hz (2f) filter is included in the DC bus where the overall experimental test rig is shown in Fig. 3.29b. The power converter module in Fig. 3.29c consists of a three-phase, three-level Neutral-Point Clamped (NPC) inverter feeding the IMs. Single-phase inverters feed auxiliary loads, such as cooling systems, control power supply units, etc. A DC-DC chopper is implemented for dissipative braking and DC bus overvoltage protection.

Normally, high-speed trains use RFOC at low speeds and CLVFC at high speeds [130]. The main system parameters are the same as those used in the simulation shown in Table A.1. The torque-flux characteristic of the motor is of the type named the extended full flux range in Fig. 3.5.

Fig. 3.30b and 3.30a show the rotor speed, modulation index, commanded and estimated torques, estimated rotor flux, and magnitude of the stator current vector during an acceleration (left) and deceleration (right) process. Fig. 3.30c and 3.30d show the spectrogram of the stator current vector. For $\omega_r < 0.12$ p.u., RFOC-SVM with a switching frequency of 850 Hz is used; the switching frequency increases to 1 kHz for $0.12 < \omega_r < 0.94$ p.u. For $\omega_r > 0.94$ p.u., CLVFC combined with SHE with one switching angle is used. Changes in the modulation method are readily observable in the spectrogram which aims to trade off switching losses and torque ripple. The control is seen to precisely follow the commanded torque and rotor flux in the whole speed range. It is noted that the changes in the estimated rotor flux observed in the flux-weakening region respond to changes in the corresponding command (not shown in the figure). Transitions between the different control and modulation strategies can be a challenge due to the high power and low switching frequencies. However, as can be observed from Fig. 3.30, such transitions are satisfactory, i.e., the spikes observed in the currents are perfectly acceptable and do not represent a risk for the power devices.
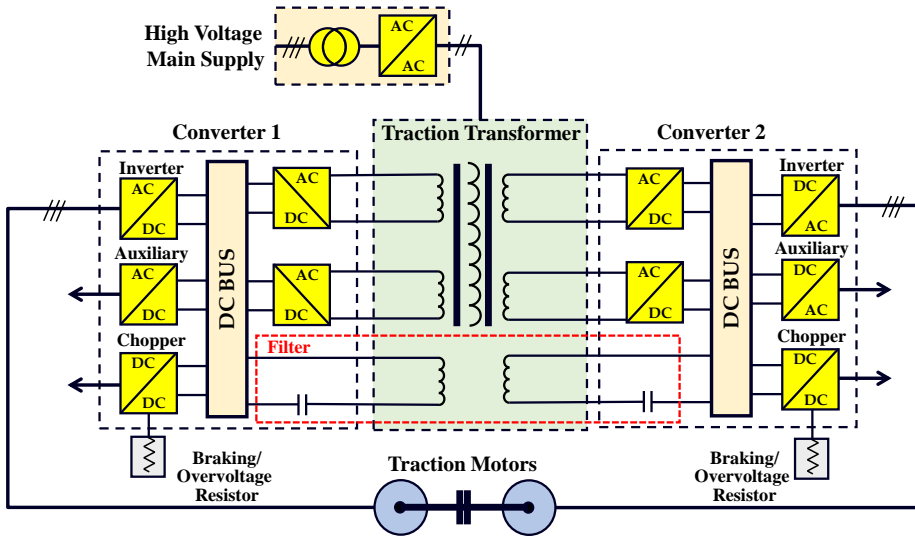
(a)
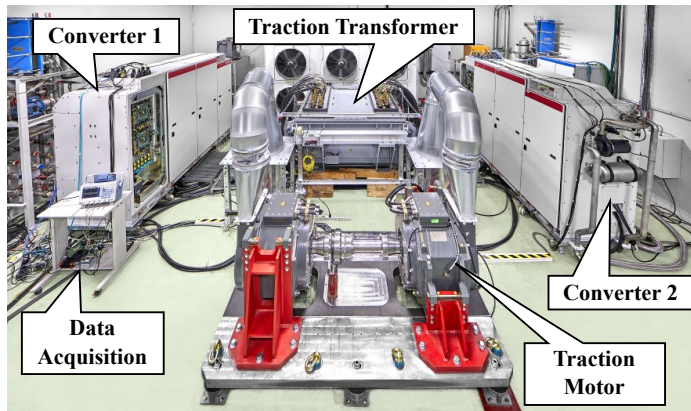
(b)
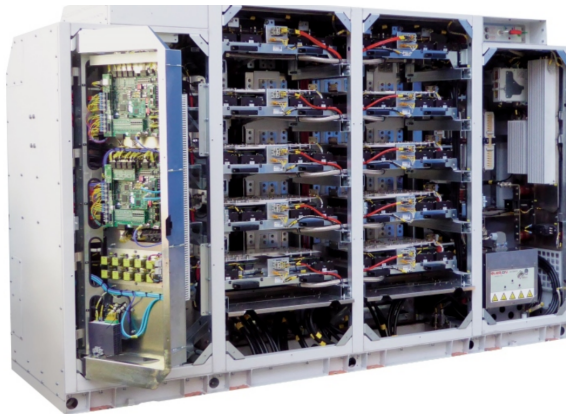
(c)

Figure 3.29: High-power traction test bench: (a) Schematic diagram; (b) Overall view of the laboratory setup; (c) Power converter module (INGETRAC).
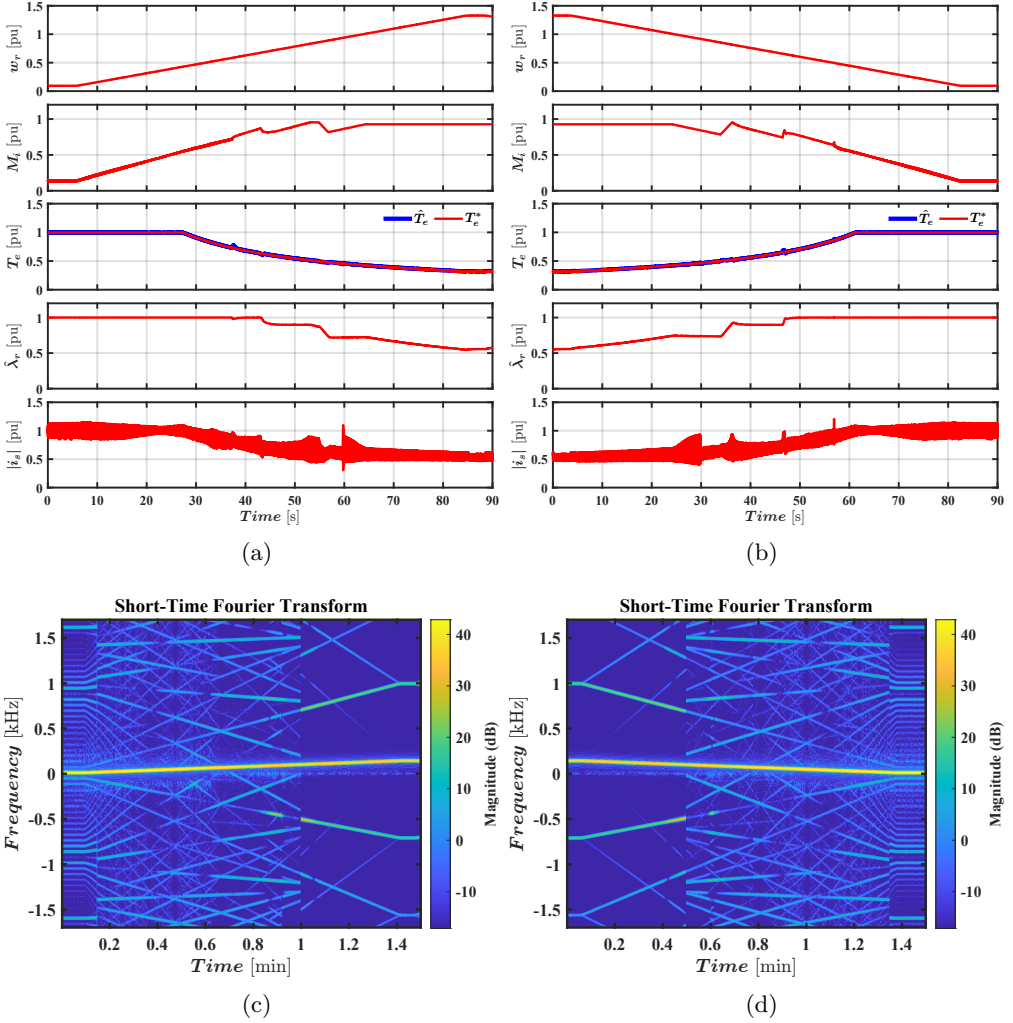
Figure 3.30: Experimental results. Acceleration (left)-deceleration (right) tests between $\omega_r = 0.1$ and $\omega_r = 1.328$ p.u. (a) From top to bottom: rotor speed, modulation index, commanded and estimated torques, estimated rotor flux, and magnitude of the stator current vector; (b) stator current vector spectrogram.

The proposed remagnetization strategy considering profile 4 was implemented and compared with the maximum possible flux strategy over the full speed range (see Fig. 3.31) in the same traction drive test bench in Fig. 3.29. It is noted that in both cases the target torque gradient of 3 kNm/s from 10% to 100% of the rated torque is achieved. The main difference can be seen in the rotor flux for the proposed method where it is reduced to $\approx 48\%$ of the rated value during light load operation compared to the conventional solution.

The corresponding d- and q-axis currents are shown in the bottom figures of Fig. 3.31.
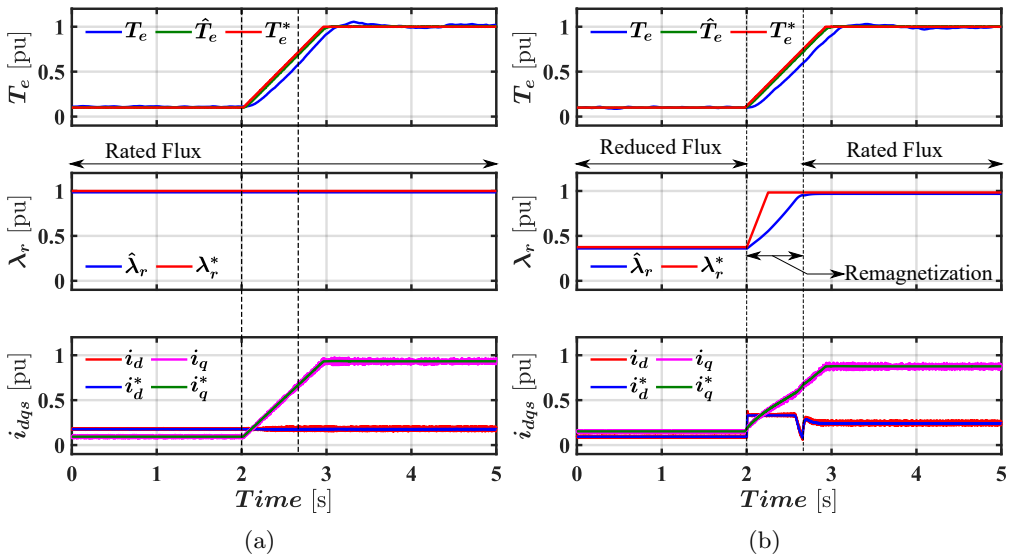
Figure 3.31: Experimental results of IM torque increase from 10% to 100% of rated torque: a) applying rated magnetizing current; b) proposed remagnetization strategy.
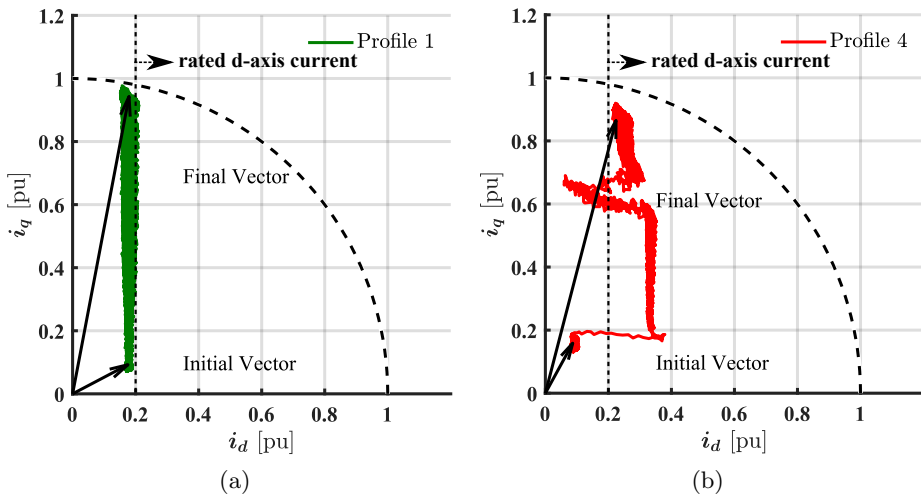
Figure 3.32: Experimental results: (a) rated step-like d-and ramp-like q-axis currents (Profile 1); (b) reduced d-axis current and constant Nm/s (Profile 4).

The d-axis current is kept at its rated value for the conventional magnetization method while the d-axis current is initially reduced during light load duration then it super-passed its rated value to build up the rotor flux quickly when the torque increase is commanded. Once the machine is fully magnetized, the d-axis current is decreased to prioritize the usage of q-axis current. The d- and q-axis current trajectories are shown in Fig. 3.32 where the maximum increase in the d-axis current in 3.32b is limited due to practical concerns.

Remagnetization process during to torque command decrease is validated experimentally in Fig. 3.33. The rotor flux is decreased following a ramp like profile as explained in Fig. 3.28b. It can be seen that the experimental results of the proposed remagnetization strategies are in good agreement with the simulation results obtained in Section 3.4.3. However, it should be noted that the ramp change rate has been chosen properly in practice to avoid demagnetization risks (see Fig. 3.33b at $t = 6$ s).
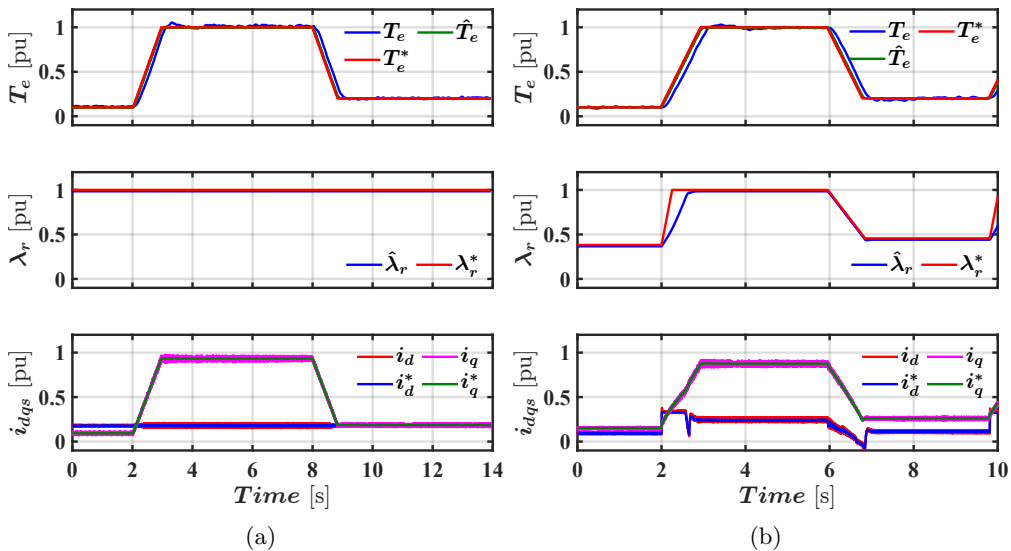
Figure 3.33: Experimental results of IM remagnetization process during increase/decrease of machine torque: (a) applying rated magnetizing current; (b) proposed remagnetization strategy.

3.6 Conclusions

Railway traction drives normally use medium-voltage, high-power induction machines. Rotor flux Oriented Control (RFOC) has been widely adopted at low

and medium speeds. However, high fundamental frequencies intrinsic to high-speed operations, combined with the need to reduce inverter losses, force the inverter to operate with reduced switching frequencies and a high modulation index or even at the six-step limit. These limitations seriously compromise the performance of RFOC at high speeds. A common practice is to use RFOC at low speeds and switch to strategies able to perform properly under severe voltage constraints at high speeds.

For high-speed operation, four different control strategies have been selected and tested by means of simulation, namely, Closed Loop V/F with flux/torque Control (CLVFC), CLVFC with feedforward (CLVFC&FF), Direct Flux Vector Control (DFVC), and Direct-Torque Control Space-Vector Modulation (DTC-SVM). The modulation methods that have been considered are PWM/SVM, SHE, and six-step. Their advantages include the easiness of operation with a high modulation index, including six-step; switching frequency; and dynamic response to both torque change demands and rotor flux change demands.

It was concluded from the simulation results that CLVFC, CLVFC & FF, and DFVC provide similar performances. However, DFVC requires a modification of the q-axis current controller gains when the drive enters the over-modulation region. Specifically, the proposed CLVFC&FF operates properly with a high modulation index, including six-step, and provides a good dynamic response. Additionally, experimental results using CLVFC in a full-scale traction drive have been provided, which are in good agreement with the simulation results, and confirm the viability of this strategy.

For traction applications, a fast dynamic response is not required as the torque rate change is limited to avoid torque shocks. Thus, a reduced remagnetizing current with a constant torque increase rate has been verified by simulation and validated experimentally through a full-scale high-power traction test bench.

The proposed remagnetization strategy calculates the initial rotor flux using MTPA algorithm at light loads. Once a change in torque command is detected, the torque and rotor flux reference will follow predefined trajectories till they reach the final value. Currently, the proposed remagnetization torque and flux trajectories are implemented offline and stored in look-up tables. Online implementation of the remagnetization trajectory is challenging and adds more complexity to the overall traction motor control.
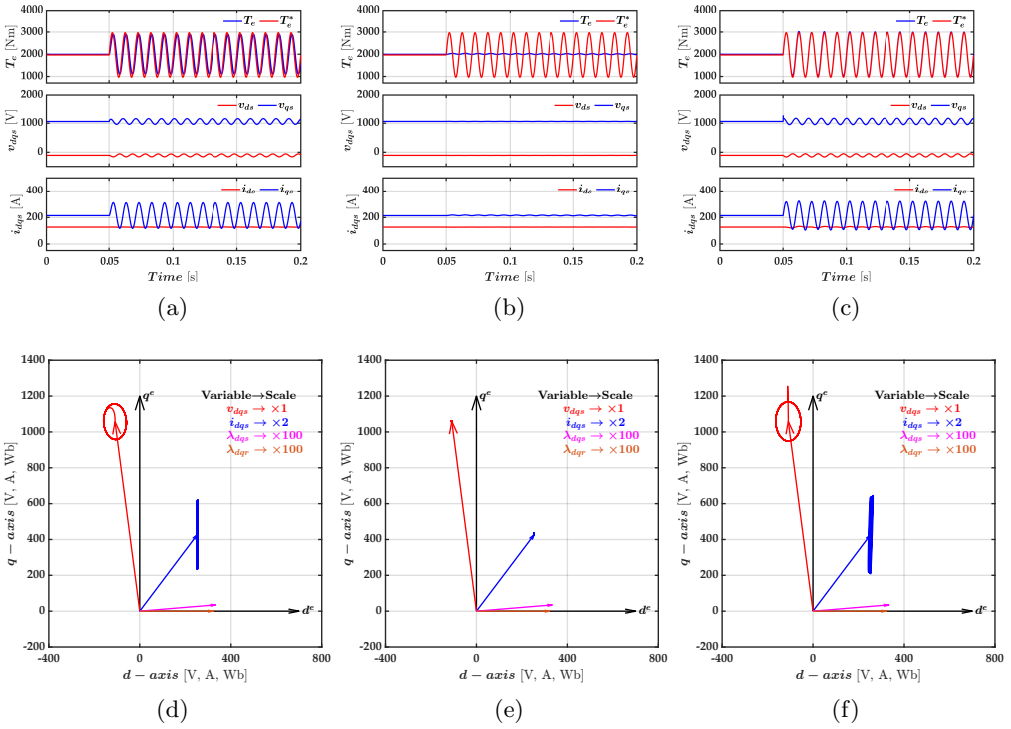
Figure 3.18: Response to commanded torque oscillation at 100 Hz: (a), (d) RFOC; (b), (e) CLVF; (c), (f) CLVF&FF. Top: time response. Bottom: vector trajectories. Solid vector: starting position. Dashed vector: steady-state position.
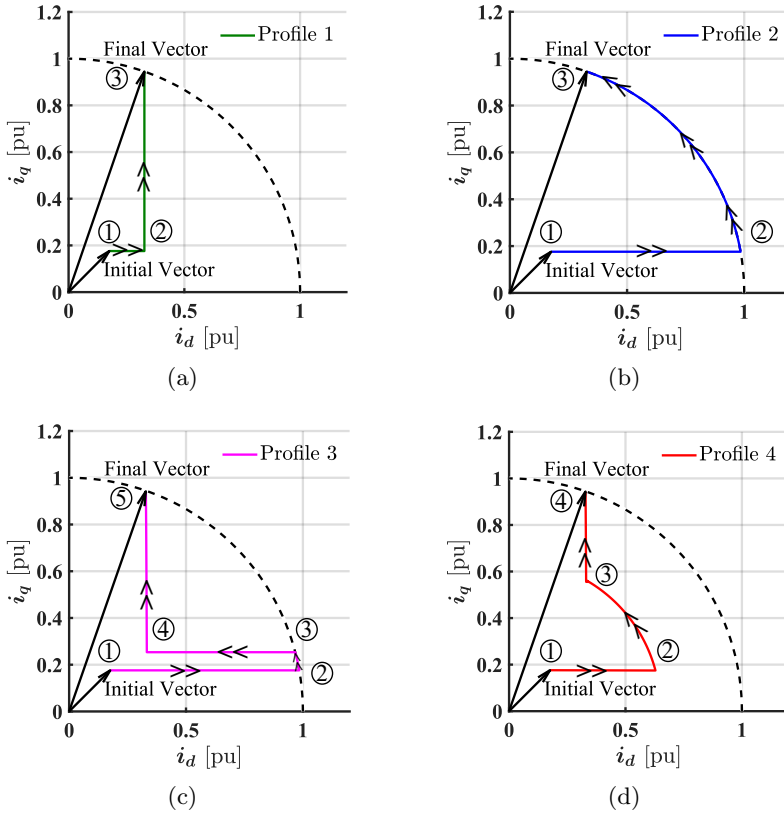
Figure 3.27: Summary of the proposed remagnetization strategies: (a) step-like rated d-axis change and ramp-like q-axis current change (Profile 1); (b) maximum d-axis current (Profile 2); (c) maximum d-axis current and constant Nm/s (Profile 3); (d) reduced d-axis current and constant Nm/s (Profile 4).

Chapter 4

Anti-Slip Control in Railway Traction Drives

4.1 Introduction

Railway vehicles often require large tractive effort. Due to the design of wheel and rail, combined with the large elastic coefficient of steel, transfer of forces between the wheel and the rail occur through a small steel-to-steel contact area. While this is advantageous regarding frictional losses, it will curb the maximum force transfer. The maximum transferable force between the wheel and rail will not only be a function of design parameters such as wheel and rail shapes and materials, vehicle weight, etc. but also will be strongly affected by the surface conditions of rail [145]. Exceeding the maximum tractive force can produce an uncontrolled wheel slip, which can result in a number of unwanted effects, including reduced acceleration/deceleration performance [145], and also the risk of triggering torsional vibration phenomena [146]. This creates an interest and necessity to study slip phenomena and develop anti-slip control methods.

Roller rigs are one of the important experimental setups that help in study and validation of the topics related to railway vehicle dynamics [147, 148], including wheel-rail contact dynamics [149], braking system [150], slip control [151] and adhesion estimation [152], etc. Test rigs can be developed in full scale, where the dimensions of the wheel and forces are unchanged compared to the actual wheels [148]; and in scaled versions, where the wheel size and the related parameters are reduced in specific ratio [153].

In this chapter, an overview of the slippage phenomenon and adhesion slip characteristics will be addressed first. Then, the development of a scaled roller rig used for adhesion coefficient estimation and slip velocity control verification will be presented. Moreover, existing slip control strategies intended for maximum utilization of the available adhesion will be discussed in detail. Two new methods for maximum adhesion tracking (MAT) will be proposed, using Fuzzy Logic Control (FLC) and Particle Swarm Optimization (PSO) respectively. Finally, a comparative analysis will be included considering Computational Simplicity, Tuning Easiness, MAT Searching Capability, Steady-state Response, and Signal Smoothness.

4.2 Overview of Slippage Phenomenon

Traction force is defined as the force developed by the traction motor being transferred to the rail through the train vehicle's wheel to achieve the desired train speed. The traction force that can be transferred to the rail will be limited by the friction between the driven wheels and the steel rail. The adhesion limit will depend on the normal load and the friction coefficient of the contact point, also known as the adhesion coefficient. Adhesion coefficient is a non-linear function of wheel slip and velocity [47]. Slip/skid phenomenon occurs when the traction force surpasses the adhesion limit during traction/braking. Excessive slip or skid will result in an increase in wheel wear and a reduction of the overall traction performance. Therefore, many efforts have been devoted to limiting the slip/skid between the wheel and the rail [43–45].

Without the slippage, traction force F_t is equal to the tangential force and is given by (4.1), where T_m is motor torque after the gear, N_m is number of motors and r_w is traction wheel radius.

$$F_t = N_m \frac{T_m}{r_w} \tag{4.1}$$

The simplified force balance equation in the real train can be defined by (4.2), where m_t is train mass, B is the friction, v_t is train linear velocity and F_{lt} is the total load force.

$$F_t - F_{lt} = m_t \frac{\mathrm{d}v_t}{\mathrm{d}t} + B \cdot v_t \tag{4.2}$$

Total load forces given by (4.3) comprise of the aerodynamic force F_{lA} (4.4), the rolling friction force F_{lR} (4.5), and the gradient force F_{lG} (4.6), which are subtracted from the adhesive force to obtain the net force F_{net} (see Fig. 4.1). Similarly, the total load torque (T_{lt}) is subtracted from the adhesive torque (T_a) to obtain net torque, T_{net}. The total load torque T_{lt} can be obtained from the load force F_{lt} using the radius of the wheel as mentioned in Fig. 4.1.

$$F_{lt} = F_{lA} + F_{lR} + F_{lG} \tag{4.3}$$

$$F_{lA} = \frac{1}{2}C_d A_f \rho v_t^2 \tag{4.4}$$

$$F_{lR} = C_r m_t g \tag{4.5}$$

$$F_{lG} = m_t g \sin \theta \tag{4.6}$$

where,

C_d the drag coefficient;
A_f frontal area;
C_r the rolling friction coefficient;
g the acceleration of gravity;
θ gradient angle in degree

Relationship between angular and linear velocities is given in (4.7) where ω_w is the angular velocity of the traction wheel.

$$v_t = \omega_w \cdot r_w \tag{4.7}$$

Adhesive force F_a is the force that can be transferred from the wheel onto the rail and is given by (4.8), where F_N is the normal force and μ is adhesion coefficient [154].
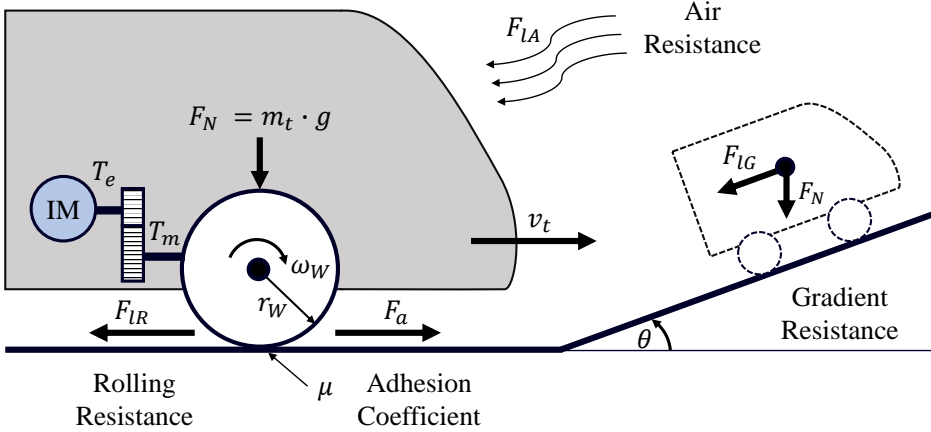
Figure 4.1: Representation of train load forces and load torque.

$$F_a = \mu \cdot F_N = \mu \cdot m_t \cdot g \tag{4.8}$$

The adhesion coefficient μ is a measure of the wheel-rail contact quality, which depends on the rail surface, environmental condition, temperature of the contact point, etc. The adhesion coefficient will be also significantly affected by the slip, which occurs when the angular velocity of the wheel doesn't match train linear velocity v_t (4.9).

$$\omega_w \cdot r_w \neq v_t \tag{4.9}$$

Variation of adhesion coefficient with respect to the slip velocity is called adhesion-slip curve. An example plot is shown in Fig. 4.2. Based on the sign of the derivative of μ with respect to slip speed, the curve shown in Fig. 4.2 can be divided into two main regions. Positive values of $d\mu/dv_s$ correspond to the stable region. In this region, an increase of slip results in an increase of μ, and consequently of the tractive effort. The stable region is seen to consist of two sub-regions: 1) linear area, the adhesion coefficient increases almost linearly with the slip velocity; 2) nonlinear area, $d\mu/dv_s$ reduces progressively, eventually reaching the maximum adhesion coefficient when $d\mu/dv_s = 0$.

If the slip surpasses this maximum, then $d\mu/dv_s < 0$, which corresponds to the unstable region. In this region, an increase of slip speed will result in a
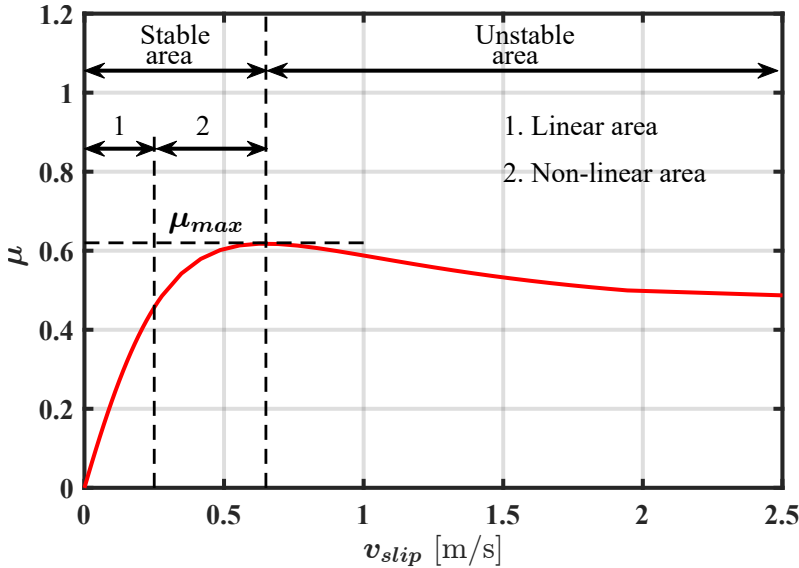
Figure 4.2: Theoretical example of adhesion-slip curve.

reduction of adhesive force. When this occurs, wheel speed is no longer linked to train speed. Equation (4.10) holds in this case, where J_a accounts for axle inertia.

$$T_m - F_a\, r_w = J_a \frac{\mathrm{d}\omega_w}{\mathrm{d}t} \tag{4.10}$$

It is observed from (4.10) that if traction motor torque T_m remains invariant, a decrease of F_a will result in a sustained increase of ω_w. Since F_a is decreasing, tractive force F_t, and consequently train speed will decrease too, slip speed consequently increasing steadily.

Maximizing the traction force leads to more efficient and faster acceleration/deceleration rates. This allows achieving the planned travel speed-distance profile precisely, avoiding trip delays and reducing energy consumption. Therefore, implementation of control methods able to maximize the traction force becomes crucial to traction systems manufacturers and train service providers. Both direct and indirect re-adhesion control methods have been proposed to limit the slip within a predefined threshold [46, 48, 50, 155]. The main demerit of these traditional re-adhesion methods is that the traction capability is not fully utilized. Slip control methods will be discussed in detail in Section 4.4.

One of the limitations perceived during the review of the state of the art was that the different methods were validated using different platforms. This makes it extremely difficult to perform a fair comparative analysis. To overcome this limitation, all the methods considered will be tested in the same test rig. System model as well as test rig design and control are presented in the following Section.

4.3   Scaled Roller Rig

Roller rigs combined with simulation verification are convenient replicas for evaluating control techniques of railway traction drives during pre-service commissioning. Full-scale or scaled roller rigs can be used for the purpose of producing the same dynamics of the actual train moving on a rail. Scaled roller rigs are preferred due to cost, size, and manufacturing obstacles. However, special care must be taken for the selection of the scaled parameters during the design process to reproduce as precisely as possible the behavior of the full-scale system. In this chapter, Manchester Metropolitan University (MMU) method is used [148]. In this approach, the locomotive mass is considered to be equally distributed amongst the wheels and the nominal linear wheel speed is scaled by 1/5 factor [156]. The full design process and scaling parameters of the scaled roller rig used in the following discussion can be found in [157].

Fig. 4.3 shows a schematic representation of the scaled roller rig where the smaller wheel represents one of the locomotive wheels and the bigger wheel, referred to as roller, represents the rail. Two induction motors (IMs) are used to drive both wheels via a transmission belt system. The normal force F_N applied to the wheel is adjusted manually with a spring system including a dynamometer for fine force tuning. The test bench has a water-spraying nozzle to emulate wheel-rail wet conditions.

Adhesion coefficient μ is defined in (4.11) as the ratio between the adhesion force F_a being transferred from the wheel to the roller and the normal force applied to the wheel F_N. Adhesion is a non-linear function that depends on the slip velocity between the wheel and roller, ambient factors such as humidity and ambient temperature, and the surface condition of the contact point [158]. The slip velocity is given by (4.12), where ω_{m_W}, ω_{m_R} and r_W, r_R are the mechanical speed of the IMs in electrical units (rad/s) and the radius of both wheel and roller in (m) respectively.
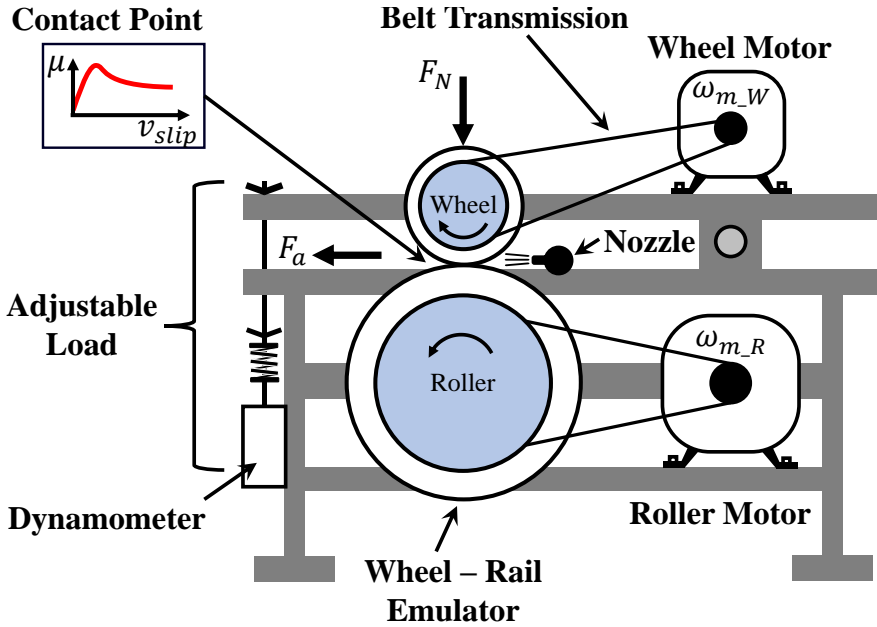
Figure 4.3: Schematic representation of the scaled roller rig.

$$\mu = \frac{F_a}{F_N} \tag{4.11}$$

$$v_{slip} = v_W - v_R \tag{4.12}$$

where $\quad v_W = \omega_{m_W} \cdot r_W; \quad v_R = \omega_{m_R} \cdot r_R$

The adhesion torque (i.e., load torque) can be expressed as the adhesion force exerted on the wheel multiplied by its radius (4.13).

$$T_W = F_a \cdot r_W = \mu \cdot F_N \cdot r_W \tag{4.13}$$

The electromagnetic torque developed by the wheel motor T_{e_W} and transferred to the wheel T_W via belt transmission is given by (4.14) where R_{g_W} is the wheel gear ratio.

$$T_{e\_W} = \frac{T_W}{R_{g\_W}} = \frac{\mu \cdot F_N \cdot r_W}{R_{g\_W}} \tag{4.14}$$
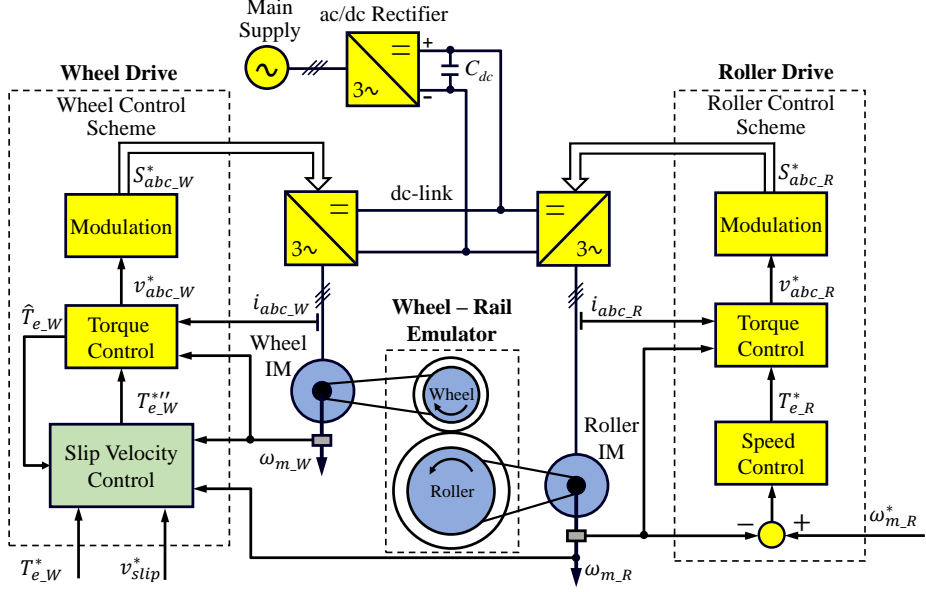
Figure 4.4: Overall control scheme of scaled roller rig for slip velocity control.

The same relation can be developed for the roller side where T_{e_R}, and R_{g_R} are the roller motor electromagnetic torque, and roller gear ratio respectively.

$$T_{e\_R} = \frac{T_R}{R_{g\_R}} = \frac{\mu \cdot F_N \cdot r_R}{R_{g\_R}} \tag{4.15}$$

Wheel and roller motors are fed from three-phase inverters which share the same DC link (see Fig. 4.4). The DC link is fed from the grid by means of a diode rectifier. A commercial drive using RFOC, mentioned in Section 3.3.2, with an outer speed control loop (see right side of Fig. 4.4) is used to control the roller.

On the other side, the wheel motor is fed from a custom drive built to implement the different control strategies for Maximum Adhesion Tracking (MAT) functionality. The control scheme of the custom drive contains the same structure as the roller commercial drive except for the speed control block that is replaced by the slip velocity control block (see the green block on the left side of Fig. 4.4). Further details are provided in Section 4.6. The slip velocity control block requires additional signals: reference torque $T_{e\_W}^*$, reference slip velocity v_{slip}^*, and torque estimate $\hat{T}_{e\_W}$. The signals involved depend on the MAT method being used. In all cases, knowledge of roller speed

is essential, which implies that real train velocity should be known in the real system.

For the following discussion and simulations, it is assumed that the roller drive control is set to speed control mode running with a constant speed. This is consistent with the case of a train that has a very large inertia. Meanwhile, the wheel drive operates with torque control; the slip velocity controller remains disabled unless the actual slip surpasses the established limit (see Fig. 4.5). The torque reference $T_{e\_W}^{*}$ is transferred to the wheel drive torque command, i.e, $T_{e\_W}^{*''} = T_{e\_W}^{*}$ unless wheel slip is detected. In this case, the slip velocity control is activated and the torque command generated from the slip speed controller is passed by the (Min) function, i.e., $T_{e\_W}^{*''} = T_{e\_W}^{*'}$. Wheel speed reference $\omega_{m\_W}^{*}$ is obtained from the slip velocity control block considering the gear ratio, i.e. $\omega_{m\_W}^{*} = \frac{R_{g\_W}}{r_W} \cdot v_W$, where v_W is the wheel linear speed in m/s. A dynamic limiter is added for the slip speed controller to avoid wind-up problems in the Proportional-Integral (PI) controller when the slip speed control is not active [157]. Different slip control modes are discussed following.
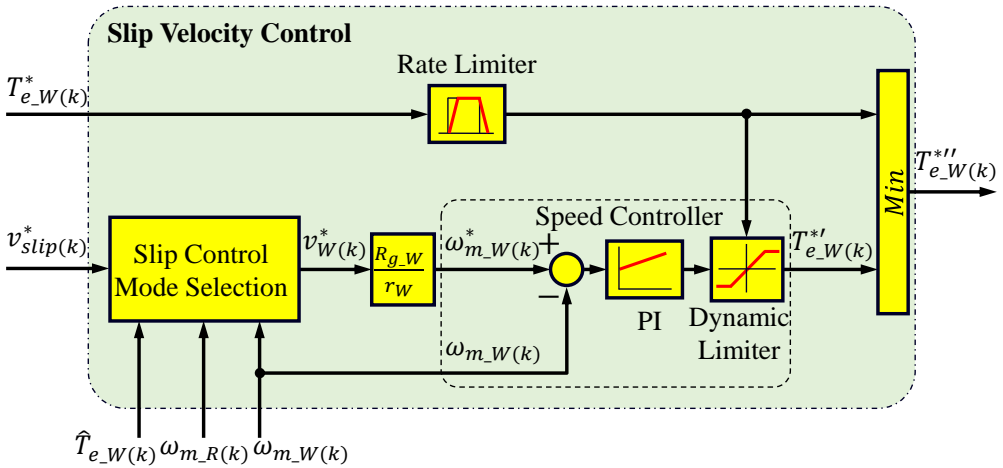
Figure 4.5: Detailed slip velocity control block diagram.

4.4   Slip Velocity Control Methods

This Section reviews the slip velocity control methods reported in the literature. The slip velocity control mode can be selected either with constant or variable slip velocity (see Fig. 4.5). Variable slip mode can be based on train speed where the slip velocity reference value is changing along the whole trip,

and continuously adapting the slip velocity command to track the maximum adhesion. The classification of the slip control mode is summarized in Fig. 4.6, and the discussion of each method is provided in the following subsection.
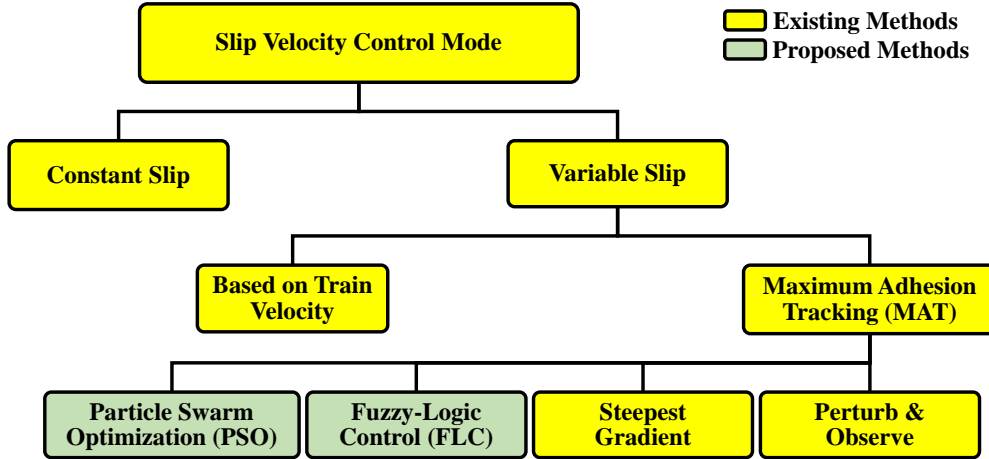
Figure 4.6: Classification of slip velocity control mode.

4.4.1 Constant Slip Velocity Control

This method is the simplest solution for slip control, being likely the most common choice for anti-slip protection in railway applications [44]. In this control mode, slip velocity reference v_{slip}^* is added to the train velocity and sent to the wheel speed controller as seen in Fig. 4.7. In this chapter, it is assumed that the train speed is measured. Methods to measure or estimate the train's linear speed can be found in [159–161]. Slip velocity reference is selected based on field tests and the train's driver experience, being generally in the range of ≈ 0.5 to 1.0 m/s [44]. Regardless of its simplicity, the main demerit of this method is that it does not usually operate at the maximum adhesion point.
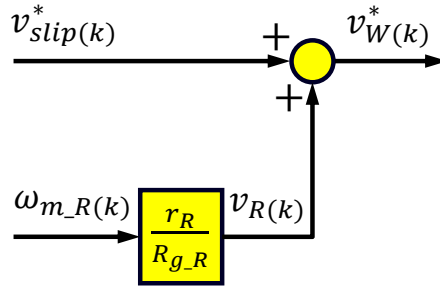
Figure 4.7: Constant slip velocity control command generation.

Fig. 4.8a shows simulation results using this method. The adhesion profiles P_1, P_2, and P_3 used are shown in Fig. 4.8b. A torque ramp with a final value of 10 Nm is commanded. The adhesion is lost when the actual torque reaches ≈ 5 Nm (see Fig. 4.8a-top). Slip velocity control is then activated with a 1.0 m/s set point (see third subplot in Fig. 4.8a). The response of slip control to changes in the wheel-roller adhesion conditions (P_1, P_2, and P_3 i.e., from high to low adhesion) is also simulated as shown in Fig. 4.8. Constant slip velocity control is seen to provide a good dynamic response, with deviations from the target sleep corrected in ≈ 1 s, and not exceeding ≈ 0.2 m/s.
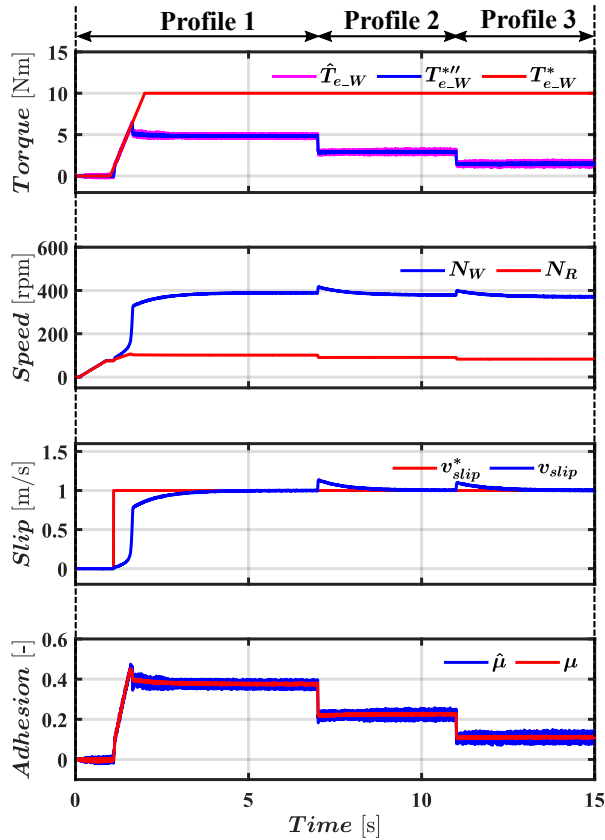
(a)
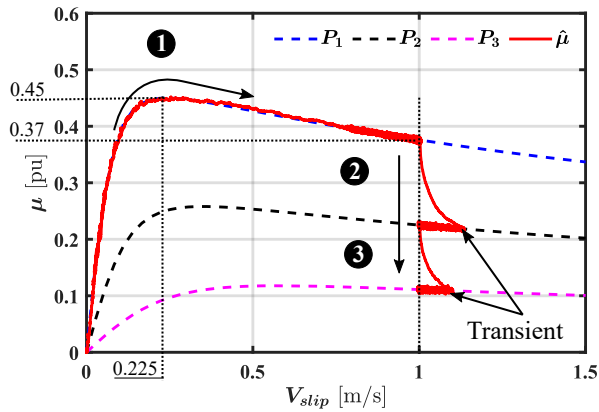
(b)

Figure 4.8: Constant slip velocity control (simulation): (a) transient response; (b) adhesion profiles. ① $P_1 : t < 7$ s; ② $P_2 : 7$ s$< t < 11$ s; ③ $P_3 : t > 11$ s.

4.4.2 Variable Slip Velocity Control with Maximum Adhesion Estimation

These methods are aimed to operate at the slip speed providing maximum adhesion. This will require maximum adhesion estimation. Subsections 4.4.2.1 and 4.4.2.2 discuss methods already reported in the literature. Two new methods will be proposed in Section 4.5

4.4.2.1 Perturb and Observe (P&O)

In this method, the slip velocity is indirectly controlled by perturbing the wheel acceleration as seen in Fig. 4.9. The wheel velocity command v_W^* is obtained by integrating the wheel acceleration command which is a combination of the current acceleration a_W and a constant value Δa as given by (4.16) and (4.17). Selection of a_0 or a_1 is based on Perturb and Observe (P&O) technique to track the maximum torque [162, 163].

$$a_0 = a_W - \Delta a \qquad (4.16)$$

$$a_1 = a_W + \Delta a \qquad (4.17)$$
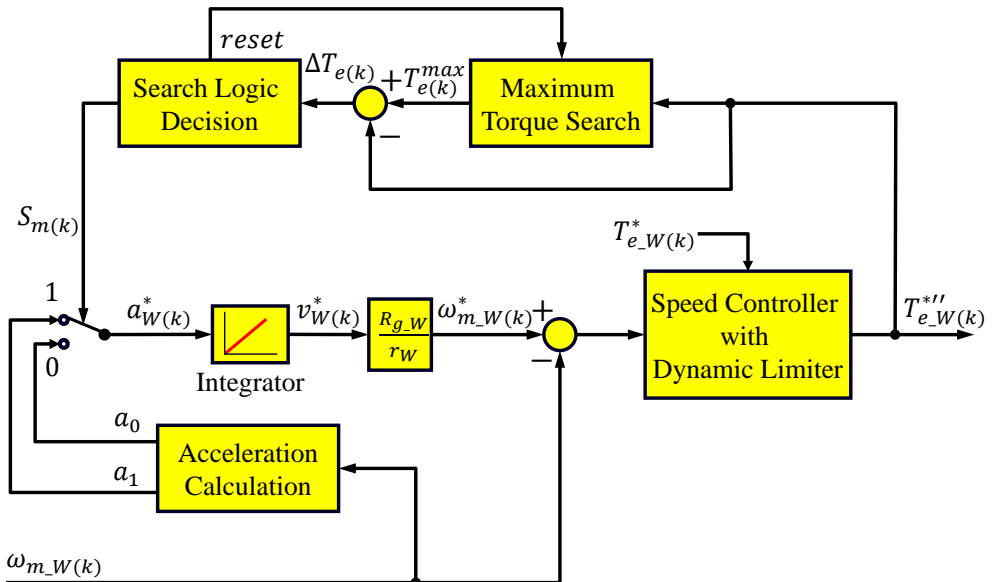
Figure 4.9: Perturb and Observe (P&O) slip velocity control mode block diagram.

The operation of MAT strategy can be summarized as follows:

- The acceleration of the traction motor wheel is initially perturbed (e.g. increased). The developed torque during this process is stored. The maximum torque value during the perturbation period $T_{e(k)}^{max}$ is held and subtracted from the current torque value obtaining ΔT_e (see Maximum Torque Search block in Fig. 4.9).

- ΔT_e is sent to the Search Logic Decision block, which will choose between a_0 and a_1 using a binary output signal $S_{m(k)}$. The search logic task is to adapt the operating point either by increasing or decreasing the acceleration command based on the current load torque compared to the maximum stored value during perturbation. If $\Delta T_e > T_{threshold}$, then the current torque $T_{e\_W}^{*\prime\prime}$ is moving apart from the peak of the adhesion curve thus the search logic block output $S_m = 0$ to decelerate the wheel and bring the operating point back to the peak of the curve (see Acceleration Calculation block in Fig. 4.9).

- A reset signal generated in the Search Logic in Fig. 4.9 is used to reset the counter in the Maximum Torque Search block which handles the perturbation period. Consequently, the operating point is expected to be alternating around the peak of the adhesion curve with no need for additional speed measurement, i.e. train velocity.

The main drawback of this method is that it creates additional ripples in the machine torque, which depend on the perturbation period. This might contribute to undesired oscillations in the mechanical drive train torsional elements [164].

Fig. 4.10 shows the simulation results of the roller rig emulator using P&O method slip velocity control. Operating conditions are the same as in Fig. 4.8. Significant excursions around the peak of the adhesion curve are observed in Fig. 4.10b, especially for the case of P_1 which corresponds to the highest adhesion level, i.e. dry condition. Also, it is found that the P&O method has a slow dynamic response while searching for the peak. Finally, peak searching capability becomes more challenging with flat adhesion curves like P_2 and P_3 (see Fig. 4.10b).
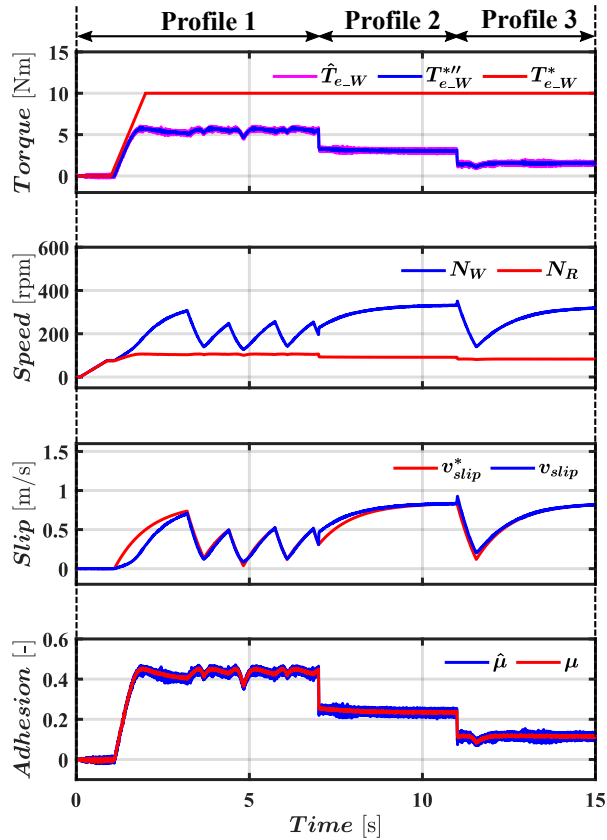
(a)
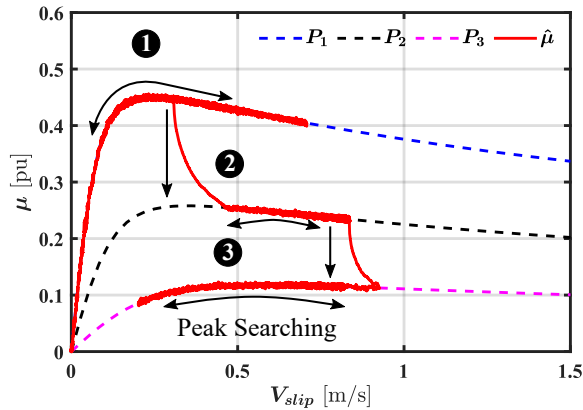
(b)

Figure 4.10: Variable slip velocity control using Perturb and Observe (P&O) (simulation): (a) transient response; (b) adhesion profiles. ① $P_1 : t < 7$ s; ② $P_2 : 7$ s$< t < 11$ s; ③ $P_3 : t > 11$ s.

4.4.2.2 Steepest Gradient

This approach takes advantage of the non-linear behavior of the adhesion-slip characteristic curve to track the maximum adhesion. As already known, the adhesion-slip characteristic is divided into two regions as shown in Fig. 4.11a: 1) micro-slip (stable) region, where the adhesion coefficient μ increases with the slip velocity v_{slip} till reaches its maximum value; 2) macro-slip (unstable), where any increase in slip velocity will decrease the adhesion coefficient and would drive the traction system to instability.

Defining the increments of the adhesion coefficient and slip velocity as (4.18) and (4.19) respectively, the slope of the adhesion-slip curve is given by (4.20).

$$\Delta \hat{\mu}_{(k)} = \hat{\mu}_{(k)} - \hat{\mu}_{(k-1)} \tag{4.18}$$

$$\Delta v_{slip(k)} = v_{slip(k)} - v_{slip(k-1)} \tag{4.19}$$

$$K_{v_{slip}(k)} = \frac{\Delta \hat{\mu}_{(k)}}{\Delta v_{slip(k)}} \tag{4.20}$$

The slope $K_{v_{slip}(k)}$ is positive in the micro-slip region, and negative in the macro-slip region, being zero at the peak of the adhesion-slip curve [see Fig. 4.11a]. Hence, tracking the maximum adhesion in the steepest gradient method would be naturally done by adding the current gradient of the adhesion-slip curve to the previous slip velocity as shown in (4.21). Gain α in (4.21) is an adaptation constant.

$$v^*_{slip(k)} = v_{slip(k-1)} + \alpha \cdot K_{v_{slip}(k)} \tag{4.21}$$

According to (4.21), if the operating point is in the micro-slip region, the adhesion-slip gradient $K_{v_{slip}(k)}$ is positive and the slip velocity command is increased. Contrarily, if the operating point falls in the macro-slip region, the gradient added is negative, and the slip velocity command is decreased. Once the maximum adhesion is reached, the adhesion-slip gradient is zero and no change is applied to the slip velocity. The block diagram of the steepest gradient method is shown in Fig. 4.11b.
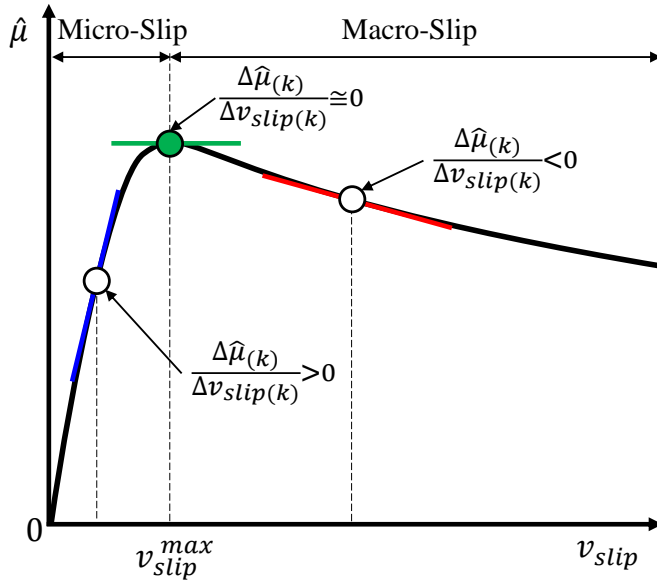
(a)
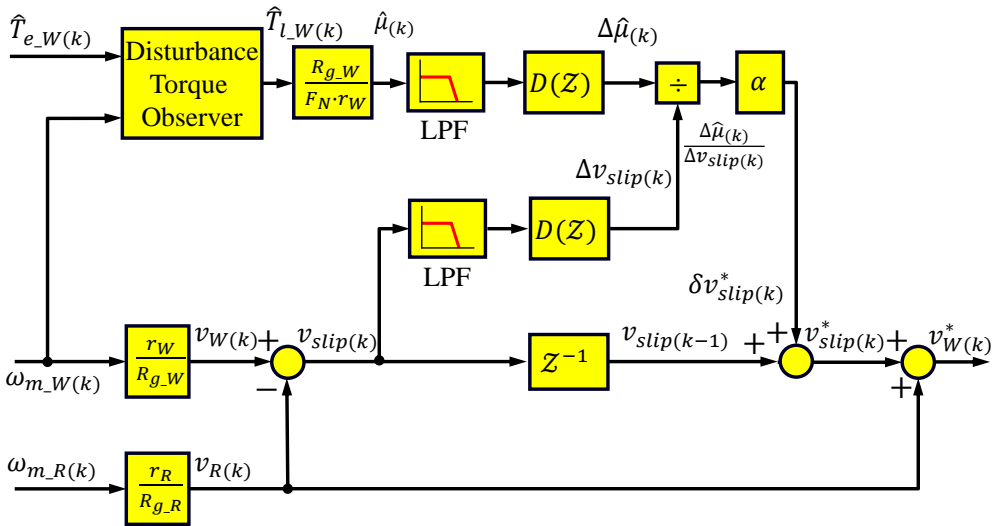
(b)

Figure 4.11: Steepest Gradient slip velocity control mode. (a) adhesion-slip curve and involved incremental variables; (b) Block diagram.

As the adhesion coefficient μ in an actual locomotive cannot be measured, estimation is required. A disturbance observer is commonly used for adhesion estimation using (4.22).

$$\hat{\mu} = \hat{T}_{l\_W} \frac{R_{g\_W}}{F_N \cdot r_W} \qquad (4.22)$$

$\hat{T}_{l\_W}$ can be estimated from (4.23), where B_m and J_m are the viscus friction and inertia of the traction wheel motor, respectively.

$$\hat{T}_{l\_W} = \hat{T}_{e\_W} - B_m \omega_{m\_W} - J_m \dot{\omega}_{m\_W} \qquad (4.23)$$

To avoid the pure derivative in (4.23), a low pass filter can be used instead (4.24).

$$\hat{T}_{l\_W(s)} = \hat{T}_{e\_W(s)} - \omega_{m\_W(s)} \left[B_{m\_W} + J_m s \left(\frac{1}{\tau s + 1} \right) \right] \qquad (4.24)$$

Two low-pass filters are used to attenuate the measurement noise in the slip velocity signal and the estimated adhesion coefficient prior to the discrete differentiation realized by $D(z)$ blocks.

Simulation results for this method are shown in Fig. 4.12. Due to the differentiation of signals used to estimate the adhesion slope $\frac{\Delta \mu_{(k)}}{\Delta v_{slip(k)}}$, Steepest Gradient (SG) method suffers from high oscillations attempting to keep the operating point at the peak of the adhesion-slip curve (see Fig. 4.12a). This becomes obvious for the adhesion profiles with higher slopes like P_1 as the resulting slope correction signal $K_{v_{slip(k)}}$ increases dramatically for the next step of the slip velocity command. Contrarily, with lower adhesion slopes such as P_2 and P_3, the correction signal moderately increases with the assumption of using constant correction factor α. However, it can be noticed in this method that the operating points are closer to the peak of the adhesion-slip curves for all the profiles. However, the peak searching space is still high (see Fig. 4.12b).
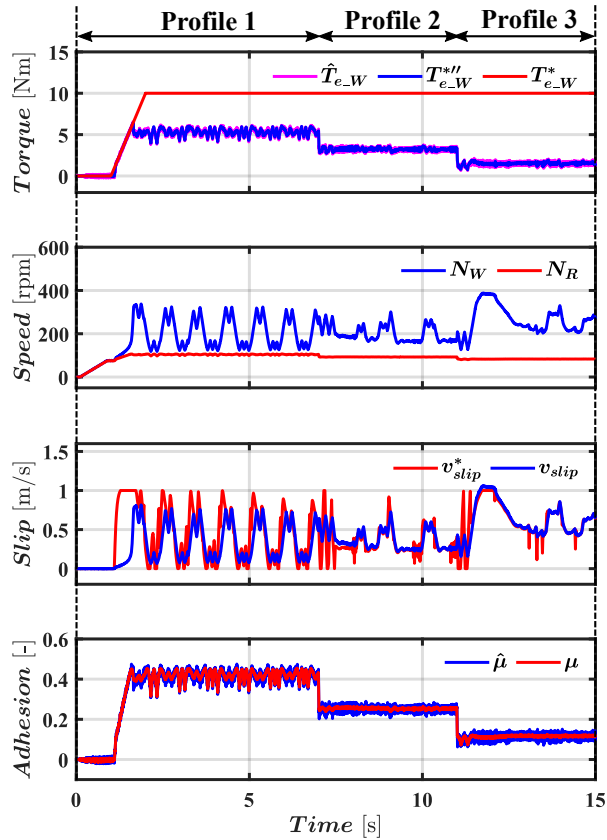
(a)
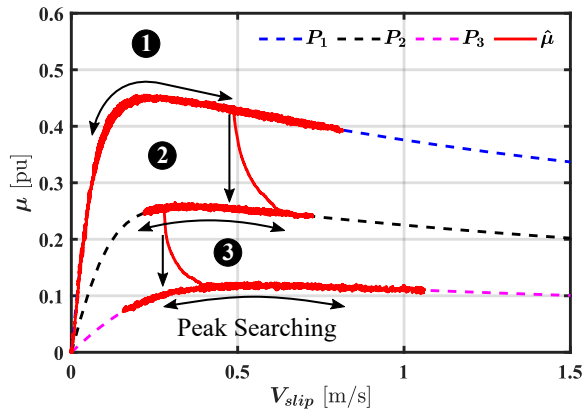
(b)

Figure 4.12: Variable slip velocity control using Steepest Gradient (SG) method (simulation): (a) transient response; (b) adhesion profiles. ① $P_1 : t < 7$ s; ② $P_2 : 7$ s$< t < 11$ s; ③ $P_3 : t > 11$ s.

4.5 Proposed MAT Techniques for Railways

As discussed in Subsection 4.4.2, operation with variable slip will require estimation of maximum adhesion. Two new methods are proposed and assessed in this Section, based on Meta-heuristic Fuzzy Logic Control and Particle Swarm Optimization respectively.

4.5.1 MAT Using Meta-heuristic Fuzzy Logic Control

Fuzzy Logic Control (FLC) is a knowledge-based control technique that uses linguistic rules designed for complex, uncertain, and non-linear systems without requiring mathematical models and/or parameter estimation [165,166]. FLC was first introduced for anti-lock braking systems (ABS) in railway traction applications to prevent wheel skid on the rail, resulting in high braking performance and consequently lower braking distance compared to conventional PID controller [51,52,167,168]. Later, FLC concept has been extended for wheel slip prevention and speed profile tracking in electric trains [169–172]. The use of FLC for MAT is developed following.

The proposed block diagram is shown in Fig. 4.13. It uses the same slip command adaptation concept of the Steepest Gradient method for tracking the peak of the adhesion curve (see Fig. 4.11a). However, the change in the slip command $v^*_{slip(k)}$ is adapted and generated automatically by the FLC block. From (4.14), it can be seen that the estimated wheel motor torque is proportional to the adhesion coefficient μ as the normal force F_N, the radius of the wheel r_W and the gear ratio R_{gW} are already known. Thus the load torque estimation $\hat{T}_{l\_W}$ using the disturbance observer in Fig. 4.11b is not required anymore and the FLC rules can be applied to the estimated motor torque $\hat{T}_{e\_W}$. $\hat{T}_{e\_W}$ is already available since it is used for the drive torque control as shown in Fig. 4.4.

The procedure for MAT using FLC is summarized in Fig. 4.14 including the flowchart shown in Fig. 4.14b.
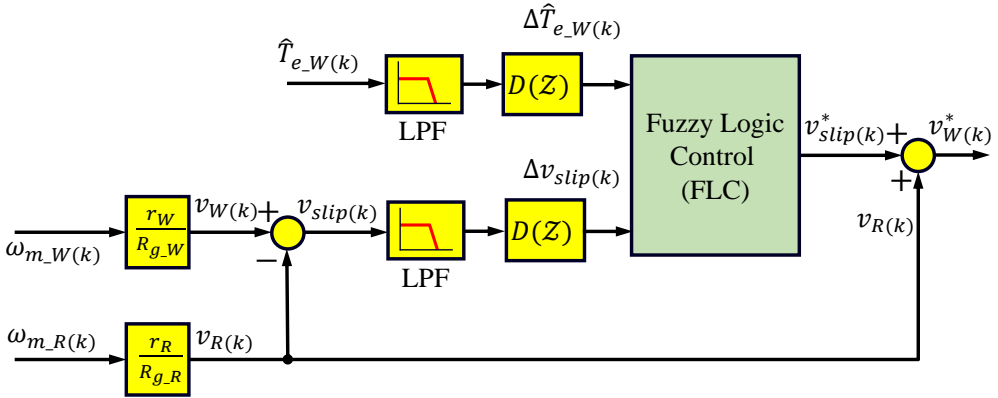
Figure 4.13: MAT using Fuzzy Logic Control (FLC) block diagram.

Like the conventional FLC structure, the FLC block of the proposed method (see Fig. 4.13) contains the input fuzzification, the fuzzy interface, and the output defuzzification respectively as seen in Fig. 4.15a. The fuzzification block consists of two membership functions that create the linguistic rules of the input variables, i.e. the $\Delta \hat{T}_{e(k)}$ and $\Delta v_{slip(k)}$. Then, the fuzzy interface correlates the linguistic rules with the knowledge base for maximum adhesion-slip curve tracking. Finally, the fuzzified output rules are transformed back to real numbers using the defuzzification membership function. The rules used in 4.15b are denoted for: NB is Negative Big; NS is Negative small; Z is zero; PS is Positive Small, and PB is Positive Big. The choice of the input and output parameters (x_2, x_1 & y_2, y_1) will depend on field tests and trains' driver expertise. For the following simulations, the input parameters are assigned as $x_2 = 15$ Nm, $x_1 = x_2/2 = 7.5$ Nm for torque increment, $x_2 = 1.0$ m/s, $x_1 = x_2/2 = 0.5$ m/s for slip velocity increment, and the output parameters are $y_2 = 0.5$ m/s, $y_1 = y_2/2 = 0.25$ m/s for the updated slip velocity command.
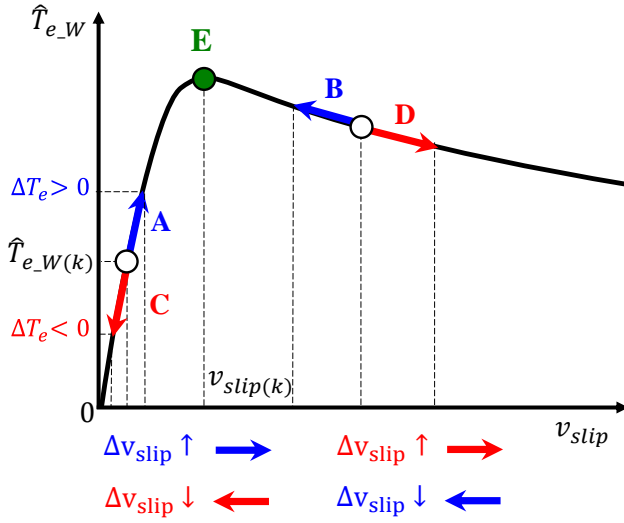
(a)
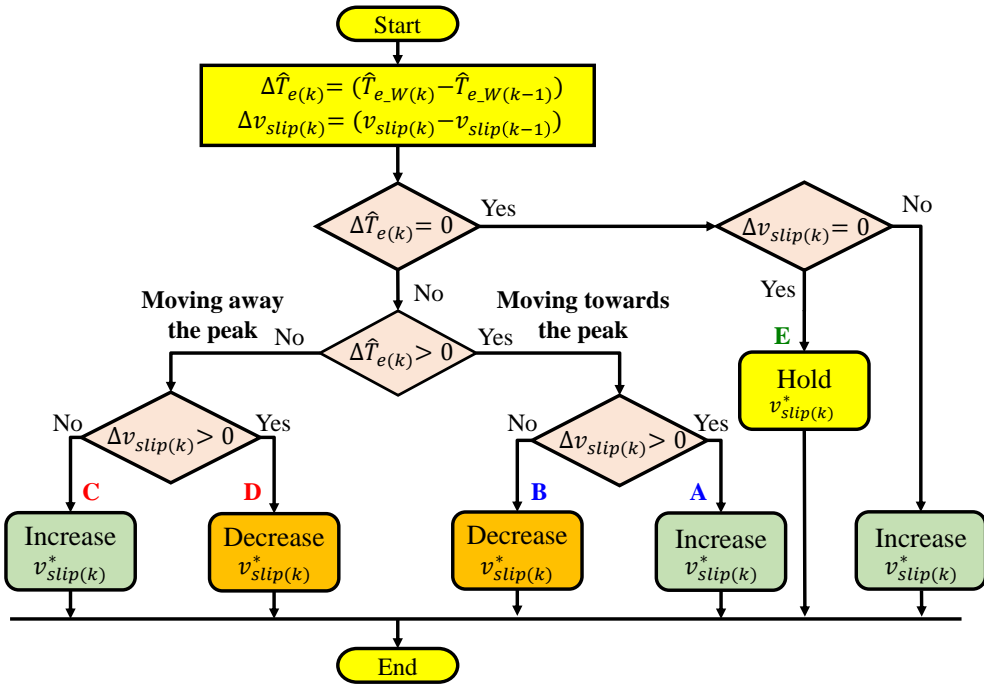
(b)

Figure 4.14: MAT using FLC procedure. (a) Adhesion-slip curve strategy; (b) Flowchart representation.

(a)

(b)
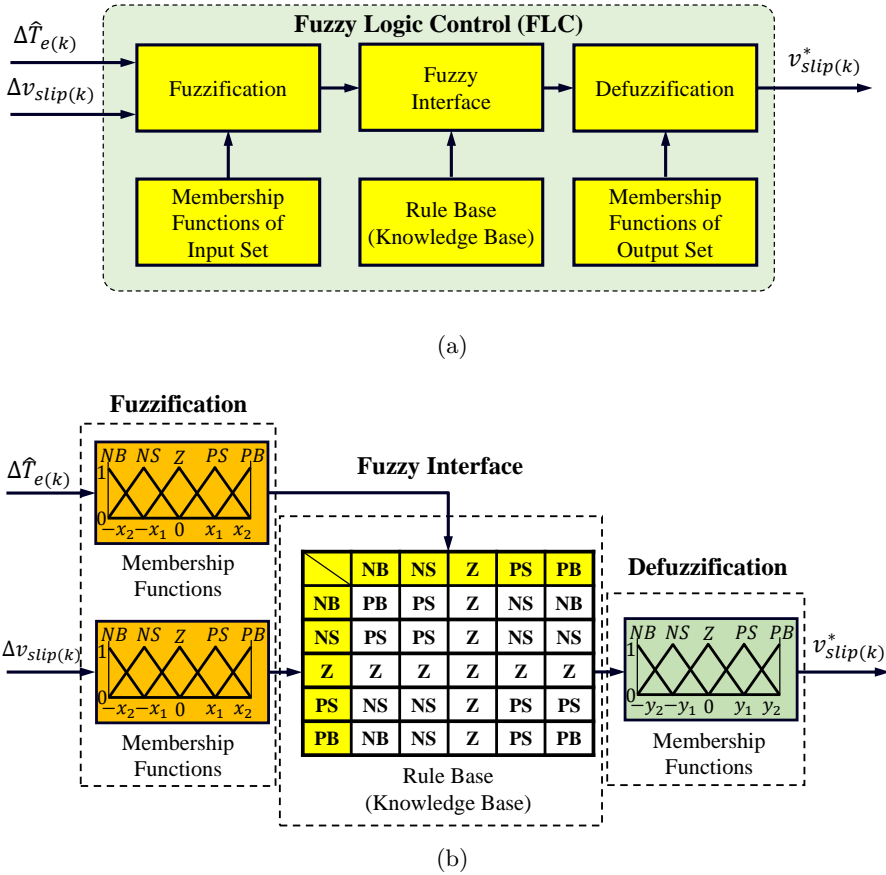
Figure 4.15: Fuzzy Logic Control (FLC) scheme. (a) Basic FLC structure; (b) Input/Output Membership functions and Rules base for MAT-FLC.

Simulation results of the proposed MAT-FLC method are shown in Fig. 4.16. The improved dynamic response and reduced oscillations are readily visible comparing Fig. 4.16a with Fig. 4.10a and 4.12a. The maximum adhesion of $\hat{\mu} = 0.45$ for P_1 is achieved in $< 1s$. The searching space is also decreased as observed comparing Fig. 4.16b with Fig. 4.10b and 4.12b.

For adhesion profiles P_1 and P_2, MAT-FLC was able to find the maximum adhesion-slip point. However, for P_3, the maximum adhesion found by the algorithm was $\approx 12\%$ smaller than the optimal value, with an error of $\approx -40\%$ in the estimated optimal slip velocity. This error can be minimized by modifying the membership functions and rules used in the FLC. Thus, adaptive tuning of FLC for multiple adhesion profiles to track the peak of the adhesion curve is needed. Implementing adaptive tuning algorithms increases the complexity of the proposed MAT-FLC [173–177]. A new approach for MAT

estimation that overcomes this problem is proposed in the next subsection.
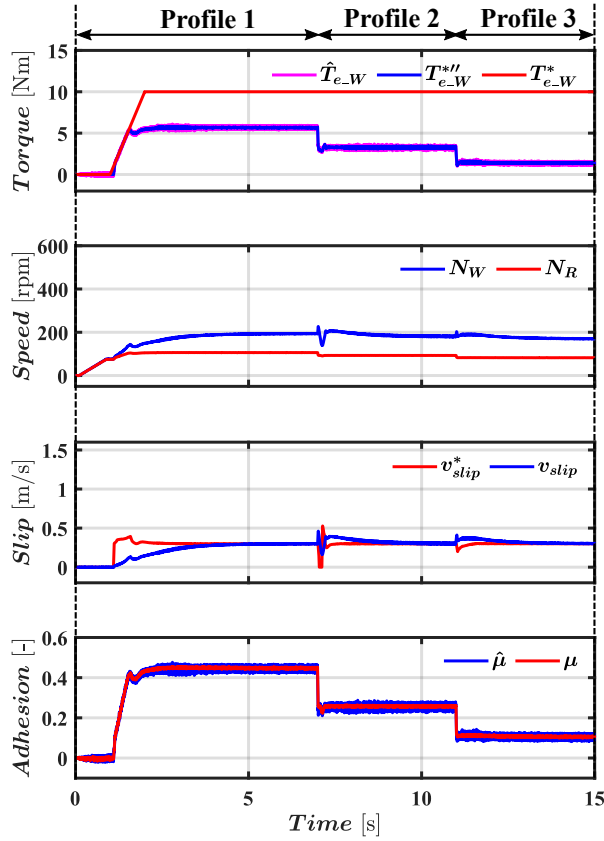
(a)
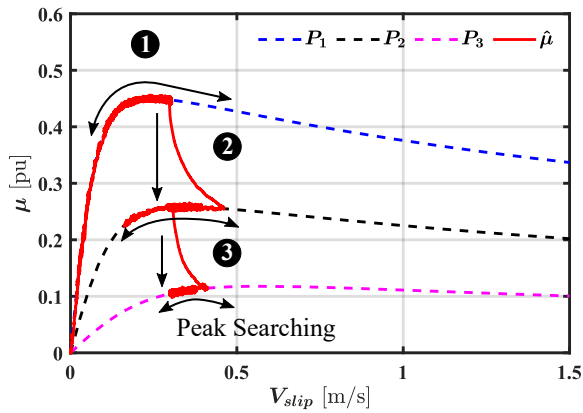
(b)

Figure 4.16: MAT using the proposed MAT-FLC (simulation): (a) transient response; (b) adhesion profiles. ① $P_1 : t < 7$ s; ② $P_2 : 7$ s$< t < 11$ s; ③ $P_3 : t > 11$ s.

4.5.2 MAT Using Particle Swarm Optimization

Particle swarm optimization (PSO) is a population-based stochastic optimization algorithm inspired by the movement of organisms such as flocks of birds or schools of fish [178]. PSO concept has roots in artificial life and evolutionary computation, intended for optimizing non-linear functions [179,180]. PSO algorithm is simple, computationally efficient, and effective in solving a variety of problems for different applications [173,181]. Maximum Power Point Tracking using Particle swarm optimization (MPPT-PSO) is considered one of the most popular evolutionary optimization algorithms in solar Photo-Voltaic (PV) systems due to its high tracking speed, ability to operate under different environmental conditions, and fast computational capability [182–187].

The PSO algorithm contains a swarm of individuals (particles) at random positions, where each particle represents a possible solution to the problem under investigation. To find the optimal solution, all particles follow a similar behavior, e.g., the position of any particle is influenced by the best particle in the neighborhood (p_{best}) as well as the best solution found by all the particles in the entire population (g_{best}). The best solution here is referred to the solution which satisfies the selected criterion (fitness function), e.g., to find the global minimum, the global maximum, etc. The particle position adjustment can be represented mathematically as (4.25) and (4.26).

$$u^i_{(k+1)} = wu^i_{(k)} + c_1 r_1 (p^i_{best} - x^i_{(k)}) + c_2 r_2 (g_{best} - x^i_{(k)}) \qquad (4.25)$$

$$x^i_{(k+1)} = x^i_{(k)} + u^i_{(k+1)} \qquad (4.26)$$

where,

$x^i_{(k+1)}$	current position of particle i;
$u^i_{(k+1)}$	current velocity of particle i ;
w	inertia weighting parameter;
c_1, c_2	acceleration coefficients;
r_1, r_2	random numbers between 0 to 1;
p^i_{best}	best solution of each particle i in the iteration k;
g_{best}	best solution of all particles in the iteration k

As in MAT-FLC, the proposed MAT technique using PSO (MAT-PSO) algorithm uses the increments of wheel motor torque $\Delta \hat{T}_{e(k)}$ and slip velocity $\Delta v_{slip(k)}$ to locate the current operating point on the adhesion-slip curve. The

output slip velocity reference signal $v^*_{slip(k)}$ is then adjusted as seen in Fig. 4.17. In the proposed method, the PSO algorithm is designed to search for the minimum absolute value of the adhesion-slip curve slope (see Fig. 4.18), as $\frac{\Delta \hat{T}_{e(k)}}{\Delta v_{slip(k)}} \approx 0$ occurs only at the peak of the adhesion-slip curve.
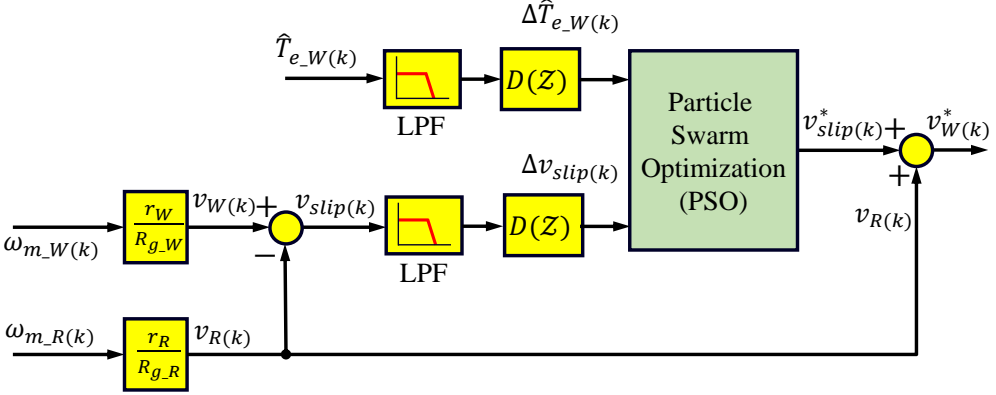
Figure 4.17: MAT using Particle Swarm Optimization (PSO) block diagram.

The flow chart of the proposed MAT-PSO method is shown in Fig. 4.19. Four particles ($N_p = 4$) were found adequate to achieve fast search speed with a computational effort suitable for real-time implementation. The algorithm starts with an initial guess of the positions of the particles (i.e. slip velocities) (see Fig. 4.18a), local best particle position p_{best}, and global best particle position g_{best} (see Fig. 4.18b). The slope of the adhesion-slip curve is first calculated for each particle and then the fitness function is evaluated individually, where the minimum value is considered to be the local best particle p_{best}, and its initial value is updated. The new p_{best} value is assigned to be the new global best particle g_{best} which other particles should follow for the next iteration. The p_{best} and g_{best} will be varying while searching for the value that satisfies the fitness function (see particle 2 in Fig. 4.18c). Afterward, the output slip velocity $v^*_{slip(k)}$ is set to be equal to the global best particle position $v^{g_{best}}_{slip(k)}$ (see Fig. 4.18d). Finally, the output slip velocity reference $v^*_{slip(k)}$ will be held constant until the reset function is activated. This occurs when the change in the wheel motor torque and the slip velocity exceeds a certain limit chosen based on the dynamics of the applied system. This situation refers to a change in the adhesion level due to changes in the track condition such as wet, ice, contaminants, etc.
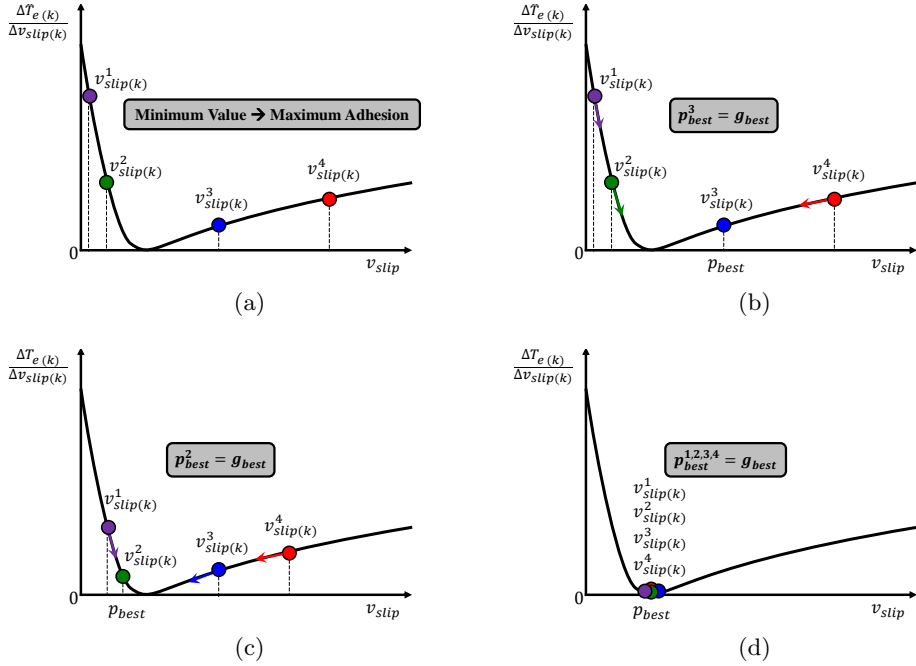
Figure 4.18: Procedure of minimum search using Particle Swarm Optimization (PSO). (a) Particle initialization; (b) Particle movements towards the global best particle after one iteration; (c) Particle swarming towards the global minimum value; (d) Particle final positions at the minimum value where the objective function is achieved.

Algorithm 1 PSO

1: Initialize a population of particles N_p with random values positions and velocities
2: **while** Termination condition not reached **do**
3:     **for** Each particle i **do**
4:         Adapt velocity of the particle using Equation (4.25)
5:         Update the position of the particle using Equation (4.26)
6:         Calculate the adhesion slope for each particle i
7:         Evaluate the fitness function $f(\overrightarrow{X}_i)$
8:         **if** $f(\overrightarrow{X}_i) < f(\overrightarrow{P}_i)$ **then**
9:             $\overrightarrow{P}_i \leftarrow \overrightarrow{X}_i$
10:         **end if**
11:         **if** $f(\overrightarrow{X}_i) < f(\overrightarrow{P}_g)$ **then**
12:             $\overrightarrow{P}_g \leftarrow \overrightarrow{X}_i$
13:         **end if**
14:     **end for**
15: **end while**

The simplified pseudo algorithm for PSO is presented in Algorithm 1 where $\overrightarrow{X}_i$ represents the current particle position vector; $\overrightarrow{P}_i$ is the best individual particle position vector, and $\overrightarrow{P}_g$ is the best global particle position vector.
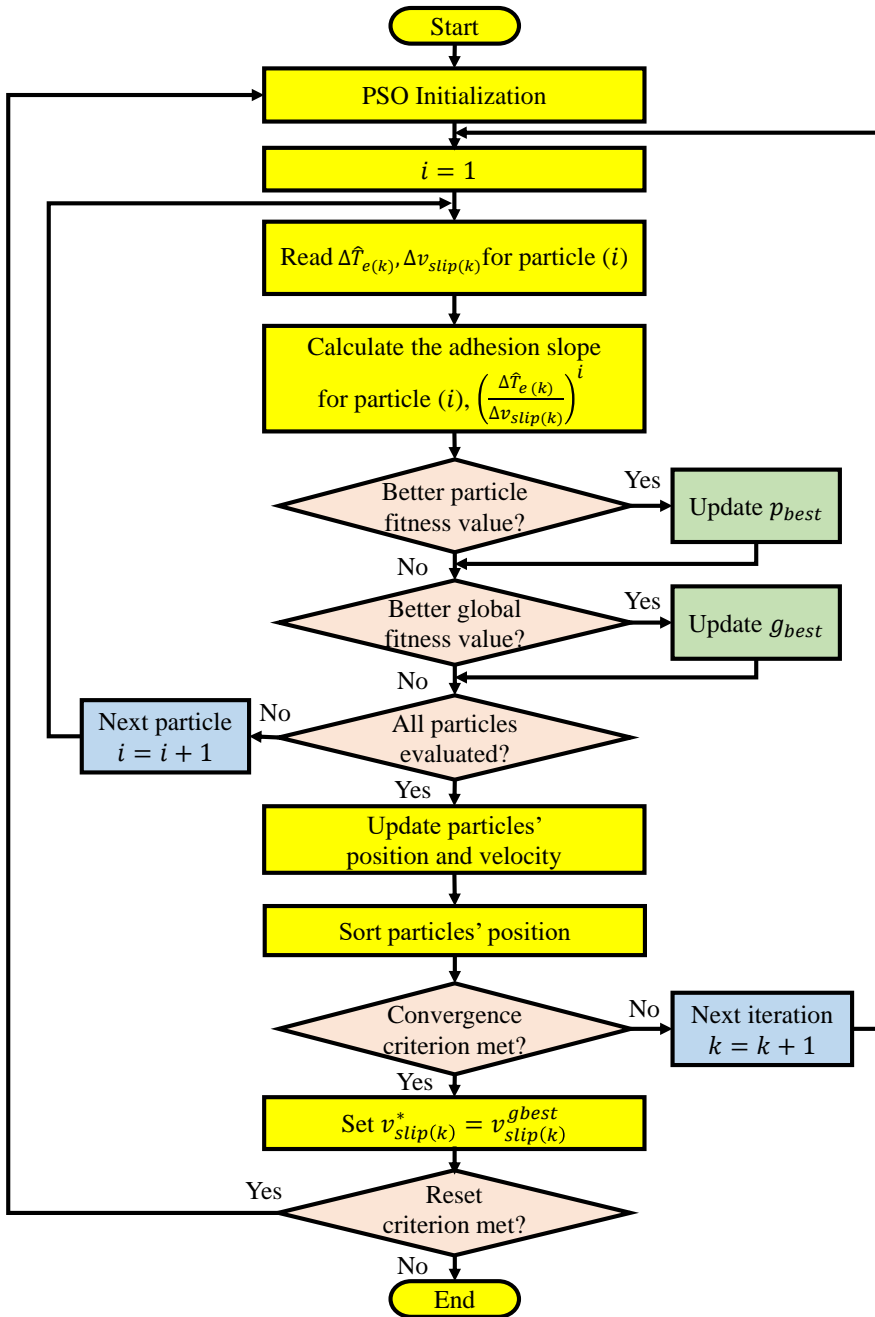
Figure 4.19: Flowchart of Particle Swarm Optimization (PSO) for minimum search.
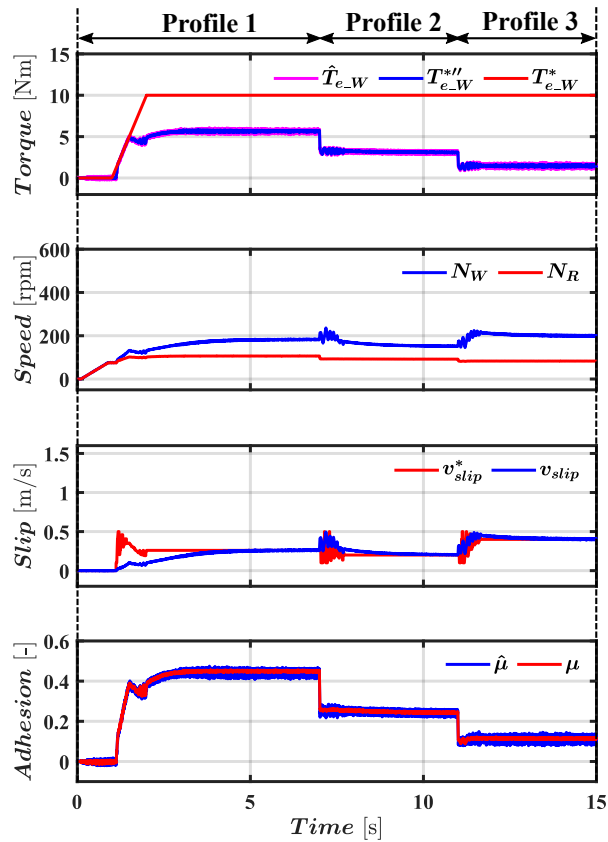
(a)
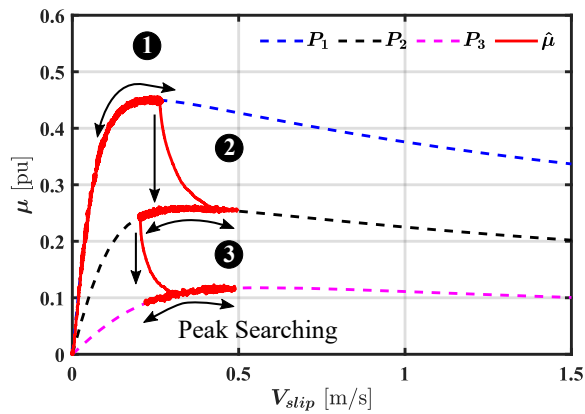
(b)

Figure 4.20: Simulation results: Proposed MAT using Particle Swarm Optimization (PSO) (MAT-PSO).

From Fig. 4.16 and Fig. 4.20, it is observed that MAT-PSO has a slightly slower response compared to MAT-FLC. This is due to the re-initialization of particles' positions and random movement when the reset function is activated (see third subplot in Fig. 4.20a). On the other hand, PSO algorithm shows a superior steady-state performance for obtaining the correct slip velocity command value at which the peak of the adhesion curve occurs. This can be noticed for P_3 where it reaches to $v_{slip}^* = 0.41$ m/s while the theoretical peak occurs at $v_{slip}^* = 0.45$ m/s (see Fig. 4.20b).

Fig. 4.21 summarizes the main characteristics and expected performance of the methods being considered. Constant slip velocity control is seen to provide excellent results in almost all the aspects being evaluated, but this is at the price of no MAT searching capability. This control mode would be beneficial for rail tracks with known adhesion characteristics. Unfortunately, this knowledge is not available in practice. The shortcomings of the constant slip method are overcome using the proposed MAT-PSO, but at the cost of implementation complexity and difficult tuning. The proposed MAT-FLC shows a moderate performance, providing some of the advantages of MAT-PSO but with less computational effort. MAT-P&O and MAT-SG show similar performance regarding tracking capability and simplicity. However, MAT-SG shows the worst performance regarding signal smoothness and steady-state response.

Figure 4.21: Comparison of slip velocity control methods.

4.6 Experimental Validation

In this Section, all methods discussed in Section 4.4 and the proposed ones in Section 4.5 are validated and evaluated experimentally.

4.6.1 Test Bench Overview

The scaled roller rig described in Subsection 4.3 is used for emulating the wheel-rail contact dynamics. The roller rig test bench is shown in Fig. 4.22a and its parameters are given in table A.2 in the appendix [157]. The roller rig load is adjusted by a spring system attached to a dynamometer for load force measurements which applies extra force on the wheel as seen in Fig. 4.22a. Additionally, a water spraying system is included for evaluation of the control strategies when the wheel-roller surface becomes wet.

Two four-pole induction motors of 4 kW (LS112M) and 5.5 kW (LSES132SU) are used for wheel and roller respectively [188]. The induction motors are driven by two independent drives where both drives use RFOC for torque control and Space-Vector Modulation technique (SVM) for voltage modulation mentioned in Sections 3.3.2 and 2.2.2. However, a commercial VACON NXP00385 Danfoss drive is used in speed control mode to keep the roller motor speed constant (see Fig. 4.22a]) [189]. While a three-phase two-level custom drive is built especially for the wheel motor to validate different slip velocity control strategies discussed in Sections 4.2 and 4.5.

The custom drive shown in Fig. 4.22b is designed and built with AECP group at the university of Oviedo which handles power up to 10 kW. The three-phase input AC source from the mains is converted into DC voltage with an average value of 540 V via three-phase power diode rectifier module DF75LB80 (see Fig. 4.21c) [190]. Two electrolytic capacitors PEH200YT4220MU2, each rated 2.2 mF, 450 V are connected in series to form a DC bus with 5% of ripple equipped with a charging circuit of approximately 3 seconds [191]. The DC bus is connected to a 7MBP100VDA120-50 three-phase Insulated Gate Bipolar Transistor (IGBT) power module which consists of 6 IGBT switches for three legs of the DC-AC inverter and a dynamic braking switch, used during braking [192]. It should be noted that a MKP386M snubber film capacitor is being connected at the DC input terminals of the power module to protect the IGBTs from the ringing effect during turn-off due to bus bars parasitic inductance and to reduce the electromagnetic interference [193]. The gate

driver unit of the inverter receives the gate pulses from the micro-controller board through the HFBR-2522Z optical fiber cable (OFC) and converts it into the gate voltage required by the power module using optocouplers which provide optical isolation to the signals [194].

(a)

(b)

(c)
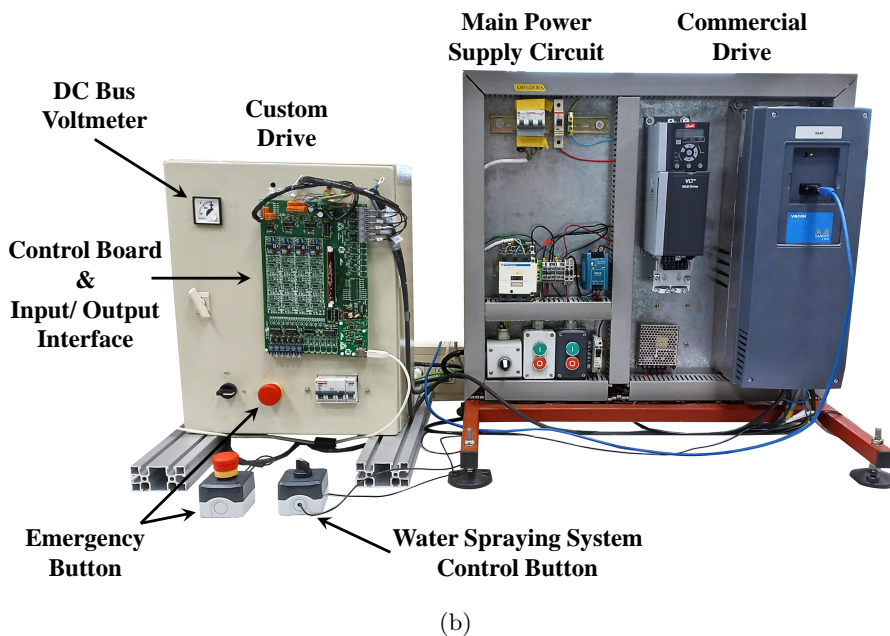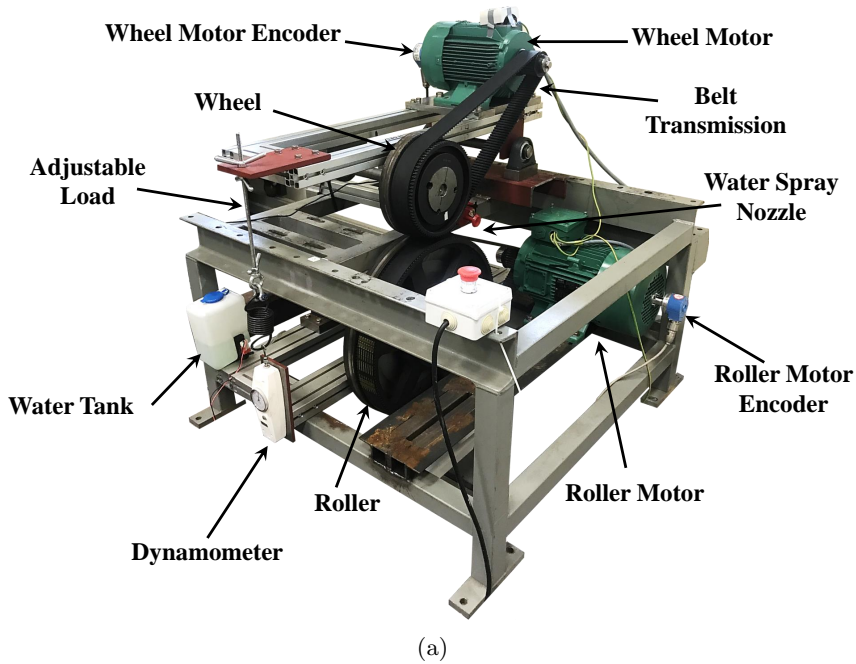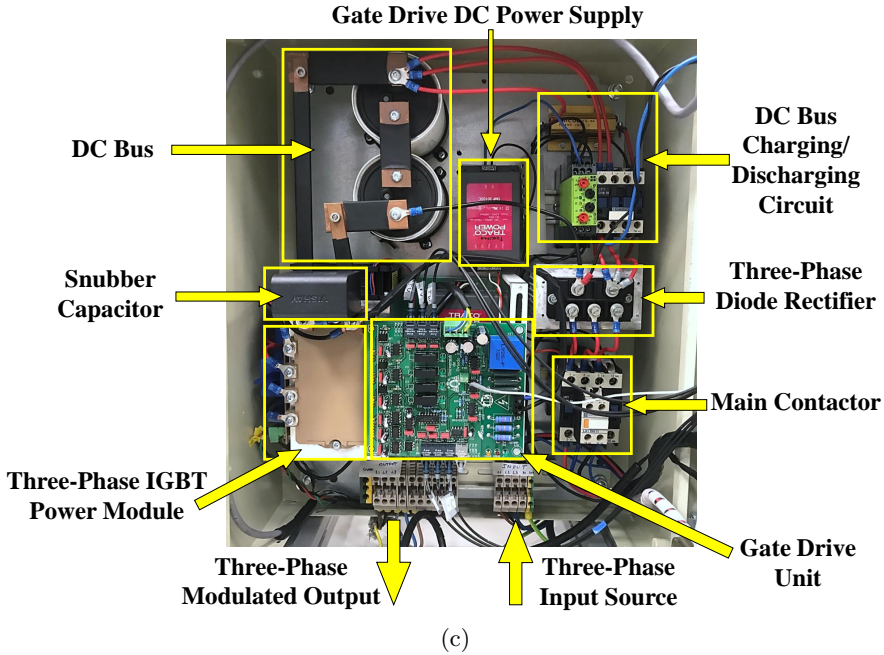
Figure 4.21: Overview of the experimental setup: (a) roller rig test bench; (b) Electrical circuit and motor drives; (c) Custom drive elements.

4.6.2 Results and Discussion

The methods discussed in Sections 4.2 and 4.5 were tested in the test bench. For each method, the experiments start with a dry wheel-roller contact point, then at $t \approx 35$ s the water spraying system is turned on till the end of the experiment with a flow rate of 140 ml/min. Fig. 4.22 and Fig. 4.23 show the response of the five methods being considered.

Overall, experimental results for all methods are in good agreement with the simulation results obtained in Sections 4.2 and 4.5. However, torque and speed oscillations in the experiments are seen to be lower than in simulation (see Fig. 4.10a & 4.12a vs. 4.22e & 4.22f). Contrary to simulation results, changes from dry to wet conditions of the contact point do not occur instantaneously in the test bench. This would explain some of the differences observed between simulation and experimental results.

For the constant slip control method (see Fig. 4.22d and 4.23a), the achieved steady-state adhesion coefficient for dry and wet conditions are $\hat{\mu} \approx 0.5$ and $\hat{\mu} \approx 0.15$ respectively. These values increase to $\hat{\mu} \approx 0.6$ and $\hat{\mu} \approx 0.25$ for all MAT methods considered in this paper (see Fig. 4.22e to Fig. 4.22h

and Fig. 4.23b to Fig. 4.23e). As expected, all the methods track the peak of the adhesion curve both in dry and wet conditions. An increase in slip velocity ($v_{slip} \approx 0.45$ m/s) is noticed while peak searching in wet condition [see Fig. 4.22f $t = 45$s to $t = 65$s] with MAT-SG due to the continuous increment of ($\Delta v^* slip(k)$) term in the slip velocity command in the case of flat adhesion curves aiming to find the maximum peak. This doesn't occur with MAT-PO as the search logic alternate between the increment/decrement of the slip velocity command.

The two proposed methods MAT-FLC and MAT-PSO show a similar response as seen in Fig. 4.22g and Fig. 4.22h, as well as Fig. 4.23d and 4.23e. However, for MAT-FLC the slip velocity command is kept at the same value ($v_{slip} \approx 0.2$ m/s) for both adhesion conditions while for MAT-PSO slip velocity is slightly differs as ($v_{slip} \approx 0.3$ m/s) and ($v_{slip} \approx 0.35$ m/s) in dry and wet conditions respectively. The difference in the performance of FLC and PSO algorithms is negligible and can be only noticed in the search space of the adhesion-slip curves, but noting the relevant differences in the implementation complexity. Therefore, the proposed MAT methods achieve the same adhesion level ($\approx 20\%$ higher than the constant slip method) with less slip velocity in steady-state compared to existing methods.
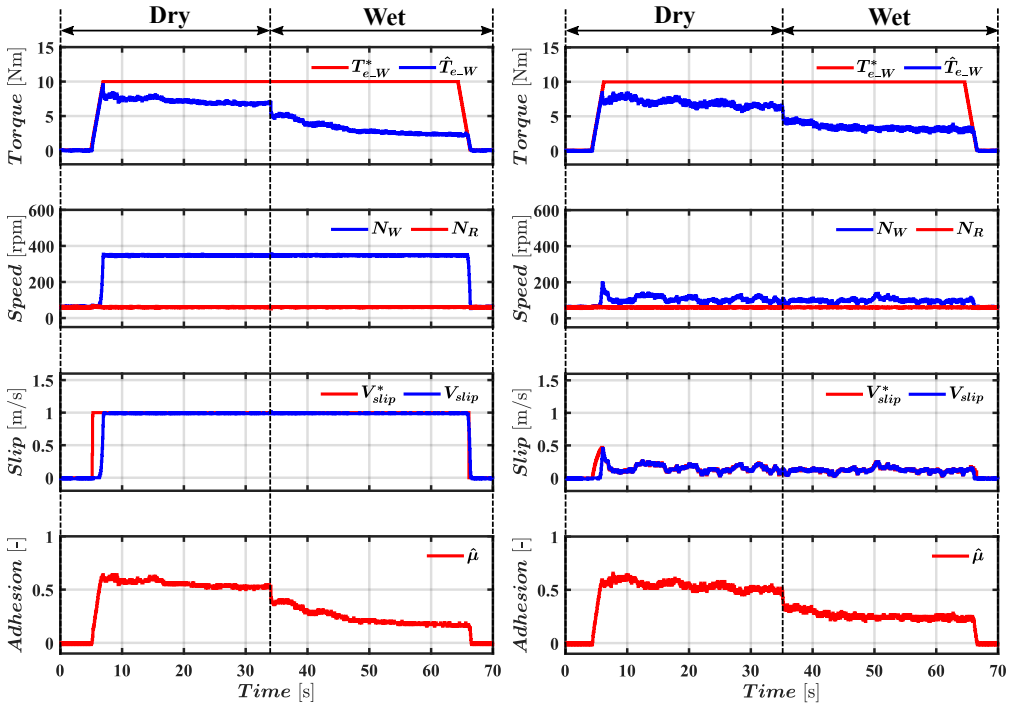
(d)

(e)
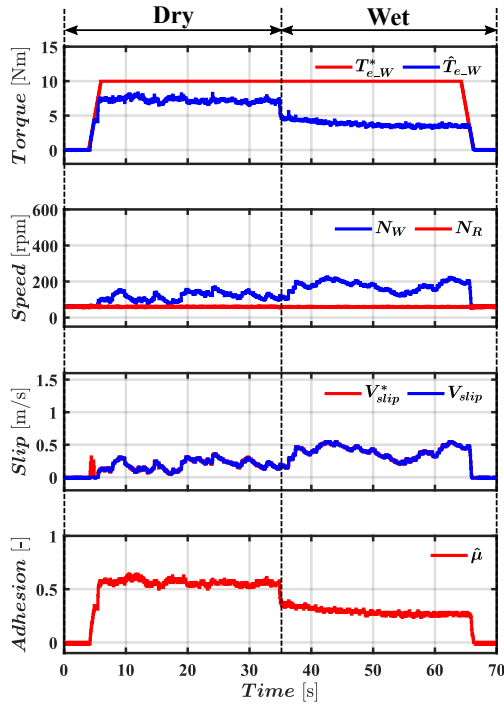
(f)
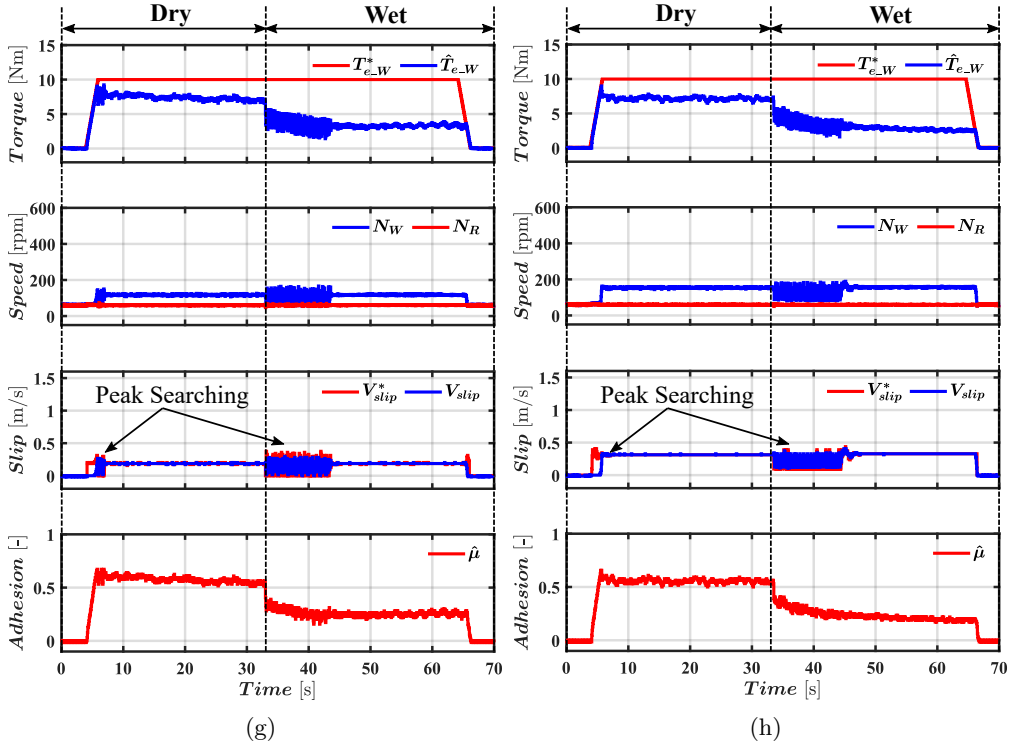
Figure 4.22: Experimental results. Response in the time domain: (a) constant slip velocity; (b) MAT-P&O; (c) MAT-SG; (d) MAT-FLC; and (e) MAT-PSO.
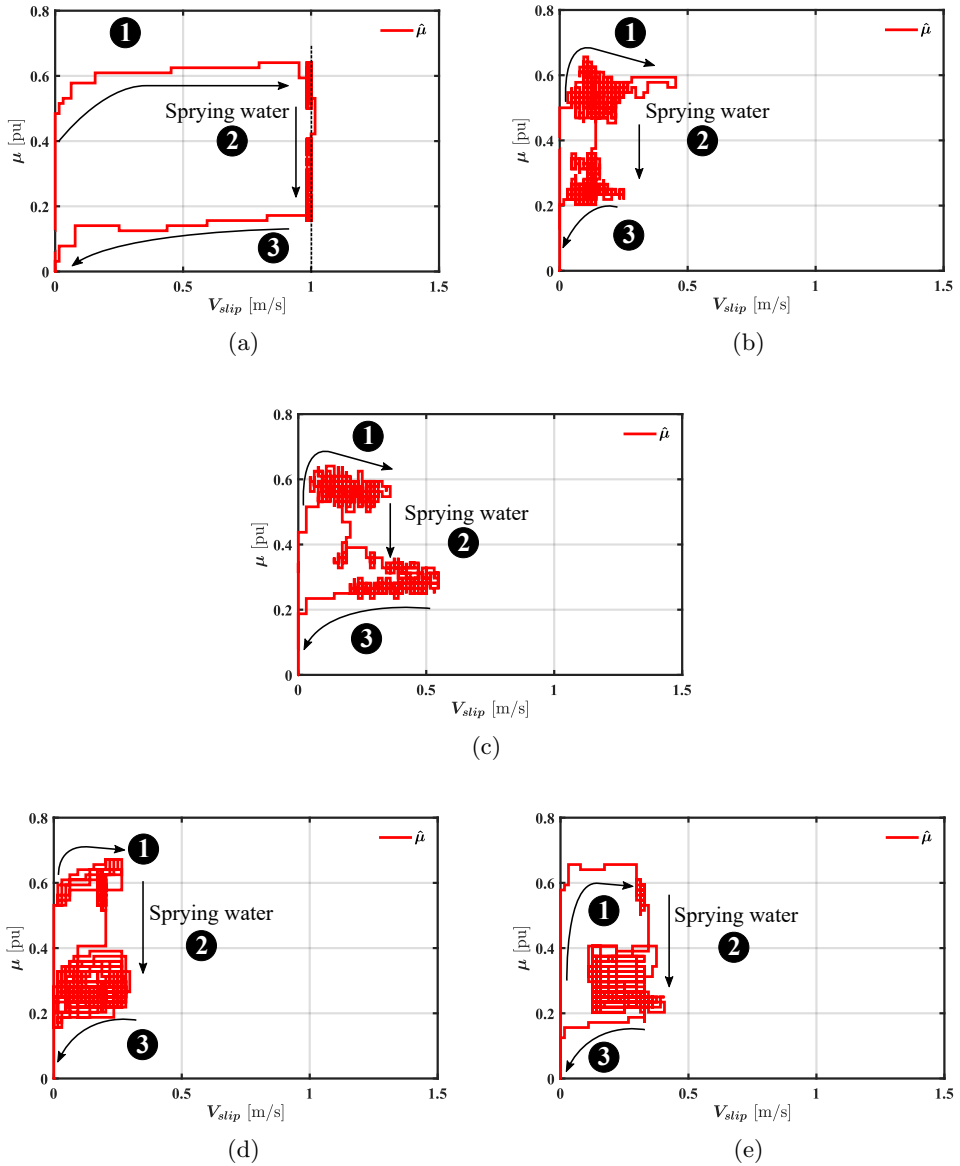
Figure 4.23: Experimental results. Adhesion-slip trajectory: (a) constant slip velocity; (b) MAT-P&O; (c) MAT-SG; (d) MAT-FLC; and (e) MAT-PSO.

4.7   Conclusions

Traction capability mainly depends on the adhesion coefficient between the wheel and the rail in railways. Improving traction capability reduces travel time and energy consumption during traction/braking. Operating at maximum adhesion coefficient is not straightforward due to its non-linear and almost unpredictable nature. In this Chapter, a comparative analysis of constant and variable slip velocity control using Maximum Adhesion Traction (MAT) has been presented.

Existing and proposed slip velocity control strategies have been simulated and validated experimentally where the wheel-rail contact point has been emulated using a scaled roller rig. It can be concluded that operating with constant slip velocity provides precise and stable operation at the cost of not fully optimizing the traction capability of the traction drive. Perturb and Observe (P&O) MAT method was able to track the maximum point of the adhesion-slip curve. However, there are two main drawbacks of this method: 1) the slip controller should be limited as it can fail with flat adhesion-slip curves as the controller tries to find the maximum adhesion point by increasing the slip velocity continuously, and 2) operating in the unstable adhesion region can excite the slip-stick vibrations in the mechanical elements of the drive-train. The MAT-P&O issues have been improved using the steepest gradient method (MAT-SG). As MAT-SG requires a disturbance torque observer, the sensitivity of the observer to measurements noise is the main concern of this method besides using derivatives that could be a problem in this case.

Finally, two new methods using Fuzzy Logic Control (MAT-FLC) and Particle Swarm Optimization (MAT-PSO) have been proposed. It has been shown that these methods provide similar performance finding the maximum adhesion point under dry and wet wheel-roller conditions with stable slip velocity value at steady-state, the implementation of MAT-FLC being simpler.

Chapter 5

Torsional Vibration Suppression in Railway Traction Drives

5.1 Introduction

As mentioned in Chapter 4, slip controllers enhanced with maximum adhesion tracking increase the utilization of tractive force for high-performance locomotives, however, they can potentially enter the unstable adhesion region during the searching. As a result, oscillations can arise in the torsional elements of the locomotives powertrain [61]. These oscillations can also be provoked by the slip-stick phenomenon due to changes in the adhesion condition and track irregularities. The most severe oscillation occurs when both wheels of the locomotive oscillate in counter-phase, which is sometimes referred as slip-stick vibration. Such vibrations add more stress on the press-fit joints of the wheelset axle, and could lead to their failure and, as a consequence, to the derailment of the locomotive.

This Chapter proposes a novel torsional vibration suppression method using a Proportional-Resonant (PR) controller. The proposed method will be shown to be robust against changes in slip velocity and wheel-rail conditions. In addition, the proposed method is insensitive to mechanical drivetrain parameter variation neither requiring adding new sensors to the wheelset. The method requires previous knowledge of the natural frequency of the wheelset

torsional mode, which can be simply obtained using free vibration analysis, but this significantly reduces the implementation complexity suffered by other anti-vibration methods.

This Chapter is organized as follows. Section 5.2 presents the detailed mechanical drivetrain and locomotive mathematical model. The torsional vibration excitation and its mitigation methods are addressed in 5.3. The proposed vibration suppression method is presented in Section 5.3.3. The proposed method is validated by simulation in Section 5.4. Finally, a summary of findings is provided in Section 5.6.

5.2 Modelling of Mechanical Drivetrain

The mechanical drivetrain of electric locomotives can be classified according to the construction design, for example, group or individual wheelset drives, and according to the orientation of the rotation axis (longitudinal or transversal). Modern high-speed trains are equipped with individual wheelset drives with transversal orientation [76]. Individual wheelset drives can be driven by a hollow-shaft hugging axle, axle-mounted traction motor, or by joint shaft. Join shaft drive is normally used with DC traction motors that have large proportions like SLM locomotives (Bombardier) [76]. Axle-mounted traction drive is typically used in freight locomotives with a maximum speed of ≈ 140 km/h such as Eurosprinter 127 series and German class 152 series [195]. This is mainly due to the usage of induction traction motors which have less mass $\approx 30 - 40\%$ resulting in less vertical forces reacting on the wheelset and the track. Hollow-shaft hugging axle drive is not new but its construction design shows good performance and is still used in modern high-speed locomotives. German class 120, Eurosprinter series, ICE1, and ICE2 are the most common locomotives that use this drivetrain type [76, 195].

5.2.1 Mathematical Model

This Section discusses the mechanical model of the drivetrain system. Axle-mounted and cardan hollow-shaft drives will modeled and analysed in details. The cardan hollow-shaft drivetrain of the German class 120 locomotive has been selected for the simulation verification of torsional vibration and its mitigation methods [162, 196].

5.2.1.1 Cardan Hollow-shaft Traction Drivetrain

The German class DB 120 series is one of the famous locomotives which uses the cardan hollow-shaft type for InterCity connection up to 200 km/h [162]. A schematic representation of the DB 120 drivetrain is shown in 5.1a. The traction drivetrain consists of six rotational masses that are connected by torsional elements in the series structure as follows (see Fig. 5.1b).

- The traction motor generates a drive torque T_e transmitted through the coupling to the gearbox T_M.

- Then the torque exerted in the gearbox T_{MG} is transmitted to the direct-driven wheel T_{HD} through the cardan hollow shaft, where the total inertia of the hollow shaft including the braking discs and couplings is divided into two rotating masses connected by an elastic shaft. The received torque at the direct driven wheel follows the transmission sequence: 1) from the gearbox to the first half of the hollow shaft (gear side) through a gear-hollow shaft coupling T_{GH} ; 2) then to the second half of the hollow shaft (wheel side) via the elastic shaft T_{HW}; 3) later to the direct-driven wheel T_{HD} through the hollow-shaft-wheel coupling.

- Finally, the torque is transmitted to the indirect-driven wheel via the wheelset axle T_{DI}.

The general motion equation is given by (5.1),

$$[J] \cdot \left[\ddot{\vartheta}\right] + [D] \cdot \left[\dot{\vartheta}\right] + [C] \cdot [\vartheta] = [T] \tag{5.1}$$

where,

J	inertia matrix;
D	damping ratio matrix;
C	stiffness matrix;
ϑ	rotational angle matrix;
$\dot{\vartheta}$	angular speed matrix;
$\ddot{\vartheta}$	acceleration matrix;
T	applied torque matrix

(a)

(b)
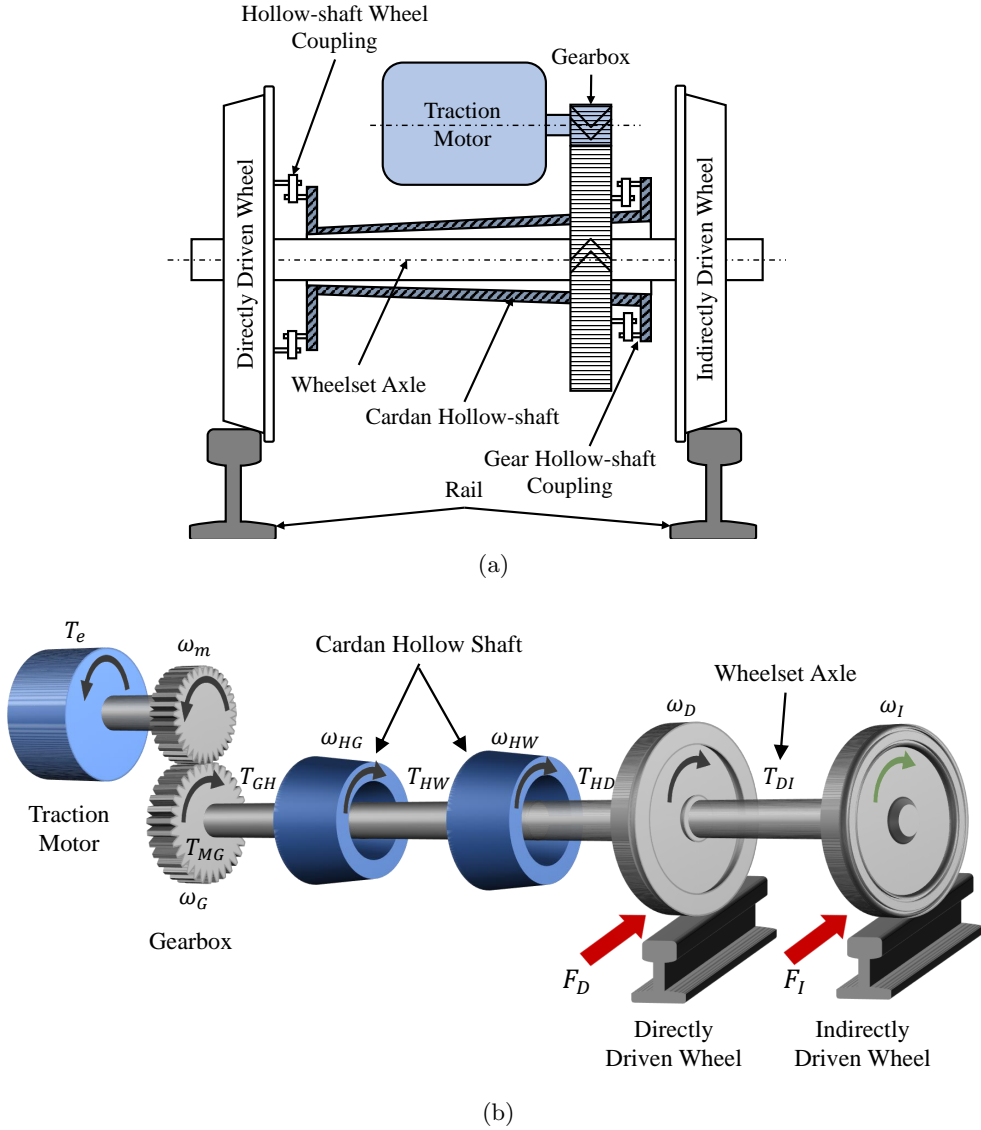
Figure 5.1: Cardan hollow-shaft traction drivetrain. (a) Schematic representation; (b) Six-inertia model. Torque transmission from the motor to direct and indirect wheels are indicated by black and green arrows respectively; adhesion forces exerted on both wheels are indicated by red arrows.

Applying (5.1) to the drivetrain in Fig. 5.1, the differential equations of the six-inertia model (5.2) are obtained. Note that all values in (5.2) are referred to the wheelset side of the drivetrain, assuming ideal gear with R_g being the gear ratio.

130

$$
\begin{bmatrix}
j_M & 0 & 0 & 0 & 0 & 0 \\
0 & j_G & 0 & 0 & 0 & 0 \\
0 & 0 & j_{HG} & 0 & 0 & 0 \\
0 & 0 & 0 & j_{HW} & 0 & 0 \\
0 & 0 & 0 & 0 & j_D & 0 \\
0 & 0 & 0 & 0 & 0 & j_I
\end{bmatrix}
\cdot
\begin{bmatrix}
\ddot{\vartheta}_M \\
\ddot{\vartheta}_G \\
\ddot{\vartheta}_{HG} \\
\ddot{\vartheta}_{HW} \\
\ddot{\vartheta}_D \\
\ddot{\vartheta}_I
\end{bmatrix}
+
$$

$$
\begin{bmatrix}
d_{MG} & -d_{MG} & 0 & 0 & 0 & 0 \\
d_{MG} & (d_{MG}+d_{GH}) & -d_{GH} & 0 & 0 & 0 \\
0 & -d_{GH} & (d_{GH}+d_{HW}) & -d_{HW} & 0 & 0 \\
0 & 0 & -d_{HW} & (d_{HW}+d_{HD}) & -d_{HD} & 0 \\
0 & 0 & 0 & -d_{HD} & (d_{HD}+d_{DI}) & -d_{DI} \\
0 & 0 & 0 & 0 & -d_{DI} & d_{DI}
\end{bmatrix}
\cdot
\begin{bmatrix}
\dot{\vartheta}_M \\
\dot{\vartheta}_G \\
\dot{\vartheta}_{HG} \\
\dot{\vartheta}_{HW} \\
\dot{\vartheta}_D \\
\dot{\vartheta}_I
\end{bmatrix}
+
$$

$$
\begin{bmatrix}
c_{MG} & -c_{MG} & 0 & 0 & 0 & 0 \\
c_{MG} & (c_{MG}+c_{GH}) & -c_{GH} & 0 & 0 & 0 \\
0 & -c_{GH} & (c_{GH}+c_{HW}) & -c_{HW} & 0 & 0 \\
0 & 0 & -d_{HW} & (c_{HW}+c_{HD}) & -c_{HD} & 0 \\
0 & 0 & 0 & -c_{HD} & (c_{HD}+c_{DI}) & -c_{DI} \\
0 & 0 & 0 & 0 & -c_{DI} & c_{DI}
\end{bmatrix}
\cdot
\begin{bmatrix}
\vartheta_M \\
\vartheta_G \\
\vartheta_{HG} \\
\vartheta_{HW} \\
\vartheta_D \\
\vartheta_I
\end{bmatrix}
=
\begin{bmatrix}
T_M \\
0 \\
0 \\
0 \\
-T_D \\
-T_I
\end{bmatrix}
\tag{5.2}
$$

where,

j_M inertia of the motor;

j_G inertia of the gear;

j_{HG} inertia of the hollow to gear half shaft;

j_{HW} inertia of the hollow to wheel half shaft;

j_D inertia of direct wheel;

j_I inertia of indirect wheel;

d_{MG}, c_{MG} damping and torsional stiffness values of the motor to the gear shaft respectively;

d_{GH}, c_{GH} damping and torsional stiffness values of the gear to the hollow shaft respectively;

d_{HW}, c_{HW} damping and torsional stiffness values of the hollow shaft gear side tothe hollow shaft wheel side respectively;

d_{HD}, c_{HD} damping and torsional stiffness values of the hollow shaft wheel side to the direct wheel respectively;

d_{DI}, c_{DI} damping and torsional stiffness values of the direct to indirect wheel shaft respectively;

T_M traction motor torque referred to wheel side;

T_D, T_I load torques applied to the direct and indirect wheels respectively

5.2.1.2 Axle-mounted Traction Drivetrain

In this drivetrain, the traction motor is directly mounted on the wheelset axle via a hollow-joint shaft attached to the gearbox (see Fig. 5.2a). This makes the torque transmitted from the traction motor onto the driven wheels is distributed into two paths through the wheelset axle. The position of the hollow-joint shaft will decide the amount of torque distribution on the wheelset axle.

(a)

(b)
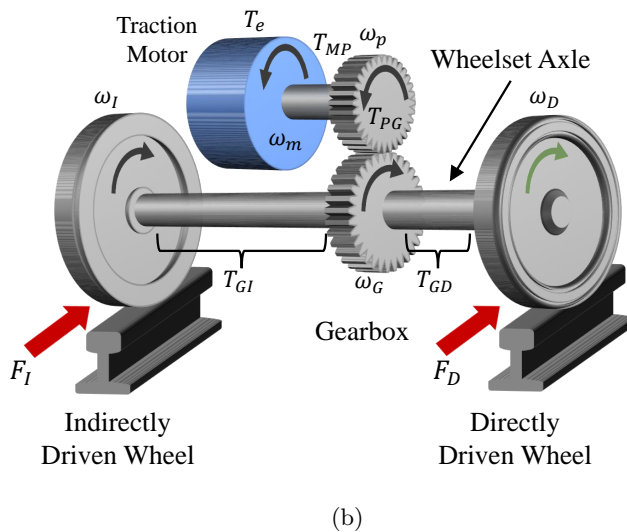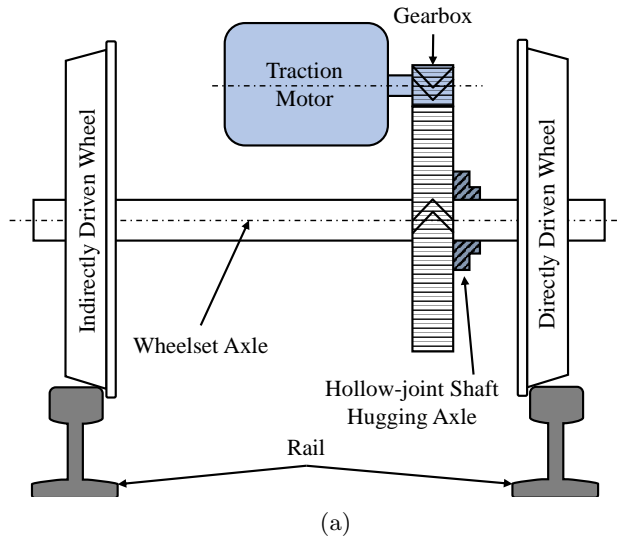
Figure 5.2: Axle-mounted traction motor drivetrain. (a) Schematic representation; (b) five-inertia model. Same legend as Fig. 5.1.

Due to manufacturing issues, the connection of the gearbox to the wheelset axle is commonly made close to one of the sides of a wheel which is referred to as the directly driven wheel. Thus the other wheel is called an indirectly driven wheel (see Fig. 5.2a).

For modeling simplification, the axle-mounted drive can be represented with five rotating masses that are connected by torsional elements in a combination of series and parallel structure (see Fig. 5.2b). Thus, the torque developed by the traction motor T_e is transmitted to the pinion through the coupling shaft T_{MP} following to the axle via the gear T_{PG}. The torque exerted on the gear is distributed into the direct wheel T_{GD} and the indirect wheel T_{GI}.

Applying (5.1) to the traction drive-train in Fig. 5.2b, the differential equations of the five-inertia model (5.3) are obtained. Note that all values in (5.3) are referred also to the wheelset side of the drive-train.

$$
\begin{bmatrix} j_M & 0 & 0 & 0 & 0 \\ 0 & j_P & 0 & 0 & 0 \\ 0 & 0 & j_G & 0 & 0 \\ 0 & 0 & 0 & j_D & 0 \\ 0 & 0 & 0 & 0 & j_I \end{bmatrix} \cdot \begin{bmatrix} \ddot{\vartheta}_M \\ \ddot{\vartheta}_P \\ \ddot{\vartheta}_G \\ \ddot{\vartheta}_D \\ \ddot{\vartheta}_I \end{bmatrix} +
$$

$$
\begin{bmatrix} d_{MP} & -d_{MP} & 0 & 0 & 0 \\ -d_{MP} & (d_{MP}+d_{PG}) & -d_{PG} & 0 & 0 \\ 0 & -d_{PG} & (d_{PG}+d_{GD}+d_{GI}) & -d_{GD} & -d_{GI} \\ 0 & 0 & -d_{GD} & d_{GD} & 0 \\ 0 & 0 & -d_{GI} & 0 & d_{GI} \end{bmatrix} \cdot \begin{bmatrix} \dot{\vartheta}_M \\ \dot{\vartheta}_P \\ \dot{\vartheta}_G \\ \dot{\vartheta}_D \\ \dot{\vartheta}_I \end{bmatrix} +
$$

$$
\begin{bmatrix} c_{MP} & -c_{MP} & 0 & 0 & 0 \\ -c_{MP} & (c_{MP}+c_{PG}) & -c_{PG} & 0 & 0 \\ 0 & -c_{PG} & (c_{PG}+c_{GD}+c_{GI}) & -c_{GD} & -c_{GI} \\ 0 & 0 & -c_{GD} & c_{GD} & 0 \\ 0 & 0 & -c_{GI} & 0 & c_{GI} \end{bmatrix} \cdot \begin{bmatrix} \vartheta_M \\ \vartheta_P \\ \vartheta_G \\ \vartheta_D \\ \vartheta_I \end{bmatrix} = \begin{bmatrix} T_M \\ 0 \\ 0 \\ -T_D \\ -T_I \end{bmatrix} \tag{5.3}
$$

where,

j_M	inertia of the motor;
j_P	inertia of the pinion;
j_G	inertia of the gear;
j_D	inertia of direct wheel;
j_I	inertia of indirect wheel;
d_{MP}, c_{MP}	damping and torsional stiffness values of the motor to the pinion shaft respectively;
d_{PG}, c_{PG}	damping and torsional stiffness values of the pinion to the gear shaft respectively;
d_{GD}, c_{GD}	damping and torsional stiffness values of the gear to the direct wheel respectively;

d_{GI}, c_{GI}	damping and torsional stiffness values of the gear to indirect wheel shaft respectively;
T_M	traction motor torque referred to wheels side;
T_D, T_I	load torques applied to direct and indirect wheels respectively

5.2.2 Modal Analysis

Modal analysis is a useful tool to identify the most stressed elements of the mechanical drivetrain from vibration characteristics, i.e. natural frequencies and mode shapes. Natural frequencies, also referred to as resonance frequencies, indicate the vibration modes of the elastic elements in the drivetrain; mode shapes indicate the relative angular displacement between adjacent elements (inertias).

Drivetrain natural frequencies and mode shapes can be obtained from the homogeneous equation (5.1) using (5.4), where λ and $[I]$ represent the eigenvalues (roots) of the system and the identity matrix respectively. It is noted that damping coefficients have been neglected, corresponding (5.4) to the worst-case scenario.

$$det \left(\lambda^2 \cdot [I] - [J]^{-1} \cdot [C] \right) = 0 \qquad (5.4)$$

Eigenvalues represent the resonance frequencies of the mechanical system, eigenvectors represent the angle deviation and the direction of rotation for each inertia relative to adjacent inertias. Mode shape is a graphical representation that shows the angle deviation between the mechanical elements at each resonance frequency (see Fig. 5.3). In this Chapter, eigenvalues and eigenvectors for the targeted (DB 120 class) drivetrain model are obtained using MATLAB and normalized based on the maximum angle deviation of all elements at each mode (see table 5.4). For instance, in the second mode, the indirect wheel has the maximum angle deviation which is selected to be the base value for the rest of the elements.

The six-inertia system consists of five torsional stiffness elements, producing five natural frequencies and mode shapes, in addition to one trivial mode as discussed following (see Fig. 5.3):

- First mode shape occurs at 0 Hz and is due to the rigid body motion.

Table 5.4: Eigenvectors of undamped six-inertia model.

Mode	1	2	3	4	5	6
f_i [Hz]	0.0	21.3	50.8	181.8	238.3	307.2
ϑ_M	1.000	-0.498	-0.1	-0.055	0.055	-0.008
ϑ_G	1.000	-0.451	-0.046	0.325	-0.592	0.154
ϑ_{HG}	1.000	-0.146	0.284	1.000	0.468	-0.990
ϑ_{HW}	1.000	0.311	0.748	-0.701	1.000	1.000
ϑ_D	1.000	0.602	1.000	-0.058	0.046	-0.027
ϑ_I	1.000	1.000	-0.790	0.002	0.001	0.003

- Second mode shape (i.e. the first vibration mode) is located at 21.3 Hz and occurs when the whole wheelset oscillates against the motor. This vibration mode can be totally damped using a proper speed controller [162].

- Third mode shape reveals the second vibration mode at 50.8 Hz, which occurs when direct and indirect wheels oscillate in the counter phase, twisting the wheelset axle. It can be noticed that this vibration mode can have a reduced impact on the motor. Detectability of the second vibration by motor control will play a key role in active damping methods, the use of speed/position sensors directly attached to the wheels might be required otherwise.

- The remaining mode shapes at higher frequencies have less influence on the traction motor and the wheelset, hence, they are normally neglected [20].

5.2.3   Approximated Model (Three-inertia Model)

Once the Eigenvalue problem is solved for the detailed model (considering the DB 120 cardan hollow-shaft drivetrain in Section 5.2.1.1) and both natural frequencies and mode shapes of the system are identified. It is convenient to develop a reduced model to include only the modes of interest for analysis [162]. This reduces the complexity and the time consumption of the analysis process. The reduced model allows to estimate the required variables in microprocessors and DSP with less computational time.
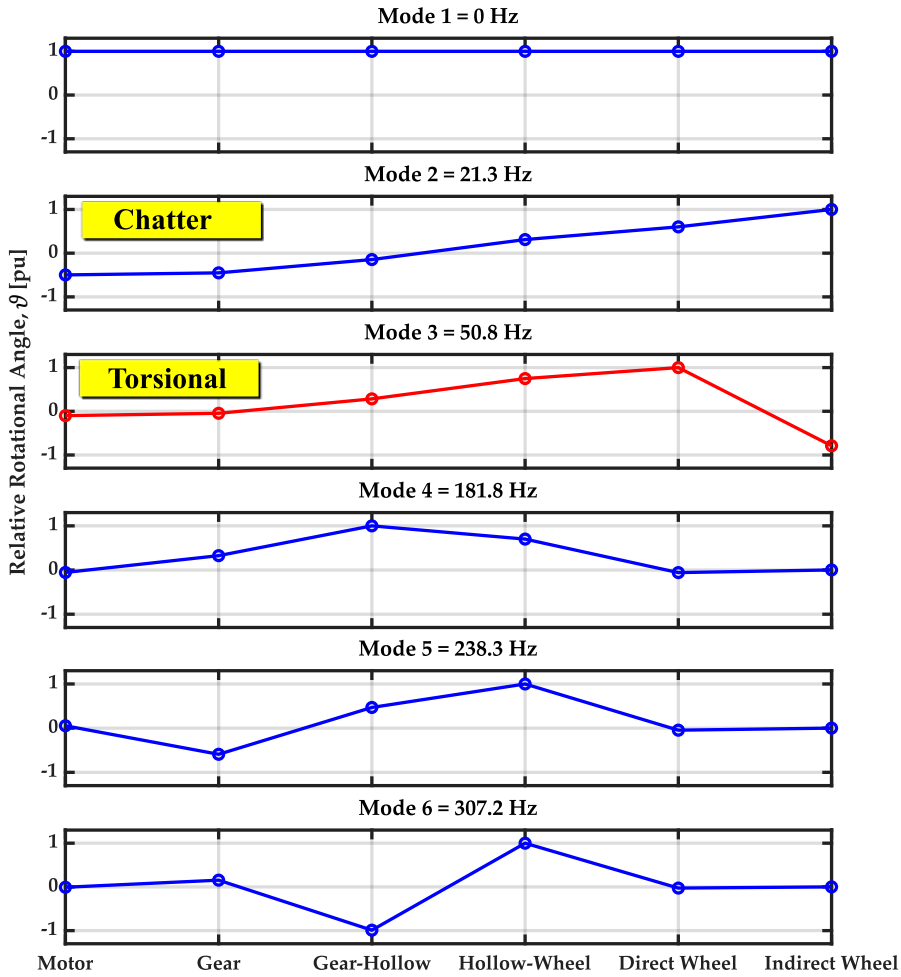
Figure 5.3: Mode shapes of the six-inertia model. Values are normalized based on the maximum absolute value at each mode.

Taking the advantage of the matrices symmetry. Only the target natural frequencies and their mode shapes are considered. For example, the first three modes are the most affecting to the system. This will create a new matrix in (5.5) where X is the eigenvector matrix, $^{(1)}$,$^{(2)}$,$^{(3)}$ are the mode numbers, and $1 \cdots n$ is the number of elements respectively.

$$X = \left[\vartheta_{1 \cdots n}^{(1)}, \vartheta_{1 \cdots n}^{(2)}, \vartheta_{1 \cdots n}^{(3)} \right] \tag{5.5}$$

The same for system elements, only the target elements are considered. For railway torsional vibration analysis, Motor, direct and indirect wheels are taken into consideration as in (5.6) where ^{T} is the matrix transportation.

$$\tilde{X} = \left[\tilde{\vartheta}_M, \tilde{\vartheta}_D, \tilde{\vartheta}_I\right]^T = \left[\vartheta_1, \vartheta_2, \vartheta_3\right]^T \tag{5.6}$$

Using the eigenvectors for the six-inertia model, the approximated three-inertia model should satisfy the equations:

$$X^T \cdot J \cdot X = \tilde{X}^T \cdot \tilde{J} \cdot \tilde{X} \tag{5.7}$$

$$X^T \cdot C \cdot X = \tilde{X}^T \cdot \tilde{C} \cdot \tilde{X} \tag{5.8}$$

$$X^T \cdot D \cdot X = \tilde{X}^T \cdot \tilde{D} \cdot \tilde{X} \tag{5.9}$$

Thus, the equivalent parameters for the reduced three-inertia model is calculated as following:

$$\tilde{J} = \tilde{X}^{T^{-1}} \cdot X^T \cdot J \cdot X \cdot \tilde{X}^{-1} \tag{5.10}$$

$$\tilde{C} = \tilde{X}^{T^{-1}} \cdot X^T \cdot C \cdot X \cdot \tilde{X}^{-1} \tag{5.11}$$

$$\tilde{D} = \tilde{X}^{T^{-1}} \cdot X^T \cdot D \cdot X \cdot \tilde{X}^{-1} \tag{5.12}$$

Finally, the general equation of motion for the approximated three-inertia model is obtained in (5.13). The equivalent model consisting of three equivalent inertias (J_1, J_2, J_3), two equivalent damping elements (d_{12}, d_{23}) and two equivalent springs with stiffness of (c_{12}, c_{23}) [162]. ϑ_{12} and ϑ_{23} represent the relative angle between the two rotating masses. The load torque is $T_L = T_{12} = c_{12} \cdot \vartheta_{12}$ and the wheelset axle torque is $T_{DI} = T_{23} = c_{23} \cdot \vartheta_{23}$, both being referred to the wheelset side. A schematic presentation of the approximated model is given in Fig. 5.4a. The mode shapes for chatter and torsional modes are found to be matched with the detailed six-inertia model shown in Fig. 5.3.

$$\begin{bmatrix} j_1 & 0 & 0 \\ 0 & j_2 & 0 \\ 0 & 0 & j_3 \end{bmatrix} \cdot \begin{bmatrix} \ddot{\vartheta}_1 \\ \ddot{\vartheta}_2 \\ \ddot{\vartheta}_3 \end{bmatrix} + \begin{bmatrix} d_{12} & -d_{12} & 0 \\ -d_{12} & (d_{12}+d_{23}) & -d_{23} \\ 0 & -d_{23} & d_{23} \end{bmatrix} \cdot \begin{bmatrix} \dot{\vartheta}_1 \\ \dot{\vartheta}_2 \\ \dot{\vartheta}_3 \end{bmatrix} +$$
$$\begin{bmatrix} c_{12} & -c_{12} & 0 \\ -c_{12} & (c_{12}+c_{23}) & -c_{23} \\ 0 & -c_{23} & c_{23} \end{bmatrix} \cdot \begin{bmatrix} \vartheta_1 \\ \vartheta_2 \\ \vartheta_3 \end{bmatrix} = \begin{bmatrix} T_L \\ -T_D \\ -T_I \end{bmatrix} \tag{5.13}$$
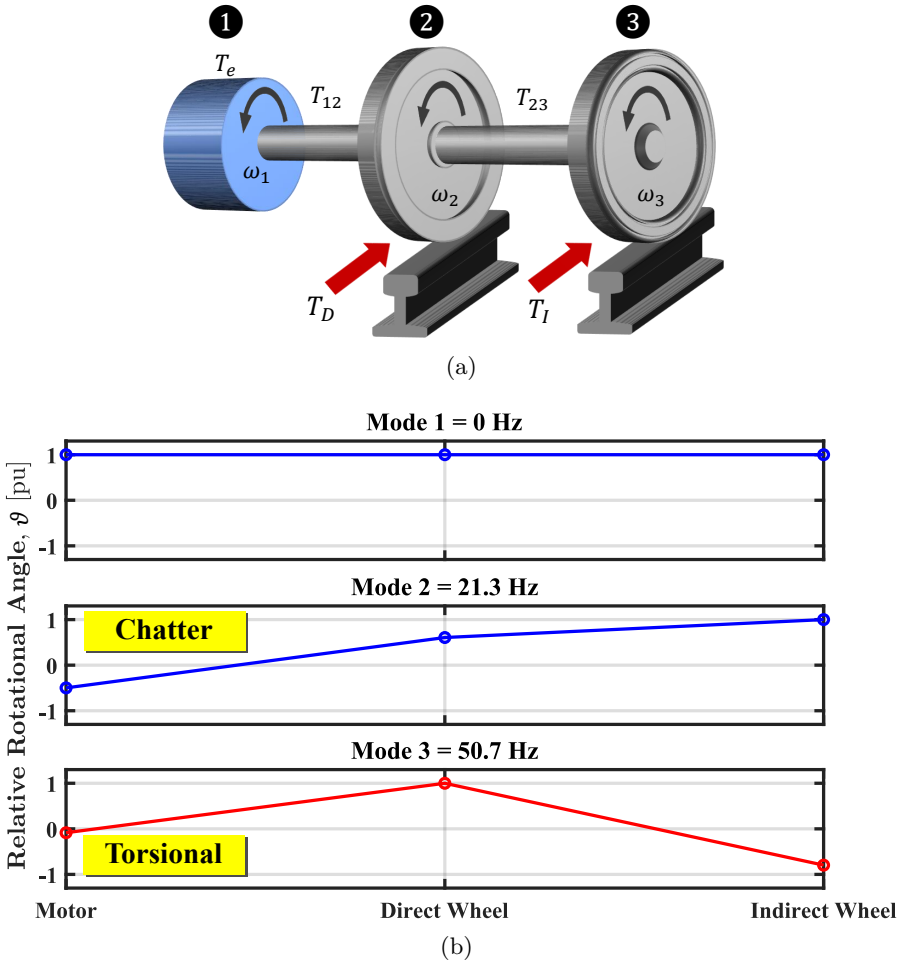
Figure 5.4: Approximated three-inertia model. (a) Schematic representation; (b) mode shapes.

5.2.4 Simulation Model

Applying Laplace transformation to (5.2), the drivetrain block diagram Fig. 5.5a is obtained. The transmitted traction forces in the wheel-rail contact point are calculated from (5.14) where r_w, $\mu_{D,I}$ and $T_{D,I}$ are the wheel radius, adhesion coefficient, and torque on each wheel, respectively; m_l, and g are the locomotive mass and the gravity constant, respectively.

$$T_{D,I} = r_w \cdot F_{D,I} = r_w \cdot \mu_{D,I} \cdot \frac{m_l \cdot g}{2 \cdot N_m} \tag{5.14}$$
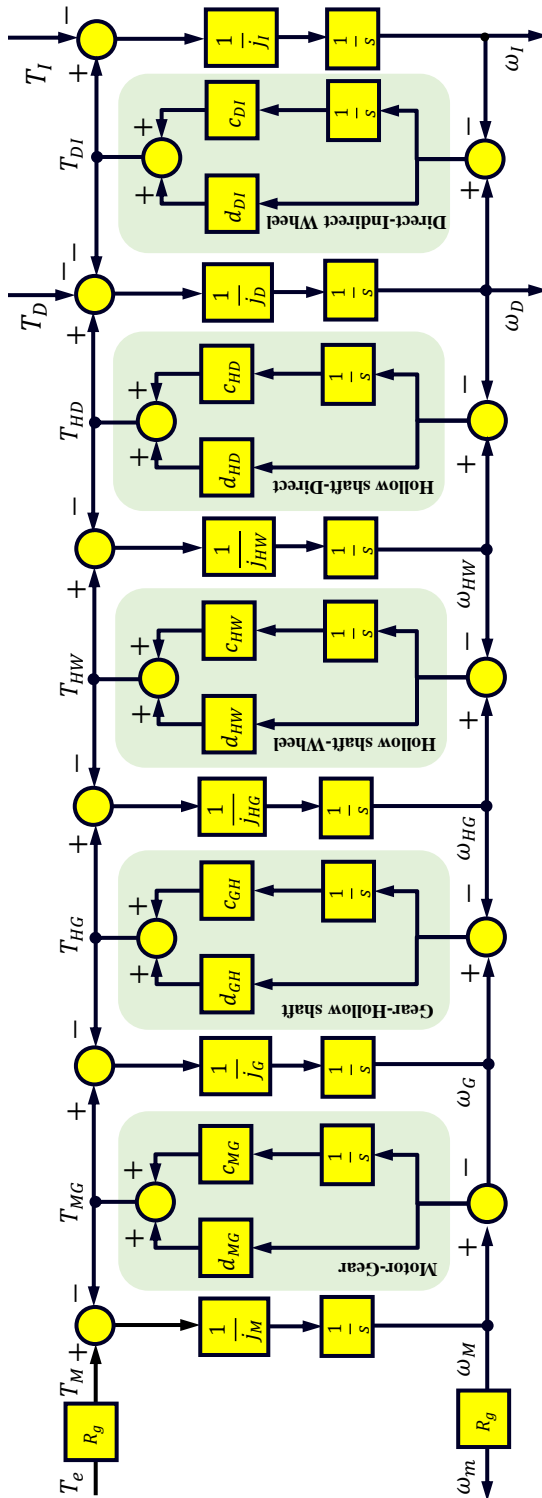
(a) Cardan hollow-shaft (six-inertia)
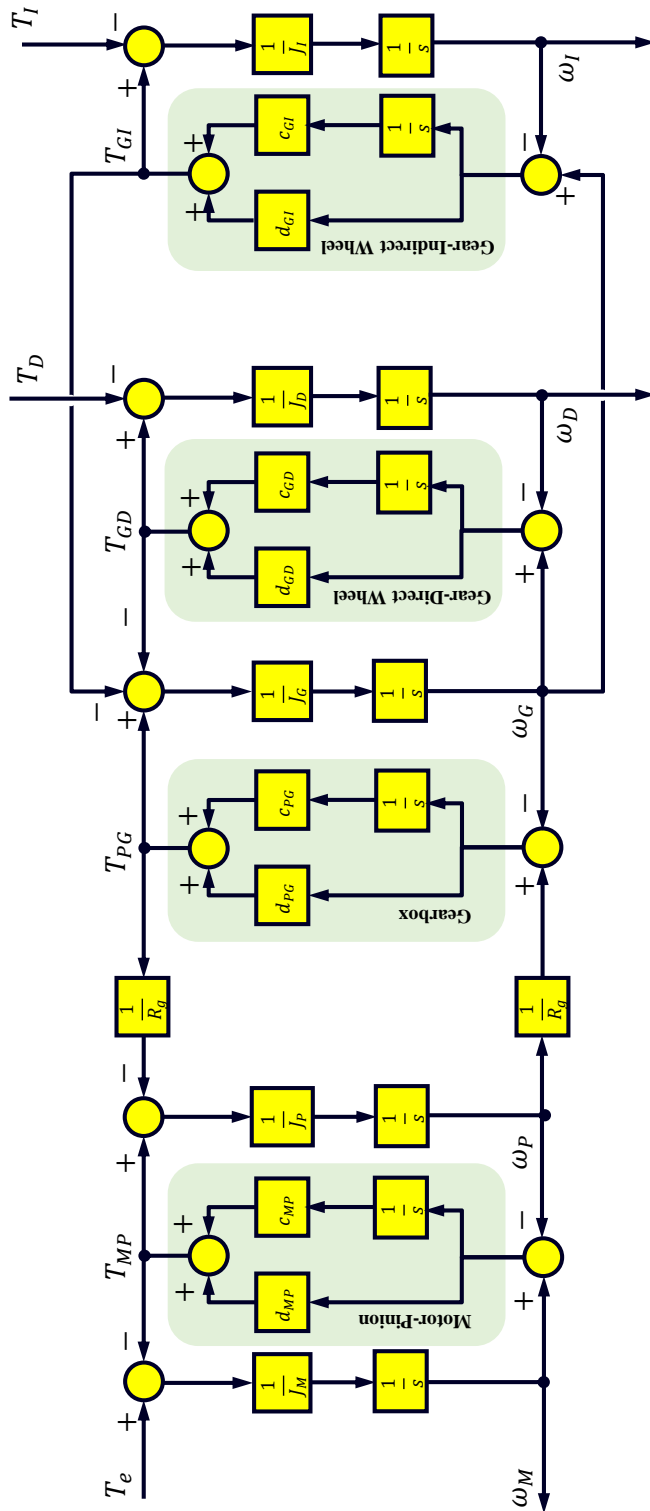
(b) Axle-mounted (Five-inertia)
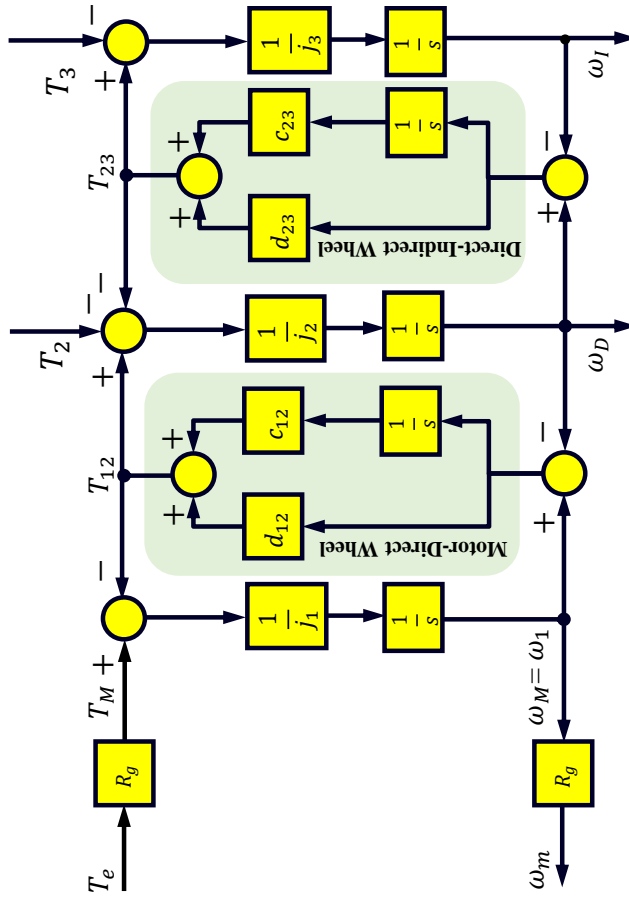
(c) Approximated model (Three-inertia)

Figure 5.5: Block diagram representation of traction drivetrain models: (a) Cardan hollow-shaft (six-inertia); (b) Axle-mounted (Five-inertia); (c) Approximated model (Three-inertia).

The adhesion characteristics for different wheel-rail conditions (dry, wet, etc.) are calculated offline and stored in a look-up table [47]. Finally, the train speed v_{train} is obtained as shown in Fig. 5.6, where m_t is the total mass of the train, F_{res} is the resistive drag force due to the air (K_{air}) and rolling (K_{roll}) resistances [196]. Forces due to track grading are not shown in this figure. It is noted that the vehicle model in Fig. 5.6 assumes that all powered axles transmit the same traction force.
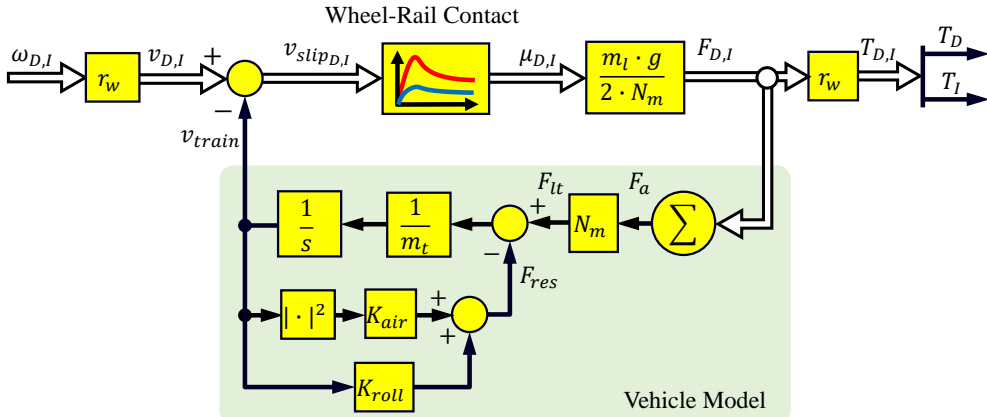
Figure 5.6: Block diagram of the wheel-rail contact model including the vehicle dynamics.

5.3 Origins and Mitigation Methods of Torsional Vibrations

This Section first discusses the slip-stick phenomenon, its effect on initiating the torsional vibrations, and the available methods for their suppression. A new method, which is the main contribution of this paper, is proposed in Section 5.3.3.

5.3.1 Slip Control and Vibration Excitation

As mentioned in Chapter 4, the traction force is regulated by adapting the slip velocity between the wheel and the rail. The slip velocity command can be modified to maximize the adhesion level with different operating conditions or simply keep it at a certain value that does not exert much wear on the rail. The slip velocity is calculated from the motor speed and the estimated train velocity. Either P or PI controllers can be used to track the commanded slip velocity. The block diagram of the traction drive control is shown in Fig. 5.7.
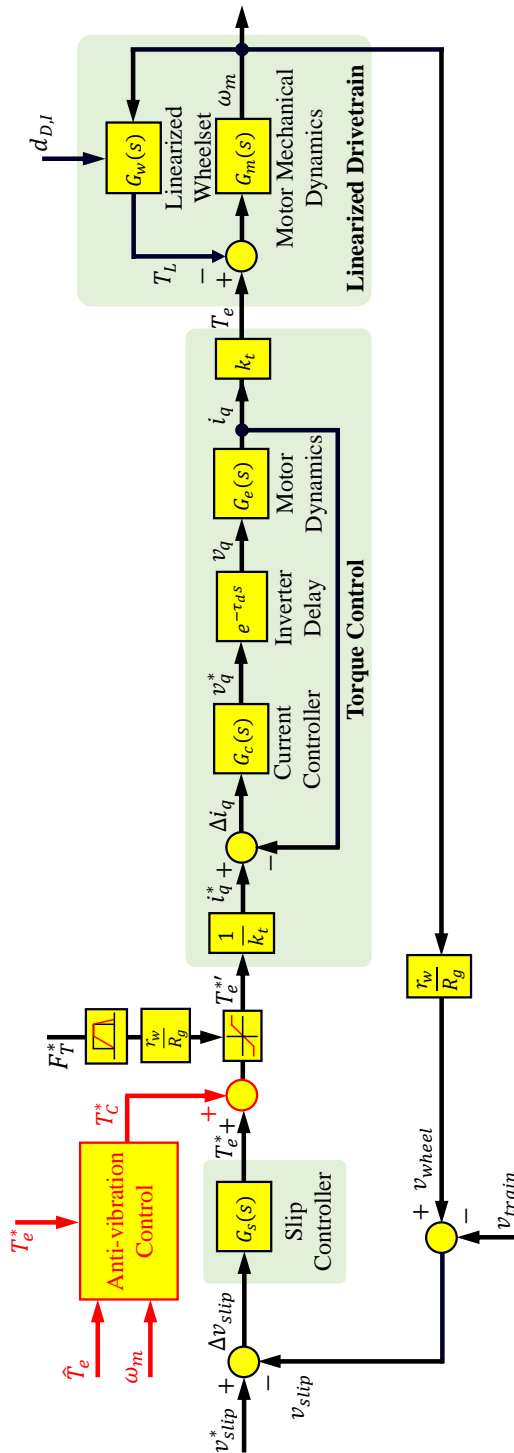
Figure 5.7: Block diagram of slip velocity control coupled with anti-vibration strategy.

Slip controller tuning is not trivial, as mechanical system dynamics depend on the non-linear wheel-rail contact characteristics. For this purpose, the linearized reduced order model including the first three mode shapes (top three traces in Fig. 5.3) discussed in Section 5.2.3 is used. The state-space representation of the approximated model is presented in (5.15) where factors d_D and d_I represent the additional damping on direct and indirect wheels when the adhesion profile changes. According to [20], these damping factors are a function of the adhesion force gradient $\frac{\Delta\mu}{\Delta v_{slip}}$ which is calculated from (5.16).

$$\dot{X} = A \cdot X + B \cdot U \qquad (5.15)$$
$$Y = C \cdot X + D \cdot U$$

$$A = \begin{bmatrix} \frac{-d_{12}}{J_1} & \frac{d_{12}}{J_1} & 0 & \frac{-c_{12}}{J_1} & 0 \\ \frac{d_{12}}{J_2} & \frac{-(d_{12}+d_{23}+d_D)}{J_2} & \frac{-d_{23}}{J_2} & \frac{c_{12}}{J_2} & \frac{-c_{23}}{J_2} \\ 0 & \frac{d_{23}}{J_3} & \frac{-(d_{23}+d_I)}{J_3} & 0 & \frac{-c_{23}}{J_3} \\ 1 & -1 & 0 & 0 & 0 \\ 0 & 1 & -1 & 0 & 0 \end{bmatrix} ;$$

$$B = \begin{bmatrix} \frac{R_g}{J_1} & 0 & 0 & 0 & 0 \end{bmatrix}^T ;$$

$$C = \begin{bmatrix} R_g & 0 & 0 & c_{12} & c_{23} \end{bmatrix} ; \quad D = [0]$$

$$X = \begin{bmatrix} \omega_1 & \omega_2 & \omega_3 & \vartheta_{12} & \vartheta_{23} \end{bmatrix}^T ;$$

$$U = \begin{bmatrix} T_e & 0 & 0 & 0 & 0 \end{bmatrix}^T ; \quad Y = \begin{bmatrix} \omega_m & 0 & 0 & T_{12} & T_{23} \end{bmatrix}^T$$

$$d_{D,I} = r_w^2 \cdot \frac{m_t \cdot g}{2 \cdot N_m} \cdot \frac{\Delta\mu_{D,I}}{\Delta v_{slip_{D,I}}} \qquad (5.16)$$

For positive adhesion force gradient, the wheelset adds damping to the drivetrain, improving the stability (P_1, P_2, P_3 in Fig. 5.8a). If the slip velocity is increased beyond the peak of the adhesion coefficient (P_1', P_2', P_3' in Fig. 5.8a), then the adhesion force gradient becomes negative which reduces the overall damping of the drivetrain, increasing the risk of instability. As the damping of the drivetrain reduces, the self-resonant frequencies start to appear, their magnitude increasing proportionally to the negative slope of the adhesion coefficient (i.e. $\frac{\Delta\mu}{\Delta v_{slip}}$).

The eigenvalue state-space wheelset model in (5.15) can be represented by an equivalent transfer function (5.17); it consists of a pure integrator while

the remaining four poles, as well as the zeros, can be proven to be complex conjugate pairs [20, 162].

$$G_{w(s)} = \frac{\omega_{m(s)}}{T_{e(s)}} = \frac{b_4 s^4 + b_2 s^2 + b_0}{s\left(a_4 s^4 + a_2 s^2 + a_0\right)} \tag{5.17}$$

Coefficients of the transfer function $b_0...b_4$, $a_0...a_4$, can be expressed as a function of drivetrain parameters where the detailed resulting expressions can be found in [20]. The detailed block diagram of the closed-loop traction drive of the slip velocity control is shown in Fig. 5.7. The closed-loop block diagram includes the slip velocity control, the torque control, the inverter time delay, and the motor electrical and mechanical dynamics respectively which are given by (5.18)-(5.21).

$$G_{s(s)} = \frac{T^*_{e(s)}}{\Delta v_{slip(s)}} = k_{ps} + \frac{k_{is}}{s} \tag{5.18}$$

$$G_{c(s)} = \frac{v^*_{q(s)}}{\Delta i_{q(s)}} = k_{pi} + \frac{k_{ii}}{s} \tag{5.19}$$

$$G_{e(s)} = \frac{T_{e(s)}}{i_{q(s)}} = \frac{1}{\hat{L}_{\sigma s} s + \hat{R}'_s} \tag{5.20}$$

$$G_{m(s)} = \frac{\omega_{m(s)}}{\Delta T_{(s)}} = \frac{1}{\hat{J}_m s + \hat{\beta}} \tag{5.21}$$

where,

k_{ps}, k_{is}	the proportional and integral (PI) gains for the slip velocity control, respectively;
k_{pi}, k_{ii}	the current controller PI gains;
$\hat{L}_{\sigma s}$, $\hat{R}'_s$	the estimated stator leakage inductance and resistance, respectively;
$\hat{J}_m$, $\hat{\beta}$	the estimated motor inertia and friction coefficient, respectively

To investigate the influence of the wheel-rail contact on the traction drive system, a range of variation of adhesion force gradient -0.12 s/m $< \frac{\Delta\mu}{\Delta v_{slip}} <$ 0.12 s/m is typically used [20]. Closed-loop pole migration of the drive-train for the two extreme cases of -0.12 s/m and 0.12 s/m are shown in Fig. 5.8b.

It is observed that by a proper selection of controller gains, the slip controller is able to damp the first vibration mode (chatter), i.e. associated closed-loop poles are moved to the left-half plane.
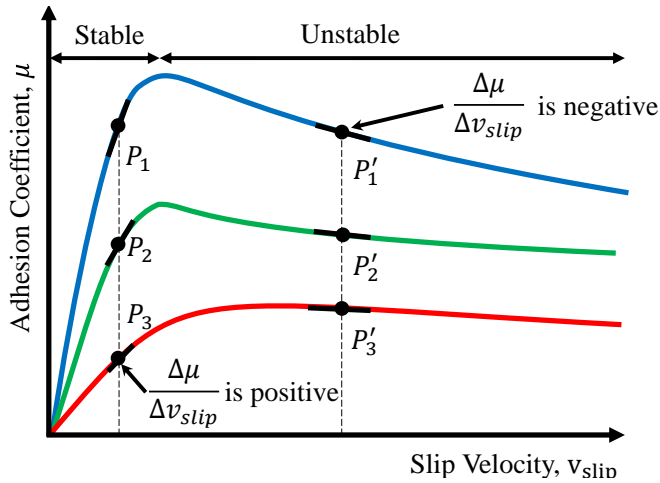
(a) Adhesion coefficient vs. slip speed
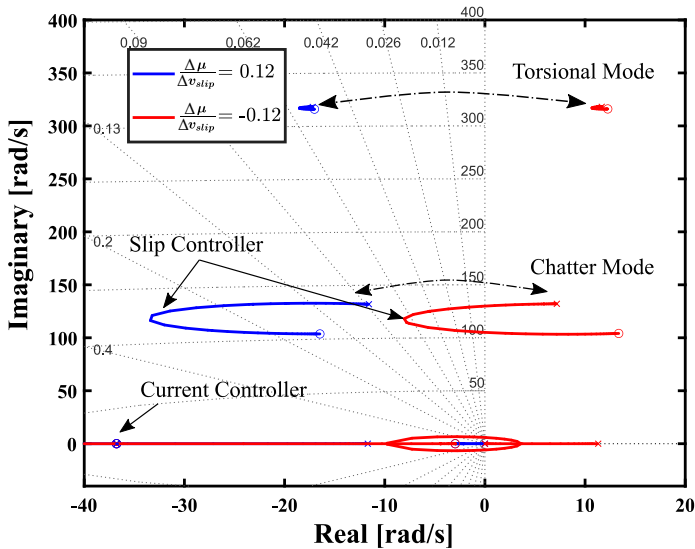
(b) Wheelset pole migration

Figure 5.8: Influence of wheel-rail contact on the traction drive-train: a) variation of adhesion force gradient over the characteristics curve; b) root locus plot of the traction drive closed-loop response for the case of the adhesion force gradient being equal -0.12 s/m and 0.12 s/m respectively.

On the other hand, the second vibration mode (torsional) is insufficiently damped; consequently, drive-train resonance due to this mode will result in torsional vibrations. An additional anti-vibration control for this specific mode is required which will be addressed next.

5.3.2 Overview of Anti-vibration Methods

Anti-vibration control is required to mitigate or suppress this specific torsional vibration mode. The conventional solution is to estimate the dynamic torque on the wheelset axle. A regular PI controller is used to limit the envelope of the oscillation (see Fig. 5.9a). A limit of 100 kNm is used; this value is obtained at the design stage of the powertrain. PI controller output T_c^* is added to the output of the slip controller (T_e^*, see Fig. 5.7). In traction mode, the magnitude of the torsional vibration is limited but at the cost of losing traction capability. Also, it is found that the conventional anti-vibration can effectively damp the vibrations for adhesion curves with negative adhesion gradients bigger than -0.04 s/m (i.e. $\frac{\Delta\mu}{\Delta v_{slip}} > -0.04$ s/m) [80]. Advanced state-space control approaches based on pole-placement techniques have been recently applied to vibration suppression strategies for negative adhesion gradients less than -0.04 s/m (i.e. $\frac{\Delta\mu}{\Delta v_{slip}} < -0.04$ s/m). A virtual absorber controller is another promising solution for actively damping not only the torsional vibrations but also improving the whole traction system dynamics [20]. The basic idea of this approach is to emulate a mechanical absorber mounted in the indirect-driven wheel by a feedback controller which is based on the estimated electromagnetic torque ($\hat{T}_e$) and the measured motor speed (ω_m). Combining two or multiple anti-vibration methods (see Fig. 5.9a) is advantageous to provide high damping to the torsional vibrations even with a very steep adhesion force gradient $\frac{\Delta\mu}{\Delta v_{slip}} < -0.12$ s/m. However, due to wear, aging, and temperature dependency of traction drivetrain elements, the vibration frequencies will increase over time. Thus, parameter estimates of the drivetrain and the virtual absorber must be very accurate, the equivalent reduced-order model should be automatically adapted accordingly. This requires additional natural identification and parameter estimation algorithms which add complexity to the system implementation [20, 197].

5.3.3 Proposed Resonant Anti-Vibration Control

From the previous discussion, it can be concluded that the traction drive control, without any additional mechanical components, and relying on motor variables only (voltage, current, speed), should be able to suppress the wheelset torsional vibrations. The key aspect of damping the vibrations is to provide the torque correction signal required to adapt the commanded torque according to the wheel-rail operating condition. Since wheel-rail contact act as a disturbance to the motor, a disturbance-observer is used to estimate the motor load torque which contains the vibration transferred from the wheelset side (see fig. 5.9b). Taking the Laplace transformation for the differential equation of motion on the motor shaft in (5.22), the load torque is estimated using (5.23) where τ is the time constant of the low-pass filter in the disturbance estimator used for noise reduction in the measured speed. Then, the estimated load torque is subtracted from the commanded torque signal to extract only the vibrating component. Finally, a proportional-resonant (PR) controller is used to suppress the torsional vibrations by injecting the correction torque signal (T_c^*) with the resonance frequency corresponding to the torsional vibration mode.

$$T_L = T_e - B\omega_m - J_m\dot{\omega}_m \tag{5.22}$$

$$\hat{T}_L(s) = \hat{T}_e(s) - B\omega_m(s) - J_m s\, \omega_m(s)\left(\frac{1}{\tau s + 1}\right) \tag{5.23}$$

The use of an ideal resonant controller is not advisable in practice due to its high sensitivity to the frequency of the input signal, which might result in instability due to the narrow bandwidths being used. Usually, the proportional-resonant controller (PR) given in (5.24) is preferred, where k_{p_r} and k_{i_r} are the proportional and resonant gains, ω_n is the resonant frequency and ω_c is the pass-band frequency range.

$$G_{pr}(s) = \frac{T_{C(s)}^*}{\Delta T_{(s)}} = k_{p_r} + \frac{2k_{r_r}\omega_c s}{(s^2 + 2\omega_c s + \omega_n^2)} \tag{5.24}$$
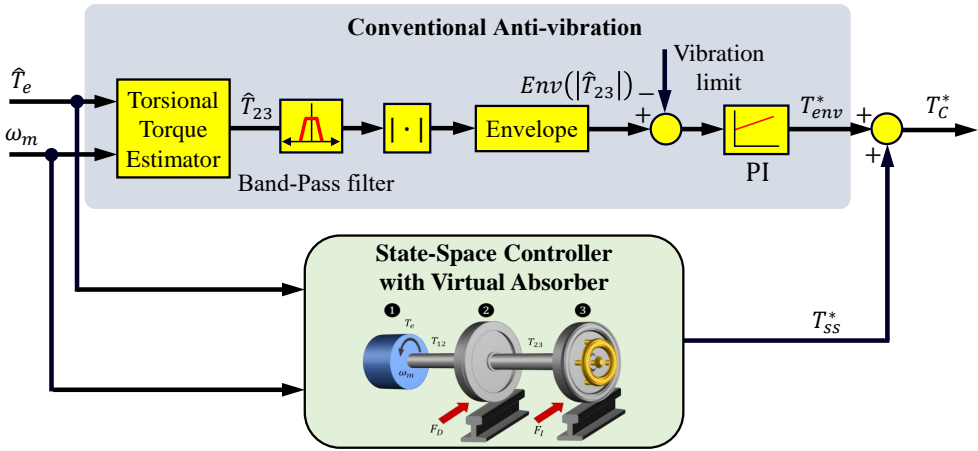
(a) Adhesion coefficient vs. slip speed
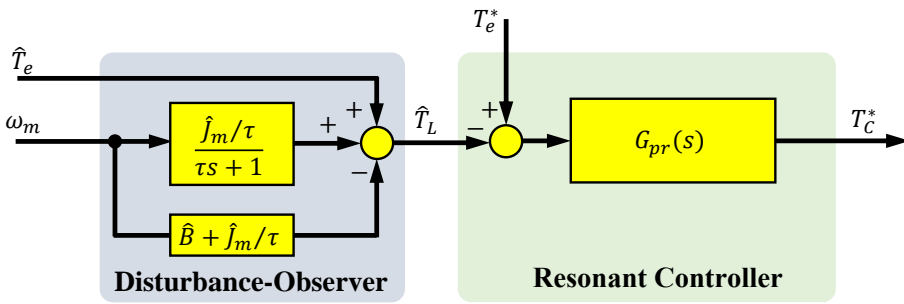
(b)

Figure 5.9: Anti-vibration control strategies based on traction motor variables: a) Existing anti-vibration control; b) Proposed vibration suppression method using PR controller.

The effectiveness of the resonant controller can be noticed for the second oscillation (torsional mode) in the Bode plot of the closed-loop slip velocity control system (see the red line in Fig. 5.10). For this specific mode, the PR controller achieves high-magnitude attenuation and cancellation of the phase delay in the closed-loop response while it does not affect the first oscillation mode. In this way, the torsional (slip-stick) vibrations are suppressed without deteriorating the traction performance and with simple control requirements.
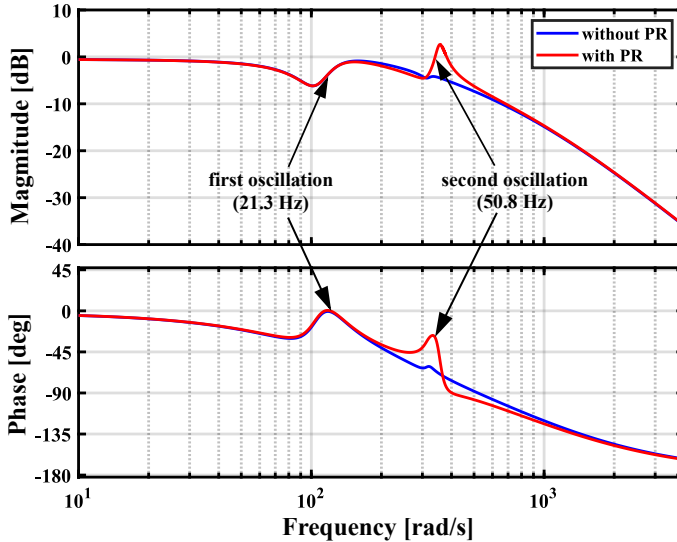
Figure 5.10: Bode plot of $\frac{\omega_m(s)}{\omega_m^*(s)}$ of the slip velocity control without (in blue) and with resonant controller (in red).

5.4   Simulation Results

To investigate the performance of the proposed vibration suppression method, the entire traction drive system is modeled and simulated using MATLAB/ Simulink following the block diagram seen in Fig. 5.11, with a simulation step of $10\,\mu$s. The detailed simulation model consists of the traction drive control, a three-level NPC inverter, the six-inertia wheelset model, the wheel-rail contact characteristics, and the vehicle model. The general specification of the loco- motive is given in table A.4; the six-mass model parameters are given in table A.3 in the appendix [162].

RFOC and SVPWM with a switching frequency of 1 kHz are used. Cur- rent controllers are tuned using the zero/pole cancellation to provide 200 Hz bandwidth, while the slip velocity controller gains are selected from the root locus closed-loop plot in Fig. 5.8b to achieve better damping of chatter vibra- tion mode. The disturbance-observer filter is chosen to have a time constant of $\tau = 1$ ms while the resonant controller is tuned at $\omega_n = 340$ rad/s with a pass-band width of $\omega_c = 12.5$ rad/s. Selection of gains k_{p_r}, ki_r is therefore extremely challenging due to the variability of operating conditions, a common practice is to follow a trial and error process to achieve sufficient damping to

the system for all operating conditions [198]. The closed-loop controller gains are given in table A.5 in the appendix.
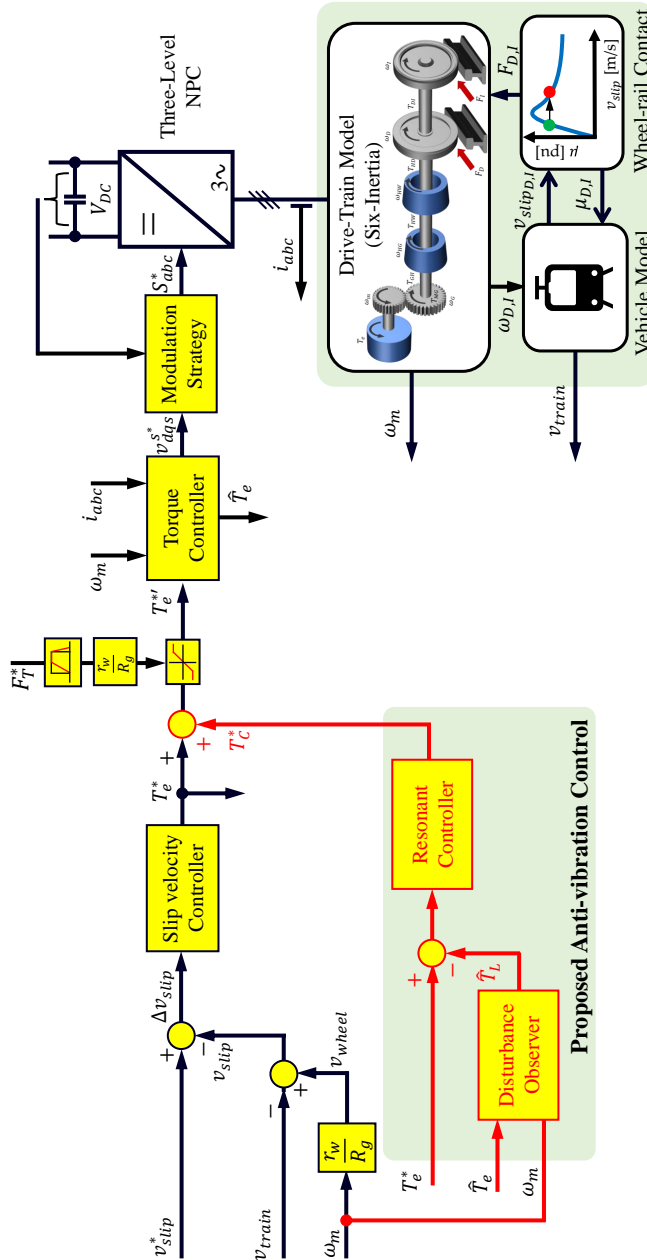
Figure 5.11: Schematic representation of the complete traction drive simulation model with the proposed anti-vibration control.

To initiate the torsional vibrations, the slip velocity command v^*_{slip} is increased from 0.1 to 1 m/s, the adhesion force gradient changing from positive to negative (see Fig. 5.8a). Fig. 5.12a shows the system response when it enters the unstable region of the adhesion-slip curve. The torsional vibration appears after approximately 3 seconds when 1 m/s slip velocity is commanded. In general, the more negative the gradient is, the sooner vibration will start. Fig. 5.12b shows the frequency spectrum of torque and speed signals when the system is in vibration mode. The vibration frequency is around 50.8 Hz, which matches the results from mode shape analysis in Subsection 5.2.2. The highest torque vibration occurs at the wheelset axle ($T_{DI} = 40$ kNm), the magnitude increasing proportionally to the (negative) adhesion force gradient. It can be also noticed the traction motor torque and the measured speed contain the vibration information, which is required to detect and further control the torsional vibration.
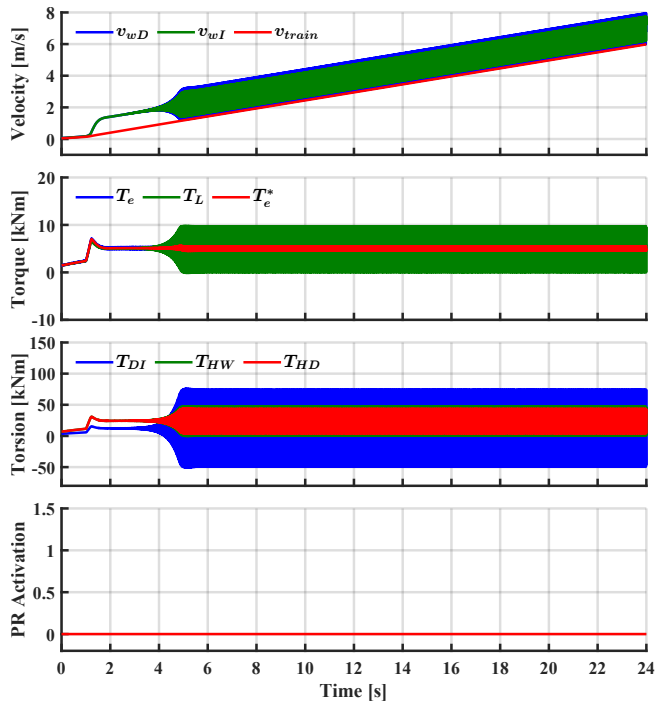
(a) Time response
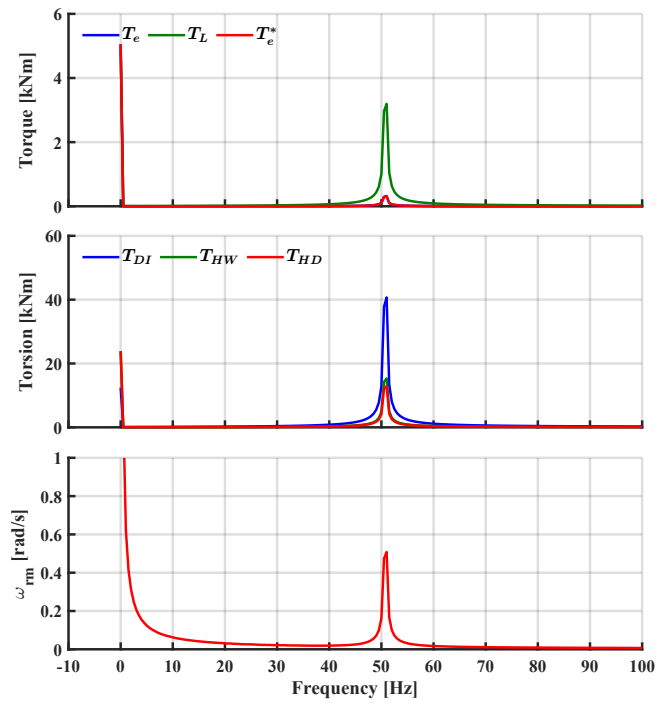
(b) —FFT—

Figure 5.12: Response of the slip velocity control while commanding 1 [m/s] at t=1 s.

The effectiveness of the proposed method in the same scenario is shown in Fig. 5.13a. PR controller is first enabled and disabled gradually (6 s $\leq$ $t \leq$ 11 s), and later suddenly at $t = 14$ s, see Fig. 5.13a-bottom). The activation process is done using a sliding factor (varying from 0 to 1) where it is multiplied by the PR output signal. It is seen that the proposed PR controller damps the torsional vibration without adverse effects observed due to sudden activation/deactivation. It is also seen that if adverse adhesion conditions remain, torsional vibrations resume a few seconds after PR control is disabled. Therefore, it is advisable to keep the PR controller enabled all the time.

A potential concern for the proposed method would be the noise in the estimated motor speed. Incremental encoders are widely used in railways. Encoder signals are normally converted into pulses to ease their acquisition and processing. However, since the encoder provides a position signal, some type of differentiation is required to obtain the angular speed. Due to the discrete nature of the encoder signal, differentiation will result in quantization noise in the estimated speed [199]. In this work, speed is estimated by combining periodmeter and frequencymeter methods [199, 200]. The effect of quantization noise in the estimated speed is shown in Fig. 5.13. A rotary incremental encoder with 4-channels 256 pulses per revolution (PPR) was used [201]. Comparing the results with ideal speed measurement in Fig. 5.13a and considering quantization noise in Fig. 5.13b, it is observed that the main difference occurs when the PR is activated suddenly. On the contrary, almost no difference is observed if PR is activated progressively, or when it remains enabled.
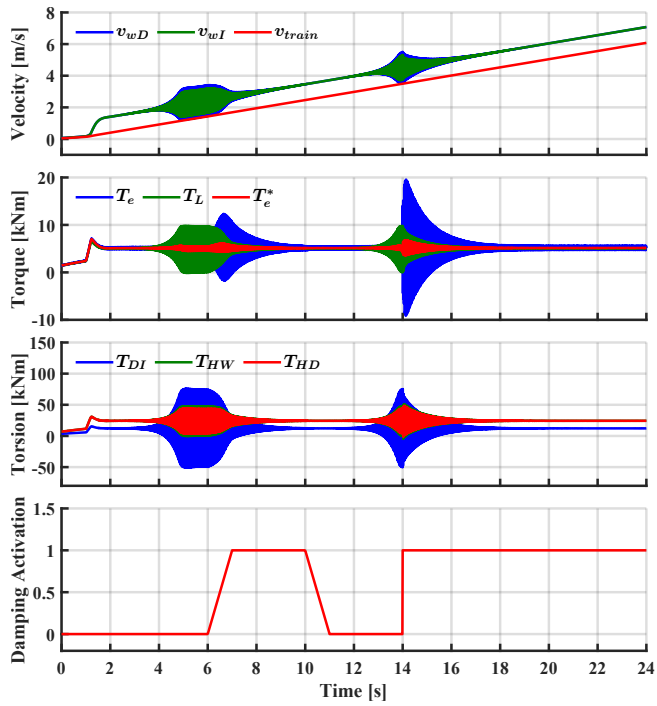
(a)
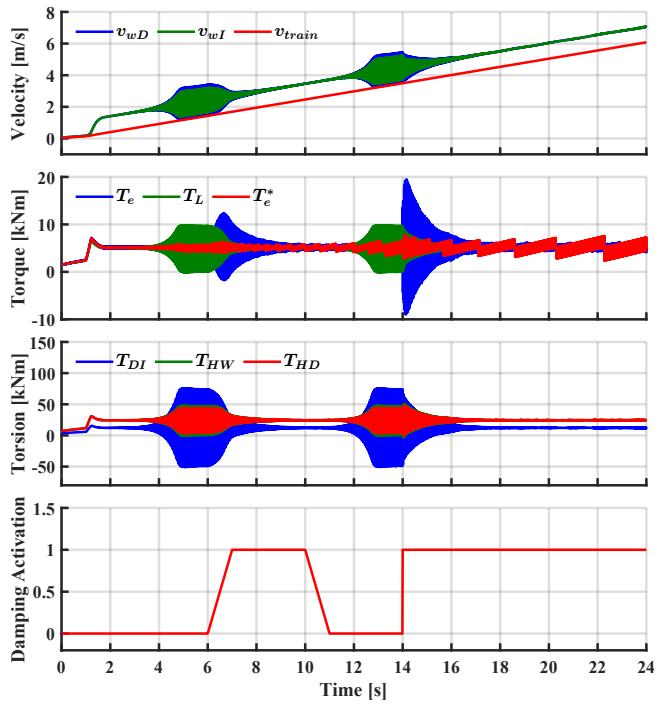
(b)

Figure 5.13: Response of the proposed method when PR is activated/deactivated gradually ($t = 6$ s $\rightarrow$ $t = 10$ s), and suddenly ($t = 14$). (a) With ideal speed measurement; (b) using and incremental encoder for speed measurement.

The proposed method is validated against the conventional vibration miti-gation method shown in Fig. 5.9a where the vibration limit is set to 20 kNm (see Fig. 5.14a vs. Fig. 5.14b). A clear observation is the loss of traction torque in the conventional suppression method (see Fig. 5.14a) to damp the oscillation. However, after suppressing the oscillation and restoring the trac-tion torque capability, the oscillations appear continuously as the slip velocity command remains at the same operating point with the negative slope of the adhesion curve (i.e. 1 m/s). In contrast, the proposed suppression method maximized the utilization of the traction torque with completely suppressing the oscillations as seen in Fig. 5.14b.
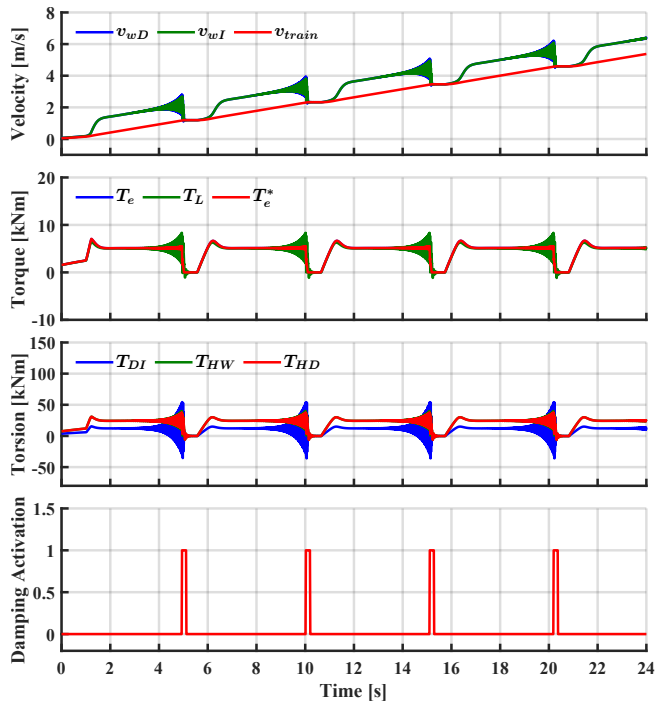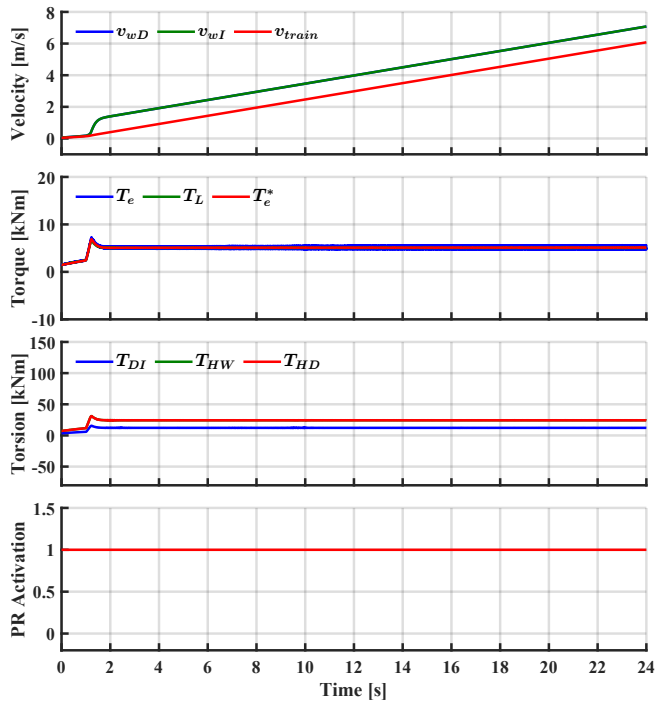
Figure 5.14: Response comparison of torsional vibration mitigation methods: (a) conventional method; (b) proposed method with active PR.

Evaluation of the proposed method under varying conditions will be discussed in the following Subsections:

5.4.1   Effects of Varying Slip Velocity and Wheel-rail Condition

Variations in the slip command can occur when the locomotive has an outer control loop implementing maximum traction force searching. This might drive the operating point into the unstable region where the torsional vibration arises. An example of the response of the proposed method to changes in the slip velocity is shown in Fig. 5.15a. Wheel-rail contact is modeled as profile 1 in the adhesion curve shown in Fig. 5.8a. The traction torque is increased from 5 kNm to 5.8 kNm by decreasing the slip velocity to 0.5 m/s. Then, the torque is decreased to 4.6 kNm when operating at the slip of 1.5 m/s. The maximum adhesion force can be achieved when $v_{slip} = 0.25$ m/s with this specific adhesion profile. However, the resonant controller was able to dampen the wheelset oscillations for all commanded slip velocities.

Variations of wheel-rail contact conditions have been reported as the main mechanism for exciting the wheelset natural frequencies leading to dynamic torque oscillations [61, 146]. Fig. 5.15b shows the response when the contact condition changes between dry to wet (profiles 1 to 3 in Fig. 5.8a). The change can occur for one wheel or both wheels, this second case is shown in the figure. The change from dry to wet decreases the adhesion force gradient $\frac{\Delta\mu}{\Delta v_{slip}}$ of both wheels initiating oscillations in the counter phase. It is observed from Fig. 5.15b that the torsional control reacts reducing torque from 5 kNm to 1 kNm at $t = 8$ s. This will keep the slip velocity at 1 m/s avoiding excessive slip. Once the wheel-rail contact returns to a dry condition, the motor torque returns to its initial value. Again, the proposed method is seen to provide a good response under challenging operating conditions.
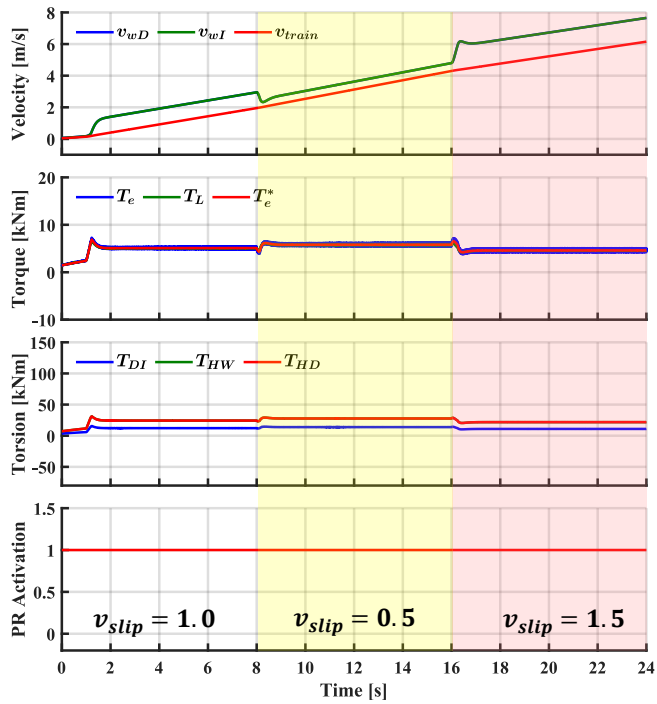
(a) Slip velocity changes
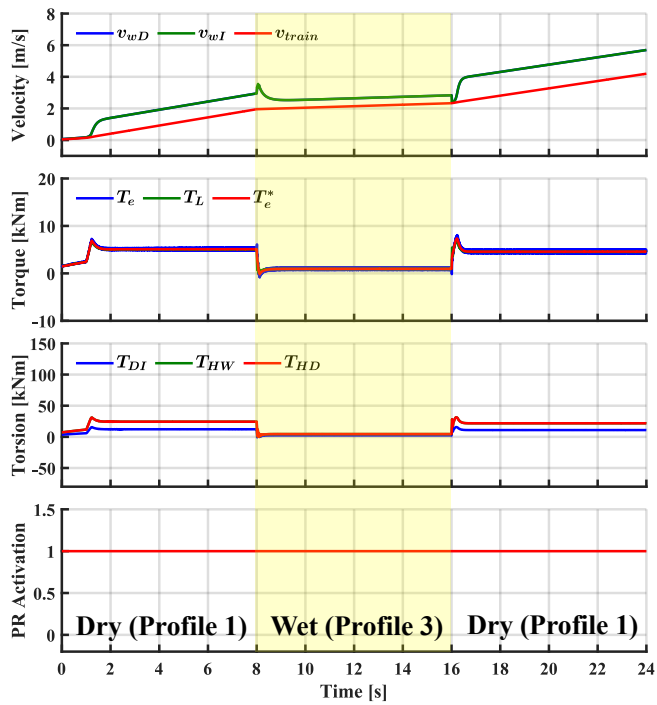
(b) Adhesion profile changes

Figure 5.15: Response of the proposed method at different operating conditions.

5.4.2 Effect of Varying Drive Control Bandwidth

In the previous simulations, fast torque control is assumed, which is achieved thanks to the use of vector control with 200 Hz bandwidth for current regulators. Frequently, drive control is switched to scalar methods at high speed, especially when the inverter is operated in the overmodulation region close to the voltage limit. A drawback of scalar control is the slow dynamic response of the torque control loop as mentioned in Section 3.3.1.

Fig. 5.16 shows the effect of the torque control bandwidth, with the same slip control setup shown in Fig. 5.11. It is clear that the lower the bandwidth, the longer the time needed to fully suppress the vibration. Interestingly, it is found that for torque control bandwidths below $<\approx 60$ Hz, oscillations are not properly cancelled. By doubling the slip controller gains, the control system is able to damp the oscillation for all bandwidths (50 to 150 Hz) (see Fig. 5.16a). However, increasing the slip velocity controller gains is not desired as it will amplify the feedback noise coming from the motor speed measurement and might also lead to oscillations in practice.

A potential concern when high-bandwidth current regulators are used is the presence of measurement noise in the measured currents. To reduce this risk, oversampling of current sensors was used [202]. A field-programmable gate array (FPGA) measures the signal every 5 μs, and averages the measurement over the whole control period. With a PWM operating with a period of 1 ms and double update (twice per period), 100 samples are therefore averaged each control period. This will reduce the noise in the signals to negligible levels [203, 204].
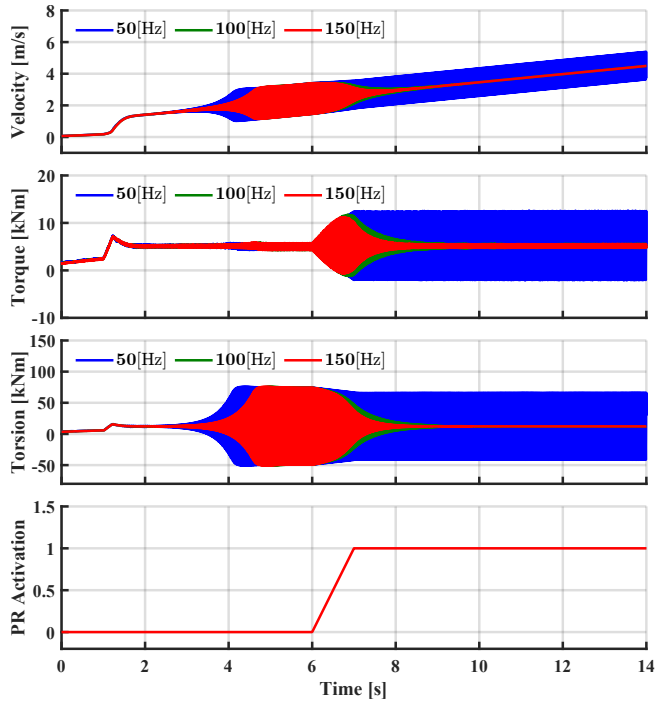
(a) $k_{p_{s1}} = 4.7 \times 10^3, k_{i_{s1}} = 1.4 \times 10^4$
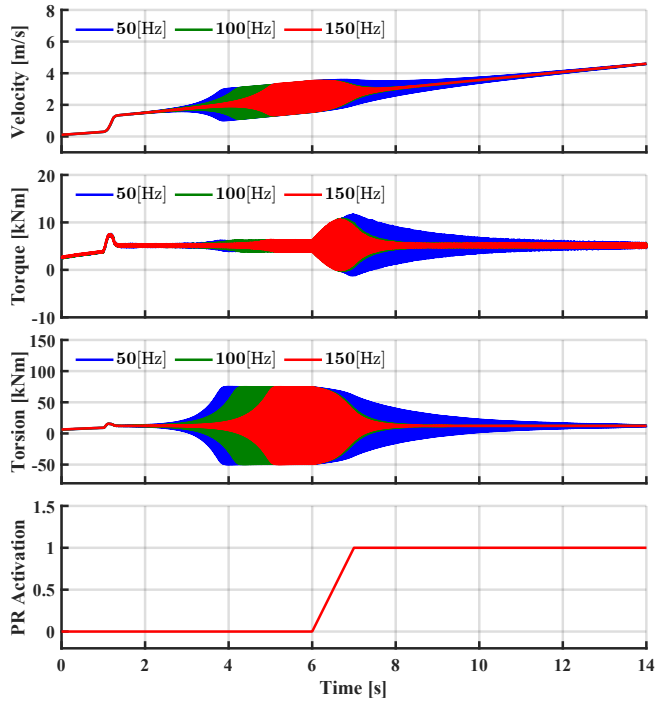
(b) $k_{p_{s2}} = 2k_{p_{s1}}, k_{i_{s2}} = 2k_{i_{s1}}$

Figure 5.16: Response of the proposed method with changing the current controller bandwidth (150, 100 and 50 Hz) for two different tuning sets of the slip velocity controller.

5.5 Co-Simulation-Based Verification and Experimental Results

In this Section, the entire traction drive system and control are modeled and simulated using MATLAB-SIMPACK co-simulation tool. Furthermore, changes in the wheel-rail conditions with activated and deactivated torsional vibration protection will be analyzed. Finally, simulation results will be compared with measured data already published in [146].

The mechanical components of the drive train are implemented in a multi-body simulation (MBS) model. Figure 5.17 shows the quarter model of a traction locomotive which is used for the investigations [196]. The mechanical model contains the masses and inertias of a hollow shaft drive train consisting of a rotor, the gear wheels, the coupling, the hollow shaft, the axle, and both wheels. The torsional stiffness and damping of the gear, the coupling, the hollow shaft, and the axle are considered. Also, the single-stage gear is included in the model.

The simulation model was built in the MBS Simpack software. The MBS model is linked to the drive controller via co-simulation. The model contains the torque transmitting components of the mechanical drive train, the wheel-rail contact as well as the friction forces and inertia forces resulting from the train set. The whole model of the drivetrain can follow the track in the longitudinal direction and can move freely in the vertical direction. The individual bodies have rotational degrees of freedom around their lateral axis.
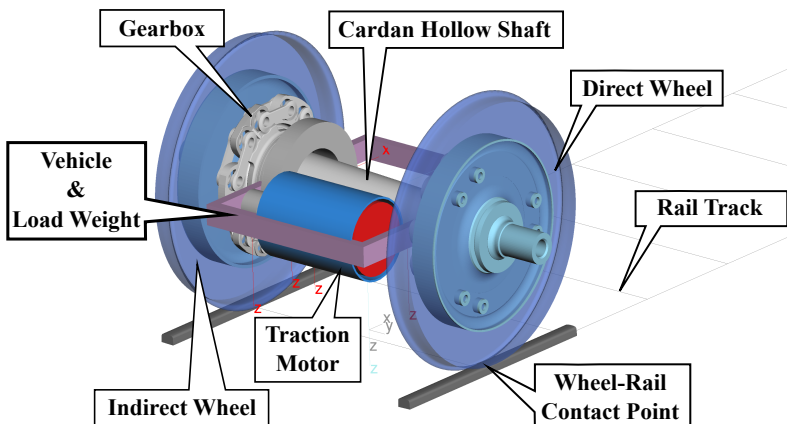
Figure 5.17: MBS model of the drivetrain with wheel-rail interaction.

For the calculation of the tangential forces in the wheel-rail contact, the analytical approach of Polach is used [47]. This approach was developed to achieve an improved fit of the adhesion characteristics in the simulation with measured data. The tangential force F calculated in Polach's formalism depends on the wheel load Q, the wheel-rail adhesion coefficient μ, and the weighting factors k_A and k_S,

$$F = \frac{2Q\mu}{\pi} \left(\frac{k_A \epsilon}{1 + (k_A \epsilon)^2} + \arctan(k_A \epsilon) \right), \quad k_S \leq k_A \leq 1 \qquad (5.25)$$

The gradient of tangential stress in the adhesion area ϵ depends on the relative (slip) velocity v_s between wheel and rail and the contact ellipse in the wheel-rail contact,

$$\epsilon = \frac{2}{3} \frac{C \pi a^2 b}{Q \mu} v_s \qquad (5.26)$$

The decrease of the wheel-rail adhesion coefficient for higher relative velocities is realized by a relative velocity v_s dependent friction value. This is highly relevant for the simulation of torsional vibrations. The slope of the adhesion coefficient above its maximum can be determined by the parameters A and B. Figure 5.18 shows the adhesion characteristics as a function of the driving speed.

$$\mu = \mu_0 \cdot \left[(1 - A) \cdot \exp^{-B \cdot |v_s|} + A \right] \qquad (5.27)$$

The traction forces are opposed by the friction and inertia forces of the train set. These opposing forces are represented in the MBS model by the following equations taken from the literature [196].

Rolling Resistance:

$$F_{roll} = M_{train} \cdot g \cdot k_{roll}, \quad k_{roll} = 1.5 \cdot 10^{-3} \qquad (5.28)$$

Air Resistance:

$$F_{air} = M_{train} \cdot g \cdot k_{air}, \quad k_{air} = 0.25 \cdot 10^{-3} \qquad (5.29)$$

Using co-simulation-based verification, the conventional vibration mitigation method will be compared experimentally with real train measurements. The passive re-adhesion controller is used (see vibration detection and protection block in Figure 5.19a). The re-adhesion controller reduces the slip
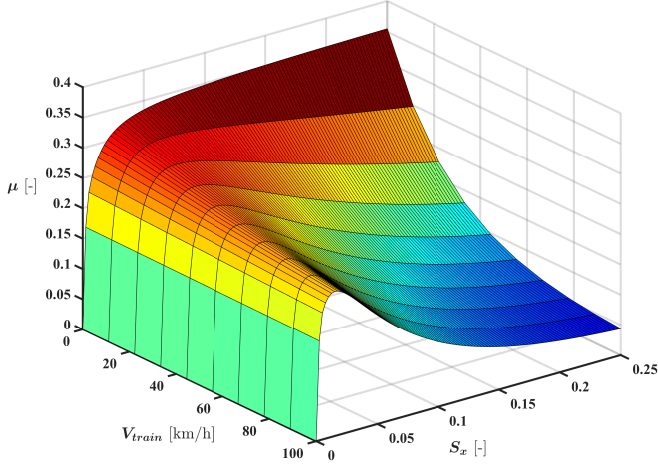
Figure 5.18: Adhesion characteristics as a function of the driving speed V_{train} and slip S_x [47].

velocity to protect the wheelset axle from excessive vibration events. This can be achieved by extracting the vibration component from the speed sensor signal of the IM ω_m using a band-pass filter. Then the envelope of the extracted vibration $Env(|v_{osc}|)$ is controlled to avoid surpassing a predefined limit $|v_{osc}|$ using a conventional PI regulator (see Figure 5.19b). The output signal Δv_{osc}^* reduces the slip velocity command once the vibration envelope exceeds the defined limit bringing the operating point back into the stable region (e.g., $P_1' \rightarrow P_1$ in Figure 5.8a). Consequently, the reference torque T_e^* is reduced during the vibration mitigation process, T_e^* being returned to its original value after vibration events clearance. Normally, passive re-adhesion control is used to limit the slip velocity, being aware of its adverse impact on traction. Alternatively, advanced control techniques can be employed to actively damp the torsional vibrations in the traction drive, but at the cost of higher complexity and parameter dependency [20].

For the following results, the entire traction drive system and control are modeled and simulated using MATLAB-SIMPACK co-simulation tool. Furthermore, changes in the wheel-rail conditions with activated and deactivated torsional vibration protection will be analyzed. Finally, simulation results will be compared with measured data already published in [146].

Based on the dependencies between maximum dynamic torque and wheel-rail conditions documented in [146,196], the wheel-rail adhesion coefficient was
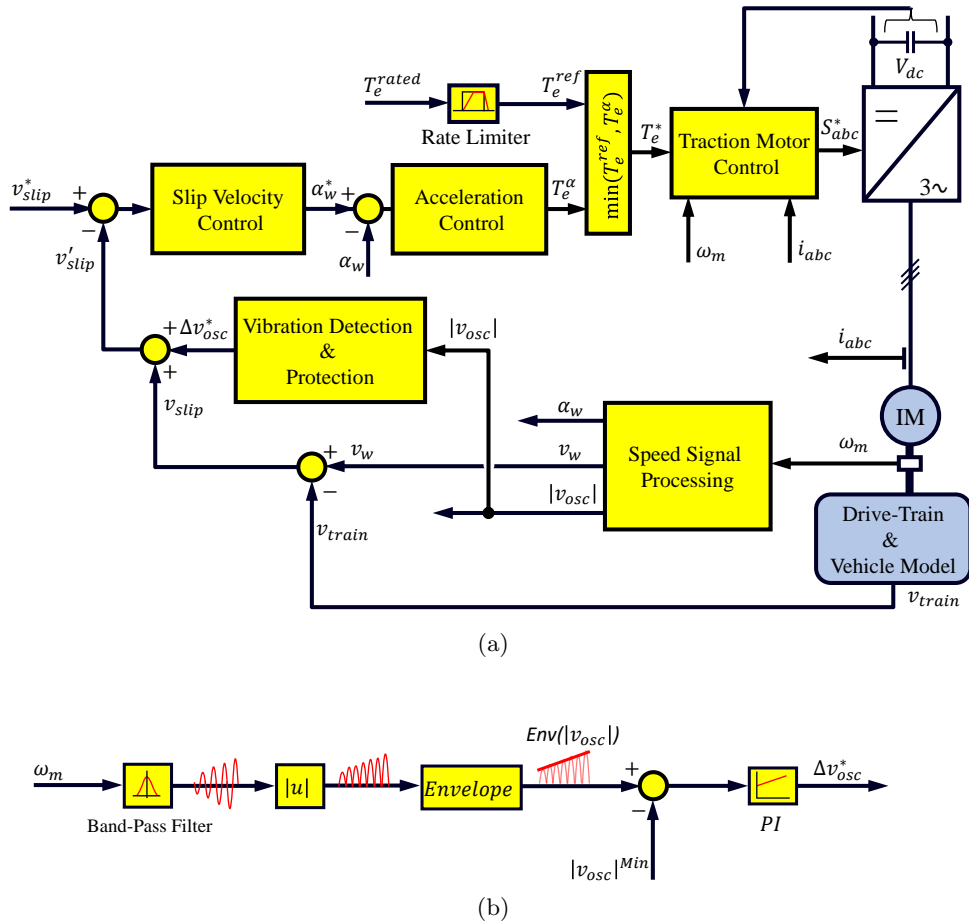
Figure 5.19: Block diagram of traction drive control including slip velocity controller: (a) Overall control scheme; (b) Detailed block diagram of conventional vibration detection and protection control.

modified during the simulation at hand during an acceleration process. For this, the introduced co-simulation tool (see Figure 5.20) was used.

The simulation batch starts by defining the number of simulations to be carried out. This depends on the ranges of train speeds and wheel-rail conditions to be tested. Variables to be set for each simulation include train velocity, adhesion coefficient, and the traveling distance where the adhesion change is applied for both wheels. The slip and vibration protection control algorithms are executed via MATLAB/Simulink toolbox where the torque command is sent to the drive train and vehicle model implemented in the SIMPACK environment. The train velocity and motor speed measurements are fed back to
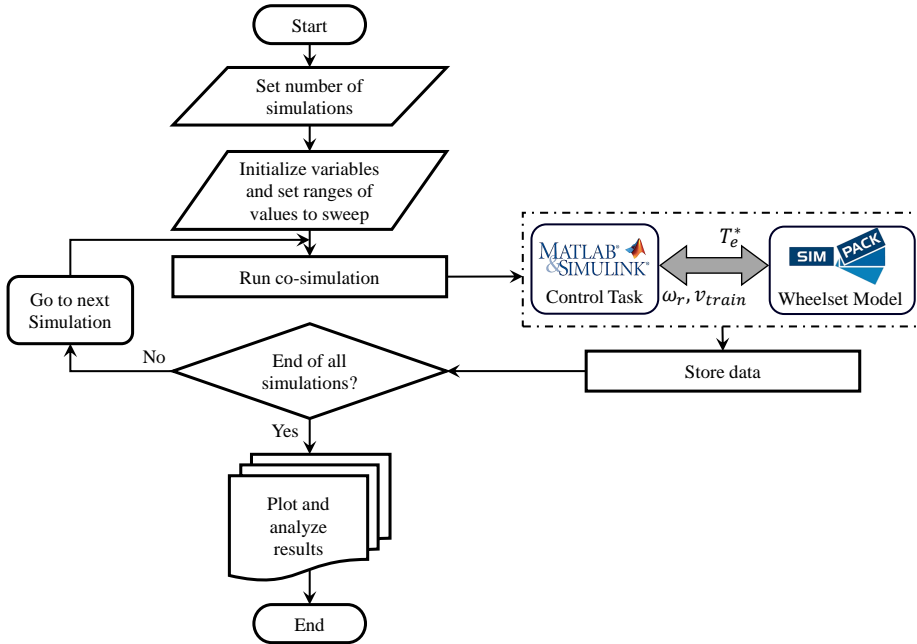
Figure 5.20: Flow chart for parametric sweep analysis of torsional vibrations in mechanical drives using MATLAB-SIMPACK co-simulation tool.

the Simulink model where the co-simulation communication is done via internet protocol (IP-Server 2000). Finally, the output data (dynamic torque, slip velocity, etc.) are stored in a vector table then the same process is repeated for the rest of the simulation steps.

Three different wheel-rail condition scenarios for both wheels were conducted to investigate the effectiveness of torsional vibration protection of electric-driven wheelsets (see Figure 5.21). $x_{1...4}$ indicates the distance at which the change of the adhesion value μ is applied (starting from 10 m to 400 m with a separation of 10 m each step). Additionally, the simulations carried out are repeated (traction and electrical braking) for different train velocities (from 0 to 200 km/h).

Figure 5.22 shows dynamic torque plotted against slip velocity where all simulation results for different adhesion scenarios (mentioned in Figure 5.21) are combined and plotted in the same graph (i.e. Figure 5.22). It is observed that without vibration protection (see left subplot in Figure 5.22), the vibration magnitude is increasing linearly with slip velocity up to the maximum value ($T_{dyn} \approx 180 \ kNm$ at $v_{slip} \approx 2.5 \ m/s$) for traction mode. It is noted that though the maximum dynamic torque is found to be less ($T_{dyn} \approx 160 \ kNm$
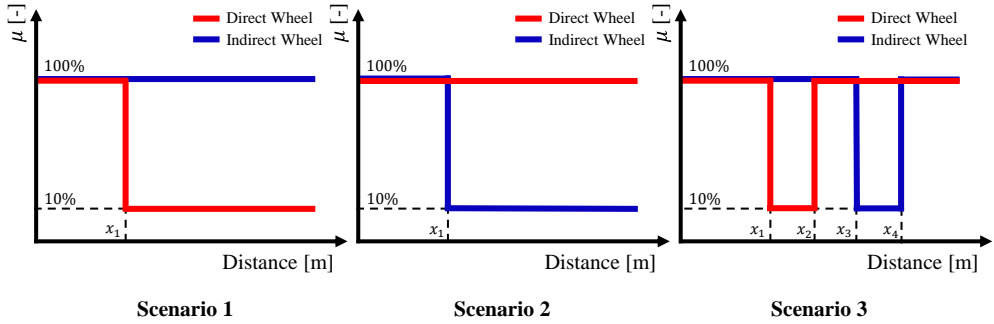
Figure 5.21: Wheel-rail contact friction configuration scenarios for SIMPACK model.

at $v_{slip} \approx 2\,m/s$) in braking mode, still the trend is the same as for traction mode.

Enabling vibration protection control limits the dynamic torque magnitude (see right subplot in Figure 5.22). The maximum dynamic torque achieved is $T_{dyn} \approx 72\,kNm$ at $v_{slip} \approx 0.7\,m/s$ for traction mode and $T_{dyn} \approx 51\,kNm$ at $v_{slip} \approx 0.6\,m/s$ for braking mode.
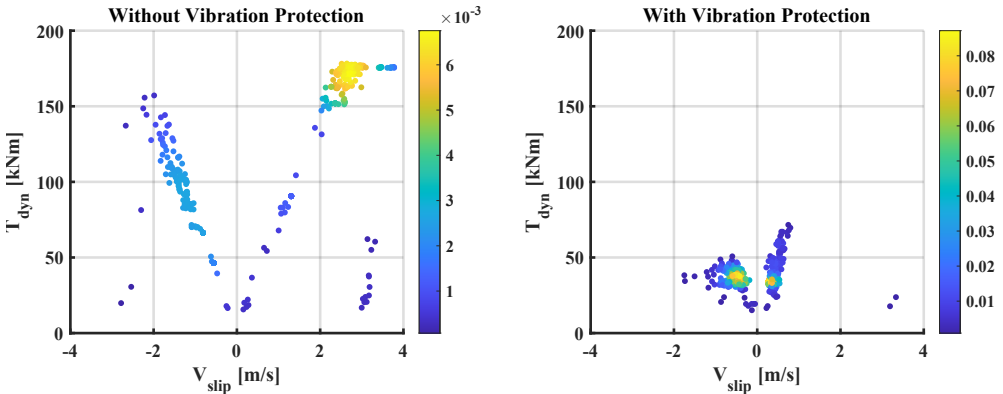
Figure 5.22: Simulation results. Dynamic torque vs. slip velocity with and without vibration protection during traction and braking, provoked by different adhesion scenarios.

As seen in Figure 5.23, likewise for measurements and for simulations. Having in mind that the adhesion characteristic is highly stochastic, it is striking, that data points resulting from simulations show good conformity with data points resulting from measurements. Measurements have been conducted with a similar drive train and traction control as the one implemented in the simulation model at hand. Measurement conduction as well as measurement data

analysis have been published in [146]. Furthermore, for both, simulations and measurements, maximum dynamic torque increases linearly by increasing slip velocity. After exceeding a certain slip velocity $v_{slip,crit} \approx 0.5\,m/s$) data points are not further increasing linearly but rather decreasing.
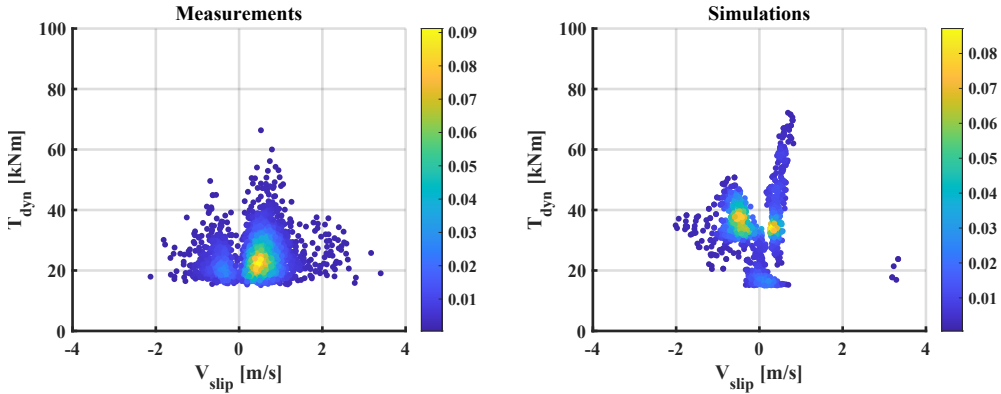
Figure 5.23: Comparison between Simulation and Measurement results. Dynamic torque vs. slip velocity during traction and braking process, provoked by different adhesion scenarios.

5.6 Conclusions

Modeling of the mechanical drivetrain and vehicle considering slippage and vibrations phenomena have been addressed in this Chapter. The conclusions of the analysis can be summarized as follows:

- The adhesion force gradient is the key factor for torsional vibration phenomena. This factor is often unpredictable. Moving this factor from positive to negative values pushes the system to the stability limit or even towards instability.

- Operating with a negative adhesion force gradient will excite the resonance frequencies of the mechanical elements in the drivetrain, their severity increasing proportionally to the negative slope of the adhesion curve.

- The first two resonance frequencies are the most affecting modes on the motor shaft and the press-fit of the wheelset axle. These two modes should be eliminated or kept as minimum value as possible to avoid fatigue and failure of the drivetrain element.

- Equipping the electric drive with a slip controller, besides preventing the wheel from slipping on the rail, can perfectly dampen the first resonance mode (chatter mode) and return the system to the stable region. However, the slip control has less influence on the second resonance mode occurring between the two wheels (torsional mode).

- Reducing the motor torque is one of the simplest solutions to dampen the torsional resonance mode but at the cost of losing traction force. Therefore, advanced control techniques are required to be added in parallel with the slip controller.

An anti-vibration method using a resonant controller has been proposed in this Chapter. A PR controller is used for this purpose, whose output is added to the torque command used to provide traction effort. Torque oscillations are obtained from the estimated traction motor load torque. Only the estimated electromagnetic torque and the measured motor speed are required, no additional sensors/cabling or drivetrain state observers are therefore needed. The proposed anti-vibration control is robust against variations of slip velocity and under changing wheel-rail conditions providing maximum available traction with no interruption. It has also been shown that proper operation of the proposed method requires torque control bandwidths in the range of 60 Hz or higher. As a general conclusion, higher bandwidths in the slip controller will improve the overall performance of the traction control system using the proposed method.

Furthermore, the implementation is realized by a co-simulation tool. In simulations, torsional vibration is provoked by changes in the wheel-rail conditions. The effectiveness of torsional vibration detection is investigated. As a first step, the functionality of the simulation model implementation has successfully been verified on measurement results. This includes the coincidence of maximum dynamic torque of simulations and measurements as well as the linear dependency of dynamic torque and slip.

As a second step, simulations have been performed to investigate the effectiveness of torsional vibration protection. The received results show that the implemented vibration protection helps to suppress torsional vibration and therefore, prevents the wheelset from high dynamic torque. Still, as torsional vibration is suppressed indirectly by dynamic torque reductions, vibration detection requires reliable wheelset rotation speed data. Linear analysis shows that rotation speed sensors of the traction motors may not provide wheel rota-

tion speed data of sufficient quality. Consequently, the presented investigations and their results verify that suppressing torsional vibration indirectly by dynamically reducing the traction torque is an effective way to prevent a railway wheelset from high dynamic torque.

Chapter 6

Conclusions and Future Work

6.1 Conclusions

Development of a cost-effective railway traction system involves a complex, iterative process to both physical elements and control strategies: 1) physical elements such as number of traction motors, motor size, inverter-rated power, cooling system, .. etc; and 2) control strategies, including modulation techniques, aim to maximize the traction performance with less energy consumption and avoid system failure due to external disturbances during the whole trip.

This dissertation gave an insightful overview of electric traction drives for railways and proposed optimized strategies to fully utilize their torque and adhesion control capabilities. The torque control capability has been utilized as follows:

- Modulation techniques, four overmodulation strategies: Minimum-Distance Error (90º), Switching-State (60º), Single-mode, and Dual-mode have been presented and compared. It has been showed that optimal performance regarding to linearity, harmonic distortion, and number of commutation can be achieved by combining Switching-State and Dual-mode methods in overmodulation region I and region II respectively.

- Fast dynamic response for full speed range operation has been achieved by involving RFOC at low speeds and CLVF&FF at high speeds.

- Minimized copper and joule losses, i.e. high IM efficiency has been achieved by using remagnetization strategy which optimally distributes stator current components (i.e. flux and torque-producing components) while the electric machine is operating at light loads.

The utilization of traction capability can be summarized as follows:

- Anti-slip control and adhesion capability, five wheel-rail slip velocity control methods: constant slip, Perturb & Observe (P&O), Steepest Gradient (SG), Fuzzy Logic Control (FLC), and Particle Swarm Optimization (PSO) have been addressed. It is shown that maximum adhesion has been achieved using the proposed MAT-FLC and MAT-PSO methods. Both proposed methods showed a similar performance, however, MAT-FLC being superior in terms of computational simplicity and implementation easiness.

- Maximization of traction capability can be achieved by the continuous operation of traction drive without any interruption due to external disturbances, in this case, oscillations in torsional elements of the mechanical drivetrain. This has been achieved by adding an active anti-vibration control using a resonant controller to correct the commanded torque obtained from slip control loop.

6.2   Contributions

The main contributions made during the development of this dissertation are summarized as follows:

- A comparative analysis of overmodulation methods for AC electric drives using induction machines is performed considering three aspects: output vs. commanded modulation index (i.e., linearity); harmonic content; and the number of commutations (i.e., switching losses). Then, a generalized form of space-vector Pulse-width modulation (PWM) in overmodulation region is proposed. The addressed overmodulation methods are simulated and validated experimentally via a commercial three-level three-phase natural-point-clamped (NPC) inverter similar to the traction inverter used in real locomotives.

- Investigating the various control strategies for induction motor drives in railways, covering the full speed range through either using a single method or a combination of multiple methods. An improvement is made to one of the control strategies to achieve a better dynamic response compared to the traditional method. Further, a novel remagnetization strategy is presented to reduce copper losses and increase the overall efficiency of induction motors while operating at high speeds with light loads. Experimental validation is conducted for the remagnetization strategy tested in real train inverter test rig.

- Developing a scaled roller rig capable of reproducing the wheel-rail slip phenomenon in railways. Then, the scaled roller rig is used to evaluate recent advances in the anti-slip control strategies. Additionally, two maximum adhesion searching techniques MAT-FLC and MAT-PSO are proposed and experimentally validated.

- The influence and the consequences of the slippage phenomenon on the mechanical elements of the drivetrain is studied. Further, an active damping control technique is proposed to mitigate the torsional vibrations exerted on the locomotive mechanical drivetrain caused by excessive slip between the wheel and rail. Finally, a new simulation strategy is introduced and verified to predict the maximum torsional vibration magnitude using the co-simulation tool of Matlab-Simpack software.

6.2.1 Contributions of the Dissertation Published in International Journals

1. Nihal V. Vantagodi, **Ahmed F. Abouzeid**, J. M. Guerrero, I. Vicente, I. Muniategui, A. Endemaño, and F. Briz, "Design of a scaled roller-rig test bench for anti-slip control development for railway traction," in *IEEE Transactions on Vehicular Technology, Early Access*, 2022, doi: 10.1109/TVT.2022.3226607.

2. **Ahmed F. Abouzeid**, F. F. Trimpe, S. Lück, M. Traupe, J. M. Guerrero, and F. Briz, "Co-Simulation-Based Verification of Torsional Vibration Protection of Electric-Driven Railway Vehicle Wheelsets," *Vibration*, vol. 5, no. 3, pp. 613–627, Sep. 2022, doi: 10.3390/vibration5030036.

3. **Ahmed F. Abouzeid**, J. M. Guerrero, I. Vicente, I. Muniategui, A. Endemaño, and F. Briz, "Torsional Vibration Suppression in Railway

Traction Drives," in *IEEE Access*, vol. 10, pp. 32855-32869, March 2022, doi: 10.1109/ACCESS.2022.3162415.

4. **Ahmed F. Abouzeid**, J. M. Guerrero, A. Endemaño, I. Muniategui, D. Ortega, I. Larrazabal, and F. Briz, "Control Strategies for Induction Motors in Railway Traction Applications," *Energies*, vol. 13, no. 3, p. 700, Feb. 2020, doi: 10.3390/en13030700.

6.2.2 Contributions of the Dissertation Published in International Conferences

1. **Ahmed F. Abouzeid**, J. M. Guerrero, I. Vicente, I. Muniategui, A. Endemaño and F. Briz, "Remagnetization Strategies for Induction Machines Operating with Reduced Flux Levels," *2022 International Conference on Electrical Machines (ICEM)*, Valencia, Spain, 2022, pp. 2249-2255, doi: 10.1109/ICEM51905.2022.9910738.

2. **Ahmed F. Abouzeid**, J. M. Guerrero, I. Muniategui, A. Endemaño, D. Ortega and F. Briz, "Torque Dynamics Enhancement of Railway Traction Drives Using Scalar Control," *2021 IEEE International Electric Machines & Drives Conference (IEMDC)*, Hartford, CT, USA, 2021, pp. 1-6, doi: 10.1109/IEMDC47953.2021.9449495.

3. **Ahmed F. Abouzeid**, J. M. Guerrero, A. Endemaño, I. Muniategui, D. Ortega and F. Briz, "Assessment of Overmodulation Strategies for AC Drives Considering Harmonics Content and Switching Losses," *2021 IEEE International Electric Machines & Drives Conference (IEMDC)*, Hartford, CT, USA, 2021, pp. 1-6, doi: 10.1109/IEMDC47953.2021.9449543.

6.2.3 Contributions of the Dissertation Under Revision in International Journals

1. **Ahmed F. Abouzeid**, J. M. Guerrero, L. Lejarza, I. Muniategui, A. Endemaño and F. Briz, "Advanced Maximum Adhesion Tracking Strategies in Railway Traction Drives," Submitted to *eTransportation*, *Elsevier*, Feb. 2023.

6.3 Future work

There are several points that could be addressed in the future in order to continue the research line of this dissertation:

- Analysing the performance of the dynamic transition between overmodulation methods in current controller drives.

- Exploring the possibility of implementing remagnetization strategies online considering inverter voltage and current limits.

- Expanding the analysis of maximum adhesion tracking methods to include more optimization algorithms like neural networks combined with fuzzy logic control, genetic algorithms, etc. Also, exploring the applicability of advanced algorithms that use machine learning or artificial intelligence.

- Adding an online modal identification algorithm for mechanical drivetrain parameters estimation. Then, explore the possibility of using a Linear-Quadratic Regulator (LQR) to actively damp torsional vibrations in electric drives operating with low torque control bandwidth.

- More investigation on maximum dynamic torque estimation and the prediction of the critical operating adhesion scenario is needed. This would save time, cost, and effort for manufacturers during the rail vehicle homologation process.

6.4 Dissertation Funding

Capítulo 7

Conclusiones y Trabajo Futuro

7.1 Conclusiones

El desarrollo de un sistema de tracción ferroviaria rentable implica un proceso complejo e iterativo que afecta tanto a los elementos físicos como a las estrategias de control: 1) los elementos físicos, como el número de motores de tracción, el tamaño del motor, la potencia nominal del inversor, el sistema de refrigeración, etc.; y 2) las estrategias de control, incluidas las técnicas de modulación, cuyo objetivo es maximizar el rendimiento de la tracción con un menor consumo de energía y evitar fallos del sistema debidos a perturbaciones externas durante todo el trayecto.

Esta tesis ofrece una visión general de los accionamientos eléctricos de tracción para ferrocarriles y propone estrategias optimizadas para aprovechar al máximo sus capacidades de control del par y la adherencia. La capacidad de control del par se ha utilizado de la siguiente manera:

- Técnicas de modulación, cuatro estrategias de sobremodulación: Se han presentado y comparado cuatro estrategias de sobremodulación: error de distancia mínima (90º), estado de conmutación (60º), modo único y modo doble. Se ha demostrado que se puede conseguir un rendimiento óptimo en cuanto a linealidad, distorsión armónica y número de conmutaciones

combinando los métodos Switching-State y Dual-mode en las regiones de sobremodulación I y II, respectivamente.

- Se ha logrado una respuesta dinámica rápida para el funcionamiento en toda la gama de velocidades mediante la participación de RFOC a bajas velocidades y CLVF&FF a altas velocidades.

- Se han minimizado las pérdidas de cobre y de joule, es decir, se ha conseguido un alto rendimiento de la MI utilizando una estrategia de remagnetización que distribuye de forma óptima los componentes de la corriente del estator (es decir, los componentes productores de flujo y par) mientras la máquina eléctrica funciona con cargas ligeras.

La utilización de la capacidad de tracción puede resumirse del siguiente modo:

- Para el control antideslizamiento y la capacidad de adherencia, se han abordado cinco métodos de control de la velocidad de deslizamiento rueda-carril: deslizamiento constante, Perturb & Observe (P&O), Steepest Gradient (SG), Fuzzy Logic Control (FLC), y Particle Swarm Optimization (PSO). Se ha demostrado que se ha conseguido la máxima adherencia utilizando los métodos MAT-FLC y MAT-PSO propuestos. Ambos métodos propuestos mostraron un rendimiento similar, sin embargo, MAT-FLC es superior en términos de simplicidad computacional y facilidad de implementación.

- La maximización de la capacidad de tracción puede lograrse mediante el funcionamiento continuo del accionamiento de tracción sin ninguna interrupción debida a perturbaciones externas, en este caso, oscilaciones en los elementos de torsión de la transmisión mecánica. Esto se ha conseguido añadiendo un control activo antivibración mediante un controlador resonante para corregir el par comandado obtenido del lazo de control de deslizamiento.

7.2 Contribuciones

Las principales aportaciones realizadas durante el desarrollo de esta tesis se resumen a continuación:

- Se realiza un análisis comparativo de los métodos de sobremodulación para accionamientos eléctricos de AC con motores de inducción teniendo en cuenta tres aspectos: el índice de modulación de salida frente al comandado (es decir, la linealidad); el contenido armónico; y el número de conmutaciones (es decir, las pérdidas por conmutación). A continuación, se propone una forma generalizada de modulación por ancho de pulsos (PWM) vectorial espacial en la región de sobremodulación. Los métodos de sobremodulación abordados se simulan y validan experimentalmente a través de un inversor trifásico comercial de tres niveles con pinza de punto natural (NPC) similar al inversor de tracción utilizado en locomotoras reales.

- Se investigan las distintas estrategias de control para accionamientos de motores de inducción en ferrocarriles, cubriendo toda la gama de velocidades mediante el uso de un único método o una combinación de varios métodos. Se introduce una mejora en una de las estrategias de control para conseguir una mejor respuesta dinámica en comparación con el método tradicional. Además, se presenta una novedosa estrategia de remagnetización para reducir las pérdidas de cobre y aumentar la eficiencia global de los motores de inducción mientras funcionan a altas velocidades con cargas ligeras. Se realiza una validación experimental de la estrategia de remagnetización probada en un banco de pruebas real de inversores de tren.

- Desarrollo de una plataforma de rodillos a escala capaz de reproducir el fenómeno del deslizamiento rueda-carril en los ferrocarriles. A continuación, se utiliza la plataforma de rodillos a escala para evaluar los avances recientes en las estrategias de control antideslizamiento. Además, se proponen y validan experimentalmente dos técnicas de búsqueda de máxima adherencia MAT-FLC y MAT-PSO.

- Se estudia la influencia y las consecuencias del fenómeno de deslizamiento sobre los elementos mecánicos de la cadena cinemática. Además, se propone una técnica de control de amortiguación activa para mitigar las vibraciones torsionales ejercidas sobre la transmisión mecánica de la locomotora causadas por un deslizamiento excesivo entre la rueda y el carril. Por último, se introduce y verifica una nueva estrategia de simulación para predecir la magnitud máxima de las vibraciones torsionales utilizando la herramienta de co-simulación del software Matlab-Simpack.

7.2.1 Contribuciones de la Tesis Doctoral Publicadas en Revistas Internacionales

1. Nihal V. Vantagodi, **Ahmed F. Abouzeid**, J. M. Guerrero, I. Vicente, I. Muniategui, A. Endemaño, and F. Briz, "Design of a scaled roller-rig test bench for anti-slip control development for railway traction," in *IEEE Transactions on Vehicular Technology, Early Access*, 2022, doi: 10.1109/TVT.2022.3226607.

2. **Ahmed F. Abouzeid**, F. F. Trimpe, S. Lück, M. Traupe, J. M. Guerrero, and F. Briz, "Co-Simulation-Based Verification of Torsional Vibration Protection of Electric-Driven Railway Vehicle Wheelsets," *Vibration*, vol. 5, no. 3, pp. 613–627, Sep. 2022, doi: 10.3390/vibration5030036.

3. **Ahmed F. Abouzeid**, J. M. Guerrero, I. Vicente, I. Muniategui, A. Endemaño, and F. Briz, "Torsional Vibration Suppression in Railway Traction Drives," in *IEEE Access*, vol. 10, pp. 32855-32869, March 2022, doi: 10.1109/ACCESS.2022.3162415.

4. **Ahmed F. Abouzeid**, J. M. Guerrero, A. Endemaño, I. Muniategui, D. Ortega, I. Larrazabal, and F. Briz, "Control Strategies for Induction Motors in Railway Traction Applications," *Energies*, vol. 13, no. 3, p. 700, Feb. 2020, doi: 10.3390/en13030700.

7.2.2 Contribuciones de la Tesis Doctoral Publicadas en Congresos Internacionales

1. **Ahmed F. Abouzeid**, J. M. Guerrero, I. Vicente, I. Muniategui, A. Endemaño and F. Briz, "Remagnetization Strategies for Induction Machines Operating with Reduced Flux Levels," *2022 International Conference on Electrical Machines (ICEM)*, Valencia, Spain, 2022, pp. 2249-2255, doi: 10.1109/ICEM51905.2022.9910738.

2. **Ahmed F. Abouzeid**, J. M. Guerrero, I. Muniategui, A. Endemaño, D. Ortega and F. Briz, "Torque Dynamics Enhancement of Railway Traction Drives Using Scalar Control," *2021 IEEE International Electric Machines & Drives Conference (IEMDC)*, Hartford, CT, USA, 2021, pp. 1-6, doi: 10.1109/IEMDC47953.2021.9449495.

3. **Ahmed F. Abouzeid**, J. M. Guerrero, A. Endemaño, I. Muniategui, D. Ortega and F. Briz, "Assessment of Overmodulation Strategies for

AC Drives Considering Harmonics Content and Switching Losses," *2021 IEEE International Electric Machines & Drives Conference (IEMDC)*, Hartford, CT, USA, 2021, pp. 1-6, doi: 10.1109/IEMDC47953.2021.9449543.

7.2.3 Contribuciones de la Tesis Doctoral en Revisión en Revistas Internacionales

1. **Ahmed F. Abouzeid**, J. M. Guerrero, L. Lejarza, I. Muniategui, A. Endemaño and F. Briz, "Advanced Maximum Adhesion Tracking Strategies in Railway Traction Drives," Submitted to *eTransportation*, *Elsevier*, Feb. 2023.

7.3 Trabajo Futuro

Hay varios puntos que podrían abordarse en el futuro para continuar la línea de investigación de esta tesis:

- Análisis del rendimiento de la transición dinámica entre métodos de sobremodulación en accionamientos con regulador de corriente.

- Exploración de la posibilidad de aplicar estrategias de remagnetización en línea teniendo en cuenta los límites de tensión y corriente del inversor.

- Ampliar el análisis de los métodos de seguimiento de máxima adherencia para incluir más algoritmos de optimización como redes neuronales combinadas con control lógico difuso, algoritmos genéticos, ... etc. Asimismo, explorar la aplicabilidad de algoritmos avanzados que utilicen aprendizaje automático o inteligencia artificial.

- Incorporación de un algoritmo de identificación modal en línea para la estimación de los parámetros de la transmisión mecánica. A continuación, se explora la posibilidad de utilizar un regulador lineal-cuadrático (LQR) para amortiguar activamente las vibraciones torsionales en accionamientos eléctricos que funcionan con un ancho de banda de control de par bajo.

- Es necesario investigar más sobre la estimación del par dinámico máximo y la predicción del escenario crítico de adherencia operativa. Esto ahorraría tiempo, costes y esfuerzo a los fabricantes durante el proceso de homologación de vehículos ferroviarios.

7.4   Entidades Financiadoras del Presente Trabajo

Appendix A

Electrical and Mechanical Parameters

A.1 Traction Motor Parameters

Table A.1: Specifications of the induction motor at base speed ω_{base} (extended full flux range design).

Parameter	Symbol	Value	Unit
DC-link voltage	V_{dc}	3600	V
Rated Power	P_n	1084	kW
Rated Voltage	V_{LL}, rms	2727	V
Pole-pairs	P	2	-
Stator resistance	R_s	55.38	mΩ
Stator inductance	L_s	26.45	mH
Torque	T_e	3241	kNm
Speed	N_r	3194	rpm

A.2 Roller Rig Parameters

Table A.2: Test bench parameters.

System	Parameter	Wheel	Roller	Unit
Wheel	Radius	0.125	0.25	m
and	Force	843	843	N
Roller	Torque	105.3	210.7	Nm
Transmission	Gear ratio	90 / 24	192/26	-
Traction **Motor**	Rating	4	5.5	kW
	Power	1.78	1.78	kW
	Torque	28.1	28.5	Nm
	Speed	604.8	595.5	rpm
	Encoder Resolution	500	500	ppr
Inverter	Rating	4	15	kW
Motor-Wheel	Inertia [1]	0.002	0.007	kgm^2

[1] Inertia is calculated in wheel and roller motor reference frame respectively.

A.3 Mechanical Drive-Train Parameters of German Class 120 Locomotive

Table A.3: Six-inertia drive-train model parameters of the German class 120 locomotive referred to the wheelset side.

Moment of inertia	Symbol	Value	Unit
Traction motor	j_M	466.6	Kgm^2
Gear	j_G	55	Kgm^2
Half of hollow shaft to the gearbox side	j_{HG}	10.13	Kgm^2
Half of hollow shaft to the wheel side	j_{HW}	9.72	Kgm^2
Direct wheel and coupling	j_D	163	Kgm^2
Indirect wheel	j_I	157.3	Kgm^2
Torsional stiffness	**Symbol**	**Value**	**Unit**
Motor shaft	c_{MG}	88.12×10^6	Nm
Coupling (Gear side)	c_{GH}	15.1×10^6	Nm
Hollow shaft	c_{HW}	10.1×10^6	Nm
Coupling (Wheel side)	c_{HD}	15.7×10^6	Nm
Wheelset axle	c_{DI}	7.06×10^6	Nm
Torsional damping ratio	**Symbol**	**Value**	**Unit**
Motor shaft	d_{MG}	920.3×10^6	Nms
Coupling (Gear side)	d_{GH}	4730.8×10^6	Nms
Hollow shaft	d_{HW}	105.5×10^6	Nms
Coupling (Wheel side)	d_{HD}	11731.4×10^6	Nms
Wheelset axle	d_{DI}	73.7×10^6	Nms

A.4 Electrical Parameters of German Class 120 Locomotive Traction Motor

Table A.4: General specifications of the German class 120 locomotive.

Parameter	Value	Unit
Centenary voltage	15	kV
Centenary frequency	16.7	Hz
Maximum power	4.4	MW
Maximum tractive effort	340	kN
Maximum speed	280	km/h
Weight	$84,000$	kg
Gear ratio	4.818	-
Wheel diameter	1.25	m
Number of motors	4	-

A.5 Anti-vibration Controllers Gains

Table A.5: Closed-loop control gains of the simulated model.

Regulator type	Controller gain	Value
Current	k_{p_i}	2.2281
	k_{i_i}	81.9413
Slip velocity	k_{p_s}	4.7×10^3
	k_{i_s}	1.4×4
Anti-vibration	k_{p_r}	0.1
	k_{r_r}	2

Appendix B

Publications

B.1   Peer-reviewed journal publications

B.1.1   Design of a Scaled Roller-rig Test Bench for Anti-slip Control Development for Railway Traction

Design of a Scaled Roller-rig Test Bench for Anti-slip Control Development for Railway Traction

Nihal Vishnu Vantagodi , Ahmed F. Abouzeid , Juan M. Guerrero , Iban Vicente, Iker Muniategui, Aitor Endemaño, Fernando Briz

Abstract—**Anti-slip control is a prominent part of modern railway traction control systems due both to performance and safety concerns. This paper explains the development of a scaled roller-rig test bench which emulates the rail and the wheel of a train. The final purpose of the developed roller-rig test bench is twofold: to study the theory/behaviour of existing anti-slip strategies and to test new designs, before their implementation in the real system. Estimation of adhesion coefficient using a disturbance observer method is explained and tested under various conditions. Anti-slip control is implemented in wheel drive using a direct method by adding a slip speed controller. The tests are conducted using both fixed roller speed and variable roller speed, i.e. dynamic roller. In this second case, train inertia emulation will be key. Two methods are proposed to emulate train inertia, being this the main contribution of this paper. Both methods are verified in simulation first, and further confirmed experimentally in the test bench.**

Index Terms—**Traction control, Anti-slip control, Roller-rig test bench, Train inertia emulation**

I. INTRODUCTION

RAILWAY vehicles often require large tractive effort. Due to the design of wheel and rail, combined with the large elastic coefficient of steel, transfer of forces between the wheel and the rail occur through a small steel-to-steel contact area. While this is advantageous regarding frictional losses, it will curb the maximum force transfer. The maximum transferable force between the wheel and rail will not only be a function of design parameters such as wheel and rail shapes and materials, vehicle weight, etc. but also will be strongly affected by the surface conditions of rail [1]. Exceeding the maximum tractive force can produce an uncontrolled wheel slip, which can result in a number of unwanted effects, including reduced acceleration/deceleration performance [1], and also the risk of triggering torsional vibration phenomena [2]. This creates an interest and necessity to study slip phenomena and to develop anti-slip control methods.

Roller rigs are one of the important experimental setup that help in study and validation of the topics related to railway vehicle dynamics [3], [4], including wheel-rail contact dynamics [5], braking system [6], slip control [7] and adhesion estimation [8], etc. Test rigs can be developed in full scale, where the dimensions of the wheel and forces are unchanged compared to the actual wheels [4]; and in scaled versions, where the wheel size and the related parameters are reduced in specific ratio [9].

In this paper, the design of a scaled roller-rig test bench intended to test anti-slip control methods is conducted. A key

TO BE ADDED FOR THE FINAL VERSION.

element for a realistic anti-slip control validation which has been ignored in literature is proper emulation of wheel/vehicle interactions, which requires train inertia emulation. The case of a train with infinite inertia will be considered first, as this significantly simplifies the control of the test bench. Then, emulation in the test bench of a finite train inertia will be considered. This will allow to reproduce the impact of anti-slip control on train speed. Two different approaches for intertia emulation are proposed in this paper: 1) using a disturbance observer; 2) using an adhesion torque observer. The proposed methods are first evaluated by means of simulation using MATLAB-Simulink. Further they are verified experimentally on the developed test rig.

The paper is structured as follows: Section II provides details about the real train system, adhesion-slip curve and the anti-slip control method being used. Section III explains the development of the roller-rig test bench. Section IV explains the anti-slip control method implemented in the wheel drive of the test bench, and the inertia emulation concept with the two proposed methods. Section V provides the experimental results obtained from the test bench on anti-slip control with inertia emulation. Section VI discusses the findings and conclusions.

II. SYSTEM DESCRIPTION

The general schematic representation of an electric locomotive traction drive is as shown in Fig. 1. The ac overhead line supplies the locomotive through the pantograph. The transformer steps down the voltage of the overhead line and feeds the four quadrant converter (4QC), which converts the ac into dc voltage. The dc link voltage is smoothed by the capacitor C_{dc} and is filtered by the (2F) filter [10]. The chopper is used for dc link over-voltage protection. Traction inverter controls the torque produced by the motors, different control strategies can be used for this purpose [11]. Motors are mechanically coupled with the gear then to the traction wheel. Advanced locomotives have the adhesion control along with the torque control. Slip control enables better performance during slippery condition, and can also contribute to reduce the risk of torsional vibration in the wheel axle [12], [13].

Without the slippage, traction force F_t is equal to the tangential force and is given by (1), where T_m is motor torque after the gear, n is number of motors and r_w is traction wheel radius.

$$F_t = n \frac{T_m}{r_w} \qquad (1)$$
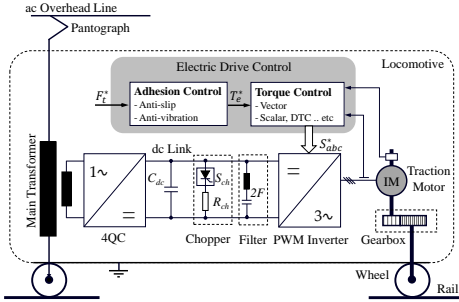
Fig. 1: Main elements of traction drive for real train.

The simplified force balance equation in the real train can be defined by (2), where m_t is train mass, B is the friction, v_t is train linear velocity and F_{lt} is the total load force.

$$F_t - F_{lt} = m_t \frac{dv_t}{dt} + B \cdot v_t \qquad (2)$$

Total load forces given by (3) comprise of the aerodynamic force F_{lA} (4), the rolling friction force F_{lR} (5), and the gradient force F_{lG} (6), which are subtracted from the adhesive force to obtain the net force F_{net} (see Fig. 2). Similarly, the total load torque (T_{lt}) is subtracted from the adhesive torque (T_a) to obtain net torque, T_{net}.

$$F_{lt} = F_{lA} + F_{lR} + F_{lG} \qquad (3)$$

$$F_{lA} = \frac{1}{2} C_d A_f \rho v_t^2 \qquad (4)$$

$$F_{lR} = C_r m_t g \qquad (5)$$

$$F_{lG} = m_t g \sin\theta \qquad (6)$$

where C_d is drag coefficient, A_f is frontal area, ρ is air density, C_r is rolling friction coefficient, g is the acceleration of gravity and θ is gradient angle in degree. The total load torque T_{lt} can be obtained from the load force F_{lt} using the radius of the wheel as mentioned in Fig. 2.

Relationship between angular and linear velocities is given in (7) where ω_w is the angular velocity of the traction wheel.

$$v_t = \omega_w \cdot r_w \qquad (7)$$

Adhesive force F_a is the force that can be transferred from the wheel onto the rail and is given by (8), where F_N is the normal force and μ is adhesion coefficient [14].

$$F_a = \mu \cdot F_N = \mu \cdot m_t \cdot g \qquad (8)$$
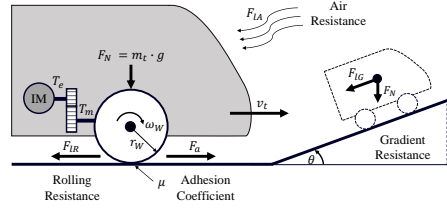
Fig. 2: Representation of train load forces and load torque.

The adhesion coefficient μ is a measure of the wheel-rail contact quality, which depends on the rail surface, environmental condition, temperature of the contact point, etc. The adhesion coefficient will be also significantly affected by the slip, which occurs when the angular velocity of the wheel doesn't match train linear velocity v_t (9).

$$\omega_w \cdot r_w \neq v_t \qquad (9)$$

A. Adhesion-Slip Relation
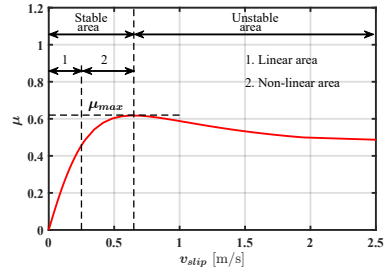
Fig. 3: Theoretical example adhesion-slip curve.

Variation of adhesion coefficient with respect to the slip velocity is called adhesion-slip curve in railway industry. An example plot is shown in Fig. 3. Based on the sign of the derivative of μ with respect to slip speed, the curve shown in Fig. 3 can be divided into two main regions. Positive values of $d\mu/dv_s$ correspond to the stable region. In this region, an increase of slip results in an increase of μ, and consequently of the tractive effort, eventually reducing slip. The stable region is seen to consist of two sub-regions: 1) linear area, the adhesion coefficient increases almost linearly with the slip velocity; 2) nonlinear area, $d\mu/dv_s$ reduces progressively, eventually reaching the maximum adhesion coefficient when $d\mu/dv_s = 0$.

If the slip surpasses this maximum, then $d\mu/dv_s < 0$, which corresponds to the unstable region. In this region, an increase of slip speed will result in a reduction of adhesive force. When this occurs, wheel speed is no longer linked to train speed.

Equation (10) holds in this case, where J_a accounts for axle inertia.

$$T_m - F_a\, r_w = J_a \frac{\mathrm{d}\omega_w}{\mathrm{d}t} \qquad (10)$$

It is observed from (10) that if traction motor torque T_m remains invariant, a decrease of F_a will result in a sustained increase of ω_w. Since F_a is decreasing, tractive force F_t, and consequently train speed will decrease too, slip speed consequently increasing steadily.

B. Anti-Slip Control

Slip control methods are aimed to maintain the slip velocity of the vehicle within the linear region and not far from the maximum adhesion coefficient value, in order to achieve the maximum possible traction effort [15]. An overview of the available slip control methods is provided in [16]. The method used in this paper being a direct type, a speed controller is used to follow the commanded slip during slippage.

The anti-slip control is implemented based on 'slip velocity control to a constant value method' [16], the control schematic is shown in Fig. 4. The torque command T^*_{mW} is provided as a ramp signal to emulate the increase in velocity of the train avoiding jerk and considering the comfort and safety of passengers. The torque reference T^{ref}_{mW} is applied to the torque controller. Fast and precise torque control is needed to avoid excessive slippage. Rotor field-oriented control (RFOC) was selected and will be used in developed the test rig as well. Voltage commands produced by RFOC are modulated using PWM to generate the pulses $S^*_{abc\_W}$ controlling inverter switches. Other control methods could be used, e.g. scalar, DTC, etc. [11], but noting that a degradation of either dynamic response of the control, or accuracy of torque estimation, will affect to the accuracy of the wheel/roller contact emulation.

Fig. 4: Wheel drive with slip control.

When the torque commanded exceeds the adhesion limit, slip occurs in the wheels. When the slip occurs, the controller maintains the slip at the reference value v^*_{slip} such that it maintains the adhesion value at maximum and in the stable region. The required slip is achieved by the speed controller. The wheel speed command ω^*_{mW} is calculated from the slip velocity reference and the train velocity v_t using the gear ratio R_{gW} and the wheel radius r_W. The controller receives

this speed command and provides the torque reference. The output of controller is saturated and this can be achieved using two methods, the static and dynamic saturation which are explained in Section IV-B. Dynamic limiter is used because of better performance compared to static limiter and the saturated output, $T^{*\prime}_{mW}$ is fed to the block which selects the minimum of the two torque values. Under operation without slip, torque from the ramp command will be fed to the torque controller block and during slippage, the torque command from speed controller will be less compared to the ramp command and hence will be provided to the torque controller block. Anti-slip control implementation in the test bench is addressed in Section IV.

III. SCALED ROLLER-RIG DESIGN

Either full scale or scaled roller rig test bench can be used to perform the tests needed to validate control strategies before introducing them in the real train. In the test bench, the actual rail is normally replaced by a wheel, which hereafter will be denoted as the roller. Use of scaled designs have obvious advantages in terms of cost and manageability. However, special care is required to ensure that key properties of the real system remain in the scaled version. This section explains the scaling and development of the test bench.

Depending on the purpose of the development of the test rig, to reduce the effect of scaling the dimensions, a suitable scientific approach must be taken while performing scaling. The scaling factors are derived based on the relation between physical quantities, the laws abiding them and the length scaling factor.

The ratio of full scale length l_f to the scaled model length l_s is the beginning step for setting the similarity of railway vehicles which is given by (11)

$$\delta_l = \frac{l_f}{l_s} \ \ (\text{length}) \qquad (11)$$

Density scaling factor is defined as (12), and using this the inertial quantities' scaling factors are defined as (13)

$$\delta_\rho = \frac{\rho_l}{\rho_s} \ \ (\text{density}) \qquad (12)$$

$$\delta_m = \frac{m_f}{m_s} = \delta_\rho \delta_l^3 \ \ (\text{mass}) \qquad (13)$$

These scaling factors form the basis of the scaling strategies. The three scaling methods which are often used in the roller rig development are MMU (Manchester Metropolitan University) method, DLR (Deutsches Zentrum für Luft- und Raumfahrt) method and INRETS (National Institute of Research on Transportation and Security) method [17]. Table I shows the parameters considered for scaling and the comparison of the scaled values in SI units using the three techniques mentioned above. As the study purpose relates to vehicle dynamics of rail, MMU similitude method is chosen.

The roller-rig test bench is developed to simulate the conditions of a locomotive of 86 t with a nominal velocity of 10.56 m/s with 8 traction wheels, further details are given in Table II. The test bench is designed to have a single wheel and

TABLE I: Comparison of roller-rig scaling techniques [17].

Scaling Variables		Scaling Method		
		MMU	DLR	INRETS
Geometry	Length	5	5	4
	Cross Section	25	25	16
Material	Density	1	0.5	1
	Mass	125	62.5	64
	Inertia	3125	1562.5	1024
System Variables	Time	1	$\sqrt{5}$	4
	Frequency	1	$1/\sqrt{5}$	$1/4$
	Velocity	5	$\sqrt{5}$	1
	Acceleration	5	1	4
	Angular velocity	1	$1/\sqrt{5}$	$1/4$

mass of the locomotive is considered to be equally distributed amongst the wheels. The scaled force F_{TR} acting on each wheel is given by (14)

$$F_{TR} = \frac{m_{loco} \cdot g}{n_{TR} \cdot \delta_m} \approx 0.843 \text{kN} \quad (14)$$

where n_{TR} is number of traction wheels of real train and δ_m is mass scaling factor in MMU method with a value of 125 mentioned in Table I.

The scaled nominal linear speed of the wheel is given by (15)

$$v_{nom_{TR}} = \frac{v_{nom}}{\delta_v} = 2.11 \text{m/s} \quad (15)$$

where δ_v is the velocity scaling factor in MMU method with a value of 5 mentioned in Table I.

The scaled wheel radius is 0.125 m. The roller radius was chosen to have twice the radius of wheel. Using the radius value and the scaled value of force and velocity (mentioned in Table II), the torque ($T = r \cdot F$) and angular speed ($\omega = v/r$) of the roller and wheel are calculated. Table II shows the parameters considered for scaling and the value obtained after the scaling using the MMU method.

TABLE II: Actual and Scaled parameters of roller-rig.

Parameter	Actual Value	Scaling Factor	Scaled Value	Unit
Wheel diameter	1.25	5	0.25	m
Roller diameter	infinite	-	0.50	m
Locomotive mass	86	125	0.688	t
Cargo mass	448.8	125	3.59	t
Force per wheel	105.4	125	0.84	kN
Velocity	10.56	5	2.11	m/s
Contact area	82-96 [18], [19]	25	3.28-3.84	mm^2
Inertia (Roll) x-axis per wheel	26113	781.2$^{(1)}$	33.42	kg m^2
Wheel Torque	5000	47.48 $^{(2)}$	105.3	Nm
Wheel Speed	3210	19.90 $^{(2)}$	161.3	r/min
Wheel Power	1084	608.9$^{(2)}$	1.78	kW

$^{(1)}$ Inertia is calculated using $J = mr^2$. For train inertia, m is mass of locomotive and cargo per wheel and r is referred to wheel radius. For scaled inertia, m is scaled mass of locomotive and cargo per wheel and r is referred to test bench roller radius.
$^{(2)}$ Derived from scaling factors and actual train and test bench gear ratios.

IV. IMPLEMENTATION AND SIMULATION OF ANTI-SLIP CONTROL INCLUDING TRAIN INERTIA EMULATION

Validation of the test rig design and proposed emulation strategies is accomplished by means of simulation. First, the adhesion coefficient of the contact point of the roller-rig test bench has been estimated; this is discussed in section IV-A. The anti-slip control method explained in Section II-B is implemented in the wheel drive of the test bench. The schematic configuration of the test bench is shown in Fig.5(a). The physical system of wheel and rail is modelled using the contact point block as shown in 5(b). Wheel and roller angular speeds are obtained from the applied torques and the corresponding inertia. Angular speeds are converted to linear velocities v_W and v_R, in wheel and roller reference frame, from which the slip velocity v_{slip} is obtained. The adhesion-slip curve was obtained during a commissioning process and stored in a look-up table allowing a precise wheel-roller contact point modeling. This will be discussed later in section V-B. The look-up table is used further to obtain the adhesive force from the measured slip speed and the known normal force. Then using the gear ratio and radius of wheel and roller, the load torque for both motors are calculated.

First, a train with an infinite inertia is considered in Section IV-B. In this case, changes in the tractive effort will have no effects on train speed. This allows decoupled wheel and roller controls, significantly simplifying the implementation, but at the price of ignoring the dynamics of the train. The approach in Sections IV-D and IV-C considers a train with a finite inertia. Changes in the tractive force will affect in this case to train (roller) speed.

(a)

(b)
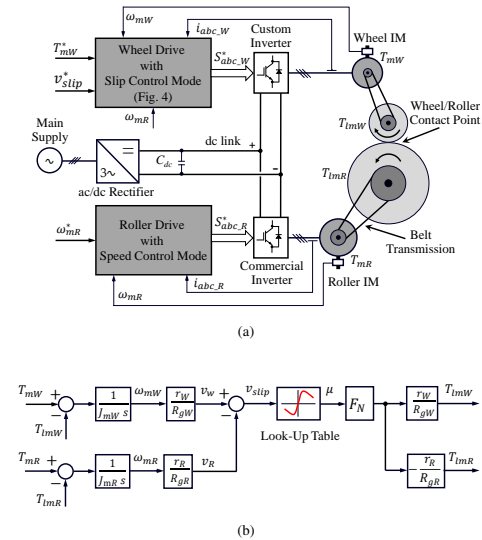
Fig. 5: Block diagram of roller-rig test bench. (a) Schematic representation of the overall control system; (b) Contact point model used in simulation. Look-up table is obtained experimentally as described in subsection V-B

A. Adhesion Estimation Using Disturbance Observer

From Fig. 5, traction motor mechanical equation is given by (16)

$$T_{mW} = J_{mW} \frac{d\omega_{mW}}{dt} + B_{mW}\omega_{mW} + T_{lmW} \qquad (16)$$

where T_{mW} and T_{lmW} are the electromagnetic torque and load torque seen by the motor respectively, J_{mW} is the combined wheel motor and inertia in motor reference, ω_{mW} is the motor speed and B_{mW} is viscous friction.

The adhesive force is calculated from the estimated load torque seen by the wheel $\hat{T}_{lW}$ and wheel radius r_W as (17), R_{gW} being the motor-to-wheel gear. Terms with a hat (^) symbol stand for estimates of the corresponding variable or parameter.

$$\hat{F}_a = \frac{\hat{T}_{lW}}{r_W} = \frac{R_{gW}\,\hat{T}_{lmW}}{r_W} \qquad (17)$$

For the motor, the load torque is the disturbance. A disturbance observer is then used to obtain the adhesion coefficient $\hat{\mu}$ [20]. Rearranging (16) for load torque and writing in Laplace domain, (18) is obtained.

$$T_{lmW(s)} = T_{mW(s)} - (J_{mW}s + B_{mW}) \cdot \omega_{mW(s)} \qquad (18)$$

To avoid the pure derivative term in the numerator a low pass filter is used as proposed in [20], the estimated load torque $\hat{T}_{lmW}$ being obtained as (19).
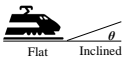
$$\hat{T}_{lmW(s)} = \hat{T}_{mW(s)} - \left(\hat{B}_{mW} + \frac{\hat{J}_{mW}}{\tau} - \frac{\hat{J}_{mW}/\tau}{\tau s + 1}\right) \cdot \omega_{mW(s)} \qquad (19)$$

Finally, combining (8) and (17), the adhesion coefficient can be estimated from the estimated motor load torque as (20).

$$\hat{\mu} = R_{gW} \frac{\hat{T}_{lmW}}{F_N \cdot r_W} \qquad (20)$$

B. Anti-Slip Control with Infinite Train Inertia

In this approach, changes on tractive force will have no effect on train speed. This might correspond to a scenario in which the gradient of railway progressively increases while the train is travelling at constant speed. This is shown schematically in Fig. 6. Tractive force increase following gradient force (6) increase might exceed the limit, causing slippage. Anti-slip control should keep the slip at the reference value in this case.

	Real Train	Test bench
Speed	Constant	Roller speed: Constant
Torque	Increases	Wheel torque: Increases
Consequence	Slip can occur	→ Slip controller activated

Fig. 6: Fixed roller speed scenario

In the described scenario, wheel is under torque control, torque command being a ramp. The roller is under speed
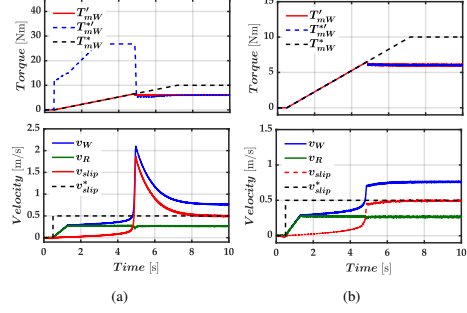
Fig. 7: Simulation results. Anti-slip control with fixed roller speed with static and dynamic saturation: (a) static limiter; (b) dynamic limiter. Top: Initial torque command T_{mW}^*; output of slip control block $T_{mW}^{*\prime}$; torque command reaching the RFOC block of wheel drive T_{mW}'. Bottom: wheel and roller linear speeds, and slip speed

control with the desired speed representing the train velocity. When the torque exceeds the limit, slip control is activated.

Special care must be taken in case saturation of the Proportional- Integral (PI) speed controller output in Fig. 4. Static saturation using rated torque as the limit is perhaps the most straightforward solution. Under normal operation, the actual slip velocity will be usually $\ll v_{slip}^*$. Thus the speed controller will saturate to rated torque in an attempt to achieve v_{slip}^*. When slip occurs, it takes time (≈ 2 s) for the slip PI controller to reduce the torque. During this time, an unacceptable overshoot of ($\approx 300\%$) in the slip velocity occurred, as seen in Fig. 7(a).

Hence to avoid this situation, a dynamic torque limiter is used which tracks the torque command and uses it as the torque limit for PI speed controller. When the ramp torque command cannot be transferred to the roller and the slip occurs, it shifts to the torque provided by the PI controller and limits the slip to the command value without having the overshoot. The results are shown in the Fig. 7(b), the improvement with respect to the static limiter case being readily observable.

C. Anti-slip Control with Proposed Train Inertia Emulation using Disturbance Observer

The tests in the previous method are performed with a fixed roller speed. As discussed, this would emulate a particular test condition wherein the gradient of the track increases but the velocity of the train remains constant. In a more general scenario, changes in the tractive force should produce changes in the train speed. To implement this, the speed of the roller, which represents the train linear speed, must change as a consequence of changes in wheel torque. It is noted that the inertia of the wheel in the test bench doesn't match the scaled train inertia. Wheel and roller inertia in motor reference frame

Fig. 8: Proposed inertia emulation using Disturbance Observer method.

Fig. 9: Proposed inertia emulation using an adhesion torque observer (a) Adhesion Torque Observer model; (b) Contact point and roller drive dynamics.
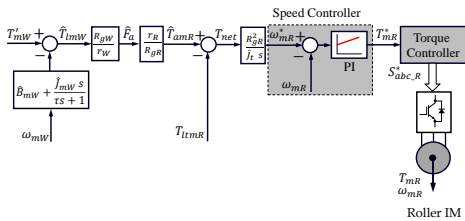
are 0.002 kgm^2 and 0.007 kgm^2 respectively while the scaled train inertia in roller motor reference $\hat{J}_{tmR}$ frame is 0.613 kgm^2 ($\hat{J}_{tmR} = \dfrac{\hat{J}_t}{R_{gR}^2}$, where $\hat{J}_t = 33.425$ kgm^2 is scaled inertia calculated in Table II). I.e. the ratio between desired and actual roller inertia is ≈ 90. Consequently, train inertia must be emulated by control.

The schematic of the inertia emulation using Disturbance Observer method is shown in Fig.8. The load torque of the wheel motor is estimated using the Disturbance Observer as in (19). The adhesive torque in roller motor reference at the wheel-rail contact, $\hat{T}_{amR}$, is estimated using the gear ratio and radius of wheel and roller. The net torque T_{net} is obtained after subtracting the total load torque (3). The roller speed command is obtained by integrating the net torque T_{net} and multiplying the inverse of equivalent train inertia in roller motor reference which is calculated dividing the scaled train inertia $\hat{J}_t$ by the square of roller gear ratio (see Fig. 8). This serves as input for the roller speed controller, the following remarks can be made:

- This method is insensitive to roller inertia and friction while emulating the train inertia. It forces the roller to follow the required torque command to emulate the scaled inertia of the train.
- Wheel drive must share its torque command signal with the roller drive. This requires a fast and reliable communication channel between both drives. Delays and/or noise in the communications can result in significant degradation of the method.

D. Anti-slip Control with Proposed Train Inertia Emulation using Adhesion Torque Observer

The drawbacks of the previous method can be overcome by emulating train inertia independently in the roller drive without employing wheel signals considering the same test conditions. The block diagram of the method developed for emulating the train inertia using an Adhesion Torque Observer is shown in Fig. 9(a). It is derived from the concept proposed in [21] to emulate a wind turbine.

The torque that is transferred by the wheel onto the roller, adhesion torque T_a, depends on the wheel-roller contact point dynamics as shown in Fig. 9(b). T_a is estimated using a 'test bench dynamic model'. Then, using the estimated adhesion
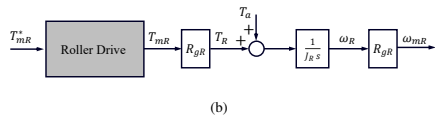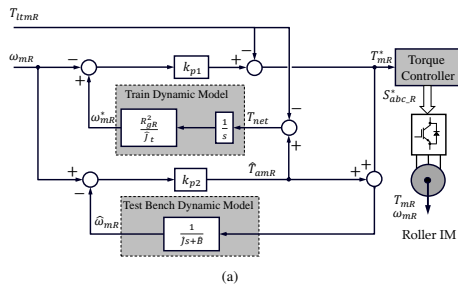
torque, a speed command for the roller, ω_{mR}^*, is obtained using a 'train dynamic model'. The test bench dynamic model accounts for the combined inertia $\hat{J}$ and friction coefficients $\hat{B}$ of the wheel, roller and the respective motors. The train dynamic model accounts for the scaled train inertia referred in roller motor reference frame.

Initially no torque is commanded to the roller. Due to T_a, the roller begins to rotate and gain speed, $T_a-$to$-\omega_R$ relationship being determined by the overall (i.e. motor and roller) roller inertia J_R.

The adhesion torque in roller motor reference frame is estimated as $\hat{T}_{amR}$ using the proportional gain k_{p2} given by (21) with the test bench dynamic model comprising of estimated roller and motor inertia.

$$\hat{T}_{amR} = k_{p2} \cdot (\omega_{mR} - \hat{\omega}_{mR}) \qquad (21)$$

where the estimated roller speed $\hat{\omega}_{mR}$ is obtained by (22)

$$\hat{\omega}_{mR} = (\hat{T}_{amR} + T_{mR}^*) \cdot \frac{1}{(\hat{J}s + \hat{B})} \qquad (22)$$

The net torque is given by (23), where T_{ltmR} is total load torque in roller motor reference frame which correspond to the load force comprising of rolling friction, gradient and aerodynamic forces shown in Fig. 2.

$$T_{net} = \hat{T}_{amR} - T_{ltmR} \qquad (23)$$

The roller motor speed command ω_{mR}^* is calculated using train dynamic model which comprise of estimated scaled train inertia $\hat{J}_t$ in roller motor reference frame and is given by (24).

$$\omega_{mR}^* = T_{net} \cdot \frac{R_{gR}^2}{\hat{J}_t} \cdot \frac{1}{s} \qquad (24)$$
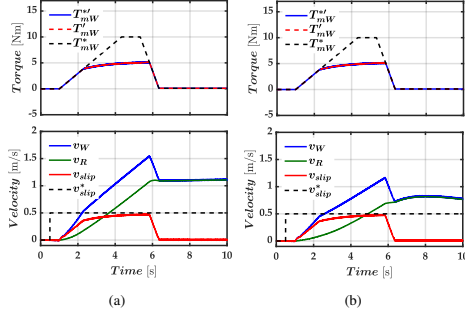
Fig. 10: Simulation results. Proposed inertia emulation methods (a) Disturbance Observer method; (b) Adhesion Torque Observer method. Top: Torque command T_{mW}^*; output of slip control block $T_{mW}^{*\prime}$; final output reaching the RFOC block of wheel drive $T_{mW}^\prime$. Bottom: wheel and roller linear speeds, and slip speed

The proportional gain k_{p1} is used to calculate the torque that forces convergence of the estimated roller motor speed $\hat{\omega}_{mR}$ and the speed command ω_{mR}^*, the roller motor torque command is given by (25).

$$T_{mR}^* = k_{p1} \cdot (\omega_{mR}^* - \omega_{mR}) \qquad (25)$$

The gain k_{p1} is limited either by the roller drive torque control bandwidth or by the sampling frequency ω_s (26) as discussed in [21]

$$\frac{k_{p1}}{J_{mR}} < \frac{\omega_s}{2} \qquad (26)$$

The gain k_{p2} is chosen to be (27) as mentioned in [21]

$$k_{p2} = \frac{2k_{p1}J_{mR}}{\hat{J}_{tmR}} \qquad (27)$$

The results of the simulation of two methods analyzed for inertia emulation are presented in Fig. 10. Torque command T_{mW}^* follows a ramp up to the value required to achieve the target acceleration, and is later removed. It can be noticed that for the same train inertia, the increase in speed of roller v_R is lower ($\approx 27\%$) in the Adhesion Torque Observer method shown in Fig. 10(b) compared to the Disturbance Observer method of inertia emulation shown in bottom subplots of Fig. 10(a). On the other hand, developed torque is seen to be same in both cases (see top subplots of Fig. 10(b) and 10(a)). This is expected as the Disturbance Observer method does not account for the roller friction and inertia, torque command being imposed only emulates train inertia. On the contrary, Adhesion Torque Observer method estimates adhesive torque from the roller speed, which accounts for test bench friction and inertia and hence has a lower speed. In both cases the slip velocity v_{slip} is achieved the reference value v_{slip}^*.

TABLE III: Wheel and Roller test bench parameters.

System	Parameter	Wheel	Roller	Unit	Variable name
Wheel and Roller	Radius	0.125	0.25	m	r_W, r_R
	Force	843	843	N	-
	Torque	105.3	210.7	Nm	-
Transmission	Gear ratio	90/24	192/26	-	R_{gW}, R_{gR}
Traction Motor	Rating	4	5.5	kW	-
	Power used	1.78	1.78	kW	-
	Torque	28.1	28.5	Nm	T_{mW}, T_{mR}
	Speed	604.8	595.5	rpm	ω_{mW}, ω_{mR}
	Encoder Resolution	500	500	ppr	-
Inverter	Rating	4	15	kW	-
Motor-Wheel	Inertia [(1)]	0.002	0.007	kgm^2	J_{mW}, J_{mR}

[(1)] Inertia is calculated in wheel and roller motor reference frame respectively.

It is noted that the adhesion estimation methods presented in this section are intended for test bench operation and might not be suitable for adhesion estimation in actual locomotives.

V. EXPERIMENTAL VALIDATION

Experimental verification of the methods discussed in section IV is addressed in this section. Roller-rig is described in subsection V-A. Adhesion-slip curves are obtained in subsection V-B. These curves were used for contact point modeling (see Fig. 5(b)) and simulation analysis and verification discussed in subsection IV-A. Finally, validation of anti-slip control using the proposed inertia emulation methods discussed in subsections IV-B−IV-D is addressed in subsections V-C-V-E respectively.

A. Hardware Setup

Test bench parameters are given in Table III. Main elements of the test bench are discussed as following:

1) Wheel and Roller: The test bench has a wheel which emulates the traction wheel of the railway locomotive and a roller, which emulates the rail. The manufacturing limit for roller diameter is 0.5 m and test rigs maintain a ratio of two or more between roller and wheel diameters. Hence, a diameter of 0.25 m was chosen for the wheel and 0.5 m for the roller (see Fig. 5(a) and Fig. 11(a)). The roller is a cylinder, i.e. its surface is flat. The surface of the wheel is provided with a circular profile with radius 0.25 m, the resulting contact area is 3.93 mm^2 close to the required scaled value shown in Table II.

2) Traction and Transmission Systems: The traction system consists of the motors and the electric drives. Four-pole induction machines of 4 kW and 5.5 kW respectively are used for wheel and roller. From the wheel parameters calculated in Table II, it can be noticed that the required power and speed of wheel/roller are small but the required torque is large when compared to the induction motors rated value. Using a transmission between the wheel/roller and the motor allows achieving the required torque and speed. The gear

(a)

(b)
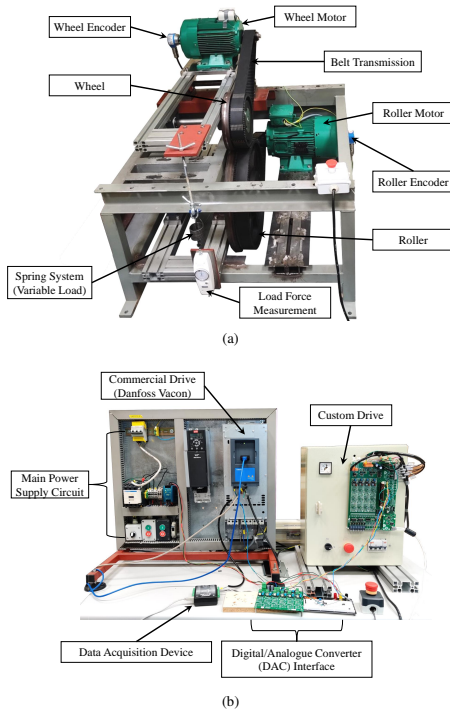
Fig. 11: Experimental setup: (a) Front view of roller rig test bench; (b) Electric Drives.

ratios of the corresponding belt transmissions were selected to match rated torque-speed of the motors to wheel and roller requirements. The details can be found in Table III. The transmission between the motors, roller and wheel can either be gear drive, belt drive or chain drive.

Owing to the non-availability and time requirement to procure the gear drive of specific ratio to match the requirement, a V-belt drive is chosen. A commercial *Vacon NXP00385 Danfoss* drive is used to control the roller motor and a custom drive is developed to control the wheel motor (see Fig. 11(b)). Both drives use rotor field-oriented control (RFOC) as mentioned in Section II-B. The Control Board of the custom drive contains the Digital Signal Controller (DSC) TMS320F28335 real time micro-controller from Texas Instruments which controls the operation of the drive with 10 kHz for both sampling and switching frequencies [22]. Additionally, the control board contains the input/output interface circuits for current, speed measurements and Pulse-Width Modulated (PWM) signals transmission for the power module.

Torque and speed of roller and wheel motors are needed for slip and torque control. Torques are estimated from RFOC

variables, i.e. stator measured currents and estimated rotor flux [11]; speeds are obtained from 500 ppr encoders attached at wheel and roller motors.

3) Wheel Load Adjustment: The force applied by the wheel on the roller can be varied by the spring system, it is measured using a force gauge. The normal force can be varied between 380 N, which occurs when the spring is not stretched and all the force is due to wheel system mass, and 1380 N (see Fig. 11(a))).

4) Visualization and Data Analysis: Roller and wheel speeds are obtained from encoders (500 ppr of resolution) attached at the corresponding motors. Torques are estimated from RFOC variables. All the relevant signals involved in wheel and roller control can be exported using Pulse-Width Modulated (PWM) signals from the drives, and captured by a multi-channel acquisition system for visualization and results analysis (see Fig. 11(b)). Results shown in Fig. 12 to Fig. 16 have been obtained using this method.

B. Adhesion-Slip Curves

To validate the proper operation of the test bench and the consistency of the results, multiple tests were conducted to obtain adhesion-slip curves between wheel and roller under different operating conditions. Both drives were operated in speed control for these tests. For each test, a base speed is fixed for the roller and then the wheel is commanded to sweep the desired slip range. The adhesion value is calculated using (20). Tests were performed varying the load applied using the spring system and the roller speed. It is observed from Fig. 12(a) that adhesion decreases as load increases. Fig. 12(b) shows that adhesion increases with increase in roller speed.

Moreover, additional tests are also conducted to obtain the adhesion curves in various conditions to have a real-world scenario. The results obtained are shown in Fig. 13. The results show that adhesion is maximum in dry conditions and reduces with water, soap water, and is least with grease. This is consistent with the results reported using the roller rig test bench in [3] and the results obtained using a real train in [23]. In this context, it is worth mentioning that the adhesion estimation accuracy is relying on the estimated wheel motor torque as seen in (19) and (20). The torque observer was calibrated and tested experimentally, the estimation error being $< 4\%$. Consequently, the steady-state error in the estimated adhesion coefficient is expected to be $< 4\%$. Transient errors will depend on the first-order low-pass filter (LPF) time constant τ in (19). The LPF time constant of $\tau = 0.01$ s was chosen for all conducted experiments.

C. Anti-slip Control with Infinite Train Inertia

This test is performed to verify the direct method of anti-slip control (Section II-B) with fixed roller speed mentioned in Section IV-B. Wheel is in torque control mode ①, a torque ramp is provided (see top sub-figure in Fig. 14) along with slip control ② as shown in Fig. 4. The roller is in speed control and commanded a fixed speed. The equivalent force will get transferred from the wheel onto the roller until the adhesion reaches the maximum value (see bottom sub-figure in Fig. 14).

195
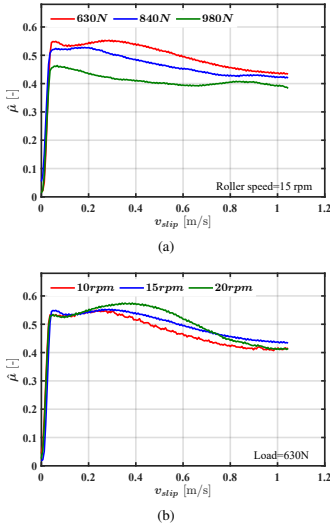
Fig. 12: Experimental results. Adhesion curve comparison at dry condition (a) Fixed roller speed, varying load; (b) Fixed load, varying roller speed.
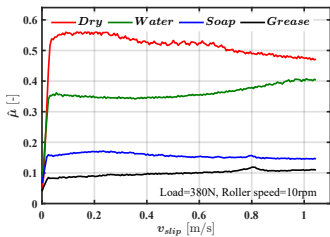
Fig. 13: Experimental results. Adhesion curve comparison for different conditions.

Once the maximum adhesion is reached, the wheels begin to slip as shown in the second sub-figure in Fig. 14 and follows the slip velocity command (see third sub-figure in Fig. 14). This is consistent with the discussion in subsection IV and the simulation results shown in Fig. 10.

D. Anti-slip Control with Proposed Train Inertia Emulation using Disturbance Observer

The method explained in Section IV-C (Fig.8) is verified in the test bench. It includes the inertia emulation proposed in this paper. In this method both wheel and roller are in torque control. A ramp torque command (Fig. 15) is provided to the wheel. Once wheel starts rotating, roller starts rotating too.
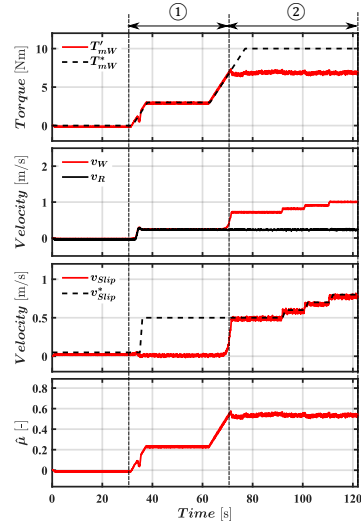
Fig. 14: Experimental results. Anti-slip control with fixed roller speed. From top to bottom: wheel torque; wheel and roller velocities; Commanded and actual slip velocities and estimated adhesion. ①: Torque control mode; ②: Slip control mode.

Inertia emulator block calculates the load torque required to emulate the train inertia, which is provided to roller drive.

Test results are shown in Fig. 15(a), the analysis being similar to the previous subsection. The ramp torque applied in Fig. 15(b) causes wheel and roller speed to increase slowly until maximum adhesion is reached. The wheel begins to slip and follows the slip command (see third sub-figure in Fig. 15(b)) after reaching the maximum adhesion value. It is observed that once the torque is removed, wheel and roller speeds remain almost constant, as would correspond to a system with a very large inertia. This effect becomes more evident in Fig. 15(a), where the system is seem to maintain an almost constant speed for a large time span. This is in agreement with the simulation results shown in Fig. 10. Interestingly, it is observed from Fig. 15(a) that when the inertia emulation is disabled, wheel and the roller come to halt in a few seconds, due to the reduced inertia and relatively large friction of the physical system compared to the one being emulated.

E. Anti-slip Control with Proposed Train Inertia Emulation using Adhesion Torque Observer

The method proposed in this paper explained in Section IV-D (Fig.9) was also verified in the test bench. The test conditions and implementation methodology are the same as for the previous subsection. Test results are shown in Fig. 16, the analysis being similar as for the previous subsection too.
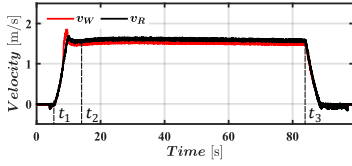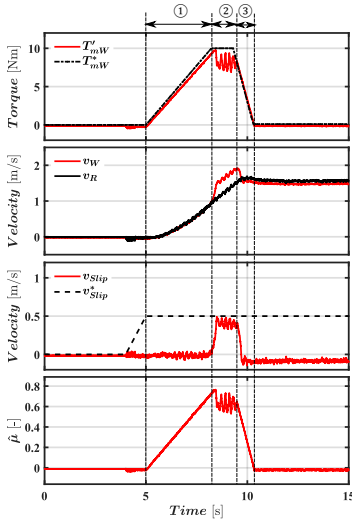
Fig. 15: Experimental results. Inertia emulator using Disturbance Observer method. (a) wheel and roller velocities. $t = t_1 \rightarrow t_2$, acceleration process; $t = t_2 \rightarrow t_3$, inertia emulation enabled; $t > t_3$, inertia emulation disabled. (b) Zoomed view of acceleration period showing from top to bottom: wheel torque; wheel and roller velocities; commanded and actual slip velocities and estimated adhesion. ① and ③: torque control mode; ②: slip control mode.

The ramp torque applied in Fig. 16(b) causes wheel and roller speed to increase slowly until maximum adhesion value is reached (see bottom sub-figure in Fig. 16(b)). The wheel begin to slip and follows the slip command (see third sub-figure in Fig. 16(b)) after reaching the maximum adhesion value. Once the torque command is reduced to zero, roller speed is seen to decrease slowly, but with a slope which is larger compared to the Disturbance Observer method shown in Fig. 15(a). This is in agreement with the simulation results shown in Fig. 10 where the slope of roller speed when the torque command is limited, is larger in Adhesion Torque Observer method compared to Disturbance Observer method for inertia emulation.
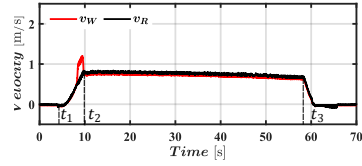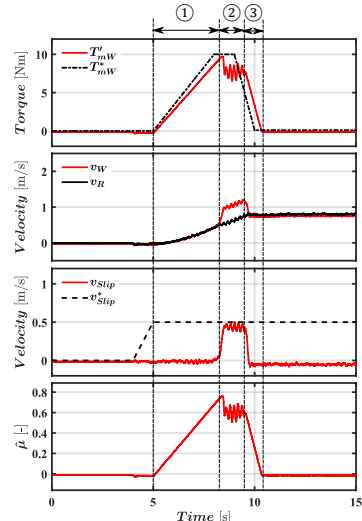
Fig. 16: Experimental results. Same legends as Fig. 15 using Adhesion Torque Observer method.

Finally, it is highlighted the importance of having a precise estimation of test bench friction $\hat{B}$ in the 'Test bench dynamic model' of Fig. 9(a). This allows isolating the adhesion force in the estimation. Fig. 17(a) and Fig. 17(b) show the effects of underestimating and overestimating the friction respectively. Underestimation of friction results in a deceleration of $-0.019 m/s^2$, which is around ten times faster than the expected value obtained using the actual train inertia and friction, which is $-2.08 \times 10^{-3} m/s^2$. Furthermore, in the case of overestimation of friction, the estimated train speed would not decrease but increase with an acceleration of $4.6 \times 10^{-3} m/s^2$. The importance of accurate test bench friction coefficient estimation becomes evident from these results.

VI. CONCLUSION

This paper explains the development of test bench intended for validation of anti-slip control for railway traction systems. System scaling and characterization of adhesion properties has been discussed in detail. The main contribution of the
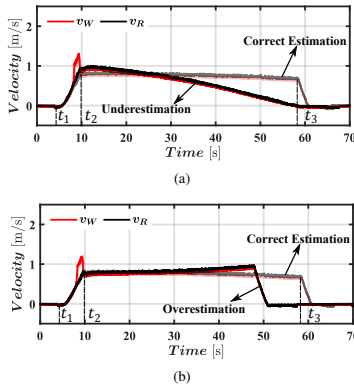
Fig. 17: Experimental results. Inertia emulator sensitivity to friction coefficient $\hat{B}$ using Adhesion Torque Observer method. Wheel and roller velocities for the case of (a) underestimated and (b) overestimated $\hat{B}$.

paper is the emulation of inertia, which is required for proper evaluation of anti-slip control. Two different approaches have been proposed. The first method uses a Disturbance Observer which emulates the train inertia irrespective of the test bench properties. The method with Adhesion Torque Observer produces torque command for the roller which reflects the desired properties of the train. This accounts for the traction force that gets transferred from wheel onto the roller including the inertia and friction of test bench. Thus the inertia emulation provides a good replica of the real train model. The concepts developed were first simulated and further verified experimentally in a roller-rig test. Train inertia emulation will require precise knowledge of roller-rig test bench inertia and friction. Roller-rig inertia can be estimated with good accuracy from the dimensions and material of the wheels. Friction estimation from system parameters is far more problematic, mainly due to the use of belts in the mechanical transmission. Therefore its adjustment has been performed experimentally. It has been shown that without proper adjustment of roller-rig parameters, inertia emulation is not reliable. Without proper inertia emulation, train acceleration and consequently the dynamic behavior of anti-slip control may be subjected to large deviations with respect to read world behavior, eventually compromising the validation process.

REFERENCES

[1] P. Pichlík, "Strategy of railway traction vehicles wheel slip control," *Czech Technical University, Prague*, 2018.
[2] F. Trimpe and C. Salander, "Wheel–rail adhesion during torsional vibration of driven railway wheelsets," *Vehicle System Dynamics*, vol. 59, no. 5, pp. 785–799, 2021.
[3] S. Iwnicki, *Handbook of railway vehicle dynamics*. CRC press, 2006.
[4] A. Jaschinski, "On the application of similarity laws to a scaled railway bogie model." 1991.
[5] R. Stock, D. T. Eadie, D. Elvidge, and K. Oldknow, "Influencing rolling contact fatigue through top of rail friction modifier application–a full scale wheel–rail test rig study," *Wear*, vol. 271, no. 1-2, pp. 134–142, 2011.
[6] R. Conti, E. Meli, and A. Ridolfi, "A full-scale roller-rig for railway vehicles: multibody modelling and hardware in the loop architecture," *Multibody System Dynamics*, vol. 37, no. 1, pp. 69–93, 2016.
[7] T. Ishrat, "Slip control for trains using induction motor drive," Ph.D. dissertation, Queensland University of Technology, 2020.
[8] X. Fang, S. Lin, Z. Yang, F. Lin, H. Sun, and L. Hu, "Adhesion control strategy based on the wheel-rail adhesion state observation for high-speed trains," *Electronics*, vol. 7, no. 5, 2018.
[9] S. Z. Meymand, M. J. Craft, and M. Ahmadian, "On the application of roller rigs for studying rail vehicle systems," in *Rail Transportation Division Conference*, vol. 56116. American Society of Mechanical Engineers, 2013, p. V001T01A015.
[10] A. F. Abouzeid, J. M. Guerrero, I. Muniategui, A. Endemaño, D. Ortega, and F. Briz, "Torque dynamics enhancement of railway traction drives using scalar control," in *2021 IEEE International Electric Machines & Drives Conference (IEMDC)*. IEEE, 2021, pp. 1–6.
[11] A. Fathy Abouzeid, J. M. Guerrero, A. Endemaño, I. Muniategui, D. Ortega, I. Larrazabal, and F. Briz, "Control strategies for induction motors in railway traction applications," *Energies*, vol. 13, no. 3, p. 700, 2020.
[12] T. Mei, J. Yu, and D. Wilson, "A mechatronic approach for anti-slip control in railway traction," *IFAC Proceedings Volumes*, vol. 41, no. 2, pp. 8275–8280, 2008.
[13] M. Fleischer, R. W. de Doncker, and D. Abel, "Traction control for railway vehicles," *Institut für Stromrichtertechnik und Elektrische Antriebe*, 2019.
[14] S. Senini, F. Flinders, and W. Oghanna, "Dynamic simulation of wheel-rail interaction for locomotive traction studies," in *Proceedings of the 1993 IEEE/ASME Joint Railroad Conference*. IEEE, 1993, pp. 27–34.
[15] K. Kondo, "Anti-slip control technologies for the railway vehicle traction," in *2012 IEEE Vehicle Power and Propulsion Conference*. IEEE, 2012, pp. 1306–1311.
[16] P. Pichlík and J. Zdeněk, "Overview of slip control methods used in locomotives," *Transactions on Electrical Engineering*, vol. 3, no. 2, pp. 38–43, 2014.
[17] A. Jaschinski, H. Chollet, S. Iwnicki, A. Wickens, and J. Würzen, "The application of roller rigs to railway vehicle dynamics," *Vehicle System Dynamics*, vol. 31, no. 5-6, pp. 345–392, 1999.
[18] M. Marshall, R. Lewis, R. Dwyer-Joyce, U. Olofsson, and S. Björklund, "Experimental characterization of wheel-rail contact patch evolution," 2006.
[19] A. Rovira, A. Roda, M. Marshall, H. Brunskill, and R. Lewis, "Experimental and numerical modelling of wheel–rail contact and wear," *Wear*, vol. 271, no. 5-6, pp. 911–924, 2011.
[20] S. H. Park, J. S. Kim, J. J. Choi, and H.-O. Yamazaki, "Modeling and control of adhesion force in railway rolling stocks," *IEEE Control Systems Magazine*, vol. 28, no. 5, pp. 44–58, 2008.
[21] J. M. Guerrero, C. Lumbreras, D. D. Reigosa, P. Garcia, and F. Briz, "Control and emulation of small wind turbines using torque estimators," *IEEE Transactions on industry applications*, vol. 53, no. 5, pp. 4863–4876, 2017.
[22] TEXAS INSTRUMENTS, TMDSCNCD28335 controlCARD. [Online]. Available: https://www.ti.com/tool/TMDSCNCD28335
[23] M. Fischer, F. Szekely, M. Frea, and S. Jennek, "Impact of slip at low adhesion conditions caused by various contaminants," *EuroBrake 2019 - Rail Wheel Contact and Adhesion*, May, 2019.

Nihal Vishnu Vantagodi (M'00) received the B.E. in Electrical and Electronics Engineering in 2017 from PES Institute of Technology, India and Erasmus Mundus joint M.S. degree in Sustainable Transportation and Electrical Power Systems from Sapienza University of Rome, Italy; University of Nottingham, UK and University of Oviedo, Spain in 2021. He is associated with AECP research group of Department of Electrical, Computer and Systems Engineering, University of Oviedo from 2021. His research interests include ac drives and traction control.

Ahmed Fathy Abouzeid (M'19) received the B.S and M.S. degrees in Electrical Engineering from Port Said University, Port Said, Egypt, in 2012 and 2017, respectively. He is currently pursuing his Ph.D. Degree at the Department of Electrical, Electronic and Computer Engineering, University of Oviedo, Gijón, Spain. From September to December 2021, he was a Visiting Researcher at Deutsche Bahn (DB) Systemtechnik GmbH, Minden, Germany. Since 2013, he joined the Department of Electrical Engineering, Port Said University, Egypt, as a researcher. Currently, he is on leave with the same department as an assistant lecturer. His research interests include power converters and ac drives, electric traction, and renewable energy systems.

Aitor Endemaño-Isasi received the Industrial Technical Engineering Degree (Electronic Design speciality) and the Industrial Automatics and Electronics Engineering Degree, from the University of Mondragon, Mondragon, Spain, in 1997 and 2000 respectively, and the PhD from Heriot-Watt University, Edinburgh, Scotland, UK, in 2003. In 2003 he joined Traction department at Ingeteam Power Technology (formerly TEAM), Zamudio, Spain, where since then he has been a Control and Regulation Engineer, involved in several traction control design projects for trams, locomotives and EMU-s. His current research interests include power converter and advanced control drives, modulation techniques, railway research issues such as AC catenary stability and mechanical vibrations in the drive-train.

Juan M. Guerrero (S'00–A'01–M'04–SM'21) received the M.E. degree in industrial engineering and the Ph.D. Degree in Electrical and Electronic Engineering from the University of Oviedo, Gijón, Spain, in 1998 and 2003, respectively. Since 1999, he has occupied different teaching and research positions with the Department of Electrical, Computer and Systems Engineering, University of Oviedo, where he is currently an Associate Professor. From February to October 2002, he was a Visiting Scholar at the University of Wisconsin, Madison. From June to December 2007, he was a Visiting Professor at the Tennessee Technological University, Cookeville. His research interests include control of electric drives and power converters, electric traction, and renewable energy generation.

Iban Vicente-Makazaga graduated in electrical engineering from University of Mondragon, Mondragon, Spain, in 2003 and the M.S. and the Ph.D. degrees from the University of Manchester, UK, in 2004 and 2009 respectively. He joined Ingeteam Power Technology (formerly TEAM), Zamudio, Spain, where he works as a Control and Regulation Engineer involved in railway traction control for trams, locomotives and EMU-s. His current research interests include power converter and advanced control drives, modulation techniques, machine parameters and speed estimation techniques as well railway research issues such as AC catenary stability and mechanical vibrations in the drive-train.

Fernando Briz (A'96–M'99–SM'06) (Senior Member, IEEE) received the M.S. and Ph.D. degrees from the University of Oviedo, Gijón, Spain, in 1990 and 1996, respectively. He is currently a Full Professor with the Department of Electrical, Computer and Systems Engineering, University of Oviedo. His research interests include electronic power converters and ac drives, power systems, machine monitoring and diagnostics, and digital signal processing. Dr. Briz was the recipient of the IEEE TRANSACTIONS ON INDUSTRY APPLICATIONS Award and nine IEEE Industry Applications Society Conference and IEEE Energy Conversion Congress and Exposition prize paper awards. He is currently Chair of the Industrial Power Conversion System Department (IPCSD) of the IAS and Deputy Editor in Chief and member of the Steering Committee of IEEE JOURNAL OF EMERGING AND SELECTED TOPICS IN POWER ELECTRONICS (JESTPE). He is also member of the Executive Board of ECCE, and Past Chair of the Industrial Drives Committee of IPCSD. He has served in scientific committees and as Vice Chair or Technical Program Chair of several conferences, including ECCE, IEMDC, ICEM, ICEMS, and SLED and is an Associate Editor of IAS Transactions.

Iker Muniategui-Aspiazu received the Industrial Technical Engineering Degree (Electronic Design speciality) and the Industrial Automatics and Electronics Engineering Degree, from the University of Mondragon, Mondragon, Spain, in 2004 and 2007 respectively. In September 2006, he joined Ingeteam Power Technology (formerly TEAM), Zamudio, Spain, where he worked as a Control and Regulation Engineer, and he is currently Control and Regulation manager of Traction department. His current research interests include power converter and advanced control drives, modulation techniques, railway research issues such as AC catenary stability and mechanical vibrations in the drive-train.

B.1.2 Co-Simulation-Based Verification of Torsional Vibration Protection of Electric-Driven Railway Vehicle Wheelsets

vibration

MDPI

Article

Co-Simulation-Based Verification of Torsional Vibration Protection of Electric-Driven Railway Vehicle Wheelsets

Ahmed Fathy Abouzeid [1,2,†,‡] [iD]**, Fritz Felix Trimpe** [3,*,‡] [iD]**, Sönke Lück** [4,‡] [iD]**, Markus Traupe** [3]**,**
Juan Manuel Guerrero [1] [iD] **and Fernando Briz** [1] [iD]

1 Electrical, Electronic, Computers and Systems Engineering, University of Oviedo, 3204 Oviedo, Spain
2 Department of Electrical Engineering, Port Said University, Port Said 42526, Egypt
3 DB Systemtechnik GmbH, 32423 Minden, Germany
4 Institute of System Dynamics and Mechatronics, University of Applied Sciences Bielefeld,
33619 Bielefeld, Germany
* Correspondence: f.trimpe@gmx.de or fritz-felix.trimpe@deutschebahn.com
† Current address: Electrical, Electronic, Computers and Systems Engineering, University of Oviedo,
3204 Oviedo, Spain.
‡ These authors contributed equally to this work.

Abstract: Torsional vibration is an oscillation phenomenon occurring at driven railway vehicle wheelsets. As the resulting dynamic stresses can be significantly larger than the maximum static motor torque, axle and press fit are at risk of failure. To prevent dangerous vibration events and with these, press fit and axle from failure, traction drive manufactures nowadays used to implement vibration suppression algorithms in drive controls. In this paper, the effectiveness of such suppression algorithms is analyzed. Furthermore, as a pilot survey, we analyze to what extend traction controls influence the excitation of torsional vibration.

Keywords: torsional vibration; railway drive train; wheel–rail contact; slip control; traction control

1. Introduction

The oscillation phenomenon torsional vibration has been known since the 1980s when the first three-phase drives with traction controls for a high force utilisation were developed. Torsional vibration was found to be a self-excited oscillation of the wheelset, which cannot actively be damped by an appropriately designed traction control. Therefore, in the following decades, torsional vibration was tolerated as no further safety concerns appeared. This changed in 2010, when wheel twists were found on traction vehicles [1]. The cause of these twists was investigated in measurements, and torsional vibration was found to result in exceeding the maximum transferable torque between wheel and axle.

Subsequently, research was undertaken to predict the highest dynamic torque resulting from torsional vibration. Railway vehicle manufacturers wanted to consider it in the design phase and enable appropriate dimensioning of a new wheelset. No suitable prediction method could be developed. However, several approaches have been published to simulate torsional vibration. Some of these models aim to predict maximum dynamic torque as described before whereas others are used to investigate the vibration phenomenon itself. A summary of these approaches is given in the following.

Yu and Breuer [2] and Weinhardt [3] tried to predict the maximum dynamic torque with empirical or semi-empirical methods. These models could not be transferred to other traction drive-wheelset configurations but to those they are based on. In a similar way, Szolc [4], Schneider [5] and Saur [6–8] used analytical simulation methods to predict maximum dynamic torque. However for these models no validation on measurements is documented.

Further investigations on the physics of torsional vibration have been performed by Liu et al. [9], Xu et al. [10], Konowrocki and Szolc [4], Meierhofer et al. [11] and

---

Fridrichovsky and Sulc [12]. First investigations on the physics of torsional vibrations have already been documented by Körner [13], Schwartz [14] and Buscher [15] in the 1980s. These investigations lack to provide dependencies between the amplitude of torsional vibration and the physical conditions under which they appear.

Finally, such dependencies were discovered in measurements documented in a study by Trimpe and Salander [16]. These dependencies are further investigated in simulations published in Trimpe et al. [17]. These simulations consider the traction control as a relevant influence for the development of torsional vibration. As the traction control used in Trimpe et al. [17] does not feature any torsional vibration suppression methods as documented in Abouzeid et al. [18], the influence of such suppression methods is investigated in this article. Basing on this, the novelty of the article at hand is firstly to introduce a simulation procedure enabling realistic simulation of torsional vibration. Here, realistic simulation especially means the implementation of vibration excitation by changing wheel–rail conditions. Secondly, the article at hand shall validate the effectiveness of a torsional vibration protection implementation.

2. System Description

In this section, a system overview for a high-performance locomotive is presented. The main circuit elements are given in Figure 1 based on the energy flow from the electrical input (overhead line) to the mechanical output (drive train) of the locomotive.

Firstly, the pantograph, mounted on top of the locomotive, transfers the electrical energy from the AC overhead line to the main transformer. The AC transmission can be 25 kV/50 Hz or 15 kV/16.7 Hz based on the country, however, cross-border locomotives are equipped with generalized transformers that meet each country's standards. The main transformer consists of a primary high-voltage winding with multiple secondary windings supplying both the traction converters and the auxiliary inverters for on-board purposes, like heating/cooling, lighting, etc.

Then, the traction converter transforms the single-phase input, connected to the main transformer winding, into the three-phase modulated output connected to the traction motor. The traction converter includes the following elements:

1.   the four-quadrant chopper (4QC),
2.   the DC-link,
3.   the switched inverter.

The 4QC is used to provide and regulate the DC voltage of the DC-link. Meanwhile, the DC-link capacitor is used to smooth the effects of power unbalances between 4QC and the inverter. A series resonant circuit (2F) is included to filter the second harmonic content of the line frequency generated by the 4QC due to the single-phase AC input. In addition, a chopper module is added to the DC-link to prevent the capacitor from overvoltages.

After that, the PWM inverter inverts the regulated DC-link voltage to a three-phase voltage with variable amplitude and frequency to feed the traction motor. This function is achieved by the electrical drive control unit which regulates the traction force according to the locomotives' driver commands. Induction machines (IMs) are commonly used in traction systems for railways due to their robustness with less maintenance requirements, their independency on rare-earth materials (e.g., magnets), and the possibility of feeding more than one motor from a single inverter [19].

Finally, the electromagnetic torque developed by the traction motor (IM) is transferred to the wheels through the mechanical drive train. This transmitted torque provides tangential (traction) force which depends on the wheel–rail condition.
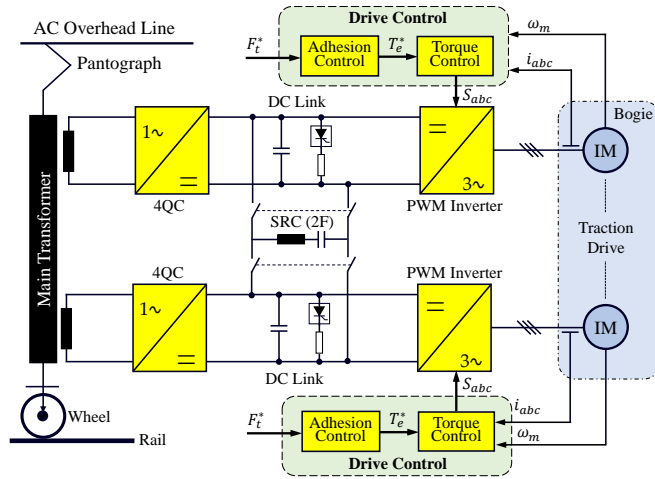
Figure 1. Main circuit elements of a high-performance locomotive [20].

2.1. Electric Drive

High performance locomotives operate with individual axle control i.e., each wheelset is fed from an independent PWM inverter (see Figure 1). Thanks to this, high utilization of wheel–rail adhesion can be achieved. The electric drive control is responsible for achieving the traction force F_t^* demanded by the locomotive driver which consists of two cascaded control loops:

1. **Adhesion control**. This control loop aims to adapt the wheel–rail adhesion level (i.e., the tractive/breaking force) besides preventing the wheel from slipping during acceleration/deceleration of the locomotive or due to changing of the wheel–rail contact conditions caused by slippery rails. More details will be discussed in Section 3.1.
2. **Torque control**. A precise, high dynamic torque control is needed to assure that the machines' actual torque follows the demanded torque T_e^* by the outer adhesion controller. Modern traction drives are equipped with different control strategies, which can change dynamically based on the operating speed [18]. Mainly, vector control schemes are used to decouple the torque and flux components of the machine's current, which allows to fully exploit machine torque capability without surpassing machine or power converter current limits. Typically rotor flux field-oriented control (RFOC) tuned with a high bandwidth is used (see Figure 2). In this scheme, the *d*-axis of the rotating reference frame is aligned with the rotor flux, i.e., $\hat{\lambda}_{dqr}^e = \hat{\lambda}_{dr}^e = \hat{\lambda}_r$, the stator voltage and the stator flux equations become (1) and (2), where ω_e is the angular speed in electrical units of the synchronous reference.

$$v_{dqs}^e = \hat{R}_s' i_{dqs}^e + p\hat{\lambda}_{dqs}^e + j\omega_e \hat{\lambda}_{dqs}^e \tag{1}$$

$$\hat{\lambda}_{dqs}^e = \frac{\hat{L}_m}{\hat{L}_r}\hat{\lambda}_{dqr}^e + \hat{L}_{\sigma s} i_{dqs}^e \tag{2}$$

$$\omega_e = \omega_r + \hat{\omega}_{sl}; \text{ where } \hat{\omega}_{sl} = \frac{\hat{L}_m}{\hat{\tau}_r |\hat{\lambda}_r|} i_{qs}^e \tag{3}$$

Thus, the electromagnetic torque T_e can be represented by (4) in terms of q-axis of stator current and the estimated rotor flux.

$$T_e = \frac{3}{2} P \frac{\hat{L}_m}{\hat{L}_r} |\hat{\lambda}_r| i_{qs}^e \tag{4}$$
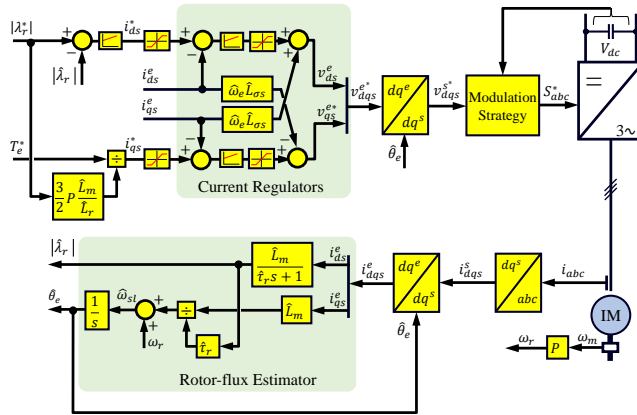
Figure 2. Rotor field-oriented control (RFOC) scheme.

The main concerns regarding RFOC methods are their sensitivity to rotor resistance, and the degradation of current regulator performance when the inverter operates near its voltage limit. Alternatively, the stator-flux orientation can be used to overcome these limitations, especially at high speeds. Direct Self-Control (DSC) was proposed for high power drives operating with low switching to fundamental frequency ratio (see Figure 3) [21]. Three hysteresis controllers determine the voltage applied to the machine by comparing the command flux magnitude and the estimated one for each phase. A two-level hysteresis torque controller determines the amount of zero voltage vector to be used. Moreover, the switching frequency is controlled by adapting the torque controller hysteresis band using either proportional or proportional-integral (P/PI) controller. DSC produces a symmetrical hexagonal stator flux trajectory to the origin increasing the robustness against input voltage disturbances. From ≈30% to ≈85% of base speed, DSC offers a high dynamic response and reduced switching losses, but at the price of a high current ripple. At high speeds (>≈85% of base speed), zero voltage vectors are not selected anymore, DSC providing, therefore, a natural transition into overmodulation and eventually into six-step [22]. Below ≈30% of the base speed there is a degradation of the control performance, a detailed description and potential remedial actions can be found in [23,24].

2.2. Mechanical Model of the Drive Train

The mechanical components of the drive train are implemented in a multibody simulation (MBS) model. Figure 4 shows the quarter model of a traction locomotive which is used for the investigations [17]. The mechanical model contains the masses and inertias of a hollow shaft drive train consisting of a rotor, the gear wheels, the coupling, the hollow shaft, the axle and both wheels. The torsional stiffness and damping of the gear, the coupling, the hollow shaft and the axle are considered. Also the single-stage gear is included in the model. Figure 4 gives an overview of the described system. The traction motor drives the gear wheel which is attached onto the cardan hollow shaft. The hollow

shaft transmits the torque by its coupling onto the directly driven wheel. Via the wheelset axle the directly driven wheel drives the indirectly driven wheel. Numerical values for the torsional stiffness and torsional damping as well as the moments of inertia used for the MBS model are obtained from [14].
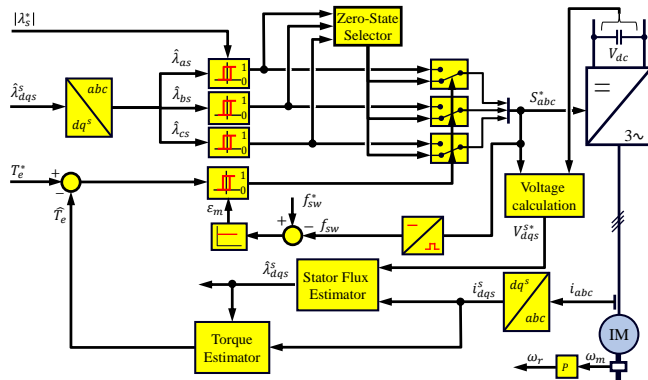
Figure 3. Direct Self-Control (DSC) scheme.
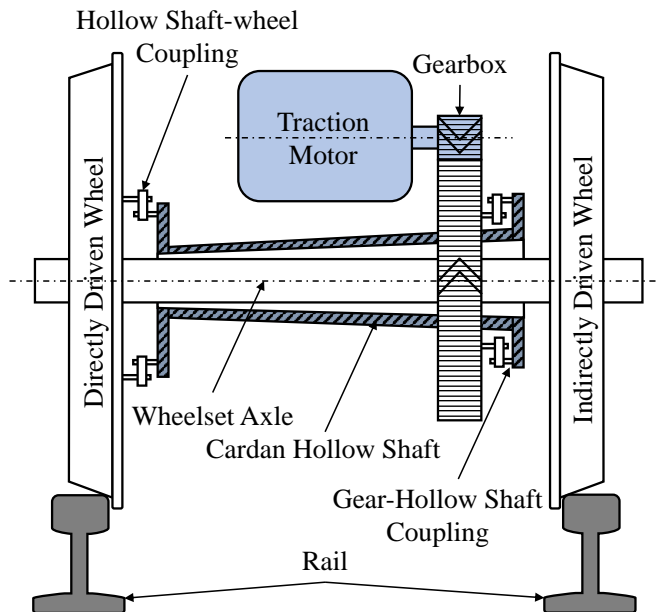
Figure 4. Structure of the mechanical model: mechanical elements of the traction drive train [25].

2.2.1. Simulation Model

The simulation model was built up in the MBS software Simpack as depicted in Figure 5. The MBS model is linked to the drive control via co-simulation. The model contains the torque transmitting components of the mechanical drive train, the wheel–rail contact, as well as the friction forces and inertia forces resulting from the train set. The whole model of the drive train can follow the track in longitudinal direction and can move freely in vertical direction. The individual bodies have rotational degrees of freedom around their lateral axis.
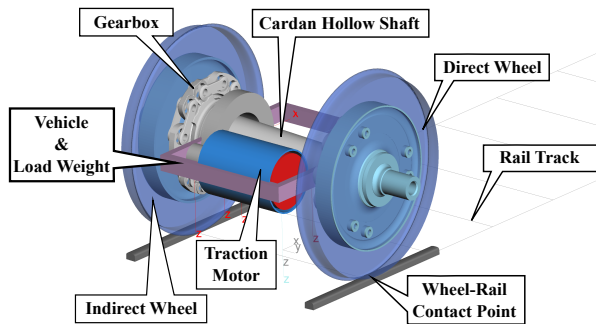
Figure 5. MBS model of the drivetrain with wheel–rail interaction.

For the calculation of the tangential forces in the wheel–rail contact, the analytical approach of Polach is used [26]. This approach was developed to achieve an improved fit of the adhesion characteristics in the simulation with measured data. The tangential force F calculated in Polach's formalism depends on the wheel load Q, the wheel–rail adhesion coefficient μ and the weighting factors k_A and k_S.

$$F = \frac{2Q\mu}{\pi} \left(\frac{k_A \epsilon}{1 + (k_A \epsilon)^2} + \arctan(k_A \epsilon) \right), \quad k_S \leq k_A \leq 1 \tag{5}$$

The gradient of tangential stress in the adhesion area ϵ is depending on the relative (slip) velocity v_s between wheel and rail and the contact ellipse in the wheel–rail contact.

$$\epsilon = \frac{2}{3} \frac{C\pi a^2 b}{Q\mu} v_s \tag{6}$$

The decrease of the wheel–rail adhesion coefficient for higher relative velocities is realized by a relative velocity v_s dependent friction value. This is highly relevant for the simulation of torsional vibrations. The slope of the adhesion coefficient above its maximum can be determined by the parameters A and B. Figure 6 shows the adhesion characteristics as a function of the driving speed.

$$\mu = \mu_0 \cdot \left((1 - A) \cdot \exp^{-B \cdot |v_s|} + A \right) \tag{7}$$

The traction forces are opposed by the friction and inertia forces of the train set. These opposing forces are represented in the MBS model by the following equations taken from the literature [17].

Rolling Resistance:

$$F_{roll} = M_{train} \cdot g \cdot k_{roll}, \quad k_{roll} = 1.5 \cdot 10^{(-3)} \tag{8}$$

206

Air Resistance:

$$F_{air} = M_{train} \cdot g \cdot k_{air}, \quad k_{air} = 0.25 \cdot 10^{(-3)} \tag{9}$$
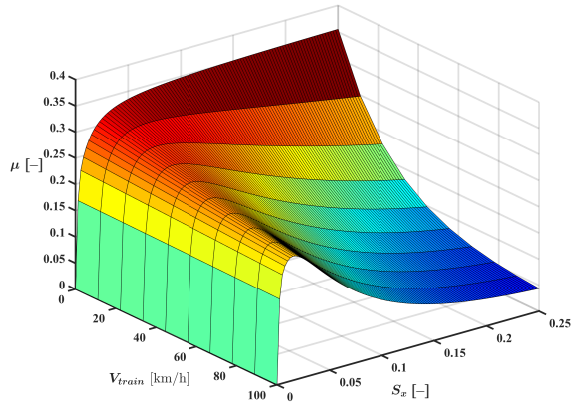
Figure 6. Adhesion characteristics as a function of the driving speed V_{train} and slip S_x [26].

2.2.2. Linear Analysis

A linear eigenvalue analysis was carried out to investigate the dynamics of the drive train. The wheel–rail contact forces are not taken into account in the analysis. The eigenmodes and the eigenfrequencies of the six-mass model were calculated (see Figure 7).

Especially, two eigenmodes are important with regard to the assessment of the drive train dynamics. For mode 2, a chatter oscillation occurs where the whole wheelset is oscillating in counter phase to rotor and gear. As the resulting oscillation amplitudes of the wheelset have a similar magnitude as the oscillation amplitudes of the rotor, chatter oscillations are detectable by the traction motor sensors. As a result, they can actively be damped by an appropriate design of the traction control [14,25].

This is different in mode 3, which is the relevant mode of torsional vibration. Here, both wheels of a wheelset oscillate in counter phase and at the same time, oscillation amplitude of the rotor are close to zero (see Figure 7). As oscillation amplitudes can hardly be detected at the rotor, torsional vibration of the wheelset cannot be actively influenced by the drive control. If wheelset torsional vibrations occur, further measures must be taken. For example, the drive torque of the motor must be reduced or the wheels must be braked.
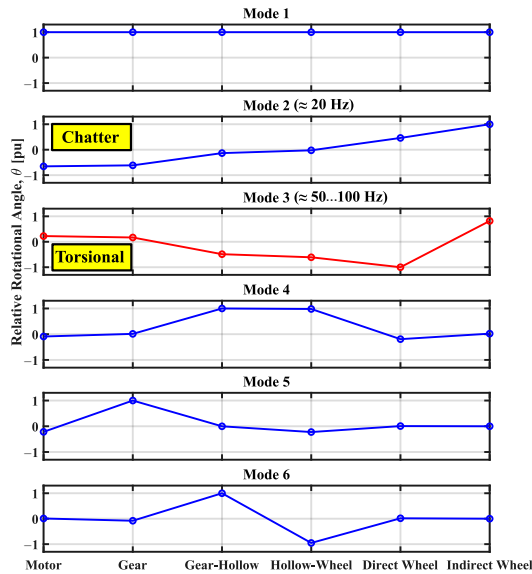
Figure 7. Mode shapes of the six-inertia model. The magnitude of the relative rotational angle is normalized based on the peak value at each mode.

3. Slip Control and Torsional Vibration Protection

3.1. Overview of Slip Control

Anti-slip control is needed in railway traction drives to reduce the wear of the wheel–rail contact surface, increase traction/breaking capability, and increase passenger comfort and safety. Commonly, the torque commanded by the train driver T_e^{ref} is sent to the traction motor control unit (TCU) meanwhile the slip control is running in parallel without any action during normal operation. Once slippage is detected, the slip control becomes active and the output torque correction signal T_e^{α} is sent to the TCU (see Figure 8). Generally, slip controller can be classified into:

- Traditional slip controllers, also known as re-adhesion controllers. They are one of the simplest and stablest solutions to limit the wheel–rail slippage to a predefined value [27–29]. The slip velocity reference can be kept at a constant value or varied with the train speed based on previous field-tests and train' driver experience [30].
- Advanced slip controllers aimed to operate at maximum possible adhesion level [15,31–36]. Due to the unpredictability of the adhesion-slip phenomena, finding the optimal slip velocity increases the complexity of the control and its real time implementation becomes more challenging.

In this article, slip velocity control is used. From the measured motor speed signal ω_m, the wheel velocity v_w and acceleration signals α_w can be obtained (see speed signal processing block in Figure 8). Slip velocity v_{slip} is obtained by subtracting wheel linear velocity v_w from train velocity v_{train}. Slip speed is compared to a preset value v_{slip}^*, the error signal feeding a conventional PI regulator. The correction signal coming out from the slip velocity controller could be the commanded torque directly. However, to ensure passengers comfort, an additional acceleration control is employed to control the acceleration/jerk of the wheel (see Figure 8). Additionally, adaptation of slip velocity Δv_{slip}^* is added to damp

208

vibrations excited in the drive train wheelset through vibration detection and protection block seen in Figure 8. Vibration suppression will be discussed in the following subsection.
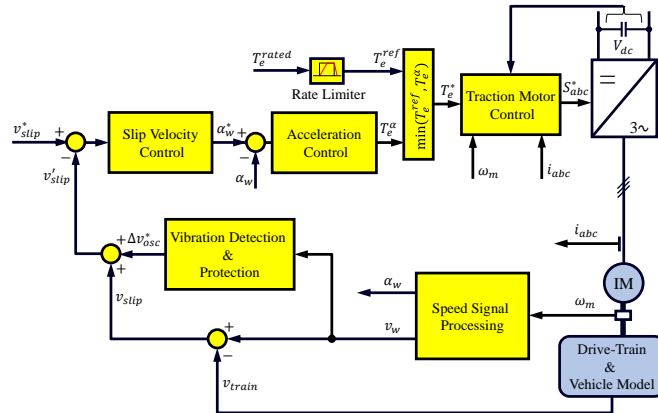
Figure 8. Overall slip control scheme with torsional vibration protection.

3.2. Torsional Vibration Control

Torsional vibrations occur in the drive trains axle due to changing of the adhesion conditions (from high to low values $P_1 \rightarrow P_3$ or vice versa), track irregularities, and/or operating at high slip velocities (i.e., unstable region in Figure 9a). The envelope magnitude of the torque vibration component, which is referred to dynamic torque $|T_{dynamic}|$, is proportional to the slope of the adhesion characteristic curve $\frac{\delta\mu}{\delta V_{slip}}$ in the unstable region (i.e., $\frac{\delta\mu_{P_1}}{\delta V_{slip_{P_1}}} > \frac{\delta\mu_{P_2}}{\delta V_{slip_{P_2}}} > \frac{\delta\mu_{P_3}}{\delta V_{slip_{P_3}}}$ in Figure 9a) [5].

To mitigate torsional vibrations in traction drive trains, passive readhesion controller is usually used (see vibration detection and protection block in Figure 8). The readhesion controller reduces the slip velocity to protect the wheelset axle from excessive vibration events. This can be achieved by extracting the vibration component from the speed sensor signal of the IM ω_m using a band-pass filter. Then the envelope of the extracted vibration $Env(|v_{osc}|)$ is controlled to avoid surpassing a predefined limit $|v_{osc}|$ using a conventional PI regulator (see Figure 9b). The output signal Δv_{osc}^* reduces the slip velocity command once the vibration envelope exceeds the defined limit bringing the operating point back into the stable region (e.g., $P_1' \rightarrow P_1$ in Figure 9a). Consequently, the reference torque T_e^* is reduced during the vibration mitigation process, T_e^* being returned to its original value after vibration events clearance. In this paper, passive readhesion control is used to limit the slip velocity, being aware of its adverse impact on traction. Alternatively, advanced control techniques can be employed to actively damp the torsional vibrations in the traction drive, but at the cost of higher complexity and parameter dependency [20,25].

(a)

(b)
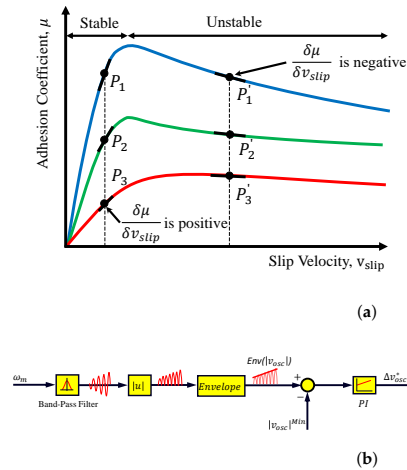
Figure 9. Torsional vibrations occurrence and mitigation method: (**a**) migration of operating point from stable (micro-slip) to unstable (macro-slip) regions, and (**b**) Vibration protection control scheme.

4. Simulation Results and Experimental Verification

In this section, the entire traction drive system and control are modeled and simulated using the MATLAB-SIMPACK co-simulation tool. Furthermore, changes in the wheel–rail conditions with activated and deactivated torsional vibration protection will be analyzed. Finally, simulation results will be compared with measured data already published in [16].

Based on the dependencies between maximum dynamic torque and wheel–rail conditions documented in [16,17], the wheel–rail adhesion coefficient was modified during the simulation at hand during an acceleration process. The introduced co-simulation tool (see Figure 10) was used.

The simulation batch starts by defining the number of simulations to be carried out. This depends on the ranges of train speeds and wheel–rail conditions to be tested. Variables to be set for each simulation include train velocity, adhesion coefficient and the travelling distance where the adhesion change is applied for both wheels. The slip and vibration protection control algorithms are executed via MATLAB/SIMULINK toolbox where the torque command is sent to the drive train and vehicle model implemented in the SIMPACK environment. The train velocity and motor speed measurements are fed back to SIMULINK model where the co-simulation communication is done via internet protocol (IP-Server 2000). Finally, the output data (dynamic torque, slip velocity, etc.) are stored in a vector table then the same process is repeated for the rest of simulation steps.
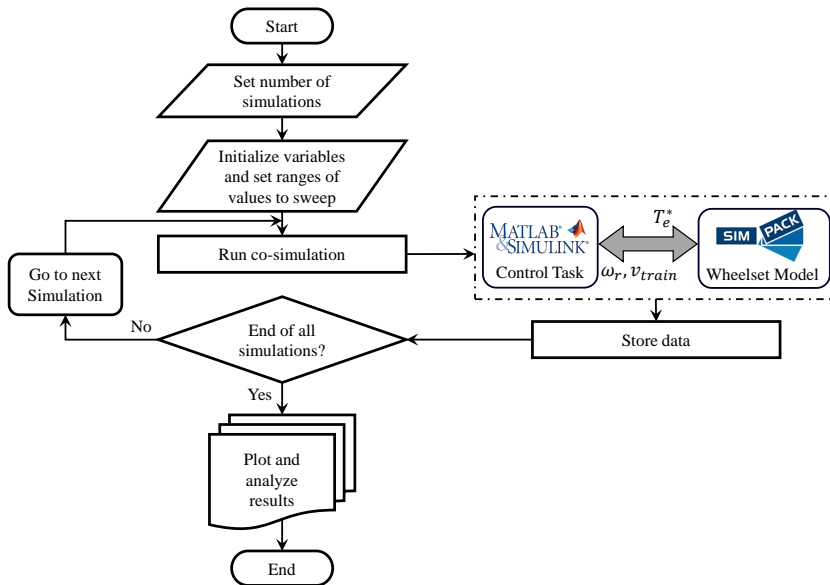
Figure 10. Flow chart for parametric sweep analyzes of torsional vibrations in mechanical drives using MATLAB-SIMPACK co-simulation tool.

Three different wheel–rail condition scenarios for both wheels were conducted to investigate effectiveness of torsional vibration protection of electric driven wheelsets (see Figure 11). $x_{1...4}$ indicates the distance at which the change of the adhesion value μ is applied (starting from 10 to 400 m with separation of 10 m each step). Additionally, the simulations carried out are repeated (traction and electrical braking) for different train velocities (from 0 to 200 km/h).
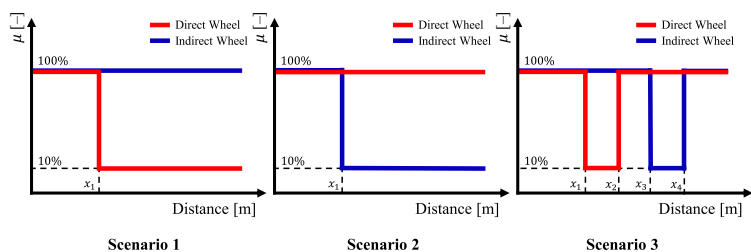
Figure 11. Wheel-rail contact friction configuration scenarios for SIMPACK model.

Figure 12 shows dynamic torque plotted against slip velocity where all simulation results for different adhesion scenarios (mentioned in Figure 11) are combined and plotted in the same graph (i.e., Figure 12). It is observed that without vibration protection (see left subplot in Figure 12), the vibration magnitude is increasing linearly with slip velocity up to the maximum value ($T_{dyn} \approx 180$ kNm at $v_{slip} \approx 2.5$ m/s) for traction mode. It is noted that though the maximum dynamic torque is found to be less ($T_{dyn} \approx 160$ kNm at $v_{slip} \approx 2$ m/s) in braking mode, still the trend is the same as for traction mode.

Enabling vibration protection control limits the dynamic torque magnitude (see right subplot in Figure 12). The maximum dynamic torque achieved is $T_{dyn} \approx$ 72 kNm at $v_{slip} \approx$ 0.7 m/s for traction mode and $T_{dyn} \approx$ 51 kNm at $v_{slip} \approx$ 0.6 m/s for braking mode.
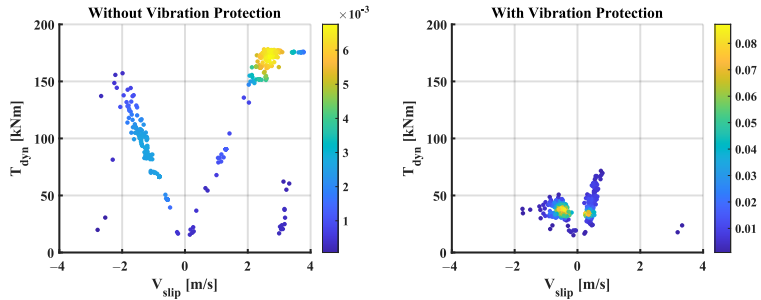
Figure 12. Simulation results. Dynamic torque vs. slip velocity with and without vibration protection during traction and braking, provoked by different adhesion scenarios.

Given that the adhesion characteristic is highly stochastic, it is striking that data points resulting from simulations show good conformity with data points resulting from measurements. Measurements have been conducted with a similar drive train and traction control as the one implemented in the simulation model at hand. Measurement conductions, as well as measurement data analysis have been published in [16]. Furthermore, for both, simulations and measurements, maximum dynamic torque increases linearly by increasing slip velocity. Although in Figure 13 this linearity appears more accurate for simulations than for measurements, conformity can be considered good as deviations in the accuracy of the linearity can be traced back to the limitations of the real test execution. After exceeding a certain slip velocity $v_{slip,crit} \approx$ 0.5 m/s data points are not increasing linearly but rather decreasing. This decreasing process of data points conforms with observations documented in other publications [2,37]. Most likely, for further increasing slip velocities above $v_{slip,crit}$, dynamic processes vanish and the wheelset transitions into global slipping.
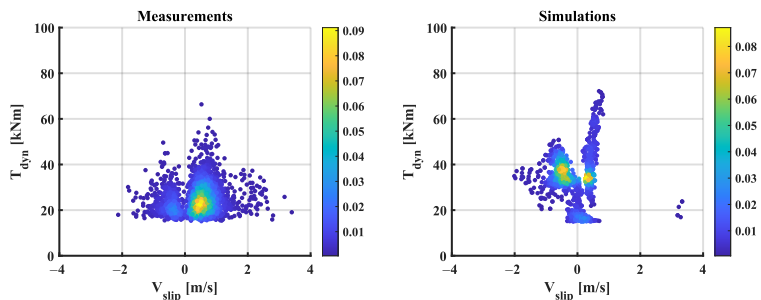
Figure 13. Comparison between Simulation and Measurement results. Dynamic torque vs. slip velocity during traction and braking process, provoked by different adhesion scenarios.

5. Conclusions and Outlook

In this article, the implementation of a complete traction drive system including electrical components, control strategies and mechanical drive train is presented. The implementation is realized by a co-simulation tool and this tool is used to simulate torsional vibration. In simulations, torsional vibration is provoked by changes of the wheel–rail conditions. Furthermore, the effectiveness of a torsional vibration detection is investigated.

For this, a torsional vibration protection is implemented as part of the traction control. Simulations are conducted with activated and deactivated vibration protection.

As a first step, the functionality of the simulation model implementation has successfully been verified on measurement results. This includes coincidence of maximum dynamic torque of simulations and measurements as well as the linear dependency of dynamic torque and slip (find further investigations on this dependency in [37]).

As a second step, simulations were performed to investigate the effectiveness of a torsional vibration protection. The received results show that the implemented vibration protection helps to suppress torsional vibration and therefore, to prevent the wheelset from high dynamic torque. As torsional vibration is suppressed indirectly by dynamic torque reductions, the vibration detection requires reliable wheelset rotation speed data. Here, linear analysis shows that rotation speed sensors of the traction motors may not provide wheel rotation speed data of sufficient quality.

Consequently, the presented investigations and results verify that suppressing torsional vibration indirectly by dynamically reducing the traction torque is an effective way to prevent a railway wheelset from high dynamic torque. Therefore, the implementation of an effective vibration protection is capable of reducing the maximum torsional loads applied to wheelset axle and press fit by a significant amount. With this, a vibration protection contributes to the safety and reliability of rail traffic.

Moreover, with the introduced model, torsional vibration has been successfully simulated in accordance with track measurements. Basing on this achievement, the simulation model shall be applied to other vehicles in order to validate prediction of maximum dynamic torque values. The capability of predicting maximum dynamic torque values is needed by railway vehicle manufacturers, to enable a more efficient development of new wheelsets. In the same way, such simulations can help manufacturers to study evidence of the effectiveness of their torsional oscillation protection implementations.

References

1. Fridrichovskỳ, T.; Šulc, B. Occurrence of Torsional Oscillations in Railway Wheelsets. *WSEAS Trans. Syst.* **2016**, *15*, 252–261.
2. Yu, M.; Breuer, W. *Energie-Methode zur Beurteilung von Kraftschlussinduzierten Eigenschwingungen von Radsatzwellen*; DVV Media Group, Eurailpress: Hamburg, Germany, 2018; Volume 142.
3. Weinhardt, M. Torsionsschwingungen in Radsätzen—Fakten und Thesen zur Anregung durch den Rad-Schiene-Kraftschluss. In Proceedings of the 15. Internationale Schienenfahrzeugtagung 2017 in Dresden, Dresden, Germany, 1 March 2017; pp. 49–51.
4. Szolc, T. Simulation of bending-torsional-lateral vibrations of the railway wheelset-track system in the medium frequency range. *Veh. Syst. Dyn.* **1998**, *30*, 473–508. [CrossRef]
5. Schneider, R. Torsionsschwingungen von Radsatzwellen—Systemanalyse Teil 1: System- und Modellbeschreibung. *ZEVrail* **2017**, *141*, 452–461.
6. Saur, F.; Weber, J. Selbsterregte Radsatz-Torsionsschwingungen in Schienenfahrzeugen: Analyse, Berechnung und Simulation. In Proceedings of the Dresdner Maschinenelemente Kolloquium (DMK 2019), Dresden, Germany, 26–27 December 2019; Technische Universität Dresden, Sierke Verlag: Göttingen, Germany, 2019; pp. 633–650.
7. Saur, F.; Weber, J. Analytische Berechnung des maximalen, dynamischen Radsatz-Torsionsmoments von Schienenfahrzeugen mit Tatzlagerantrieb. *Eisenbahntechnische Rundsch.* **2021**, *4*, 69–73.

8. Saur, F.; Weber, J. Auslegung von Radsatzwellen unter Berücksichtigung des maximalen, dynamischen Torsionsmoments. *Eisenbahntechnische Rundsch.* **2021**, *10*, 86–90.
9. Liu, J.; Zhao, H.; Zhai, W. Mechanism of self-excited torsional vibration of locomotive driving system. *Front. Mech. Eng. China* **2010**, *5*, 465–469. [CrossRef]
10. Xu, K.; Zeng, J.; Wei, L. An analysis of the self-excited torsional vibration of high-speed train drive system. *J. Mech. Sci. Technol.* **2019**, *33*, 1149–1158. [CrossRef]
11. Meierhofer, A.; Simon, G.; Simunek, D.; Weber, F.J.; Six, K. Welche Worst-Case-Kraftschluss Szenarien verursachen die maximale Rollierschwingung? In Proceedings of the 18 Internationale Schienenfahrzeugtagung 2021 in Dresden, Dresden, Germany, 22 September 2021; pp. 42–43.
12. Fridrichovskỳ, T.; Šulc, B. Investigation of Torsional Oscillations in Railway Vehicles. In *Proceedings of the MATEC Web of Conferences in Corfu Island, Greece*; EDP Sciences: Les Ulis, France, 2016; Volume 76, p. 02052.
13. Körner, E. *Reibschwingungen Eines Elektrischen Triebfahrzeuges an der Haftwertgrenze*; TU Graz: Graz, Austria, 1988.
14. Schwartz, H.J. *Regelung der Radsatzdrehzahl zur maximalen Kraftschlussausnutzung bei elektrischen Triebfahrzeugen*; VDI-Verlag: Düsseldorf, Germany, 1992.
15. Buscher, M. *Radschlupfregelung zur maximalen Kraftschlussausnutzung bei elektrischen Traktionsantrieben*; Verlag Shaker: Herzogenrath, Germany, 1995.
16. Trimpe, F.; Salander, C. Wheel—Rail adhesion during torsional vibration of driven railway wheelsets. *Veh. Syst. Dyn.* **2021**, *59*, 785–799. [CrossRef]
17. Trimpe, F.; Lück, S.; Naumann, R.; Salander, C. Simulation of torsional vibration of driven railway wheelsets respecting the drive control response on the vibration excitation in the wheel–rail contact point. *Vibration* **2020**, *4*, 30–48. [CrossRef]
18. Fathy Abouzeid, A.; Guerrero, J.M.; Endemaño, A.; Muniategui, I.; Ortega, D.; Larrazabal, I.; Briz, F. Control strategies for induction motors in railway traction applications. *Energies* **2020**, *13*, 700. [CrossRef]
19. El-Refaie, A.M. Motors/generators for traction/propulsion applications: A review. *IEEE Veh. Technol. Mag.* **2013**, *8*, 90–99. [CrossRef]
20. Fleischer, M.; de Doncker, R.W.; Abel, D. *Traction Control for Railway Vehicles*; Technical Report; Institut für Stromrichtertechnik und Elektrische Antriebe: Brighton, The Netherlands, 2019.
21. Depenbrock, M. Direct self-control (DSC) of inverter fed induktion machine. In Proceedings of the 1987 IEEE Power Electronics Specialists Conference, Blacksburg, VA, USA, 21–26 June 1987; pp. 632–641.
22. Buja, G.S.; Kazmierkowski, M.P. Direct torque control of PWM inverter-fed AC motors-a survey. *IEEE Trans. Ind. Electron.* **2004**, *51*, 744–757. [CrossRef]
23. Spichartz, M.; Heising, C.; Staudt, V.; Steimel, A. Indirect Stator-Quantities control as benchmark for highly dynamic induction machine control in the full operating range. In Proceedings of the 14th International Power Electronics and Motion Control Conference EPE-PEMC 2010, Ohrid, North Macedonia, 6–8 September 2010; pp. T3–T13.
24. Steimel, A. Direct self-control and synchronous pulse techniques for high-power traction inverters in comparison. *IEEE Trans. Ind. Electron.* **2004**, *51*, 810–820. [CrossRef]
25. Abouzeid, A.F.; Guerrero, J.M.; Vicente-Makazaga, I.; Muniategui-Aspiazu, I.; Endemaño-Isasi, A.; Briz, F. Torsional Vibration Suppression in Railway Traction Drives. *IEEE Access* **2022**, *10*, 32855–32869. [CrossRef]
26. Polach, O. Creep forces in simulations of traction vehicles running on adhesion limit. *Wear* **2005**, *258*, 992–1000. [CrossRef]
27. Watanabe, T. Anti-slip readhesion control with presumed adhesion force-Method of presuming adhesion force and running test results of High-speed shinkansen train. *Q. Rep. RTRI* **2000**, *41*, 32–36. [CrossRef]
28. Park, D.Y.; Kim, M.S.; Hwang, D.H.; Lee, J.H.; Kim, Y.J. Hybrid re-adhesion control method for traction system of high-speed railway. In Proceedings of the ICEMS'2001. Proceedings of the Fifth International Conference on Electrical Machines and Systems (IEEE Cat. No. 01EX501), Shenyang, China, 18–20 August 2001; Volume 2, pp. 739–742.
29. Yamashita, M.; Soeda, T. Anti-slip re-adhesion control method for increasing the tractive force of locomotives through the early detection of wheel slip convergence. In Proceedings of the 2015 17th European conference on power electronics and applications (EPE'15 ECCE-Europe), Geneva, Switzerland, 8–10 September 2015; pp. 1–10.
30. Cheok, A.D.; Shiomi, S. Combined heuristic knowledge and limited measurement based fuzzy logic antiskid control for railway applications. *IEEE Trans. Syst. Man Cybern. Part Appl. Rev.* **2000**, *30*, 557–568. [CrossRef]
31. Spiryagin, M.; Lee, K.S.; Yoo, H.H. Control system for maximum use of adhesive forces of a railway vehicle in a tractive mode. *Mech. Syst. Signal Process* **2008**, *22*, 709–720. [CrossRef]
32. Ohishi, K.; Hata, T.; Sano, T.; Yasukawa, S. Realization of anti-slip/skid re-adhesion control for electric commuter train based on disturbance observer. *IEEJ Trans. Electr. Electron. Eng.* **2009**, *4*, 199–209. [CrossRef]
33. Sadr, S.; Khaburi, D.A.; Rodríguez, J. Predictive slip control for electrical trains. *IEEE Trans. Ind. Electron.* **2016**, *63*, 3446–3457. [CrossRef]
34. Ishrat, T.; Ledwich, G.; Vilathgamuwa, M.; Borghesani, P. Identification scheme of maximum traction force using recursive least square for traction control in electric locomotives. In Proceedings of the 2017 IEEE 12th International Conference on Power Electronics and Drive Systems (PEDS), Honolulu, HI, USA, 12–15 December 2017; pp. 1–120.
35. Fang, X.; Lin, S.; Yang, Z.; Lin, F.; Sun, H.; Hu, L. Adhesion control strategy based on the wheel–rail adhesion state observation for high-speed trains. *Electronics* **2018**, *7*, 70. [CrossRef]

214

36. Can, K.; Jingchun, H.; Wenqi, D.; Xiaokang, W. Adhesion control method based on optimal slip velocity searching and tracking. In Proceedings of the 2019 14th IEEE International Conference on Electronic Measurement & Instruments (ICEMI), Changsha, China, 1–3 November 2019; pp. 1200–1207.

37. Trimpe, F.; Friedrich, S.; Traupe, M. Untersuchung der Gleitgeschwindigkeit während dynamischer Torsionsbelastungen von Radsatzwellen. In Proceedings of the 17 Internationale Schienenfahrzeugtagung 2020 in Dresden, Dresden, Germany, 26–28 February 2020; pp. 61–63.

B.1.3 Torsional Vibration Suppression in Railway Traction Drives

Torsional Vibration Suppression in Railway Traction Drives

AHMED FATHY ABOUZEID[1,2], (Member, IEEE), **JUAN M. GUERRERO**[1], (Senior Member, IEEE), **IBAN VICENTE-MAKAZAGA**[3], **IKER MUNIATEGUI-ASPIAZU**[3], **AITOR ENDEMAÑO-ISASI**[3], **AND FERNANDO BRIZ**[1], (Senior Member, IEEE)

[1]Department of Electrical, Electronic and Computer Engineering, University of Oviedo, 33003 Oviedo, Spain
[2]Department of Electrical Engineering, Port Said University, Port Said 42526, Egypt
[3]Department of Traction Systems, Ingeteam Power Technology, 48170 Zamudio, Spain

Corresponding author: Ahmed Fathy Abouzeid (abouzeidahmed@uniovi.es)

ABSTRACT Torsional vibrations phenomena are self-excited vibrations that occur in the wheelset of railway powertrains due to the counter-phase oscillation of both wheels. Long-lasting events of this type may lead to the catastrophic failures. Therefore, torsional vibration suppression and mitigation methods have drawn significant attention from the railway industry in the recent few years. Conventional vibration suppression methods reduce motor torque once the oscillation is detected. However, this can result in trip delays. Design of methods which do not compromise the traction capability is challenging. This paper proposes a novel torsional vibration suppression method using a Proportional-Resonant (PR) controller. The proposed method is insensitive to mechanical drive-train parameter variation neither requires adding new sensors to the wheelset. The method requires previous knowledge of the natural frequency of the wheelset torsional mode but this significantly reduces the implementation complexity suffered by other anti-vibration methods. Furthermore, the method will be shown to provide reduced sensitivity to slip velocities and wheel-rail conditions.

INDEX TERMS Railway traction drives, torsional vibrations, slip-stick phenomenon, slip control, field-oriented control, proportional-resonant controller.

I. INTRODUCTION

Derailment is one of the serious problems that should be avoided in railways for ensuring passengers' safety and reducing maintenance costs. Derailment occurs when the train vehicle comes off the track (i.e. the rail) which could lead to major accidents and collisions [1]. Failure in the mechanical components of the vehicle, track geometry defect (due to excessive wear of wheels or rails), and wheel-rail interaction such as excessive creepage are the most significant reasons for the train vehicle derailment [2], [3]. Therefore, many efforts have been devoted to limiting the creep (i.e. slip) between the wheel and the rail [4]–[6].

A certain amount of slip between wheel and rail is needed to increase the tractive force generated by the traction motor

The associate editor coordinating the review of this manuscript and approving it for publication was Zhuang Xu.

to the rail. Traditional creep controllers, also known as re-adhesion controllers, avoid slippage (i.e. the condition when the wheel-rail slip velocity dramatically increases) by limiting the slip velocity within a predefined threshold [7], [8]. They can be divided into two types:

1) Direct methods: they compare either the wheel circumference slip velocity or the wheel acceleration with a predefined threshold [9]–[11]. The threshold is chosen based on field-tests and trains' driver experience [12], [13]. The main drawback of the direct methods is that the re-adhesion controller cannot optimally utilize the adhesion in different rail surface conditions.

2) Indirect methods: they are intended for rolling stocks where multiple motors are fed from the same inverter. It is assumed that the speed of all paralleled motors is not measured [14], some form of sensorless vector control is therefore normally used. Slip is detected in

this case from unbalances in the current consumed by the paralleled motors. An obvious limitation of this method is that it can only be used when the traction converter feeds multiple motors.

Modern high-speed railway traction drives are often equipped with slip controllers aimed to operate at the possible maximum adhesion point while preventing slippage. Slip controllers make use of the adhesion-slip characteristic curve; reported approaches include:

1) Direct adaptation of the torque command using an adhesion force controller. Maximum adhesion occurs when the adhesion force gradient equals to zero (i.e. at the peak of the adhesion-slip curve). Steepest gradient method or Proportional-Integral (PI) controllers aimed to keep the adhesion slope equal to zero are commonly used for this purpose. [15]–[20].

2) Regulation of the slip velocity using an additional speed controller [21]–[23]. In this case, the slip velocity reference is increased progressively in small steps, the commanded torque being monitored. When a slip increase results in a decrease in the commanded torque, it is considered that maximum adhesion has been surpassed.

Finding the optimal slip velocity is a challenging task due to the high unpredictability of adhesion-slip phenomena and the subsequent uncertainty in the estimations. Several approaches have been proposed for this purpose, including: perturb and observe methods (P&O) [24], [25]; recursive least squares searching [26]–[28]. Model predictive control and particle swarm intelligence methods are also be found in [29], [30]. However, these searching algorithms increase the complexity of the control and their implementation in real trains has not been reported in the literature.

While slip controllers enhanced with maximum adhesion tracking increase the utilization of tractive force for high-performance locomotives, they can potentially enter the unstable adhesion region during the searching. As a result, oscillations can arise in the torsional elements of the locomotives power train [31]. These oscillations can also be provoked by slip-stick phenomenon due to changes in the adhesion condition and track irregularities. The most severe oscillation occurs when both wheels of the locomotive oscillate in counter-phase, which is sometimes referred as slip-stick vibration. Such vibrations add more stress on the press-fit joints of the wheelset axle, and could lead to their failure and, as a consequence, to the derailment of the locomotive.

Excitation of torsional resonances by the torque ripple and the interaction between the electric and mechanical elements are the main source of such vibrations [32]. Torsional vibrations in mechanical systems fed from electrical drives can be either passively or actively damped [33]. Passive cancellation can be implemented using Infinite Impulse Response (IIR) notch filters. The filter is designed to remove dangerous oscillations from the torque command [34], avoid-

ing their propagation to the mechanical system. However, notch filters might fail to suppress completely the resonant frequency due to the output delays and the uncertainty in the location of the resonance poles and zeros due to changes of the inertia constant of the mechanical system. A Finite Impulse Response (FIR) notch filter compensator can be used instead [35], taking advantage of FIR systems intrinsic stability and linear phase shift [36], [37]. Excitation of resonant modes can be also avoided using an FIR compensator by halving the output of the speed controller and delaying one of the halves by half the resonance period, later adding it to the non-modified half signal, which eventually cancels the oscillation [35]. The limitation of this approach relies on torque control transient response and the noise in the feedback speed sensor.

Active damping of torsional vibration can be achieved by using state feedback compensation where the torque command can be adapted through the feedback signals of torque control loop, speed control loop, or both [38]. Thus, all system poles can be placed at the desired location by choosing the appropriate feedback gains [39], [40]. Usually, these methods require an estimator or observer for non-measurable states [40], [41]. Moreover, advanced control techniques using Linear Quadratic Regulator (LQR), Linear Quadratic Gaussian (LQC), and H_∞ have been also proposed in [42]–[44]. However, these methods are highly sensitive to system parameters, meaning that for successful implementation they might need to be combined with parameter identification methods. Furthermore, the aforementioned torsional vibration methods use simplified mechanical models, ignoring therefore system dynamics, sensor noise, and other unexpected disturbances, which can be highly relevant in railways due to wheel-rail slippage phenomena.

Analysis and modeling of self-excited torsional vibrations phenomena in railways has been discussed in [45]–[48]. In [49], an indirect passive anti-vibration control is proposed. Torsional vibrations are extracted from the estimated dynamic of the wheelset axle. If they exceed a predefined limit, the control reduces the torque command. The effectiveness of this method strongly relies on quick detection of slip. While simple and therefore easy to implement, the main shortcomings of this method are a decrease of traction capability during the oscillation mitigation process, and the need for additional wheel sensors, which increase the cost and require the reconfiguration of existing locomotives in service. In [50], a state-space active anti-vibration control integrated with a slip re-adhesion control is proposed. This control strategy was capable of damping slip-stick vibrations up to a certain negative gradient of the adhesion force characteristic. The method was further improved by adding a virtual absorber at the indirectly driven wheel to suppress the torsional vibrations [51]. Complete vibration damping at any negative value of adhesion force gradient and without losing the traction capability is feasible with the virtual damper approach. The drawbacks of this method are its complexity

218
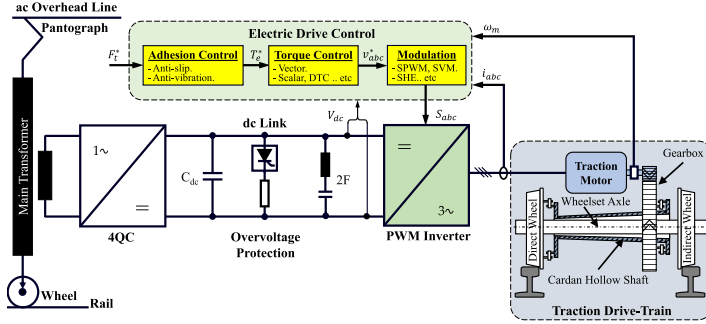
FIGURE 1. Schematic representation of a single-driven axle for a high-performance locomotive.

and the difficult tuning of the controller and the observer. Furthermore, natural frequencies identification is required to adapt the mechanical drive-train parameters to reflect variations due to wear and aging.

This paper proposes a torsional vibration suppression method using a resonant controller. The proposed method will be shown to be robust against changes in slip velocity and wheel-rail conditions. The paper is organized as follows. Section II describes the traction drive system for railways. Section III presents the detailed mechanical drive-train and locomotive model. The slip velocity control and the proposed vibration suppression method are addressed in IV. The proposed method is validated by simulation in section V. Finally, a summary of findings is provided in section VI.

II. SYSTEM DESCRIPTION

This section overviews the powertrain for high-performance locomotives (Fig. 1). The pantograph transfers the electrical power from the overhead line (ac or dc) to the locomotive. The ac transmission voltage can be 25 kV/50 Hz or 15 kV/16.7 Hz while the dc voltage can be 3 kV or 1.5 kV. For ac catenaries, the main transformer normally consists of a primary high-voltage winding with multiple secondary windings supplying both the traction converters and the auxiliary systems for heating, ventilation, and air conditioning (HVAC), lighting, etc.

A four-quadrant power converter (4QC) provides the dc-link voltage feeding the traction inverters, which are responsible for controlling the torque produced by motors according to the locomotive driver commands. Motor torque is transferred to the wheels through the mechanical drive-train, producing the traction force.

The electric drive control is responsible for achieving the traction force F_t^* commanded by the driver. As shown in Fig. 1, it consists of three main blocks: modulation, torque control, and adhesion control.
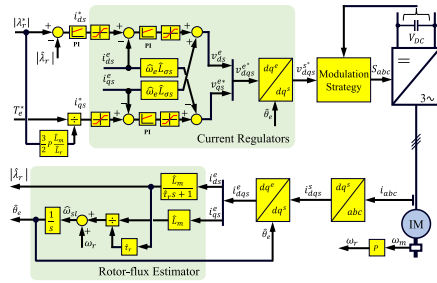
FIGURE 2. Rotor field-oriented control (RFOC) scheme.

A. TORQUE CONTROL AND MODULATION TECHNIQUE

Vector control schemes are preferred at low speed since they allow precise control of torque and flux, which is achieved employing high-performance current regulators. Typically rotor flux field-oriented control (RFOC) is used (see Fig. 2). The electromagnetic torque T_e using RFOC can be represented by (1). As observed from (1), torque can be controlled through the q-axis current i_{qs}^e; high bandwidth current regulators are used for this purpose.

$$T_e = \frac{3}{2} P \frac{L_m}{L_r} \lambda_r i_{qs}^e \qquad (1)$$

where P is the number of pole-pairs; L_m, L_r are the magnetizing and rotor inductances respectively; λ_r is the rotor flux.

At low speeds with RFOC, the inverter usually operates with constant switching frequency using either carrier-based Pulse-Width Modulation (PWM) with triplen harmonic injection or Space Vector PWM. Both two-level and three-level neutral-point clamped voltage-source inverters (3L-NPC-VSI) using insulated-gate bipolar transistors (IGBTs)

are of common use for traction drive [52]. The 3L-NPC-VSI will be used in this paper.

For high-speed operation, the inverter often operates with low switching-to-fundamental frequency ratios and high modulation indexes, including full-wave. Due to this, synchronous modulation methods, including Selective Harmonic Elimination (SHE), combined with scalar control, are a common choice in this case [53].

The electric drive control strategy can play a major role in the implementation of torsional vibration cancellation. A key aspect to consider is the bandwidth of the torque control, ROFC being in general advantageous over scalar control methods in this regard. This issue is addressed in section V-B.

B. ADHESION CONTROL

This block is responsible for adjusting the traction force to the wheel-rail adhesion level to prevent the wheel from slipping out, especially during acceleration/deceleration of the locomotive or in the event of sudden changes of the wheel-rail contact conditions. Recently with the rising awareness of torsional vibrations and their side effects on the wheelset axle, the adhesion control block has been enhanced with an additional anti-vibration control strategy. The details on the slip and anti-vibration control method will be discussed in section IV.

III. MECHANICAL DRIVE-TRAIN MODEL

This section discusses the mechanical model of the drive-train system. The hollow shaft drive-train of the German class 120 locomotive has been selected for the analysis [54], [55].

A. MATHEMATICAL MODEL

The traction drive-train consists of six rotational masses that are connected by torsional elements in the series structure as follows (see Fig. 3).

- The induction motor generates a drive torque T_e transmitted through the coupling to the gearbox T_M.
- Then the torque exerted in the gearbox T_{MG} is transmitted to the direct-driven wheel T_{HD} through the cardan hollow shaft, where the total inertia of the hollow shaft including the braking discs and couplings is divided into two rotating masses connected by an elastic shaft. The received torque at the direct driven wheel follows the transmission sequence: 1) from the gearbox to the first half of hollow shaft (gear side) through a gear-hollow shaft coupling T_{GH}; 2) then to the second half of the hollow shaft (wheel side) via the elastic shaft T_{HW}; 3) afterward to the direct-driven wheel T_{HD} through the hollow shaft-wheel coupling.
- Finally, the torque is transmitted to the indirect-driven wheel via the wheelset axle T_{DI}.

The general motion equation is given by (2),

$$[J] \cdot \left[\ddot{\theta}\right] + [D] \cdot \left[\dot{\theta}\right] + [C] \cdot [\theta] = [T] \qquad (2)$$

where J, D, and C are the inertia, damping ratio, and stiffness matrices, respectively. θ, $\dot{\theta}$ and $\ddot{\theta}$ are the rotational angle, its
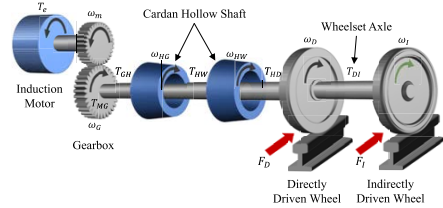
FIGURE 3. Six-inertia model of the mechanical traction drive-train. Torque transmission from motor to direct and indirect wheels are indicated by black and green arrows respectively; adhesion forces exerted on both wheels are indicated by red arrows.

first and second derivatives matrices, respectively. T is the applied torque matrix.

Applying (2) to the drive-train in Fig. 3, the differential equations of the six-inertia model (3), as shown at the bottom of the next page, are obtained, where: j_M, j_G, j_{HG}, j_{HW}, j_D and j_I represent the inertia of the motor, the gear, the hollow-gear, the hollow-wheel, the direct and the indirect wheels respectively; d_{MG}, d_{GH}, d_{HW}, d_{HD}, and d_{DI}; c_{MG}, c_{GH}, c_{HW}, c_{HD}, and c_{DI} are the torsional damping and stiffness values of the motor to the gear, the gear to the hollow shaft, the hollow shaft gear side to the hollow shaft wheel side, the hollow shaft wheel side to the direct wheel and the direct to indirect wheels respectively. T_M, T_D, and T_I are the motor torque and the traction torques applied to the direct and indirect wheels respectively. Note that all values in (3) are referred to the wheelset side of the drive-train, with R_g being the gear ratio.

B. SIMULATION MODEL

Applying Laplace transformation to (3), the drive-train block diagram Fig. 4 is obtained. The transmitted traction forces in the wheel-rail contact point are calculated from (4) where r_w, $\mu_{D,I}$ and $T_{D,I}$ are the wheel radius, adhesion coefficient and torque on each wheel, respectively; m_l, N_m, g are the locomotive mass, the total number of motors and the gravity constant, respectively.

$$T_{D,I} = r_w \cdot F_{D,I} = r_w \cdot \mu_{D,I} \cdot \frac{m_l \cdot g}{2 \cdot N_m} \qquad (4)$$

The adhesion characteristics for different wheel-rail conditions (dry, wet, …etc.) are calculated offline and stored in a look-up table [7]. Finally, the train speed v_{train} is obtained as shown in Fig. 5, where m_t is the total mass of the train, F_{res} is the resistive force due to the air (K_{air}) and rolling (K_{roll}) resistances [55]. Forces due to track grading are not shown in this figure. It is noted that the vehicle model in Fig. 5 assumes that all powered axles transmit the same traction force.

C. MODAL ANALYSIS

Modal analysis is a useful tool to identify the most stressed elements of the mechanical drive-train from vibration characteristics, i.e. natural frequencies and mode shapes. Natural frequencies, also referred to as resonance frequencies,
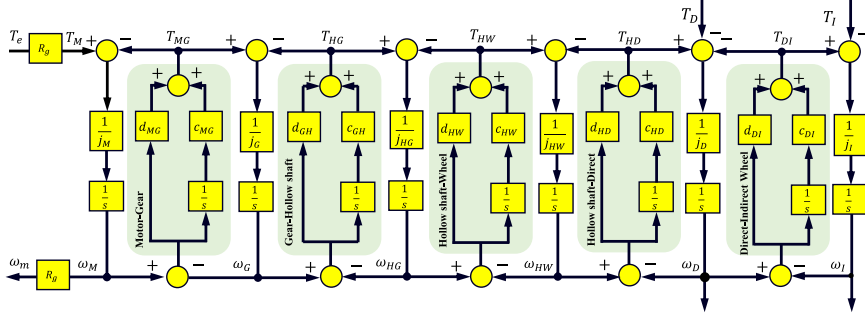
FIGURE 4. Block diagram of the six-inertia drive-train model.
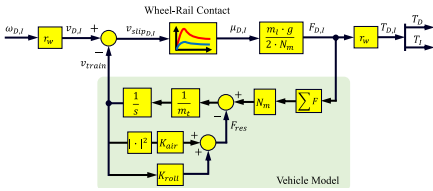
FIGURE 5. Block diagram of the wheel-rail contact model including the vehicle dynamics.

indicate the vibration modes of the elastic elements in the drive-train; mode shapes indicate the relative displacement between adjacent elements (inertias).

Drive-train natural frequencies and mode shapes can be obtained from the homogeneous equation (2) using (5), where λ, $[I]$ represent the eigenvalues (roots) of the system and the identity matrix respectively. It is noted that damping

coefficients have been neglected, which corresponds to the worst-case scenario.

$$det\left(\lambda^2 \cdot [I] - [J]^{-1} \cdot [C]\right) = 0 \qquad (5)$$

where eigenvalues represent the resonance frequencies of the mechanical system, eigenvectors represent the angle deviation and the direction of rotation for each inertia relative to adjacent inertias. Mode shape is a graphical representation that shows the angle deviation between the mechanical element at each resonance frequency (see Fig. 6). Eigenvalues and eigenvectors problems for the targeted drive-train model are obtained using MATLAB and normalized based on the maximum angle deviation found from all elements at each mode. For instance, in the second mode, the indirect wheel has the maximum angle deviation which is selected to be the base value for the rest of the elements. The six-inertia system consists of five torsional stiffness elements, producing five natural frequencies and mode shapes, in addition to one trivial mode as the discussed following (see Fig. 6):

$$
\begin{bmatrix}
j_M & 0 & 0 & 0 & 0 & 0 \\
0 & j_G & 0 & 0 & 0 & 0 \\
0 & 0 & j_{HG} & 0 & 0 & 0 \\
0 & 0 & 0 & j_{HW} & 0 & 0 \\
0 & 0 & 0 & 0 & j_D & 0 \\
0 & 0 & 0 & 0 & 0 & j_I
\end{bmatrix}
\cdot
\begin{bmatrix}
\ddot{\theta}_M \\
\ddot{\theta}_G \\
\ddot{\theta}_{HG} \\
\ddot{\theta}_{HW} \\
\ddot{\theta}_D \\
\ddot{\theta}_I
\end{bmatrix}
$$

$$
+
\begin{bmatrix}
d_{MG} & -d_{MG} & 0 & 0 & 0 & 0 \\
d_{MG} & (d_{MG}+d_{GH}) & -d_{GH} & 0 & 0 & 0 \\
0 & -d_{GH} & (d_{GH}+d_{HW}) & -d_{HW} & 0 & 0 \\
0 & 0 & -d_{HW} & (d_{HW}+d_{HD}) & -d_{HD} & 0 \\
0 & 0 & 0 & -d_{HD} & (d_{HD}+d_{DI}) & -d_{DI} \\
0 & 0 & 0 & 0 & -d_{DI} & d_{DI}
\end{bmatrix}
\cdot
\begin{bmatrix}
\dot{\theta}_M \\
\dot{\theta}_G \\
\dot{\theta}_{HG} \\
\dot{\theta}_{HW} \\
\dot{\theta}_D \\
\dot{\theta}_I
\end{bmatrix}
$$

$$
+
\begin{bmatrix}
c_{MG} & -c_{MG} & 0 & 0 & 0 & 0 \\
c_{MG} & (c_{MG}+c_{GH}) & -c_{GH} & 0 & 0 & 0 \\
0 & -c_{GH} & (c_{GH}+c_{HW}) & -c_{HW} & 0 & 0 \\
0 & 0 & -d_{HW} & (c_{HW}+c_{HD}) & -c_{HD} & 0 \\
0 & 0 & 0 & -c_{HD} & (c_{HD}+c_{DI}) & -c_{DI} \\
0 & 0 & 0 & 0 & -c_{DI} & c_{DI}
\end{bmatrix}
\cdot
\begin{bmatrix}
\theta_M \\
\theta_G \\
\theta_{HG} \\
\theta_{HW} \\
\theta_D \\
\theta_I
\end{bmatrix}
=
\begin{bmatrix}
T_M \\
0 \\
0 \\
0 \\
-T_D \\
-T_I
\end{bmatrix}
\qquad (3)
$$

FIGURE 6. Mode shapes of the six-inertia model.

- First mode shape occurs at 0 Hz and is due to the rigid body motion.
- Second mode shape (i.e. the first vibration mode) is located at 21.3 Hz and occurs when the whole wheelset oscillates against the motor. This vibration mode can be totally damped using a proper speed controller [54].
- Third mode shape reveals the second vibration mode at 50.8 Hz, which occurs when direct and indirect wheels oscillate in the counter phase, twisting the wheelset axle. It can be noticed that this vibration mode can have a reduced impact on the motor. Detectability of the second vibration by motor control will play a key role for active damping methods, use of speed/position sensors directly attached to the wheels might be required otherwise.
- The remaining mode shapes at higher frequencies have less influence on the traction motor and the wheelset, hence, they are normally neglected [51].

IV. WHEEL-RAIL SLIP CONTROL AND PROPOSED TORSIONAL VIBRATIONS SUPPRESSION

This section first discusses slip-stick phenomenon, its effect on initiating the torsional vibrations and the available methods for their suppression. A new method, which is the main contribution of this paper, is proposed in Section IV-C.

A. SLIP CONTROL AND VIBRATION EXCITATION

As mentioned in section II-B, the traction force is regulated by adapting the slip velocity between the wheel and the rail. The slip velocity command can be modified to maximize the adhesion level with different operating conditions or simply kept at a certain value that does not exert much wear on the rail. The slip velocity is calculated from the motor speed and

the estimated train velocity. Either P or PI controllers can be used to track the commanded slip velocity. The block diagram of the traction drive control is shown in Fig. 7.

Slip controller tuning is not trivial, as mechanical system dynamics depend on the non-linear wheel-rail contact characteristics. For this purpose, a linearized reduced order model including the first three mode shapes (top three traces in Fig. 6) can be obtained from the six-inertia drive-train model [54]. Using modal approximation method, the equivalent model (6), as shown at the bottom of the next page, consisting of three equivalent inertias (J_1, J_2, J_3), two equivalent damping (d_{12}, d_{23}) and two equivalent stiffness (c_{12}, c_{23}) elements is obtained [54]. θ_{12} and θ_{23} represent the relative angle between the two rotating masses. The load torque is $T_L = T_{12} = c_{12}\theta_{12}$ and the wheelset axle torque is $T_{DI} = T_{23} = c_{23}\theta_{23}$, both being referred to the wheelset side. Factors d_D and d_I represent the additional damping on direct and indirect wheels when the adhesion profile changes. According to [51], these damping factors are function of the adhesion force gradient $\frac{\delta\mu}{\delta v_{slip}}$ which is calculated from (7), as shown at the bottom of the next page.

For positive adhesion force gradient, the wheelset adds damping to the drive-train, improving the stability (P_1, P_2, P_3 in Fig. 8a). If the slip velocity is increased beyond the peak of the adhesion coefficient (P'_1, P'_2, P'_3 in Fig. 8a), then the adhesion force gradient becomes negative which reduces the overall damping of the drive-train, increasing the risk of instability. As the damping of the drive-train reduces, the self-resonant frequencies start to appear, their magnitude increasing proportionally to the negative slope of the adhesion coefficient (i.e. $\frac{\delta\mu}{\delta v_{slip}}$).

The eigenvalues state-space wheelset model in (6) can be represented by an equivalent transfer function (8); it consists of a pure integrator while the remaining four poles, as well as the zeros, can be proven to be complex conjugate pairs [51], [54].

$$G_w(s) = \frac{b_4 s^4 + b_2 s^2 + b_0}{s\left(a_4 s^4 + a_2 s^2 + a_0\right)} \tag{8}$$

Coefficients of the transfer function $b_0 \ldots b_4$, $a_0 \ldots a_4$, can be expressed a function of drive-train parameters, the resulting expressions are omitted due to the room constraints [51]. The detailed block diagram of the closed-loop traction drive of the slip velocity control is shown in Fig. 7. The closed-loop block diagram includes the slip velocity control, the torque control, the inverter time delay, the motor electrical and mechanical dynamics respectively which are given by (9)-(12).

$$G_s(s) = k_{ps} + \frac{k_{is}}{s} \tag{9}$$

$$G_c(s) = k_{pi} + \frac{k_{ii}}{s} \tag{10}$$

$$G_e(s) = \frac{1}{\hat{L}_{\sigma s} s + \hat{R}'_s} \tag{11}$$

$$G_m(s) = \frac{1}{\hat{J}_m s + \hat{\beta}} \tag{12}$$
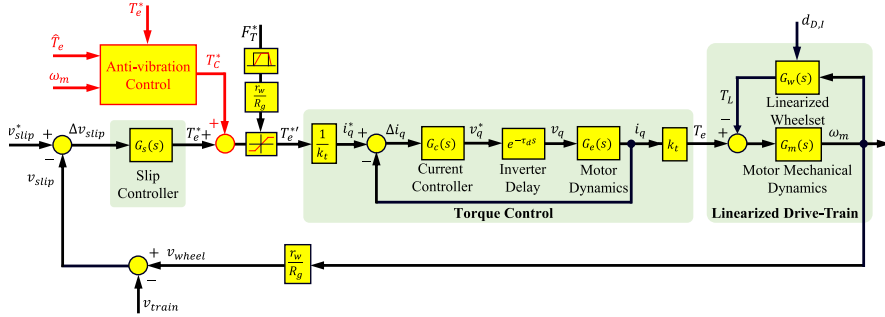
FIGURE 7. Block diagram of slip velocity control coupled with anti-vibration strategy.

where k_{ps} and k_{is} are the proportional and integral (PI) gains for the slip velocity control, respectively; k_{pi} and k_{ii} are the current controller PI gains, respectively; $\hat{L}_{\sigma s}$ and $\hat{R}'_{s}$ are the estimated stator leakage inductance and resistance, respectively; $\hat{J}_m$ and $\hat{\beta}$ are the estimated motor inertia and friction coefficient, respectively.

To investigate the influence of the wheel-rail contact on the traction drive system, a range of variation of adhesion force gradient -0.12 s/m $< \frac{\delta\mu}{\delta v_{slip}} < 0.12$ s/m is typically used [51]. Closed-loop poles migration of the drive-train for the two extreme cases of -0.12 s/m and 0.12 s/m are shown in Fig. 8b. It is observed that by a proper selection of controller gains, the slip controller is able to damp the first vibration mode (chatter), i.e. associated closed-loop poles are moved to the left-half plane. On the other hand, the second vibration mode (torsional) is insufficiently damped;

consequently, drive-train resonance due to this mode will result in torsional vibrations. An additional anti-vibration control for this specific mode is required which will be addressed next.

B. OVERVIEW OF ANTI-VIBRATION METHODS

Anti-vibration control is required to mitigate or suppress this specific torsional vibration mode. The conventional solution is to estimate the dynamic torque on the wheelset axle. A regular PI controller is used to limit the envelope of the oscillation (see Fig. 9a). A limit of 100 kNm is used, this value being obtained at the design stage of the powertrain. PI controller output T_c^* is added to the output of the slip controller (T_e^*, see Fig. 7). In traction mode, the magnitude of the torsional vibration is limited but at the cost of losing traction capability. Also, it is found that the conventional

$$\dot{X} = A \cdot X + B \cdot U$$
$$Y = C \cdot X + D \cdot U$$

$$A = \begin{bmatrix} \dfrac{-d_{12}}{J_1} & \dfrac{d_{12}}{J_1} & 0 & \dfrac{-c_{12}}{J_1} & 0 \\ \dfrac{d_{12}}{J_2} & -(d_{12}+d_{23}+d_D) & \dfrac{-d_{23}}{J_2} & \dfrac{c_{12}}{J_2} & \dfrac{-c_{23}}{J_2} \\ 0 & \dfrac{d_{23}}{J_3} & -(d_{23}+d_I) & 0 & \dfrac{-c_{23}}{J_3} \\ 1 & -1 & 0 & 0 & 0 \\ 0 & 1 & -1 & 0 & 0 \end{bmatrix};$$

$$B = \begin{bmatrix} \dfrac{R_g}{J_1} & 0 & 0 & 0 & 0 \end{bmatrix}^T;$$

$$C = \begin{bmatrix} R_g & 0 & 0 & c_{12} & c_{23} \end{bmatrix}; \quad D = [0]$$

$$X = \begin{bmatrix} \omega_1 & \omega_2 & \omega_3 & \theta_{12} & \theta_{23} \end{bmatrix}^T;$$

$$U = \begin{bmatrix} T_e & 0 & 0 & 0 & 0 \end{bmatrix}^T; \quad Y = \begin{bmatrix} \omega_m & 0 & 0 & T_{12} & T_{23} \end{bmatrix}^T \tag{6}$$

$$d_{D,I} = r_w^2 \cdot \frac{m_t \cdot g}{2 \cdot N_m} \cdot \frac{\delta\mu_{D,I}}{\delta v_{slip_{D,I}}} \tag{7}$$

(a) Adhesion coefficient vs. slip speed

(b) Wheelset pole migration

FIGURE 8. Influence of wheel-rail contact on the traction drive-train: a) variation of adhesion force gradient over the characteristics curve; b) Root locus plot of the traction drive closed-loop response for the case of the adhesion force gradient being equal −0.12 s/m and 0.12 s/m respectively.

anti-vibration can effectively damp the vibrations for adhesion curves with negative adhesion gradients bigger than −0.04 s/m (i.e. $\frac{\delta\mu}{\delta v_{slip}}$ >−0.04 s/m) [50]. Advanced state-space control approaches based on pole-placement techniques have been recently applied to vibration suppression strategies for negative adhesion gradients less than −0.04 s/m (i.e. $\frac{\delta\mu}{\delta v_{slip}}$ <−0.04 s/m). Virtual absorber controller is another promising solution for actively damping not only the torsional vibrations but also improving the whole traction system dynamics [51]. The basic idea of this approach is to emulate a mechanical absorber mounted in the indirect-driven wheel by a feedback controller which is based on the estimated electromagnetic torque ($\hat{T}_e$) and the measured motor speed (ω_m). Combining two or multiple anti-vibration methods (see Fig. 9a) is advantageous to provide high damping to the torsional vibrations even with a very steep adhesion force gradient $\frac{\delta\mu}{\delta v_{slip}}$ <−0.12 s/m. However, due to wear, aging, and temperature-dependent of the traction drive-train elements, the vibration frequencies will increase over time. Thus, parameters estimates of the drive-train and the virtual absorber must be very accurate, the equivalent reduced-order model should be automatically adapted accordingly.
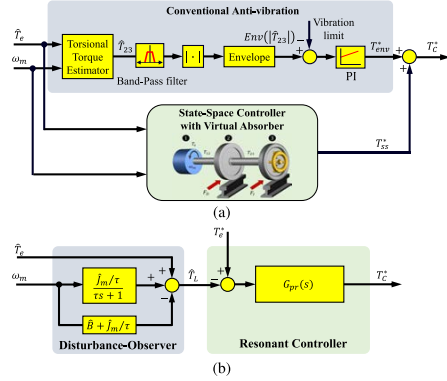
FIGURE 9. Anti-vibration control strategies based on traction motor variables: a) Existing anti-vibration control; b) Proposed vibration suppression method using PR controller.

This requires additional natural identification and parameter estimation algorithms which add complexity to the system implementation.

C. PROPOSED PROPORTIONAL-RESONANT ANTI-VIBRATION CONTROL

From the previous discussion, it can be concluded that the traction drive control, without any additional mechanical components, and relying on motor variables only (voltage, current, speed), should be able to suppress the wheelset torsional vibrations. The key aspect of damping the vibrations is to provide the torque correction signal required to adapt the commanded torque according to the wheel-rail operating condition. Since wheel-rail contact act as a disturbance to the motor, a disturbance-observer is used to estimate the motor load torque which contains the vibration transferred from the wheelset side (see fig. 9b). Taking the Laplace transformation for the differential equation of motion on the motor shaft in (13), the load torque is estimated using (14) where τ is the time constant of the low-pass filter in the disturbance observer used for noise reduction in the measured speed. Then, the estimated load torque is subtracted from the commanded torque signal to extract only the vibrating component. Finally, a proportional-resonant (PR) controller is used to suppress the torsional vibrations by injecting the correction torque signal (T_c^*) with the resonance frequency corresponding to the torsional vibration mode.

$$T_L = T_e - \beta\omega_m - J_m\dot{\omega}_m \tag{13}$$

$$\hat{T}_L(s) = \hat{T}_e(s) - \beta\omega_m(s) - J_m s\, \omega_m(s)\left(\frac{1}{\tau s + 1}\right) \tag{14}$$

The use of an ideal resonant controller is not advisable in practice due to its high sensitivity to the frequency of
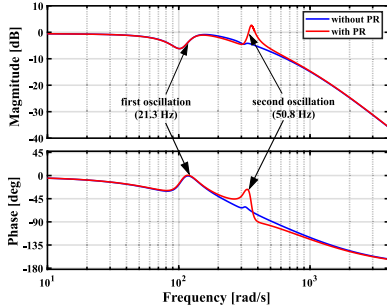
the input signal, which might result in instability due to the narrow bandwidths being used. Usually, the resonant controller (PR) given in (15) is preferred, where k_{p_r} and k_{i_r} are the proportional and integral gains, ω_n is the resonant frequency and ω_c is the pass-band frequency range.

$$G_{pr}(s) = k_{p_r} + \frac{2k_{r_r}\omega_c s}{(s^2 + 2\omega_c s + \omega_n^2)} \qquad (15)$$

The effectiveness of the resonant controller can be noticed for the second oscillation (torsional mode) in the bode plot of the closed-loop slip velocity control system (see the red line in Fig. 10). For this specific mode, the PR controller achieves high magnitude attenuation with eliminating the phase delay in the closed-loop response while it does not affect the first oscillation mode. In this way, the torsional (slip-stick) vibrations are suppressed without deteriorating the traction performance and with simple control requirements.

V. SIMULATION RESULTS

To investigate the performance of the proposed vibration suppression method, the entire traction drive system is modeled and simulated using MATLAB/Simulink following the block diagram seen in Fig. 11, with a simulation step of 10 μs. The detailed simulation model consists of the traction drive control, a three-level NPC inverter, the six-inertia wheelset model, the wheel-rail contact characteristics, and the vehicle model. The general specification of the locomotive is given in table 1; the six-mass model parameters are given in table 2 in the appendix A [54]. RFOC and SVPWM with a switching frequency of 1 kHz are used. Current controllers are tuned using the zero/pole cancellation to provide 200 Hz bandwidth, while the slip velocity controller gains are selected from the root locus closed-loop plot in Fig. 8b to achieve better damping of chatter vibration mode. The disturbance-observer filter is chosen to have a time constant of $\tau = 1$ ms while the resonant controller is tuned at $\omega_n = 340$ rad/s with a pass-band width of $\omega_c = 12.5$ rad/s. Selection of gains k_{p_r}, ki_r is therefore extremely

TABLE 1. General specifications of the German class 120 locomotive.

Parameter	Value	Unit
Centenary voltage	15	kV
Centenary frequency	16.7	Hz
Maximum power	4.4	MW
Maximum tractive effort	340	kN
Maximum speed	280	km/h
Weight	84,000	kg
Gear ratio	4.818	-
Wheel diameter	1.25	m
Number of motors	4	-

challenging due to the variability of operating conditions, a common practice is to follow a trial and error process to achieve sufficient damping to the system for all operating conditions [56].The close-loop controllers gains are given in table 3 in the appendix B.

To initiate the torsional vibrations, the slip velocity command v_{slip}^* is increased from 0.1 to 1 m/s, the adhesion force gradient changing from positive to negative (see Fig. 8a). Fig. 12a shows the system response when it enters the unstable region of the adhesion-slip curve. The torsional vibration appears after ≈ 3 seconds when 1 m/s slip velocity is commanded. In general, the more negative is the gradient, the sooner vibration will start. Fig. 12b shows the frequency spectrum of torque and speed signals when the system is in vibration mode. Vibration frequency is around 50.8 Hz, which matches the results from mode shape analysis in subsection III-C. The highest torque vibration occurs at the wheelset axle ($T_{DI} = 40$ kNm), the magnitude increasing proportionally to the (negative) adhesion force gradient. It can be also noticed the traction motor torque and the measured speed contains the vibration information, which is required to detect and further control the torsional vibration.

The effectiveness of the proposed method in the same scenario is shown in Fig. 13a. PR controller is first enabled and disabled gradually ($6 \text{ s} \leq t \leq 11 \text{ s}$), and latter suddenly at $t = 14$ s, see Fig. 13a-bottom). The activation process is done using a sliding factor (varying from 0 to 1) where it is multiplied by the PR output signal. It is seen that the proposed PR controller damps the torsional vibration, no adverse effects are observed due to sudden activation/deactivation. It is also seen that if adverse adhesion conditions remain, torsional vibrations resume a few seconds after PR control is disabled. Therefore, it is advisable to keep the PR controller enabled all the time.

A potential concern for the proposed method would be the noise in the estimated motor speed. Incremental encoders are widely used in railway. Encoder signals are normally converted into pulses to ease their acquisition and processing. However, since the encoder provides a position signal, some type of differentiation is required to obtain the angular speed. Due to the discrete nature of encoder signal, differentiation will result in quantization noise in the estimated speed [57]. In this work, speed is estimated by combining periodimeter and frequencimeter methods [57], [58].

A. F. Abouzeid *et al.*: Torsional Vibration Suppression in Railway Traction Drives
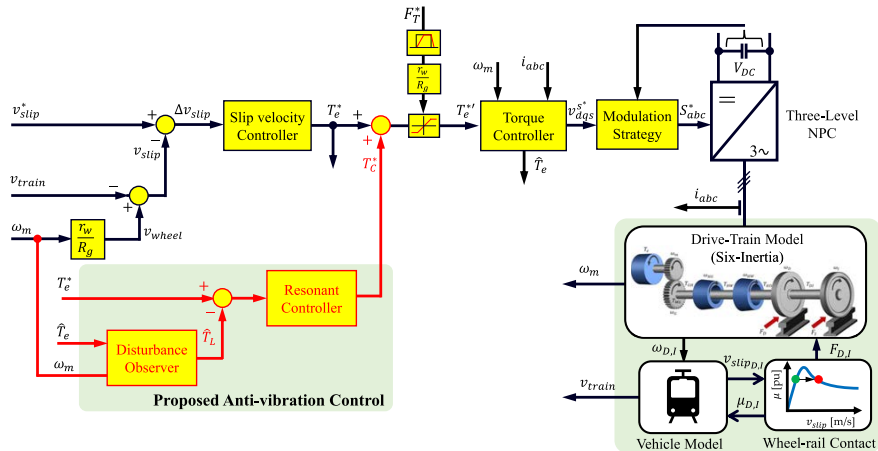
FIGURE 11. Schematic representation of the complete traction drive simulation model with the proposed anti-vibration control.

(a) Time response

(b) |FFT|
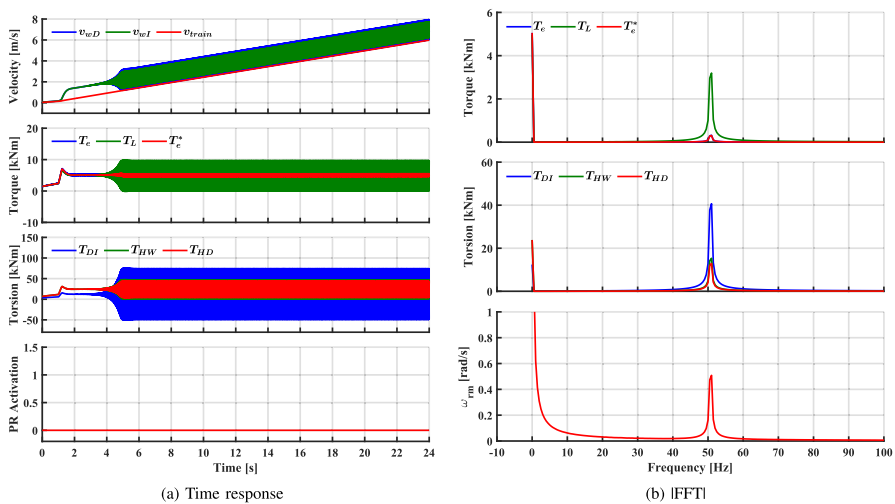
FIGURE 12. Response of the slip velocity control while commanding 1 [m/s] at t = 1 s.

The effect of quantization noise in the estimated speed is shown in Fig. 13. A rotary incremental encoder with 4-channels 256 pulse per revolution (PPR) was used [59]. Comparing the results with ideal speed measurement in Fig. 13a and considering quantization noise in Fig. 13b, it is observed that the main difference occurs when the PR is activated suddenly. On the contrary, almost no difference is

observed if PR is activated progressively, or when it remains enabled.

The proposed method is validated against the conventional vibration mitigation method shown in Fig. 9a where the vibration limit is set to 20 kNm (see Fig. 14 vs. Fig. 13a from $t = 6 \rightarrow 11$ s and $t = 14 \rightarrow 24$ s). A clear observation is the loss of traction torque in the conventional suppression
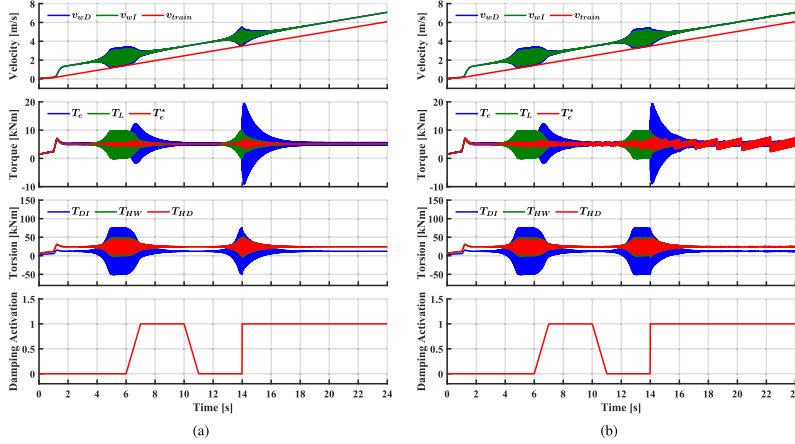
FIGURE 13. Response of the proposed method when PR is activated/deactivated gradually ($t = 6$ s → $t = 10$ s), and suddenly ($t = 14$). (a) With ideal speed measurement; (b) using and incremental encoder for speed measurement.
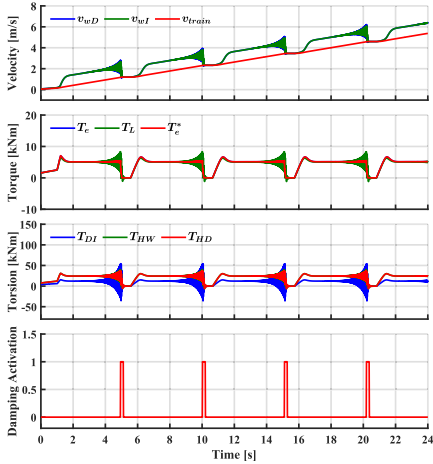
FIGURE 14. Response of conventional torsional vibration mitigation method.

method (see Fig. 14) to damp the oscillation. However, after suppressing the oscillation and restoring the traction torque capability, the oscillations appear continuously as the slip velocity command remains at the same operating point with the negative slope of the adhesion curve (i.e. 1 m/s). In the contrast, the proposed suppression method maximized the utilisation of the traction torque with completely suppressing the oscillations as seen in Fig. 13a.

Evaluation of the proposed method under varying conditions will be discussed in the following subsections:

A. EFFECTS OF VARYING SLIP VELOCITY AND WHEEL-RAIL CONDITION

Variations in the slip command can occur when the locomotive has an outer control loop implementing maximum traction force searching. This might drive the operating point into the unstable region where the torsional vibration arises. An example of the response of the proposed method to changes in the slip velocity is shown in Fig. 15a. Wheel-rail contact is modeled as profile 1 in the adhesion curve shown in Fig. 8a. The traction torque is increased from 5 kNm to 5.8 kNm by decreasing the slip velocity to 0.5 m/s. Then, the torque is decreased to 4.6 kNm when operating at the slip of 1.5 m/s. The maximum adhesion force can be achieved when $v_{slip} = 0.25$ m/s with this specific adhesion profile. However, the resonant controller was able to dampen the wheelset oscillations for all commanded slip velocities.

Variations of wheel-rail contact conditions have been reported as the main mechanism for exciting the wheelset natural frequencies leading to dynamic torque oscillations [31], [60]. Fig. 15b shows the response when the contact condition changes between dry to wet (profiles 1 to 3 in Fig. 8a). The change can occur for one wheel or both wheels, this second case is shown in the figure. The change from dry to wet decreases the adhesion force gradient $\frac{\delta\mu}{\delta v_{slip}}$ of both wheels initiating oscillations in the counter phase. It is observed from Fig. 15b that the torsional control reacts reducing torque from 5 kNm to 1 kNm at $t = 8$ s. This will keep the slip velocity at 1 m/s avoiding excessive slip. Once the wheel-rail contact returns to a dry condition, the

227

A. F. Abouzeid *et al.*: Torsional Vibration Suppression in Railway Traction Drives

(a) Slip velocity changes

(b) Adhesion profile changes
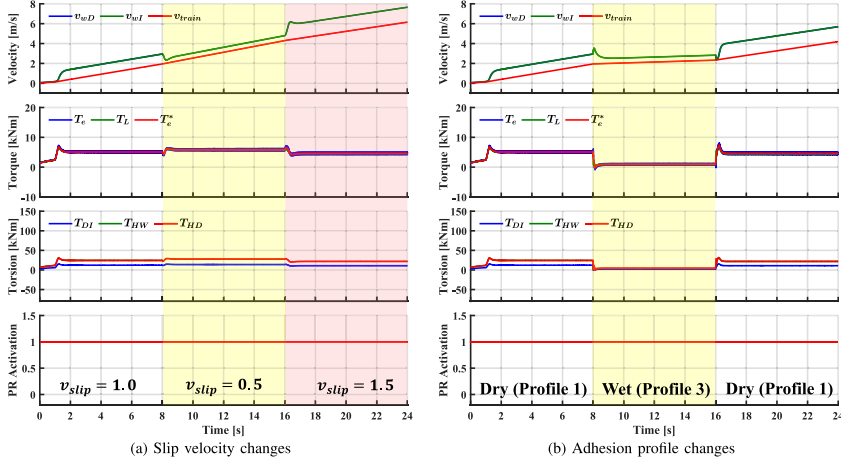
FIGURE 15. Response of the proposed method at different operating conditions.

(a) $k_{p_{s1}} = 4.7 \times 10^3$, $k_{i_{s1}} = 1.4 \times 10^4$

(b) $k_{p_{s2}} = 2k_{p_{s1}}$, $k_{i_{s2}} = 2k_{i_{s1}}$
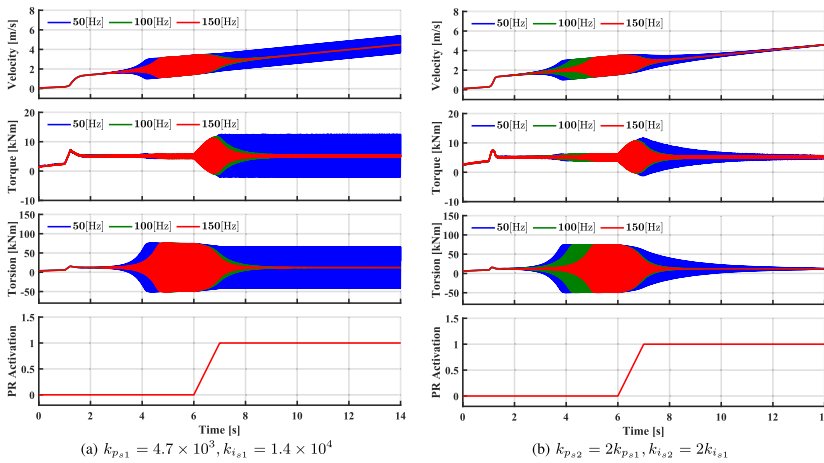
FIGURE 16. Response of the proposed method with changing the current controller bandwidth (150, 100 and 50 Hz) for two different tuning sets of the slip velocity controller.

motor torque returns to its initial value. Again, the proposed method is seen to provide a good response under challenging operating conditions.

B. EFFECT OF THE DRIVE CONTROL BANDWIDTH

In the previous simulations, fast torque control is assumed, which is achieved thanks to the use of vector control with 200 Hz bandwidth for current regulators. Frequently, drive control is switched to scalar methods at high speed,

especially when the inverter is operated in the overmodulation region close to the voltage limit. A drawback of scalar control is the slow dynamic response of the torque control loop.

Fig. 16b shows the effect of the torque control bandwidth, with the same slip control setup shown in Fig. 11. It is clear that the lower the bandwidth, the longer the time needed to fully suppress the vibration. Interestingly, it is found that for torque control bandwidths below $< \approx 60$ Hz, oscillations are not properly cancelled. By doubling the slip controller

gains, the control system is able to damp the oscillation for all bandwidths (50 to 150 Hz) (see Fig. 16a). However, increasing the slip velocity controller gains is not desired as it will amplify the feedback noise coming from the motor speed measurement and might also lead to oscillations in practice.

A potential concern when high bandwidth current regulators are used, is the presence of electrical noise in the measured currents. The reduce this risk, oversampling of current sensors was used [61]. A field-programmable gate array (FPGA) measures the signal every 5 μs, and averages the measurement over the whole control period. The PWM operates with a period of 1 ms and with double update, 100 samples being therefore averaged each control period. This will reduce the noise in the signals to negligible levels [62], [63].

VI. CONCLUSION
Design and analysis of dynamic torque control for railways have been addressed in this paper. Modeling of the electric drive, mechanical drive-train, and vehicle considering slippage and vibrations phenomena have been presented. The conclusions of the analysis can be summarized as follows:

- The adhesion force gradient is the key factor for torsional vibration phenomena. This factor is often unpredictable. Moving this factor from positive to negative values pushes the system to the stability limit or even towards the instability.
- Operating with negative adhesion force gradient will excite the resonance frequencies of the mechanical elements in the drive-train, their severity increasing proportionally to the negative slope of the adhesion curve.
- The first two resonance frequencies are the most affecting modes on the motor shaft and the press-fit of the wheelset axle. These two modes should be eliminated or kept as minimum value as possible to avoid fatigue and failure of the drive-train element.
- Equipping the electric drive with a slip controller, besides preventing the wheel from slipping on the rail, can perfectly dampen the first resonance mode (chatter mode) and return the system to the stable region. However, the slip control has less influence on the second resonance mode occurring between the two wheels (torsional mode).
- Reducing the motor torque is one of the simplest solutions to damp the torsional resonance mode but at the cost of losing traction force. Therefore, advanced control techniques are required to be added in parallel with the slip controller.

An anti-vibration method using a resonant controller has been proposed in this paper. A PR controller is used for this purpose, whose output is added to the torque command used to provide traction effort. Torque oscillations are obtained from the estimated traction motor load torque. Only the estimated electromagnetic torque and the measured motor speed are required, no additional sensors/cabling or drive-train state observers are therefore needed. The proposed

anti-vibration control is robust against variations of slip velocity and under changing wheel-rail conditions providing maximum available traction with no interruption. It has also been shown that proper operation of the proposed method requires torque control bandwidths in the range of 60 Hz or higher. As a general conclusion, higher bandwidths in the slip controller will improve the overall performance of the traction control system using the proposed method.

APPENDIX A
MECHANICAL DRIVE-TRAIN PARAMETERS

TABLE 2. Six-inertia drive-train model parameters of the German class 120 locomotive referred to the wheelset side [54], [55].

Moment of inertia	Symbol	Value	Unit
Traction motor	j_M	466.6	Kgm^2
Gear	j_G	55	Kgm^2
Half of hollow shaft to the gearbox side	j_{HG}	10.13	Kgm^2
Half of hollow shaft to the wheel side	j_{HW}	9.72	Kgm^2
Direct wheel and coupling	j_D	163	Kgm^2
Indirect wheel	j_I	157.3	Kgm^2
Torsional stiffness	**Symbol**	**Value**	**Unit**
Motor shaft	c_{MG}	88.12×10^6	Nm
Coupling (Gear side)	c_{GH}	15.1×10^6	Nm
Hollow shaft	c_{HW}	10.1×10^6	Nm
Coupling (Wheel side)	c_{HD}	15.7×10^6	Nm
Wheelset axle	c_{DI}	7.06×10^6	Nm
Torsional damping ratio	**Symbol**	**Value**	**Unit**
Motor shaft	d_{MG}	920.3×10^6	Nms
Coupling (Gear side)	d_{GH}	4730.8×10^6	Nms
Hollow shaft	d_{HW}	105.5×10^6	Nms
Coupling (Wheel side)	d_{HD}	11731.4×10^6	Nms
Wheelset axle	d_{DI}	73.7×10^6	Nms

APPENDIX B
CONTROLLERS GAINS

TABLE 3. Closed-loop control gains of the simulated model.

Regulator type	Controller gain	Value
Current	k_{p_i}	2.2281
	k_{i_i}	81.9413
Slip velocity	k_{p_s}	4.7×10^3
	k_{i_s}	1.4×4
Anti-vibration	k_{p_r}	0.1
	k_{r_r}	2

REFERENCES
[1] European Union Agency for Railways. (2018). *Report on Railway Safety and Interoperability in the EU*. [Online]. Available: https://www.era.europa.eu/sites/default/files/library/docs/safety_inter%operability_progress_reports/railway_safety_and_interoperability_in_eu_2018_en%.pdf
[2] J. Zeng and P. Wu, "Study on the wheel/rail interaction and derailment safety," *Wear*, vol. 265, nos. 9–10, pp. 1452–1459, 2008.
[3] J. Santamaria, E. Vadillo, and J. Gomez, "Influence of creep forces on the risk of derailment of railway vehicles," *Vehicle Syst. Dyn.*, vol. 47, no. 6, pp. 721–752, 2009.
[4] K. Kondo, "Anti-slip control technologies for the railway vehicle traction," in *Proc. IEEE Vehicle Power Propuls. Conf.*, Oct. 2012, pp. 1306–1311.
[5] P. Pichlík and J. Zdeněk, "Overview of slip control methods used in locomotives," *Trans. Electr. Eng.*, vol. 3, no. 2, pp. 38–43, 2014.
[6] U. Caglar, G. Metin, and B. Seta, "Comparison of the re-adhesion control strategies in high-speed train," *Proc. Inst. Mech. Eng., I, J. Syst. Control Eng.*, vol. 232, no. 1, pp. 92–105, 2018.
[7] O. Polach, "Creep forces in simulations of traction vehicles running on adhesion limit," *Wear*, vol. 258, nos. 7–8, pp. 992–1000, 2005.

[8] D.-Y. Park, M.-S. Kim, D.-H. Hwang, J.-H. Lee, and Y.-J. Kim, "Hybrid re-adhesion control method for traction system of high-speed railway," in *Proc. 5th Int. Conf. Electr. Mach. Syst. (ICEMS)*, vol. 2, Aug. 2001, pp. 739–742.

[9] T. WATANABE, "Anti-slip readhesion control with presumed adhesion force-method of presuming adhesion force and running test results of high-speed shinkansen train," *Quart. Rep. RTRI*, vol. 41, no. 1, pp. 32–36, 2000.

[10] J. Huang, J. Xiao, and H. Weiss, "Simulation study on adhesion control of electric locomotives based on multidisciplinary virtual prototyping," in *Proc. IEEE Int. Conf. Ind. Technol.*, Apr. 2008, pp. 1–4.

[11] M. Yamashita and T. Soeda, "Anti-slip re-adhesion control method for increasing the tractive force of locomotives through the early detection of wheel slip convergence," in *Proc. 17th Eur. Conf. Power Electron. Appl. (EPE ECCE-Eur.)*, Sep. 2015, pp. 1–10.

[12] A. D. Cheok and S. Shiomi, "A fuzzy logic based anti-skid control system for railway applications," in *Proc. 2nd Int. Conf. Knowl.-Based Intell. Electron. Syst. Proc. (KES)*, vol. 1, Apr. 1998, pp. 195–201.

[13] A. D. Cheok and S. Shiomi, "Combined heuristic knowledge and limited measurement based fuzzy logic antiskid control for railway applications," *IEEE Trans. Syst., Man, Cybern. C, Appl. Rev.*, vol. 30, no. 4, pp. 557–568, Nov. 2000.

[14] T. Watanabe and M. Yamashita, "A novel anti-slip control without speed sensor for electric railway vehicles," in *Proc. 27th Annu. Conf. IEEE Ind. Electron. Soc. (IECON)*, vol. 2, Dec. 2001, pp. 1382–1387.

[15] K. Ohishi, Y. Ogawa, I. Miyashita, and S. Yasukawa, "Anti-slip re-adhesion control of electric motor coach based on force control using disturbance observer," in *Proc. Conf. Rec. IEEE Ind. Appl. Conf.*, vol. 2, Oct. 2000, pp. 1001–1007.

[16] M. Spiryagin, K. S. Lee, and H. H. Yoo, "Control system for maximum use of adhesive forces of a railway vehicle in a traction mode," *Mech. Syst. signal Process.*, vol. 22, no. 3, pp. 709–720, 2008.

[17] K. Ohishi, T. Hata, T. Sano, and S. Yasukawa, "Realization of anti-slip/skid re-adhesion control for electric commuter train based on disturbance observer," *IEEJ Trans. Electr. Electron. Eng.*, vol. 4, no. 2, pp. 199–209, 2009.

[18] L. Diao, L. Zhao, Z. Jin, L. Wang, and S. M. Sharkh, "Taking traction control to task: High-adhesion-point tracking based on a disturbance observer in railway vehicles," *IEEE Ind. Electron. Mag.*, vol. 11, no. 1, pp. 51–62, Mar. 2017.

[19] P. Pichlik and J. Zdenek, "Locomotive wheel slip control method based on an unscented Kalman filter," *IEEE Trans. Veh. Technol.*, vol. 67, no. 7, pp. 5730–5739, Jul. 2018.

[20] P. Pichlik and J. Bauer, "Adhesion characteristic slope estimation for wheel slip control purpose based on UKF," *IEEE Trans. Veh. Technol.*, vol. 70, no. 5, pp. 4303–4311, 2021.

[21] M. Buscher, *Radschlupfregelung Zur Maximalen Kraftschlussausnutzung Bei Elektrischen Traktionsantrieben*. Aachen, Germany: Verlag Shaker, 1995.

[22] H. Ryoo, S. Kim, G. Rim, Y. Kim, and M. Kim, "Novel anti-slip/slide control algorithm for Korean high-speed train," in *Proc. 29th Annu. Conf. IEEE Ind. Electron. Soc. (IECON)*, vol. 3, Nov. 2003, pp. 2570–2574.

[23] X. Fang, S. Lin, Z. Yang, F. Lin, H. Sun, and L. Hu, "Adhesion control strategy based on the wheel-rail adhesion state observation for high-speed trains," *Electronics*, vol. 7, no. 5, p. 70, 2018.

[24] S. Sadr, D. A. Khaburi, and J. Rodríguez, "Predictive slip control for electrical trains," *IEEE Trans. Ind. Electron.*, vol. 63, no. 6, pp. 3446–3457, Jun. 2016.

[25] K. Can, H. Jingchun, D. Wenqi, and W. Xiaokang, "Adhesion control method based on optimal slip velocity searching and tracking," in *Proc. 14th IEEE Int. Conf. Electron. Meas. Instrum. (ICEMI)*, Nov. 2019, pp. 1200–1207.

[26] S. H. Park, J. S. Kim, J. J. Choi, and H. Yamazaki, "Modeling and control of adhesion force in railway rolling stocks," *IEEE Control Syst. Mag.*, vol. 28, no. 5, pp. 44–58, Oct. 2008.

[27] T. Ishrat, G. Ledwich, M. Vilathgamuwa, and P. Borghesani, "Identification scheme of maximum traction force using recursive least square for traction control in electric locomotives," in *Proc. IEEE 12th Int. Conf. Power Electron. Drive Syst. (PEDS)*, Dec. 2017, pp. 1–120.

[28] Z. Huang, W. Du, B. Chen, K. Gao, Y. Liu, X. Tang, and Y. Yang, "An online super-twisting sliding mode anti-slip control strategy," *Energies*, vol. 13, no. 7, p. 1823, 2020.

[29] X. Wen, J. Huang, and S. Zhang, "Anti-slip re-adhesion control strategy of electric locomotive based on distributed MPC," in *Proc. IEEE 21st Int. Conf. High Perform. Comput. Commun. IEEE 17th Int. Conf. Smart City, IEEE 5th Int. Conf. Data Sci. Syst. (HPCC/SmartCity/DSS)*, Aug. 2019, pp. 2708–2713.

[30] A. Zirek and A. Onat, "A novel anti-slip control approach for railway vehicles with traction based on adhesion estimation with swarm intelligence," *Railway Eng. Sci.*, vol. 28, no. 4, pp. 346–364, 2020.

[31] T. Fridrichovský and B. Šulc, "Investigation of torsional oscillations in railway vehicles," in *Proc. MATEC Web Conf.*, vol. 76, 2016, Art. no. 02052.

[32] H. Wu, P. Wu, K. Xu, J. Li, and F. Li, "Research on vibration characteristics and stress analysis of gearbox housing in high-speed trains," *IEEE Access*, vol. 7, pp. 102508–102518, 2019.

[33] M. Bruha and Z. Peroutka, "Torsional vibration in large variable speed drive systems: Origin and mitigation methods," in *Proc. 17th Eur. Conf. Power Electron. Appl. (EPE ECCE-Eur.)*, Sep. 2015, pp. 1–10.

[34] J. Pacas, A. John, and T. Eutebach, "Automatic identification and damping of torsional vibrations in high-dynamic-drives," in *Proc. IEEE Int. Symp. Ind. Electron. (ISIE)*, vol. 1, Dec. 2000, pp. 201–206.

[35] S. N. Vukosavic and M. R. Stojic, "Suppression of torsional oscillations in a high-performance speed servo drive," *IEEE Trans. Ind. Electron.*, vol. 45, no. 1, pp. 108–117, Feb. 1998.

[36] K.-K. Shyu and C.-Y. Chang, "Modified FIR filter with phase compensation technique to feedforward active noise controller design," *IEEE Trans. Ind. Electron.*, vol. 47, no. 2, pp. 444–453, Apr. 2000.

[37] L. Litwin, "FIR and IIR digital filters," *IEEE Potentials*, vol. 19, no. 4, pp. 28–31, Oct. 2000.

[38] T. Ohmae, T. Matsuda, M. Kanno, K. Saito, and T. Sukegawa, "A microprocessor-based motor speed regulator using fast-response state observer for reduction of torsional vibration," *IEEE Trans. Ind. Appl.*, vol. IA-23, no. 5, pp. 863–871, Sep. 1987.

[39] Y. Hori, H. Iseki, and K. Sugiura, "Basic consideration of vibration suppression and disturbance rejection control of multi-inertia system using SFLAC (state feedback and load acceleration control)," *IEEE Trans. Ind. Appl.*, vol. 30, no. 4, pp. 889–896, Jul./Aug. 1994.

[40] K. Sugiura and Y. Hori, "Vibration suppression in 2-and 3-mass system based on the feedback of imperfect derivative of the estimated torsional torque," *IEEE Trans. Ind. Electron.*, vol. 43, no. 1, pp. 56–64, Feb. 1996.

[41] M. Neshati, T. Jersch, and J. Wenske, "Model based active damping of drive train torsional oscillations for a full-scale wind turbine nacelle test rig," in *Proc. Amer. Control Conf. (ACC)*, Jul. 2016, pp. 2283–2288.

[42] J.-K. Ji and S.-K. Sul, "Kalman filter and LQ based speed controller for torsional vibration suppression in a 2-mass motor drive system," *IEEE Trans. Ind. Electron.*, vol. 42, no. 6, pp. 564–571, Dec. 1995.

[43] E. Omine, T. Goya, U. Akie, T. Senjyu, A. Yona, N. Urasaki, and T. Funabashi, "Torsional torque suppression of decentralized generators using h∞ observer," *Renew. Energy*, vol. 35, no. 9, pp. 1908–1913, 2010.

[44] Y. Wang, Q. Zheng, H. Zhang, and M. Chen, "The LQG/LTR control method for turboshaft engine with variable rotor speed based on torsional vibration suppression," *J. Low Freq. Noise, Vibrat. Act. Control*, vol. 39, no. 4, pp. 1145–1158, 2020.

[45] T. Hirotsu, S. KASAI, and H. TAKAI, "Self-excited vibration during slippage of parallel cardan drives for electric railcars: Vibration, control engineering, engineering for industry," *JSME Int. J.*, vol. 30, no. 266, pp. 1304–1310, 1987.

[46] M. Lata, "The modern wheelset drive system and possibilities of modelling the torsion dynamics," *Transport*, vol. 23, no. 2, pp. 172–181, 2008.

[47] R. Konowrocki and T. Szolc, "An analysis of the self-excited torsional vibrations of the electromechanical drive system," *Vib. Phys. Syst.*, vol. 27, pp. 187–194, 2016.

[48] K. Xu, J. Zeng, and L. Wei, "An analysis of the self-excited torsional vibration of high-speed train drive system," *J. Mech. Sci. Technol.*, vol. 33, no. 3, pp. 1149–1158, 2019.

[49] T. Mei, J. Yu, and D. Wilson, "A mechatronic approach for anti-slip control in railway traction," *IFAC Proc. Volumes*, vol. 41, no. 2, pp. 8275–8280, 2008.

[50] M. Fleischer and K. Kondo, "Slip-stick vibration suppression by modal state control for traction drive-trains," *IEEJ J. Ind. Appl.*, vol. 5, no. 1, pp. 1–9, 2016.

[51] M. Fleischer, R. W. De Doncker, and D. Abel, "Traction control for railway vehicles," Institut für Stromrichtertechnik und Elektrische Antriebe, Aachen Univ., Aachen, Germany, 2019, vol. 128.

[52] R. Teichmann and S. Bernet, "A comparison of three-level converters versus two-level converters for low-voltage drives, traction, and utility applications," *IEEE Trans. Ind. Appl.*, vol. 41, no. 3, pp. 855–865, May 2005.

[53] A. F. Abouzeid, J. M. Guerrero, A. Endemano, I. Muniategui, D. Ortega, I. Larrazabal, and F. Briz, "Control strategies for induction motors in railway traction applications," *Energies*, vol. 13, no. 3, p. 700, 2020.

[54] H. J. Schwartz, *Regelung Der Radsatzdrehzahl Zur Maximalen Kraftschlussausnutzung Bei Elektrischen Triebfahrzeugen*. Düsseldorf, Germany: VDI-Verlag, 1992.

[55] F. Trimpe, S. Lück, R. Naumann, and C. Salander, "Simulation of torsional vibration of driven railway wheelsets respecting the drive control response on the vibration excitation in the wheel-rail contact point," *Vibration*, vol. 4, no. 1, pp. 30–48, 2021. [Online]. Available: https://www.mdpi.com/2571-631X/4/1/3

[56] R. Chattopadhyay, A. De, and S. Bhattacharya, "Comparison of PR controller and damped pr controller for grid current control of LCL filter based grid-tied inverter under frequency variation and grid distortion," in *Proc. IEEE Energy Convers. Congr. Expo. (ECCE)*, Sep. 2014, pp. 3634–3641.

[57] F. Briz, J. Cancelas, and A. Diez, "Speed measurement using rotary encoders for high performance ac drives," in *Proc. 20th Annu. Conf. IEEE Ind. Electron. (IECON)*, vol. 1, Sep. 1994, pp. 538–542.

[58] Y. Li, F. Gu, G. Harris, A. Ball, N. Bennett, and K. Travis, "The measurement of instantaneous angular speed," *Mech. Syst. Signal Process.*, vol. 19, no. 4, pp. 786–805, 2005.

[59] *Lenord + Bauer.Speed Sensors & Rotary Pulse Encoders: Rail Speed Sensor Gel 2477*. Accessed: Feb. 14, 2022. [Online]. Available: https://www.sensorprod.com/lenord/speed-sensor-gel-2477.php

[60] F. Trimpe and C. Salander, "Wheel-rail adhesion during torsional vibration of driven railway wheelsets," *Vehicle Syst. Dyn.*, vol. 59, no. 5, pp. 785–799, 2021.

[61] J. Böcker and O. Buchholz, "Can oversampling improve the dynamics of PWM controls?" in *Proc. IEEE Int. Conf. Ind. Technol. (ICIT)*, Feb. 2013, pp. 1818–1824.

[62] M.-W. Naouar, E. Monmasson, A. A. Naassani, I. Slama-Belkhodja, and N. Patin, "FPGA-based current controllers for ac machine drives—A review," *IEEE Trans. Ind. Electron.*, vol. 54, no. 4, pp. 1907–1925, Jul. 2007.

[63] E. Monmasson, L. Idkhajine, and M. W. Naouar, "FPGA-based controllers," *IEEE Ind. Electron. Mag.*, vol. 5, no. 1, pp. 14–26, Mar. 2011.

AHMED FATHY ABOUZEID (Member, IEEE) received the B.S. and M.S. degrees in electrical engineering from Port Said University, Port Said, Egypt, in 2012 and 2017, respectively. He is currently pursuing the Ph.D. degree with the Department of Electrical, Electronic and Computer Engineering, University of Oviedo, Gijón, Spain. In 2013, he joined the Department of Electrical Engineering, Port Said University, as a Teaching Assistant. He is on leave with the Department of Electrical Engineering as an Assistant Lecturer. He is partially supported by the Scholarship from the Ministry of Higher Education and Scientific Research of Egypt. His research interests include power converters and ac drives, electric traction, and renewable energy systems.

JUAN M. GUERRERO (Senior Member, IEEE) received the M.E. degree in industrial engineering and the Ph.D. degree in electrical and electronic engineering from the University of Oviedo, Gijón, Spain, in 1998 and 2003, respectively. Since 1999, he has been occupied different teaching and research positions with the Department of Electrical, Computer and Systems Engineering, University of Oviedo, where he is currently an Associate Professor. From February 2002 to October 2002, he was a Visiting Scholar at the University of Wisconsin, Madison. From June 2007 to December 2007, he was a Visiting Professor at Tennessee Technological University, Cookeville. His research interests include control of electric drives and power converters, electric traction, and renewable energy generation. He is an Associate Editor of the IEEE Transactions on Industry Applications.

IBAN VICENTE-MAKAZAGA graduated in electrical engineering from the University of Mondragon, Mondragon, Spain, in 2003, and the M.S. and Ph.D. degrees from The University of Manchester, U.K., in 2004 and 2009, respectively. He joined Ingeteam Power Technology (formerly TEAM), Zamudio, Spain, where he currently works as a Control and Regulation Engineer involved in railway traction control for trams, locomotives, and EMU-s. His current research interests include power converter and advanced control drives, modulation techniques, machine parameters, speed estimation techniques, and railway research issues, such as AC catenary stability and mechanical vibrations in the drive-train.

IKER MUNIATEGUI-ASPIAZU received the Industrial Technical Engineering degree (electronic design specialty) and the Industrial Automatics and Electronics Engineering degree from the University of Mondragon, Mondragon, Spain, in 2004 and 2007, respectively. In September 2006, he joined Ingeteam Power Technology (formerly TEAM), Zamudio, Spain, where he worked as a Control and Regulation Engineer and he is currently a Control and Regulation Manager of the Traction Department. His current research interests include power converter and advanced control drives, modulation techniques, and railway research issues, such as AC catenary stability and mechanical vibrations in the drive-train.
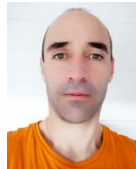
AITOR ENDEMAÑO-ISASI received the Industrial Technical Engineering degree (electronic design specialty) and the Industrial Automatics and Electronics Engineering degree from the University of Mondragon, Mondragon, Spain, in 1997 and 2000, respectively, and the Ph.D. degree from Heriot-Watt University, Edinburgh, U.K., in 2003. In 2003, he joined the Traction Department, Ingeteam Power Technology (formerly TEAM), Zamudio, Spain, where he has been a Control and Regulation Engineer (since then), involved in several traction control design projects for trams, locomotives, and EMU-s. His current research interests include power converter and advanced control drives, modulation techniques, and railway research issues, such as AC catenary stability and mechanical vibrations in the drive-train.

FERNANDO BRIZ (Senior Member, IEEE) received the M.S. and Ph.D. degrees from the University of Oviedo, Gijón, Spain, in 1990 and 1996, respectively. He is currently a Full Professor with the Department of Electrical, Computer and Systems Engineering, University of Oviedo. His research interests include electronic power converters and ac drives, power systems, machine monitoring and diagnostics, and digital signal processing. He is a member of the Executive Board of ECCE. He was a recipient of the IEEE Transactions on Industry Applications Award and the nine IEEE Industry Applications Society Conference and IEEE Energy Conversion Congress and Exposition Prize Paper Awards. He is the Chair of the Industrial Power Conversion System Department (IPCSD) of the IAS. He is the Past Chair of the Industrial Drives Committee of IPCSD. He has served for scientific committees and as the Vice Chair or the Technical Program Chair for several conferences, including ECCE, IEMDC, ICEM, ICEMS, and SLED. He is the Deputy Editor-in-Chief and a member of the Steering Committee of IEEE Journal of Emerging and Selected Topics in Power Electronics. He is an Associate Editor of IEEE Transactions on Industry Applications.

• • •

231

B.1.4 Control Strategies for Induction Motors in Railway Traction Applications

energies

Review

Control Strategies for Induction Motors in Railway Traction Applications

Ahmed Fathy Abouzeid [1], **Juan Manuel Guerrero [1]**, **Aitor Endemaño [2]**, **Iker Muniategui [2]**, **David Ortega [2]**, **Igor Larrazabal [2]** and **Fernando Briz [1,*]**

[1] Electrical, Electronic, Computers and Systems Engineering, University of Oviedo, 3204 Oviedo, Spain; abouzeidahmed@uniovi.es (A.F.A.); guerrero@uniovi.es (J.M.G.)

[2] Ingeteam Power Technology S.A.—Traction, 48170 Zamudio, Spain; aitor.endemano@ingeteam.com (A.E.); iker.muniategui@ingeteam.com (I.M.); David.Ortega@ingeteam.com (D.O.); igor.larrazabal@ingeteam.com (I.L.)

* Correspondence: fbriz@uniovi.es

check for updates

Abstract: This paper analyzes control strategies for induction motors in railway applications. The paper will focus on drives operating with a low switching to fundamental frequency ratio and in the overmodulation region or six-step operation, as these are the most challenging cases. Modulation methods, efficient modes of operation of the drive and the implications for its dynamic performance, and machine design will also be discussed. Extensive simulation results, as well as experimental results, obtained from a railway traction drive, are provided.

Keywords: railway traction drives; induction motor drives; high-speed drives; maximum torque per ampere; overmodulation and six-step operation

1. Introduction

Despite being one of the most energy-efficient means for mass transportation (see Figure 1) [1], there is pressure to develop a more efficient, reliable, cheap, and compact railway traction system, which should be achieved without compromising customer satisfaction.
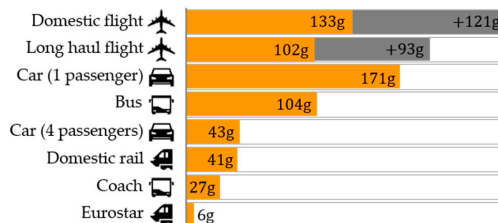
Figure 1. Emissions per passenger per km from different modes of transport. From the UK Department for Business, Energy and Industrial Strategy 2019 Government Greenhouse Gas Conversion Factors [1].

Three-phase induction motors (IMs) were adopted in the 1990s for traction systems in railways replacing DC machines [2] due to their increased robustness and reduced cost and maintenance requirements. In addition, precise control of the IM torque/speed is perfectly possible thanks to the development of new power devices and digital signal processors, combined with the advances in AC-driven control methods. Furthermore, the inherent slip of IM allows multiple motors to be fed from a single inverter, even if they rotate at different speeds due to differences in wheel diameters. As a

result, the voltage-source inverter-fed IM drive (VSI-IM) is currently the preferred option in traction systems for railways [3]. While Permanent Magnet Synchronous Machines (PMSM) have also been considered and can be found in several traction systems, cost and reliability concerns intrinsic to this type of machine, mainly due to magnets, have so far prevented their widespread use [4].

Rolling stock can be classified according to the power level of the traction system, ranging from several tens of kW for Light Rail systems, to several MW for High-Speed Trains (HST) and Heavy Rail Locomotives [5]. Traction systems can be concentrated or distributed. In concentrated systems, one or more locomotives pull unmotorized coaches. On the contrary, distributed traction systems use Electric Multiple Units (EMU), i.e., self-propelled carriages. Both options have advantages and disadvantages. EMUs can provide a superior performance in terms of the acceleration and deceleration times, adhesion effort, and transport capacity. However, passenger comfort, maintenance, and pantograph operation can be compromised in this case [6,7]. For the case of HST, European manufacturers have predominantly adopted the concentrated traction option, while the distributed option has been preferred by Japanese manufacturers [8].

The two main elements in a traction system are the electric motor and the inverter. The development of a cost-effective traction system for a given application involves a complex, iterative process to decide the number of traction motors, motor size, inverter rated power, cooling system, etc. Once the physical elements of the traction system have been defined, the control and modulation strategies need to be defined. Additionally, in this case, a complex iterative process can be required as the traction system must comply with a number of requirements. These include those imposed by the desired train performance (e.g., torque-speed characteristic, maximum torque and speed, acceleration/deceleration times, etc.), electric drive performance (e.g., machine and inverter efficiency, temperature limits, maximum torque ripple, etc.), existing standards (e.g., electromagnetic interference, acoustic noise, etc.), and so on. However, these targets will often be in conflict. The reduction of inverter losses requires low switching frequencies, which in turn result in higher losses and large torque pulsations in the motor, and can also compromise the dynamic response or even the stability of the drive. Especially challenging is the operation of the traction drive at high speeds. The large back-electromotive force, in this case, forces the inverter to operate in the overmodulation region, including square-wave modes. The control operates in this case with a reduced (or even no) voltage margin and large distortions in the currents, which can further deteriorate the drive performance.

Figure 2 shows a schematic representation of the main blocks involved in the operation of a traction drive. The drive will normally receive a torque command coming from outer control loops (e.g., the train driver or speed control loop). From the torque command and in the operating condition of the machine, a flux command is derived; different criteria can be followed for this purpose, as shown in Figure 2. Torque and flux are controlled by the inner control loops; a number of solutions are available for this purpose. Inner control loops will provide the voltage command to the Voltage Source Inverter (VSI) feeding the machine, with selection of the modulation method being of the highest importance.
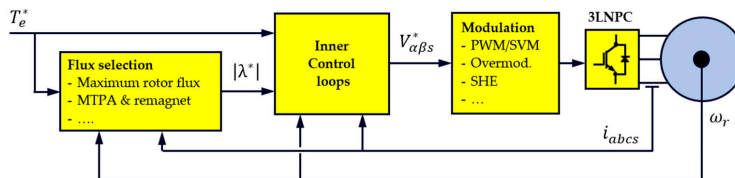
Figure 2. Main blocks of a traction drive.

This paper presents a review of the different aspects involved in the control of IM motor drives for railway applications. Section 2 reviews the IM motor model, including a discussion on the machine characteristics. Section 3 discusses control strategies, with a special focus on their suitability for use

234

at high speed and low switching frequencies, as this is the most frequent and challenging mode of operation for traction drives. Modulation is discussed in Section 4. Section 5 discusses efficient modes of operation and remagnetization strategies. Sections 6 and 7 provide simulation and experimental results, respectively. Section 8 summarizes the conclusions.

2. Induction Motor Model and Machine Characteristics

2.1. Induction Motor Model

Complex vectors allow a compact, insightful dynamic representation of the physical effects occurring in AC machines, i.e., the relationships among electromagnetic variables (voltages, currents, and fluxes) and shaft variables (torque and speed) [9]. Equations (1)–(4) show the electromagnetic complex vector equations describing the squirrel cage induction machine in a synchronous reference frame rotating at the flux angular frequency ω_e, where v_{dqs} denotes the stator voltage; i_{dqs} and i_{dqr} are the stator and rotor currents, respectively; λ_{dqs} and λ_{dqr} represent the stator and rotor fluxes, respectively; R_s and R_r are the stator and rotor resistances, respectively; L_s, L_r, and L_m are the stator, rotor, and mutual inductances, respectively; ω_r is the rotor angular speed in electrical units; and p is the derivative operator.

$$v_{dqs} = R_s i_{dqs} + p\lambda_{dqs} + j\omega_e \lambda_{dqs} \tag{1}$$

$$0 = R_r i_{dqr} + p\lambda_{dqr} + j(\omega_e - \omega_r)\lambda_{dqr} \tag{2}$$

$$\lambda_{dqs} = L_s i_{dqs} + L_m i_{dqr} \tag{3}$$

$$\lambda_{dqr} = L_m i_{dqs} + L_r i_{dqr} \tag{4}$$

The electromagnetic torque T_e can be expressed as the cross product of stator and rotor currents (5). P is the number of pole-pairs, and "*Im*" and "‡" denote the imaginary part and complex conjugate, respectively.

$$T_e = \frac{3}{2} P L_m Im\left\{i_{dqs} i_{dqr}^{\ddagger}\right\} \tag{5}$$

Equations (1)–(4) can be particularized for the case when the d-axis is aligned with the rotor flux, i.e., $\lambda_{dqr} = \lambda_{dr} = \lambda_r$, which is the base of rotor field-oriented control (RFOC). The stator voltage equation in scalar form is, in this case (6), the rotor flux dynamics being given by (7), where τ_r is the rotor time constant and σ is the leakage factor.

$$\left.\begin{array}{l} v_{ds} = R_s i_{ds} + \sigma L_s p i_{ds} - \omega_e \sigma L_s i_{qs} + \frac{L_m}{L_r} p \lambda_r \\ v_{qs} = R_s i_{qs} + \sigma L_s p i_{qs} + \omega_e \sigma L_s i_{ds} + \omega_e \frac{L_m}{L_r} \lambda_r \end{array}\right\} \tag{6}$$

$$\tau_r \frac{d\lambda_r}{dt} + \lambda_r = L_m i_{ds} \; ; \; \tau_r = \frac{L_r}{R_r} \; ; \; \sigma = 1 - \frac{L_m^2}{L_s L_r} \tag{7}$$

The torque Equation (5) can be rewritten as (8) in this case. Other forms of the torque equation can be obtained by combining (2)–(4) and (5) and will be the basis of different control strategies, as will be discussed in further sections.

$$T_e = \frac{3}{2} P \frac{L_m}{L_r} \lambda_r i_{qs} \tag{8}$$

2.2. Machine Characteristics

Traction drives commonly receive a torque command from an outer control loop, which is responsible for speed control. The maximum torque that can be produced at a given speed will essentially depend on the current limits of the machine and power converter (due to losses) and on the maximum flux, which is limited by saturation and the available DC link voltage. For most IM designs, the maximum voltage and field weakening occur at the same speed, i.e., field weakening is a direct consequence of reaching the voltage limit. This is shown schematically in Figure 3 (continuous line case). For rotor speeds $\omega_r < \omega_1$, the machine operates with a rated flux and current, with the voltage increasing proportionally to the rotor speed, mainly due to the back-emf. If $\omega_r > \omega_1$, the flux, and consequently torque, must be decreased. The current (Figure 3b) can still be maintained at its rated value until the machine enters field-weakening region II (not shown in the figure) [10]. Therefore, for the machine denoted as conventional in Figure 3, region ① corresponds to a constant torque operation, while regions ②+③ have constant power.
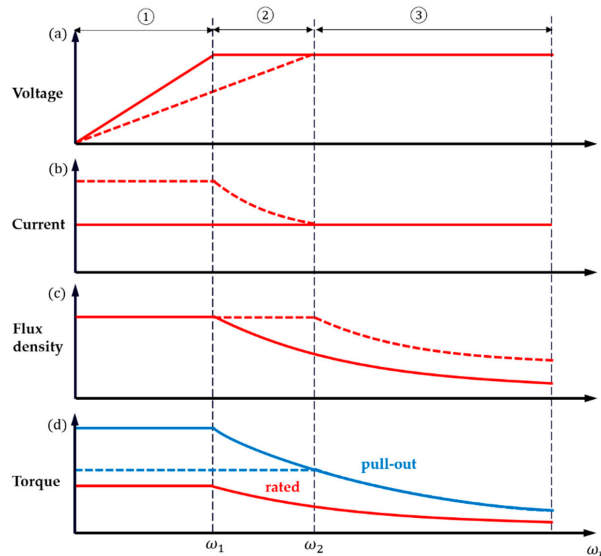
Figure 3. Conventional (−) and extended full flux range (--) induction motor (IM) design behavior: **(a)** Stator voltage magnitude; **(b)** Stator current magnitude; **(c)** Flux density; **(d)** Electromagnetic torque (rated&pull-out). Both machines are designed to provide the same torque vs. speed characteristic and have the same voltage limit.

IM designs for railway traction are often aimed at reducing the size of the machine, which can be desirable or even imperative due to room constraints. For this purpose, the voltage characteristic of the conventional design in Figure 3 can be modified by rewinding the stator, varying the number of turns, and gauging the wire [10,11]. If the modification is made such that $N_2 < N_1$, with N_1 and N_2 being the number of turns for the conventional and modified designs, respectively, and the active conductor area in each stator slot remaining unchanged, i.e., $N_1 \cdot S_1 = N_2 \cdot S_2$, and S_1 and S_2 being the area of the conductor for the conventional and modified designs, respectively, both machines should be able to produce the same amount of torque, as the total current circulating within the stator slots and the rest of the machine dimensions are the same in both cases [11]. Since the number of turns has been reduced, the voltage vs. speed characteristic is also modified. As seen in Figure 3a (dashed line), for $\omega_r = \omega_1$,

the machine is far from its voltage limit. It can also be observed that for $\omega_r < \omega_1$, the current of the modified machine design is N_1/N_2 larger than for the conventional design. This does not imply an increase of joule losses, as the wire in the modified design is thicker, and the current density is the same in both cases. Since, at $\omega_r = \omega_1$, the modified machine operates well below its voltage limit, there is no need to decrease the flux at this point; instead, the nominal air gap flux density can be maintained until $\omega_r = \omega_2$ (region ② in Figure 3), i.e., the full flux range is extended. The fact that the flux weakening region is reduced while the torque characteristic remains unchanged enables a reduction of the stator current for $\omega_r > \omega_1$, as can be readily deduced from (8). Consequently, assuming that the dimensions of the machine do not change, the extended full flux range design in Figure 3 would allow a significant decrease of the current density in regions ② and ③ (i.e., at high train speeds) and consequently of Joule losses, i.e., would be more efficient compared to the conventional design.

However, the design with an extended full flux range offers other possibilities. The torque of an IM can be written as (9), where V_{rotor} is the active volume of the rotor, J is the stator surface current density, B is the air gap flux density, $\varnothing$ is the angle between J and B vectors, and k_1 is a constant which depends on the machine winding design [11].

$$T_e = k_1 \cdot V_{rotor} \cdot J \cdot B \cdot \cos(\varnothing) \tag{9}$$

As the extended full flux range design provides higher flux densities at high speeds and the current density J remains constant, it is possible to reduce the volume of the rotor, and consequently the size of the machine, without affecting the torque production capability, i.e., the extended full flux design in Figure 3 will be smaller.

It must be noted, however, that redesigning the machine brings drawbacks that must also be considered. First, the size of the inverter is increased, as the current that the semiconductors must handle is increased by a factor of N_1/N_2, while the voltage and power remain unaffected. However, this penalty is not so relevant nowadays thanks to the latest developments in power devices [10]. Second, the pull-out torque in the low-speed region is significantly decreased, as shown in Figure 3d [11], which must be considered to guarantee that the machine meets the application requirements.

3. Overview of Control Methods for Three-Phase Induction Machines

This section discusses control strategies for IMs in railway applications. The drives must be able to perform properly from zero to relatively high rotational frequencies. On the other hand, the switching frequencies are often limited to several hundred Hz due to the switching losses of high-power semiconductor devices. At low rotational frequencies, the switching to fundamental frequency ratio is still relatively large and the inverter will operate far from its voltage limit. On the contrary, operation at high speeds is characterized by a reduced switching to fundamental frequency ratio and a reduced (or even inexistent) voltage margin in the inverter. Due to this, both control and modulation strategies are often dynamically modified, depending on the IM speed. The following discussion will primarily focus on the most challenging high-speed case.

Control methods for IMs can be classified into scalar and vector types, as shown in Figure 4. Scalar methods are derived from the machine equivalent circuit in a steady-state. Consequently, they can operate properly in applications in which fast changes in the operating conditions of the machine (torque, speed, flux, . . .) are not required. On the contrary, vector control methods are based on the dynamic equations of the machine, which, combined with proper control loops, allow the machine's torque capabilities to be fully exploited, without surpassing machine or power converter limits. Both types of methods are briefly discussed in the following. It must be noted, however, that the borderline between scalar- and vector-based methods is sometimes blurred, as there have been several proposals to enhance the dynamic response of scalar methods by adding control loops based on dynamic models.

Figure 4. Control methods for IMs.

3.1. Scalar-Based Control

3.1.1. Open-loop V/F

Open-loop V/F varies the stator voltage magnitude proportional to the frequency. This results in an (almost) constant flux. While simple, V/F control has some relevant limitations. The rotor speed is not precisely controlled due to slip. Additionally, an incorrect voltage to frequency ratio, voltage drop in the stator resistance, variations of the DC link voltage feeding the inverter, etc., will result in incorrect flux levels, eventually modifying the operating point of the machine from the desired value.

3.1.2. V/F with Feedback Control

Closed-loop speed control with slip regulation (Figure 5) has been widely used in IM traction drives [12]. Speed error generates the slip command ω_{sl}^* through a Proportional-Integrator (PI) controller, which, when added to the measured speed, provides the angular frequency of the stator voltage ω_e^*.
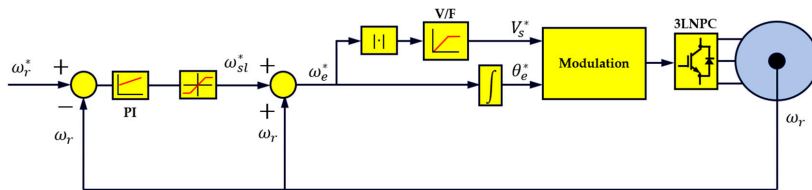
Figure 5. V/F with speed control scheme.

Flux and torque control loops can be used instead of the V/F ratio to obtain the desired stator voltage magnitude and angle (Figure 6). Torque and flux can be estimated from the (commanded) stator voltages and the (measured) stator currents using the voltage model (10); "^" indicates estimated variables/parameters. The pure integrator in (10) is replaced in practice by a first-order system to avoid the drift problems derived from the integrator infinite gain at DC [13]. The torque is obtained using (11).

$$\hat{\lambda}_{\alpha\beta s} = \int \left(V_{\alpha\beta s}^* - \hat{R}_s i_{\alpha\beta s} \right) dt \tag{10}$$

$$\hat{T}_e = \frac{3}{2} P \left(\hat{\lambda}_{\alpha s} i_{\beta s} - \hat{\lambda}_{\beta s} i_{\alpha s} \right) \tag{11}$$

Figure 6. Torque-flux scalar control scheme.

The methods in Figures 5 and 6 are relatively simple to implement, with the second enabling precise control of the machine's operating point in a steady-state. A further advantage of scalar methods is that operation near or at the inverter voltage limit is relatively easy to achieve. However, the fact that coupling between flux and torque is not considered for the control design requires a very slow dynamic response to avoid over currents and torque pulsations.

3.1.3. Torque/Flux Scalar Control with Feedforward

The dynamic response of the closed-loop V/F control scheme in Figure 6 can be enhanced by adding two feedforward terms, as can be seen in Figure 7. The first uses the desired V/F characteristic to provide the base value of the stator voltage magnitude $V_{s\_vf}^*$, with the rotor flux regulator providing the incremental voltage required to track the desired rotor flux with no error. The second provides the base value for the slip $\omega_{sl\_ff}^*$, which is obtained from the desired torque and the estimated rotor flux using (12). The torque regulator corrects the slip so that the desired torque is followed with no error.

$$\omega_{sl\_ff}^* = \frac{2}{3}\frac{1}{P}\frac{\hat{R}_r}{\left|\hat{\lambda}_r\right|^2}T_e^* \tag{12}$$

Figure 7. Closed-loop V/F with torque/flux control (CLVFC) scheme.

Due to the fact that the voltage command magnitude and phase angle are independently controlled, flux and torque controllers must be tuned for relatively low bandwidths. A dynamic response eventually

relies on the accuracy of the feedforward terms. As for the scheme in Figure 6, the scheme in Figure 7 can easily operate in the field-weakening region, including that of six-step.

An alternative approach for the implementation of the feedforward action is to use the machine *d-q* model in the rotor flux reference frame. The desired d- and q-axis currents are first obtained from the commanded torque and rotor flux using (7) and (8) (see Figure 8). The d- and q-axis stator voltages required to achieve the desired currents are the middle terms in (13), which are obtained from (6).

$$
\left.
\begin{aligned}
v^*_{ds\_ff} &= \hat{R}_s i^*_{ds} + \hat{o}\hat{L}_s p i^*_{ds} - \omega^*_e \hat{o}\hat{L}_s i^*_{qs} + \frac{\hat{L}_m}{\hat{L}_r} p \lambda^*_{dr} \cong -\omega^*_e \hat{o}\hat{L}_s i^*_{qs} \\
v^*_{qs\_ff} &= \hat{R}_s i^*_{qs} + \hat{o}\hat{L}_s p i^*_{qs} + \omega^*_e \hat{o}\hat{L}_s i^*_{ds} + \omega^*_e \frac{\hat{L}_m}{\hat{L}_r} \lambda^*_{dr} \cong \omega^*_e \hat{o}\hat{L}_s i^*_{ds} + \omega^*_e \frac{\hat{L}_m}{\hat{L}_r} \lambda^*_{dr}
\end{aligned}
\right\}
\tag{13}
$$

Figure 8. Closed loop V/F with torque/flux control and feedforward (CLVFC&FF) scheme.

Ideally, (13) will produce the voltage needed to obtain the desired torque and rotor flux with no error. However, there are a number of issues to consider. Mismatch between model and actual parameters must be expected and will produce errors in the feedforward voltages. In addition, (13) includes derivatives which are problematic in practice. It is noted, however, that the signals affected by the derivative (13) are (clean) commanded variables, i.e., do not involve (noisy) measured variables. Furthermore, the torque derivative will be limited by the application, meaning that the derivative of q-axis current and flux commands will be limited too. Finally, the terms depending on the stator resistance will have a reduced weight considering that the control is only intended to operate at a high speed. Based on the previous considerations, the feedforward voltage can be safely simplified to form the right hand of (13). The resulting block diagram is shown in Figure 8, with the feedforward term being either the complete or simplified voltage equation in (13).

3.2. Vector-Based Control

Vector control methods are aimed at directly manipulating the IM fields and torque. These methods are based on well-known *d-q* models. Field-Oriented Control (FOC) represents flux and torque as a function of stator currents in a synchronous reference frame, with high-bandwidth current regulators being used to provide the voltage command to the inverter. Alternatively, Direct Torque Control (DTC) methods implement torque and flux controllers which directly provide the IGBT gate signals for the inverter, i.e., without the explicit control of stator currents.

3.2.1. Rotor Field-Oriented Control (RFOC)

RFOC (see Figure 9) is one of the most popular options for the high-performance control of IM drives [14,15], although its discussion is beyond the scope of this paper. RFOC is often used in HST at relatively low speeds, the inverter operates in the linear region and with an adequate switching to fundamental frequency ratio. However, its use at high speeds presents multiple problems, including the lack of a voltage margin in the inverter for proper operation of the current regulator, distortions in the currents due to overmodulation, and delays intrinsic to the reduced switching frequency. The modification of RFOC to enable operation at the voltage limit was discussed in [16].
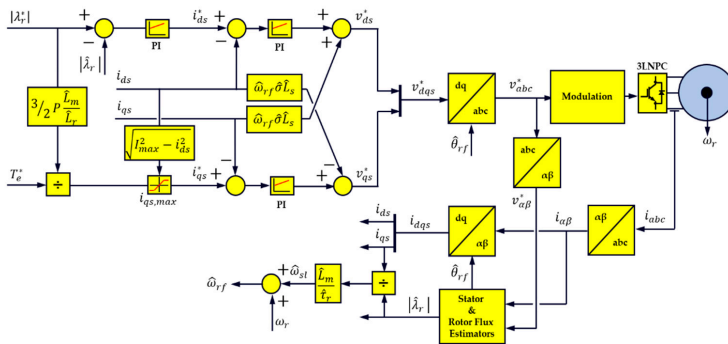
Figure 9. Rotor field-oriented control (RFOC) scheme.

3.2.2. Direct Flux Vector Control (DFVC)

DFVC [17] is a stator-flux-oriented control approach. By writing the voltage Equation (1) in stator flux, reference frame (14) can be obtained. It can be observed from (14) that the stator flux variation can be regulated through the d-axis voltage, and the torque is then controlled through the q-axis current (15), with a current regulator being used for this purpose. The DFVC scheme is shown in Figure 10.

$$\left.\begin{array}{l} v_{ds} = \hat{R}_s i_{ds} + p\hat{\lambda}_{ds} \\ v_{qs} = \hat{R}_s i_{qs} + \hat{\omega}_{sf}\hat{\lambda}_{ds} \end{array}\right\} \tag{14}$$

$$T_e = \frac{3}{2}P\hat{\lambda}_{ds}i_{qs} \tag{15}$$

Stator flux $\alpha\beta$-components are estimated from the voltage-model-based flux estimator. The synchronous frequency can be obtained from the estimated stator flux and back-emf (16) [18], avoiding the use of stator flux angle derivative and time-consuming trigonometric functions.

$$\hat{\omega}_{sf} = p\hat{\theta}_{sf} = \frac{d}{dt}\left[tan^{-1}\left(\frac{\hat{\lambda}_{\beta s}}{\hat{\lambda}_{\alpha s}}\right)\right] = \frac{\hat{\lambda}_{\alpha s}\cdot\hat{e}_{\beta s} - \hat{\lambda}_{\beta s}\cdot\hat{e}_{\alpha s}}{|\hat{\lambda}_s|^2} \tag{16}$$

At low speeds, DFVC can operate either with rated stator flux or a maximum torque per ampere (MTPA) strategy to improve the efficiency. Above the base speed, flux is reduced according to (17), where V_{max} is the maximum output voltage of the inverter, which depends on the available DC-link voltage and the modulation method. Operation in overmodulation is feasible, but a voltage margin must be preserved for proper operation of the q-axis current regulator, meaning that operation with a maximum output voltage (i.e., six-step) is not possible. Furthermore, operation in overmodulation

forces a reduction of the current regulator bandwidth to mitigate the effects of the resulting current harmonics in this case. Therefore, current regulator gains may need to be adapted with machine speeds.

$$\lambda_s^* \leq \frac{V_{max} - \hat{R}_s i_{qs}}{|\hat{\omega}_{sf}|} \tag{17}$$

It is finally noted that Figure 10 includes a mechanism to limit the torque angle δ between the stator and rotor fluxes so that it is smaller than the pull-out torque angle of $\delta = 45$ electrical degrees [17].

Figure 10. Direct Flux Vector Control (DFVC) scheme.

3.2.3. Direct Torque Control (DTC)

IM torque can be expressed as (18), with δ being the torque angle. DTC methods control torque by controlling the stator flux magnitude and angle with respect to rotor flux. Stator flux is controlled through the stator voltage (19) (stator resistance neglected), with V_s being the inverter output voltage vector.

$$T_e = \frac{L_m}{\sigma L_s L_r} \lambda_s \lambda_r sin(\delta) \tag{18}$$

$$\lambda_s = \int V_s dt \tag{19}$$

Switching-Table-Based (ST-DTC) was introduced by Takahashi and Noguchi [19] in the mid-1980s. Two hysteresis controllers are used to control the stator flux and torque directly. The hysteresis control signals are sent to a look-up table to select the voltage vectors required to achieve high dynamics (see Figure 11). The fact that the switching frequency is not defined and operation in overmodulation and six-step is not straightforward makes this method inadequate for high-power railway drives [20].

Direct-Self Control (DSC) was proposed by Depenbrock [21] for high-power drives. Three hysteresis controllers determine the voltage applied to the machine by comparing a flux magnitude command with the estimated flux for each phase, and a two-level hysteresis torque controller determines the amount of zero voltage (see Figure 12). DSC produces a hexagonal stator flux trajectory, which enables a smooth transition into overmodulation and eventually six-step. However, hexagonal flux trajectories make DSC problematic below ≈30% of the base speed, and remedial actions can be found in [22,23].

Figure 11. Switching-Table-Based Direct Torque Control (ST-DTC) scheme.

Figure 12. Direct-Self Control (DSC) scheme.

Several modifications have been proposed to overcome the limitations of DTC methods [24]. DTC with a constant switching frequency calculates the required stator voltage vector over a sampling period to achieve the desired torque and stator flux. The voltage vector is synthesized using Space-Vector Modulation (SVM), and these methods are often referred to as DTC-SVM. In the implementation in Figure 13, a PI controls the torque through the torque angle [25]. The stator flux angle is obtained from the estimated rotor flux angle and the commanded torque angle. The stator voltage vector command $V_{\alpha\beta s}^*$ employed to cancel the stator flux error $\Delta\lambda_{\alpha\beta s}^*$ at the end of the next sampling period Δt is obtained as:

$$V_{\alpha\beta s}^* = \frac{\Delta\lambda_{\alpha\beta s}^*}{\Delta t} + \hat{R}_s i_{\alpha\beta s}. \tag{20}$$
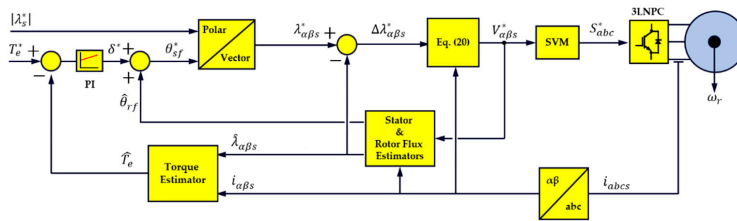
Figure 13. Direct-Torque Control Space-Vector Modulation (DTC-SVM) block diagram.

The scheme in Figure 13 is easy to implement and retains the fast dynamics of DTC if the inverter operates in the linear region. However, voltage distortions intrinsic to overmodulation can result in magnitude and phase deviations of the actual stator flux vector, leading to instability problems. Furthermore, (20) effectively cancels the flux error for relatively small values of Δt, but can result in large steady-state errors in the case of low switching frequencies. DTC-SVM suffers from the same limitation as ST-DTC when operating in overmodulation and six-step, which raises concerns on their use for high-power, high-speed railway traction drives. A predictive term for mitigating the stator flux delay and extending the operation to six-step was proposed in [26]. However, this was at the price of a significant complexity increase.

3.3. Control Strategies Summary

Table 1 summarizes the main conclusions for the control methods discussed in this section, including controlled variables and the easiness of operation at low speeds, overmodulation (high speed), and the transition to six-step. Regarding the dynamic response, it is important to note that the torque ramp is normally limited in railway traction. Consequently, not only the maximum dynamic response (e.g., the minimum time required to respond to a step-like torque command) is relevant, but also the capability of the drive to meet the maximum torque ramp requested by the application, especially when the machine operates at a high speed in the field-weakening region. CLVFC, CLVFC&FF, DFVC, and DTC-SVM have been selected as a representative subset of the methods in Table 1, and their behavior will be analyzed by means of simulation in Section 6.

Table 1. Summary of the presented control schemes for traction applications.

Properties/ Performance	V/Hz with Feedback			FOC		DTC		
	V/Hz (Figure 5)	CLVFC (Figure 7)	CLVFC&FF (Figure 8)	RFOC (Figure 9)	DFVC (Figure 10)	DTC (Figure 11)	DSC (Figure 12)	DTC-SVM (Figure 13)
Reference frame	λ_r	λ_r	λ_r	λ_r	λ_s	SRF.	SRF	λ_r
Controlled variables	ω_r [†]	$\lambda_r; T_e$	$\lambda_r; T_e$	$\lambda_r \& i_{ds}; i_{qs}$	$\lambda_s; i_{qs}$	$\lambda_s; T_e$	$\lambda_s; T_e$	$\lambda_s; T_e$
Defined switching frequency	Yes	Yes	Yes	Yes	Yes	No	No	Yes
Low speed (linear mod.)	✔	✔	✔	✔	✔	✗	✗	✔
High speed (overmodulation)	✔	✔	✔	—	—	✗	✔	✗
Six-step operation	✔	✔	✔	✗	✗	✗	✔	✗
Dynamic response [††]	✗/✗	✗/—	—/✔	✔/—	✔/—	✔/✗	✔/✔	✔/✗

✔: favorable; —: neutral; ✗: unfavorable; "SRF" stands for stationary reference frame. [†]: Implementation of an outer speed control loop for the rest of the methods is straightforward. [††]: (1) maximum torque dynamic response/ (2) capability to provide 3 kNm/s in the overmodulation region.

4. Modulation Techniques

High-power traction drives usually operate with low switching frequencies (<1 kHz) to reduce switching losses. This results in significant current and consequently torque ripples, which can have implications for mechanical transmission stress, train comfort, standards compliance, etc. Trading-off switching losses and torque pulsations is a challenge for the selection of modulation methods. Furthermore, modulation and control strategies often change with the output frequency. Figure 14 shows an example of this [27]. Asynchronous Pulse-Width Modulation (PWM) is used at low speeds, changing to synchronous modulation with Selective Harmonic Elimination (SHE) and finally single pulse modes as the speed increases. The three options are briefly described in the following, and are particularized for a three-level Neutral-Point-Clamped (3L-NPC) scheme [28], as this is the configuration used in this project.
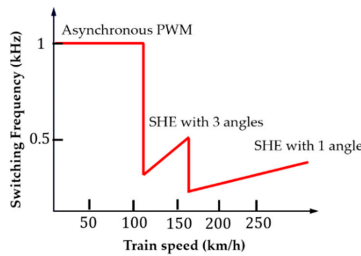
Figure 14. Modulation technique vs. train speed for a High-Speed Train (HST).

4.1. Asynchronous Modulation

Carrier-Based Pulse-Width Modulation (PWM) or Space-Vector Modulation (SVM) can be used at low speeds. The first compares the reference voltages V^*_{abc} with two carriers, as shown in Figure 15a. A level-shifted carrier is normally preferred as it results in a lower voltage harmonic content [28]. A common-mode (homopolar) voltage should be added to fully use the available DC link voltage. Space-Vector Modulation (SVM) for three-level inverters shares the same basic principles as that for two-level inverters, but 24 active voltage and three zero vectors are available. The implementation of SVM is shown in Figure 15b. It typically consists of three steps: (1) sector identification, (2) region identification, and (3) the selection of an appropriate switching sequence. Redundant states are used to balance DC link capacitor voltages. SVM offers the same DC voltage utilization as the PWM with a homopolar voltage, and it has a larger computational burden, but makes better use of the redundant states [29,30].

(a)   (b)
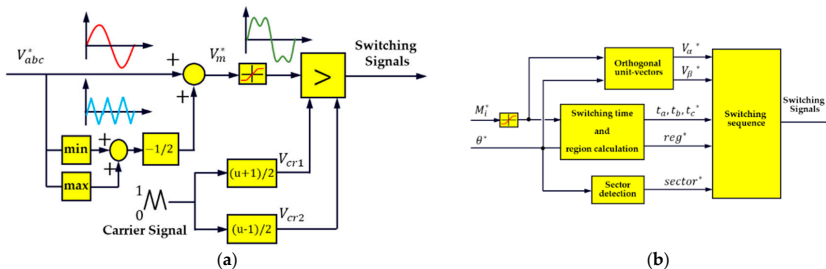
Figure 15. Asynchronous modulation techniques: (**a**) Pulse-Width Modulation (PWM) with triple harmonic injection; (**b**) Space-Vector Modulation (SVM).

4.2. Synchronous Modulation—Selective Harmonic Elimination (SHE)

SHE performs a predefined number of commutations per quarter of the fundamental cycle. Commutations are synchronized with the fundamental wave. Commutation angles are pre-calculated via Fourier analysis [31], with the aim of eliminating specific harmonics of the output voltage. An example of SHE with three switching angles is shown in Figure 16a. With three angles, it is possible to cancel two harmonics of the output voltage (typically the 5th and 7th), in addition to controlling the magnitude of the fundamental voltage. As the speed increases, SHE changes to one pulse mode (Figure 16b) to reduce switching losses. SHE implementation is schematically shown in Figure 16c.
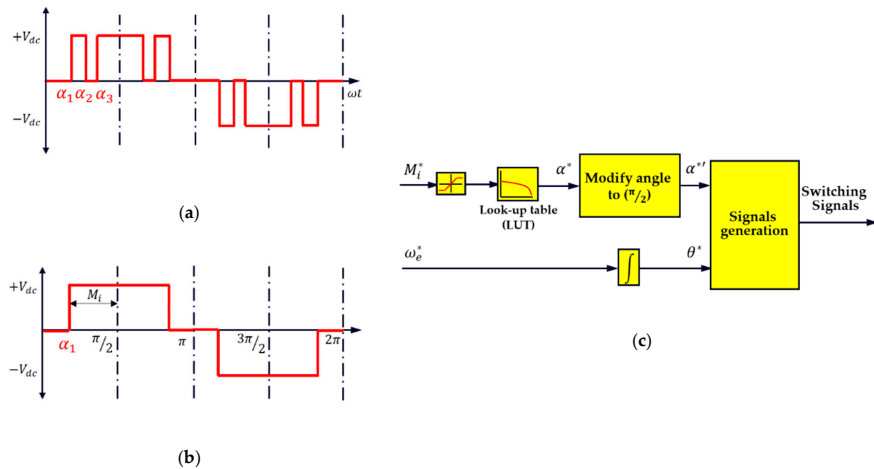
Figure 16. Selective Harmonic Elimination (SHE) for three-level Neutral-Point-Clamped (3L-NPC): (**a**) Phase voltage for the case of three switching angles; (**b**) phase voltage for the case of one switching angle; (**c**) Selective Harmonic Elimination (SHE) block diagram.

5. Operation with Reduced Flux and Remagnetization Strategies

Electric drives in high-speed traction applications can work for certain periods of time with light loads. It is possible in this case to decrease the flux level to reduce the stator current and consequently Joule losses, which is commonly termed MTPA [32]. However, operating with reduced flux levels will penalize the dynamic response of the drive. If a torque increase is demanded, the machine must be remagnetized first. The remagnetization time is determined by the rotor time constant (7) and applied magnetizing current. Due to the relatively large values of the rotor time constant, fast torque changes of torque are not feasible. It must be noted, however, that fast torque changes are not desirable for traction applications, as they might exert stress on the mechanical transmission, produce wheel slip, and raise comfort concerns. The maximum torque-allowed gradient will depend on the application. For the machine considered in this paper, it has a value of 3 kNm/s.

Figure 17 shows two possible remagnetization strategies. RFOC principles are used for the discussion. It is noted, however, that equivalent strategies can be used with other control methods by simply transforming *d-q* axis current commands into other commands, e.g., stator flux and slip.

(**a**) Profile 1: step-like d-axis, ramp-like q axis   (**b**) Profile 2: 3kNm/s torque ramp, minimum current
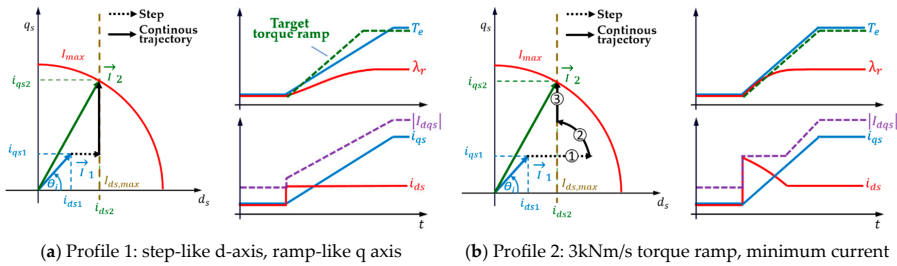
Figure 17. Remagnetization (**a**) using the rated d-axis current and (**b**) target torque gradient. Left: Current trajectories in the *d-q* plane; right: torque, rotor flux, and current trajectories vs. time.

The strategy in Figure 14a uses a step-like d-axis current command. While simple, this results in a slow remagnetization, with the 3 kNm/s target not being achieved. The option in Figure 14b is derived from the method described in [33] and is aimed at providing a target torque ramp with the smallest possible current during the remagnetization process. This reduces the stress in the power devices and the risk of surpassing their current limit. This strategy will be used for the simulation results in the next section.

6. Simulation Results

Selected control methods from Section 3 have been evaluated by means of simulation using MATLAB/Simulink. IM parameters for the base speed are given in Table 2. The simulation model implements asynchronous SVM with a switching frequency of 1 kHz at low speeds and SHE at high speeds, as shown in Figure 14.

Table 2. Specifications of the induction motor at base speed ω_{base} (extended full flux range design).

Variable	Value	Unit
DC-link voltage	3600	V
Rated Power	1084	kW
Rated Voltage (L-L, rms)	2727	V
Pole-pairs (P)	2	Pole
Stator resistance (R_s)	55.38	mΩ
Stator inductance (L_s)	26.45	mH
Torque	3241	Nm
Speed	3194	rpm

Since the main focus of this paper is high-speed operation, only results at high speed using SHE are provided in this section. Infinite inertia is assumed. Consequently, the rotor speed remained constant throughout the simulation. This assumption is realistic and has no effect on the conclusions. Profile 2 in Figure 17b was used during remagnetization. The maximum torque ramp was limited to 3 kNm/s, which was imposed by the application. Simulation results are shown in Figure 18.

The most remarkable difference is the slowest transient response of CLVFC due to dynamic limitations intrinsic to scalar control. The dynamic response is seen to improve and be comparable to the other methods when the feedforward defined by (13) is used (CLVFC&FF in Figure 18b).

DFVC and DTC-SVM are seen to provide similar dynamic responses to CLVFC&FF. Regarding DFVC, it must be noted that to achieve proper operation in the overmodulation region, the q-axis current regulator bandwidth was reduced in the range of ten times to avoid a current regulator reaction to low-order current harmonics due to the non-linear operation of the inverter. The need to dynamically adapt the gains of the current regulator in the high-speed region is an obvious concern.

It can be observed that DTC-SVM suffers from a steady-state error in the controlled flux due to the low sampling frequency (Δt) when SHE is used in the inverter. This results in an increase in the load angle. This could lead to overcurrent or instability if the load angle is not monitored.

Figure 19 summarizes the performance in a steady state for the four control methods, i.e., once the machine is providing its maximum torque. The steady-state error in the flux for DTC-SVM is seen to affect the modulation index and slip. This will eventually affect the machine loss distribution, which is a concern as traction motors can be required to operate close to their thermal limit. CLVFC and CLVFC&FF are seen to have a higher torque error compared to DFVC, but with little impact on the modulation index and slip. It is noted that a torque error in the range of 1% is perfectly assumable.

Figure 18. Simulation results of using (**a**) CLVFC, (**b**) CLVFC&FF, (**c**) DFVC, and (**d**) DTC-SVM control methods with SHE. Rotor speed $\omega_r = 1.328\omega_{base}$; torque was increased from 10% (i.e., with the machine operating with reduced flux in MTPA) to 100%. From top to bottom: commanded and actual torque; d- and q-axis currents; commanded and estimated flux (can be stator or rotor flux, depending on the method); and output voltage magnitude. All the variables are shown in p.u.
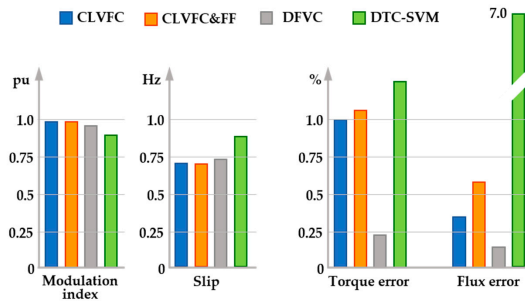
Figure 19. From left to right: modulation index, slip, torque error, and error in the flux being controlled for the four control methods being considered, once the machine has reached a steady state, i.e., is its maximum torque. Torque and slip have been low-pass filtered to eliminate the harmonic content produced by SHE modulation.

It can be concluded that CLVFC&FF is more adequate compared to the simulated schemes at high speeds due to its high dynamics, and the controllers are not affected by low-order harmonics resulting from a square-wave operation, i.e., six-step, as in the case of DFVC, and are simple to implement.

7. Experimental Results

A schematic diagram of the high-power traction system test bench is shown in Figure 20a. It consists of two identical IMs and converters connected back-to-back, which are supplied from a High-Voltage (HV) DC power supply. The power converter module (see Figure 20b) consists of a three-phase, three-level Neutral-Point Clamped (NPC) inverter feeding the IMs. Single-phase inverters feed auxiliary loads, such as cooling systems, control power supply units, etc. A DC-DC chopper is implemented for dissipative braking and DC bus overvoltage protection. A specially designed traction transformer is used to filter off catenary harmonics and allow the interconnection of the different converters. A 100 Hz (2f) filter is included in the DC bus. The overall experimental test rig is shown in Figure 20c.
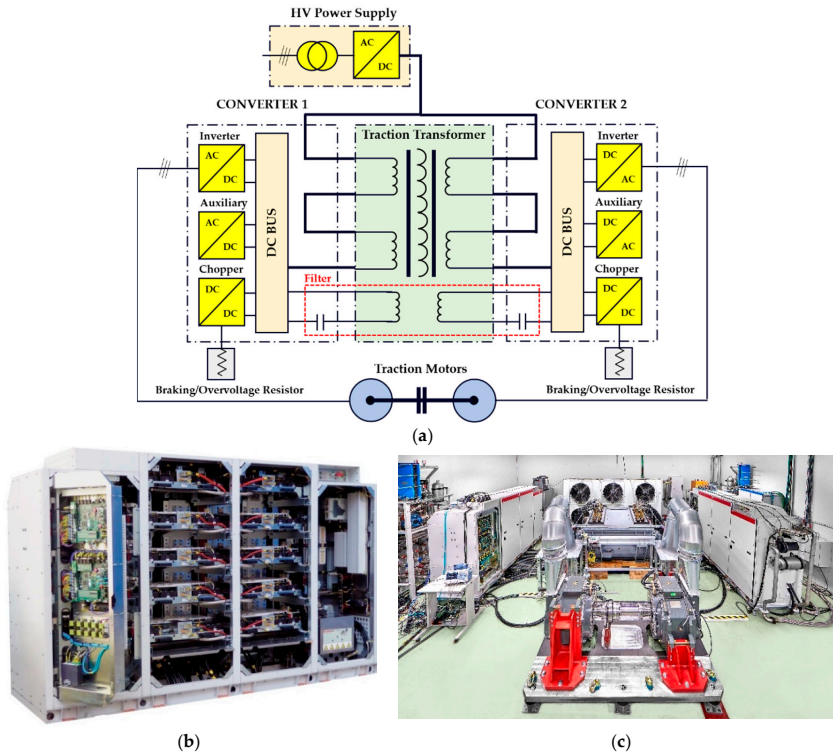
Figure 20. High-power traction test bench: (**a**) Schematic diagram; (**b**) power converter module (INGETRAC); and (**c**) overall view of the laboratory setup.

Preliminary experimental results for a full-scale HS traction drive are presented in the following. The control uses RFOC at low speeds and CLVFC at high speeds. The main system parameters are the same as those used in the simulation shown in Table 2. The torque-flux characteristic of the motor is of the type named as the extended full flux range in Figure 3.

Figure 21a shows the rotor speed, modulation index, commanded and estimated torques, estimated rotor flux, and magnitude of the stator current vector during an acceleration (left) and deceleration (right) process. Figure 21b shows the spectrogram of the stator current vector. For $\omega_r < 0.12$ p.u., RFOC-SVM with a switching frequency of 850 Hz is used; the switching frequency increases to 1 kHz for $0.12 < \omega_r < 0.94$ p.u. For $\omega_r > 0.94$ p.u., CLVFC combined with SHE with one switching angle is used. Changes in the modulation method are readily observable in the spectrogram of Figure 21b, and are aim to trade-off switching losses and torque ripple. The control is seen to precisely follow the commanded torque and rotor flux in the whole speed range. It is noted that the changes in the estimated rotor flux observed in the flux-weakening region respond to changes in the corresponding command (not shown in the figure). Transitions between the different control and modulation strategies can be a challenge due to the high power and low switching frequencies. However, as can be observed from Figure 21, such transitions are satisfactory, i.e., the spikes observed in the currents are perfectly acceptable and do not represent a risk for the power devices. Implementation of the other control methods and remagnetization strategies discussed in Sections 3 and 6 is ongoing.
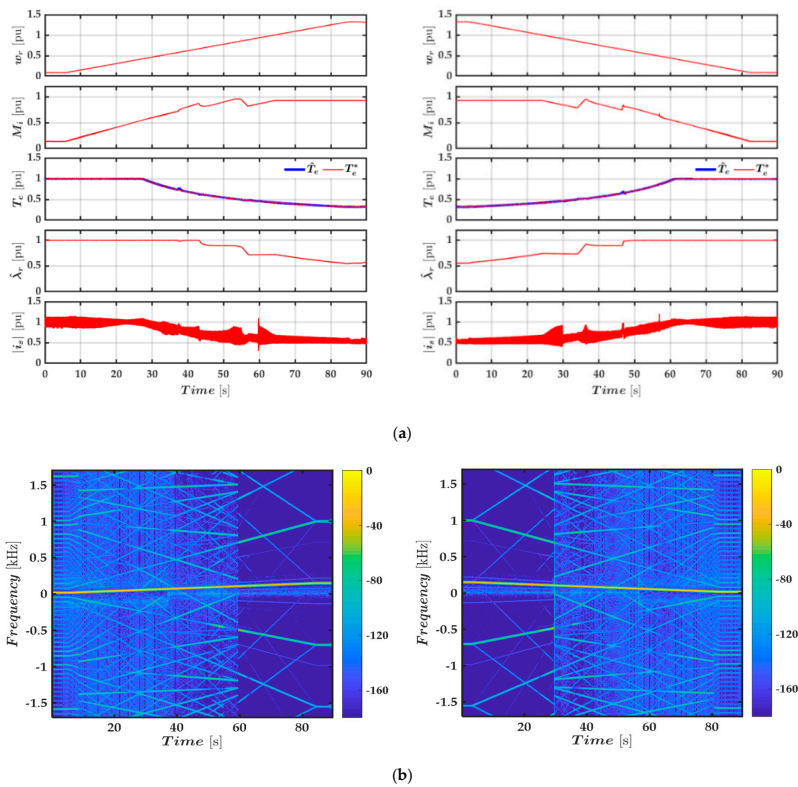
Figure 21. Experimental results. Acceleration (left)-deceleration (right) tests between $\omega_r = 0.1$ and $\omega_r = 1.328$ p.u. (**a**) From top to bottom: rotor speed, modulation index, commanded and estimated torques, estimated rotor flux, and magnitude of the stator current vector; (**b**) stator current vector spectrogram.

8. Conclusions

In this paper, a comparative analysis of scalar and vector control strategies for railway traction applications has been presented, with a special focus on their operation at high speeds.

HSTs normally use medium-voltage, high-power IMs. Rotor flux Oriented Control (RFOC) has been widely adopted at low and medium speeds. However, high fundamental frequencies intrinsic to high-speed operations, combined with the need to reduce inverter losses, force the inverter to operate with reduced switching frequencies and a high modulation index or even at the six-step limit. These limitations seriously compromise the performance of RFOC at high speeds. A common practice is to use RFOC at low speeds, rather than switch to strategies able to perform properly under severe voltage constraints at high speeds.

Methods considered for the analysis included different types of Closed-loop Voltage/Frequency (V/F), Field-Oriented Control (FOC), and Direct-Torque Control (DTC) strategies. Four different control strategies have been selected and tested by means of simulation, namely, Closed Loop V/F with flux/torque Control (CLVFC), CLVFC with feedforward (CLVFC&FF), Direct Flux Vector Control (DFVC), and Direct-Torque Control Space-Vector Modulation (DTC-SVM). The modulation methods that have been considered are PWM/SVM, SHE, and six-step. Their advantages include the easiness

of operation with a high modulation index, including six-step; switching frequency; and dynamic response to both torque change demands and rotor flux change demands during remagntization.

The CLVFC&FF method described in Section 3.1.3 and the remagnetization strategy discussed in Section 5 are the original contributions of this paper.

It was concluded from the simulation results that CLVFC, CLVFC&FF, and DFVC provide similar performances. However, DFVC requires a modification of the q-axis current controller gains when the drive enters the overmodulation region. Specifically, CLVFC&FF proposed in this paper operates properly with a high modulation index, including six-step, and provides a good dynamic response during remagnetization.

Preliminary experimental results using CLVFC in a full-scale traction drive have been provided, which are in good agreement with the simulation results, and confirm the viability of this strategy. Implementation of the other strategies, including remagnetization, is ongoing.

Author Contributions: Conceptualization, F.B. and D.O.; methodology, F.B., J.M.G. and D.O.; formal analysis, A.F.A., J.M.G. and F.B.; simulation and programing, A.F.A., A.E. and I.M.; validation, A.F.A., A.E. and I.M.; writing—original draft preparation, A.F.A.; writing—review and editing F.B. and J.M.G.; supervision, F.B., D.O. and I.L.; All authors have read and agreed to the published version of the manuscript.

Conflicts of Interest: The authors declare no conflict of interest.

References

1. Nikolas Hill, E.K. *2019 Government Greenhouse Gas Conversion Factors for Company Reporting: Methodology Paper for Emission Factors Final*; Government UK: London, UK, 2019.
2. Hill, R.J. Electric railway traction. Part 2: Traction drives with three-phase induction motors. *Power Eng. J.* **1994**, *8*, 143–152. [CrossRef]
3. El-Refaie, A.M. Motors/generators for traction/propulsion applications: A review. *IEEE Veh. Technol. Mag.* **2013**, *8*, 90–99. [CrossRef]
4. Buyukdegirmenci, V.T.; Bazzi, A.M.; Krein, P.T. Evaluation of induction and permanent-magnet synchronous machines using drive-cycle energy and loss minimization in traction applications. *IEEE Trans. Ind. Appl.* **2014**, *50*, 395–403. [CrossRef]
5. Ronanki, D.; Singh, S.A.; Williamson, S.S. Comprehensive Topological Overview of Rolling Stock Architectures and Recent Trends in Electric Railway Traction Systems. *IEEE Trans. Transp. Electrif.* **2017**, *3*, 724–738. [CrossRef]
6. McGean, T.J. Developing IEEE rail transit vehicle standards. In Proceedings of the 1998 ASME/IEEE Joint Railroad Conference, Philadelphia, PA, USA, 16 April 1998; pp. 95–105.
7. Drofenik, U.; Canales, F. European trends and technologies in traction. In Proceedings of the 2014 International Power Electronics Conference IPEC-Hiroshima—ECCE Asia, Hiroshima, Japan, 18–21 May 2014; pp. 1043–1049.
8. Sato, K.; Yoshizawa, M.; Fukushima, T. Traction systems using power electronics for Shinkansen High-speed Electric Multiple Units. In Proceedings of the 2010 International Power Electronics Conference IPEC—ECCE Asia, Sapporo, Japan, 21–24 June 2010; pp. 2859–2866.
9. Krause, P.C.; Thomas, C.H. Simulation of Symmetrical Induction Machinery. *IEEE Trans. Power Appar. Syst.* **1965**, *84*, 1038–1053. [CrossRef]
10. Ikeda, R.; Yusya, S.; Kondo, K. Study on Design Method for Increasing Power Density of Induction Motors for Electric Railway Vehicle Traction. In Proceedings of the 2019 IEEE International Electric Machines & Drives Conference (IEMDC), San Diego, CA, USA, 12–15 May 2019; pp. 1545–1550.
11. Buhrkall, L. Traction System Case Study. In Proceedings of the 2008 IET Professional Development Course on Electric Traction Systems, Manchester, UK, 3–7 November 2008; pp. 45–63.
12. Bose, B.K. *Modern Power Electronics and AC Drives*; Prentice-Hall, Inc.: Upper Saddle River, NJ, USA, 2002.

13. Holtz, J. Sensorless control of induction machines—With or without signal injection? *IEEE Trans. Ind. Electron.* **2006**, *53*, 7–30. [CrossRef]

14. Blaschke, F. The principle of field orientation as applied to the new TRANSVECTOR closed loop control system for rotating field machines. *J. Chem. Inf. Model.* **1972**, *34*, 217–220.

15. Kubota, H.; Matsuse, K. Speed sensorless field-oriented control of induction motor with rotor resistance adaptation. *IEEE Trans. Ind. Appl.* **1994**, *30*, 1219–1224. [CrossRef]

16. Kwon, Y.-C.; Kim, S.; Sul, S.-K. Six-Step Operation of PMSM With Instantaneous Current Control. *IEEE Trans. Ind. Appl.* **2014**, *50*, 2614–2625. [CrossRef]

17. Pellegrino, G.; Bojoi, R.I.; Guglielmi, P. Unified direct-flux vector control for AC motor drives. *IEEE Trans. Ind. Appl.* **2011**, *47*, 2093–2102. [CrossRef]

18. Novotny, D.W. Implementation of Direct Stator Flux Orientation Control on a Versatile dsp Based System. *IEEE Trans. Ind. Appl.* **1991**, *27*, 694–700.

19. Takahashi, I.; Noguchi, T. A New Quick-Response and High-Efficiency Control Strategy of an Induction Motor. *IEEE Trans. Ind. Appl.* **1986**, *IA-22*, 820–827. [CrossRef]

20. Casadei, D.; Serra, G.; Stefani, A.; Tani, A.; Zarri, L. DTC drives for wide speed range applications using a robust flux-weakening algorithm. *IEEE Trans. Ind. Electron.* **2007**, *54*, 2451–2461. [CrossRef]

21. Depenbrock, M. Direct self-control (DSC) of inverter fed induktion machine. In Proceedings of the 1987 IEEE Power Electronics Specialists Conference, Blacksburg, VA, USA, 21–26 June 1987; pp. 632–641.

22. Steimel, A. Direct self-control and synchronous pulse techniques for high-power traction inverters in comparison. *IEEE Trans. Ind. Electron.* **2004**, *51*, 810–820. [CrossRef]

23. Spichartz, M.; Heising, C.; Staudt, V.; Steimel, A. Indirect Stator-Quantities Control as Benchmark for Highly Dynamic Induction Machine Control in the Full Operating Range. In Proceedings of the 14th International Power Electronics and Motion Control Conference EPE-PEMC, Ohrid, Macedonia, 6–8 September 2010; pp. T3–T13.

24. Buja, G.S.; Kazmierkowski, M.P. Direct Torque Control of PWM Inverter-Fed AC Motors—A Survey. *IEEE Trans. Ind. Electron.* **2004**, *51*, 744–757. [CrossRef]

25. Rodríguez, J.; Pontt, J.; Silva, C.; Kouro, S.; Miranda, H. A novel direct torque control scheme for induction machines with space vector modulation. In Proceedings of the 2004 IEEE 35th Annual Power Electronics Specialists Conference (IEEE Cat. No.04CH37551), Aachen, Germany, 20–25 June 2004; Volume 2, pp. 1392–1397.

26. Tripathi, A.; Khambadkone, A.M.; Panda, S.K. Stator flux based space-vector modulation and closed loop control of the stator flux vector in overmodulation into six-step mode. *IEEE Trans. Power Electron.* **2004**, *19*, 775–782. [CrossRef]

27. Yano, M.; Iwahori, M. Transition from Slip-Frequency Control to Vector Control for Induction Motor Drives of Traction Applications in Japan. In Proceedings of the Fifth International Conference on Power Electronics and Drive Systems, Singapore, 17–20 November 2003; pp. 1246–1251.

28. Rodriguez, J.; Bernet, S.; Steimer, P.K.; Lizama, I.E. A survey on neutral-point-clamped inverters. *IEEE Trans. Ind. Electron.* **2010**, *57*, 2219–2230. [CrossRef]

29. Wang, F. Sine-triangle versus space-vector modulation for three-level PWM voltage-source inverters. *IEEE Trans. Ind. Appl.* **2002**, *38*, 500–506. [CrossRef]

30. Attique, Q.M. A Survey on Space-Vector Pulse Width Modulation for Multilevel Inverters. *CPSS Trans. Power Electron. Appl.* **2017**, *2*, 226–236. [CrossRef]

31. Al-Hitmi, M.; Ahmad, S.; Iqbal, A.; Padmanaban, S.; Ashraf, I. Selective harmonic elimination in awide modulation range using modified Newton-raphson and pattern generation methods for a multilevel inverter. *Energies* **2018**, *11*, 458. [CrossRef]

32. Wasynczuk, O.; Sudhoff, S.D.; Corzine, K.A.; Tichenor, J.L.; Krause, P.C.; Hansen, I.G.; Taylor, L.M. A maximum torque per ampere control strategy for induction motor drives. *IEEE Trans. Energy Convers.* **1998**, *13*, 163–169. [CrossRef]

33. Popov, A.; Lapshina, V.; Briz, F.; Gulyaev, I. Estimation of the Required Voltage for Improved MTPA Algorithm. In Proceedings of the 2018 X International Conference Electrical Power Drive Systems (ICEPDS), Novocherkassk, Russia, 3–8 October 2018; pp. 1–4.

B.2 Conference publications

B.2.1 Remagnetization Strategies for Induction Machines Operating with Reduced Flux Levels

Remagnetization Strategies for Induction Machines Operating with Reduced Flux Levels

Ahmed F. Abouzeid, *Student Member, IEEE* , Juan M. Guerrero, *Senior Member, IEEE*, Iban Vicente, Iker Muniategui, Aitor Endemaño, and Fernando Briz, *Senior Member, IEEE*

Abstract—**Induction Machines (IMs) drives are the preferred option for high-speed railway traction drives. Electric drives in this application can work for certain periods of time with light load levels. It is possible in this case to decrease the flux level to reduce the stator current and consequently both joule and hysteresis losses. A drawback of this approach is that if a torque increase is demanded, the machine must be firstly remagnetized. Remagnetization time is determined by the rotor time constant and the applied magnetizing current. Due to the relatively large values of the rotor time constant, fast torque changes are not feasible, which eventually penalizes the dynamic response of the drive. This paper presents strategies for the remagnetization of Induction Machines. Though proposed methods are primarily intended for railways traction, they can be easily extended to other uses of IM drives.**

Index Terms—**Induction Machines; Field-Oriented Control; Scalar Control; Maximum-Torque-Per-Ampere (MTPA); Re-magnetization.**

I. INTRODUCTION

TRACTION electrification gained more attention in recent years due to fuel costs and environmental concerns. Thanks to the continuous development of renewable energy conversion systems and power electronic converters, the electric traction drive systems (ETDS) have been drastically improved [1]. Efficiency, performance, torque and power densities are the key aspects of ETDSs. Compromising these aspects over a wide speed range is a challenging task. This can be achieved either by traction machine type, electric drive control, or a combination of both [2]. Permanent-magnet (PM) synchronous machines are widely used for traction applications due to their high efficiency, high torque, and high power densities [3]. However, cost and rare-earth material availability are the main limitations of PMs [4]. Induction machines (IMs), besides being robust with fewer maintenance

Ahmed Fathy Abouzeid is with the Department of Electrical, Electronic and Computer Engineering, University of Oviedo, Gijón, Spain (e-mail: abouzeidahmed@uniovi.es). He is on leave with the Department of Electrical Engineering, Port-Said University, Egypt (e-mail: ahmed_abouzeid@eng.psu.edu.eg).

Iban Vicente, Iker Muniategui, Aitor Endemaño are with the Department of Traction systems, Ingeteam Power Technology, Zamudio, Spain (e-mail: iban.vicente@ingeteam.com; iker.muniategui@ingeteam.com; aitor.endemano@ingeteam.com).

Juan Manuel Guerrero and Fernando Briz are with the Department of Electrical, Electronic and Computer Engineering, University of Oviedo, Gijón, Spain (e-mail: guerrero@uniovi.es; fbriz@uniovi.es).

requirements, are considered the promising alternative of PMs in traction applications [5]. Rewinding the machine combined with optimized control techniques of the electric drive, IMs can achieve comparable performance to PMs [6], [7]. Furthermore, for specific applications like traction, the overall efficiency of the IM operating at partial load can be improved by reducing the air gap flux level [8].

IMs control optimization techniques objective may include minimization of total losses, maximization of power transfer and/or maximization of torque production [9], [10]. Optimal efficiency control or also called loss minimization control aims to select the appropriate machines' flux level minimizing the joule and hysteresis losses of the machine [11]. Maximum-Torque-per-Ampere (MTPA) method aims to optimally select the flux and torque producing components of machines' stator current to achieve maximum torque with minimum losses considering inverter voltage limits [12]. Similarly, Maximum-Torque-per-Voltage (MTPV) method is used to fulfill the optimization criteria taking into consideration both inverter voltage and current constraints [10].

Regardless of the optimization technique used, the IM operates at a reduced flux level during light loads. Hence, at any instant, if the load torque is increased, the machine flux has to be re-established (i.e. remagnetized) quickly for producing the required torque. While the aforementioned optimization techniques are intended for steady-state operation, an additional approach should be imposed to control the transient dynamics. Few attempts have been made for improving the transient response and minimizing the machine's losses during flux remagnetization. In [13], an optimal dynamic current sharing algorithm is proposed to mitigate machine speed drops for sudden torque increases while the machine is initially operating at reduced flux. Alternative power loss minimization techniques using model predictive control in transient states of speed controller machines are presented in [14], [15]. In [16], different stator current sharing techniques have been proposed for improving the dynamic response of the IM, however, the proposed methods were intended for Field Oriented Control (FOC) schemes.

In this paper, the problem of operating the IM with reduced flux will be addressed. In addition, different flux remagnetization strategies considering the dynamic response and inverter limits will be proposed. The proposed strategy generates the optimum torque and flux trajectories that meet the application requirements and it can be used for vector and scalar control schemes.

II. MODELLING, OPERATING REGIONS AND CONTROL OF INDUCTION MACHINES

A. IM model using complex vector notation

Complex vectors are a powerful tool for the modeling of three-phase symmetric ac machines [17]. The sinusoidal variation of mutual inductances with respect to the rotor angle is eliminated by transforming the electrical variables of stator and rotor to a common reference frame. This frame can be either fixed to the stator or rotated with the electromagnetic quantities of the machine, being denoted as stationary and synchronous reference frames respectively [18]. In this paper, rotor-flux field-orientation (RFOC) will be used as it allows decoupled control of rotor flux and torque [19].

Stator voltage equation in a rotor-flux reference frame is given by (1), where σL_s is the stator transient inductance, R'_s is stator transient resistance and τ_r is the rotor time constant (2); R_s and R_r are the stator and rotor resistances, respectively; L_s, L_r, and L_m are the stator, rotor, and mutual inductances, respectively; ω_e is the rotor flux angular frequency; ω_r is the rotor angular frequency.

Rotor flux and torque equations for the IM in the rotor-flux reference frame are given by (3)-(4), with P being the number of pole-pairs. The slip frequency ω_{slip} is given by (5), the rotor flux angular frequency ω_e and angle θ_e being obtained as shown in (6).

$$v_{dqs} = \sigma L_s \frac{di_{dqs}}{dt} + \left(R'_s + \sigma L_s j\omega_e\right) i_{dqs} - \frac{L_m}{L_r}\left(\frac{1}{\tau_r} - j\omega_r\right)\lambda_r \tag{1}$$

$$\sigma = 1 - \frac{L_m^2}{L_s L_r}; \ \ R'_s = R_s + \left(\frac{L_m}{L_r}\right)^2 R_r; \ \ \tau_r = \frac{L_r}{R_r} \tag{2}$$

$$\frac{d\lambda_r}{dt}\tau_r + \lambda_r = L_m i_{ds} \tag{3}$$

$$T_e = \frac{3}{2}P\frac{L_m}{L_r}\lambda_{dr}i_{qs} \tag{4}$$

$$\omega_{slip} = \frac{L_m}{\tau_r \lambda_r}i_{qs} \tag{5}$$

$$\omega_e = \omega_r + \omega_{slip}; \quad \theta_e = \int \omega_e dt \tag{6}$$

B. Regions of operation of the IM

Fig. 1 shows the operating regions of IMs considering that torque reduction and field weakening occur at the same frequency at which the inverter reaches its voltage limit. The full range of operation is considered: 1) MTPA; 2) rated flux; 3) field weakening region I, and 4) field weakening region II. Transitions from region 2) to 3) and from region 3) to 4) are the result of voltage constraints. In segment 4-5 the machine operates with MTPV operation. The behavior and constraints of the machine in steady-state are defined by the stator voltage equation (7) (determined by dc-link voltage V_{dc}
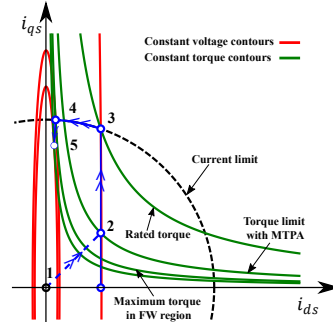
Fig. 1: Regions of operation of the induction machine for the case rated voltage and rated speed occur at the same frequency (Segment 1-2: MTPA region; Segment 2-3: rated flux region; Segment 3-4: field weakening region 1; Segment 4-5: field weakening region 2 (MTPV)).

and modulation strategy, being $v_{dqs_{limit}} = V_{dc}/\sqrt{3}$ for linear operation of inverter), current limit (mainly due to thermal issues) (8) where V_{dc} is the dc-link voltage.

$$\left(\omega_e \sigma L_s i_{qs}\right)^2 + \left(\omega_e L_s i_{ds}\right)^2 \leq v_{dqs_{limit}}^2 \tag{7}$$

$$\sqrt{i_{ds}^2 + i_{qs}^2} \leq i_{dqs_{rated}} \tag{8}$$

MTPA can be implemented in segment 1-2 (see Fig. 1) while operation at rated flux applies between 2 and 3. In point 3 the machine operates at is rated values of voltage (9), current (10).

$$\left(\omega_e \sigma L_s i_{qs_{rated}}\right)^2 + \left(\omega_e L_s i_{ds_{rated}}\right)^2 = v_{dqs_{limit}}^2 \tag{9}$$

$$i_{qs_{rated}} = \sqrt{i_{dqs_{rated}}^2 - i_{ds_{rated}}^2}; \ i_{ds_{rated}} = \frac{\lambda_{r_{rated}}}{L_m} \tag{10}$$

Field weakening region I corresponds to the segment 3-4 in Fig. 1. In this region, the machine operates with rated voltage and current, but with reduced d-axis current and therefore reduced rotor flux. The d-axis current can be written as a function of the fundamental frequency (11), which is obtained from (8) and (9), the q-axis current being (12). The maximum fundamental frequency in field weakening region I occurs when the constant voltage ellipsis and the constant torque hyperbola do not intersect to each other but the ellipsis become tangent (operating point 4 in Fig. 1).

$$i_{ds} = \sqrt{\frac{\left(\frac{v_{dqs_{limit}}}{\omega_e}\right)^2 - \left(\sigma L_s i_{dqs_{rated}}\right)^2}{L_s^2\left(1 - \sigma^2\right)}} < i_{ds_{rated}} \tag{11}$$

2250

$$i_{qs} = \sqrt{i_{dqs_{rated}}^2 - i_{ds}^2} = \sqrt{\frac{\left(L_s i_{dqs_{rated}}\right)^2 - \left(\frac{v_{dqs_{limit}}}{\omega_e}\right)^2}{L_s^2 \left(1 - \sigma^2\right)}} \tag{12}$$

In field weakening region II (see segment 4-5 in Fig. 1), the machine operates with MTPV, i.e. constant voltage ellipsis are tangent to constant torque hyperbolas. d- and q-axis in this region can be obtained by replacing the q-axis in (12) into the torque equation (4), (13) being obtained. Making the derivative of the torque with respect to the d-axis current equal to zero (3.14), produces the currents (14).

$$T_e = \frac{3}{2} P \frac{L_m^2}{L_r} i_{ds}^e \sqrt{\frac{\left(L_s i_{dqs_{rated}}\right)^2 - \left(\frac{v_{dqs_{limit}}}{\omega_e}\right)^2}{L_s^2 \left(1 - \sigma^2\right)}} \tag{13}$$

$$i_{ds} = \frac{v_{dqs_{limit}}}{\sqrt{2}\omega_e L_s}; \; i_{qs} = \frac{v_{dqs_{limit}}}{\sqrt{2}\omega_e \sigma L_s} \tag{14}$$

C. Control strategies of IMs

High power electric drives must be able to properly operate from zero to relatively high rotational frequencies while switching frequencies are often limited to several hundred Hz. Control of the electric drive at low rotational frequencies where switching to fundamental frequency ratio is relatively large and the inverter operates far from its voltage limit, is significantly easier compared to the case of operation at high speeds characterized by reduced switching to fundamental frequency ratio and reduced (or even no) voltage margin in the inverter. Due to this, both control and modulation strategies are often dynamically changed depending on the frequency of operation [20]. A common practice in high-speed drives is using rotor flux field-oriented control (RFOC) in the low-speed range and switch to scalar or direct torque control in the high-speed range. That strategy ensures a high dynamic response of the electric drive without deterioration of the control system [21], [22].

III. PROPOSED REMAGNETIZATION STRATEGIES FOR INDUCTION MACHINES

In high-speed traction applications, the electric drive can work for certain periods of time with light loads. It is possible in this case to decrease the flux level to reduce the stator current and consequently joule losses. However, if higher torque is demanded, the machine must be magnetized first to achieve a proper flux level corresponding to the demanded torque. MTPA strategy is one of the most efficient and used strategies in motor drives for a wide speed range [23], [24]. In this paper, the map-based approach introduced in [25] will be used for selecting the current references to achieve MTPA control, taking into consideration the machine saturation. However, the main limitation of the presented map-based MTPA strategy is that it controls only the steady-state behavior of the stator current dq-axis trajectories regardless of the dynamic behavior during torque variations.

Operation with reduced flux levels will deteriorate the dynamic response of the electric drive to torque demands. The machine must be remagnetized first, where the remagnetization time is determined by the rotor time constant and by the applied magnetizing current. Generally, the goal of a remagnetization strategy is to determine the optimal torque and flux trajectories between initial ($T_{e_{ini}}$, $\lambda_{r_{ini}}$) and maximum possible torque/flux values ($T_{e_{max}}$, $\lambda_{r_{max}}$) for the corresponding speed. Due to the relatively large values of the rotor time constant fast torque changes of torque are not feasible specifically for traction applications. Fast torque variations might stress the mechanical transmission, produce wheel slip and also raise comfort concerns. Therefore, the optimization of the torque/flux trajectories should satisfy the following criteria:

- Minimization of the settling time Δt.
- Avoidance of torque impacts, i.e. sudden changes in the torque.
- Loss minimization during the transient.

in addition, other considerations must be also taken:

- Over-currents are not allowed.
- It is assumed that the load has a very large mechanical inertia, and consequently the rotor speed can be assumed to remain constant during the transient.

Some of these targets can conflict, e.g. minimization of losses and of settling time. Thus, the optimal remagnetization process may differ for each application.

Strategies for the simultaneous increase of torque and rotor flux (remagnetization) are discussed following:

A. Remagnetization with step-like rated d-axis change and ramp-like q-axis current change:

If FOC is being used, the straightest remagnetization strategy to achieve rated rotor flux and torque (for the actual operating speed) is to apply the rated d- axis current as fast as possible (step increase segment 1-2 in Fig. 2a) and increase the q-axis current gradually (segment 2-3 in Fig. 2a). The main drawback of this solution is the large settling time for the torque during the machine remagnetizing process (in the range of three rotor time constants).

B. Remagnetization with maximum d-axis current:

This strategy prioritizes remagnetization over torque production. As shown in Fig. 2b, following an increased torque command, all the available current is used in the d-axis for this purpose (segment 1-2 in Fig. 2b). Once the rotor flux is fully established, d-axis current is reduced to the level required to maintain the rotor flux at its target level, the remaining available current being transferred to the q-axis to produce the maximum torque (segment 2-3 in Fig. 2b). This strategy reduces the time required to produce the desired final torque (i.e. settling time) and provides the fastest torque production. However, in traction applications, fast torque variation is not allowed as mentioned above.
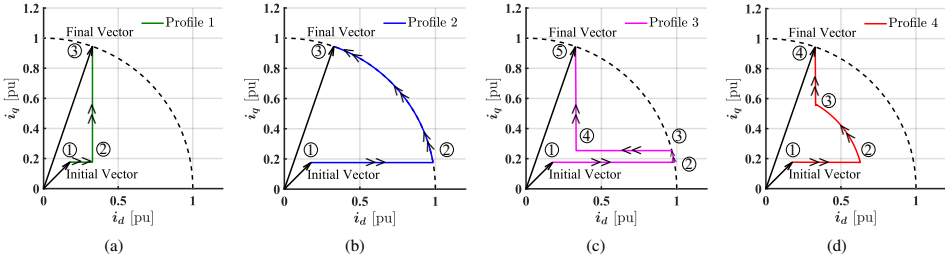
Fig. 2: Summary of different proposed remagnetization strategies: a) step-like rated d-axis change and ramp-like q-axis current change (Profile 1); b) maximum d-axis current (Profile 2); b) maximum d-axis current and constant Nm/s (Profile 3); c) reduced d-axis current and constant Nm/s (Profile 4).

C. Remagnetization with maximum d-axis current and constant Nm/s:

The main idea behind this strategy is to control the torque to follow a ramp (15), where K_{T_e} is the slope in Nm/s.

$$T_e^* = T_{e_{ini}} + K_{T_e} t \ \text{ for } \ t_1 < t < t_2 \qquad (15)$$

To minimize the settling time of flux, K_{T_e} must be selected such that the maximum current is used during the whole transient (16).

$$\sqrt{i_{ds}^{*\,2} + i_{qs}^{*\,2}} = I_{s_{max}} \qquad (16)$$

The desired torque and flux trajectories can be obtained by solving (3), (4) and (16). Analytical solution of this system is not feasible, numerical methods can be used instead. It is seen that at the beginning of the transient all the available current is transferred to the d-axis current (segment 1-2 in Fig. 2c), the remaining current being transferred to the q-axis to establish the rotor flux quickly (segment 2-3 in Fig. 2c). Then, the d-axis current is reduced to its rated value (segment 3-4 in Fig. 2c) while increasing the q-axis current smoothly taking into consideration that fast changes in q-axis current are avoided as they would produce torque impacts (segment 4-5 in Fig. 2c).

D. Remagnetization with reduced d-axis current and constant Nm/s:

The strategy in Fig. 2d provides the same torque ramp as in Fig. 2c but uses the smallest possible current during segment 2-3. This reduces the stress in the power devices, as well as the risk of surpassing the maximum current in case of overshoot due to controller detuning. Thus, the segment 3-4 in Fig. 2c is omitted to have a continuous trajectory of d-q axis currents. However, this strategy is not straightforward, and the minimum current value changes depending on the initial torque value. One of the possible solutions is to assign profile 3 strategy with a lower current magnitude but at cost of longer magnetization time.

The proposed remagnetization strategy (see Fig. 3) includes the following process:

1) At light load, the initial rotor flux reference value is obtained from MTPA method using a look-up table or polynomial function approximation according to the operating speed.
2) Once an increase/decrease is detected in the reference torque, the torque and rotor flux references will follow one of the predefined trajectories (see Fig. 2) with rates limited to the application until reach to the new target values.
3) The rotor flux reference is limited in the field-weakening region according to the operating speed.
4) The rotor flux trajectory can be a ramp, exponential convergence or other profiles obtained from optimization methods (profiles 1-to-4, in this paper) that meets the application constraints.

The aforementioned remagnetization profiles will be simulated and evaluated in section IV.
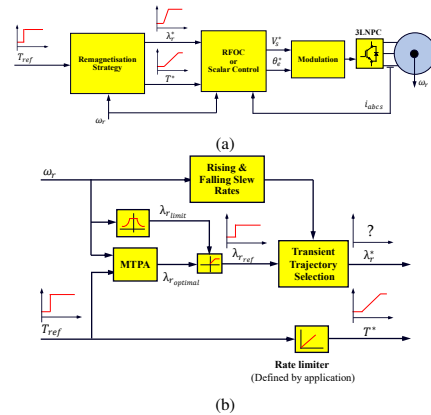
Fig. 3: Proposed remagnetization strategy: a) overall control scheme; b) detailed block diagram of the proposed method.

2252

IV. SIMULATION RESULTS AND EXPERIMENTAL VALIDATION

The proposed remagnetization strategies discussed in section III have been simulated using MATLAB environment with a sample time of 200 μs. The dynamic d-q model in rotor flux reference frame is used for modeling the induction machine. IM parameters for the base speed are given in Table I.

TABLE I: Specifications of the IM at base speed (107 Hz).

| Parameter	Value	Unit
DC-link voltage, (V_{dc})	3600	V
Rated Power	1084	kW
Rated Voltage, (V_{LL}, RMS)	2727	V
Pole-pairs (P)	2	-
Stator resistance (R_s)	55.38	mΩ
Stator inductance (L_s)	26.45	mH
Torque	3241	Nm
Speed	3194	rpm

Fig. 4 shows a summary of the simulation results for the machine operating at base speed, assuming that the IM is connected to an ideal inverter (i.e. linear voltage source). The IM torque is increased from 10% to 100% of the rated torque at t=0.25 s following the four remagnetization profiles proposed in subsections III-A, III-B, III-C and III-D respectively. It is noted that the slowest torque production is obtained by magnetizing the machine with profile 1, i.e. d-axis current is increased to its rated value then the q-axis current is increased gradually. The final torque will be achieved when the machine flux is fully established which could take some time ($\approx$ 3 to 4 times the rotor time constant see Fig. 4).
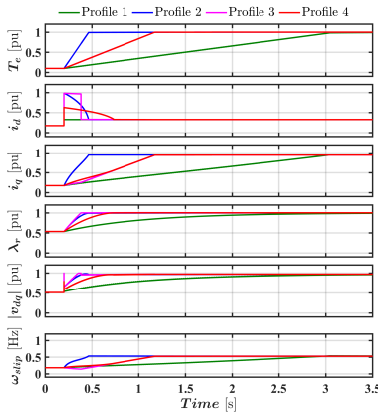
Fig. 4: Simulation results: Time response of different proposed remagnetization strategies.

On the other side, the fastest torque production is reached
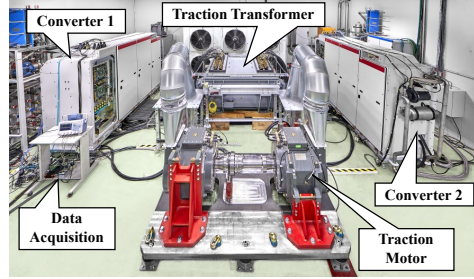
Fig. 5: Overall view of the full scale high-power traction test bench.

following profile 2 (see the blue color in Fig. 4) where all the stator current is used to magnetize the machine. Afterward, the stator current vector follows the current limit trajectory sharing the remaining current into the q-axis component assuring that the total current is not surpassed.

Profiles 3 and 4 show similar torque production rates (magenta vs. red color in Fig. 4) as these strategies are designed to follow a predefined kNm/s rate (in this application 3 kNm/s is used), however, each strategy dynamically behaves different. Profile 3 prioritize the use of stator current vector on the d-axis component in order to expedite flux establishment then the priority moves to the q-axis component for torque production (see second sub-figure Fig. 4). A reduced remaganetization can be used for profile 4 which will penalize the dynamic response of the rotor flux which is not a concern in traction applications as a fast torque increase is not needed. The main advantage of this strategy is it balances the dynamic response of the remaganetization process with the current stress on the switches of the inverter.

The proposed remagnetization strategy has been experimentally validated using high-power traction system test bench shown in Fig. 5. It consists of two identical IMs and two converters connected back-to-back, which are supplied from a High-Voltage (HV) dc power supply. The power converter module consists of a three-phase, three-level Neutral-Point Clamped (NPC) inverter feeding the IMs. Single-phase inverters feed auxiliary loads, such as cooling systems, control power supply units, etc. A dc-dc chopper is implemented for dissipative braking and dc bus overvoltage protection. A specially designed traction transformer is used to filter off catenary harmonics and allow the interconnection of the different converters. A 100 Hz (2f) filter is included in the dc bus. Preliminary experimental results for a full-scale high-speed traction drive are presented in the following. The control uses RFOC at low speeds and closed-loop scalar control at high speeds. The main system parameters are the same as those used in the simulation shown in table I.

The proposed remagnetization strategy is validated by comparing the conventional magnetization solution (applying maximum possible flux for the full speed range see Fig. 6a)

against the proposed remagnetization profile 4 (see Fig. 6b). It is noted that both methods are able to reach the target torque with the same increase rate (3 kNm/s) from 10% to 100% of the rated torque. The main difference can be seen in the rotor flux for the proposed method where it is reduced to ≈ 48% of the rated value during light load operation compared to the conventional solution. The corresponding d- and q-axis currents are shown in the bottom figures of Fig. 6. The d-axis current is kept at its rated value for the conventional magnetization method while the d-axis current is initially reduced during light load duration then it superpassed its rated value to build up the rotor flux quickly when the torque increase is commanded. Once the machine is fully magnetized, the d-axis current is decreased to prioritize the usage of q-axis current.
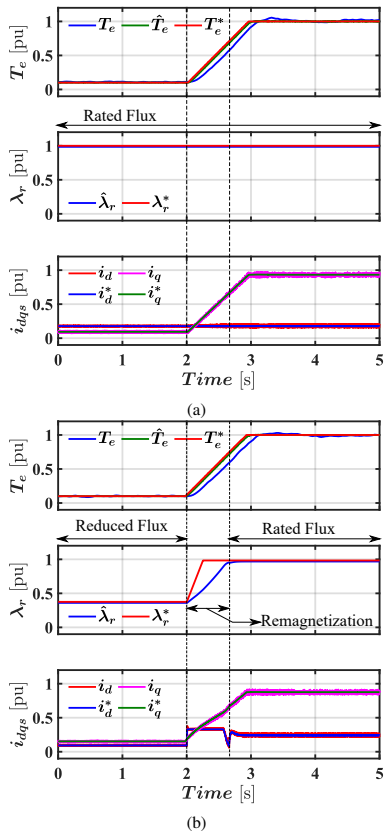
Fig. 6: Experimental results of IM torque increase from 10% to 100% of rated torque: a) applying rated magnetizing current; b) proposed remagnetization strategy.

V. CONCLUSIONS

Optimal efficiency and loss minimization control techniques have been proposed in the technical literature for optimally distributing stator current components (i.e. flux and torque producing components) while the electric machine is operating at light loads. MTPA method is commonly used in electric drives providing maximum available torque with minimum losses. However, MTPA algorithms provide the steady-state set points for the electric drive control, transients being uncontrolled and dictated by the machine time constant and the coupling between torque and flux components. Few approaches attempting to improve the torque transient response can be found in the literature. Computational complexity and approximated solutions for specific conditions limit the widespread usage of those approaches in the industry.

This paper proposes different remagnetization strategies for induction machines during torque transients. Based on the application, the remagnetization strategy can be selected to prioritize the torque dynamic response where the machine can operate at inverter limits for a portion of time. Another solution is to operate far from inverter limits at the cost of a lower dynamic response. Compromising dynamic response with system operational requirements would be the optimum solution.

The proposed remagnetization strategy calculates the initial rotor flux using MTPA algorithm at light loads. Once a change in torque command is detected, the torque and rotor flux reference will follow predefined trajectories till reach the final value. The proposed strategy at four different torque and flux components trajectories is evaluated through simulations. For traction applications, a fast dynamic response is not required as the torque rate change is limited to avoid torque shocks. Thus, a reduced remagnetizing current with constant torque increase rate has been validated experimentally through a full-scale high-power traction test bench. Currently, the proposed remagnetization torque and flux trajectories are implemented offline and stored in look-up tables. Online implementation of the remagnetization trajectory is ongoing.

REFERENCES

[1] ENERGY EFFICIENCY & RENEWABLE ENERGY Office, "U.S. DRIVE electrical and electronics technical team roadmap", 2017 [Online] Available: https://www.energy.gov/eere/vehicles/downloads/us-drive-electrical-and-electronics-technical-team-roadmap.

[2] C. Liu, "Emerging electric machines and drives—an overview," *IEEE Transactions on Energy Conversion*, vol. 33, no. 4, pp. 2270–2280, 2018.

[3] Z. Yang, F. Shang, I. P. Brown, and M. Krishnamurthy, "Comparative study of interior permanent magnet, induction, and switched reluctance motor drives for EV and HEV applications," *IEEE Transactions on Transportation Electrification*, vol. 1, no. 3, pp. 245–254, 2015.

[4] J.-R. Riba, C. López-Torres, L. Romeral, and A. Garcia, "Rare-earth-free propulsion motors for electric vehicles: A technology review," *Renewable and Sustainable Energy Reviews*, vol. 57, pp. 367–379, 2016.

[5] V. T. Buyukdegirmenci, A. M. Bazzi, and P. T. Krein, "Evaluation of induction and permanent-magnet synchronous machines using drive-cycle energy and loss minimization in traction applications," *IEEE Transactions on Industry Applications*, vol. 50, no. 1, pp. 395–403, 2013.

2254

[6] L. Buhrkall, "Traction system case study," in *The 9th Institution of Engineering and Technology Professional Development Course on Electric Traction Systems*. IET, 2006, pp. 53–71.

[7] G. Pellegrino, A. Vagati, B. Boazzo, and P. Guglielmi, "Comparison of induction and PM synchronous motor drives for EV application including design examples," *IEEE Transactions on industry applications*, vol. 48, no. 6, pp. 2322–2332, 2012.

[8] D. S. Kirschen, D. W. Novotny, and W. Suwanwisoot, "Minimizing induction motor losses by excitation control in variable frequency drives," *IEEE Transactions on Industry Applications*, no. 5, pp. 1244–1250, 1984.

[9] D. Biswas, K. Mukherjee, and N. C. Kar, "A novel approach towards electrical loss minimization in vector controlled induction machine drive for EV/HEV," in *2012 IEEE Transportation Electrification Conference and Expo (ITEC)*. IEEE, 2012, pp. 1–5.

[10] R. Tarvirdilu-Asl, S. Nalakath, Z. Xia, Y. Sun, J. Wiseman, and A. Emadi, "Improved online optimization-based optimal tracking control method for induction motor drives," *IEEE Transactions on Power Electronics*, vol. 35, no. 10, pp. 10654–10672, 2020.

[11] D. S. Kirschen, D. W. Novotny, and T. A. Lipo, "On-line efficiency optimization of a variable frequency induction motor drive," *IEEE transactions on industry applications*, no. 3, pp. 610–616, 1985.

[12] S. Bozhko, S. Dymko, S. Kovbasa, and S. M. Peresada, "Maximum torque-per-amp control for traction im: Theory and experimental results," *IEEE Transactions on Industry Applications*, vol. 53, no. 1, pp. 181–193, 2016.

[13] S. N. Vukosavic and E. Levi, "A method for transient torque response improvement in optimum efficiency induction motor drives," *IEEE transactions on energy conversion*, vol. 18, no. 4, pp. 484–493, 2003.

[14] J.-F. Stumper, A. Dötlinger, and R. Kennel, "Loss minimization of induction machines in dynamic operation," *IEEE transactions on energy conversion*, vol. 28, no. 3, pp. 726–735, 2013.

[15] Z. Hu, Q. Liu, and K. Hameyer, "Loss minimization of speed controlled induction machines in transient states considering system constraints," in *2014 17th International Conference on Electrical Machines and Systems (ICEMS)*. IEEE, 2014, pp. 123–129.

[16] A. Popov, V. Lapshina, I. Gulyaev, and F. Briz, "Improving the dynamic response of FOC induction machines operated with reduced rotor flux," in *2018 25th International Workshop on Electric Drives: Optimization in Control of Electric Drives (IWED)*. IEEE, 2018, pp. 1–4.

[17] P. C. Krause and C. Thomas, "Simulation of symmetrical induction machinery," *IEEE transactions on power apparatus and systems*, vol. 84, no. 11, pp. 1038–1053, 1965.

[18] A. M. Khambadkone and J. Holtz, "Vector-controlled induction motor drive with a self-commissioning scheme," *IEEE Transactions on Industrial Electronics*, vol. 38, no. 5, pp. 322–327, 1991.

[19] F. Blaschke, "The principle of field orientation as applied to the new transvektor closed-loop control system for rotating field machines," *Siemens review*, vol. 34, no. 1, 1972.

[20] A. Fathy Abouzeid, J. M. Guerrero, A. Endemaño, I. Muniategui, D. Ortega, I. Larrazabal, and F. Briz, "Control strategies for induction motors in railway traction applications," *Energies*, vol. 13, no. 3, p. 700, 2020.

[21] T. H. Nguyen, T. L. Van, D.-C. Lee, J.-H. Park, and J.-H. Hwang, "Control mode switching of induction machine drives between vector control and v/f control in overmodulation range," *Journal of Power Electronics*, vol. 11, no. 6, pp. 846–855, 2011.

[22] A. F. Abouzeid, J. M. Guerrero, I. Muniategui, A. Endemaño, D. Ortega, and F. Briz, "Torque dynamics enhancement of railway traction drives using scalar control," in *2021 IEEE International Electric Machines & Drives Conference (IEMDC)*. IEEE, 2021, pp. 1–6.

[23] O. Wasynczuk, S. Sudhoff, K. Corzine, J. L. Tichenor, P. Krause, I. Hansen, and L. Taylor, "A maximum torque per ampere control strategy for induction motor drives," *IEEE Transactions on Energy Conversion*, vol. 13, no. 2, pp. 163–169, 1998.

[24] H. Kouns, J.-S. Lai, and C. E. Konrad, "Analysis of a traction induction motor drive operating under maximum efficiency and maximum torque per ampere conditions," in *Nineteenth Annual IEEE Applied Power Electronics Conference and Exposition, 2004. APEC'04.*, vol. 1. IEEE, 2004, pp. 545–551.

[25] R. Bojoi, Z. Li, S. Odhano, G. Griva, and A. Tenconi, "Unified direct-flux vector control of induction motor drives with maximum torque per ampere operation," in *2013 IEEE Energy Conversion Congress and Exposition*. IEEE, 2013, pp. 3888–3895.

VI. Biographies

Ahmed Fathy Abouzeid (M'19) received the B.S and M.S. degrees in Electrical Engineering from Port Said University, Port Said, Egypt, in 2012 and 2017, respectively. He is currently pursuing his Ph.D. Degree at the Department of Electrical, Electronic and Computer Engineering, University of Oviedo, Gijón, Spain. In 2013, he joined the Department of Electrical Engineering, Port Said University, Egypt, as a Teaching Assistant. Currently, he is on leave with the same department as an Assistant Lecturer. He is partially supported by a scholarship from the Ministry of Higher Education and Scientific Research of Egypt. His research interests include power converters and ac drives, electric traction, and renewable energy systems.

Juan M. Guerrero (S'00–A'01–M'04–SM'21) received the M.E. degree in industrial engineering and the Ph.D. Degree in Electrical and Electronic Engineering from the University of Oviedo, Gijón, Spain, in 1998 and 2003, respectively. Since 1999, he has occupied different teaching and research positions with the Department of Electrical, Computer and Systems Engineering, University of Oviedo, where he is currently an Associate Professor. From February to October 2002, he was a Visiting Scholar at the University of Wisconsin, Madison. From June to December 2007, he was a Visiting Professor at the Tennessee Technological University, Cookeville. He is Associate Editor of the IEEE Trans. on Industry Applications. His research interests include control of electric drives and power converters, electric traction, and renewable energy generation.

Iban Vicente-Makazaga graduated in electrical engineering from University of Mondragon, Mondragon, Spain, in 2003 and the M.S. and the Ph.D. degrees from the University of Manchester, UK, in 2004 and 2009 respectively. He joined Ingeteam Power Technology (formerly TEAM), Zamudio, Spain, where he works as a Control and Regulation Engineer involved in railway traction control for trams, locomotives and EMU-s. His current research interests include power converter and advanced control drives, modulation techniques, machine parameters and speed estimation techniques as well railway research issues such as AC catenary stability and mechanical vibrations in the drive-train.

Iker Muniategui-Aspiazu received the Industrial Technical Engineering Degree (Electronic Design speciality) and the Industrial Automatics and Electronics Engineering Degree, from the University of Mondragon, Mondragon, Spain, in 2004 and 2007 respectively. In September 2006, he joined Ingeteam Power Technology (formerly TEAM), Zamudio, Spain, where he worked as a Control and Regulation Engineer, and he is currently Control and Regulation manager of Traction department. His current research interests include power converter and advanced control drives, modulation techniques, railway research issues such as AC catenary stability and mechanical vibrations in the drive-train.

Aitor Endemaño-Isasi received the Industrial Technical Engineering Degree (Electronic Design speciality) and the Industrial Automatics and Electronics Engineering Degree, from the University of Mondragon, Mondragon, Spain, in 1997 and 2000 respectively, and the PhD from Heriot-Watt University, Edinburgh, Scotland, UK, in 2003. In 2003 he joined Traction department at Ingeteam Power Technology (formerly TEAM), Zamudio, Spain, where since then he has been a Control and Regulation Engineer, involved in several traction control design projects for trams, locomotives and EMU-s. His current research interests include power converter and advanced control drives, modulation techniques, railway research issues such as AC catenary stability and mechanical vibrations in the drive-train.

Fernando Briz (A'96–M'99–SM'06) received the M.S. and Ph.D. degrees from the University of Oviedo, Gijón, Spain, in 1990 and 1996, respectively. He is currently a Full Professor with the Department of Electrical, Computer and Systems Engineering, University of Oviedo. Dr. Briz received an IEEE TRANSACTIONS ON INDUSTRY APPLICATIONS Award and nine IEEE Industry Applications Society Conference and IEEE Energy Conversion Congress and Exposition prize paper awards. He is Past Chair of the Industrial Drives Committee of the Industrial Power Conversion System Department (IPCSD) of the IAS. Currently he is Vice Chair of IPCSD. He has served in scientific committees and as Vice Chair or Technical Program Chair of several conferences, including ECCE, IEMDC, ICEM, ICEMS and SLED. He is a Member of the Steering Committee of IEEE Journal of Emerging and Selected Topics in Power Electronics (JESTPE), Editor of JESTPE Transactions and Associate Editor of IAS Transactions. His topics of interest include electronic power converters and ac drives, power systems, machine monitoring and diagnostics and digital signal processing.

2255

B.2.2 Torque Dynamics Enhancement of Railway Traction Drives Using Scalar Control

Torque Dynamics Enhancement of Railway Traction Drives Using Scalar Control

Ahmed Fathy Abouzeid
Dept. of Electrical Engineering
University of Oviedo
Gijón, Spain
abouzeidahmed@uniovi.es

Juan Manuel Guerrero
Dept. of Electrical Engineering
University of Oviedo
Gijón, Spain
guerrero@uniovi.es

Iker Muniategui
Traction systems
Ingeteam Power Technology
Zamudio, Spain
iker.muniategui@ingeteam.com

Aitor Endemaño
Traction systems
Ingeteam Power Technology
Zamudio, Spain
aitor.endemano@ingeteam.com

David Ortega
Traction systems
Ingeteam Power Technology
Zamudio, Spain
David.Ortega@ingeteam.com

Fernando Briz
Dept. of Electrical Engineering
University of Oviedo
Gijón, Spain
fbriz@uniovi.es

Abstract—Traction systems for railway typically use rotor field-oriented control (RFOC) at low speeds, and scalar control at high speeds to overcome the deterioration of the current regulator performance in the overmodulation region. Well-known limitations of scalar control are the slow dynamic response due to the coupling between torque and flux, as well as the risk of overcurrents. While this is not a problem for normal operation, as fast torque variations are not required, there are specific operating conditions in which fast torque response of scalar control might be required. This would include adhesion control, torsional torque vibration mitigation and torque ripple cancellation for traction systems fed from ac catenaries without a 2F filter in the dc-link. This paper proposes a method to enhance the dynamic response of scalar control. The principles of the proposed method are derived from vector control concepts. While the method could be applied to any electric drive using scalar control, the discussion presented in this paper will be targeted towards high power railway traction drives.

Index Terms—Scalar V/F control; railway traction drives; induction motors; beatless control; torsional torque oscillations.

I. INTRODUCTION

Voltage-Source Inverter-fed Induction Machines (VSI-IM) are the preferred choice in railway traction systems due to their robustness and the slip inherent to IM, which allows multiple motors to be fed from a single inverter [1], [2]. VSI-IM traction drive systems can be fed from different power sources. For the specific case of ac catenaries, a four-quadrant converter (4QC) is required to supply the VSI-IM dc link. The fact that the catenary is single-phase results in well-known power oscillations at twice the catenary voltage frequency (2F), which has to be considered for the design of the traction system.

Fig. 1 shows the main circuit elements for a single-driven axle of a high-performance locomotive fed from an ac catenary. High-performance locomotive drives control consists of two control layers; an inner control layer aimed to provide the desired torque T_e^* and an outer control layer that oversees traction force F_t^* which can comprise several functionalities
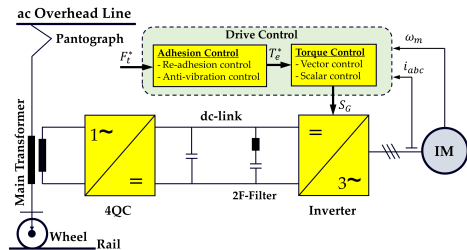
Fig. 1: Main circuit diagram for single driven axle of a high-performance locomotive.

as re-adhesion control, anti-slip control, torsional torque vibration mitigation, 2F oscillations cancellation, etc. Regarding the inner loop, RFOC with Pulse-Width Modulation/Space-Vector Modulation (PWM/SVM) is typically used at low-medium speeds, where the voltage margin and the switching to fundamental frequency ratio are sufficient for proper operation of the current regulators [3]. At high speeds, the lack of a voltage margin and the reduced switching to fundamental frequency ratio can seriously compromise the performance of FOC. Several attempts have been made to improve vector control performance in the overmodulation region, but this is at the price of increased complexity and parameter sensitivity, which has prevented their widespread use [4]–[6].

Scalar control is widely used when the drive operates close or at the voltage limit, constant V/F being the simplest implementation. Modulation strategies aimed to reduce switching losses and/or harmonic content are often used in this case [7]. Scalar control methods show slow torque dynamics due to the coupling between torque and flux and the need to prevent overcurrents. This is not a concern for normal operation of

traction drives. However, modern trains may require fast torque dynamics for advanced modes of operation, such as adhesion control, torsional torque vibration mitigation, and cancellation of torque ripple in traction drives fed from ac catenaries without an intermediate 2F filter (see Fig. 1) [8], [9].

Several methods aimed to improve the dynamic response of scalar control have been reported in the literature [10]–[15]. In [10], a feedforward term is added to the voltage magnitude command to compensate for the voltage variation caused by torque changes, which is claimed to decouple torque and flux and improve both the dynamic and steady-state response of the V/F control. Parameters required by the decoupling block change with the operating point. This involves the use of look-up tables which are built during a commissioning stage, what increases the complexity of the proposed method. In [13], [14], a transient voltage vector is estimated and added to the voltage vector command improving the transient response of the scalar V/F method. However, the estimated transient vector is obtained from d-q current regulators operating in parallel of the main V/F controllers which could be problematic when the machine enters the overmodulation region and the voltage margin required for the normal operation of the current controller is lost. Methods reported in [11], [12], [15] are targeted to overcome the limitations of scalar control at low fundamental frequencies only, being therefore disregarded.

In this paper, a method for enhancing the torque dynamics of scalar control when the drive operates at high fundamental frequencies in the overmodulation region, including six-step, is developed. The proposed method can potentially achieve dynamic responses comparable to those of vector controlled drives, but without the drawbacks of current regulators. The effectiveness of the proposed method will be validated through MATLAB/Simulink simulations in this paper. Construction of a test bench for experimental verification is ongoing.

II. INDUCTION MOTOR MODEL

For the discussions following, variables in the stationary reference frame, stator voltage reference frame and rotor flux reference frame will be denoted by superscripts "s", "slf" and "rf" respectively.

The complex vector notation of an induction motor, with the stator current and the rotor flux as the state variables, are given by (1)-(2). v_{dqs}^s denotes the stator voltage; i_{dqs}^s is the stator current; $\hat{\lambda}_{dqr}^s$ represents the estimated rotor flux; $\hat{R}_s$ and $\hat{R}_r$ are the estimated stator and rotor resistances; $\hat{L}_s$, $\hat{L}_r$ and $\hat{L}_m$ are the estimated stator, rotor, and mutual inductances, respectively; ω_r is the rotor angular speed in electrical units; and p is the derivative operator.

$$p i_{dqs}^s = \frac{1}{\hat{L}_{\sigma s}} \left(v_{dqs}^s - \hat{R}_s' i_{dqs}^s + \frac{\hat{L}_m}{\hat{L}_r} \omega_{br} \hat{\lambda}_{dqr}^s \right) \quad (1)$$

$$p \hat{\lambda}_{dqr}^s = \frac{\hat{L}_m}{\hat{L}_r} \hat{R}_r i_{dqs}^s - \omega_{br} \hat{\lambda}_{dqr}^s \quad (2)$$

where

$$\hat{R}_s' = \hat{R}_s + \hat{R}_r \left(\frac{\hat{L}_m}{\hat{L}_r} \right)^2 \; ; \; \hat{L}_{\sigma s} = \hat{L}_s - \frac{\hat{L}_m^2}{\hat{L}_r} \; ; \omega_{br} = \frac{\hat{R}_r}{\hat{L}_r} - j\omega_r$$

$\hat{R}_s'$ and $\hat{\sigma}$ are the estimated stator transient resistance and leakage inductance respectively. The electromagnetic torque T_e is given by (3) in terms of stator current and rotor flux where P is the pole-pairs.

$$T_e = \frac{3}{2} P \frac{\hat{L}_m}{\hat{L}_r} \left(\hat{\lambda}_{dr}^s i_{qs}^s - \hat{\lambda}_{qr}^s i_{ds}^s \right) \quad (3)$$

By aligning the d-axis of the rotating reference frame with the rotor flux, i.e., $\hat{\lambda}_{dqr}^{rf} = \hat{\lambda}_{dr}^{rf} = \hat{\lambda}_r$, the stator voltage and the stator flux equations become (4) and (5), where ω_e is the angular speed in electrical units of the synchronous reference frame.

$$v_{dqs}^{rf} = \hat{R}_s' i_{dqs}^{rf} + p\hat{\lambda}_{dqs}^{rf} + j\omega_e \hat{\lambda}_{dqs}^{rf} \quad (4)$$

$$\hat{\lambda}_{dqs}^{rf} = \frac{\hat{L}_m}{\hat{L}_r} \hat{\lambda}_{dqr}^{rf} + \hat{L}_{\sigma s} i_{dqs}^{rf} \quad (5)$$

III. VECTOR VS. SCALAR CONTROL

Vector control uses the dynamic equations of the machine to achieve decoupled control of torque and flux (see Fig. 2a). This allows to fully exploit machine torque capability without surpassing machine or power converter current limits. On the contrary, open-loop scalar V/F control schemes make the stator voltage magnitude proportional to the frequency, leading to an almost constant flux in the machine. Nevertheless, there is a number of issues e.g. incorrect voltage to frequency ratios, voltage drops in the stator resistance, or variations of the inverter dc-link voltage, etc. which could drift the actual operating point from the desired value. To overcome these effects, the performance of V/F control can be improved with the addition of feedback loops [16].

Closed-loop V/F control has been widely used in traction drives. Flux and the torque are regulated in this case using Proportional-Integral (PI) controllers. This closed-loop scheme is known as slip/flux scalar V/F control (SLF), (see Fig. 2b), which consists of two terms: 1) the first term provides the base value of the stator voltage magnitude through the V/F characteristic, with adapting the rotor flux level through a PI regulator. 2) the second term provides the base value for the slip, then the torque is controlled by regulating the slip with no error [7]. Closed-loop V/F control is usually applied at high speed operation where power converter operates close to its voltage limit, including overmodulation and six-step [3]. This enables precise control of the machines' operating point in steady-state avoiding the deterioration of the current regulators due to the generated harmonic components of the machine current during the over-modulation. However, closed-loop V/F schemes have slower dynamic response compared to rotor flux field-oriented control (RFOC). Since the voltage magnitude and phase angle commands are independently obtained, both flux and torque controllers must be tuned for relatively low bandwidths to avoid cross-coupling interactions.
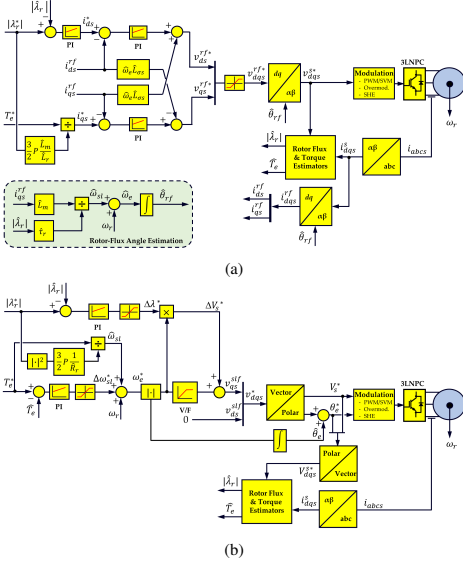
(a)

(b)

Fig. 2: Block diagram of closed-loop control scheme for induction motors: a) Rotor flux field-oriented control (RFOC); b) Stator voltage oriented V/F with slip & flux control (SLF).

IV. SCALAR CONTROL WITH ENHANCED DYNAMICS

The following discussion assumes that the induction machine in Fig. 2 is operating at relatively high speed. The q-axis of the synchronous reference is defined to be aligned with the stator voltage vector (6b). If a sudden change in the torque command is applied, the slip angular speed $\hat{\omega}_{sl}$ will increase proportionally (see Fig. 2b), increasing therefore the angular speed of the stator voltage vector. The magnitude of the stator voltage v_{qs}^{slf} will also increase according to the predefined V/Hz ratio to keep the flux constant. Such sudden changes of the stator voltage angle and magnitude can result in large transient currents. Due to this, the rate of variation of the torque command, i.e. the dynamic response of the scalar control, must be limited.

$$\begin{cases} v_{ds}^{slf} &= 0 & \text{(6a)} \\ v_{qs}^{slf} &= V_s^* = |\hat{R}_s I_s + j\hat{\omega}_e \hat{\lambda}_s| \cong |\hat{\omega}_e \hat{\lambda}_s| & \text{(6b)} \end{cases}$$

To understand how the dynamic response of the scalar control can be enhanced, it is useful to analyze the behavior of the stator voltage from a rotor flux oriented control perspective. Using (5) and (4), it is possible rewrite (6a) and (6b) in a rotor
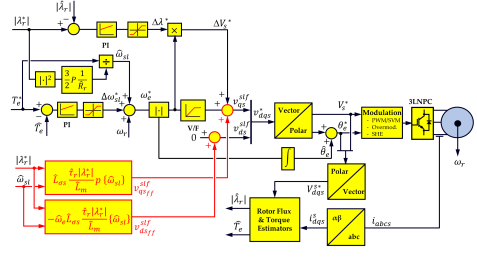
flux reference frame (7a) and (7b).

$$\begin{cases} v_{ds}^{rf} &= \hat{R}_s' i_{ds}^{rf} + \hat{L}_{\sigma s} p i_{ds}^{rf} - \hat{\omega}_e \hat{L}_{\sigma s} i_{qs}^{rf} - \hat{R}_r \frac{\hat{L}_m}{\hat{L}_r^2} \lambda_{dr}^{rf} & \text{(7a)} \\ v_{qs}^{rf} &= \hat{R}_s' i_{qs}^{rf} + \hat{L}_{\sigma s} p i_{qs}^{rf} + \hat{\omega}_e \hat{L}_{\sigma s} i_{ds}^{rf} + \hat{\omega}_r \frac{\hat{L}_m}{\hat{L}_r} \hat{\lambda}_{dr}^{rf} & \text{(7b)} \end{cases}$$

Equations (7a) and (7b) can be used to define feedforward terms aimed to improve the dynamic response of the scalar control in Fig. 2. Despite of its apparent complexity, and the associated parameter sensitivity, a number of simplifications are feasible: 1) The resistive voltage drops $\hat{R}_s' i_{ds}^{rf}$ and $\hat{R}_s' i_{qs}^{rf}$ can be neglected in high speed operation; 2) $\hat{L}_{\sigma s} p i_{ds}^{rf}$ equals zero assuming that the flux is kept constant; 3) $\hat{R}_r \frac{\hat{L}_m}{\hat{L}_r^2} \hat{\lambda}_{dr}^{rf}$ can be shown to be negligible as the rotor flux and rotor resistance values of high power machines are small compared to low power machines. The relationship between the stator voltage, q-axis current and flux can be then simplified as:

$$\begin{cases} v_{ds}^{rf} &\cong -\hat{\omega}_e \hat{L}_{\sigma s} i_{qs}^{rf} & \text{(8a)} \\ v_{qs}^{rf} &\cong \hat{L}_{\sigma s} p i_{qs}^{rf} + \hat{\omega}_e \hat{L}_{\sigma s} i_{ds}^{rf} + \hat{\omega}_r \frac{\hat{L}_m}{\hat{L}_r} \hat{\lambda}_{dr}^{rf} & \text{(8b)} \end{cases}$$

Equation (8a) shows the feedforward term to be added to the d-axis voltage component v_{ds}^{rf} to take into account changes in the torque (i.e. q-axis current). The transient response improvement is achieved by the $\hat{L}_{\sigma s} p i_{qs}^{rf}$ term of the stator voltage q-axis component in (8b). This term is a function of the q-axis current derivative and enhances therefore torque dynamic behavior. Since this action must be applied to the scalar control, the q-axis current is transformed into the slip angular speed using (9).

$$\hat{\omega}_{sl} = \frac{\hat{L}_m}{\hat{\tau}_r |\lambda_r^*|} i_{qs}^{rf} \tag{9}$$

Finally, the feedforward terms aimed to improve the dynamic response are given in (10a)&(10b) by substituting (9) in (8a)&(8b), where the steady-state value is nearly achieved from the V/F relation, i.e. $|\hat{\omega}_e \hat{\lambda}_s| \cong \hat{\omega}_e \hat{L}_{\sigma s} i_{ds}^{rf} + \hat{\omega}_r \frac{\hat{L}_m}{\hat{L}_r} \hat{\lambda}_{dr}^{rf}$ in (6b). Fig. 3 shows the block diagram of the proposed method.

$$\begin{cases} v_{ds_{ff}}^{slf} &\cong -\hat{\omega}_e \hat{L}_{\sigma s} \frac{\hat{\tau}_r |\lambda_r^*|}{\hat{L}_m} \hat{\omega}_{sl} & \text{(10a)} \\ v_{qs_{ff}}^{slf} &\cong \hat{L}_{\sigma s} \frac{\hat{\tau}_r |\lambda_r^*|}{\hat{L}_m} p\hat{\omega}_{sl} & \text{(10b)} \end{cases}$$

Fig. 3: Proposed feedforward compensation for stator voltage oriented scalar V/F control.
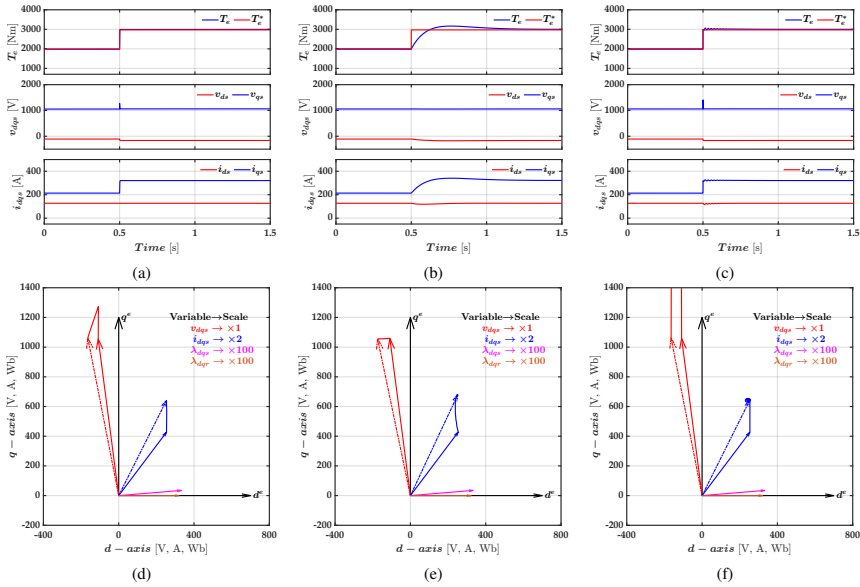
Fig. 4: Response to a torque command step change: (a), (d) RFOC; (b), (e) SLF; (c), (f) SLF with full feedforward terms. Top: time response. Bottom: vector trajectories. Solid vector: starting position. Dashed vector: steady-state position.

V. SIMULATION RESULTS

The performance of the proposed method has been validated by simulation using MATLAB/Simulink. The induction motor parameters at base speed are given in Table I. The dynamic response of the proposed method is validated first with the IM connected to an ideal (linear) voltage. Further a Three-Level Neutral-Point-Clamped (3LNPC) inverter will be used. Usually high-power traction drives operate with low switching frequencies to reduce switching losses, Space-Vector PWM (SVPWM) with a switching frequency of 1 kHz will be used. An infinite inertia is assumed; consequently, the rotor speed remains constant. This assumption is realistic in railway traction drives during short periods of time due to train inertia.

TABLE I: Specifications of the induction motor and nominal values at base speed

Variable	Value	Unit
DC-link voltage	3600	V
Rated Power	1084	kW
Rated Voltage (V_{LL}, rms)	2727	V
Pole-pairs (P)	2	Poles
Stator resistance (R_s)	55.38	mΩ
Stator inductance (L_s)	26.45	mH
Torque	3241	Nm
Speed	3194	rpm

Fig. 4 shows the response to a torque step from 2 kNm

to 3 kNm of RFOC (Fig. 2a), scalar control (SLF) (Fig. 2b), and scalar control (SLF) with both dq-axis feedforward terms (Fig. 3). Top subfigures show the torque, stator voltage and current vectors response in the time domain while bottom subfigures show the vector diagrams. For the sake of comparison, all vector diagrams are shown in the rotor-flux reference frame.

The superior dynamic performance of RFOC over scalar control is readily observed from Fig. 4a and Fig. 4b. The differences in the trajectories followed by the voltage in Fig. 4d and Fig. 4e explain this behavior. For the RFOC case, current controllers force the current to move along the q-axis, while for the scalar control case, a deviation from the desired trajectory is observed. Adding the d-axis feedforward term is seen to improve the dynamic response providing the correct position of the stator voltage vector, but at the price of inadmissible torque and current oscillations. The dynamic response with only d-axis feedforward has been omitted as it provides an unsatisfactory response. Full feedforward (Fig. 4c and Fig. 4f) are seen to provide a dynamic response comparable to that of field-oriented control. However, it is seen the the stator voltage vector reached its limits. In practice, this behavior is undesired, but can be avoided by limiting the maximum slope of the torque command, which is a common practice in traction drives.

While thew fast changes in the torque command shown
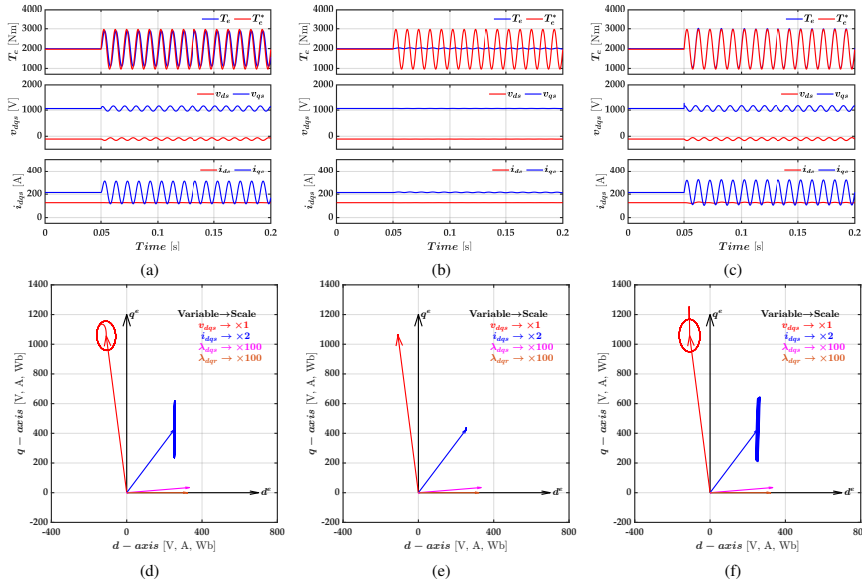
Fig. 5: Response to commanded torque oscillation at 100 Hz: (a), (d) RFOC; (b), (e) SLF; (c), (f) SLF with full feedforward terms. Top: time response. Bottom: vector trajectories. Solid vector: starting position. Dashed vector: steady-state position.

in Fig. 4 are not normally needed, there is a number of operating conditions in which they might be required. This would include to mitigate torque ripples produced by the 2F oscillation of the dc-link voltage in ac catenaries when a 2F filter is not used; to implement anti-slip control and for active cancellation of torsional torque vibrations. In all these case, the control should be able to produce torque oscillations at frequencies around twice the catenary frequency [17].

Fig. 5 shows the dynamic response of the control schemes under discussion subjected to a torque command oscillating at 100 Hz (which corresponds to 2F for 50 Hz catenaries). While RFOC (see Fig. 5a) precisely follows the torque command, SLF is unable to track such fast torque variations (see Fig. 5b). Use of full feedforward 5c) is seen to produce a dynamic response comparable fo the of RFOC.

All the simulation results shown so far used a linear voltage source. While useful for validation of the concepts, the use of the linear voltage source hides effects as the now due to commutation and the delays intrinsic to PWM which can play a relevant role in the real system. The proposed method has also also been validated when feeding the IM from a 3LNPC, as shown in Fig. 6. A step of 2 kNm is applied at $t = 0.5$s then a ramp of 1 kNm is applied at $t = 1.5$s (see Fig. the left column of Fig. 6).
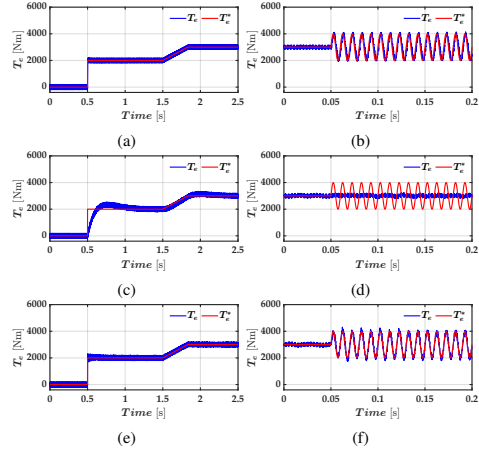

Fig. 6: Response of IM connected to 3LNPC: (a), (b) RFOC; (c), (d) SLF; (e), (f) SLF with full feedforward terms. Left: with step/ramp torque command. Right: with 100 Hz injected oscillation torque command.

The maximum allowable torque gradient will depend on each application. A 3 kNm/s has been chosen for the machine considered in this paper. The torque oscillation injection results are shown in the right column of Fig. 6. The results confirm the effectiveness of the proposed method.

VI. CONCLUSIONS

This paper proposes a method to improve the dynamic response of electric drives using scalar control. The proposed method uses vector control concepts to obtain feedforward voltage terms to be applied to the scalar control, being suitable for its use with electric drives operating at high fundamental frequencies, and with high modulation indexes, including six-step.

The proposed methods can achieve a similar dynamic performance as RFOC. By this way, the deterioration of the RFOC current regulators performance operating at overmodulation range can be avoided without affecting the overall performance of the traction drive.

While the proposed concepts can be applied to any electric drive using scalar control, the specific application being considered are traction drives for railway. Potential uses would include mitigation of torque pulsations in ac catenaries for traction drives operating without 2F filter; anti-slip control and suppression of torsional torque vibrations.

Preliminary simulation results have been provided in this paper. Construction of the testbench for experimental validation is ongoing.

REFERENCES

[1] R. Hill, "Electric railway traction. ii. traction drives with three-phase induction motors," *Power Engineering Journal*, vol. 8, no. 3, pp. 143–152, 1994.

[2] A. M. El-Refaie, "Motors/generators for traction/propulsion applications: A review," *IEEE Vehicular Technology Magazine*, vol. 8, no. 1, pp. 90–99, 2013.

[3] T. H. Nguyen, T. L. Van, D.-C. Lee, J.-H. Park, and J.-H. Hwang, "Control mode switching of induction machine drives between vector control and v/f control in overmodulation range," *Journal of Power Electronics*, vol. 11, no. 6, pp. 846–855, 2011.

[4] Y. Kwon, S. Kim, and S. Sul, "Six-step operation of pmsm with instantaneous current control," *IEEE Transactions on Industry Applications*, vol. 50, no. 4, pp. 2614–2625, 2014.

[5] X. Fang, Z. Tian, H. Li, Z. Yang, F. Lin, and S. Hillmansen, "Current closed-loop control and field orientation analysis of an induction motor in six-step operation for railway applications," *IET Power Electronics*, vol. 12, no. 6, pp. 1462–1469, 2019.

[6] J. Holtz and N. Oikonomou, "Estimation of the fundamental current in low switching frequency high-dynamic medium voltage drives," in *2007 IEEE Industry Applications Annual Meeting*. IEEE, 2007, pp. 993–1000.

[7] A. Fathy Abouzeid, J. M. Guerrero, A. Endemaño, I. Muniategui, D. Ortega, I. Larrazabal, and F. Briz, "Control strategies for induction motors in railway traction applications," *Energies*, vol. 13, no. 3, p. 700, 2020.

[8] M. Fleischer and K. Kondo, "Slip-stick vibration suppression by modal state control for traction drive-trains," *IEEJ Journal of Industry Applications*, vol. 5, no. 1, pp. 1–9, 2016.

[9] B. Gou, X. Feng, W. Song, K. Han, and X. Ge, "Analysis and compensation of beat phenomenon for railway traction drive system fed with fluctuating dc-link voltage," in *Proceedings of The 7th International Power Electronics and Motion Control Conference*, vol. 1. IEEE, 2012, pp. 654–659.

[10] B. K. Bose, "Scalar decoupled control of induction motor," *IEEE transactions on industry applications*, no. 1, pp. 216–225, 1984.

[11] A. Smith, S. Gadoue, M. Armstrong, and J. Finch, "Improved method for the scalar control of induction motor drives," *IET Electric Power Applications*, vol. 7, no. 6, pp. 487–498, 2013.

[12] I. Boldea, A. Moldovan, and L. Tutelea, "Scalar v/f and i-f control of ac motor drives: An overview," in *2015 Intl Aegean Conference on Electrical Machines Power Electronics (ACEMP), 2015 Intl Conference on Optimization of Electrical Electronic Equipment (OPTIM) 2015 Intl Symposium on Advanced Electromechanical Motion Systems (ELECTROMOTION)*, 2015, pp. 8–17.

[13] S. R. P. Reddy and U. Loganathan, "Robust and high-dynamic-performance control of induction motor drive using transient vector estimator," *IEEE Transactions on Industrial Electronics*, vol. 66, no. 10, pp. 7529–7538, 2018.

[14] ——, "Improving the dynamic response of scalar control of induction machine drive using phase angle control," in *IECON 2018-44th Annual Conference of the IEEE Industrial Electronics Society*. IEEE, 2018, pp. 541–546.

[15] Z. Zhang and A. M. Bazzi, "Robust sensorless scalar control of induction motor drives with torque capability enhancement at low speeds," in *2019 IEEE International Electric Machines & Drives Conference (IEMDC)*. IEEE, 2019, pp. 1706–1710.

[16] B. Bose, "Modern power electronics and ac drives-prentice-hall," *Inc, Publication*, pp. 70–74, 2002.

[17] Y. Lei, K. Wang, L. Zhao, and Q. Ge, "An improved beatless control method of ac drives for railway traction converters," in *2016 19th International Conference on Electrical Machines and Systems (ICEMS)*. IEEE, 2016, pp. 1–5.

B.2.3 Assessment of Overmodulation Strategies for AC Drives Considering Harmonics Content and Switching Losses

Assessment of Overmodulation Strategies for AC Drives Considering Harmonics Content and Switching Losses

Ahmed Fathy Abouzeid
Dept. of Electrical Engineering
University of Oviedo
Gijón, Spain
abouzeidahmed@uniovi.es

Juan Manuel Guerrero
Dept. of Electrical Engineering
University of Oviedo
Gijón, Spain
guerrero@uniovi.es

Aitor Endemaño
Traction systems
Ingeteam Power Technology
Zamudio, Spain
iker.muniategui@ingeteam.com

Iker Muniategui
Traction systems
Ingeteam Power Technology
Zamudio, Spain
aitor.endemano@ingeteam.com

David Ortega
Traction systems
Ingeteam Power Technology
Zamudio, Spain
David.Ortega@ingeteam.com

Fernando Briz
Dept. of Electrical Engineering
University of Oviedo
Gijón, Spain
fbriz@uniovi.es

Abstract—This paper performs a comparative analysis of overmodulation methods for AC electric drives. Criteria for the analysis considers three aspects: output vs. commanded modulation index (i.e., linearity); harmonic content; and the number of commutations (i.e., switching losses). The analysis focuses on existing methods reported in the literature. Improvements for the existing methods will be proposed as a result of the analysis. The analysis is experimentally validated on a three-phase three-level Neutral-Point-Clamped (NPC) inverter.

I. INTRODUCTION

Overmodulation is used in electric drives to increase the fundamental output voltage of the inverter. This has two beneficial effects: 1) an increase of the fundamental output voltage allows to get more torque at high speed, and consequently more power; 2) the number of commutations, and consequently, the switching losses in the inverter are reduced [1]. Unfortunately, this is at the price of an increase of the distortion of the currents creating torque harmonics with the subsequent effects as noise, vibration, additional losses in the machine, etc [2]. Many efforts have been devoted to improving drive performance in overmodulation [3]–[9]. However, the analyses reported in the literature primarily focuses on voltage utilization and harmonic content, the effect on switching losses being normally ignored. This paper presents a comparative analysis of overmodulation methods for AC electric drives using three criteria: output vs. commanded modulation index (i.e. linearity); harmonic content; and number of commutations (i.e. switching losses). Thus, the analysis will primarily focus on existing methods reported in the literature, followed by a generalized form for improving some of these methods will be also addressed. Though the methods discussed in this paper can be applied to any electric drive, they will be of especial relevance in high power applications in which machine and/or power converter need to operate close to their thermal limits, as often occurs in railway traction drives.

II. VOLTAGE SYNTHESIS SUMMARY OF OVERMODULATION STRATEGIES

The modulation index (M_i) of a three-phase inverter is given by (1), where V is the peak value of the phase voltage fundamental component and V_{dc} is the inverter dc input voltage. Modulation methods as Space-Vector Modulation (SVM) or sine-triangle Pulse-Width Modulation (PWM) with triplen harmonic injection allow linear operation of the inverter (i.e. $M_i = M_i^*$) up to $M_i = 0.907$, $M_i = 1$ being achieved with six-step modulation.

$$M_i = \frac{V}{\frac{2}{\pi}V_{dc}} \tag{1}$$

In the overmodulation range ($0.907 \leq M_i \leq 1$), the voltage waveform is distorted, which results in odd harmonics. In addition, the relationship between commanded and actual modulation index, M_i^* and M_i, becomes non-linear. Several overmodulation methods that have been reported in the literature will be summarized following (see Fig. 2), and their performance will be discussed in Section IV:

A. Minimum-Phase Error (MPE), V_{s1}^*

In this strategy, when the reference voltage vector V_s^* is outside the hexagon, the applied voltage is obtained as the intersection between the voltage command and the hexagon boundary [10]. The results for this method has been omitted from the paper as it requires infinity gain to reach six-step operation.
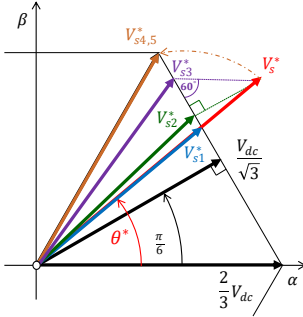
Fig. 1: Space-vector representation of the modified voltage vector vs. the reference voltage vector for overmodulation.

Fig. 3: Proposed generalized form overmodulation strategy: a) Reference voltage vector, V_s^*; b) Modified reference voltage vector with an arbitrary angle γ, V_{sm}^*.

B. Minimum-Distance/Magnitude Error (MDE), V_{s2}^*

When the reference voltage vector is outside the hexagon, the output voltage is obtained as the projection of the voltage command orthogonal to the hexagon boundary (see Fig. 2a) [10].

C. Switching-state (60°), V_{s3}^*

The output voltage vector is modified to a point in which the vector difference between the reference and the output voltage vector makes a 60° lagging/leading with the hexagon boundary on the first/second half of each hexagon sector respectively (see Fig. 2b) [10].

D. Single-mode, V_{s4}^*

When the reference vector exceeds the hexagon boundary, the output voltage vector is obtained by rotating the reference voltage, keeping its magnitude constant, until it touches the hexagon boundary (see Fig. 2c). With this method, six-step operation is reached when $V^* = \frac{2}{3}V_{dc}$ [11]. Due to holding the reference voltage vector at the intersection point, the phase angle of the reference vector is shifting to the next or the previous intersection point depending on its location in the sector. This results in a significant increase of harmonic components in the output voltage.

E. Dual-mode, V_{s5}^*

This method is intended to overcome the single-mode high harmonic content [12], [13]. Overmodulation is divided into two modes: a) Mode I ($0.907 < M_i \leq 0.952$): only the magnitude of the reference vector is changed while the phase angle is kept as its reference. If the reference vector is outside the hexagon boundary, the output vector is limited to the hexagon bounds. When the reference vector is inside the hexagon, the output vector magnitude is increased with an appropriate value to compensate for the difference in the reference vector during the operation outside the hexagon limit.

The modified vector magnitude is a function of the reference angle α_r. b) Mode II ($0.952 < M_i \leq 1$): both vector magnitude and phase angle are changed to ensure a smooth transition of the output voltage vector into square wave, i.e. six-step (see Fig. 2d). The output voltage vector is limited to the hexagon boundary while the output phase angle is modified according to a holding angle α_h which is gradually increased from zero to $\frac{\pi}{6}$ at six-step. For online implementation both the reference and the holding angles are linearized as a function of the modulation index [13].

III. GENERALIZED FORM OF SPACE-VECTOR PWM IN OVERMODULATION

From the previous discussion, it can be noticed that the Minimum-Phase Error, Minimum-Distance Error and Switching-State methods are based on similar principles, the only difference being the angle between the voltage vector being added to the original voltage command and the hexagon boundary (0°, 90° and 60° respectively), as seen in Fig. 1. This type of overmodulation can be generalized to any arbitrary angle γ as described following:

1) Assuming the reference voltage vector is located in the first sector. The reference vector magnitude limited to the hexagon boundary is calculated in (2), where θ^* is the angle of the reference voltage vector.

$$|V_{hex}^*| = \frac{V_{dc}}{\sqrt{3}\cos\left(\theta^* - \frac{\pi}{6}\right)} \qquad (2)$$

2) For a given angle γ the triangle ABC shown in Fig. 3 is formed, with the angles α and β being obtained as:

$$\alpha = \begin{cases} \theta^* + \frac{\pi}{3}, & \text{if } 0 \leq \theta^* \leq \frac{\pi}{6} \\ \pi - \theta^* - \frac{\pi}{3}, & \text{if } \frac{\pi}{6} < \theta^* \leq \frac{\pi}{3} \end{cases} \qquad (3)$$

$$\beta = \pi - \alpha - \gamma. \qquad (4)$$
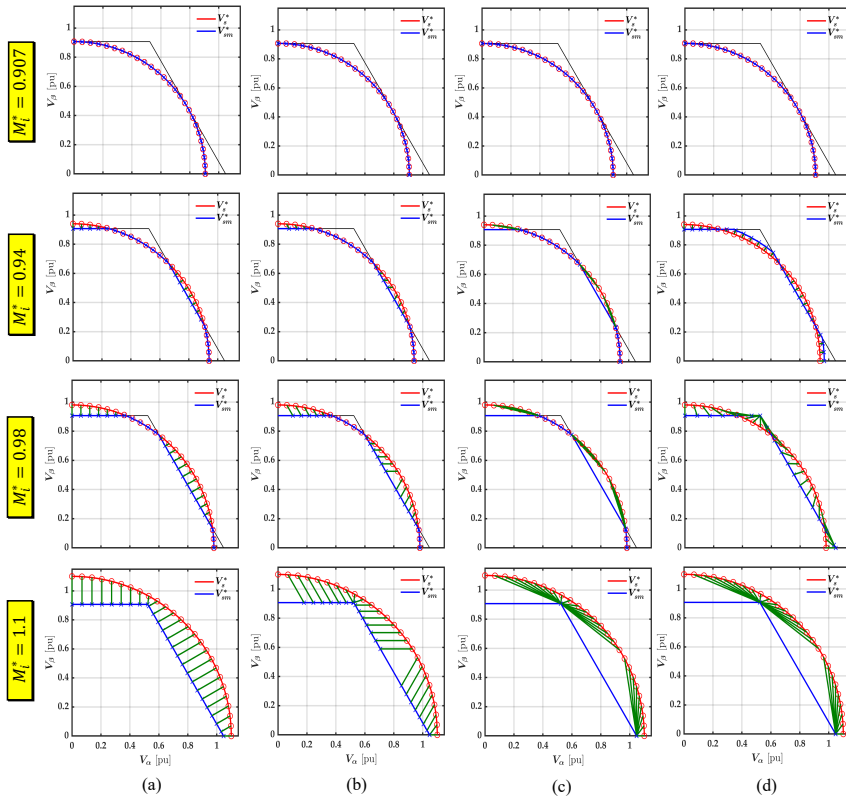
Fig. 2: Reference voltage vector synthesize using different overmodulation methods: (a) Minimum-Distance Error (90°); (b) Switching-State (60°); (c) Single-mode; (d) Dual-mode. Red: reference voltage vector. Blue: modified reference voltage vector. Green: difference between reference and modified voltage vectors.

3) The modified reference vector can be calculated as follows:

$$|A| = |V_s^*| - |V_{hex}^*| \tag{5}$$

$$|C| = |A|\frac{\sin(\beta)}{\sin(\gamma)} \tag{6}$$

$$\overrightarrow{V}_{sm}^* = \begin{cases} \overrightarrow{V}_{hex}^* + |C|\,e^{-j\frac{\pi}{3}}, & \text{if } 0 \le \theta^* \le \frac{\pi}{6} \\ \overrightarrow{V}_{hex}^* + |C|\,e^{j\frac{2\pi}{3}}, & \text{if } \frac{\pi}{6} < \theta^* \le \frac{\pi}{3} \end{cases} \tag{7}$$

4) Finally, the modified reference voltage vector $\overrightarrow{V}_{sm}^*$ is rotated for the remaining sectors.

IV. COMPARATIVE ANALYSIS OF OVERMODULATIONM STRATEGIES

This section compares the performance of the different overmodulation strategies. As already stated, three aspects will be considered: a) output to commanded modulation index (linearity); b) harmonic distortion; and c) number of commutations. The analysis will focus on strategies which can reach six-step operation; hence the Minimum-Phase Error (MPE) method is disregarded as it requires an infinite reference modulation index to reach six-step.

Fig. 4a shows the actual (M_i) vs. commanded (M_i^*) modulation index for the overmodulation methods stated in section II. It is seen that the Dual-mode strategy provides a nearly

273

Fig. 4: Comparative analysis: a) M_i versus M_i^*; b) THD, c) -5th, d) 7th, e) -11th and f) 13th harmonic components vs. M_i respectively.

differences are observed. The individual harmonic distortion for the -5th, 7th, -11th and 13th components are shown in Fig. 4c-f respectively. It is seen that Minimum-Distance Error and Dual-mode have lower harmonic content for most of the overmodulation range. However, the Switching-State method has lower distortion in certain harmonic components for a specifi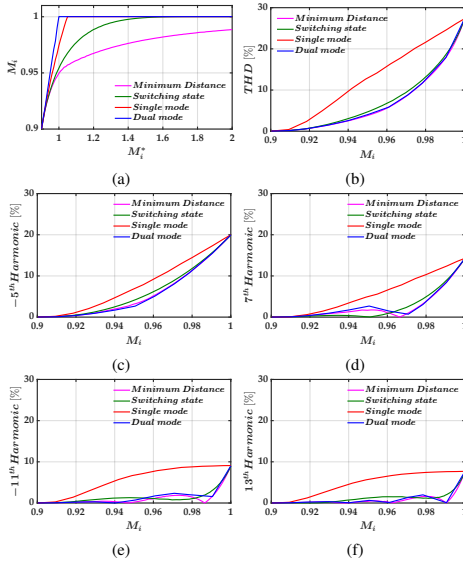c modulation index range. For instance, the 7th from $M_i^* = 0.9$ to $M_i^* = 0.95$ and the -11th from $M_i^* = 0.958$ to $M_i^* = 0.98$, Switching-State method becomes superior for these ranges regarding to harmonic content.

Another important aspect which is often neglected in the literature are the switching losses, which are especially relevant for medium-voltage high-power drives. The number of commutations per quarter of cycle was obtained by means of simulation. This number is a function of the modulation index and the ratio between switching frequency and fundamental frequency, ($\frac{\omega_{sw}}{\omega_f}$). Fig. 5 shows the results for a ratio of 100 and 10 respectively. The Single-mode strategy shows the worst performance, while none of the other methods is superior (i.e., has less commutations) for all modulation indexes and switching to fundamental ratios.

Fig. 5: Number of commutations per quarter cycle of the fundamental frequency, of the different overmodulation methods vs. M_i for a switching to fundamental frequency ratio: a) $\frac{\omega_{sw}}{\omega_f} = 100$; b) $\frac{\omega_{sw}}{\omega_f} = 10$.

The same analyses was repeated using the proposed general form discussed in section III. By comparing the results in Fig. 6 and Fig. 7, it can be concluded that the lower the angle, the higher the linearity, THD, and number of commutations. The maximum output voltage is found at 1.047 of the commanded modulation indexes, which is similar to the Single-mode method. But again, taking into consideration the individual low-order harmonic components, none of the angles provides the best solution over the whole overmodulation range.

Optimal overmodulation strategy can be achieved by combining at least two overmodulation methods as a function of modulation index. As the minimum number of commutations and minimum low-order harmonic distortion (especially -5th & 7th) are usually the requirements for traction drives, a combination of Switching-State and Dual-mode could provide the best performance over the whole overmodulation range.

V. EXPERIMENTAL VALIDATION

Fig. 8 shows the hardware setup of the test bench used for experimental verification. Control is implemented on a

linear relationship between the reference and the output voltage while the Minimum-Distance Error (MDE) one shows the worse behavior in this regard. The six-step operation is reached at a very high (in the range of thousands) value of the reference modulation index, therefore the reference modulation index in Fig. 4a is only showed up to the value of 2 for clear visualization and comparison with other methods. Switching-State strategy modifies the reference voltage vector to be 60° from the hexagon boundary. Six-step operation is achieved in this case for $M_i^* \cong 1.5$. Holding the reference voltage vector at the hexagon boundary to compensate for the interval being outside the hexagon (i.e. Single-mode), will fasten the achievability of the six-step operation to $M_i^* \cong 1.047$ [11].

To conclude this discussion, it is important to note that the non-linear relationship between the commanded and actual modulation index can potentially be compensated by prewarping the commanded modulation index, either a look-up table or an analytical function can be used for this purpose.

The main concern using overmodulation are the low-order harmonics introduced in the output voltage waveform, which will be transferred to the currents and eventually to torque. Fig. 4b shows the Total Harmonic Distortion (THD) considering the -5th, 7th, -11th and 13th harmonic components. It is noted that the Single-mode method shows the worst behavior, while for the other methods subject of this analysis only minor

Fig. 6: Comparative analysis as a function of γ angle: a) M_i versus M_i^*; b) THD, c) -5th, d) 7th, e) -11th and f) 13th harmonic components vs. M_i respectively.

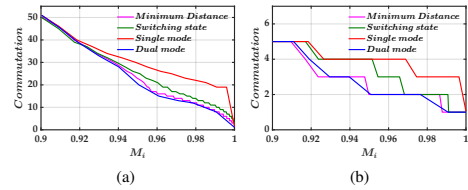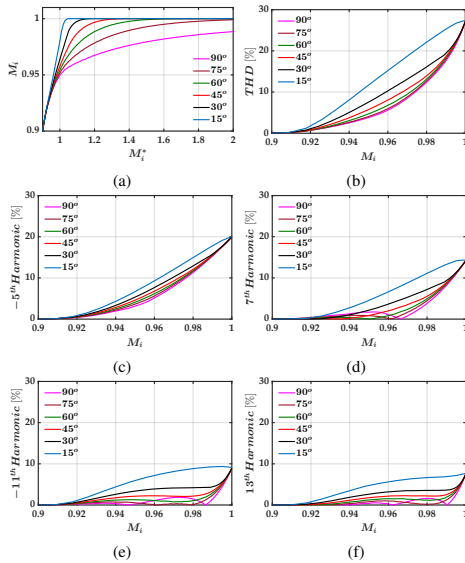Fig. 7: Number of commutations per quarter cycle of the fundamental frequency, of the different overmodulation methods as a function of γ angle vs. M_i for a switching to fundamental frequency ratio: a) $\frac{\omega_{sw}}{\omega_f} = 100$; b) $\frac{\omega_{sw}}{\omega_f} = 10$.

TMS320F28335 DSP. A three-level 4 kV NPC three-phase inverter was used. For the experiments presented in this paper, the dc-link was limited to 600V. The switching and sampling frequencies are 1 kHz, a dead-time of 4 μs is used.

The measured phase-a to dc mid-point voltages is shown in Fig. 9. It can be noticed that the switching pattern of Minimum-Distance Error and Switching-State methods are still far from six-step operation even at ($M_i^* = 1.1$). The transition from linear modulation to six-step is achieved in both Single-mode (see Fig. 9c) and Dual-mode (see Fig. 9d). However, Dual-mode reaches six-step faster with less number

(a)
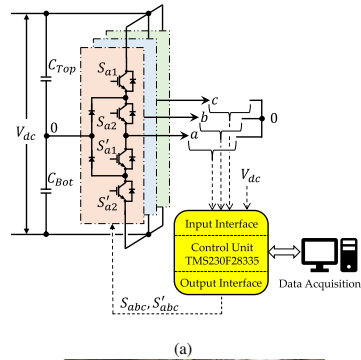
(b)

Fig. 8: Test bench for overmodulation strategies: a) Schematic representation of the laboratory setup; b) 4 kV/40A three-level NPC ELINSA inverter.

of commutations which confirms the simulation results in section IV (see Fig. 9c vs. Fig. 9d at $M_i^* = 0.94$ and $M_i^* = 0.98$).

Despite of the main aspects compared in this section, the dynamic performance plays an important role in selecting the appropriate overmodulation strategy for electric drives. Usually, overmodulation methods with larger gains are preferred for such applications which involves current regulators [14], [15]. Further investigation of the dynamic performance of overmodulation strategies and the transition from one method to another for optimal overmodulation is ongoing.

VI. CONCLUSIONS

In this paper, comparative analysis of four overmodulation strategies for electric drives reported in the literature is performed: Minimum-Distance Error (90°), Switching-State (60°), Single-mode, and Dual-mode. Furthermore, a generalized overmodulation method with an arbitrary angle γ is presented. Criteria considered for the analysis are: 1) linearity,

Fig. 9: Measured voltage of phase a to dc mid-point of three-level NPC (V_{a0}) for different overmodulation methods: (a) Minimum-Distance Error (90°); (b) Switching-State (60°); (c) Single-mode; (d) Dual-mode.

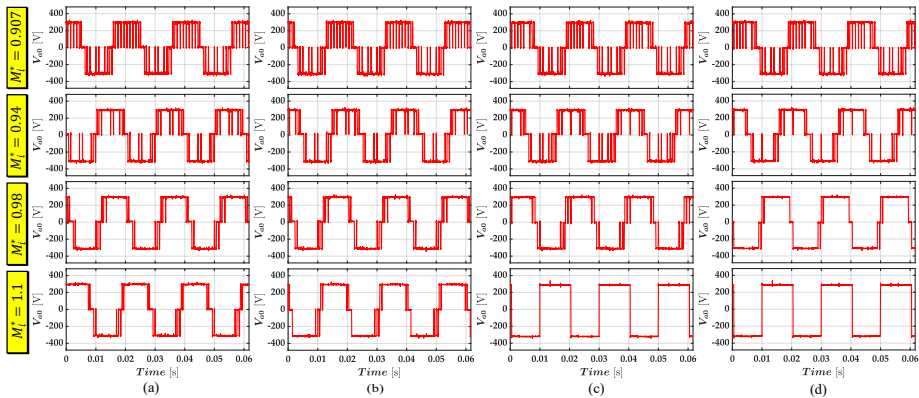2) harmonic distortion, and 3) number of commutations. A finding is that by decreasing the angle between the voltage vector added to the original voltage command and the hexagon boundary, linearity is increased at the price of an increase in the harmonic distortion and number of commutations. It is concluded that none of the analyzed methods achieve the best performance for the whole overmodulation range and switching to fundamental frequency ratio. Optimal performance would be achieved by combining Switching-State and the Dual-mode. Preliminary simulation and experimental results have been provided.

Analysis of the dynamic transition between different overmodulation methods, both for open loop operation as well as in current controlled drives is a subject of ongoing research.

REFERENCES

[1] X. Guo, M. He, and Y. Yang, "Over modulation strategy of power converters: A review," *IEEE Access*, vol. 6, pp. 69 528–69 544, 2018.

[2] H. Mahlfeld, T. Schuhmann, R. Döbler, and B. Cebulski, "Impact of overmodulation methods on inverter and machine losses in voltage-fed induction motor drives," in *2016 XXII International Conference on Electrical Machines (ICEM)*. IEEE, 2016, pp. 1064–1070.

[3] S. Halasz, I. Varjasi, and A. Zacharov, "Overmodulation strategies of inverter-fed ac drives," in *Proceedings of the Power Conversion Conference-Osaka 2002 (Cat. No. 02TH8579)*, vol. 3. IEEE, 2002, pp. 1346–1351.

[4] G. Narayanan and V. T. Ranganathan, "Extension of operation of space vector pwm strategies with low switching frequencies using different overmodulation algorithms," *IEEE Transactions on Power Electronics*, vol. 17, no. 5, pp. 788–798, 2002.

[5] S. K. Mondal, B. K. Bose, V. Oleschuk, and J. O. P. Pinto, "Space vector pulse width modulation of three-level inverter extending operation into overmodulation region," *IEEE Transactions on Power Electronics*, vol. 18, no. 2, pp. 604–611, 2003.

[6] A. K. Gupta and A. M. Khambadkone, "A general space vector pwm algorithm for multilevel inverters, including operation in overmodulation range," *IEEE Transactions on Power Electronics*, vol. 22, no. 2, pp. 517–526, 2007.

[7] J. Prieto, F. Barrero, M. J. Durán, S. T. Marín, and M. A. Perales, "Svm procedure for n-phase vsi with low harmonic distortion in the overmodulation region," *IEEE Transactions on Industrial Electronics*, vol. 61, no. 1, pp. 92–97, 2013.

[8] P. Stumpf and S. Halász, "Optimization of pwm for the overmodulation region of two-level inverters," *Ieee transactions on industry applications*, vol. 54, no. 4, pp. 3393–3404, 2018.

[9] J. Chen, R. Ni, T. Li, R. Qiu, and Z. Liu, "The harmonic characteristic of the advanced synchronous svpwm overmodulation strategy," *IEEE Access*, vol. 7, pp. 148 934–148 949, 2019.

[10] A. M. Hava, R. J. Kerkman, and T. A. Lipo, "Carrier-based pwm-vsi overmodulation strategies: analysis, comparison, and design," *IEEE Transactions on Power Electronics*, vol. 13, no. 4, pp. 674–689, 1998.

[11] S. Bolognani and M. Zigliotto, "Novel digital continuous control of svm inverters in the overmodulation range," *IEEE Transactions on Industry Applications*, vol. 33, no. 2, pp. 525–530, 1997.

[12] J. Holtz, W. Lotzkat, and A. M. Khambadkone, "On continuous control of pwm inverters in the overmodulation range including the six-step mode," *IEEE Transactions on Power Electronics*, vol. 8, no. 4, pp. 546–553, 1993.

[13] Dong-Choon Lee and G-Myoung Lee, "A novel overmodulation technique for space-vector pwm inverters," *IEEE Transactions on Power Electronics*, vol. 13, no. 6, pp. 1144–1151, 1998.

[14] A. M. Hava, S.-K. Sul, R. J. Kerkman, and T. A. Lipo, "Dynamic overmodulation characteristics of triangle intersection pwm methods," *IEEE Transactions on Industry Applications*, vol. 35, no. 4, pp. 896–907, 1999.

[15] Y.-C. Kwon, S. Kim, and S.-K. Sul, "Six-step operation of pmsm with instantaneous current control," *IEEE Transactions on Industry Applications*, vol. 50, no. 4, pp. 2614–2625, 2014.

B.3 Under review publications

B.3.1 Advanced Maximum Adhesion Tracking Strategies in Railway Traction Drives

Advanced Maximum Adhesion Tracking Strategies in Railway Traction Drives

Ahmed Fathy Abouzeid[a,b,*], Juan Manuel Guerrero[a], Lander Lejarza[c], Iker Muniategui[c], Aitor Endemaño[c] and Fernando Briz[a]

[a]*AECP Group, Department of Electrical, Electronic and Computer Engineering, University of Oviedo, Gijón, Spain*
[b]*Department of Electrical Engineering, Faculty of Engineering, Port-Said University, Egypt*
[c]*R&D Group, Department of Traction Systems, Ingeteam Power Technology, Zamudio, Spain*

ARTICLE INFO

ABSTRACT

Modern railway traction systems are equipped with anti-slip control to avoid excessive slipping of locomotive wheels, which is compulsory due to both performance and safety concerns. A certain amount of slip is often needed to increase the torque transferred by the traction motors onto the rail. Finding the slip at which maximum traction force is achieved is challenging due to the non-linear relationship between slip and wheel-rail adhesion coefficient, as well as to its dependence on rail and wheel conditions. The constant slip control strategy can be used instead but at the price of not fully utilizing the train traction/braking capability, which will penalize train performance.

In this paper three slip control strategies are compared: constant slip velocity; perturb and observe (P&O); and steepest gradient (SG), the last two methods being intended for maximum adhesion tracking (MAT). Additionally, new advanced MAT strategies using Fuzzy Logic Controller (FLC) and Particle Swarm Optimization (PSO) will be proposed. All the methods will be simulated and further validated experimentally and compared using a scaled Roller Rig.

1. Introduction

Optimized utilization of traction/braking force is a key aspect in modern railway traction systems for multiple reasons, including safety, performance, reliability, and energy efficiency.

Traction force is defined as the force developed by the traction motor being transferred to the rail through the train vehicle's wheel to achieve the desired train speed. Maximizing the traction force leads to more efficient and faster acceleration/deceleration rates. This allows achieving the planned travel speed-distance profile precisely, avoiding trip delays and reducing energy consumption. Therefore, implementation of control methods able to maximize the traction force becomes crucial to traction systems manufacturers and train service providers.

The traction force that can be transferred to the rail will be limited by the friction between the driven wheels and the steel rail. The adhesion limit will depend on the normal load and the friction coefficient of the contact point, also known as the adhesion coefficient. Adhesion coefficient is a non-linear function slip [1]. Slip/skid phenomenon occurs when the traction force surpasses the adhesion limit during traction/braking. Excessive slip or skid will result in an increase in wheel wear and a reduction of the overall traction performance. Therefore, many efforts have been devoted to limiting the slip/skid between the wheel and the rail [2, 3, 4].

✉ abouzeidahmed@uniovi.es; ahmed_abouzeid@eng.psu.edu.eg (A.F. Abouzeid); guerrero@uniovi.es (J.M. Guerrero); lander.lejarza@ingeteam.com (L. Lejarza); iker.muniategui@ingeteam.com (I. Muniategui); aitor.endemano@ingeteam.com (A. Endemaño); fbriz@uniovi.es (F. Briz)

ORCID(s): 0000-0002-2239-7972 (A.F. Abouzeid); 0000-0001-5529-9837 (J.M. Guerrero); 0000-0002-6658-8746 (F. Briz)

Both direct and indirect re-adhesion control methods have been proposed to limit the slip within a predefined threshold [5, 6, 7, 8]. The main demerit of these traditional re-adhesion methods is that the traction capability is not fully utilized.

Finding the slip velocity at which the maximum adhesion occurs is a challenging task. This is due to the unpredictability of the wheel-rail contact condition, and consequently the difficulty of estimating the adhesion coefficient. In [9], Perturb and Observe (P&O) method similar to those used for photovoltaic panels was applied for MAT. The slip controller increases the slip velocity command gradually and the tractive force is monitored and stored. If the maximum point is overstepped, the slip velocity command is decreased to bring the operating point back to the stable region. In [10] authors propose to use the adhesion force derivative. The slip velocity command is corrected according to the slope of the adhesion curve, i.e., the slip command increases when the slope of the curve is positive which means that the operating point is in the stable region. If the slope of the adhesion curve is negative, the operating point is in the unstable region and the slip command should be decreased. The previous two methods will be discussed in more detail and tested in this paper.

Several approaches have been proposed using Kalman Filters to avoid measurement noise and the computation of derivatives used in [10]. However, these methods rely on the mathematical model of the mechanical drive train and require accurate parameter estimates [11, 12, 13]. The authors in [14] proposed an adaptive sliding mode control to stabilize wheel slip and improve traction performance but this method requires accurate measurement of the adhesion force, which is not easy to achieve in practice. Additionally, advanced slip control techniques using model predictive

control and adhesion swarm intelligence can be found in [15, 16, 17, 18, 19]. Though these methods show good adhesion performance, they either lack experimental validation [16, 17, 18] or suffer from implementation complexity and high computational burden [15, 19].

The aim of this paper is twofold: First, existing slip control strategies intended for maximum utilization of the available adhesion will be discussed. Then, two new methods for MAT will be proposed, using Fuzzy Logic Control (FLC) and Particle Swarm Optimization (PSO) respectively. Existing and proposed slip control methods will be simulated and validated experimentally on a scaled roller rig. A comparative analysis will be included considering computational burden, tuning easiness, MAT searching capability, steady-state response, and Signal Smoothness.

The structure of the article is summarized as follows: section 2 includes an overview of the design and the overall control scheme of the scaled roller rig with wheel-rail contact emulator; section 3 summarizes the existing slip velocity control methods considered for MAT applied in real trains; section 4 includes the two proposed MAT strategies; section 5 includes an assessment and comparative analysis of all the methods being considered; conclusions are finally discussed in section 6.

2. System Model and Test bench Description

One of the limitations perceived during the review of the state of the art was that the different methods were validated using different platforms. This makes it extremely difficult to perform a fair comparative analysis. To overcome this limitation, all the methods considered in this paper will be tested in the same test rig. System model as well as test rig design and control are presented in this section.

2.1. Wheel-rail contact emulator

Roller rigs combined with simulation verification are convenient replicas for evaluating control techniques of railway traction drives during pre-service commissioning. Full-scale or scaled roller rigs can be used for the purpose of producing the same dynamics of the actual train moving on a rail. Scaled roller rigs are preferred due to cost, size, and manufacturing obstacles. However, special care must be taken for the selection of the scaled parameters during the design process to reproduce as precisely as possible the behavior of the full-scale system. In this paper, Manchester Metropolitan University (MMU) method is used [20]. In this approach, the locomotive mass is considered to be equally distributed amongst the wheels and the nominal linear wheel speed is scaled by 1/5 factor [21]. The full design process and scaling parameters of the scaled roller rig used in this paper can be found in [22].

Fig. 1 shows a schematic representation of the scaled roller rig where the smaller wheel represents one of the locomotive wheels and the bigger wheel, referred to as roller, represents the rail. Two induction motors (IMs) are used to drive both wheels via a transmission belt system. The normal force F_N applied to the wheel is adjusted manually with a
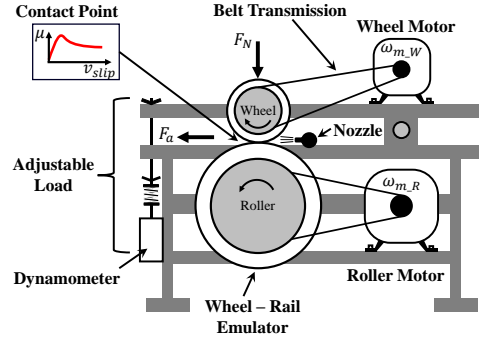
Figure 1: Schematic representation of the scaled roller rig.

spring system including a dynamometer for fine force tuning. The test bench has a water-spraying nozzle to emulate wheel-rail wet conditions.

Adhesion coefficient μ is defined in (1) as the ratio between the adhesion force F_a being transferred from the wheel to the roller and the normal force applied to the wheel F_N. Adhesion is a non-linear function that depends on the slip velocity between the wheel and roller, ambient factors such as humidity and ambient temperature, and the surface condition of the contact point [23]. The slip velocity is given by (2), where ω_{m_W}, ω_{m_R} and r_W, r_R are the mechanical speed of the induction motors (IM) in electrical units (rad/s) and the radius of both wheel and roller respectively.

$$\mu = \frac{F_a}{F_N} \tag{1}$$

$$v_{slip} = v_W - v_R \tag{2}$$

where $v_W = \omega_{m_W} \cdot r_W; \quad v_R = \omega_{m_R} \cdot r_R$

The adhesion torque (i.e., load torque) can be expressed as the adhesion force exerted on the wheel multiplied by its radius (3).

$$T_W = F_a \cdot r_W = \mu \cdot F_N \cdot r_W \tag{3}$$

The electromagnetic torque developed by the wheel motor T_{e_W} and transferred to the wheel T_W via belt transmission is given by (4) where R_{g_W} is the wheel gear ratio.

$$T_{e\_W} = \frac{T_W}{R_{g\_W}} = \frac{\mu \cdot F_N \cdot r_W}{R_{g\_W}} \tag{4}$$

The same relation can be developed for the roller side where T_{e_R}, and R_{g_R} are the roller motor electromagnetic torque, and roller gear ratio respectively.

$$T_{e\_R} = \frac{T_R}{R_{g\_R}} = \frac{\mu \cdot F_N \cdot r_R}{R_{g\_R}} \tag{5}$$

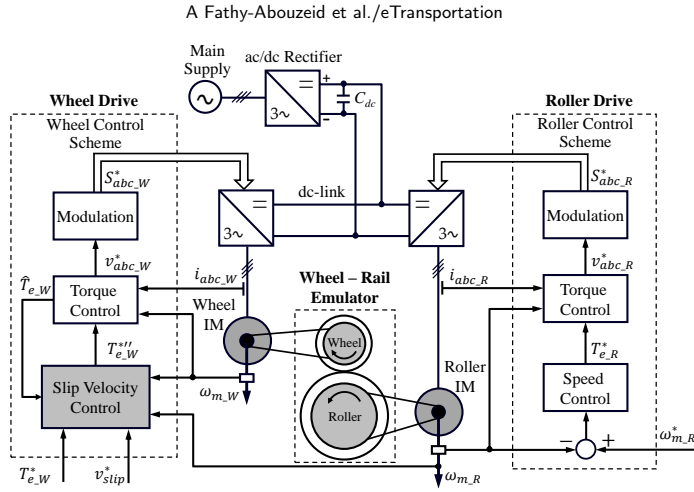**Figure 2:** Overall control scheme of scaled roller rig for slip velocity control.

2.2. Scaled roller rig overall control scheme

Wheel and roller motors are fed from three-phase inverters which share the same dc link (see Fig. 2). The dc link is fed from the grid by means of a diode rectifier. A commercial drive using Rotor Field Oriented Control (RFOC) with an outer speed control loop (see right side of Fig. 2) is used to control the roller.

On the other side, the wheel motor is fed from a custom drive built to implement the different control strategies for MAT functionality. The control scheme of the custom drive contains the same structure as the roller commercial drive except for the speed control block that is replaced by the slip velocity control block (see the gray block on the left side of Fig. 2). Further details are provided in Section 5. The slip velocity control block requires additional signals: reference torque $T_{e\_W}^*$, reference slip velocity v_{slip}^*, and torque estimate $\hat{T}_{e\_W}$. The signals involved depend on the MAT method being used. In all cases, knowledge of roller speed is essential, which implies that real train velocity should be known in the real system.

For the following discussion and simulations, it is assumed that the roller drive control is set to speed control mode running with a constant speed. This is consistent with the case of a train that has a very large inertia. Meanwhile, the wheel drive operates with torque control; the slip velocity controller remains disabled unless the actual slip surpasses the established limit (see Fig. 3). The torque reference $T_{e\_W}^*$ is transferred to the wheel drive torque command, i.e, $T_{e\_W}^{*\prime\prime} = T_{e\_W}^*$ unless wheel slip is detected. In this case, the slip velocity control is activated and the torque command generated from the slip speed controller is passed by the (Min) function, i.e., $T_{e\_W}^{*\prime\prime} = T_{e\_W}^{*\prime}$. Wheel speed reference $\omega_{m\_W}^*$ is obtained from the slip velocity control block considering the gear ratio, i.e. $\omega_{m\_W}^* = \frac{R_{g\_W}}{r_W} \cdot v_W$,

where v_W is the wheel linear speed in m/s. A dynamic limiter is added for the slip speed controller to avoid wind-up problems in the Propositional-Integral (PI) controller when the slip speed control is not active [22]. Different slip control modes are discussed following.
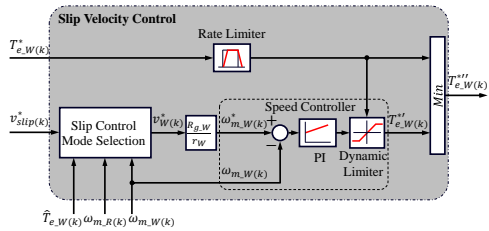
Figure 3: Detailed slip velocity control block diagram. Slip Control Mode Selection block is explained in Sections 3 and 4.

3. Overview of Wheel-Rail Slip Velocity Control Methods

This section reviews the slip velocity control methods reported in the literature. Simulation results using the downscaled test rig are provided. Experimental results will be shown in section 5.

The slip velocity control mode in Fig. 3 can be selected either with constant or variable slip velocity. Variable slip mode can be based on train speed where the slip velocity reference value is changing along the whole trip, and continuously adapting the slip velocity command to track the maximum adhesion. The classification of the slip control mode is summarized in Fig. 4, and the discussion of each method is provided in the following subsection.

Figure 4: Classification of slip velocity control mode.

3.1. Constant slip velocity control

This method is the simplest solution for slip control, being likely the most common choice for anti-slip protection in railway applications [3]. In this control mode, slip velocity reference v^*_{slip} is added to the train velocity and sent to the wheel speed controller as seen in Fig. 5. In this paper, it is assumed that the train speed is measured. Methods to measure or estimate the train's linear speed can be found in [24, 25, 26]. Slip velocity reference is selected based on field tests and the train's driver experience, being generally in the range of $\approx$ 0.5 to 1.0 m/s [3]. Regardless of its simplicity, the main demerit of this method is that it does not usually operate at the maximum adhesion point.
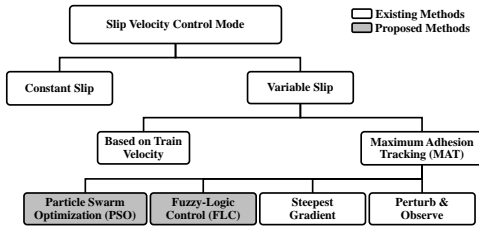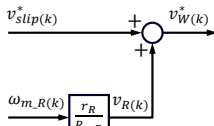

Figure 5: Constant slip velocity control command generation.

Fig. 6(a) shows simulation results using this method. The adhesion profiles used are shown in Fig. 6(b). A torque ramp with a final value of 10 Nm is commanded. The adhesion is lost when the actual torque reaches $\approx$ 5 Nm (see Fig. 6(a)-top). Slip velocity control is then activated with a 1.0 m/s set point (see third subplot in Fig. 6(a)). The response of slip control to changes in the wheel-roller adhesion conditions is also simulated as shown in Fig. 6. Constant slip velocity control is seen to provide a good dynamic response, with deviations from the target sleep corrected in $\approx$ 1 s, and not exceeding $\approx$ 0.2 m/s.

3.2. Variable slip velocity control with maximum adhesion estimation

These methods are aimed to operate at the slip speed providing maximum adhesion. This will require maximum adhesion estimation. Subsections 3.2.1 and 3.2.2 discuss methods already reported in the literature. Two new methods will be proposed in Section 4
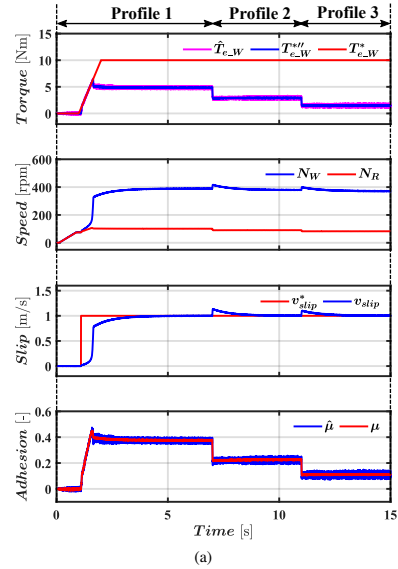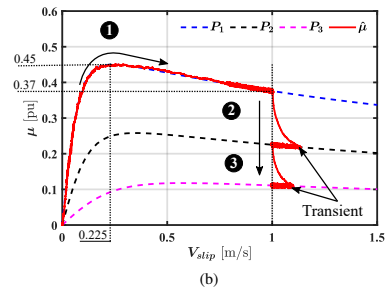
Figure 6: Constant slip velocity control (simulation): (a) transient response; (b) adhesion profiles. ① P_1 : $t < 7$ s; ② P_2 : 7 s< $t < 11$ s; ③ P_3 : $t > 11$ s.

3.2.1. Perturb and Observe (P&O)

In this method, the slip velocity is indirectly controlled by perturbing the wheel acceleration as seen in Fig. 7. The wheel velocity command v^*_W is obtained by integrating the wheel acceleration command which is a combination of the current acceleration a_W and a constant value Δa as given by (6) and (7). Selection of a_0 or a_1 is based on Perturb and Observe (P&O) technique to track the maximum torque [9, 27].

$$a_0 = a_W - \Delta a \tag{6}$$
$$a_1 = a_W + \Delta a \tag{7}$$

The operation of MAT strategy can be summarized as follows:

Figure 7: Perturb and Observe (P&O) slip velocity control mode block diagram.

- The acceleration of the traction motor wheel is initially perturbed (e.g. increased). The developed torque during this process is stored. The maximum torque value during the perturbation period $T_{e(k)}^{max}$ is held and subtracted from the current torque value obtaining ΔT_e (see Maximum Torque Search block in Fig. 7).
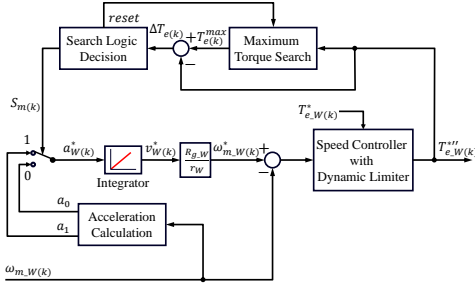
- ΔT_e is sent to the Search Logic Decision block, which will choose between a_0 and a_1 using a binary output signal $S_{m(k)}$. The search logic task is to adapt the operating point either by increasing or decreasing the acceleration command based on the current load torque compared to the maximum stored value during perturbation. If $\Delta T_e > T_{threshold}$, then the current torque $T_{e\_W}^{*''}$ is moving apart from the peak of the adhesion curve thus the search logic block output $S_m = 0$ to decelerate the wheel and bring the operating point back to the peak of the curve (see Signal Adaptation block in Fig. 7).

- A reset signal generated in the Search Logic in Fig. 7 is used to reset the counter in the Maximum Torque Search block which handles the perturbation period. Consequently, the operating point is expected to be alternating around the peak of the adhesion curve with no need for additional speed measurement, i.e. train velocity.

The main drawback of this method is that it creates additional ripples in the machine torque, which depend on the perturbation period. This might contribute to undesired oscillations in the mechanical drive train torsional elements [28].

Fig. 8 shows the simulation results of the roller rig emulator using P&O method slip velocity control. Operating conditions are the same as in Fig. 6. Significant excursions around the peak of the adhesion curve are observed in Fig. 8(b), especially for the case of P_1 which corresponds to the highest adhesion level, i.e. dry condition. Also, it is found that the P&O method has a slow dynamic response while searching for the peak. Finally, peak searching capability
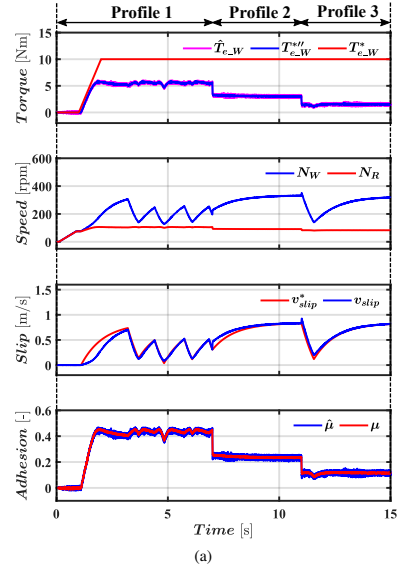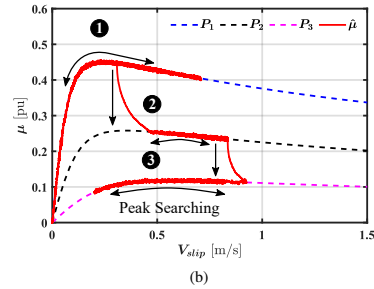
Figure 8: Variable slip velocity control using Perturb and Observe (P&O) (simulation): (a) transient response; (b) adhesion profiles. ① $P_1 : t < 7$ s; ② $P_2 : 7$ s$< t < 11$ s; ③ $P_3 : t > 11$ s.

becomes more challenging with flat adhesion curves like P_2 and P_3 (see Fig. 8(b)).

3.2.2. Steepest Gradient

This approach takes advantage of the non-linear behavior of the adhesion-slip characteristic curve to track the maximum adhesion. As already known, the adhesion-slip characteristic is divided into two regions as shown in Fig. 9(a): 1) micro-slip (stable) region, where the adhesion coefficient μ increases with the slip velocity v_{slip} till reaches its maximum value; 2) macro-slip (unstable), where any increase in slip velocity will decrease the adhesion coefficient and would drive the traction system to instability.

Defining the increments of the adhesion coefficient and slip velocity as (8) and (9) respectively, the slope of the adhesion-slip curve is given by (10).

$$\Delta \hat{\mu}_{(k)} = \hat{\mu}_{(k)} - \hat{\mu}_{(k-1)} \tag{8}$$

$$\Delta v_{slip(k)} = v_{slip(k)} - v_{slip(k-1)} \tag{9}$$

$$K_{v_{slip}(k)} = \frac{\Delta \hat{\mu}_{(k)}}{\Delta v_{slip(k)}} \tag{10}$$

The slope $K_{v_{slip}(k)}$ is positive in the micro-slip region, and negative in the macro-slip region, being zero at the peak of the adhesion-slip curve [see Fig. 9(a)]. Hence, tracking the maximum adhesion in the steepest gradient method would be naturally done by adding the current gradient of the adhesion-slip curve to the previous slip velocity as shown in (11). Gain α in (11) is an adaptation constant.

$$v_{slip(k)}^* = v_{slip(k-1)} + \alpha \cdot K_{v_{slip}(k)} \tag{11}$$

According to (11), if the operating point is in the micro-slip region, the adhesion-slip gradient $K_{v_{slip}(k)}$ is positive and the slip velocity command is increased. Contrarily, if the operating point falls in the macro-slip region, the gradient added is negative, and the slip velocity command is decreased. Once the maximum adhesion is reached, the adhesion-slip gradient is zero and no change is applied to the slip velocity. The block diagram of the steepest gradient method is shown in Fig. 9(b).

As the adhesion coefficient μ in an actual locomotive cannot be measured, estimation is required. A disturbance observer is commonly used for adhesion estimation using (12).

$$\hat{\mu} = \hat{T}_{l\_W} \frac{R_{g\_W}}{F_N \cdot r_W} \tag{12}$$

$\hat{T}_{l\_W}$ can be estimated from (13), where β_m and J_m are the viscus friction and inertia of the traction wheel motor, respectively.

$$\hat{T}_{l\_W} = \hat{T}_{e\_W} - \beta_m \omega_{m\_W} - J_m \dot{\omega}_{m\_W} \tag{13}$$

To avoid the pure derivative in (13), a low pass filter can be used instead (14).

$$\hat{T}_{l\_W(s)} = \hat{T}_{e\_W(s)} - \omega_{m\_W(s)} \left[\beta_{m\_W} + J_m s \left(\frac{1}{\tau s + 1} \right) \right] \tag{14}$$

Two low-pass filters are used to attenuate the measurement noise in the slip velocity signal and the estimated adhesion coefficient prior to the discrete differentiation realized by $D(z)$ blocks.
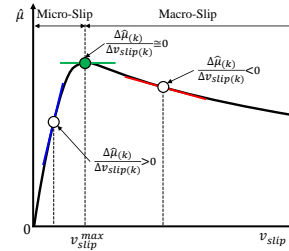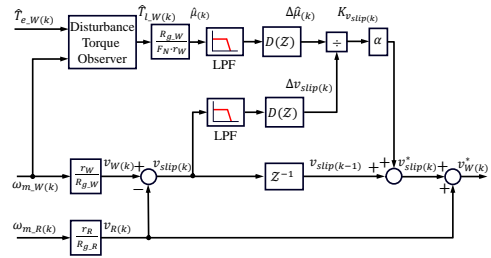
Figure 9: Steepest Gradient slip velocity control mode. (a) adhesion-slip curve and involved incremental variables; (b) Block diagram.

Simulation results for this method are shown in Fig. 10. Due to the differentiation of signals used to estimate the adhesion slope $\frac{\Delta \hat{\mu}_{(k)}}{\Delta v_{slip(k)}}$, Steepest Gradient (SG) method suffers from high oscillations attempting to keep the operating point at the peak of the adhesion-slip curve [see Fig. 10(a)]. This becomes obvious for the adhesion profiles with higher slopes like P_1 as the resulting slope correction signal $K_{v_{slip}(k)}$ increases dramatically for the next step of the slip velocity command. Contrarily, with lower adhesion slopes such as P_2 and P_3, the correction signal moderately increases with the assumption of using constant correction factor α. However, it can be noticed in this method that the operating points are closer to the peak of the adhesion-slip curves for all the profiles. However, the peak searching space is still high [see Fig. 10(b)].

4. Proposed MAT Techniques for Railways

As discussed in subsection 3.2, operation with variable slip will require estimation of maximum adhesion. Two new methods are proposed and assessed in this section, based on Meta-heuristic Fuzzy Logic Control and Particle Swarm Optimization respectively.

(a)

(b)
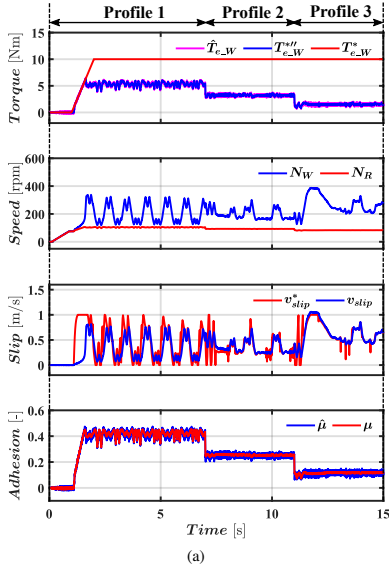
Figure 10: Variable slip velocity control using Steepest Gradient method (simulation): (a) transient response; (b) adhesion profiles. ① P_1 : $t < 7$ s; ② P_2 : 7 s$< t < 11$ s; ③ P_3 : $t > 11$ s.

4.1. MAT Using Meta-heuristic Fuzzy Logic Control

Fuzzy Logic Control (FLC) is a knowledge-based control technique that uses linguistic rules designed for complex, uncertain, and non-linear systems without requiring mathematical models and/or parameter estimation [29, 30]. FLC was first introduced for anti-lock braking systems (ABS) in railway traction applications to prevent wheel skid on the rail, resulting in high braking performance and consequently lower braking distance compared to conventional PID controller [31, 32, 33, 34]. Later, FLC concept has been extended for wheel slip prevention and speed profile tracking in electric trains [35, 36, 37, 38]. The use of FLC for MAT is developed following.
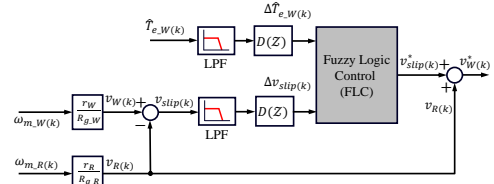
Figure 11: MAT using Fuzzy Logic Control (FLC) block diagram.

(a)

(b)
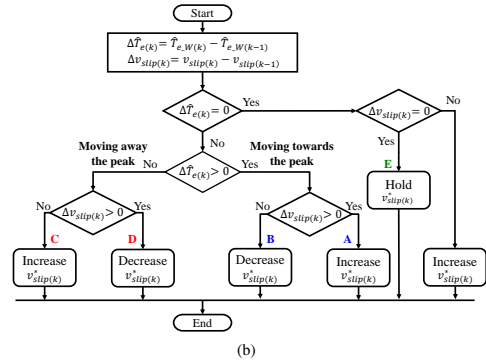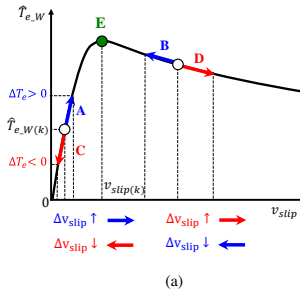
Figure 12: MAT using FLC procedure. (a) Adhesion-slip curve strategy; (b) Flowchart representation.

The proposed block diagram is shown in Fig. 11. It uses the same slip command adaptation concept of the Steepest Gradient method for tracking the peak of the adhesion curve [see Fig. 9(a)]. However, the change in the slip command $v^*_{slip(k)}$ is adapted and generated automatically by the FLC block. From (4), it can be seen that the estimated wheel motor torque is proportional to the adhesion coefficient μ as the normal force F_N, the radius of the wheel r_W and the gear ratio R_{g_W} are already known. Thus the load torque estimation $\hat{T}_{l\_W}$ using the disturbance observer in Fig. 9(b) is not required anymore and the FLC rules can be applied to

the estimated motor torque $\hat{T}_{e\_W}$. $\hat{T}_{e\_W}$ is already available since it is used for the drive torque control as shown in Fig. 2.

The procedure for MAT using FLC is summarized in Fig. 12 including the flowchart shown in Fig. 12(b).

Like the conventional FLC structure, the FLC block of the proposed method (see Fig. 11) contains the input fuzzification, the fuzzy interface, and the output defuzzification respectively as seen in 13(a). The fuzzification block consists of two membership functions that create the linguistic rules of the input variables, i.e. the $\Delta\hat{T}_{e(k)}$ and $\Delta v_{slip(k)}$. Then, the fuzzy interface correlates the linguistic rules with the knowledge base for maximum adhesion-slip curve tracking. Finally, the fuzzified output rules are transformed back to real numbers using the defuzzification membership function. The rules used in 13(b) are denoted for: NB is Negative Big; NS is Negative small; Z is zero; PS is Positive Small, and PB is Positive Big. The choice of the input and output parameters $(x_2, x_1 \& y_2, y_1)$ will depend on field tests and trains' driver expertise. In this paper, the input parameters are assigned as $x_2 = 15$ Nm, $x_1 = x_2/2 = 7.5$ Nm for torque increment, $x_2 = 1.0$ m/s, $x_1 = x_2/2 = 0.5$ m/s for slip velocity increment, and the output parameters are $y_2 = 0.5$ m/s, $y_1 = y_2/2 = 0.25$ m/s for the updated slip velocity command.

(a)

(b)
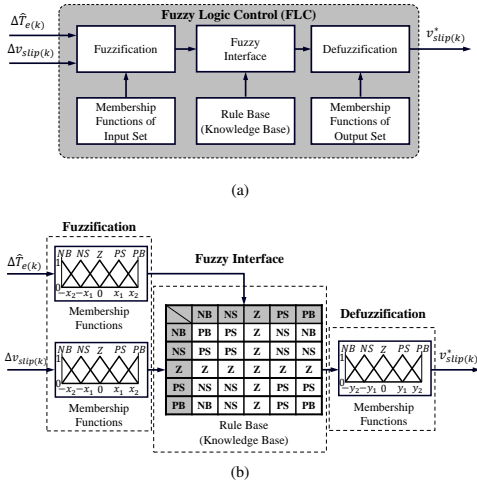
Figure 13: Fuzzy Logic Control (FLC) scheme. (a) Basic FLC structure; (b) Input/Output Membership functions and Rules base for MAT-FLC.

Simulation results of the proposed MAT-FLC method are shown in Fig. 14. The improved dynamic response and reduced oscillations are readily visible comparing Fig. 14(a) with Fig. 8(a) and 10(a). The maximum adhesion of $\hat{\mu} = 0.45$ for P_1 is achieved in < 1s. The searching space is also decreased as observed comparing Fig. 14(b) with Fig. 8(b) and 10(b).

(a)

(b)
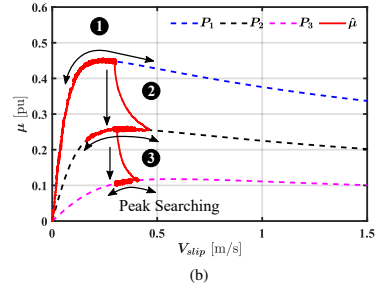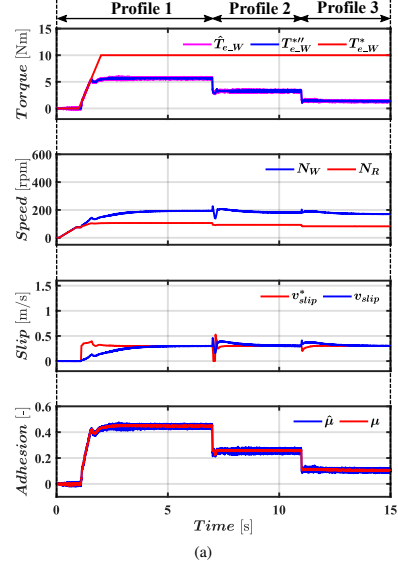
Figure 14: MAT using the proposed MAT-FLC (simulation): (a) transient response; (b) adhesion profiles. ① P_1 : $t < 7$ s; ② P_2 : 7 s< $t < 11$ s; ③ P_3 : $t > 11$ s.

For adhesion profiles P_1 and P_2, MAT-FLC was able to find the maximum adhesion-slip point. However, for P_3, the maximum adhesion found by the algorithm was ≈ 12% smaller than the optimal value, with an error of ≈ −40% in the estimated optimal slip velocity. This error can be minimized by modifying the membership functions and rules used in the FLC. Thus, adaptive tuning of FLC for multiple adhesion profiles to track the peak of the adhesion curve is needed. Implementing adaptive tuning algorithms increases the complexity of the proposed MAT-FLC [39, 40, 41, 42, 43]. A new approach for MAT estimation that overcomes this problem is proposed in the next subsection.

A Fathy-Abouzeid et al./eTransportation

4.2. MAT Using Particle Swarm Optimization

Particle swarm optimization (PSO) is a population-based stochastic optimization algorithm inspired by the movement of organisms such as flocks of birds or schools of fish [44]. PSO concept has roots in artificial life and evolutionary computation, intended for optimizing non-linear functions [45, 46]. PSO algorithm is simple, computationally efficient, and effective in solving a variety of problems for different applications [39, 47]. Maximum Power Point Tracking using Particle swarm optimization (MPPT-PSO) is considered one of the most popular evolutionary optimization algorithms in solar Photo-Voltaic (PV) systems due to its high tracking speed, ability to operate under different environmental conditions, and fast computational capability [48, 49, 50, 51, 52, 53].
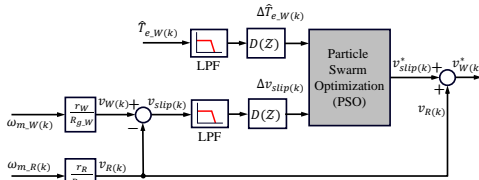
Figure 15: MAT using Particle Swarm Optimization (PSO) block diagram.

The PSO algorithm contains a swarm of individuals (particles) at random positions, where each particle represents a possible solution to the problem under investigation. To find the optimal solution, all particles follow a similar behavior, e.g., the position of any particle is influenced by the best particle in the neighborhood (p_{best}) as well as the best solution found by all the particles in the entire population (g_{best}). The best solution here is referred to the solution which satisfies the selected criterion (fitness function), e.g., to find the global minimum, the global maximum, etc. The particle position adjustment can be represented mathematically as (15) and (16), where $x^i_{(k+1)}$ and $u^i_{(k+1)}$ represent the current position and velocity of particle i respectively; w is an inertia weighting parameter; c_1 and c_2 are acceleration coefficients; r_1 and r_2 are random numbers between 0 to 1; p^i_{best} is the best solution of particle i in the previous iteration k, g_{best} is the best solution of all particles in the previous iteration k.

$$x^i_{(k+1)} = x^i_{(k)} + u^i_{(k+1)} \tag{15}$$

$$u^i_{(k+1)} = wu^i_{(k)} + c_1 r_1 (p^i_{best} - x^i_{(k)}) + c_2 r_2 (g_{best} - x^i_{(k)}) \tag{16}$$

As in MAT-FLC, the proposed MAT technique using PSO (MAT-PSO) algorithm uses the increments of wheel motor torque $\Delta \hat{T}_{e(k)}$ and slip velocity $\Delta v_{slip(k)}$ to locate the current operating point on the adhesion-slip curve. The output slip velocity reference signal $v^*_{slip(k)}$ is then adjusted as
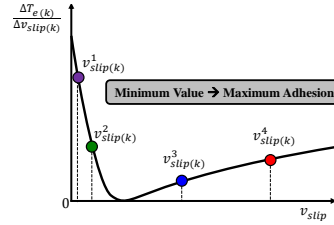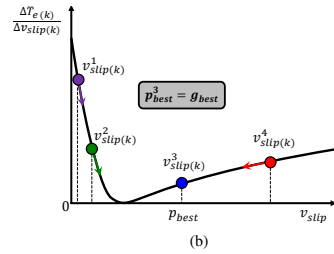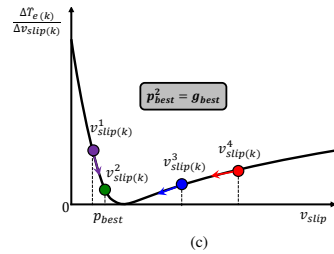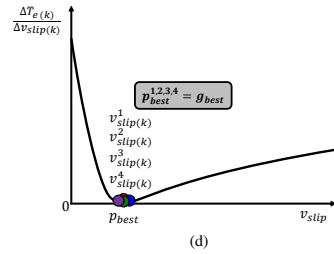
Figure 16: Procedure of minimum search using Particle Swarm Optimization (PSO). (a) Particle initialization; (b) Particle movements towards the global best particle after one iteration; (c) Particle swarming towards the global minimum value; (d) Particle final positions at the minimum value where the objective function is achieved.

seen in Fig. 15. In the proposed method, the PSO algorithm is designed to search for the minimum absolute value of the adhesion-slip curve slope [see Fig. 16], as $\frac{\Delta \hat{T}_{e(k)}}{\Delta v_{slip(k)}} \approx 0$ occurs only at the peak of the adhesion-slip curve.

286

A Fathy-Abouzeid et al./eTransportation
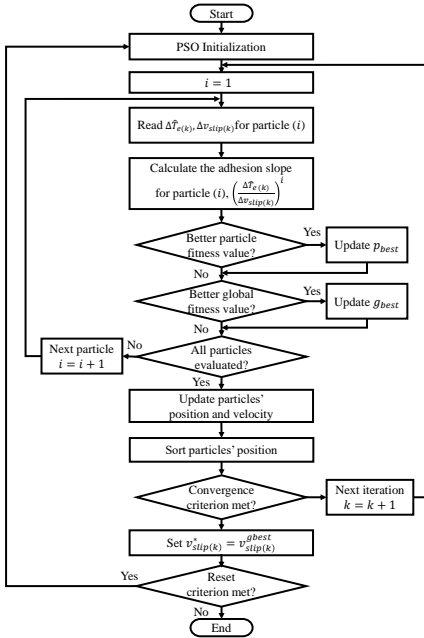
Figure 17: Flowchart of Particle Swarm Optimization (PSO) for minimum search.

Figure 18: Simulation results: Proposed MAT using Particle Swarm Optimization (PSO) (MAT-PSO).

The flow chart of the proposed MAT-PSO method is shown in Fig. 17. Four particles ($N_p = 4$) were found adequate to achieve fast search speed with a computational effort suitable for real-time implementation. The algorithm starts with an initial guess of the positions of the particles (i.e. slip velocities) [see Fig. 16(a)], local best particle position p_{best}, and global best particle position g_{best} [see Fig. 16(b)]. The slope of the adhesion-slip curve is first calculated for each particle and then the fitness function is evaluated individually, where the minimum value is considered to be the local best particle p_{best}, and its initial value is updated. The new p_{best} value is assigned to be the new global best particle g_{best} which other particles should follow for the next iteration. The p_{best} and g_{best} will be varying while searching for the value that satisfies the fitness function [see particle 2 in Fig. 16(c)]. Afterward, the output slip velocity $v^*_{slip(k)}$ is set to be equal to the global best particle position $v^{gbest}_{slip(k)}$ [see Fig. 16(d)]. Finally, the output slip velocity reference $v^*_{slip(k)}$ will be held constant until the reset function is activated. This occurs when the change in the wheel motor torque and the slip velocity exceeds a certain limit chosen based on the dynamics of the applied system. This situation refers to a change in the adhesion level due to changes in the track condition such as wet, ice, contaminants, etc. From Fig. 14 and Fig. 18, it is observed that MAT-PSO has a slightly slower response compared to MAT-FLC. This is due
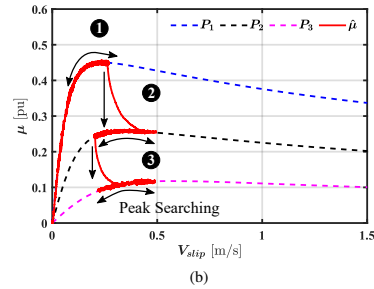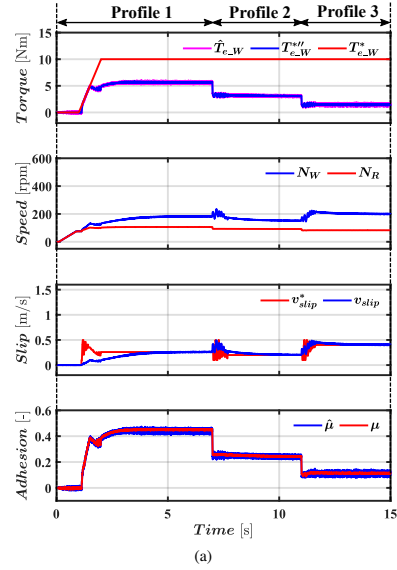
to the re-initialization of particles' positions and random movement when the reset function is activated [see third subplot in Fig. 18(a)]. On the other hand, PSO algorithm shows a superior steady-state performance for obtaining the correct slip velocity command value at which the peak of the adhesion curve occurs. This can be noticed for P_3 where it reaches to $v^*_{slip} = 0.41$ m/s while the theoretical peak occurs at $v^*_{slip} = 0.45$ m/s [see Fig. 18(b)].

Fig. 19 summarizes the main characteristics and expected performance of the methods being considered. Constant slip velocity control is seen to provide excellent results in almost all the aspects being evaluated, but this is at the price of no MAT searching capability. This control mode would be beneficial for rail tracks with known adhesion characteristics. Unfortunately, this knowledge is not available in practice. The shortcomings of the constant slip

method are overcome using the proposed MAT-PSO, but at the cost of implementation complexity and difficult tuning. The proposed MAT-FLC shows a moderate performance, providing some of the advantages of MAT-PSO but with less computational effort. MAT-P&O and MAT-SG show similar performance regarding tracking capability and simplicity. However, MAT-SG shows the worst performance regarding signal smoothness and steady-state response.

Figure 19: Comparison of slip velocity control methods.

5. Experimental Validation

In this section, all methods discussed in section 3 and the proposed ones in section 4 are validated evaluated experimentally.

5.1. Test Bench Design

The scaled roller rig described in subsection 2.1 is used for emulating the wheel-rail contact dynamics. The roller rig test bench is shown in Fig. 20(a) and its parameters are given in table 1 [22]. The roller rig load is adjusted by a spring system attached to a dynamometer for load force measurements which applies extra force on the wheel as seen in Fig. 20(a). Additionally, a water spraying system is included for evaluation of the control strategies when the wheel-roller surface becomes wet.

Two four-pole induction motors of 4 kW and 5.5 kW are used for wheel and roller respectively (see Fig. 20(a)). The induction motors are driven by two drives, both using rotor field-oriented control (RFOC) (see Fig. 20(b)) [54, 55]. A commercial VACON NXP00385 Danfoss drive is used in speed control mode to keep the roller motor speed constant. A custom drive is used to feed the wheel motor. All the methods discussed in this paper are implemented in a TMDSCNCD28335 digital signal processor used to control the custom drive 3 and 4.

5.2. Results and Discussion

The methods discussed in Sections 3 and 4 were tested in the test bench. For each method, the experiments start with a dry wheel-roller contact point, then at $t \approx 35$ s the water

Table 1
roller rig test bench parameters.

System	Parameter	Wheel	Roller	Unit
Wheel and Roller	Radius	0.125	0.25	m
	Force	843	843	N
	Torque	105.3	210.7	Nm
Transmission	Gear ratio	90 / 24	192/26	-
Traction Motor	Rating	4	5.5	kW
	Power	1.78	1.78	kW
	Torque	28.1	28.5	Nm
	Speed	604.8	595.5	rpm
	Encoder Resolution	500	500	ppr
Inverter	Rating	4	15	kW
Motor-Wheel	Inertia [1]	0.002	0.007	kgm^2

[1] Inertia is calculated in wheel and roller motor reference frame respectively.

spraying system is turned on till the end of the experiment with a flow rate of 140 ml/min. Fig. 21 and 22 show the response of the five methods being considered.

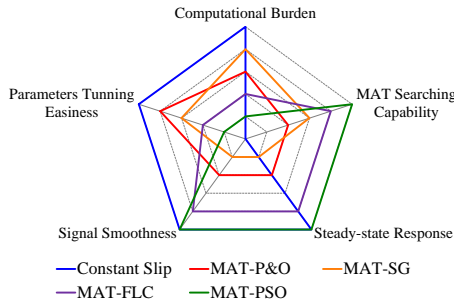Overall, experimental results for all methods are in good agreement with the simulation results obtained in Sections 3 and 4. However, torque and speed oscillations in the experiments are seen to be lower than in simulation (see Fig. 8(a) & 10(a) vs. 21(b) & 21(c)). Contrary to simulation results, changes from dry to wet conditions of the contact point do not occur instantaneously in the test bench. This would explain some of the differences observed between simulation and experimental results.

For the constant slip control method (see Fig. 21(a) and 22(a)), the achieved steady-state adhesion coefficient for dry and wet conditions are $\hat{\mu} \approx 0.5$ and $\hat{\mu} \approx 0.15$ respectively. These values increase to $\hat{\mu} \approx 0.6$ and $\hat{\mu} \approx 0.25$ for all MAT methods considered in this paper (see Fig. 21(b) to Fig. 21(e) and Fig. 22(b) to Fig. 22(e)). As expected, all the methods track the peak of the adhesion curve both in dry and wet conditions. An increase in slip velocity ($v_{slip} \approx 0.45$ m/s) is noticed while peak searching in wet condition (see Fig. 21(c) $t = 45s$ to $t = 65s$) with MAT-SG due to the continuous increment of $(\Delta v^* slip(k))$ term in the slip velocity command in the case of flat adhesion curves aiming to find the maximum peak. This doesn't occur with MAT-PO as the search logic alternate between the increment/decrement of the slip velocity command.

The two proposed methods MAT-FLC and MAT-PSO show a similar response as seen in Fig. 21(d) and Fig. 21(e), as well as Fig. 22(d) and 22(e). However, for MAT-FLC the slip velocity command is kept at the same value ($v_{slip} \approx 0.2$ m/s) for both adhesion conditions while for MAT-PSO slip velocity is slightly differs as ($v_{slip} \approx 0.3$ m/s) and ($v_{slip} \approx 0.35$ m/s) in dry and wet conditions respectively. The difference in the performance of FLC and PSO algorithms is negligible and can be only noticed in the search space of the adhesion-slip curves, but noting the relevant differences in the implementation complexity. Therefore, the proposed MAT methods achieve the same

(a)

(b)

(c)
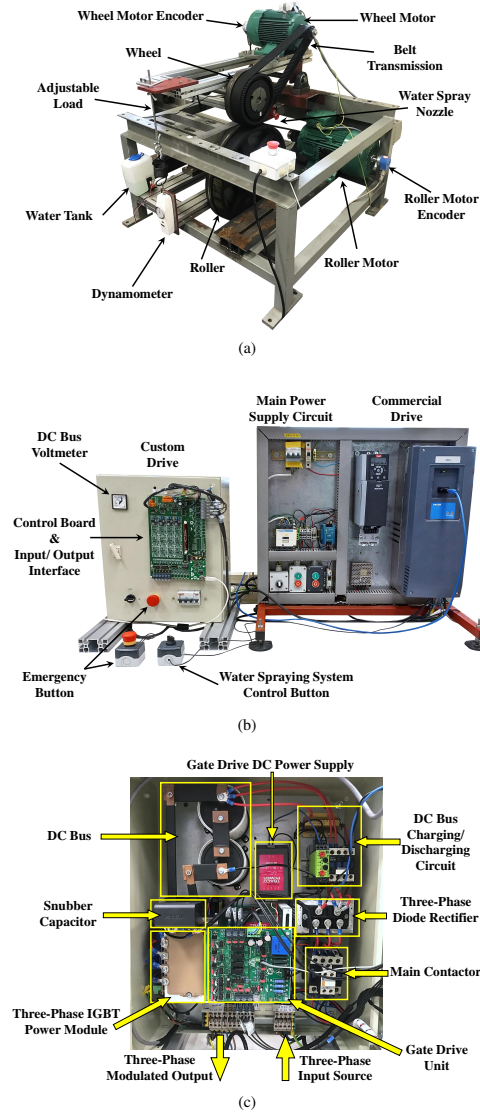
Figure 20: Overview of experimental setup: (a) roller rig test bench; (b) Electrical circuit and motor drives; (c) Custom drive elements.

adhesion level ($\approx$ 20% higher than the constant slip method) with less slip velocity in steady-state compared to existing methods.

6. Conclusion

Traction capability mainly depends on the adhesion co-efficient between the wheel and the rail in railways. Improving traction capability reduces travel time and energy consumption during traction/braking. Operating at maximum adhesion coefficient is not straightforward due to its non-linear and almost unpredictable nature. In this paper, a comparative analysis of constant and variable slip velocity control using MAT has been presented.

Existing and proposed slip velocity control strategies have been simulated and validated experimentally where the wheel-rail contact point has been emulated using a scaled roller rig. It can be concluded that operating with constant slip velocity provides precise and stable operation at the cost of not fully optimizing the traction capability of the traction drive. Perturb and Observe (P&O) MAT method was able to track the maximum point of the adhesion-slip curve. However, there are two main drawbacks of this method: 1) the slip controller should be limited as it can fail with flat adhesion-slip curves as the controller tries to find the maximum adhesion point by increasing the slip velocity continuously, and 2) operating in the unstable adhesion region can excite the slip-stick vibrations in the mechanical elements of the drive-train. The MAT-P&O issues have been improved using the steepest gradient method (MAT-SG). As MAT-SG requires a disturbance torque observer, the sensitivity of the observer to measurements noise is the main concern of this method besides using derivatives that could be a problem in this case.

Finally, two new methods using Fuzzy Logic Control (MAT-FLC) and Particle Swarm Optimization (MAT-PSO) have been proposed. It has been shown that these methods provide similar performance finding the maximum adhesion point under dry and wet wheel-roller conditions with stable slip velocity value at steady-state, the implementation of MAT-FLC being simpler.

CRediT authorship contribution statement

Ahmed Fathy Abouzeid: Conceptualization of this study, Software, Hardware, Writing-Original draft. **Juan Manuel Guerrero:** Software, Hardware, Review & Editing. **Lander Lejarza:** Methodology, Data curation. **Iker Muniategui:** Investigation, Methodology. **Aitor Endemaño:** Investigation, Data curation. **Fernando Briz:** Conceptualization of this study, Methodology, Review & Editing.

Declaration of interests

The authors declare that they have no known competing financial interests or personal relationships that could have appeared to influence the work reported in this paper.

Data availability

Data will be made available on request.

A Fathy-Abouzeid et al./eTransportation
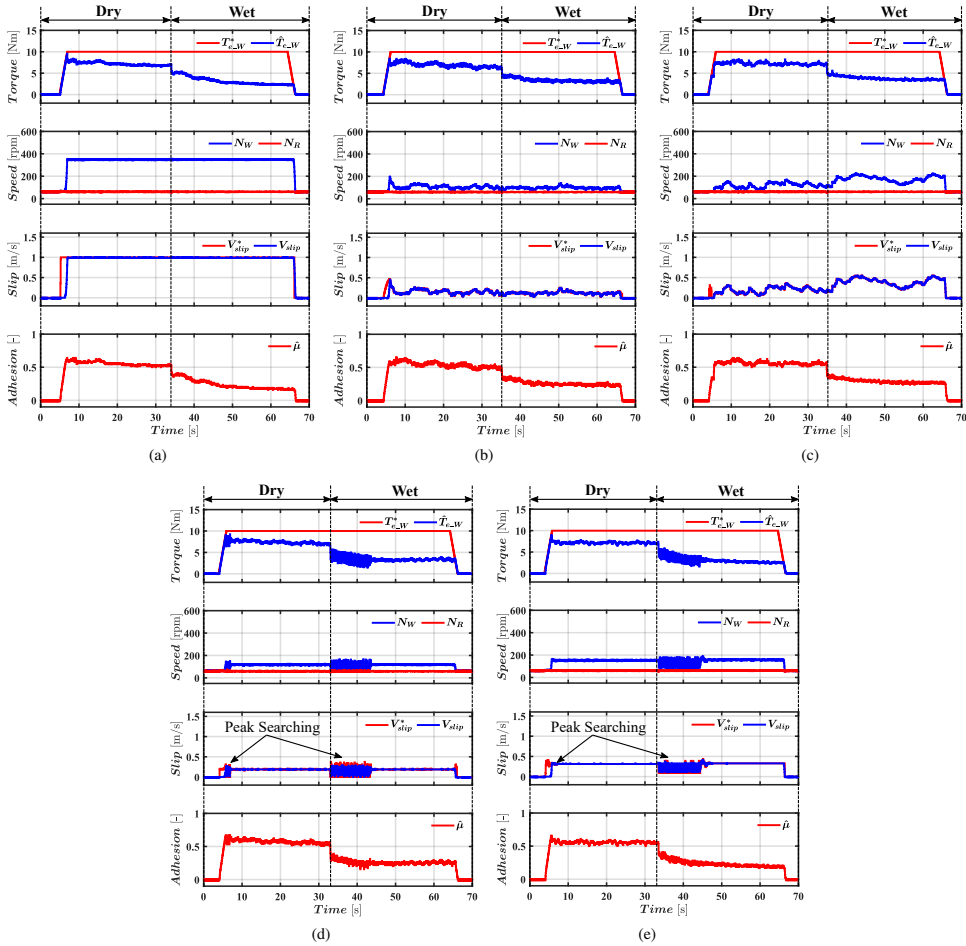
Figure 21: Experimental results. Response in the time domain: (a) constant slip velocity; (b) MAT-P&O; (c) MAT-SG; (d) MAT-FLC; and (e) MAT-PSO.

References

[1] O. Polach. Creep forces in simulations of traction vehicles running on adhesion limit. *Wear*, 258(7-8):992–1000, 2005.

[2] K. Kondo. Anti-slip control technologies for the railway vehicle traction. In *2012 IEEE Vehicle Power and Propulsion Conference*, pages 1306–1311. IEEE, 2012.

[3] P. Pichlík and J. Zdeněk. Overview of slip control methods used in locomotives. *Transactions on Electrical Engineering*, 3(2):38–43, 2014.

[4] C. Uyulan, M. Gokasan, and S. Bogosyan. Comparison of the re-adhesion control strategies in high-speed train. *Proceedings of the Institution of Mechanical Engineers, Part I: Journal of Systems and Control Engineering*, 232(1):92–105, 2018.

[5] D.-Y. Park, M.-S. Kim, D.-H. Hwang, J.-H. Lee, and Y.-J. Kim. Hybrid re-adhesion control method for traction system of high-speed railway. In *ICEMS'2001. Proceedings of the Fifth International Conference on Electrical Machines and Systems (IEEE Cat. No. 01EX501)*, volume 2, pages 739–742. IEEE, 2001.
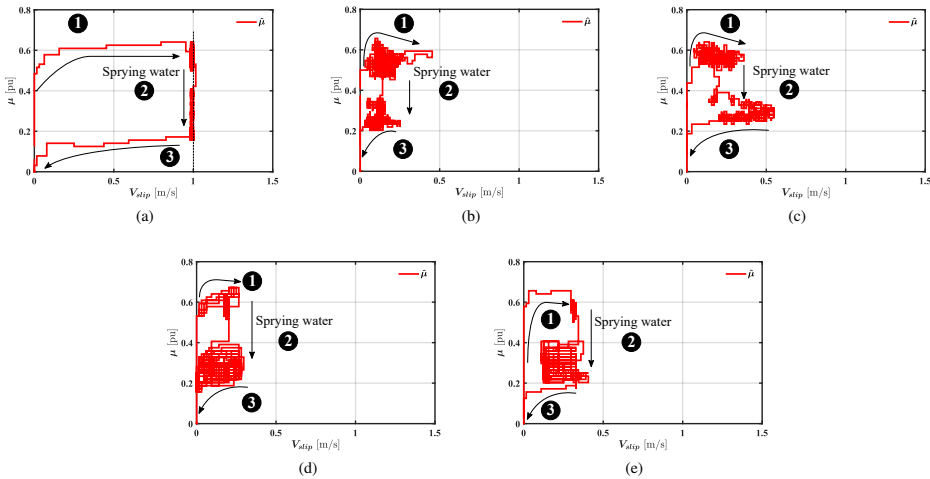
290

A Fathy-Abouzeid et al./eTransportation

Figure 22: Experimental results. Adhesion-slip trajectory: (a) constant slip velocity; (b) MAT-P&O; (c) MAT-SG; (d) MAT-FLC; and (e) MAT-PSO.

[6] T. WATANABE. Anti-slip readhesion control with presumed adhesion force-method of presuming adhesion force and running test results of high-speed shinkansen train. *Quarterly Report of RTRI*, 41(1):32–36, 2000.

[7] H. Ryoo, S. Kim, G. Rim, Y. Kim, and M. Kim. Novel anti-slip/slide control algorithm for korean high-speed train. In *IECON'03. 29th Annual Conference of the IEEE Industrial Electronics Society (IEEE Cat. No. 03CH37468)*, volume 3, pages 2570–2574. IEEE, 2003.

[8] M. Yamashita and T. Soeda. Anti-slip re-adhesion control method for increasing the tractive force of locomotives through the early detection of wheel slip convergence. In *2015 17th European conference on power electronics and applications (EPE'15 ECCE-Europe)*, pages 1–10. IEEE, 2015.

[9] H. J. Schwartz. *Regelung der Radsatzdrehzahl zur maximalen Kraftschlussausnutzung bei elektrischen Triebfahrzeugen*. VDI-Verlag, 1992.

[10] A. Kawamura, T. Furuya, K. Takeuchi, Y. Takaoka, K. Yoshimoto, and M. Cao. Maximum adhesion control for shinkansen using the tractive force tester. In *IEEE 2002 28th Annual Conference of the Industrial Electronics Society. IECON 02*, volume 1, pages 567–572. IEEE, 2002.

[11] J. Liu, Q. Peng, Z. Huang, H. Li, D. Wang, Y. Chen, and F. LinZhou. A novel estimation of adhesion force of railway vehicles braking systems and reference speed calculation. In *2017 29th Chinese control and decision conference (CCDC)*, pages 7606–7611. IEEE, 2017.

[12] P. Pichlik and J. Zdenek. Locomotive wheel slip control method based on an unscented kalman filter. *IEEE Transactions on Vehicular Technology*, 67(7):5730–5739, 2018.

[13] P. Pichlik and J. Bauer. Adhesion characteristic slope estimation for wheel slip control purpose based on ukf. *IEEE Transactions on Vehicular Technology*, 70(5):4303–4311, 2021.

[14] A. Zirek, P. Voltr, M. Lata, and J. Novák. An adaptive sliding mode control to stabilize wheel slip and improve traction performance. *Proceedings of the Institution of Mechanical Engineers, Part F: Journal of Rail and Rapid Transit*, 232(10):2392–2405, 2018.

[15] S. Sadr, D. A. Khaburi, and J. Rodríguez. Predictive slip control for electrical trains. *IEEE Transactions on Industrial Electronics*, 63(6):3446–3457, 2016.

[16] X. Wen, J. Huang, and S. Zhang. Anti-slip re-adhesion control strategy of electric locomotive based on distributed MPC. In *2019 IEEE 21st International Conference on High Performance Computing and Communications; IEEE 17th International Conference on Smart City; IEEE 5th International Conference on Data Science and Systems (HPCC/SmartCity/DSS)*, pages 2708–2713. IEEE, 2019.

[17] Z. Huang, W. Du, B. Chen, K. Gao, Y. Liu, X. Tang, and Y. Yang. An online super-twisting sliding mode anti-slip control strategy. *Energies*, 13(7):1823, 2020.

[18] A. Molavi and F. Rashidi Fathabadi. Robust model predictive anti-slip controller and speed profile tracking of an electric train based on lmi approach. *International Journal of Dynamics and Control*, pages 1–12, 2022.

[19] A. Zirek and A. Onat. A novel anti-slip control approach for railway vehicles with traction based on adhesion estimation with swarm intelligence. *Railway Engineering Science*, 28(4):346–364, 2020.

[20] A. Jaschinski. *On the application of similarity laws to a scaled railway bogie model*. PhD thesis, Delft University of Technology, 1991.

[21] A. Jaschinski, H. Chollet, S. Iwnicki, A. Wickens, and J. Würzen. The application of roller rigs to railway vehicle dynamics. *Vehicle System Dynamics*, 31(5-6):345–392, 1999.

[22] N. V. Vantagodi, A. F. Abouzeid, J. M. Guerrero, I. Vicente, I. Muniategui, A. Endemaño, and F. Briz. Design of a scaled roller-rig test bench for anti-slip control development for railway traction. *IEEE Transactions on Vehicular Technology*, 2022.

[23] E. Vollebregt, K. Six, and O. Polach. Challenges and progress in the understanding and modelling of the wheel–rail creep forces. *Vehicle System Dynamics*, 59(7):1026–1068, 2021.

[24] M. Malvezzi, P. Toni, B. Allotta, and V. Colla. Train speed and position evaluation using wheel velocity measurements. In *2001 IEEE/ASME International Conference on Advanced Intelligent Mechatronics. Proceedings (Cat. No. 01TH8556)*, volume 1, pages 220–224. IEEE, 2001.

[25] T. Mei and H. Li. A novel approach for the measurement of absolute train speed. *Vehicle System Dynamics*, 46(S1):705–715, 2008.

[26] J. Guzinski, H. Abu-Rub, M. Diguet, Z. Krzeminski, and A. Lewicki. Speed and load torque observer application in high-speed train electric drive. *IEEE Transactions on Industrial Electronics*, 57(2):565–574,

A Fathy-Abouzeid et al./eTransportation

2009.

[27] M. Buscher. *Radschlupfregelung zur maximalen Kraftschlussausnutzung bei elektrischen Traktionsantrieben*. Verlag Shaker, 1995.

[28] A. F. Abouzeid, J. M. Guerrero, I. Vicente-Makazaga, I. Muniategui-Aspiazu, A. Endemaño-Isasi, and F. Briz. Torsional vibration suppression in railway traction drives. *IEEE Access*, 10:32855–32869, 2022.

[29] C.-C. Lee. Fuzzy logic in control systems: fuzzy logic controller. i. *IEEE Transactions on systems, man, and cybernetics*, 20(2):404–418, 1990.

[30] C.-Y. Su and Y. Stepanenko. Adaptive control of a class of nonlinear systems with fuzzy logic. *IEEE Transactions on Fuzzy Systems*, 2(4):285–294, 1994.

[31] A. D. Cheok and S. Shiomi. A fuzzy logic based anti-skid control system for railway applications. In *1998 Second International Conference. Knowledge-Based Intelligent Electronic Systems. Proceedings KES'98 (Cat. No. 98EX111)*, volume 1, pages 195–201. IEEE, 1998.

[32] A. D. Cheok and S. Shiomi. Combined heuristic knowledge and limited measurement based fuzzy logic antiskid control for railway applications. *IEEE Transactions on Systems, Man, and Cybernetics, Part C (Applications and Reviews)*, 30(4):557–568, 2000.

[33] C.-M. Lin and C.-F. Hsu. Self-learning fuzzy sliding-mode control for antilock braking systems. *IEEE Transactions on Control Systems Technology*, 11(2):273–278, 2003.

[34] A. Mirzaei, M. Moallem, B. Mirzaeian, and B. Fahimi. Design of an optimal fuzzy controller for antilock braking systems. In *2005 IEEE Vehicle Power and Propulsion Conference*, pages 823–828. IEEE, 2005.

[35] L. B. Jordan Jr. Locomotive traction control system using fuzzy logic, June 13 1995. US Patent 5,424,948.

[36] M. Garcia-Rivera, R. Sanz, and J. A. Perez-Rodriguez. An antislipping fuzzy logic controller for a railway traction system. In *Proceedings of 6th International Fuzzy Systems Conference*, volume 1, pages 119–124. IEEE, 1997.

[37] P. Khatun, C. Bingham, and P. Mellor. Comparison of control methods for electric vehicle antilock braking/traction control systems. Technical report, SAE Technical Paper, 2001.

[38] B. Moaveni, F. Rashidi Fathabadi, and A. Molavi. Fuzzy control system design for wheel slip prevention and tracking of desired speed profile in electric trains. *Asian Journal of Control*, 24(1):388–400, 2022.

[39] Y. Shi and R. C. Eberhart. Empirical study of particle swarm optimization. In *Proceedings of the 1999 congress on evolutionary computation-CEC99 (Cat. No. 99TH8406)*, volume 3, pages 1945–1950. IEEE, 1999.

[40] F. Herrera, M. Lozano, and J. L. Verdegay. Tuning fuzzy logic controllers by genetic algorithms. *International Journal of Approximate Reasoning*, 12(3-4):299–315, 1995.

[41] Y. Shi and M. Mizumoto. A new approach of neuro-fuzzy learning algorithm for tuning fuzzy rules. *Fuzzy sets and systems*, 112(1):99–116, 2000.

[42] O. Guenounou, B. Dahhou, and F. Chabour. Adaptive fuzzy controller based mppt for photovoltaic systems. *Energy Conversion and Management*, 78:843–850, 2014.

[43] N. Patcharaprakiti, S. Premrudeepreechacharn, and Y. Sriuthaisiriwong. Maximum power point tracking using adaptive fuzzy logic control for grid-connected photovoltaic system. *Renewable Energy*, 30(11):1771–1788, 2005.

[44] J. Kennedy and R. Eberhart. Particle swarm optimization. In *Proceedings of ICNN'95-international conference on neural networks*, volume 4, pages 1942–1948. IEEE, 1995.

[45] R. Poli, J. Kennedy, and T. Blackwell. Particle swarm optimization. *Swarm intelligence*, 1(1):33–57, 2007.

[46] D. Wang, D. Tan, and L. Liu. Particle swarm optimization algorithm: an overview. *Soft computing*, 22(2):387–408, 2018.

[47] Y. Shi et al. Particle swarm optimization: developments, applications and resources. In *Proceedings of the 2001 congress on evolutionary computation (IEEE Cat. No. 01TH8546)*, volume 1, pages 81–86.

IEEE, 2001.

[48] Y.-H. Liu, S.-C. Huang, J.-W. Huang, and W.-C. Liang. A particle swarm optimization-based maximum power point tracking algorithm for pv systems operating under partially shaded conditions. *IEEE Transactions on Energy Conversion*, 27(4):1027–1035, 2012.

[49] K. Ishaque, Z. Salam, M. Amjad, and S. Mekhilef. An improved particle swarm optimization (PSO)–based mppt for pv with reduced steady-state oscillation. *IEEE Transactions on Power Electronics*, 27(8):3627–3638, 2012.

[50] H. Li, D. Yang, W. Su, J. Lü, and X. Yu. An overall distribution particle swarm optimization mppt algorithm for photovoltaic system under partial shading. *IEEE Transactions on Industrial Electronics*, 66(1):265–275, 2018.

[51] L. Xu, R. Cheng, Z. Xia, and Z. Shen. Improved particle swarm optimization (PSO)-based mppt method for pv string under partially shading and uniform irradiance condition. In *2020 Asia Energy and Electrical Engineering Symposium (AEEES)*, pages 771–775. IEEE, 2020.

[52] D. Diaz Martinez, R. Trujillo Codorniu, R. Giral, and L. Vazquez Seisdedos. Evaluation of particle swarm optimization techniques applied to maximum power point tracking in photovoltaic systems. *International Journal of Circuit Theory and Applications*, 49(7):1849–1867, 2021.

[53] P. Verma, A. Alam, A. Sarwar, M. Tariq, H. Vahedi, D. Gupta, S. Ahmad, and A. Shah Noor Mohamed. Meta-heuristic optimization techniques used for maximum power point tracking in solar pv system. *Electronics*, 10(19):2419, 2021.

[54] F. Blaschke. The principle of field orientation as applied to the new transvector closed-loop system for rotating-field machines. *Siemens review*, 34(3):217–220, 1972.

[55] K. Zhou and D. Wang. Relationship between space-vector modulation and three-phase carrier-based pwm: a comprehensive analysis [three-phase inverters]. *IEEE transactions on industrial electronics*, 49(1):186–196, 2002.

Ahmed Fathy Abouzeid received the B.S and M.S. degrees in Electrical Engineering from Port Said University, Port Said, Egypt, in 2012 and 2017, respectively. He is currently pursuing his Ph.D. Degree at the Department of Electrical, Electronic and Computer Engineering, University of Oviedo, Gijón, Spain. From September to December 2021, he was a Visiting Researcher at Deutsche Bahn (DB) Systemtechnik GmbH, Minden, Germany. In 2013, he joined the Department of Electrical Engineering, Port Said University, Egypt, as a researcher. Currently, he is on leave with the same department as an assistant lecturer. His research interests include power converters and ac drives, electric traction, and renewable energy systems.

Juan M. Guerrero received the M.E. degree in industrial engineering and the Ph.D. Degree in Electrical and Electronic Engineering from the University of Oviedo, Gijón, Spain, in 1998 and 2003, respectively. Since 1999, he has occupied different teaching and research positions with the Department of Electrical, Computer and Systems Engineering, University of Oviedo, where he is currently a Full Professor. From February 2002 to October 2002, he was a Visiting Scholar at the University of Wisconsin, Madison. From June to December 2007, he was a Visiting Professor at the Tennessee Technological University, Cookeville. His research interests include control of electric drives and power converters, electric traction, and renewable energy generation. He is an Associate

Editor of the IEEE TRANSACTIONS ON IN-DUSTRY APPLICATIONS.

Lander Lejarza-Lasuen received the B.Sc. degree in electronics engineering, and the M.Sc. degree in control, automatics and robotics from the University of the Basque Country (UPV/EHU), Bilbao, Spain, in 2017 and 2019, respectively. He joined Ingeteam Power Technology, Zamudio, Spain, in July 2019, where he works as a Control and Regulation Engineer involved in railway traction control for trams, locomotives and EMU-s. His current research interests include power converter and advanced control drives, modeling, modulation techniques, and digital signal processing, as well as railway research issues such as mechanical vibrations in the drive-train.

Iker Muniategui-Aspiazu received the Industrial Technical Engineering Degree (Electronic Design specialty) and the Industrial Automatics and Electronics Engineering Degree, from the University of Mondragon, Mondragon, Spain, in 2004 and 2007 respectively. In September 2006, he joined Ingeteam Power Technology (formerly TEAM), Zamudio, Spain, where he worked as a Control and Regulation Engineer, and he is currently Control and Regulation manager of Traction department. His current research interests include power converter and advanced control drives, modulation techniques, and railway research issues such as AC catenary stability and mechanical vibrations in the drive-train.

Aitor Endemaño-Isasi received the Industrial Technical Engineering Degree (Electronic Design speciality) and the Industrial Automatics and Electronics Engineering Degree, from the University of Mondragon, Mondragon, Spain, in 1997 and 2000 respectively, and the Ph.D. from Heriot-Watt University, Edinburgh, Scotland, UK, in 2003. In 2003 he joined Traction department at Ingeteam Power Technology (formerly TEAM), Zamudio, Spain, where since then he has been a Control and Regulation Engineer, involved in several traction control design projects for trams, locomotives and EMU-s. His current research interests include power converter and advanced control drives, modulation techniques, railway research issues such as AC catenary stability and mechanical vibrations in the drive-train.

Fernando Briz received the M.S. and Ph.D. degrees from the University of Oviedo, Gijón, Spain, in 1990 and 1996, respectively. He is currently a Full Professor with the Department of Electrical, Computer and Systems Engineering, University of Oviedo. His research interests include electronic power converters and ac drives, power systems, machine monitoring and diagnostics, and digital signal processing. He is a member of the Executive Board of ECCE. He was a recipient of the IEEE TRANSACTIONS ON INDUSTRY APPLICATIONS Award and the nine IEEE Industry Applications Society Conference and IEEE Energy

Conversion Congress and Exposition Prize Paper Awards. He is the Chair of the Industrial Power Conversion System Department (IPCSD) of the IAS. He is the Past Chair of the Industrial Drives Committee of IPCSD. He has served for scientific committees and as the Vice Chair or the Technical Program Chair for several conferences, including ECCE, IEMDC, ICEM, ICEMS, and SLED. He is the Deputy Editor-in-Chief and a member of the Steering Committee of IEEE JOURNAL OF EMERGING AND SELECTED TOPICS IN POWER ELECTRONICS. He is an Associate Editor of IEEE TRANSACTIONS ON INDUSTRY APPLICATIONS.

Bibliography

[1] V. V. Georgatzi, Y. Stamboulis, and A. Vetsikas, "Examining the determinants of co2 emissions caused by the transport sector: Empirical evidence from 12 european countries," *Economic Analysis and Policy*, vol. 65, pp. 11–20, 2020.

[2] N. L. Panwar, S. C. Kaushik, and S. Kothari, "Role of renewable energy sources in environmental protection: A review," *Renewable and sustainable energy reviews*, vol. 15, no. 3, pp. 1513–1524, 2011.

[3] D. Gielen, F. Boshell, D. Saygin, M. D. Bazilian, N. Wagner, and R. Gorini, "The role of renewable energy in the global energy transformation," *Energy strategy reviews*, vol. 24, pp. 38–50, 2019.

[4] P. A. Owusu and S. Asumadu-Sarkodie, "A review of renewable energy sources, sustainability issues and climate change mitigation," *Cogent Engineering*, vol. 3, no. 1, p. 1167990, 2016.

[5] D. McCollum, V. Krey, P. Kolp, Y. Nagai, and K. Riahi, "Transport electrification: A key element for energy system transformation and climate stabilization," *Climatic change*, vol. 123, pp. 651–664, 2014.

[6] R. Zhang and S. Fujimori, "The role of transport electrification in global climate change mitigation scenarios," *Environmental Research Letters*, vol. 15, no. 3, p. 034019, 2020.

[7] M. Seredynski, "Pathways to reducing the negative impact of urban transport on climate change," *IET Smart Cities*, 2022.

[8] G. Wu, X. Zhang, and Z. Dong, "Powertrain architectures of electrified vehicles: Review, classification and comparison," *Journal of the Franklin Institute*, vol. 352, no. 2, pp. 425–448, 2015.

[9] J. C. González Palencia, V. T. Nguyen, M. Araki, and S. Shiga, "The role of powertrain electrification in achieving deep decarbonization in road freight transport," *Energies*, vol. 13, no. 10, p. 2459, 2020.

[10] G. Conway, A. Joshi, F. Leach, A. García, and P. K. Senecal, "A review of current and future powertrain technologies and trends in 2020," *Transportation Engineering*, vol. 5, p. 100080, 2021.

[11] I. M. Sebastiaan Boschmans and S. Ochelen, "Decarbonising road transport — the role of vehicles, fuels and transport demand," *Transport and environment report, European Environment Agency ©EEA, Luxembourg*, 2022.

[12] N. Lutsey, "Global climate change mitigation potential from a transition to electric vehicles," *The International Council on Clean Transportation*, vol. 5, 2015.

[13] L. A.-W. Ellingsen, B. Singh, and A. H. Strømman, "The size and range effect: lifecycle greenhouse gas emissions of electric vehicles," *Environmental Research Letters*, vol. 11, no. 5, p. 054010, 2016.

[14] X. Sun, Z. Li, X. Wang, and C. Li, "Technology development of electric vehicles: A review," *Energies*, vol. 13, no. 1, p. 90, 2019.

[15] J. A. Sanguesa, V. Torres-Sanz, P. Garrido, F. J. Martinez, and J. M. Marquez-Barja, "A review on electric vehicles: Technologies and challenges," *Smart Cities*, vol. 4, no. 1, pp. 372–404, 2021.

[16] D. Ronanki, S. A. Singh, and S. S. Williamson, "Comprehensive topological overview of rolling stock architectures and recent trends in electric railway traction systems," *IEEE Transactions on transportation Electrification*, vol. 3, no. 3, pp. 724–738, 2017.

[17] T. McGean, "Developing ieee rail transit vehicle standards," in *Proceedings of the 1998 ASME/IEEE Joint Railroad Conference*, pp. 95–105, IEEE, 1998.

[18] U. Drofenik and F. Canales, "European trends and technologies in traction," in *2014 International Power Electronics Conference (IPEC-Hiroshima 2014-ECCE ASIA)*, pp. 1043–1049, IEEE, 2014.

[19] K. Sato, M. Yoshizawa, and T. Fukushima, "Traction systems using power electronics for shinkansen high-speed electric multiple units," in

The 2010 International Power Electronics Conference-ECCE ASIA-, pp. 2859–2866, IEEE, 2010.

[20] M. Fleischer, R. W. de Doncker, and D. Abel, "Traction control for railway vehicles," *Institut für Stromrichtertechnik und Elektrische Antriebe*, 2019.

[21] L. Chapman, "Transport and climate change: a review," *Journal of transport geography*, vol. 15, no. 5, pp. 354–367, 2007.

[22] Z. Chen, J. Xue, A. Z. Rose, and K. E. Haynes, "The impact of high-speed rail investment on economic and environmental change in china: A dynamic cge analysis," *Transportation Research Part A: Policy and Practice*, vol. 92, pp. 232–245, 2016.

[23] Y. Lin, Y. Qin, J. Wu, and M. Xu, "Impact of high-speed rail on road traffic and greenhouse gas emissions," *Nature Climate Change*, vol. 11, no. 11, pp. 952–957, 2021.

[24] T. Koseki, "Technical trends of railway traction in the world," in *The 2010 International Power Electronics Conference-ECCE ASIA-*, pp. 2836–2831, IEEE, 2010.

[25] A. Miller, K. Hess, D. Barnes, and T. Erickson, "System design of a large fuel cell hybrid locomotive," *Journal of Power Sources*, vol. 173, no. 2, pp. 935–942, 2007.

[26] N. Ghaviha, J. Campillo, M. Bohlin, and E. Dahlquist, "Review of application of energy storage devices in railway transportation," *Energy Procedia*, vol. 105, pp. 4561–4568, 2017.

[27] R. Hill, "Electric railway traction. ii. traction drives with three-phase induction motors," *Power Engineering Journal*, vol. 8, no. 3, pp. 143–152, 1994.

[28] A. M. El-Refaie, "Motors/generators for traction/propulsion applications: A review," *IEEE Vehicular Technology Magazine*, vol. 8, no. 1, pp. 90–99, 2013.

[29] V. T. Buyukdegirmenci, A. M. Bazzi, and P. T. Krein, "Evaluation of induction and permanent-magnet synchronous machines using drive-cycle energy and loss minimization in traction applications," *IEEE Transactions on Industry Applications*, vol. 50, no. 1, pp. 395–403, 2013.

[30] M. Yano and M. Iwahori, "Transition from slip-frequency control to vector control for induction motor drives of traction applications in japan," in *The Fifth International Conference on Power Electronics and Drive Systems, 2003. PEDS 2003.*, vol. 2, pp. 1246–1251, IEEE, 2003.

[31] X. Guo, M. He, and Y. Yang, "Over modulation strategy of power converters: A review," *IEEE Access*, vol. 6, pp. 69528–69544, 2018.

[32] H. Mahlfeld, T. Schuhmann, R. Döbler, and B. Cebulski, "Impact of overmodulation methods on inverter and machine losses in voltage-fed induction motor drives," in *2016 XXII International Conference on Electrical Machines (ICEM)*, pp. 1064–1070, IEEE, 2016.

[33] S. Halasz, I. Varjasi, and A. Zacharov, "Overmodulation strategies of inverter-fed ac drives," in *Proceedings of the Power Conversion Conference-Osaka 2002 (Cat. No. 02TH8579)*, vol. 3, pp. 1346–1351, IEEE, 2002.

[34] G. Narayanan and V. T. Ranganathan, "Extension of operation of space vector pwm strategies with low switching frequencies using different overmodulation algorithms," *IEEE Transactions on Power Electronics*, vol. 17, no. 5, pp. 788–798, 2002.

[35] S. K. Mondal, B. K. Bose, V. Oleschuk, and J. O. P. Pinto, "Space vector pulse width modulation of three-level inverter extending operation into overmodulation region," *IEEE Transactions on Power Electronics*, vol. 18, no. 2, pp. 604–611, 2003.

[36] A. K. Gupta and A. M. Khambadkone, "A general space vector pwm algorithm for multilevel inverters, including operation in overmodulation range," *IEEE Transactions on Power Electronics*, vol. 22, no. 2, pp. 517–526, 2007.

[37] J. Prieto, F. Barrero, M. J. Durán, S. T. Marín, and M. A. Perales, "Svm procedure for n-phase vsi with low harmonic distortion in the overmodulation region," *IEEE Transactions on Industrial Electronics*, vol. 61, no. 1, pp. 92–97, 2013.

[38] P. Stumpf and S. Halász, "Optimization of pwm for the overmodulation region of two-level inverters," *Ieee transactions on industry applications*, vol. 54, no. 4, pp. 3393–3404, 2018.

[39] J. Chen, R. Ni, T. Li, R. Qiu, and Z. Liu, "The harmonic characteristic of the advanced synchronous svpwm overmodulation strategy," *IEEE Access*, vol. 7, pp. 148934–148949, 2019.

[40] European Union Agency for Railways, "Report on Railway Safety and Interoperability in the EU", 2018. Available: `https://www.era.europa.eu/sites/default/files/library/docs/safety_interoperability_progress_reports/railway_safety_and_interoperability_in_eu_2018_en.pdf`.

[41] J. Zeng and P. Wu, "Study on the wheel/rail interaction and derailment safety," *Wear*, vol. 265, no. 9-10, pp. 1452–1459, 2008.

[42] J. Santamaria, E. Vadillo, and J. Gomez, "Influence of creep forces on the risk of derailment of railway vehicles," *Vehicle System Dynamics*, vol. 47, no. 6, pp. 721–752, 2009.

[43] K. Kondo, "Anti-slip control technologies for the railway vehicle traction," in *2012 IEEE Vehicle Power and Propulsion Conference*, pp. 1306–1311, IEEE, 2012.

[44] P. Pichlík and J. Zdeněk, "Overview of slip control methods used in locomotives," *Transactions on Electrical Engineering*, vol. 3, no. 2, pp. 38–43, 2014.

[45] C. Uyulan, M. Gokasan, and S. Bogosyan, "Comparison of the re-adhesion control strategies in high-speed train," *Proceedings of the Institution of Mechanical Engineers, Part I: Journal of Systems and Control Engineering*, vol. 232, no. 1, pp. 92–105, 2018.

[46] D.-Y. Park, M.-S. Kim, D.-H. Hwang, J.-H. Lee, and Y.-J. Kim, "Hybrid re-adhesion control method for traction system of high-speed railway," in *ICEMS'2001. Proceedings of the Fifth International Conference on Electrical Machines and Systems (IEEE Cat. No. 01EX501)*, vol. 2, pp. 739–742, IEEE, 2001.

[47] O. Polach, "Creep forces in simulations of traction vehicles running on adhesion limit," *Wear*, vol. 258, no. 7-8, pp. 992–1000, 2005.

[48] T. WATANABE, "Anti-slip readhesion control with presumed adhesion force-method of presuming adhesion force and running test results of high-speed shinkansen train," *Quarterly Report of RTRI*, vol. 41, no. 1, pp. 32–36, 2000.

299

[49] J. Huang, J. Xiao, and H. Weiss, "Simulation study on adhesion control of electric locomotives based on multidisciplinary virtual prototyping," in *2008 IEEE International Conference on Industrial Technology*, pp. 1–4, IEEE, 2008.

[50] M. Yamashita and T. Soeda, "Anti-slip re-adhesion control method for increasing the tractive force of locomotives through the early detection of wheel slip convergence," in *2015 17th European conference on power electronics and applications (EPE'15 ECCE-Europe)*, pp. 1–10, IEEE, 2015.

[51] A. D. Cheok and S. Shiomi, "A fuzzy logic based anti-skid control system for railway applications," in *1998 Second International Conference. Knowledge-Based Intelligent Electronic Systems. Proceedings KES'98 (Cat. No. 98EX111)*, vol. 1, pp. 195–201, IEEE, 1998.

[52] A. D. Cheok and S. Shiomi, "Combined heuristic knowledge and limited measurement based fuzzy logic antiskid control for railway applications," *IEEE Transactions on Systems, Man, and Cybernetics, Part C (Applications and Reviews)*, vol. 30, no. 4, pp. 557–568, 2000.

[53] T. Watanabe and M. Yamashita, "A novel anti-slip control without speed sensor for electric railway vehicles," in *IECON'01. 27th Annual Conference of the IEEE Industrial Electronics Society (Cat. No. 37243)*, vol. 2, pp. 1382–1387, IEEE, 2001.

[54] S. Sadr, D. A. Khaburi, and J. Rodríguez, "Predictive slip control for electrical trains," *IEEE Transactions on Industrial Electronics*, vol. 63, no. 6, pp. 3446–3457, 2016.

[55] K. Can, H. Jingchun, D. Wenqi, and W. Xiaokang, "Adhesion control method based on optimal slip velocity searching and tracking," in *2019 14th IEEE International Conference on Electronic Measurement & Instruments (ICEMI)*, pp. 1200–1207, IEEE, 2019.

[56] S. H. Park, J. S. Kim, J. J. Choi, and H.-O. Yamazaki, "Modeling and control of adhesion force in railway rolling stocks," *IEEE Control Systems Magazine*, vol. 28, no. 5, pp. 44–58, 2008.

[57] T. Ishrat, G. Ledwich, M. Vilathgamuwa, and P. Borghesani, "Identification scheme of maximum traction force using recursive least square

for traction control in electric locomotives," in *2017 IEEE 12th International Conference on Power Electronics and Drive Systems (PEDS)*, pp. 1–120, IEEE, 2017.

[58] Z. Huang, W. Du, B. Chen, K. Gao, Y. Liu, X. Tang, and Y. Yang, "An online super-twisting sliding mode anti-slip control strategy," *Energies*, vol. 13, no. 7, p. 1823, 2020.

[59] X. Wen, J. Huang, and S. Zhang, "Anti-slip re-adhesion control strategy of electric locomotive based on distributed MPC," in *2019 IEEE 21st International Conference on High Performance Computing and Communications; IEEE 17th International Conference on Smart City; IEEE 5th International Conference on Data Science and Systems (HPCC/SmartCity/DSS)*, pp. 2708–2713, IEEE, 2019.

[60] A. Zirek and A. Onat, "A novel anti-slip control approach for railway vehicles with traction based on adhesion estimation with swarm intelligence," *Railway Engineering Science*, vol. 28, no. 4, pp. 346–364, 2020.

[61] T. Fridrichovskỳ and B. Šulc, "Investigation of torsional oscillations in railway vehicles," in *MATEC Web of Conferences*, vol. 76, p. 02052, EDP Sciences, 2016.

[62] H. Wu, P. Wu, K. Xu, J. Li, and F. Li, "Research on vibration characteristics and stress analysis of gearbox housing in high-speed trains," *IEEE Access*, vol. 7, pp. 102508–102518, 2019.

[63] M. Bruha and Z. Peroutka, "Torsional vibration in large variable speed drive systems: Origin and mitigation methods," in *2015 17th European Conference on Power Electronics and Applications (EPE'15 ECCE-Europe)*, pp. 1–10, IEEE, 2015.

[64] J. Pacas, A. John, and T. Eutebach, "Automatic identification and damping of torsional vibrations in high-dynamic-drives," in *ISIE'2000. Proceedings of the 2000 IEEE International Symposium on Industrial Electronics (Cat. No. 00TH8543)*, vol. 1, pp. 201–206, IEEE, 2000.

[65] S. N. Vukosavic and M. R. Stojic, "Suppression of torsional oscillations in a high-performance speed servo drive," *IEEE Transactions on Industrial Electronics*, vol. 45, no. 1, pp. 108–117, 1998.

[66] K.-K. Shyu and C.-Y. Chang, "Modified FIR filter with phase compensation technique to feedforward active noise controller design," *IEEE Transactions on Industrial Electronics*, vol. 47, no. 2, pp. 444–453, 2000.

[67] L. Litwin, "FIR and IIR digital filters," *IEEE potentials*, vol. 19, no. 4, pp. 28–31, 2000.

[68] T. Ohmae, T. Matsuda, M. Kanno, K. Saito, and T. Sukegawa, "A microprocessor-based motor speed regulator using fast-response state observer for reduction of torsional vibration," *IEEE transactions on industry applications*, no. 5, pp. 863–871, 1987.

[69] Y. Hori, H. Iseki, and K. Sugiura, "Basic consideration of vibration suppression and disturbance rejection control of multi-inertia system using SFLAC (state feedback and load acceleration control)," *IEEE Transactions on Industry Applications*, vol. 30, no. 4, pp. 889–896, 1994.

[70] K. Sugiura and Y. Hori, "Vibration suppression in 2-and 3-mass system based on the feedback of imperfect derivative of the estimated torsional torque," *IEEE Transactions on Industrial Electronics*, vol. 43, no. 1, pp. 56–64, 1996.

[71] M. Neshati, T. Jersch, and J. Wenske, "Model based active damping of drive train torsional oscillations for a full-scale wind turbine nacelle test rig," in *2016 American Control Conference (ACC)*, pp. 2283–2288, IEEE, 2016.

[72] J.-K. Ji and S.-K. Sul, "Kalman filter and LQ based speed controller for torsional vibration suppression in a 2-mass motor drive system," *IEEE Transactions on industrial electronics*, vol. 42, no. 6, pp. 564–571, 1995.

[73] E. Omine, T. Goya, U. Akie, T. Senjyu, A. Yona, N. Urasaki, and T. Funabashi, "Torsional torque suppression of decentralized generators using h∞ observer," *Renewable Energy*, vol. 35, no. 9, pp. 1908–1913, 2010.

[74] Y. Wang, Q. Zheng, H. Zhang, and M. Chen, "The LQG/LTR control method for turboshaft engine with variable rotor speed based on torsional vibration suppression," *Journal of Low Frequency Noise, Vibration and Active Control*, vol. 39, no. 4, pp. 1145–1158, 2020.

[75] T. Hirotsu, S. KASAI, and H. TAKAI, "Self-excited vibration during slippage of parallel cardan drives for electric railcars: Vibration, con-

trol engineering, engineering for industry," *JSME international journal*, vol. 30, no. 266, pp. 1304–1310, 1987.

[76] M. Lata, "The modern wheelset drive system and possibilities of modelling the torsion dynamics," *Transport*, vol. 23, no. 2, pp. 172–181, 2008.

[77] R. Konowrocki and T. Szolc, "An analysis of the self-excited torsional vibrations of the electromechanical drive system," *Vibrations in Physical Systems*, vol. 27, 2016.

[78] K. Xu, J. Zeng, and L. Wei, "An analysis of the self-excited torsional vibration of high-speed train drive system.," *Journal of Mechanical Science & Technology*, vol. 33, no. 3, 2019.

[79] T. Mei, J. Yu, and D. Wilson, "A mechatronic approach for anti-slip control in railway traction," *IFAC Proceedings Volumes*, vol. 41, no. 2, pp. 8275–8280, 2008.

[80] M. Fleischer and K. Kondo, "Slip-stick vibration suppression by modal state control for traction drive-trains," *IEEJ Journal of Industry Applications*, vol. 5, no. 1, pp. 1–9, 2016.

[81] A. M. Hava, R. J. Kerkman, and T. A. Lipo, "Simple analytical and graphical methods for carrier-based pwm-vsi drives," *IEEE transactions on power electronics*, vol. 14, no. 1, pp. 49–61, 1999.

[82] A. Nabae, I. Takahashi, and H. Akagi, "A new neutral-point-clamped pwm inverter," *IEEE Transactions on industry applications*, no. 5, pp. 518–523, 1981.

[83] L. Wei, Y. Wu, C. Li, H. Wang, S. Liu, and F. Li, "A novel space vector control of three-level pwm converter," in *Proceedings of the IEEE 1999 International Conference on Power Electronics and Drive Systems. PEDS'99 (Cat. No. 99TH8475)*, vol. 2, pp. 745–750, IEEE, 1999.

[84] N. Celanovic and D. Boroyevich, "A comprehensive study of neutral-point voltage balancing problem in three-level neutral-point-clamped voltage source pwm inverters," *IEEE Transactions on power electronics*, vol. 15, no. 2, pp. 242–249, 2000.

[85] A. M. Hava, R. J. Kerkman, and T. A. Lipo, "A high-performance generalized discontinuous pwm algorithm," *IEEE Transactions on Industry applications*, vol. 34, no. 5, pp. 1059–1071, 1998.

[86] A. M. Hava, R. J. Kerkman, and T. A. Lipo, "Carrier-based pwm-vsi overmodulation strategies: analysis, comparison, and design," *IEEE Transactions on Power Electronics*, vol. 13, no. 4, pp. 674–689, 1998.

[87] J. S. Kim and S. K. Sul, "A novel voltage modulation technique of the space vector pwm," *Chongi Hakhoe Nonmunchi (Transactions of the Korean Institute of Electrical Engineers)*, vol. 44, 1995.

[88] D.-W. Chung, J.-S. Kim, and S.-K. Sul, "Unified voltage modulation technique for real-time three-phase power conversion," *IEEE Transactions on Industry applications*, vol. 34, no. 2, pp. 374–380, 1998.

[89] M. Al-Hitmi, S. Ahmad, A. Iqbal, S. Padmanaban, and I. Ashraf, "Selective harmonic elimination in a wide modulation range using modified newton–raphson and pattern generation methods for a multilevel inverter," *Energies*, vol. 11, no. 2, p. 458, 2018.

[90] A. M. Amjad and Z. Salam, "A review of soft computing methods for harmonics elimination pwm for inverters in renewable energy conversion systems," *Renewable and Sustainable Energy Reviews*, vol. 33, pp. 141–153, 2014.

[91] N. Rai and S. Chakravorty, "Generalized formulations and solving techniques for selective harmonic elimination pwm strategy: A review," *Journal of The Institution of Engineers (India): Series B*, vol. 100, no. 6, pp. 649–664, 2019.

[92] Y. Sahali and M. Fellah, "Selective harmonic eliminated pulse-width modulation technique (she pwm) applied to three-level inverter/converter," in *2003 IEEE International Symposium on Industrial Electronics (Cat. No. 03TH8692)*, vol. 2, pp. 1112–1117, IEEE, 2003.

[93] S. Bolognani and M. Zigliotto, "Novel digital continuous control of svm inverters in the overmodulation range," *IEEE Transactions on Industry Applications*, vol. 33, no. 2, pp. 525–530, 1997.

[94] Dong-Choon Lee and G-Myoung Lee, "A novel overmodulation technique for space-vector pwm inverters," *IEEE Transactions on Power Electronics*, vol. 13, no. 6, pp. 1144–1151, 1998.

[95] "ELINSA three-phase three-level natural-point-clamped (NPC) inverter." https://www.elinsa.org/en/

`manufacturing-of-electrical-equipment-and-power-electronics`. Accessed: 2023-03-08.

[96] "Magna DC MT series programmable DC power supply." `https://magna-power.com/products/magnadc/mt`. Accessed: 2023-03-08.

[97] A. M. Hava, S.-K. Sul, R. J. Kerkman, and T. A. Lipo, "Dynamic overmodulation characteristics of triangle intersection pwm methods," *IEEE Transactions on Industry Applications*, vol. 35, no. 4, pp. 896–907, 1999.

[98] Y.-C. Kwon, S. Kim, and S.-K. Sul, "Six-step operation of pmsm with instantaneous current control," *IEEE Transactions on Industry Applications*, vol. 50, no. 4, pp. 2614–2625, 2014.

[99] S. K. Mondal, B. K. Bose, V. Oleschuk, and J. O. Pinto, "Space vector pulse width modulation of three-level inverter extending operation into overmodulation region," *IEEE Transactions on Power Electronics*, vol. 18, no. 2, pp. 604–611, 2003.

[100] X. Fang, Z. Tian, H. Li, Z. Yang, F. Lin, and S. Hillmansen, "Current closed-loop control and field orientation analysis of an induction motor in six-step operation for railway applications," *IET Power Electronics*, vol. 12, no. 6, pp. 1462–1469, 2019.

[101] B. Wang, X. Zhang, Y. Yu, J. Zhang, and D. Xu, "Maximum torque analysis and extension in six-step mode-combined field-weakening control for induction motor drives," *IEEE Transactions on Industrial Electronics*, vol. 66, no. 12, pp. 9129–9138, 2019.

[102] A. G. Yepes and J. Doval-Gandoy, "Overmodulation method with adaptive x-y current limitation for five-phase induction motor drives," *IEEE Transactions on Industrial Electronics*, vol. 69, no. 3, pp. 2240–2251, 2021.

[103] J. Zhang, B. Wang, Y. Yu, X. Zhang, and D. Xu, "Overmodulation harmonic modeling and suppression for induction motor field-weakening control with extended voltage tracking method," *IEEE Transactions on Industrial Electronics*, 2022.

[104] D. W. Novotny and T. A. Lipo, *Vector control and dynamics of AC drives*, vol. 41. Oxford university press, 1996.

[105] G. Abad, *Power electronics and electric drives for traction applications*. John Wiley & Sons, 2016.

[106] R. Ikeda, S. Yusya, and K. Kondo, "Study on design method for increasing power density of induction motors for electric railway vehicle traction," in *2019 IEEE International Electric Machines & Drives Conference (IEMDC)*, pp. 1545–1550, IEEE, 2019.

[107] L. Buhrkall, "Traction system case study," in *The 9th Institution of Engineering and Technology Professional Development Course on Electric Traction Systems*, pp. 53–71, IET, 2006.

[108] B. Bose, "Modern power electronics and ac drives-prentice-hall," *Inc, Publication*, pp. 70–74, 2002.

[109] J. Holtz, "Sensorless control of induction machines—with or without signal injection?," *IEEE transactions on industrial electronics*, vol. 53, no. 1, pp. 7–30, 2006.

[110] P. Vas, "Vector control of ac machines," *Monographs in Electrical and Electronic Engineering*, vol. 22, 1990.

[111] F. Blaschke, "The principle of field orientation as applied to the new transvektor closed-loop control system for rotating field machines," *Siemens review*, vol. 34, no. 1, 1972.

[112] G. Pellegrino, R. I. Bojoi, and P. Guglielmi, "Unified direct-flux vector control for ac motor drives," *IEEE Transactions on Industry Applications*, vol. 47, no. 5, pp. 2093–2102, 2011.

[113] X. Xu and D. W. Novotny, "Implementation of direct stator flux orientation control on a versatile dsp based system," *IEEE Transactions on Industry Applications*, vol. 27, no. 4, pp. 694–700, 1991.

[114] I. Takahashi and T. Noguchi, "A new quick-response and high-efficiency control strategy of an induction motor," *IEEE Transactions on Industry applications*, no. 5, pp. 820–827, 1986.

[115] D. Casadei, G. Serra, A. Stefani, A. Tani, and L. Zarri, "Dtc drives for wide speed range applications using a robust flux-weakening algorithm," *IEEE transactions on industrial electronics*, vol. 54, no. 5, pp. 2451–2461, 2007.

[116] M. Depenbrock, "Direct self-control (dsc) of inverter fed induktion machine," in *1987 IEEE Power Electronics Specialists Conference*, pp. 632–641, IEEE, 1987.

[117] G. S. Buja and M. P. Kazmierkowski, "Direct torque control of pwm inverter-fed ac motors-a survey," *IEEE Transactions on industrial electronics*, vol. 51, no. 4, pp. 744–757, 2004.

[118] A. Steimel, "Direct self-control and synchronous pulse techniques for high-power traction inverters in comparison," *IEEE Transactions on Industrial Electronics*, vol. 51, no. 4, pp. 810–820, 2004.

[119] M. Spichartz, C. Heising, V. Staudt, and A. Steimel, "Indirect stator-quantities control as benchmark for highly dynamic induction machine control in the full operating range," in *Proceedings of 14th International Power Electronics and Motion Control Conference EPE-PEMC 2010*, pp. T3–13, IEEE, 2010.

[120] C. Lascu, I. Boldea, and F. Blaabjerg, "A modified direct torque control for induction motor sensorless drive," *IEEE Transactions on industry applications*, vol. 36, no. 1, pp. 122–130, 2000.

[121] L. Tang, L. Zhong, M. F. Rahman, and Y. Hu, "A novel direct torque controlled interior permanent magnet synchronous machine drive with low ripple in flux and torque and fixed switching frequency," *IEEE Transactions on power electronics*, vol. 19, no. 2, pp. 346–354, 2004.

[122] J. Rodriguez, J. Pontt, C. Silva, S. Kouro, and H. Miranda, "A novel direct torque control scheme for induction machines with space vector modulation," in *2004 IEEE 35th Annual Power Electronics Specialists Conference (IEEE Cat. No. 04CH37551)*, vol. 2, pp. 1392–1397, IEEE, 2004.

[123] A. Tripathi, A. M. Khambadkone, and S. K. Panda, "Stator flux based space-vector modulation and closed loop control of the stator flux vector in overmodulation into six-step mode," *IEEE Transactions on Power Electronics*, vol. 19, no. 3, pp. 775–782, 2004.

[124] B. K. Bose, "Scalar decoupled control of induction motor," *IEEE transactions on industry applications*, no. 1, pp. 216–225, 1984.

[125] A. Smith, S. Gadoue, M. Armstrong, and J. Finch, "Improved method for the scalar control of induction motor drives," *IET Electric Power Applications*, vol. 7, no. 6, pp. 487–498, 2013.

[126] I. Boldea, A. Moldovan, and L. Tutelea, "Scalar v/f and i-f control of ac motor drives: An overview," in *2015 Intl Aegean Conference on Electrical Machines Power Electronics (ACEMP), 2015 Intl Conference on Optimization of Electrical Electronic Equipment (OPTIM) 2015 Intl Symposium on Advanced Electromechanical Motion Systems (ELECTROMOTION)*, pp. 8–17, 2015.

[127] S. R. P. Reddy and U. Loganathan, "Robust and high-dynamic-performance control of induction motor drive using transient vector estimator," *IEEE Transactions on Industrial Electronics*, vol. 66, no. 10, pp. 7529–7538, 2018.

[128] S. R. P. Reddy and U. Loganathan, "Improving the dynamic response of scalar control of induction machine drive using phase angle control," in *IECON 2018-44th Annual Conference of the IEEE Industrial Electronics Society*, pp. 541–546, IEEE, 2018.

[129] Z. Zhang and A. M. Bazzi, "Robust sensorless scalar control of induction motor drives with torque capability enhancement at low speeds," in *2019 IEEE International Electric Machines & Drives Conference (IEMDC)*, pp. 1706–1710, IEEE, 2019.

[130] T. H. Nguyen, T. L. Van, D.-C. Lee, J.-H. Park, and J.-H. Hwang, "Control mode switching of induction machine drives between vector control and v/f control in overmodulation range," *Journal of Power Electronics*, vol. 11, no. 6, pp. 846–855, 2011.

[131] B. Gou, X. Feng, W. Song, K. Han, and X. Ge, "Analysis and compensation of beat phenomenon for railway traction drive system fed with fluctuating dc-link voltage," in *Proceedings of The 7th International Power Electronics and Motion Control Conference*, vol. 1, pp. 654–659, IEEE, 2012.

[132] Y. Lei, K. Wang, L. Zhao, and Q. Ge, "An improved beatless control method of ac drives for railway traction converters," in *2016 19th International Conference on Electrical Machines and Systems (ICEMS)*, pp. 1–5, IEEE, 2016.

[133] J. Kullick and C. M. Hackl, "Generic machine identification and maximum efficiency operation of induction machines," *arXiv preprint arXiv:1812.02431*, 2018.

[134] S. Lim and K. Nam, "Loss-minimising control scheme for induction motors," *IEE Proceedings-Electric Power Applications*, vol. 151, no. 4, pp. 385–397, 2004.

[135] D. S. Kirschen, D. W. Novotny, and T. A. Lipo, "On-line efficiency optimization of a variable frequency induction motor drive," *IEEE transactions on industry applications*, no. 3, pp. 610–616, 1985.

[136] O. Wasynczuk, S. Sudhoff, K. Corzine, J. L. Tichenor, P. Krause, I. Hansen, and L. Taylor, "A maximum torque per ampere control strategy for induction motor drives," *IEEE Transactions on Energy Conversion*, vol. 13, no. 2, pp. 163–169, 1998.

[137] A. Dianov, F. Tinazzi, S. Calligaro, and S. Bolognani, "Review and classification of mtpa control algorithms for synchronous motors," *IEEE Transactions on Power Electronics*, 2021.

[138] H. Kouns, J.-S. Lai, and C. E. Konrad, "Analysis of a traction induction motor drive operating under maximum efficiency and maximum torque per ampere conditions," in *Nineteenth Annual IEEE Applied Power Electronics Conference and Exposition, 2004. APEC'04.*, vol. 1, pp. 545–551, IEEE, 2004.

[139] M. Hrkel, J. Vittek, and Z. Biel, "Maximum torque per ampere control strategy of induction motor with iron losses," in *2012 ELEKTRO*, pp. 185–190, IEEE, 2012.

[140] Y. Liu and A. Bazzi, "Improved maximum torque-per-ampere control of induction machines by considering iron loss," in *2017 IEEE international electric machines and drives conference (IEMDC)*, pp. 1–6, IEEE, 2017.

[141] S. N. Vukosavic and E. Levi, "A method for transient torque response improvement in optimum efficiency induction motor drives," *IEEE transactions on energy conversion*, vol. 18, no. 4, pp. 484–493, 2003.

[142] J.-F. Stumper, A. Dötlinger, and R. Kennel, "Loss minimization of induction machines in dynamic operation," *IEEE transactions on energy conversion*, vol. 28, no. 3, pp. 726–735, 2013.

[143] Z. Hu, Q. Liu, and K. Hameyer, "Loss minimization of speed controlled induction machines in transient states considering system constraints," in *2014 17th International Conference on Electrical Machines and Systems (ICEMS)*, pp. 123–129, IEEE, 2014.

[144] "INGETRAC: High power traction converters." `https://www.ingeteam.com/en-us/sectors/railways/p15_59_596_586/ingetrac-traction-converters-high-power.aspx`. Accessed: 2022-11-24.

[145] P. Pichlík, "Strategy of railway traction vehicles wheel slip control," *Czech Technical University, Prague*, 2018.

[146] F. Trimpe and C. Salander, "Wheel–rail adhesion during torsional vibration of driven railway wheelsets," *Vehicle System Dynamics*, vol. 59, no. 5, pp. 785–799, 2021.

[147] S. Iwnicki, *Handbook of railway vehicle dynamics*. CRC press, 2006.

[148] A. Jaschinski, *On the application of similarity laws to a scaled railway bogie model*. PhD thesis, Delft University of Technology, 1991.

[149] R. Stock, D. T. Eadie, D. Elvidge, and K. Oldknow, "Influencing rolling contact fatigue through top of rail friction modifier application–a full scale wheel–rail test rig study," *Wear*, vol. 271, no. 1-2, pp. 134–142, 2011.

[150] R. Conti, E. Meli, and A. Ridolfi, "A full-scale roller-rig for railway vehicles: multibody modelling and hardware in the loop architecture," *Multibody System Dynamics*, vol. 37, no. 1, pp. 69–93, 2016.

[151] T. Ishrat, *Slip control for trains using induction motor drive*. PhD thesis, Queensland University of Technology, 2020.

[152] X. Fang, S. Lin, Z. Yang, F. Lin, H. Sun, and L. Hu, "Adhesion control strategy based on the wheel-rail adhesion state observation for high-speed trains," *Electronics*, vol. 7, no. 5, 2018.

[153] S. Z. Meymand, M. J. Craft, and M. Ahmadian, "On the application of roller rigs for studying rail vehicle systems," in *Rail Transportation Division Conference*, vol. 56116, p. V001T01A015, American Society of Mechanical Engineers, 2013.

[154] S. Senini, F. Flinders, and W. Oghanna, "Dynamic simulation of wheel-rail interaction for locomotive traction studies," in *Proceedings of the 1993 IEEE/ASME Joint Railroad Conference*, pp. 27–34, IEEE, 1993.

[155] H. Ryoo, S. Kim, G. Rim, Y. Kim, and M. Kim, "Novel anti-slip/slide control algorithm for korean high-speed train," in *IECON'03. 29th Annual Conference of the IEEE Industrial Electronics Society (IEEE Cat. No. 03CH37468)*, vol. 3, pp. 2570–2574, IEEE, 2003.

[156] A. Jaschinski, H. Chollet, S. Iwnicki, A. Wickens, and J. Würzen, "The application of roller rigs to railway vehicle dynamics," *Vehicle System Dynamics*, vol. 31, no. 5-6, pp. 345–392, 1999.

[157] N. V. Vantagodi, A. F. Abouzeid, J. M. Guerrero, I. Vicente, I. Muniategui, A. Endemaño, and F. Briz, "Design of a scaled roller-rig test bench for anti-slip control development for railway traction," *IEEE Transactions on Vehicular Technology*, 2022.

[158] E. Vollebregt, K. Six, and O. Polach, "Challenges and progress in the understanding and modelling of the wheel–rail creep forces," *Vehicle System Dynamics*, vol. 59, no. 7, pp. 1026–1068, 2021.

[159] M. Malvezzi, P. Toni, B. Allotta, and V. Colla, "Train speed and position evaluation using wheel velocity measurements," in *2001 IEEE/ASME International Conference on Advanced Intelligent Mechatronics. Proceedings (Cat. No. 01TH8556)*, vol. 1, pp. 220–224, IEEE, 2001.

[160] T. Mei and H. Li, "A novel approach for the measurement of absolute train speed," *Vehicle System Dynamics*, vol. 46, no. S1, pp. 705–715, 2008.

[161] J. Guzinski, H. Abu-Rub, M. Diguet, Z. Krzeminski, and A. Lewicki, "Speed and load torque observer application in high-speed train electric drive," *IEEE Transactions on Industrial Electronics*, vol. 57, no. 2, pp. 565–574, 2009.

[162] H. J. Schwartz, *Regelung der Radsatzdrehzahl zur maximalen Kraftschlussausnutzung bei elektrischen Triebfahrzeugen*. VDI-Verlag, 1992.

[163] M. Buscher, *Radschlupfregelung zur maximalen Kraftschlussausnutzung bei elektrischen Traktionsantrieben*. Verlag Shaker, 1995.

[164] A. F. Abouzeid, J. M. Guerrero, I. Vicente-Makazaga, I. Muniategui-Aspiazu, A. Endemaño-Isasi, and F. Briz, "Torsional vibration suppression in railway traction drives," *IEEE Access*, vol. 10, pp. 32855–32869, 2022.

[165] C.-C. Lee, "Fuzzy logic in control systems: fuzzy logic controller. i," *IEEE Transactions on systems, man, and cybernetics*, vol. 20, no. 2, pp. 404–418, 1990.

[166] C.-Y. Su and Y. Stepanenko, "Adaptive control of a class of nonlinear systems with fuzzy logic," *IEEE Transactions on Fuzzy Systems*, vol. 2, no. 4, pp. 285–294, 1994.

[167] C.-M. Lin and C.-F. Hsu, "Self-learning fuzzy sliding-mode control for antilock braking systems," *IEEE Transactions on Control Systems Technology*, vol. 11, no. 2, pp. 273–278, 2003.

[168] A. Mirzaei, M. Moallem, B. Mirzaeian, and B. Fahimi, "Design of an optimal fuzzy controller for antilock braking systems," in *2005 IEEE Vehicle Power and Propulsion Conference*, pp. 823–828, IEEE, 2005.

[169] L. B. Jordan Jr, "Locomotive traction control system using fuzzy logic," June 13 1995. US Patent 5,424,948.

[170] M. Garcia-Rivera, R. Sanz, and J. A. Perez-Rodriguez, "An antislipping fuzzy logic controller for a railway traction system," in *Proceedings of 6th International Fuzzy Systems Conference*, vol. 1, pp. 119–124, IEEE, 1997.

[171] P. Khatun, C. Bingham, and P. Mellor, "Comparison of control methods for electric vehicle antilock braking/traction control systems," tech. rep., SAE Technical Paper, 2001.

[172] B. Moaveni, F. Rashidi Fathabadi, and A. Molavi, "Fuzzy control system design for wheel slip prevention and tracking of desired speed profile in electric trains," *Asian Journal of Control*, vol. 24, no. 1, pp. 388–400, 2022.

[173] Y. Shi and R. C. Eberhart, "Empirical study of particle swarm optimization," in *Proceedings of the 1999 congress on evolutionary computation-CEC99 (Cat. No. 99TH8406)*, vol. 3, pp. 1945–1950, IEEE, 1999.

[174] F. Herrera, M. Lozano, and J. L. Verdegay, "Tuning fuzzy logic controllers by genetic algorithms," *International Journal of Approximate Reasoning*, vol. 12, no. 3-4, pp. 299–315, 1995.

[175] Y. Shi and M. Mizumoto, "A new approach of neuro-fuzzy learning algorithm for tuning fuzzy rules," *Fuzzy sets and systems*, vol. 112, no. 1, pp. 99–116, 2000.

[176] O. Guenounou, B. Dahhou, and F. Chabour, "Adaptive fuzzy controller based mppt for photovoltaic systems," *Energy Conversion and Management*, vol. 78, pp. 843–850, 2014.

[177] N. Patcharaprakiti, S. Premrudeepreechacharn, and Y. Sriuthaisiriwong, "Maximum power point tracking using adaptive fuzzy logic control for grid-connected photovoltaic system," *Renewable Energy*, vol. 30, no. 11, pp. 1771–1788, 2005.

[178] J. Kennedy and R. Eberhart, "Particle swarm optimization," in *Proceedings of ICNN'95-international conference on neural networks*, vol. 4, pp. 1942–1948, IEEE, 1995.

[179] R. Poli, J. Kennedy, and T. Blackwell, "Particle swarm optimization," *Swarm intelligence*, vol. 1, no. 1, pp. 33–57, 2007.

[180] D. Wang, D. Tan, and L. Liu, "Particle swarm optimization algorithm: an overview," *Soft computing*, vol. 22, no. 2, pp. 387–408, 2018.

[181] Y. Shi *et al.*, "Particle swarm optimization: developments, applications and resources," in *Proceedings of the 2001 congress on evolutionary computation (IEEE Cat. No. 01TH8546)*, vol. 1, pp. 81–86, IEEE, 2001.

[182] Y.-H. Liu, S.-C. Huang, J.-W. Huang, and W.-C. Liang, "A particle swarm optimization-based maximum power point tracking algorithm for pv systems operating under partially shaded conditions," *IEEE Transactions on Energy Conversion*, vol. 27, no. 4, pp. 1027–1035, 2012.

[183] K. Ishaque, Z. Salam, M. Amjad, and S. Mekhilef, "An improved particle swarm optimization (PSO)–based mppt for pv with reduced steady-state oscillation," *IEEE Transactions on Power Electronics*, vol. 27, no. 8, pp. 3627–3638, 2012.

[184] H. Li, D. Yang, W. Su, J. Lü, and X. Yu, "An overall distribution particle swarm optimization mppt algorithm for photovoltaic system under

partial shading," *IEEE Transactions on Industrial Electronics*, vol. 66, no. 1, pp. 265–275, 2018.

[185] L. Xu, R. Cheng, Z. Xia, and Z. Shen, "Improved particle swarm optimization (PSO)-based mppt method for pv string under partially shading and uniform irradiance condition," in *2020 Asia Energy and Electrical Engineering Symposium (AEEES)*, pp. 771–775, IEEE, 2020.

[186] D. Diaz Martinez, R. Trujillo Codorniu, R. Giral, and L. Vazquez Seisdedos, "Evaluation of particle swarm optimization techniques applied to maximum power point tracking in photovoltaic systems," *International Journal of Circuit Theory and Applications*, vol. 49, no. 7, pp. 1849–1867, 2021.

[187] P. Verma, A. Alam, A. Sarwar, M. Tariq, H. Vahedi, D. Gupta, S. Ahmad, and A. Shah Noor Mohamed, "Meta-heuristic optimization techniques used for maximum power point tracking in solar pv system," *Electronics*, vol. 10, no. 19, p. 2419, 2021.

[188] LEORY-SOMER. IMfinity® 3-phase induction motors - IE2 - powered by the drive with IP55 Aluminum frame.

[189] Danfoss. VACON® NXP Air Cooled Motor Drive.

[190] SanRex. Three-phase Power Diode Module DF75LB80.

[191] KEMET. PEH200, Aluminum Electrolytic, 2,200 uF, 20%, 450 VDC.

[192] Fuji Electric. 7MBP100VDA120-50, Three-phase IGBT Power Module.

[193] VISHAY. MKP386M Snubber, Metallized Polypropylene Film Capacitor Radial Snubber Type.

[194] AVAGO. HFBR-2522Z, Versatile Fiber Optic Connection.

[195] A. Jöckel, *Aktive Schwingungsdämpfung im Antriebsstrang von Triebfahrzeugen auf der Grundlage von Systemmodellierung und Betriebsmessungen*. Shaker, 1999.

[196] F. Trimpe, S. Lück, R. Naumann, and C. Salander, "Simulation of torsional vibration of driven railway wheelsets respecting the drive control response on the vibration excitation in the wheel-rail contact point," *Vibration*, vol. 4, no. 1, pp. 30–48, 2021.

[197] P. Pichlik and J. Bauer, "Adhesion characteristic slope estimation for wheel slip control purpose based on ukf," *IEEE Transactions on Vehicular Technology*, vol. 70, no. 5, pp. 4303–4311, 2021.

[198] R. Chattopadhyay, A. De, and S. Bhattacharya, "Comparison of PR controller and damped pr controller for grid current control of LCL filter based grid-tied inverter under frequency variation and grid distortion," in *2014 IEEE Energy Conversion Congress and Exposition (ECCE)*, pp. 3634–3641, Ieee, 2014.

[199] F. Briz, J. Cancelas, and A. Diez, "Speed measurement using rotary encoders for high performance ac drives," in *Proceedings of IECON'94-20th Annual Conference of IEEE Industrial Electronics*, vol. 1, pp. 538–542, IEEE, 1994.

[200] Y. Li, F. Gu, G. Harris, A. Ball, N. Bennett, and K. Travis, "The measurement of instantaneous angular speed," *Mechanical Systems and Signal Processing*, vol. 19, no. 4, pp. 786–805, 2005.

[201] Lenord + Bauer.Speed Sensors & Rotary Pulse Encoders: Rail Speed Sensor Gel 2477. Available at `https://www.sensorprod.com/lenord/speed-sensor-gel-2477.php`, accessed 14-February-2022.

[202] J. Böcker and O. Buchholz, "Can oversampling improve the dynamics of PWM controls?," in *2013 IEEE International Conference on Industrial Technology (ICIT)*, pp. 1818–1824, IEEE, 2013.

[203] M.-W. Naouar, E. Monmasson, A. A. Naassani, I. Slama-Belkhodja, and N. Patin, "FPGA-based current controllers for ac machine drives-a review," *IEEE Transactions on Industrial Electronics*, vol. 54, no. 4, pp. 1907–1925, 2007.

[204] E. Monmasson, L. Idkhajine, and M. W. Naouar, "FPGA-based controllers," *IEEE Industrial Electronics Magazine*, vol. 5, no. 1, pp. 14–26, 2011.